Dynamics of hydrofracturing and microseismic signals in porous versus tight rocks

Janis Aleksans
BSc

Submitted in the fulfilment of the requirements for the degree of Doctor of Philosophy

School of Geographical and Earth Sciences
College of Science and Engineering
University of Glasgow

October 2018

Abstract

This work discusses the dynamic development of hydraulic fractures, their evolution and the resulting seismicity during fluid injection in a coupled numerical model. The model describes coupling between a solid that can fracture dynamically and a compressible fluid that can push back at the rock and open fractures. With a series of numerical simulations it is shown how the fracture pattern and seismicity change depending on changes in depth, injection rate, Young's modulus and breaking strength. Simulations indicate that the Young's modulus has the largest influence on the fracture dynamics and also the related seismicity. Simulations of rocks with a Young's modulus smaller than 10 GPa show dominant mode I failure and a growth of fracture aperture with a decrease in Young's modulus. Simulations of rocks with a Young's modulus higher than 10 GPa show fractures with a constant aperture and fracture growth that is mainly governed by a growth in crack length and an increasing amount of mode II failure. This change in fracture geometry evolution has an effect on the observed seismicity. Rocks with a Young's modulus of 10 GPa have the smallest moment magnitude while both decrease and increase of Young's modulus value contribute to a growth of the seismic moment magnitude. The signal is further altered by non-linear change in dip and tensile angle depending on the Young's modulus value. It is proposed that two distinct failure regimes are observed in the simulations. Below 10 GPa a fracture propagates through growth in aperture, this causes the fracture tip to be under constant extension. For rocks above 10 GPa, the aperture is small and the fracture is under compression. In this case fracture growth is driven by stress intensification at the crack tip, which causes fracture opening to have greater proportion of mode II compared to mode I. To suppliment the observations made from numerical simulations, laboratory experiments with air injection into vertically orientated Hele-Shaw cell were carried out. Strain analysis of the recorded experiments showed stress regimes that are very similar to the ones observed during numerical simulations with soft rocks. In both cases negative strain fields could be observed in front of the fracture tip. This indicates that fracture propagation for soft materials is driven by tensile failure and walls being pushed apart. Further analysis on fracture propagation mechanisms and solid media response were carried out.

These results are applicable to the prediction of fracture dynamics and seismicity during fluid injection, especially since we see a transition from one failure regime to another at around 10 GPa, a Young's modulus that lies in the middle of possible values for natural shale rocks.

Table of Contents

List of Tables

List of Figures

Acknowledgement

“Not All Who Wander Are Lost”

A line of J. R. R. Tolkien’s poem full meaning of which is revealed to me at the end of this journey. And what a journey it was. Full of ups and downs. Moments of despair, when nothing seemed to work, and moments of eureka when finally all the jigsaw puzzle pieces fell into place. This thesis was an emotional and physical challenge, a whole new experience of the academic world. There were moments in the last four years when I was wondering, what did I get myself into. But I was lucky enough to have people around me through thick and thin to whom I am most grateful.

First and foremost, my greatest gratitude goes to my PhD supervisor Dr Daniel Koehn. For believing in a freshly graduated BSc student and giving me an opportunity to prove myself by offering me this PhD position. For having enormous amounts of patience and devoting all that time guiding me through numerous challenges of this PhD. For never letting myself loose motivation and drive to achieve this ultimate goal. It was my greatest honour being able to work with him.

I would like to further thank Professor Renaud Toussaint for his sincere effort in contributing to me succeeding in this work. Without his help it would not be possible to conduct Hele-Shaw cell experiments. I am sincerely grateful to him for helping organise my stay at the University of Strasbourg and making me feel so welcome there. I would like to further thank Dr Guillaume Daniel for providing me with constant support in regards of the seismological processes’ theory and being able to meet with me on so many occasions.

This research was done as a part of NERC CDT in Oil and Gas and I would like to extend my gratitude for making this research possible. I would like to thank Dr John Underhill for being the driving force behind the training academy, which I was lucky enough to be the part of, as well as to Anna Clark, who made close to miraculous effort in organising so many training courses in so many places. Special thanks goes to all my fellow PhD students on the course who made all 100 days of the training an unforgettable, once in a life time experience, which I am sure I will be nostalgic about.

I would like to thank all the amazing people I met here at the University of Glasgow, both among the staff and the students, who made this a wonderful

experience. I would like to offer a special gratitude to my dear friends Arman and Ena, who had an enormous amount of patience and willpower to proofread my thesis.

I cannot thank enough my parents for upbringing me the way I am today. Our family has faced many challenges, but despite that, they always prioritized my higher education above everything else in the world. I would not be standing where I am today without my mom and dad.

Last but not least, I could have not accomplished this research without the support from my wife Valeriya. She has seen me in my darkest hour but not for a moment she had lost faith in me. In the moments when there seemed to be no light at the end of the tunnel, she reminded me what truly matters in this life, which kept me moving forward. I am extremely lucky to have you in my life.

Author's Declaration

I hereby declare and confirm that this thesis is my own work and materials from other sources have been properly and fully acknowledged. The thesis represents my interpretation of results and my own views. I also confirm that the presented material has not been submitted to any other degrees at the University of Glasgow or any other institutions.

Janis Aleksans

October 2018, Glasgow

1. Introduction

1.1. A brief history of Hydrofracturing

1.1.1. The discovery of induced artificial fracturing.

The early roots of hydraulic fracturing can be traced back to 1862. During the battle of Fredericksburg of the American Civil War, Colonel Edward A.L. Roberts keenly observed what could be accomplished when firing explosive artillery into a narrow canal that obstructed the battlefield. He described it as "superincumbent fluid tamping" (Borowski, 2012).

Edward Roberts was able to receive his first of many patents on the April 26th, 1865, for an "Improvement" in exploding torpedoes in artesian wells. In November of 1866, Edwards Roberts was awarded patent number 59 936 known as the "Exploding Torpedo" (Fig 1.1) (Teska, 2011).

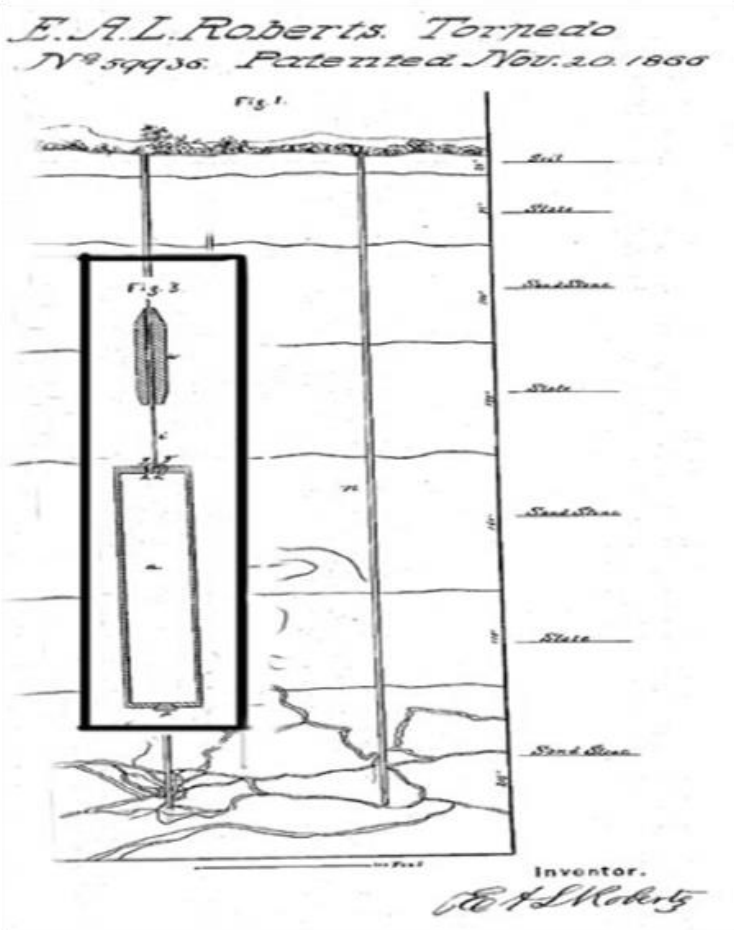

Figure 1.1. Sketch of "exploding torpedo" submitted to the patent office alongside the patent by Edward Roberts in 1864 (Borowski, 2012).

The method of extraction was implemented by putting a torpedo into an iron case together with 15-20 pounds of powder. The case was then lowered into the oil well and placed in a spot closest to the oil reserves. Once placed, the borehole would be flooded with water to dampen the explosion, preventing any debris blowing back up the hole and amplifying its effects. The torpedo would then be detonated via a wire connecting the top of the shell with the surface.

As a result of implementing this invention into practice, oil production was increased up to 1200 percent in some wells. The efficiency of this method created a massive demand for its implementation, and thus led to the foundation of Roberts Petroleum Torpedo Company, which would charge $100-$200 per torpedo, plus a royalty of 1/15 of the profits generated from the product. Their legacy lives on with the Otto Cupler Torpedo Company, which still shoots wells with modern explosives and rigorous safety procedures (Borowski, 2012; Teska, 2011).

1.1.2 The rise of commercial fracturing.

The method developed during the American Civil War was widely used for more than half a century before undergoing any form of innovation in the 1930s, when drillers used acid as a non-explosive alternative to nitroglycerine. The wells fractured in this manner proved to be more resistant to having fractures closing down, and thus improving the productivity (Warner and Sharipo, 2013).

It then took another decade until Floyd Farris of Stanolind Oil began a study on the relationship between oil and gas production output, and the amount of pressurised treatment being used on each well. He proposed that fracturing a rock formation through hydraulic pressure might increase well productivity (Teska, 2011).

The first officially recorded experiment of hydraulic fracturing was conducted at Hugoton gas field, Kansas, in 1947. About 1000 gallons of gasoline gel mixed with sand were injected into a gas producing limestone formation followed by injection of the gel breaker. While the experiment failed to produce a significant increase in production, it marked the start of hydraulic fracturing (Heinberg, 2013).

This was followed by an experiment conducted by Halliburton in 1949, Oklahoma. This proved to be the first economically viable hydrofracturing operation. The Halliburton Oil Well Cementing Company obtained an exclusive licence (subsequently extended to other qualified companies) for the hydraulic fracturing

process. In the first year of operations, 332 oil wells were treated with crude oil or a combination of crude oil, gasoline and sand. The wells on average increased production by 75%. From 1953, water was also used as a fracturing fluid, and various additives were tried to improve its performance. By 1968, hydrofracturing was being used in oil and gas wells across the United States, but its application was limited to the less difficult geological formations (Heinberg, 2013).
In the United Kingdom, the first hydraulic fracturing operation was carried out in the North Sea in 1965 shortly after the discovery of the West Sole field (Morton, 2013). In 1970 industry started to use intermediate and high strength proppants leading to hydrofracturing becoming a common practice in the North Sea. In 1980 the first hydraulic operation was carried out from the ship in the British Southern North Sea (Detlef, 1989).

1.1.3 Modern day hydrofracturing.

Shale rock presented a particular challenge because of the difficulty in accessing the hydrocarbons in these tight formations. In the mid-1970s, the US Department of Energy (DOE) and the Gas Research Institute (GRI), in partnership with private operators, began developing techniques to produce natural gas from shale. The oil shale boom began in the 1990s with the innovative approach of George P. Mitchell who combined hydrofracturing with horizontal drilling, a new technology developed in the late 1980s (Morton, 2013). This allowed to significantly reduce the drilling cost as the same horizontal drilling well extended the range of fracturing sideways along a rock formation rather than contacting it vertically. The technology initially developed in the Barnett Shale formation, after its initial success, rapidly spread to shale exploration in Texas, Oklahoma, Arkansas, Louisiana, Pennsylvania, West Virginia and the Rockies (Morton, 2013).
Although hydrofracturing is mainly known due to its role in hydrocarbon extraction, it is only one of the many modern practical applications where it is considered an invaluable tool:

- Groundwater well stimulation;
- Enhancing electricity generation via geothermal systems;
- Increasing injection rates for geological sequestration of CO2 (more commonly known as CCS or Carbon Capture and Storage);
- Soil remediation and disposal of waste by deep rock injection;

- Measuring stress in the Earth for academic and geotechnical purposes.

These are just but a few of the examples where hydrofracturing is nowadays commonly applied (Aamodt and Kuriyagawa, 1981; Frank and Barkley, 1995; Banks et al., 1996; Brown, 2003;2007; Bell, 2004; Miller, 2005; DiPippo, 2012).

1.2. Rock Deformation

1.2.1. Stress and Strain

Rocks are a subject to constant influence by forces that might lead to deformation. This can result in significant changes in the rocks' physical properties and mechanical behavior, and thus it is important to understand the driving processes behind deformation.

Deformation is an umbrella term applied to several processes behind the transformation of a rock body. It consists of a combination of four constituent deformation elements: strain (distortion), rotation, translation and volume change (van der Pluijm and Marshak, 2004). The rock becomes deformed due to the force applied to the surface of the rock. The force applied per unit of area at any given point at the surface is referred to as "stress" (σ). It is measured in SI units as Newtons per square meter (N/m^2) or Pascals (Pa).

Stress field is defined as a distribution of internal tractions that balance a given set of external tractions and body forces (Bower, 2009). External tractions are expressed as bound vectors, meaning they cannot translate to another location without losing the same properties (Peters and Ranson, 1982). Therefore traction vector cannot be described unless both the force and the surface upon which force acts are fully specified. From here the traction vector T can be described as

$$T = \lim_{\Delta s \to 0} \frac{\Delta F}{\Delta s} \tag{1.1}$$

where ΔF denotes the infinitesimal resultant force acting on the surface element Δs (Fig 1.2).

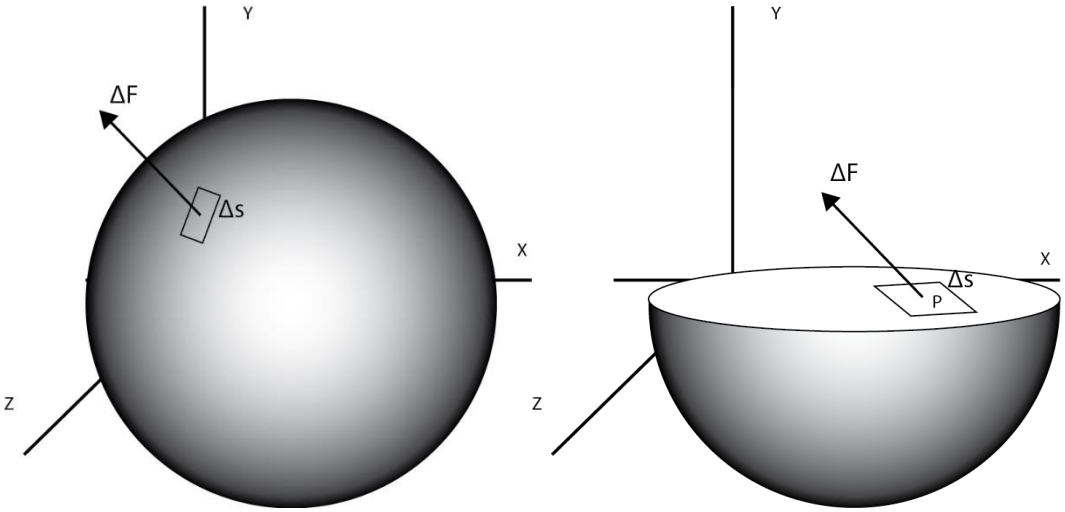

Figure 1.2. Left: arbitrary body with an external traction force ΔF acting on the surface element Δs. Right: Internal traction force acting on a point *P* within the solid body expressed as resultant force ΔF acting on the surface element Δs while $\Delta s \rightarrow 0$.

Counterpart to the external traction is internal traction or stress. It can be expressed using the same equation as for the external traction for any point *P* within the solid body (Fig 1.2).

One therefore can define stress as internal tractions that act upon a point within an internal plane. Stress then can be decomposed into three components: normal stress (σ_n), which is perpendicular to the stressed surface and two components tangential to the surface, which represent shear stress (σ_s). Aligning set of internal planes with the Cartesian coordinates allows to describe stress state at an internal point *P* relative to the *x, y* and *z* coordinate directions. An infinitesimal cube with three stress components at each side can be used to represent the stress state at point *P* (Fig 1.3).

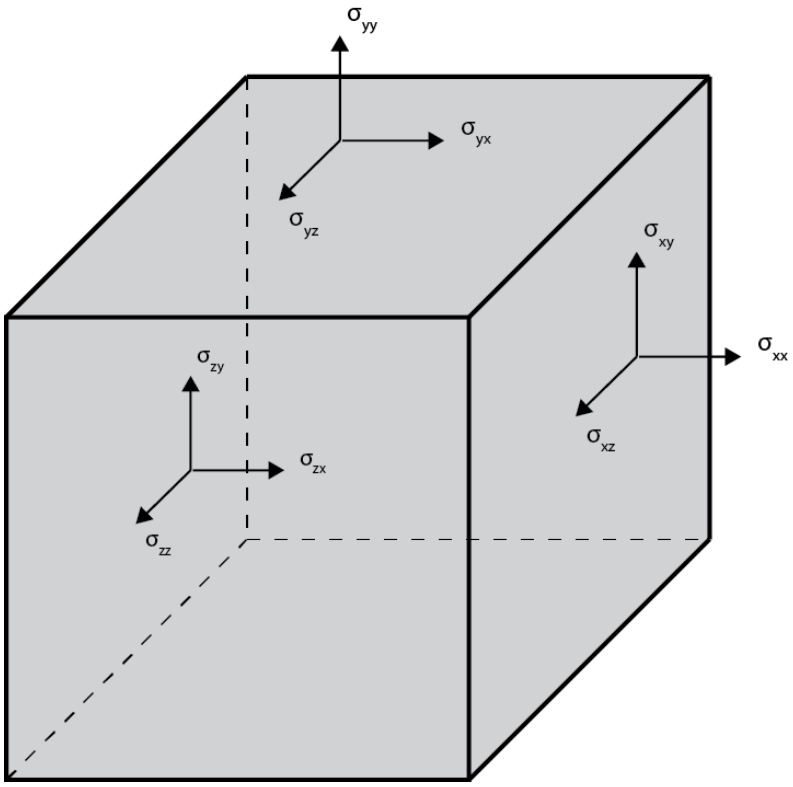

Figure 1.3. An infinitesimal cube with three stress components at each side representing the stress state at point *P.*

The nine stress components can be written in the form of a matrix such as

$$\begin{vmatrix} \sigma_{xx} & \sigma_{xy} & \sigma_{xz} \\ \sigma_{yx} & \sigma_{yy} & \sigma_{yz} \\ \sigma_{zx} & \sigma_{zy} & \sigma_{zz} \end{vmatrix} \quad (1.2)$$

where the diagonal component are the normal stresses along the three Cartesian coordinate axis. As the system is in static equilibrium (no net moment), opposing shear stresses are identical ($\sigma_{xy} = \sigma_{yx};\ \sigma_{xz} = \sigma_{zx};\ \sigma_{yz} = \sigma_{zy}$) making the matrix symmetrical.

Visually stress states can be represented by the stress ellipsoid where the axes represent the normal stresses $\sigma_1, \sigma_2, \sigma_3$, where $\sigma_1 > \sigma_2 > \sigma_3$ (Fig. 1.4)

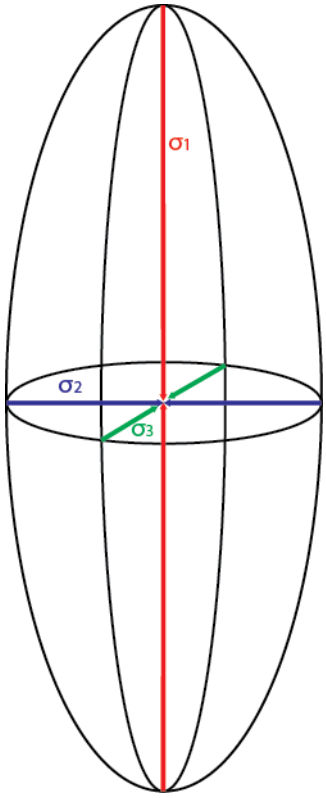

Figure 1.4. Stress ellipsoid where three principal stresses are represented on the three main axis where $\sigma_1 > \sigma_2 > \sigma_3$.

Materials such as fluids in most cases have no shear resistance (some fluids have very low shear resistance) (Bird, 2004). Force applied perpendicularly to the unit of area for fluid is regarded to as pressure (P) (Dean and Dalrymple, 1991; Fay, 1994). Pressure is expressed in the same SI units as stress but is a scalar quantity rather than a tensor meaning its projected magnitude is uniform in all directions. In this case the stress can be written in a form of matrix as:

$$\begin{vmatrix} \sigma_{xx} & 0 & 0 \\ 0 & \sigma_{yy} & 0 \\ 0 & 0 & \sigma_{zz} \end{vmatrix} \tag{1.3}$$

where $\sigma_{xx} = \sigma_{yy} = \sigma_{zz}$.

A relevant example to this is a hydrostatic pressure, which by definition is pressure generated by a static fluid column upon the unit of area of the pore surface within the rock. It is expressed as a function of gravitational acceleration, the density of the fluid and height of the fluid column ($P_f = g\rho h$). If we assume that rocks have very low to no shear resistance, they can also be subject to pressure. In that case, stress becomes independent of the direction and forms an isotropic stress

condition ($\sigma_1 = \sigma_2 = \sigma_3$). The stress ellipsoid would be represented by a sphere. Stress then is controlled solely by the depth at which the rock is located, the gravitational acceleration constant and the rock's density and is referred to as lithospheric stress.

There is a large number of mechanisms and factors present in the nature that can trigger rock deformation (Patterson and Wong, 2005). Some of the processes that act upon the rock are: tectonic forces (extensional and compressional), gravity-driven compaction, expansion due to increased temperature and anthropologically induced stresses (e.g., drilling). The magnitude of deformation is not governed just by stress and strain, which is induced by external factors, but also by physical and material properties of the rock itself, such as rock fabric, grain size and rigidity. For example, an increase in temperature decreases the shear and tensile strength of the rock (Sibson, 1977), meaning that fracturing will occur at lower differential stresses. Pre-existing fabric in the rock will also create anisotropy which can act as planes of weakness and will be reactivated as preferred direction of fracture propagation (White et al., 1986). Grain size variations cause a similar effect (Eberhardt et al., 1999). Grain boundaries act as potential planes of weakness. Increase in the size of boundaries is proportional to increase in the grain size, meaning that isotropy and uniformity of the rock decreases. Grains act as physical obstacle for fluid flow; decrease in grain grain size leads to increase in the number of grains and thus in the surface volume. Surface creates friction which fluid has to overcome as it migrates.

The amount of the deformation is measured through strain. It represents the displacement of the particles within the body relative to their original configuration (Patterson and Wong, 2005). Strain is dimensionless and is typically expressed as a percentage. It is also a tensor quantity and can be decomposed into normal and shear strain. Longitudinal strains can be expressed along axis (n) parallel to the force applied as:

$$\varepsilon_n = \frac{amount\ of\ extension}{original\ length\ along\ axis\ n} = \frac{\partial u_n}{\partial n} \tag{1.4}$$

Lateral strain can be calculated using same equation (1.4) measuring change in length perpendicular to the direction of force applied. The shear strain γ_{xy} is then defined as change in the angle A (Fig 1.5).

$$\gamma_{xy} = \alpha + \beta = \tan\left(\frac{\frac{\partial u_y}{\partial x}}{1 + \frac{\partial u_x}{\partial x}}\right) + \tan\left(\frac{\frac{\partial u_x}{\partial y}}{1 + \frac{\partial u_y}{\partial y}}\right) \quad (1.5)$$

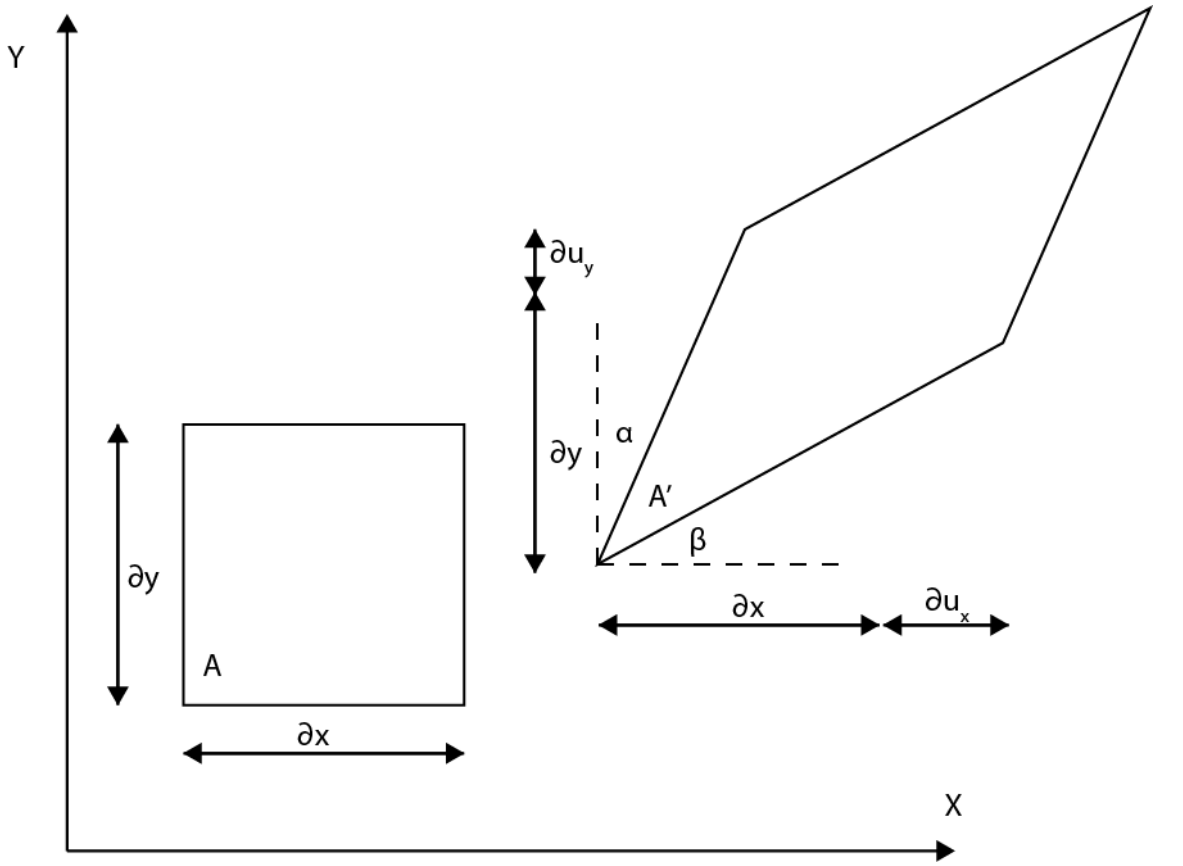

Figure 1.5. Rectangular shaped body before (left) and after (right) deformation. The shear strain is calculated as a change in *A* which is derived from changing dimensions of unit along *x* and *y* axis.

For small rotations where α and β are $\ll 1$ shear strain can be written as

$$\gamma_{xy} = \alpha + \beta = \frac{\partial u_y}{\partial x} + \frac{\partial u_x}{\partial y} \quad (1.6)$$

Depending on the α and β values special cases of shear strain can be identified:

- $\alpha = \beta$: pure shear;
- $\alpha = 0$ or $\beta = 0$: simple shear;

The infinitesimal strain tensor can then be written using symmetrical matrix as:

$$\varepsilon = \begin{bmatrix} \varepsilon_x & \frac{1}{2}\gamma_{xy} & \frac{1}{2}\gamma_{xz} \\ \frac{1}{2}\gamma_{yx} & \varepsilon_y & \frac{1}{2}\gamma_{yz} \\ \frac{1}{2}\gamma_{zy} & \frac{1}{2}\gamma_{zy} & \varepsilon_z \end{bmatrix}$$

(1.7)

Deformation can be expressed as a function of time as strain rate. For the longitudinal and lateral strain components strain rate is described by the change in length of the unit Δu_n along the axis *n* over the time $t\left(\varepsilon_n(t) = \frac{\Delta u_n}{t}\right)$. Shear strain rate can be calculated in a similar manner where relative change in γ_{ij} is measured as a function of time (Patterson and Wong, 2005). If the strain rate is high, it means more deformation will be applied to the rock over the same amount of time. The rock then might not be able to accumulate the strain at a sufficient rate and will fracture faster.

The parameter that relates strain to the stress applied is known as Young's modulus (E) or stiffness of the rock. Young's modulus by definition characterizes elasticity of the material and is expressed as the amount of force required to apply to a unit of area to compact it by the amount of strain achieved. The units in the SI system are N/m^2 or Pa.

$$E = \frac{\sigma}{\varepsilon}$$

(1.8)

Thus it is proportional to the applied stress and inversely proportional to the elongation. This relation is called the Hooke's law, and it is used to describe the linear elasticity of the solid materials

$$F \propto x$$

(1.9)

where F denotes force applied being proportional to achieved x amount of elongation (Tullis and Tullis, 1986).

When deformation affects material dimensions along one axis, the dimensions along other axis will change as well. If compressed, the material can compact by molecular compaction (Gercek, 2007). However, it can do it only to a certain extent after which material will be displaced along the axis of least stress that is perpendicular to the axis of compaction. The phenomenon in which a material tends to expand in directions perpendicular to the direction of compression is

called Poisson's Effect. Poisson's ratio is be the ratio of relative contraction to relative expansion. It is calculated as $\nu = -\varepsilon_{trans}/\varepsilon_{axial}$ where ε_{trans} is a transverse strain with positive values for compaction and ε_{axial} is an axial strain with negative values for compaction (Greaves et al., 2011). Ideally incompressible material would exhibit Poisson's ratio of 0.5, while material, which shows no expansion along one axis while being compressed along other axis, would have it of 0. Most materials have a Poisson's ratio value between 0.3 and 0.5 (Gercek, 2007; Greaves et al., 2011).

Depending on the type of the rock, Young's modulus and Poisson's ratio can vary greatly. Elastic parameters of a material are obtained from seismic wave propagation speeds that depend upon the density, and thus, molecular structure (Gercek, 2007). Igneous and metamorphic rocks tend to have higher density and thus higher elastic constants, due to crystalline rather than granular structure (Lake, 2007). However, even in sedimentary rocks such as shales, sandstones and limestones, Young's modulus can vary on a scale up to 40GPa (Lake, 2007). Elastic parameters in the sedimentary rocks vary due to variations in grain size and undergone diagenetic processes. Rocks with higher Young's modulus require larger stress to be applied for it to achieve same level of strain compared to rocks with lower E. Poisson's ratio for sandstones can vary from 0.05 to 0.4 (Gercek, 2007). This means that different amount of distortion can be achieved by applying the same amount of stress even to the same type of rock.

In addition to the elastic deformation, where deformation is reversed and material returns to the original state once the applied stress is removed, there is also permanent deformation. If the stress applied exceeds a critical value (yield point), the deformation regime changes from elastic to plastic, meaning that the strain applied is irreversible and the rock deforms (Beer et al, 2001; Avallone, Baumeister, 2017). During such deformation strain applied is redistributed across the material. Such deformation is known as "ductile". Examples of ductile deformation are folds and shear zones. The last stage is achieved if the stress applied exceeds either critical tensile strength or shear strength of the rock. In this case, the strain becomes localized, and then stress is relieved through deformation mode known as "brittle". Examples of brittle deformation are cracks, fractures and faults.

For the fluids viscosity (μ) term is used to measure its resistance towards shearing relative to the stress applied as:

$$\mu = \tau/\dot{\varepsilon} \tag{1.10}$$

where τ is the shearing component of the stress, and $\dot{\varepsilon}$ is the shear strain rate. Rearranging this equation as

$$\dot{\varepsilon} = \tau/\mu \tag{1.11}$$

shows that the material with a higher viscosity is going to have lower strain rate than a material with a lower viscosity given the same stress applied (McBirney and Muras. 1984).

1.2.2. Brittle deformation and fracturing

The material undergoes brittle deformation when there is sudden local loss of cohesive strength. This does not necessarily mean that material will fail. In the case of poorly consolidated materials, deformation can consist of grain rotation and frictional sliding along the grain contacts. Such behaviour is typical of granular media, however, they are still solids. These cases are relatively rare and most materials behave as solids, which means that fractures will form. Fractures are described as areas of the material where there is a localised loss of cohesion and observable displacement (Anderson, 2005). They form when the internal and/or external force applied to a rock exceeds the material's critical tensile or shear strength (Inglis, 1913; Grifith, 1920, Irwin 1953, 1954). The length of the fracture is proportional to the surplus stress applied and reversely proportional to the strength of the rock. Depending on the scenario, fractures can form from micron scale (microcracks) up to kilometer scale (faults). They are usually classified depending on the relative displacement of the material on the opposing sides of the fracture. When the displacement of the opposing walls of the fracture is perpendicular in relation to the imaginary fracture plane, it is classified as a Mode I fracture (Fig. 1.6). In the opposite case scenario, where walls of the fracture move in opposing directions but parallel to the fracture plane, it is known as a Mode II fracture. Mode III fracture is a special case known as tearing or out of plane shearing. It incorporates an additional axis as walls move parallel to the plane of fracture but, in contrast to Mode II, walls move perpendicularly rather

than parallel to the axis of fracture propagation. Even as pure Mode II fractures are widely common, pure Mode I fractures are quite rare. In the geological setting most fractures that exhibit Mode I opening behaviour have some parallel movement vector component to them and are perceived rather as a mixture of Mode I and Mode II regimes (Ou, 2008).

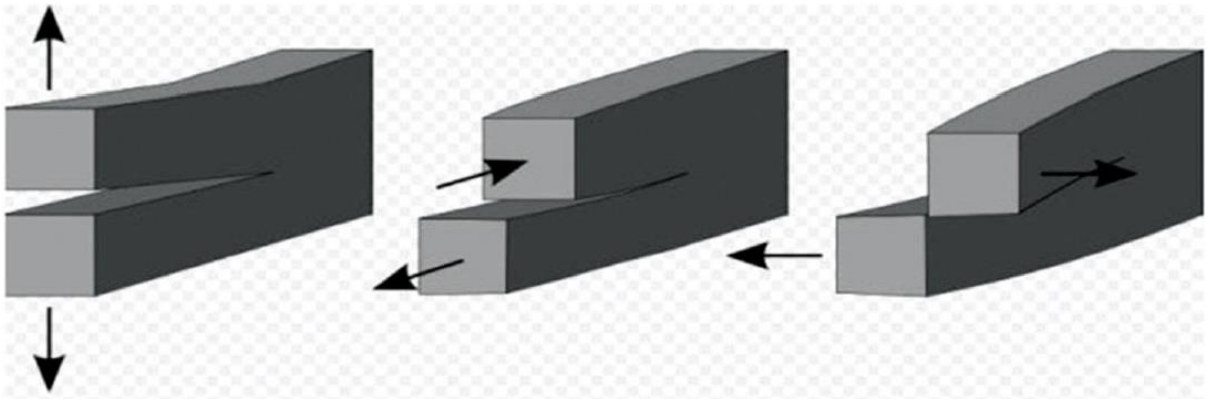

Figure 1.6. Three modes of fracturing. From left to right: a) Mode I fracture where fracture walls are displaced perpendicularly the imaginary fracture plane, b) Mode II fracture where displacement of the walls are parallel to the imaginary fracture plane, c) Mode III fracture where displacement of the walls is parallel to the fracture plane, but perpendicular to the fracture propagation direction vector (Figure after Eaton and Forouhideh, 2010).

A textbook visual representation tool used to analyse the mode of fracturing, as well as stress states and fracture plane orientation, is the Mohr circle (Fig.1.7). It is used in combination with Mohr-Coulomb-Griffith failure criterion and provides information on how failure planes are oriented and displaced depending on the principal stress orientation. When plotting the Mohr circle, the x-axis represents normal stress (σ_n) while the y-axis represents shear stress (σ_s). The circle can be plotted if largest (σ_1) and the smallest (σ_3) stresses are known and represented on the x-axis. The centre of the circle is then in the middle of these two stresses ($(\sigma_1 + \sigma_3)/2$). The diameter of the circle is the differential stress ($\Delta\sigma = \sigma_1 - \sigma_3$) and each point of the circle represents a potential plane on which shear and normal stress act. The angle between σ_1 and the normal to the plane is represented by a. This angle is equal to the angle between σ_3 and the plane. The stress state of the plane can be plotted by measuring $2a$ from σ_1 and plotting the point on the Mohr circle. From this point, both normal stress (σ_n) and shear stress (σ_s) can be read from the axis. The plane has a conjugate pair, which is plotted then on the opposite side of the circle and has a negative σ_s sign as its force vector is pointing in the opposite direction (Fig 1.7).

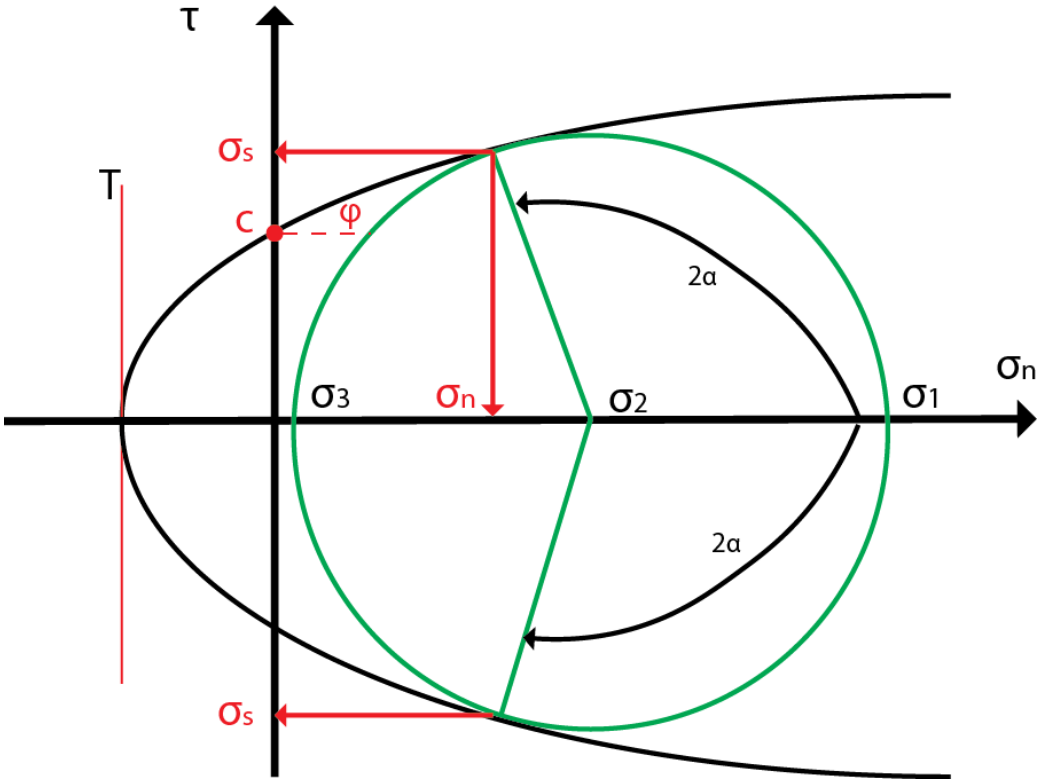

Figure 1.7. Mohr circle, which represents shear failure. The stress state of the plane can be plotted by measuring 2*α* from σ_1. Normal stress (σ_n) and shear stress (σ_s) can be read from the corresponding axis. The plane has a conjugate pair, which is plotted then on the opposite side of the circle and has a negative σ_s sign. The failure plain crosses T which is the tensile strength of the rock and is plotted on the negative side of the x axis. Failure plane crosses y axis at point which equals the cohesion value *c* and is continued to the right of the y axis at *φ*, where *φ* is the friction angle of the material.

Brittle failure of rocks is governed by their mechanical properties. Anisotropies, such as preexisting fractures, cleavages and bedding planes provide potential planes of weakness with already lowered cohesive strength (Anderson, 2005). Another factor is the physical properties of the rock itself such as Poisson's ratio and Young's modulus. Both of these parameters then further determine how much deformation the rock can take through accommodating stress elastically. The value that represents the maximum amount of stress that rock can withstand without failing is called breaking strength (Bell, 2003). The critical breaking strength can then be further subdivided into two components. Firstly, the critical tensile strength governs how much extensional stress the rock can tolerate. Secondly, a critical shear strength of a rock defines the amount of stress that the rock can withstand when applied parallel to the fracture plane. The tensile strength of the rock defines where the tensile failure curve will cross the *x* axis on the Mohr circle diagram. It will always be located on the negative value side. The cohesive strength of the rock will define where the failure envelope will then

cross the y axis. The failure envelope will then increase towards the right hand side at an angle of φ, where φ is the friction angle of the rock. The combined breaking strength of the rock is measured as a combination of both components. If the Mohr circle touches the failure envelope on the right hand side of the y axis, this results in Mode II fractures. Mode I fractures are formed if the circle touches failure curve at the point of it intersecting x axis. If the circle touches curve anywhere on the left side of the y axis with any σ_s component present that yields to the creation of fractures which have both Mode I and Mode II elements to them.

1.2.3. Fluids present in the rock and their role in hydrofracturing

There is a constant presence of fluids in the Earth's crust due to various processes. Natural processes involve water being trapped in pore spaces during marine sedimentation that can be of meteoric origin (rainwater and meltwater drainage), expelled from magma in thermal regimes (White, 1957) or migrated upwards during dehydration reactions of hydrous minerals such as chlorite and clay minerals (Johns and Shimoyama, 1972; Aoyagi and Kazama, 1980). The amount of fluid in the rocks depends upon the physical properties of the rock itself as well as the sedimentation rate. Depending on the rock type there can be a great variation of grain size and sorting and thus porosity. Rock types such as sandstones tend to have a higher porosity compared to shales and non-sedimentary rocks. Porosity in sandstones can reach up to 45% (Todd, 1959; Keller and Frischknecht, 1966, Nimmo 2004), meaning more fluids can be retained. Grain size variation plays a significant role as a uniform grain size distribution creates larger porosity (Schmidt and Macdonald, 1979; Nimmo, 2004). Grain size itself plays a large role in governing permeability of the rock as well. Permeability (K) is a measure of the ability of a porous material to allow fluids to pass through it. Its relationship to porosity and grain size in an ideal, isotropic medium is represented by the Kozeny-Carman relation

$$K(\phi) = \frac{d^2(\phi)^3}{180(1-\phi)^2} \tag{1.12}$$

where ϕ is porosity, *d* is the particle diameter and 1/180 is an empirical constant for packing of spheres (Carman, 1939). Smaller grain size results in larger surface

to volume ratio. Surfaces are no-slip boundaries which increase the friction of the fluid flow thus making it harder for the fluid to escape. Another factor that governs the amount of fluids present in the rock is temporal. Slow sedimentation rate means that there is enough time for the fluid to migrate, as fast sedimentation rates, in contrast, mean that the fluid might get trapped. In this case, it gets expelled later during the stages of further sediment compaction and lithification. This is one of the causes for naturally occurring hydrofracturing. Hydrofractures are fluid driven fractures.

Fluid, like any other material in the crust, being subject to numerous tectonic, sedimentary, volcanic and hydrothermal processes, can produce pressure on the surrounding rock. In the simplest case, where all the pores in the material are interconnected with each other and with the surface, the fluid exerts hydrostatic pressure, e.g., pressure caused by its gravitational force pull of the vertical column of water. Depending on the geological heterogeneity of the basin, hydrostatic fluid pressure can be present up to 4000m in depth (Mann and Mackenzie, 1990). Processes that cause the fluid pressure to increase can be in most cases attributed to one of the three categories: increasing compressive stress, changes in the volume of the fluid or porosity withholding the fluid and dynamic fluid migration (Barker, 1972; Green and Wang, 1986; Tobin and Saffer, 2009). Tectonic processes such as compression or sedimentation (increase in overburden) cause for compressive stress to increase. This in turn causes grains within the rock to compact. If the fluid volume stays the same and there is decrease in the pore volume, it leads to relative increase in the pore pressure. The other factor which can influence fluid pressure is a change in the volume of the fluid. This can be caused by a number of naturally occurring mechanisms (thermal expansion of water, hydrocarbon generation, water expulsion due to mineral transformation (Bethke, 1985; Oliver, 1986). A fluid volume increase leads to a higher fluid pressure if the pore space volume stays the same and the fluid cannot escape. Lastly, dynamic fluid migration and geological heterogeneity can cause fluid pressure to increase in some areas while it decreases in other. This creates the possibility for the fluid pressure redistribution through high permeability channels such as fractures, faults or high permeability rock beds and lenses. This can also be influenced by low permeability anisotropies which can create a seal. This prevents fluid from migrating causing local fluid pressure

increase with a gradual decrease towards the upper boundary of the seal (Cobbold and Rodrigues, 2007). This is regarded as “overpressure”.

There are two groups of processes that cause for changes in the fluid pressure: a) tectonic and b) sedimentary. Deformation due to tectonic processes has the effect on the fluid pressure change as it causes fracturing (increase in permeability) (Cox, 2005), compression (decrease in pore volume) or folding (Fyfe et al., 1978). Sedimentation processes such as secondary cementation, depositional heterogeneities with higher permeability (river channels, submarine depositional channels) cause further change in fluid pressure. Burial due to sedimentation increases temperature which causes thermal expansion of fluids (change in fluid volume) as well as hydrocarbon generation and mineral transportation (Oliver, 1986).

It is important to notice that for the fluid pressure to increase, the drainage rate has to be significantly lower than the rate of fluid pressure increase. If one or more mechanisms cause for the pore/fluid volume ratio to change faster than the fluid can migrate to area where there is lower pore pressure it causes for the overpressure to form, which is commonly assumed to cause tensile fracturing (Fig 1.8) (Sachau et al., 2015). For overpressure to form there must be a limiting factor that prevents fluid from migrating. On a basin scale that can be a cap rock sealing structure, which limits lateral fluid migration (Osbourne and Swarbrick, 1997). On a local scale overpressure can form in a single low permeability unit. An example of that would be shale rock with low permeability during the formation of hydrocarbons. Hydrocarbons then act as a point source for the overpressure as their mobility is limited by the low permeability of the host rock (Bowker, 2007).

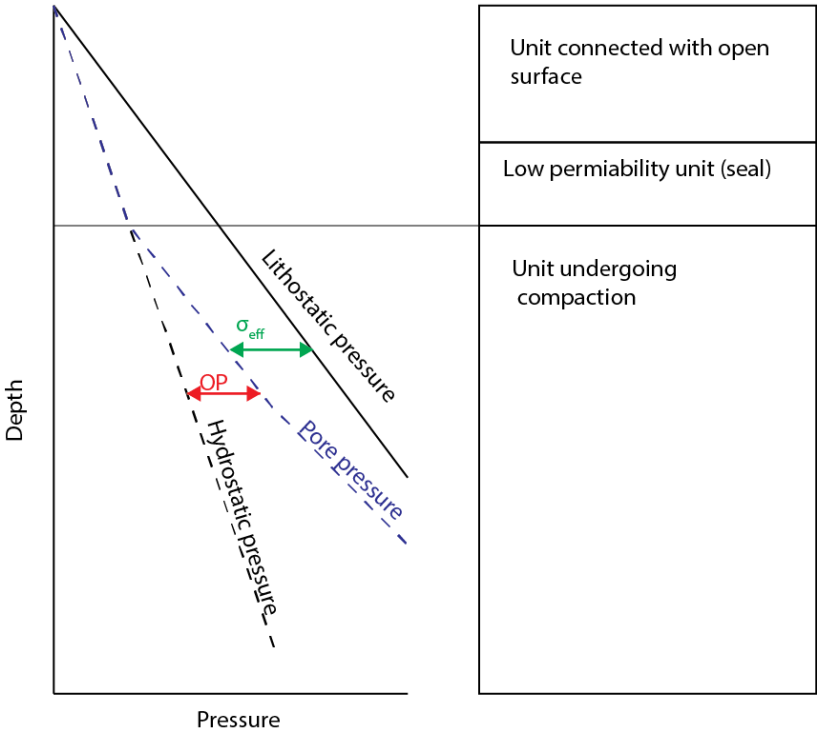

Figure 1.8. Representation of the pore pressure evolution in the scenario where there is a cap rock present and lateral fluid migration is limited. The unit below cap rock is assumed to be undergoing compaction, meaning decrease in the pore volume and increase in the pore pressure. Pore pressure follows hydrostatic fluid pressure gradient up to the top of the compacted unit. The difference between the hydrostatic pressure gradient and pore pressure is termed overpressure while difference between the lithostatic pressure gradient and fluid pressure is represented by effective stress σ_{eff}.

Hydraulic fracturing is the process of creating cracks within a rock volume by increasing the fluid pressure until the rock fractures (Hubbert and Willis, 1957; Nordgren, 1972; Valko and Ecomides, 1995). It can be both of natural and anthropological origin. It plays an important role in the geophysical, geomechanical and structural mechanics of the Earth's crust in a wide variety of geological settings (Fyfe et al., 1978) and has a growing interest in geotechnical and industrial applications (Baria et al., 1999; Urbancic et al., 1999; Warpinski et al., 1999). A hydrofracture develops if the fluid overpressure exceeds the sum of the least compressive stress and the tensile strength of the rock (Cobbold and Rodrigues, 2007). During industrial hydrofracturing, large quantities of fluid are pumped into a finite pore volume generating an overpressure and an outward push, which will lead to the brittle failure and the development of fractures (Pearson, 1981; Zoback and Harjes, 1997; Niebling et al., 2012). This is done with an aim to increase the local permeability of the rock. That results in an enhanced well productivity as hydrocarbon flow towards the wellbore increases. There also

have been in-situ experiments where hydrofracturing was applied to measure the stress state in the surrounding rock at the site (Hickman and Zoback, 1983). For these studies viscous mud is injected into the rock to generate fractures that would open in the direction of the least effective stress and thus provide the insight of the stress regime of the study area.

Natural hydrofracturing follows similar principles as the industrial hydrofracturing at sites with high local overpressure (Engelder and Lacazette, 1990; Rodrigues et al., 2009). In such a system fluid pressure and fluid pressure gradient is separated from the solid pressure, however both interact with each other creating a two-fold stress system. The fluid pressure system is acting in an opposing way to the stress applied to the rock, resulting in resistance to the compaction. This leads to the decrease of the stress state and is regarded to as effective stress (σ'_{ij}) (Terzaghi, 1923; Biot, 1941) and can be described by Terzaghi's law:

$$\sigma'_{ij} = \sigma_{ij} - P_f \delta_{ij} \tag{1.13}$$

where σ_{ij} is the stress tensor, P_f is fluid pressure and δ_{ij} is Kronecker delta with positive sign conversion.

Applying this transformation to the Mohr circle, shifts the circle to the left by the amount equal to the fluid pressure. If the fluid pressure exceeds the sum of the minimum principal stress (σ_3) and the tensile strength of the rock, the effective mean stress decreases as well and the Mohr circle shifts to the left until it reaches the failure envelope creating tensile (Mode I) fractures (Fig.1.9a). Once the rock fails, the stress is relieved and fluid pressure drops, as the fractures provide space for the fluid to escape (Sachau et al., 2015). If the fluid supply is not constant, this can lead to fracture closure if the fluid pressure drops below minimum principal stress. Typically, rocks are porous and thus the fluid overpressure can diffuse into the rock. According to Biot's poroelastic theory (Detournay and Cheng, 1993), this pressure diffusion influences the effective stress, since the fluid overpressure is reduced. Ghani et al. (2013) have shown that the feedback between the fluid and solid leads to an initial build-up of fluid overpressure and diffusion of fluid into the rock, an increase in pressure gradient and final fracturing (Fig. 1.9b). The fractures, in turn, enhance the permeability and allow the fluid overpressure to be reduced. The crack propagates upwards and as the fluid escapes, crack closes down again. The existing fractures may then even be pushed open by the developing fluid pressure gradients leading to a more dynamic system

of overpressure release (Sachau et al., 2015). It is important to understand the full scope of this dynamic feedback to analyse hydrofracture dynamics.

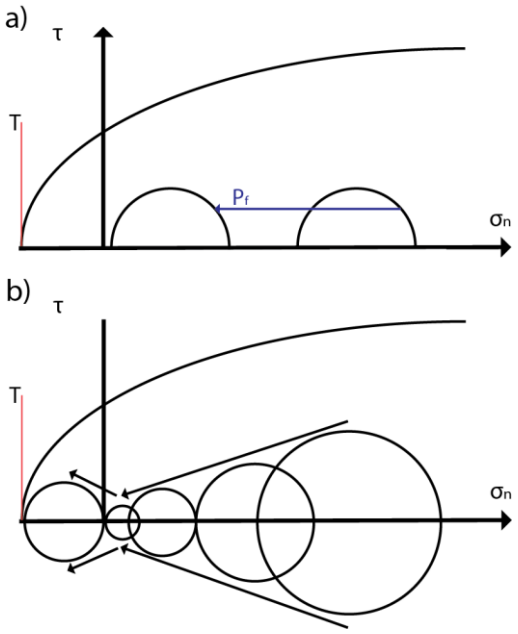

Figure 1.9. a) Standard Mohr circle diagram of effective stress showing how an increase in fluid pressure shifts the Mohr circle from its initial compressive stress state at the right hand side to the left into the tensile regime leading to failure; Note that the differential stress remains constant. b) Mohr circle diagram of effective stress in the model illustrating the anisotropy of stress changes when fluid overpressure or pressure gradients are taken into account. Locally the system will fluidize, the differential stress goes to zero or becomes very small leading to mainly mode I failure.

The classical textbook example of effective stress assumes that the stress state in the system does not alter and the effective differential stress stays constant. Cobbold and Rodrigues (2007), as well as Ghani et al. (2015), have shown that this is an oversimplification. Studies by Rozhko et al. (2007) and Rozhko (2010) show that the migrating fluid exerts a drag force on the solid particles within the solid framework termed “seepage forces”. Another parameter that has to be taken into account is a static fluid pressure gradient. The pore pressure is differentiated throughout the same reservoir depending on the depth. Fluid pressure gradient is then calculated as a difference in the fluid pressure over the distance given. Because there is inequality in the fluid pressure, the fluid pressure gradient force is exerted from the area of high fluid pressure in the direction of low fluid pressure. In this case, contrary to the seepage force, fluids do not necessarily migrate (Fay, 1994; Munson et al., 2013). Seepage forces and fluid pressure gradient forces have two main consequences. First, they lower the total stress and, second, they change the orientation of the stress tensors. The second effect is achieved due to σ_1, being independent value, while σ_3 becomes coupled to it

(Hillis, 2003). The result is anisotropic stress state changes, where σ_3 decreases at a slower rate than σ_1. Such condition is typical to a sedimentary basin to occur under a sealing cap rock. The percentage of difference between the change in σ_1 and σ_3 depends upon the Poisson's ratio (Hillis, 2003).

This effect means that the Mohr circle for the effective stress state as such is still moving towards the left-hand side into the regime of tensile failure, however, the circle is shrinking at the same time (Fig. 1.9b).

The important role that fluid pressure plays in the deformation process of the host rock makes it directly relevant to the studies associated with hydrocarbon reservoir modelling and management, geothermal resource development, CO_2 storage and nuclear waste underground management.

1.3. Induced seismicity.

Seismicity is a measure that describes the disturbances in the surrounding media caused by the earthquakes as well as earthquake occurrences and mechanisms (Richter and Gutenberg, 1941). The term induced seismicity refers to any seismic activity generated by physical processes (loading constraints and triggering rupture) which can be non-exclusively tectonic. Thus, we can distinguish two categories of induced seismicity. First, seismicity fully induced due to loading and non-tectonic triggering. This means that the probability of occurrence of these earthquakes would be zero without the intervention of non-tectonic factors. Second, seismicity linked to a tectonic loading that can be triggered by a non-tectonic factor (Schilen, 1972). This means that the intervention of the non-tectonic factor accelerates the occurrence time of the seismic event that would happen indifferently of the intervention. The accelerating non-tectonic factors can be either natural (volcanoes (Jay et al., 2012), geothermal activity (Majer et al., 2007)) or anthropogenic (nuclear explosion tests (Boucher et al., 1969), industrial activity (McGarr et al., 2003; Ellsworth, 2013)).

1.3.1. Naturally induced seismicity.

Small scale naturally induced seismicity of non-tectonic origin in most cases includes seismicity generated either by volcanoes or geothermal areas (Majer et al., 2007). Even if these geological areas are a consequence of Earth's tectonic

processes, the seismicity that occurs there is not initially caused directly by tectonic stresses but is instead a result of the geological processes related to these particular areas. Seismicity in the volcanic areas can be attributed to melt movement within the crust, while in geothermal areas it is induced by fluid migration. The earthquakes induced by volcanism can be classified into two major categories (Sherburn et al., 1998). First of all, the "volcano-tectonic earthquakes" produced on faults in response to indirectly induced stress variations due to the circulation of magmas and hydrothermal fluids (Chouet, 1996). The most notable example is earthquakes accompanying volcanic eruptions. The mechanism at the source, in this case, will include significant mode I components associated with the fractures opening due to magma penetrating the upper layers of the crust which indicates a combination of both opening and shearing along the fault plane (Miller et al., 1998). The other major group is that of earthquakes in the volcanic regions generated by the movement of magmas and gas bubbles in the volcanic structures. These earthquakes are created by the dynamic mass movement of the melt rather than fracturing (Chouet, 2003).

Lesser known occurrences of earthquakes can be triggered by the lunisolar tides. A small increase in stress, caused by the pull of the moon and the sun on the Earth's crust, can act as a triggering mechanism for an earthquake if its state of stress is at a critical condition for an outbreak (Heaton, 1982, Tsuruoka et al., 1995).

1.3.2. Anthropogenically induced seismicity

Seismicity that has been induced by human activity can be generally categorized into three groups: seismicity induced by fluid injection (Ellsworth, 2013), seismicity induced by fluid extraction (Segall, 1989), seismicity induced by solid extraction (McGarr, 1994). We are going to focus in detail on the first of the three groups.

The first observation of seismic activity induced by water injection goes back to 1960s in Colorado were earthquakes of magnitudes <5.1 were recorded following injection of large volumes of water into deep rocks (Healy et al., 1968). Nowadays, fluid injections have many different industrial applications, and in most cases, these are accompanied by seismic or microseismic activity (Warpinski et al., 2001). In oil reservoirs, fluid is injected to flush hydrocarbons towards the

extraction wells or to hydraulically fracture the rock to increase the permeability. In the chemical industry water injections are used for brine production by dissolving salt layers at depth. Lastly, fluid injection is a common practice in projects associated with geothermal reservoir exploitation with the main function of increasing permeability of the fracture network, and thus increasing output, where the cold water is injected into dry hot reservoir rocks and then recovered at another well once it goes through the fracture network and, in the meantime, heats up.

Moment magnitude is a logarithmic scale measure that is conventionally used to describe amount of energy released during the earthquake. It is designed so that its values correspond to ones of the outdated Richter scale (Hanks & Kanamori, 1972). Because of their very small magnitude, generally in negative values, the earthquakes induced by fluid injection rarely can be recorded by the networks on the surface (Kochnev et al, 2007; Eisner, 2010). For reference, people are generally unable to feel earthquakes below moment magnitude of 2. In addition, the fluid injection operation sites are very noisy due to injection pumps which also create a relatively large amount of background surface vibrations. This is the reason why microseismic activity associated with fluid injection is generally recorded by sensors installed in observation wells. However, these facilities are quite costly, that is the reason why a number of sensors deployed on the operation site is limited. Further, the positioning of the sensors depends on the operation location and logistics, and therefore, the network configuration is not always optimal (Eisner, 2010).

Many studies have already examined the relationship between fluid injection and observed seismicity (Fehler 1989, Cornet et al. 1997, Talebi et al., 1998; Fischer et al., 2008). Figure 1.10 shows a correlation between the injected fluid flow, the pressure of the injected fluid and the number of events recorded during the injection operation in a sedimentary rock during the hydraulic fracturing operation in East Texas (Rutledge et al., 2003). In fact, Cornet and Jianmin (1995) show that

seismicity does not directly reflect the injection flow, but only the pressure of the liquid in the pores of the rock.

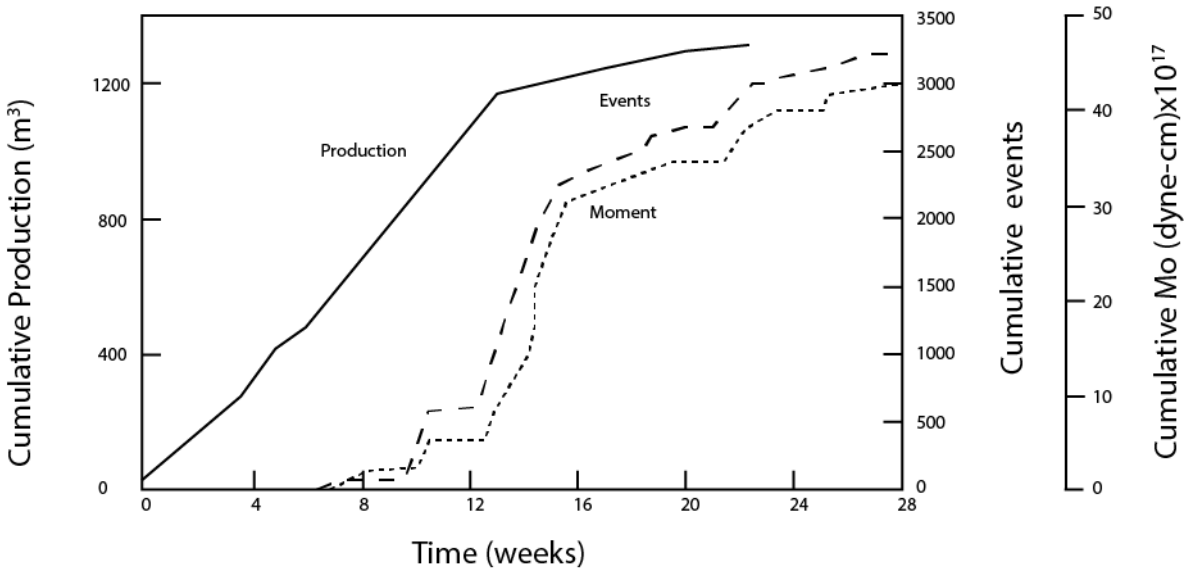

Figure 1.10. Correlation between volume of fluid injected (production used as proxy as it is linear to injected volume) and number of seismic events recorded as well as their cumulative seismic moment (after Rutledge et al., 2003).

The development of a shear fracture, which translates into movement along the fracture plane, is triggered by the decrease of the effective stress. This drop in effective stress is caused by the increase in the pore pressure due to the fluid injection into the rock. The conditions under which the failure occurs can be illustrated by Mohr's circle, which shows the relation between the constraint shear stress τ and normal stress σ on the fault plane. The values of σ, τ of the opposing direction of the plane are shown on a circle which's diameter equals to $\sigma_1 - \sigma_3$ and which's centre is oriented at the value of $((\sigma_1 - \sigma_3)/2)$ where σ_1 and σ_3 are respectively the maximum principal stress and the minimum main constraint. The fracturing occurs when the circle touches "the failure envelope". Figure 1.11a illustrates shear failure caused by natural tectonic loading. In this case main stress σ_1 and shear τ increase gradually until failure occurs The Figure 1.11b illustrates shear failure caused by fluid overpressure. In this case, the normal stress at the fault plane is reduced until it reaches the breaking point, which is depicted on the Mohr's diagram by displacing the circle to the left. The second case is a tensile failure, which was discussed in Chapter 1.2.3 (Fig. 1.7). This can occur if the differential stress is small enough for the Mohr circle to be able to move to the negative side of x axis (tensile regime), without touching the failure curve.

Another possibility is if seepage forces and fluid pressure gradient force is actively changing differential stress.

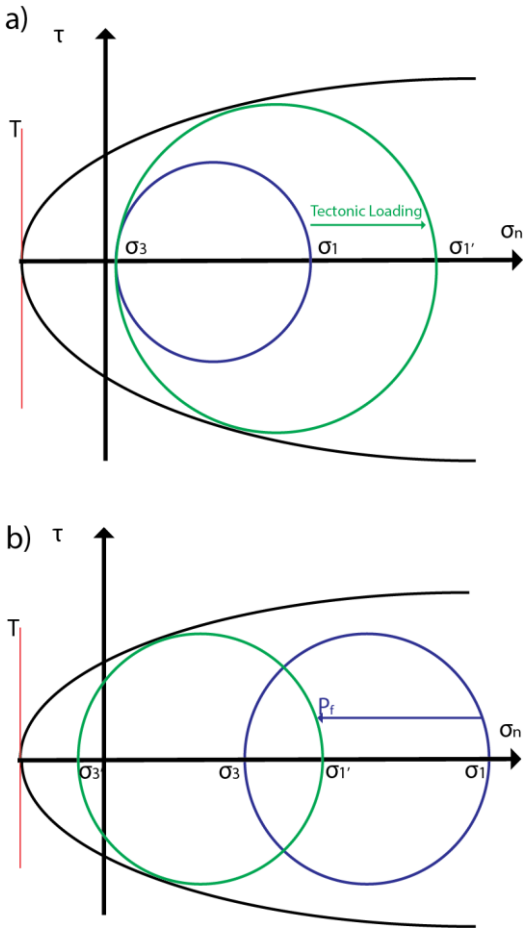

Figure 1.11. a) Mohr circle diagram illustrating differential stress increase due to increase in σ_1 due to tectonic loading. Eventually Mohr circle reaches failure envelope and shear failure occurs. b) Mohr circle illustrating fluid pressure influence to the system where differential stress remains the same while circle is being shifted to the left until it touches failure envelope, which causes shear failure.

1.3.3. Microseismicity and its role in hydrofracturing

When conducting unconventional hydrocarbon well stimulation operations, engineers use geomechanical and fracture models to plan where to initiate fracture stimulation as well as to predict where the fractures might propagate in the reservoir (Eaton and Forouhideh, 2010). As already discussed, the reservoirs are a complex system with a variety of variables. This means that these models require calibration and validation. Microseismic monitoring has proven itself as a viable mean of providing empirical data for these purposes.

Microseismic monitoring is a technique that records and locates the microseismic events, which are bursts of seismic wave energy caused by rock mass movements in response to changes in the in-situ stress due to artificially increased fluid

pressure (Le Calvez et al., 2016). When studying active hydrofractures in the Earth's crust, microseismic activity has been used to map the fracture's height, extent, orientation as well as magnitude of the fracturing event in order to monitor fractures during geothermal energy extraction (Baria et al., 1999), reservoir stimulation (Urbancic et al., 1999), and waste reinjection (Warpinski et al., 1999). Laboratory experiments of acoustic emission observation during hydrofracturing (Scott et al., 2000; Groenboom and van Dam, 2000) as well as modelling of such emissions (Guest and Settari, 2010; Murphy et al., 2013; Rutqvist et al., 2013) can also be used to better understand the fracturing process and its aspects such as direction of fracture propagation and fluid injection induced static stress perturbation. Inversion of seismic data allows to determine the moment tensor during hydrofracturing and thus the movement of the fracture walls relative to each other (Hazzard and Young, 2002; Guest and Settari, 2010; Vavrycuk, 2011).

Typically, the moment magnitudes of the seismic activity caused by the hydraulic fracturing do not reach positive values on the scale (Shapiro et al., 2007). Moment magnitude is scaled to be similar to outdated Richter scale (Hanks and Kanamori, 1972). Humans, generally, are unable to feel events below magnitude of 2. Statistically, a record of microseismicity for the typical hydrofracturing operation will form a normal distribution in between values of -4 and 0, with most of them being around the value of -2 (Kamei et al., 2015). An event of the magnitude of -2 is about a billion times weaker than what can be felt by a person on the surface. However, there are still risks involved in association with hydrofracturing induced seismicity. In the US there has been a dramatic increase in the seismic events of magnitude >3, meaning they could be felt on the surface. Increase has happened from an average of 24 M≥3 earthquakes per year in the years 1973–2008 to an average of 193 M≥3 earthquakes in 2009–2014, with 688 occurring in 2014 alone (Rubinstein & Mahani, 2015). Most of them are attributed not to the hydrofracturing operations themselves but rather to the wastewater disposal (Gallegos et al., 2015). In the UK Cuadrilla Resources Ltd. hydraulically fractured the UK's first shale gas wells at Preese Hall in April and May 2011. Two seismic events followed this activity, the largest of which had a magnitude of 2.3. Investigations carried out concluded that the seismicity was linked to the direct injection of fluids into an adjacent fault zone (Green et al., 2012; Prpich, 2015).

Not all hydrofracturing induced seismicity is associated with hydrocarbon extraction. The most known case is the incident that occurred in December 2006 near Basel, Switzerland, where water was injected into a 5km deep borehole in efforts to fracture the crystalline basement to create an enhanced geothermal system. That generated about ~10500 events with some of them reaching a magnitude of 3.4 (Deichmann and Giardini, 2009). This was caused due to underestimation of the amount of fluid that would leak into a nearby thrust fault (Dyer et al., 2010; Goertz-Allmann, 2011). Recent reports show the situation has deteriorated since then as the reactivation of the fault also contributed to the formation of new fracture networks and re-opening of previously sealed fractures. Due to this, there is a constant fluid migration to the borehole site which causes overpressure and repeated seismic events, some of which still reach magnitudes of 1.8. To avoid this, wellbore must be regularly kept open to release overpressure, resulting in substantial amounts of mud flow-back (Kraft et al., 2018).

Relatively recently, in November 2017, earthquake of magnitude 5.5 occurred near Pohang, South Korea. Although not yet completely proven, the general concensus is that it most likely occurred due to development of enhanced geothermal systems near the city of Pohang where the fluids leaked into nearby fault system (Grigoli et al., 2018).

Another example is the unnatural increase in the frequency of magnitude >3 earthquakes in Oklahoma, US, in the period since 2007 with an earthquake of 5.7 magnitudes in 2011. The main cause behind this phenomenon is argued to be deep rock injection of wastewater associated with unconventional hydrocarbon extraction (Keranen et al., 2014). It is believed that wastewater has enhanced the activity of nearby Nemaha fault complex, with the main fault itself being able to cause an earthquake of magnitude >7 (Wells and Coppersmith, 1994), in accordance to the scaling law between fault length and magnitude derived by Kanamori and Anderson (1975).

In order to alleviate any risk during future hydrofracturing operation, it is of vital importance to understand how different rock types break during hydrofracturing, what seismic signals are emitted during this process and also how microseismicity can be used to monitor fluid movement and hydrofracturing.

1.4. Research motivations and questions

This research has been carried out as a part of the National Environment Research Council's UK-wide Centre for Doctoral Training in Oil and Gas framework, which had four main themes. The one under which this research was carried out, was to better understand unconventional reservoirs.

The core of the project was anthropologically induced hydrofracturing and dynamics of the fracture propagation. There are still many unanswered questions regarding the dynamics of solid and fluid interaction in the geological systems during hydrofracturing. Monitoring fluid movement and fracturing is one of the key research aspects in the modern unconventional hydrocarbon industry. There are models present that deal with the process, however many of them lack the component to study the geometries of the created fractures and associated dynamics in detail. Further, there are few known modelling attempts that have coupled solid-state deformation with the dynamics of the fluid phase and quantified generated seismicity. Microseismicity observation is currently the best available monitoring tool for such operations. Hydrofracturing associated seismicity has been of great concern to the public in the recent years. This adds the necessity to better understand the characteristics and possibilities of the seismicity generated by simulated hydrofracturing operations in different scenarios. Therefore, it is important to provide a model that can incorporate all the elements of the real time hydrofracturing operation.

In order to further understand and possibly validate the model results, experimental work has been carried out. We have chosen the Hele-Shaw cell method, which has a number of beneficial properties. Most of the laboratory experiments that have been conducted to study hydrofracture propagation have been carried out using solid materials. Due to their nature, solid materials require a pre-existing notch for fracturing initiation and thus introduce bias to the experiment. Hele-Shaw cell allows to look at the displacement dynamics not only of the fracture itself but also in the surrounding solid media, which adds great potential to better understand the hydrofracturing process.

This research has been then further inspired by the possibility to broaden the existing knowledge base on the given topic by addressing the following questions:

- What are the dynamics of the solid and fluid phases in the system during hydrofracturing?

- Which mechanical rock properties, natural conditions and anthropologically controlled factors have the largest effect on the characteristics of the developed fracture networks?
- How do the fracture network geometries change in response to alteration of upper-mentioned variables?
- How does the stress state evolve in the system during hydrofracturing?
- What are the dynamics of a single propagating fracture?
- Can we quantify possible fracture network geometries from the input parameters?
- Can we observe any patterns in the generated seismicity depending on the characteristics of the hydrofracturing operation?

These questions have been approached using the combination of numerical modelling and laboratory experiments in an effort to broaden our knowledge on the rock dynamic processes and associated seismicity caused by the hydraulic fracturing.

1.5. Thesis structure

The thesis has three main parts to it: (1) exploring into fracturing dynamics using numerical modelling; (2) laboratory experiments studying fracture pattern development and propagation in a vertically orientated Hele-Shaw cell and (3) detailed analysis of the seismicity generated during modelled hydraulic fracturing. This order was chosen as first numerical modelling was carried out to see how the system reacts to alteration of different input parameters. Next Hele-Shaw cell experiments were conducted in order to reproduce experiments that are similar in their setup to the numerical model. This was done to further understand the processes within the solid media ongoing during hydraulic fracturing and to see if these observations can help us better explain the results gathered from the numerical modelling. The last chapter then focuses on the generated seismicity. It is explored very last as by this point the most important variables within the

system have been established and the generated signal can be analysed depending on their alteration.

First, I present the literature review chapter, which presents the most important literature regarding each topic as well explores methodologies available to study each of the questions presented in this thesis. This is followed by the methodology chapter which studies in depth methods used to gather and analyse the data as well as in detail presents the analytical solution developed specifically to study fracturing dynamics using the given numerical model. The next three chapters present the main results and findings. Each topic is presented as a separate chapter, where results, specific to the question of the interest, are presented. This is followed by discussion and conclusion. The thesis ends with a brief summary of the work accomplished as well as final comments on the research.

2. Literature review

2.1 Numerical modelling of rock deformation processes

Rock deformation studies are used to understand some of the fundamental geological processes and features found in nature such as folds, thrusts, faults and fractures (Bons et al., 2007). As these can be on a multi-kilometre scale in size as well as form over a very long time, we almost always see only the very final stage of the formation process. Other anthropologically induced processes such as hydraulic fracturing occur in depth, despite being short on a temporal and spatial scale. This means there are no visual observation possibilities, and other investigative methods such as microseismic monitoring provide only a fraction of the information related to the rock deformation (Kamei et al., 2015). Due to this reason, geologists must apply other means of investigation than field studies. Tools developed need to be able to test a broad spectrum of possible scenarios. These involve different boundary conditions (pressure, temperature, strain) that cause the deformation as well as the different mechanical properties of the rock (Young's modulus, Poisson's ratio) (Bons et al., 2007). Another goal for these tools is to vary the temporal component, meaning that models should be able to simulate processes that would otherwise take a very long time to happen in nature. One of the main tools applied for this purpose is numerical modelling (Cundall and Hart, 1992; Cundall, 2001). Depending on the complexity of the model, it is possible to vary a number of parameters to produce a range of scenarios. As rock deformation can occur on a very large scale and has a long temporal component, numerical modelling has a significant advantage over the laboratory experiments where such conditions cannot be created. Lastly, the nature of the modelling process makes it possible to look at the interim results during the deformation, giving in-depth insight into the ongoing dynamics and not only the result.

There is a range of numerical model types developed based on their purpose and running algorithms (Ciarlet and Lions, 1990; Bons et al., 2007). Some of the examples that are commonly used in the modelling of geological processes include:

- Finite Element Models (FEM) – Subdivides continuous space into smaller elements each with its set of properties. Used to simulate linear and non-linear processes in material mechanics, such as fracturing, as well as physical processes, such as magnetization.
    - Finite Difference Model (FDM) – Type of the FEM where differential equations are solved. This allows looking at physical property variation over the time and space (Liszka and Orkisz, 1980). Compared to FEM, particles do not vary in size.
    - Finite Volume Model (FVM) – Also a type of FEM where space is subdivided into volumes, then differential equations are employed to observe the change in volume as a function of conservation or balance of physical quantities, like mass and energy. Commonly used in the fluid dynamics calculations (Versteeg and Malalasekera, 2007). Both FDM and FVM are the simplification of the FEM approach designed to better solve specific problems.
    - Bonundary Element Model (BEM) – Subtype of the FEM which is used for solving linear partial differential equations which have been formulated as integral equations (i.e. in boundary integral form), including fluid mechanics, acoustics, electromagnetics, fracture mechanics, and contact mechanics (Jing, 2003).
- Spectral Model (SM) – Similar to FEM, but employs Fast Fourier Transform from the sum of multiple simple equations. Then it is possible to derive a differential equation for the whole system rather than each partial element on the mesh. This means that further equation take into account variable states across the entire system and not just individual cells. This method is used for calculation of parameters that have high variability over space and time. An example of a problem solved using this method is shockwave spread (Marshall, 1970).
- Discrete Element Model (DEM) – The main idea of this approach is to portray an object or media modelled as an assemblage of smaller particles (Munjiza et al., 1995). Each particle then is given its own set of parameters which is updated every iteration (in a way similar to finite volume).
- Lattice-Boltzmann model – the model type which employs multiple cores build in one thus allowing to parallelize algorithms (Chen and Doolen,

1998). This also allows for dealing with complex boundary conditions where one algorithm cannot be efficiently used to account for all of them. Most commonly used for calculating fluid dynamics for liquids where the classical Navier-Stokes method is non-applicable.

Every model type is used or has been specifically designed for its own area of purpose. Each method has its own advantages and disadvantages. For the purpose of simulating hydraulical fracturing, DEM and FEM are the most commonly used approaches (Lisjak and Grasselli, 2014). Further, we are going to look in more detail at working principles of the DEM. Examples from the literature, where DEMs have been used to solve similar problems, will be presented.

2.1.2 Discrete Element Models

The DEMs provide a framework where the body is represented as a lattice of particles (Cundall and Strack, 1979). Each particle is treated as an individual entity with their own set of calculable parameters and degrees of freedom. For every particle, number of nearest neighbour particles are then determined. This is required as a set of interaction forces (normal, tangential and contact forces) among these particles are being accounted for. Another term to account for, the cohesion, is introduced, thus adding another level of complexity. In contrast to above-mentioned interaction forces, cohesion holds the particles together and interaction forces then have to be calculated in regards of the cohesion force (Scholtes and Donze, 2013). The model then acts in a quasi-static fashion, meaning that the set of the mechanical properties are being updated every increment of the experiment. The most common approach is to calculate the mechanical properties as temporal derivatives, and thus increments commonly being referred to as “time steps”.

Because particles are being treated as separate entities DEM codes require significant computational power. For that reason, one must make a compromise between the complexity of the model and its time efficiency (Cundall and Strack, 1979). Particles themselves tend to be represented as spheres. If the model is in 2D, cylinder shapes are typically used. This involves relatively simple calculations when describing their physical properties as well as simplifies calculating inter-particle interaction parameters. When dealing with spheres, the distance from

the centre of one particle to the boundary of another is independent of their juxtapositioning angle. Despite each particle being treated individually, the sum of them needs to represent a unified body, and therefore interactions between particles have a fundamental role (Cundall and Strack, 1979). Again, to simplify calculation, most DEMs use the very basic triangular mesh setup (Lisjak and Grasselli, 2014). The reasons for that are that a) in the initial setup every particle will be located equal distance apart from all of its closest neighbours, b) the triangular setup allows using the basic trigonometrical functions c) it can be easily upgraded to more complex shapes such as hexagons, without having to change the trigonometric base approach for the geometrical calculations if additional computational power is available (Ashurst and Hoover, 1976; Wang et al., 2000; Place et al., 2002). Also, there are several approaches on how and which particles should be connected. In classical DEM, particles have interaction among themselves if they are in direct contact (Wang and Mora, 2008). Alternatively, in cases where particles can compact each other, inter-particle relations are looked at only if the distance between the particle centres is smaller than the sum of both particle radii (Chareyre et al., 2012). For more complex approaches, the zoning method is used where particles interact among themselves even if they are not in direct contact but are in the same "zone" (Scholtes and Donze, 2013). In the case of DEMs used for solid materials, there is a layer of cohesion calculations involved. For such scenarios, particles are usually connected by "springs". Which particles are connected that can be determined and applied by the algorithm that assigns set of nearest neighbours to every particle. The structure of the model and which particles are connected plays a fundamental role in how the kinetic energy will be distributed during the deformation modelling and will determine how the model will behave. Therefore, when designing an experiment, the model setup must be chosen so that represents the modelled parameter of interest to the best possible standard.

There are two computational algorithm cycles involved in the classical DEM approach. Firstly, the above-mentioned interaction forces are being calculated using the following laws. Secondly, once these have been applied, particles must be relocated to their new positions. This is achieved by applying Newton's Second Law of Motion (Sholtes and Donze, 2012; Scholtes and Donze, 2013). The result is translational and rotational acceleration which then is integrated over the

temporal value of a single time step of the model. At the end of the time step, new particle positions and their coordinates are recorded. These then are used to update interaction forces among them.

The user imposed outer force effects, such as in-situ stress, strain and gravitational compaction, can be applied through boundary conditions (Jing, 2003; Jing and Hudson, 2002). The DEM usually has boundary walls that are essentially the outer rows of the model. The particles in the boundary walls, contrary to the other particles in the model, are not affected by the particle interaction algorithm (Ghani et al., 2013). This allows them to maintain their original position throughout simulation imposing the user-defined forces on the rest of the model. DEMs are very flexible and efficient despite their simplicity. This allows them to be used to simulate a range of different processes. Simplicity is an attractive property as it requires relatively small computational power. It is achieved by a small number of input parameters that allows measuring small-scale specific mechanical properties (Jing, 2003). Discontinuous characteristics in combination with cohesive property implementation in DEMs make them a powerful tool to simulate physical processes in the solid phase such as rock (Malthe-Sorensen et al., 1998; Walmann et al., 1996, Lisjak and Grasselli, 2014). However, as previously discussed, when dealing with deformation of the rock, the fluid has a major role in the process. Every rock is porous to some degree, and this pore space can be filled either by pore fluids or influenced by external fluid flow. DEMs alone cannot account for the forces generated by a fluid phase, and therefore we need to implement a model that can account for both the solid and fluid phase. Such models are referred to as coupled hydro-mechanical models, and are one of the most abundantly used tools to model and simulate hydrofracturing processes.

2.1.3 Hydro-mechanical models

Being able to model processes in saturated porous media has great potential as it is applicable both to natural processes (liquefaction (Clément et al., 2018; Zeev et al., 2017) and natural hydrofracturing (Zienkiewicz and Shiomi, 1984)) as well as industrial and geotechnical processes (reservoir modelling (Hicks et al., 1996), human-induced hydrofracturing (Ghani et al., 2015), rock and soil stability (Parez et al., 2016)). Coupled models need to solve an array of complex interconnected issues such as solid phase deformation due to fluid pressure, fracture propagation

due to deformation, fluid flow in the solid and changes in the fluid pressure caused by the fracturing. As it can be seen, all three are interlinked and there is a feedback loop among all of them.

There are different approaches to solving the problem of coupling fluid and solid phases. However, most of the approaches can be binned into two larger groups: continuum and microscale models (Jerry, 2005). The continuum-based approach uses an additional grid which usually supersedes DEM layout base unit size and overlays the initial DEM lattice. The variables such as porosity and permeability are averaged over the mesh. Quite often, a tent function is used to assign these values to DEM particles as it averages them proportionally to four nearby points on the continuum (Ghani et al., 2013). This approach is beneficial from the perspective of computational power required. However, due to the large scale of the continuum and averaging of the values, this approach can be problematic when trying to model fine-scale processes (Jerry, 2005). Microscale models employ a method which is opposite in its approach of adding fluid phase representation. For example, Lattice-Boltzmann models introduce smaller fluid meshes that can dynamically adapt their size (Chen and Doolen, 1998). This approach yields great resolution and precision of the experiments, however, computational power required is very high, which results in long simulation run times.

Due to lack of widespread access to high capacity computational facilities, DEM is the most commonly used modelling approach for most mechanical processes (Jing, 2003; Dorren, 2003; Jerry, 2005). Such DEMs present us with a body that is partially constituted of the solid media and pore space in between the solid is filled with fluid. This setup is mimicking a porous media which deforms due to variations in pore pressure that result in a fluid pressure gradient. The very core concept of the coupling is the change in the porosity and permeability caused by the deformation, with the main emphasis on fracture generation and opening of fractures. Changes in porosity and permeability then have a strong feedback on the fluid pressure evolution.

One of the first investigations into how this could be accomplished was done in the study by Flekkoy et al. (2002). The solid media was represented by a triangular lattice of disc-shaped particles. Particles were then connected by elastic springs with pre-assigned tensile strength. Fracturing occurred when tensile strength of the spring was exceeded. A “broken” bond was removed from the lattice, which

enabled only for the Mode I fractures to occur. Despite bonds breaking under the extension on the local scale, this still enabled representing shearing processes on the larger scale. Some theoretical work on fluid pressure evolution and its coupling to the solid media has been previously carried out by McNamara et al. (2000) and earlier by Tanaka et al. (1993) as well as Andrews and O'Rourke (1996). The idea was to use Darcy flow together with fluid and solid mass conservation to calculate the fluid pressure evolution. The Flekkoy et al. (2002) model implemented very basic principles and had to make a number of assumptions to simplify the calculations. It did not account for the local scale porosity variations and fluid pressure response to volumetric changes in the solid phase. The initial setup had a pre-assigned permeability parameter that would change during the fracturing as a function of solid mass fraction reduction (Flekkoy et al., 2002; Ghani et al., 2013; Ghani et al., 2015). To avoid abrupt irregularities in the solid phase density, the smoothing function was used. It is used by linking each solid phase particle to four nearest fluid phase nodes. Then the forces exerted on each particle from the four nearby nodes would be calculated as a sum of ratios derived from the distance of the particle to the node. That means that the closest node would have the greater impact on the particle while the furthest would have the least impact. The deformation is then calculated by combining the force applied by the combination of four nearby nodes and particles attached by elastic springs. More analytical framework of the mathematical and physical principles used is provided in Chapter 3.1.

There are a number of models which use the principles described in the work by McNamara et al. (2002) (Ghani et al., 2013; Ghani et al., 2015; Niebling et al., 2010; Niebling et al., 2012; Niebling et al., 2013; Vinningland et al., 2007; Johnsen et al., 2006). There, however, seems to be a split in the approaches where some models consider the fluid to be compressible (McNamara et al., 2002; Vinningland et al., 2007; Ghani et al., 2015) while others consider it to be incompressible (Niebling et al., 2012). Niebling et al. (2010) argue by presenting their 2D closed Hele-Shaw cell numerical calculations that fluid compressibility had a minimal effect on the solid phase dynamics as fluid compressibility is very limited under the shallow crust conditions.

Another significant split in the opinion that can be found in the literature is whether poroelasticity has a significant enough role in the fracturing dynamics.

Poroelasticity is a term used to describe the two way interaction between the pore pressure alteration and porous solid deformation (Biot, 1941). Authors of porosity driven models argue that poroelasticity has significant feedback on fluid pressure which in turn is the driving mechanism behind hydraulic fracturing (Ghani et al., 2013; Ghani et al., 2015; Flekkoy et al., 2002; Olson et al., 1989, Olson et al., 2009; Cobbold and Rodrigues, 2007; Mourgues and Cobbold, 2003). The other side of the view tends to ignore the poroelasticity effect mainly due to two reasons. Firstly, the classical model of fluid pressure impact on the stress state does not involve a change in the differential stress (when shifted towards the left, the Mohr circle does not change size, see Chapter 1). This view has been lately challenged by numerous analytical and numerical studies (Holtz and Kovacs, 1981; Teufel et al., 1991; Cobbold and Rodrigues, 2007; Ghani et al., 2015). The other reason is that poroelasticity is often excluded from numerical calculation due to its complex nature and complex effects that it has on both the fluid and solid phase (Wang, 2016). However, that approach is being less frequent in the recent studies once the machine calculation capacities available have increased.

2.2 Other Hydrofracturing models and approaches to coupling of solid and fluid phases

2.2.1 Coupling solid and fluid phases using the discrete fracture network method

With the advance of high capacity computational opportunities, models that look into alternative ways of how to represent fluid flow in the solid rock mass have emerged. One of the approaches is to look at the pre-existing fracture network instead of porosity as the main way of fluid transportation and migration mechanism. Such an approach was implemented by Damjanac et al. (2013). Porosity is considered as a mechanism that provides pathways for the fluid leak-off, and thus drops in the fluid pressure. However, the pore pressure itself in this type of simulation cannot trigger new fracture generation.

This type of model coupling was developed using the synthetic rock mass (SRM) concept (Pierce et al., 2007). SRM has two constituents to it: a) the bounded particle model (BMP) for characterising deformation and fracturing processes in the intact rock and b) the smooth joint model (SJM) to characterise discontinuities

in the rock as well as fluid migration pathways. The BMP component is built on the basis of DEM of quasi-randomly located arrays of nodes in a 3D space. The particles are then assigned mass and are interconnected by a pair of springs. One of the springs represents shear stiffness while a second spring represents normal stiffness. This is the same as for most of the classic DEMs where particles mimic the solid rock mass while its elastic properties and macroscopic strength are being calibrated through varying spring properties. During the running of the model, once the displacement and velocity (transitional and rotational) are calculated in tri-axial space, it is integrated over the time step to gain acceleration. Finally, Newton's Second Law of Motion is applied to calculate for the force applied from the acceleration components in all the three directions. If the force applied exceeds either normal or shear stiffness of the rock, a spring is removed and a fracture forms.

The second component is the smooth joint model (Mas Ivars et al., 2008; Chiu et al., 2013). It is acquired through blending user defined discrete fracture network, which is supposed to represent the pre-existing fracture network in the rock, with the DEM used in the first stage to mark the coordinates of the fractures. This is done by marking springs which are located closest to the planes as "joints" or "fractures". These discontinuities then can be characterised through the user input parameters. Fluid then migrates through the network of "pipes" from the centre of one node to another, where "nodes" are springs designated as pre-existing fractures or springs which were removed due to active fracturing during the experiment. As described above, DEM has a pre-assigned static porosity value which does not change throughout the experiment and acts only as means of fluid leak off. The fluid network structure is dynamic and is updated every time step to incorporate newly broken springs into it. The rate of fluid migration is then calculated via the lubrication equation as a function of fracture aperture, fluid viscosity and differential of fluid pressure in the two nearby nodes, relative permeability and saturation.

The model then is coupled through a three-phase loop:

1) The deformation of the solid phase affects the fracture aperture and via that the permeability;
2) The effective stress is calculated as a function of fluid pressure. This drives the deformation process and affects the strength of the rock;

3) The fluid pressure is determined by the permeability of the solid phase and apertures of the fractures.

The approach of using fractures as a proxy for the fluid phase is a novice and has great potential. It can be very precise for simulating scenarios in the sites from which rock samples are available and all the needed parameters for the model can be obtained by basic laboratory experiments.
The downside of this approach is that it is very reliant on the rock to have the network of the pre-existing fractures to work. Lack of seepage forces in the fluid phase equations in the model makes it impossible to model the deformation in the intact rock without pre-existing discontinuities where pore fluid pressure is the driving failure mechanism. Also, the existence of separate springs for shear and normal stiffness limits the failure mode only to pure Mode I or Mode II regime whereas, in reality, it is quite rarely the case. Most failures are to some extent a combination of both modes and failure criterion should be viewed as a proportional equation of the two stiffness values (Sachau et al., 2013).

2.2.2 FEMDEM coupling models

Another idea, which became available for modellers, to be run only in recent times is the multi-stage coupling approach. This approach means that for the same model multiple model types are being blended into the same model and are calculated for simultaneously. Until recently, there was no conventional computing power available to do that. The theoretical ideas of how to bring together methodologies used in finite element models (FEM) with discrete element models (DEM) was first described by Munjiza (1992). Applications for the code were very limited at the time. The idea of FEMDEM incorporates possibility to model dynamic elasticity variability of solids presented by FEM with the particle tracking possibilities of DEM. Such an approach was designed by Munjiza (1992) to solve for the fragmentation problems. The main novice idea, introduced to hydrofracturing problem solving by the FEMDEM approach, is that if the stresses are sufficiently high, they will fracture the individual particles, and then DEM algorithm will continue to track their location in the system. To simplify things, for the DEM-part of the calculations, all the particles are assumed to be of the classical built up – three-node triangular setup. This shape is also then kept during

the breakup of the given particles. Such an approach yields that blocks that are away from the injection point stay large in size throughout the experiment and require relatively little calculations and computational power. Blocks that are close to the injection point get fragmented into smaller entities. This allows for very precise geometries to be calculated. This is often regarded as an adaptive mesh approach (Fig. 2.1) (Park et al., 2012; Obeysekara, 2016). The upside to such model setup is that it produces very precise results. On the other hand, the number of FEM elements tends to grow in a geometrical progression towards the later stages of the experiment, meaning that depending on the number of parameters involved the calculations take very long time to be processed.

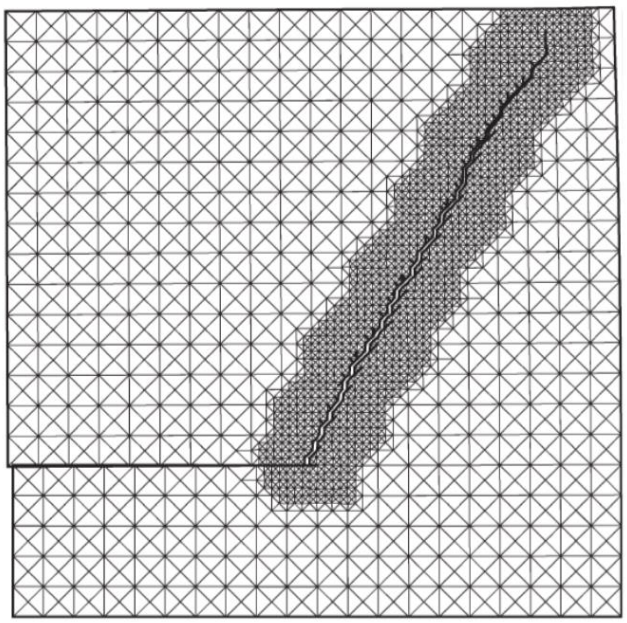

Figure 2.1. Adaptive mesh FEMDEM model illustration. Figure from Park et al. (2012).

Similar to the previously described method is the discrete fracture network layer that is superimposed upon this model to track the location and variability of the fractures (Lei et al., 2014). The difference in the current approach is that the adaptive mesh method is further applied to the fracture network layer as well. As a result, model coupling mechanism has to account for two fine detailed structures. Because of the fractionation, the coordinates of the solid nodes and fractures usually end up chaotically juxta-positioned. The coupling mechanism then uses mesh-to-mesh interpolation between solids and fluids. This is done by annotating “nodes” on the fractures and then balancing the two-way acting forces between them and “nodes” of the nearby solid fractals. Due to such an approach, the computational burden increases even further and a balance has to be made

between the number of free degrees and output values. This can result in poorer resolution results. Otherwise, great computational capacities and time are required.

2.3 Experimental studies of rock deformation processes

Numerical modelling solutions for rock deformation processes can be very useful from the perspective where they can be configured using a multitude of degrees of freedom and produce a large number of observable parameters (Jing, 2003; Jing et al., 2002). However, the fundamental knowledge of the rock mechanics is always obtained from the practical experiments or field samples. Natural examples obtainable in the field provide only a snapshot of the time, and we often see just the result of the deformation process where many unknowns remain. For this reason, laboratory experiments are carried out with the purpose to understand how different types of rock behave under controlled stress conditions. Understanding of the mechanical characteristics is fundamental in a number of scientific and engineering branches. The differentiation in mechanical behaviour usually depends on the environmental conditions and scale in space and time (Patterson and Wong, 2004). It can range from small-scale, momentary elastic strains during earthquake wave propagation (Aki and Richards, 2002) to irreversible, slow deformations in Earth's crust and mantle during such processes as ocean floor spreading and continental evolution.

Due to differences in the problems being solved and questions being answered, experimental research on the mechanical deformation behaviour of rocks has developed to some extent independently in several directions, which are not closely related to each other (Patterson and Wong, 2004). Particular separation in approaches can be seen between the civil engineering and mining engineering in contrast to studies aimed at geological process understanding. Petroleum engineering (Bobok, 1993), environmental and groundwater pollution problem (Yong, 2000) as well as nuclear waste storage specialists (Whiterspoon et al., 1981) further study deformation in the context of fluid movement through the rock and its pores (Committee on Fracture Characterization and Fluid Flow, 1996).

In the civil engineering sector, the problems are usually associated with the possible failure of the support and slope stability (Morgenstern and Price, 1965; Abramson et al., 2002). They do not tend to deal with large strains, but the

knowledge of the fracture propagation is vital. For that reason, engineering rock mechanics tend to be mostly focused on the brittle deformation. However, some engineering branches, such as mechanical engineering associated with turbine design, have to account for ductile deformation of material and associate it with material fatigue (Matthews et al., 2007).

As the material sciences first studied deformation processes in the simple cubic systems, the obtained laws of deformation were then applied in more complicated mediums, such as rocks in Earth Science (Patterson and Wong, 2005). In Earth Sciences, a lot of effort is spent on looking at brittle deformation as well. The context for that is faulting and earthquake mechanics. However, geology looks at different scale deformation from small, penetrative tests at a scale of hand specimens to a tectonic scale deformation processes, which involve the rock undergoing significant plastic deformation. Thus, Earth Science approaches involves looking at both brittle and ductile deformations. Despite having different applications and study focuses, results from deformation studies in both Earth Sciences and engineering can be transferable across both disciplines (Patterson, 2013).

2.3.1 Rock strength and triaxial test

When testing mechanical strength of most metallic materials, the applied stress is uniaxial and two other principal stresses remain zero throughout the test. In the case of rocks and soil, the experiments carried out are usually made so that all three principal stress values are non-zero. In the classical approach, these stresses tend to be compressive. To some extent, such practice is being used as triaxial stress more effectively simulates situations when the overburden is involved (Fig. 2.2). The main reason for such an approach is that the failure criteria of the rock strongly depends on both the normal and shear component of the stress.

Most commonly experimental approach used to test a rock's mechanical properties is the triaxial test. The concept was theorised as early as 1910 by Love (2013). However, for a long time, it could not be practically implemented as there were technical challenges in maintaining the axis of principal stresses from switching. The first stable design of a triaxial testing apparatus was introduced by Bishop and Henkel (1957). The principle is relatively simple. A cylindrical rock sample is being placed in a sealed off chamber, it is filled with liquid and

pressurised to mimic σ_3. The confining σ_3 is typically maintained stable throughout the experiments. Additional stress is then applied from the top with a piston to simulate σ_1 (Deshpande and Fleck, 2001; Haimson and Chang, 2000). There is a possibility provided for fluids to drain or remain depending on whether the experiment design requires for the pore pressure to stay constant or drop (Bishop and Henkel, 1957; Hoek and Franklin, 1967).

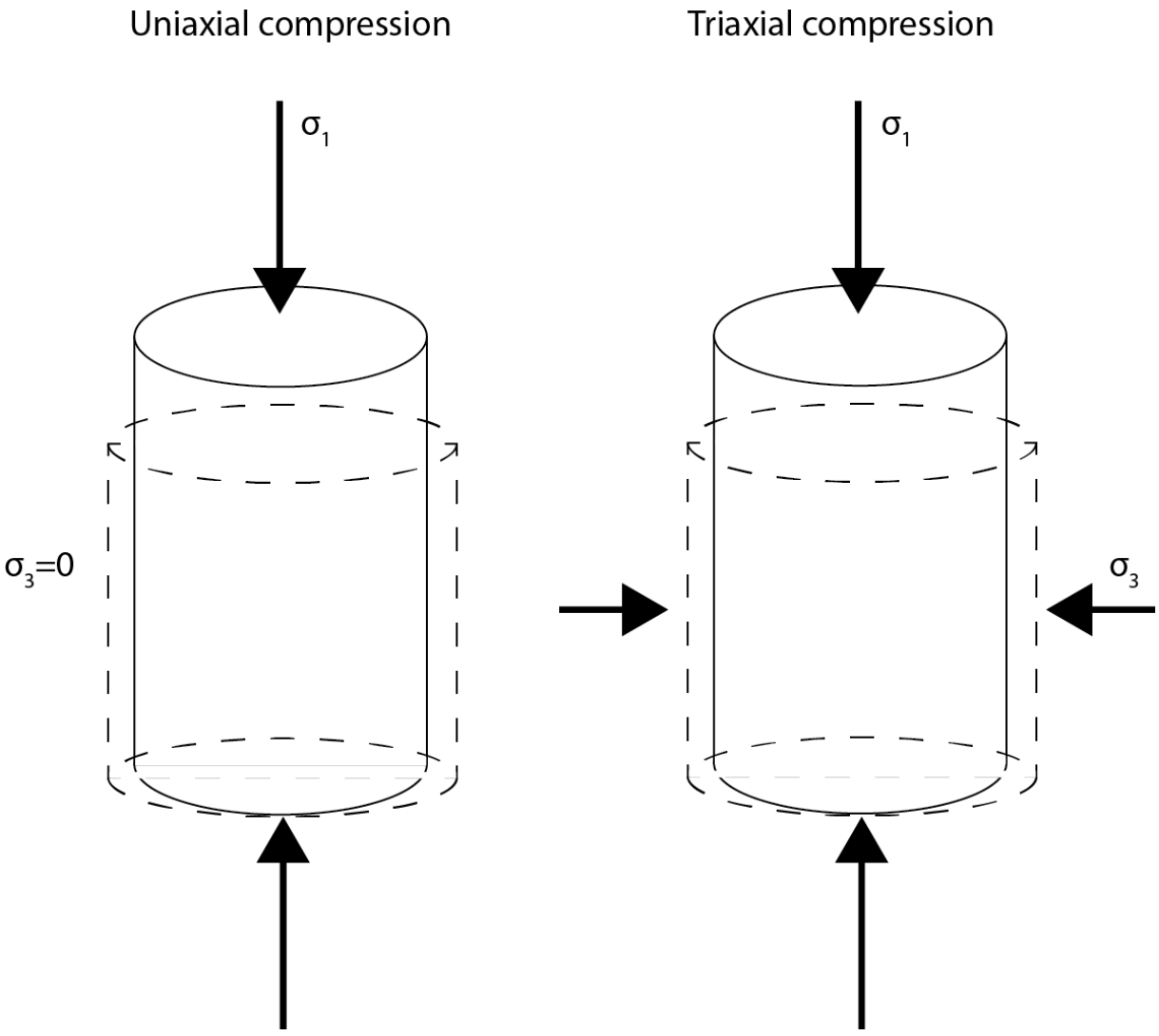

Figure 2.2. Unixial and triaxial stress test setups. Uniaxial stress test involves stress applied only along one axis. Triaxial stress test has an addition of the confining stress perpendicular to the main stress applied. This is better suited to illustrate conditions of the buried rock, as rocks at depth are a subject to confining stresses.

The two primary parameters measured during a triaxial test at constant confining pressure are a net axial force and axial strain. Those then can be used to plot differential stress versus axial strain. In some occasions, the change in volume of the specimen is also measured. The pressure then can be applied until brittle

failure occurs. The basic parameters that are derived from that are the cohesion, internal angle of friction and shear strength of the rock.

The effect of porosity change during the compaction is also widely investigated during the triaxial testing. For such studies, more advanced equipment is required. The most common relationship investigated is one between the change in permeability during the compaction as a function of porosity decrease. The second parameter of interest is the bulk modulus of both drained and undrained rock (fluid being absent or present in the pores) as well as stiffness comparisons between the drained and undrained samples of the same rock (Bishop and Donald, 1961).

In order to understand failure better and in order to locate failure planes in a specimen, acoustic emissions during the brittle failure of rocks are studied. Looking into correlations between the jumps in strains and the number of acoustic events occurring provides very useful insight into fault plane nucleation dynamics (Tang et al., 2002). To conduct such an experiment, a multichannel recording system is used to acquire the full waveforms. The polarity is acquired through the first motion. Then the focal mechanism and location of each event can be deduced. These experiments provided valuable insights into how fractures propagate in porous versus tight rocks. It was seen that in porous rocks the acoustic emissions do not follow a specific pattern and tend to form a cluster during the pre-fail stages of loading. Once the failure stage is reached the main failure plain develops through the network of the clustered microfractures (Warpinski, 2009; Bonamy and Bouchaud, 2011). In tight rock specimen, no obvious clustering of events during the pre-failure stages was observed. By contrast, very active clustering of the events happens in the post-fail stage where events cluster along an elongate volume that propagates progressively to develop a through-going shear band across the sample (Lockner et al., 1992). Another interesting aspect is the analysis of the focal mechanisms of the acoustic events. For the tight rock samples, most of the events presented as “double couples” indicating Mode II type of failure. For porous rocks, only about 15% were of Mode II while about a third showed extensionally Mode I behaviour, and the rest were classified as “complex” events with no evidence showing either Mode I or Mode II being dominant mechanism (Shah and Labuz, 1995; Satoh et al., 1996; Zang et al., 1998).

The triaxial compressive test is also used during the investigation of the seismic properties of the rock. One of the main characteristics looked upon is the change of the velocity of both P and S waves during compaction. The theory behind this is that microfractures in an uncompressed natural rock markedly decrease propagation velocities of both the compressional wave Vp and the shear wave Vs (Castagna et al., 1985). *Vp* is affected more than *Vs* so the ratio *Vp/ Vs* also tends to decrease. The change in a decrease of wave velocities and the ratio is the same in all the directions when there is no preferred orientation of the cracks. In the scenario where there is a preferred orientation of the cracks, the change in velocities and ratios becomes anisotropic due to different natures of the waves. When applying hydrostatic pressure to the rock of at least a few hundred megapascals, the effect of microfracture closure is achieved. This leads to an initial rapid increase in the wave velocity. After the initial cracks are closed, the wave velocity increase halts and stays constant despite the further applied stress. If stress is increased further, a new network of microcracks forms, and the wave velocity drops again. This effect is not so adverse in rocks which have pores filled with fluids.

Similar to wave velocity, elastic wave propagation dynamic can be observed with another parameter: attenuation. Seismic attenuation factor quantifies the loss of the wave amplitude due to the fluid flow and grain boundary friction in the solid, through which the seismic wave travels (Johnston and Toksöz, 1980). The quantitative measure of attenuation is given by a specific attenuation factor Q (Knopoff, 1964; O'Connell and Budiansky, 1978). It is very sensitive to the presence of cracks and fluids in the rock, as indicated by the relative amplitude of the received signals. Attenuation in the porous rocks is known to be of magnitude higher than that in crystalline rocks (Nowick and Berry, 1972) and is even further increased if fluids are present in the rock. Attenuation is associated with the light contact of points at crack tips and scattering of the elastic waves if the wavelength is comparable to the scale of cracks and pores (Knopoff, 1964; Winkler and Murphy 1995; Wulff and Burkhardt, 1997). Similarly to the wave propagation velocity, the increase in applied pressure has a positive effect on attenuation. It appears that this trend reverses after reaching roughly half of the macroscopic stress required to cause brittle failure. At this point, attenuation begins to increase again. This is believed to be correlated with the proliferation

of cracking associated with dilatancy prior to macroscopic fracturing (Rao and Ramana, 1974; Meredith and Murrell, 1995; Wulff et al., 1999).
Loading stress tests such as a triaxial loading test provide invaluable insights into investigating rock mechanical properties and fracturing dynamics during loading. However, such tests alone do not provide enough insight into fracturing dynamics during hydraulical stimulation as in this case failure is tensile, and thus extensional rather than compressional mechanisms are in operation.

2.3.2 Hydraulic fracture laboratory experiments

The very first detailed investigation into the mechanics of hydraulic fracturing was made by Hubbert and Willis (1957). Their research was first to focus into how newly formed fractures tend to be oriented in the rock. Their novel approach was to propose that fractures are orientated depending on the stress state rather than depending on the microstructural features such as microcrack orientation. Also, they challenged the idea that stress in the rock is mainly hydrostatic, and correctly assumed that it is predominantly determined by tectonic forces. Volcanic dykes were used as a natural example representing such a view. The idea that newly developed fractures can form independently of a pre-existing fracture direction was widely unpopular and can be seen to be disputed by Reynolds and Coffer (Hubbert and Willis, 1957). Hubbert and Willis (1957) used a simple, yet effective method to demonstrate their point. Gelatin was used as an elastic material that fractures easily. It was moulded onto a tube to mimic a borehole with an open well section. The two samples of gelatin then were stressed in a manner where the first sample had dominant vertical stress while the second had dominant horizontal stress. A plaster-of-Paris slurry was then used as an injection fluid and was applied to the samples. In both cases, the fracture opened in the direction of the least effective stress. Authors then formulated their findings using the Mohr circle diagrams, an approach and same principles that are employed today.
Early investigations, however, did not report dynamics of the fracture development and growth. Detailed fracture characterisation such as measuring fracture extent and width was also not a common practice. Most early contributions report borehole pressure versus time and fracture geometry at the end of the experiment. One of such studies is by Agarwal et al., (1979) as well as Hanson et al., (1981) where it was attempted to cross-correlate fluid injection

volumes with depth and production rates are made to derive cumulative fractured area of analysed project sites.

Quite often hydraulic fracturing would be used as a technique to determine the in-situ stress in different boreholes around the world (Haimson, 1978) rather than a tool to look into mechanics of fracture growth. This approach was developed mostly by the efforts of Zoback et al. (1977) and Zoback et al., (1978) who were investigating how fluid viscosity determines the fracture growth and fracture length relationship in regards to the stress intensity factor. They discovered that viscous mud is needed to generate fractures that are always opening in the direction of the least effective stress as in this case mud would not be able to penetrate the pre-existing weaknesses in the rock.

One of the first significant investigations into geometrical aspects of hydrofracturing was carried out by Garagash and Detournay (1996) as a follow-up investigation of results found by Haimson and Zhao (1991) and Schmitt and Zoback (1992). Initially a study of pressure drop rate during the hydrofracturing was carried out, and fracture geometries were used for the description of the leak-off function and lubrication equations, which govern the rate of fluid pressure loss through the porosity over the area of the fracture and fluid flow rate in the fracture respectively. Similar research was carried out by Detournay and Cheng (1995) where the effects of poroelasticity on the pressure drop were investigated and numerical solutions to describe it were derived. Fracture opening aperture was discovered to play an important role in describing this relation. In their earlier study Detournay and Cheng (1991) have investigated geometries (aperture and length) of the fracture and created profiles for fractures with different poroelastic responses. These studies were initially showing that fracture length and aperture relationship is not linear for rocks, even when only poroelasticity was being changed and that the behaviour of fracture geometries can be more complex.

Leguillon (2001) performed a theoretical calculation using field observation data on fracture opening and propagation from the naturally occurring hydrofractures. He used empirical data from Parvizi et al. (1978) measurements of crack lengths in limestones as well as results from plexi-glass fracturing experiments from Hutchinson (2000) and Mohammed and Leichti (2000) to correlate the lengths of the fractures formed to the critical stress intensity factor of the material.

A detailed investigation into a parametric dependency of the fluid driven fracture propagation was carried out by Garagash (2006) and Bunger et al. (2005). These authors firstly differentiated between plane strain fractures and radially symmetric (penny-shaped) fractures. They provide a complex mathematical formulation based on linear elastic fracture mechanics and Newtonian fluid mechanics for calculating fracture geometry describing parameters such as length and aperture. The theoretical fracture length is expressed as a function of material physical properties, such as Young's modulus, Poisson's ratio, fracture toughness and fluid properties, such as viscosity, injection rate and leak-off coefficient (a function of the permeability and porosity). The conclusion that authors derive at is that the mechanical properties of the rock have relevance in determining the fracture length only on a small scale. When it comes to scales which are more characteristic of a typical hydrofracturing operation, changes in the fluid viscosity have the most effect on the formed fracture length. Bunger and Detournay (2008) carried out a number of practical experiments where they hydraulically fractured and measured the aperture of the fracture in polymethyl methacrylate (PMMA) and glass. The fracture aperture was plotted against the distance from the crack tip. The relationship between the two parameters followed a 2/3 asymptote for the region closer to the fracture tip while the region closer to the injection point followed a 1/2 asymptote. Lecampion et al. (2017) then took that theory a step further and assumed that fluid might not be present at the fracture tip at the moment of fracturing. Their discoveries through a series of experiments showed that there is a significant dependency on the fluid lag, meaning that at the moment of the fracturing there is no fluid in the fracture tip. The lubrication equation is then used to account for the time required for the fluid to cover the distance between the injection point and crack tip. This assumption was then further experimentally confirmed by Xing et al. (2017). This approach provides a robust physical and mathematical solution, which has been throughout backed up by laboratory experiments. However, it lacks some details that are more typical to the real world application. As one of the examples, all the laboratory experiments have a predesignated notch at the injection point, meaning the direction of fracture propagation is predetermined. Another downside to this approach is the fact that the materials used have near zero porosity, and therefore no seepage forces are active. Although this approach

provides a robust problem solution in the laboratory environment, it lacks several important aspects that can be found in real life rocks.

2.3.3 Hele-Shaw cell

The Hele-Shaw cell was first developed by a British inventor, scientist and engineer Henry Selby Hele-Shaw. While teaching fluid mechanics at the University College Liverpool, Hele-Shaw was designing experiments to demonstrate various fluid properties to his students. In an attempt to demonstrate fluid flow dynamics, when the fluid has to flow around the object, Hele-Shaw combined two glass plates with the viscous fluid in between them. After running demonstration, he realised that fluid flow would remain laminar at all velocities. This concept was firstly published by Hele-Shaw in 1897, and further apparatus schematics and discussion on the working principles were made available to now widely known publications in 1898 and 1899 (Hele-Shaw, 1898; Hele-Shaw, 1899).

Since then the Hele-Shaw cell has been used for a multitude of research purposes by mathematicians (Howison, 1986), physicists (McLean and Saffman, 1981), engineers (Paterson, 1981) and lately also geologists (Mango et al., 2004; Tsai et al., 2013; Perugini and Pol, 2005). The concept that one fluid or multiple fluids with different viscosities are going to have laminar flow at all times allows to greatly simplify quantitative analysis behind the processes observed. The classical Hele-Shaw cell has been used to study the interaction between two fluids of different viscosities (Saffman and Taylor, 1958). One of the most famous problems described in the literature is the Hele-Shaw free boundary problem, which has been studied for more than 60 years. The problem can be illustrated as if a blob of viscous fluid will be injected into space in a Hele-Shaw cell, which is occupied by another fluid of negligible viscosity. The two fluids are immiscible, and a fluid blob of the first substance is growing through injection at the middle of the horizontally oriented Hele-Shaw cell. The free boundary problem then can be characterised by the resulting motion of the interface between the two fluids and finding the shape of the evolving interface (Sethian and Smeraka, 2003). The fact that two fluids are immiscible means they mix on neither molecular nor macroscopic levels, meaning there is always a sharp boundary between them. In the geological concept, this idea has been used to study gas bubbles in magma (Sun and Beckermann, 2010).

The Hele-Shaw cell has also been used by mathematicians in studying pattern evolution (Islam and Gandhi, 2017). For this purpose, typically one fluid of varied viscosity is injected into space between the plates and then one of the plates is lifted. Besides the viscosity of the injected fluid, the velocity and vector of motion of the removed plate can be varied to study pattern forming processes (Islam and Gandhi, 2017). One of the first geological applications of the Hele-Shaw cells can be traced back to the study of Lemaire at al. (1991), where an effort to distinguish between viscous fingering and visco-elastic fracturing is made. The water was injected into smectite material with differentiated water ratio in it and angles between the fractures were measured. This approach was taken from a study by Viscek and Kertész (1988) where they let the injected water into bentonite filled Hele-Shaw cell and then left it open to let it dry. A similar study was carried out earlier by Van Damme and Lemaire (1990), where they analysed the geometries of cracks produced by air injections into mud. They discovered that despite fractures having different geometries and crack tip shapes in different viscosity muds, the branching scaling law stays the same. That means that the frequency on the fracture branching is proportional to the crack aperture. This shows that in theory even poorly consolidated materials can be used to recreate hydrofracturing conditions in the Hele-Shaw cell. In fact, it can even be used as an advantage as due to the softness of the material, the particle displacement response is a lot more exaggerated compared to tough materials. This will allow to better observe small-scale dynamics.

This idea has been recognised, and lately, significant research effort is put into investigating dynamics of fracturing in granular media. A numerical model was developed by McNamara et al. (2000) confirming with Hele-Shaw experiments that the gas follows Darcy's law while granular media acts according to Newtonian physics. Initially, this relationship was intensely studied to better understand bed fluidisation during sedimentation as a function of burden overpressure (Vinningland et al., 2007a; Vinningland et al., 2007b). Another research direction was studying the formation of the patterns of air being injected into compacted granular medium. The first study, where the methodology resembling the one employed in this study (described in Chapter 3) was used, was carried out by Johnsen et al. (2006). The experiment consisted of a horizontally oriented, confined radial Hele-Shaw cell with the injection point at the centre of the cell.

Both Newtonian and Non-Newtonian fluids were injected at varied pressures, and four displacement regimes were determined depending on the injection pressure. In the first case, no fracture was created, and only local particle displacement in the surrounding area was registered as injected fluid dissipated through the pore space in between the grains. In the second case radial, equal in length fractures would start forming. If the pressure was increased further, the radial symmetry was lost, and branching occurred. The length of the structure would then be proportional to the increase in the injected fluid pressure rate. Following the Saffmann-Taylor instability, the driving pressure gradient was larger ahead of the most developed fracture, and it tended to grow at the expense of the other fractures. Lastly, at the largest of the injection pressures, the surrounding granular media would fluidise. This behaviour is unwelcome when studying fracture propagation, thus injected fluid pressure must be carefully calibrated. A similar setup was used by Cheng et al. (2008). They used air injection into granular media in the radial Hele-Shaw cell to study fractal growth. They as well discovered that branching and fracture length can be scaled with the injected pressure rate. However, the more significant observation was that fractures tend to widen before they branch off, which shows signs of elastic behaviour in the granular medium. These experiments were carried out in a zero-surface tension setup. Therefore, in a regular setup, elastic behaviour would be expressed stronger. The follow-up study by Johnsen et al. (2008) looked at what parameters determine the characteristics in the fractures formed and tried varying viscosity of the injected fluid (oil versus air), the thickness of the granular media and injection pressure. They discovered that mobilities of the two systems are the same when scaled with the respect to fluid viscosity. However, the mobility of both, oil and air, systems is an increasing function of the cell thickness. This demonstrates that fluid viscosity does not play a significant role in the fractures generated when scaled accordingly but the packaging of the granular media does. The more compressed it is, the more it behaves like a solid. Another conclusion that authors made is that air tends to seep through the pore spaces among the granular elements and decompacts them. This creates zones on the sides of the fractures as well as in front of them through which stress buildup is released alongside the fracturing process. A similar study was carried out by Niebling et al. (2012), where they were injecting air into an elongated horizontally oriented Hele-Shaw cell. Instead of

changing viscosity, the only degree of freedom in the experiments was the gas injection rate. It was determined that the fracture propagation position in time increases with the square root of the injection pressure. Also, they did a geometrical description of the formed fractures and found that higher injection rates generate features that more closely resemble fractures and that these are more branched. However, again if pressures are too high the system fluidizes.

2.4 Source Mechanism

The source mechanism describes the geometry of a homogeneous displacement on a fault plane (Aki, 1968). The recordings (seismograms) of the waves emitted by the slip are used to study the geometry of the fracture. This operation is based on the fact that the radiation pattern of the seismic waves depends on the geometry of the fault (Kwiatek, 2013). In the majority of the cases, an assimilated seismic source in the homogeneous medium can be described by a value called general seismic moment tensor (Jost and Hermann, 1989, Vavrycuk, 2001).

2.4.1 Thermodynamics and elastic dynamics.

The first law of thermodynamics implies that the energy balance during active material deformation can be written down as

$$d\Omega/dt + dQ/dt = d(K + U)/dt \tag{2.1}$$

where Ω, Q, K and U are mechanical work, heat, kinetic energy and internal energy, respectively, all in SI units expressed per unit mass or volume. Internal energy refers to an intrinsic potential such as elastic strain energy, magnetic field and gravity (Ben-Zion, 2003). In the case, when internal energy is known and is expressed as a function of strain ε and entropy S, it forms a complete equation of state, which allows to obtain all the other equilibrium properties of a deforming system, such as specific heat and stress-strain relation via differentiation. For this application, it is preferable to use strain and temperature T as independent variables, in which case the equation of state can be expressed as

$$F = U - TS \tag{2.2}$$

where *F* is force, *U* and *S* are per unit mass or volume.

The second law of thermodynamics states that inside the closed system entropy production rate must be either null or positive

$$dS \geq 0 \tag{2.3}$$

where being 0 characterizes reversible processes (elastic deformation), while positive values indicate irreversible ones (plastic deformation, e.g. fractures).

The moduli tensor c_{ijkl} and stress tensor σ_{ij} of the elastic deformation are derived from the strain density function *W* as

$$c_{ijkl} = \partial^2 W / \partial\varepsilon_{ij}\,\partial\varepsilon_{kl} \tag{2.4}$$

and

$$\sigma_{ij} = \rho' \,\partial \mathrm{W} / \partial\varepsilon_{ij} \tag{2.5}$$

where ρ' is mass density in situations where *W* energy density refers to cases per unit or 1 in situations where mass density is per unit volume (Aki and Richards, 1980). For deformation in adiabatic conditions (energy is transferred purely as work, without heat exchange) *W* can be described by *U*, while isothermal deformation is *F* (Lakshminarayana, 1995).

Elastic moduli, strain and stress tensors all have the following symmetry properties.

$$c_{ijkl} = c_{jikl} = c_{ijlk} = c_{klij} \tag{2.6}$$

$$\varepsilon_{ij} = \varepsilon_{ji} \tag{2.7}$$

$$\sigma_{ij} = \sigma_{ji} \tag{2.8}$$

Taking into account the abovementioned properties and definition, the strain energy density per unit volume in the linear elastic solid is

$$W = \frac{1}{2} c_{ijkl}\varepsilon_{ij}\varepsilon_{kl} = \frac{1}{2}\sigma_{ij}\varepsilon_{ij} \tag{2.9}$$

Since the strain and stress are symmetric and real-valued, these values can be transformed and diagonalised to a coordinate system consisting of three orthogonal directions (principal axes) that are normal to planes subjected to normal stress and strain components (principal stresses and strain values).

The stress-strain relation for a linear isotropic elastic solid can be expressed as

$$\sigma_{ij} = \lambda\delta_{ij}\varepsilon_{kk} + 2\mu\varepsilon_{ij} \tag{2.10}$$

which is governed by the two independent elastic moduli, called the Lame constants λ and μ (Malvern, 1969) where δ is the Kronecker delta function. Lame constants and bulk modulus K can be defined in terms of Young's modulus E and Poisson ratio v as

$$\mu = E/[2(1+\nu)] \tag{2.11}$$

$$\lambda = \nu E/[(1+\nu)(1-2\nu)] \tag{2.12}$$

$$K = E/[3(1-2\nu)] = \lambda + 2\mu/3 \tag{2.13}$$

In the case of uniaxial elastic deformation of the homogeneous isotropic material under tensile stress σ_{11}, the axial strain is $\varepsilon_{11} = \sigma_{11}/E$, $\varepsilon_{22} = \varepsilon_{33} = v\varepsilon_{11}$ and shear strain values are zero. For infinitesimal deformation of a homogeneous isotropic elastic solid under pressure $-p$, the normal stress components are all equal to the pressure applied $\sigma_{11} = \sigma_{22} = \sigma_{33} = -p$ and the relative reduction in volume can be expressed as $\Delta V/V = (\varepsilon_{11} + \varepsilon_{22} + \varepsilon_{33}) = -p/K$.

The Cauchy equation of motion for a continuum in terms of stress and displacement u is

$$\sigma_{ij,j} + f_i = \rho\ddot{u}_i \tag{2.14}$$

where f_i is the i component of body force per unit volume and $\ddot{u}_i$ is the time derivative of the displacement (Lay and Wallace, 1995).

Combining equations 2.10 and 2.14, and taking into account the definition of infinitesimal strain as a function of displacement gradients $\varepsilon_{ij} = \frac{1}{2}(u_{i,j} + u_{j,i})$, gives us Navier equation of motion for the linear homogeneous elastic solid

$$(\lambda+\mu)u_{k,ki} + \mu u_{i,kk} + f_i = \rho\ddot{u}_i \tag{2.15}$$

For the two types of plain body waves, equation 2.15 has solution $u(x,t) = \hat{p}u(\hat{n} \cdot x - ct)$, where u is an arbitrary pulse shape propagating in a direction $\hat{n}$, c is velocity, and $\hat{p}$ represents particle motion polarization (Aki and Richards, 1980). For longitudinal dilatational P waves, equations stand as

$$c = v_p \equiv \sqrt{\frac{\lambda + 2\mu}{\rho}} \qquad and \qquad \hat{p} \times \hat{n} = 0 \tag{2.16}$$

while for transverse shear S waves, it is

$$c = v_s \equiv \sqrt{\frac{\mu}{\rho}} \qquad and \qquad \hat{p} \cdot \hat{n} = 0 \tag{2.17}$$

The strain energy in a linear isotropic elastic solid per unit volume of a plane P or S wave is

$$W = \frac{1}{2}\sigma_{ij}\varepsilon_{ij} = \frac{1}{2}\rho\dot{u}^2 = K \tag{2.18}$$

where K is the kinetic energy density per unit volume. The energy transmission rate of flux (energy per unit time across the area unit propagating in a perpendicular direction to the plane) is $v_s\rho\dot{u}^2$ for S waves and $v_p\rho\dot{u}^2$ for P waves (Vavrycuk, 2001).

The elastodynamic Green function $G_{ij}(x,t;x',t')$ can be used to synthesize the displacement field generated by a distribution of body forces and surface traction, giving the *i* component of displacement at source location x at time t as can be seen due to localized unit body force at observation location x' at time t' propagating in the *j* direction (Aki and Richards, 1980; Aki and Richards, 2002). The elastodynamic Green function satisfies the Navier equation of motion for a linear elastic solid

$$\rho\frac{\partial^2}{\partial t^2}G_{ij} = \delta_{ij}\delta(x - x')\delta(t - t') + \frac{\partial}{\partial x_n}(c_{inkl}\frac{\partial}{\partial x_l}G_{kj}) \tag{2.19}$$

where $\delta()$ is Dirac delta function. To be a valid function from an algebraic perspective, determination of G_{ij} must meet initial conditions ($G = \frac{\partial G}{\partial t} = 0$ for $t \leq t'$ and $x \neq x'$).

If G_{ij} satisfies homogeneous boundary conditions (zero traction or zero displacement) on S, it has the following spatiotemporal reciprocity properties

$$G_{ij}(x,t;x',t') = G_{ij}(x',-t';x,-t) \tag{2.20}$$

The displacement field in a solid described by volume *V* and surface *S* altered by the body force *f* and surface traction *T* can be expressed using the Green function response that satisfies stress-free boundary conditions on *S* (Farrell, 1972) as

$$u_i(x,t) = \int_{-\infty}^{t} dt' \int_V G_{ij}(x,t;x'.t') f_j(x',t') d^3\,x' + \int_{-\infty}^{t} dt' \int_S G_{ij}(x,t;x',t') T_j(x',t') d^2x'. \tag{2.21}$$

2.4.2 The general seismic moment tensor and representation integrals

The total strain at (x,t) may be expressed as a sum of elastic and plastic contributors (Fig 2.3) (Jost and Hermann. 1989). The plastic strain tensor, also referred to as transformational strain, defines the seismic potency density tensor per unit volume

$$\varepsilon_{ij}^{P}(x,t) \equiv seismic\ potency\ density\ tensor. \tag{2.22}$$

The corresponding transformational stress (the glut stress) defines the seismic moment density per unit volume

$$c_{ijkl}\varepsilon_{kl}^{P}(x,t) \equiv m_{ij}(x,t) \equiv seismic\ moment\ density\ tensor. \tag{2.23}$$

It is assumed in the upper mentioned relation that the elastic moduli tensor is time invariant (Kostrov, 1974). Since that is not the case during faulting, c_{ijkl} should be interpreted as a tensor of effective elastic constants, where actual values vary depending on the application. This allows, as in the case where ε_{kl}^{P} is identified as the elastic strain drop tensor during faulting, to interpret m_{ij} as the corresponding stress drop tensor $\Delta\sigma_{ij}$ and c_{ijkl} as an effective elastic constant linking drop in elastic strain tensor to the stress drop tensor (Ben-Zion et al., 2003).

Further, the seismic potency tensor can be described as

$$P_{ij}(t) = \int_V \varepsilon_{ij}^P \, dV \tag{2.24}$$

where the integral represents an inelastically deformed volume in the faulting source region. This allows expressing the seismic moment tensor as

$$M_{ij}(t) = \int_V c_{ijkl} \, \varepsilon_{ij}^P \, dV = \int_V \Delta\sigma_{ij} \, dV \tag{2.25}$$

The seismic potency for the case of discontinuity Δu across surface S with a vector normal $\hat{n}$ can be described as

$$P_{ij}(t) = \frac{1}{2}\int_S \left(\Delta u_i n_j + \Delta u_j n_i\right) dS \tag{2.26}$$

This allows expressing the moment tensor for the isotropic media as

$$M_{ij}(t) = \int_S c_{ijkl} \Delta u_k n_l \, dS \tag{2.27}$$

In the scalar values, the potency of the fault slip on a planar surface is the amount of relative fault wall movement to each other integrated over the fault area or, in other terms, the equivalent of the spatial average of movement of fault fragments over the fault area A (Scholz, 2002)

$$P_o = \langle \Delta u \rangle A \tag{2.28}$$

This gives us the corresponding scalar seismic moment as

$$M_o = \mu P_o = \mu \langle \Delta u \rangle A \tag{2.29}$$

where μ is the effective rigidity of the source area.

If the given values are applied in the terms of observed displacement field at (x, t), it can be expressed as a function of m_{jk} $(= c_{jkpq} n_q \Delta u_p)$ along the internal surface of the fault S (Aki and Richards, 2002)

$$u_i(x,t) = \int_{-\infty}^{t} dt' \int_S c_{jkpq}(x') n_p(x') \Delta u_p(x', t') \times [\partial G_{ij}(x, t; x't') / \partial x'_k] d^2x' \tag{2.30}$$

Because the displacement along the surface S is discontinuous, equation 2.30 needs to be rewritten to accommodate for the distribution of the displacements

$$u_i(x,t) = \int_{-\infty}^{t} dt' \int_S \Delta u_j(x',t') B_{ij}(x,t;x',t',\hat{n}) d^2x' \tag{2.31}$$

where B_{ij} represents the *i* component of displacement at (x,t) due to point unit dislocation in the *j* direction at (x',t') across the surface S where $\hat{n}(x')$ is unit normal. The two end members of the displacement mode are represent by $\hat{e}^j \cdot \hat{n} = 0$ ($\hat{e}^j$ being the movement vector in the *j* direction) for the scenario of the shear crack and $\hat{e}^j \times \hat{n} = 0$ in the case of a tensile crack.

2.4.3 Moment tensor properties

If we rewrite equation 2.27 the general moment tensor of the fault movement is described as

$$M_{pq} = c_{jkpq} A \Delta u \, v_k n_j \tag{2.32}$$

where *c* is the tensor of the elastic properties

$$c_{jkpq} = \lambda \delta_{jk} \delta_{pq} + \mu(\delta_{jk}\delta_{pq} + \delta_{jp}\delta_{kq}) \tag{2.33}$$

where the Kronecker delta function is used. As per other parameters in equation 2.32, A is the area of the fault, *u* is an amount of homogeneous displacement of the fault, v_k and n_j are respectively vectors normal and perpendicular to the fault surface. The first three terms represent the magnitude of the moment tensor. The moment tensor is the second order tensor representing nine force systems (Jost and Herrmann, 1989).

$$M = \begin{bmatrix} M_{11} & M_{12} & M_{13} \\ M_{21} & M_{22} & M_{23} \\ M_{31} & M_{32} & M_{33} \end{bmatrix} \tag{2.34}$$

For the computational purposes the moment tensor for tensile fault segment can be decomposed into a series of functions of fault-parallel movement (v) and fault-normal movement (n) vectors (Gasperini and Vannucci, 2003; Vavrycuk, 2011) such as:

$$M_{ij} = M_o \begin{bmatrix} 2n_x v_x & n_x v_y + n_y v_x & n_x v_z + n_z v_x \\ n_x v_y + n_y v_x & 2n_y v_y & n_y v_z + n_z v_y \\ n_x v_z + n_z v_x & n_y v_z + n_z v_y & 2n_z v_z \end{bmatrix} \tag{2.35}$$

where

$$n_x = -\sin\delta \sin\phi_s \tag{2.36a}$$

$$n_y = \sin\delta \sin\phi_s \tag{2.36b}$$

$$n_z = -\cos\delta \tag{2.36c}$$

and

$$v_x = (\cos\lambda \cos\phi_s + \cos\delta \sin\lambda \sin\phi_s)\cos\alpha - \sin\delta \sin\phi_s \sin\alpha \tag{2.37a}$$

$$v_y = (\cos\lambda \sin\phi_s + \cos\delta \sin\lambda \cos\phi_s)\cos\alpha - \sin\delta \cos\phi_s \sin\alpha \tag{2.37b}$$

$$v_z = -\sin\lambda \sin\delta \cos\alpha - \cos\delta \sin\alpha \tag{2.37c}$$

In this case, the coordinate system x, y and z are directed to the North, East and down, respectively. The four degrees of freedom are angles ϕ_s (strike), δ (dip), λ (rake) and α (tensile angle or angle between the fault surface and fault wall relative displacement vector) (Fig. 2.7).

The moment tensor depends on the seismic source orientation and strength. The three diagonal elements represent vector dipoles while the six off-diagonal elements represent force couples. The sum of the eigenvalues denotes a change in the source, the “isotropic part” (“IP”). A positive sum indicates an “explosion” (e.g., nuclear test), and a negative sum indicates an “implosion”. If one of the eigenvalues vanishes, the deviatoric moment tensor represents a pure “double couple” (“DC”). If none of the eigenvalues vanishes and their sum is still zero, the tensor can be decomposed into a major and minor double couple – or into a double couple and a compensated linear vector dipole (“CLVD”), a vector that is corrected for the effect of the volume change (Jost and Hermann, 1989; Vavrycuk, 2001).

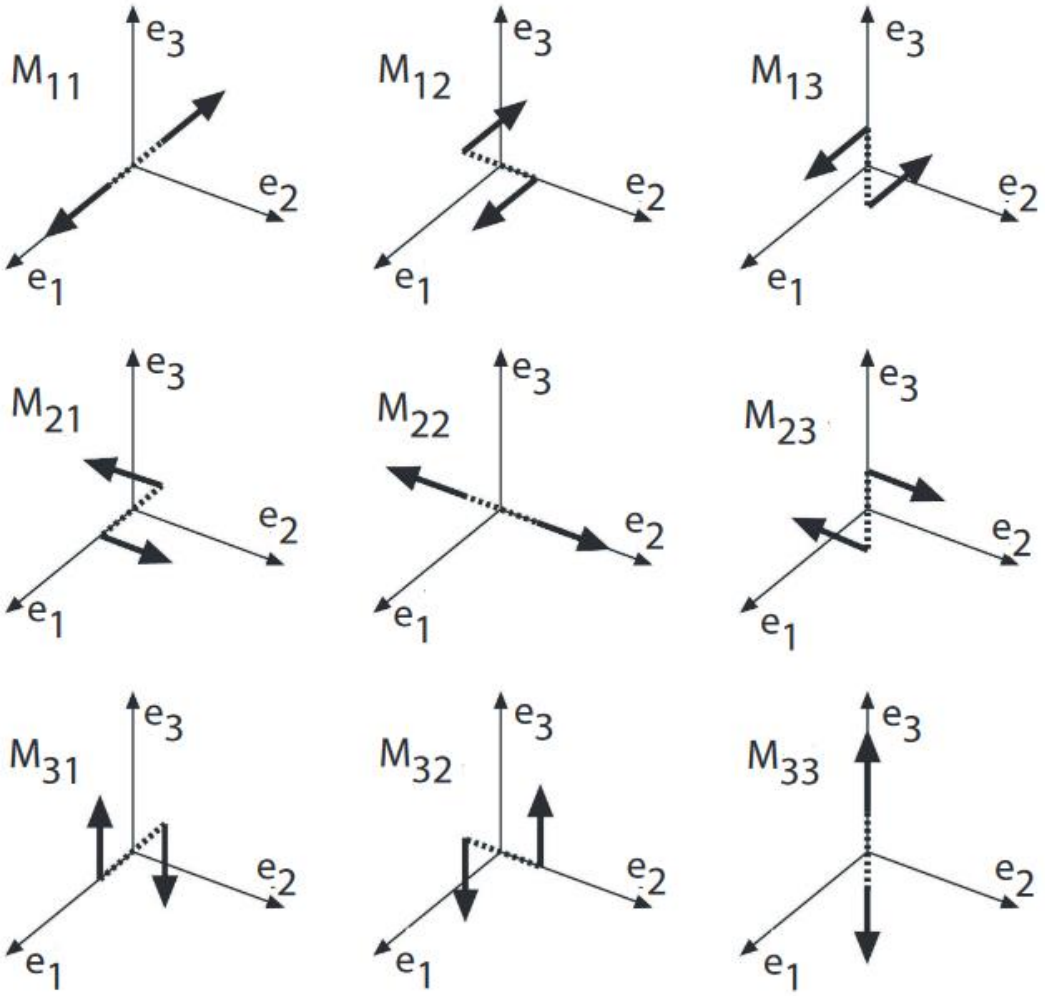

Figure 2.3. Visual representation of the nine seismic source components. Moment tensor depends on the seismic source orientation and strength. The three diagonal elements represent vector dipoles towards North, East and Down in the Cartesian coordinate system, while the six off-diagonal elements represent force couples (Jost and Hermann, 1989).

A simple way to decompose the moment tensor via deviatoric eigenvalues $M_1 \geq M_2 \geq M_3$, where we compute ε = -M_3/M_1 is as

$$M = \begin{bmatrix} M_1 & 0 & 0 \\ 0 & M_2 & 0 \\ 0 & 0 & M_3 \end{bmatrix} = m_{iso} + m_{dev}$$

(2.38)

where

$$m_{iso} = \frac{1}{3}\begin{bmatrix} tr(M) & 0 & 0 \\ 0 & tr(M) & 0 \\ 0 & 0 & tr(M) \end{bmatrix} \qquad (Isotropic\ part)$$

(2.39a)

$$m_{dev} = (1-2\varepsilon)\begin{bmatrix} 0 & 0 & 0 \\ 0 & -M_3 & 0 \\ 0 & 0 & -M_3 \end{bmatrix} \qquad \left(Douple\ Couple\ (DC)\right)$$

(2.39b)

$$+\varepsilon\begin{bmatrix} -M_3 & 0 & 0 \\ 0 & -M_3 & 0 \\ 0 & 0 & -M_3 \end{bmatrix} \ (Compnesated\ Linear\ Vector\ Dipole\ (CLVD))$$

(2.39c)

with $tr(M)$ being the trace of the diagonilised moment tensor M and ε is the measure of the size of CLVD component compared to the DC and Isotropic part. ε=0 for a pure double couple and 0.5 for a pure CLVD (Vavrycuk, 2007).

Lastly, we can calculate the percentage of all the three components by looking at the proportions of the three components of the moment tensor (Vavrycuk, 2005).

$$P_{ISO}^{\%} = \frac{\frac{1}{3}tr(M)}{|M_1|}.100$$

(2.40a)

$$P_{CLVD}^{\%} = 2|\varepsilon|(100 - \left|P_{ISO}^{\%}\right|)$$

(2.40b)

$$P_{DC}^{\%} = 100 - \left|P_{ISO}^{\%}\right| - \left|P_{CLVD}^{\%}\right|$$

(2.40c)

where M_1 is the largest absolute value of the three eigenvalues. The percentage for the isotropic component is always positive, while CLVD and double couple components are positive for the expansive motions and negative for the compaction events (Vavrycuk, 2001).

The double couple mechanism describes sliding over a fault surface and is used to describe tectonic earthquakes. The CLVD tensor can describe several types of seismic sources. Combination of a CLVD and isotropic tensor describes the tensile opening of the fracture. Therefore, sources with the CLVD can be found in magmatic zones and also in reservoirs which are under the subject of fluid injection operations (Aki, 1984; Kanamori. 1994). Figure 2.4. shows the basic representation of the three possible force systems used for isotropic, double-couple and CLVD compositions as well as radiation patterns that they emit (Equation 2.41)

$$\mathrm{F}^k(\phi, i) = \left(\sum_{i=1}^{6} M_i\right) \vec{\gamma}\,(\phi, i)\, \overrightarrow{\gamma'}\,(\phi, i) \tag{2.41}$$

where F^k is the radiation pattern for the wave *k* (P, S, SH or SV), ϕ is the azimuth of the seismic wave radiating from the source, $\vec{\gamma}$ is a direction vector to the source and $\overrightarrow{\gamma'}$ is the particle movement direction vector.

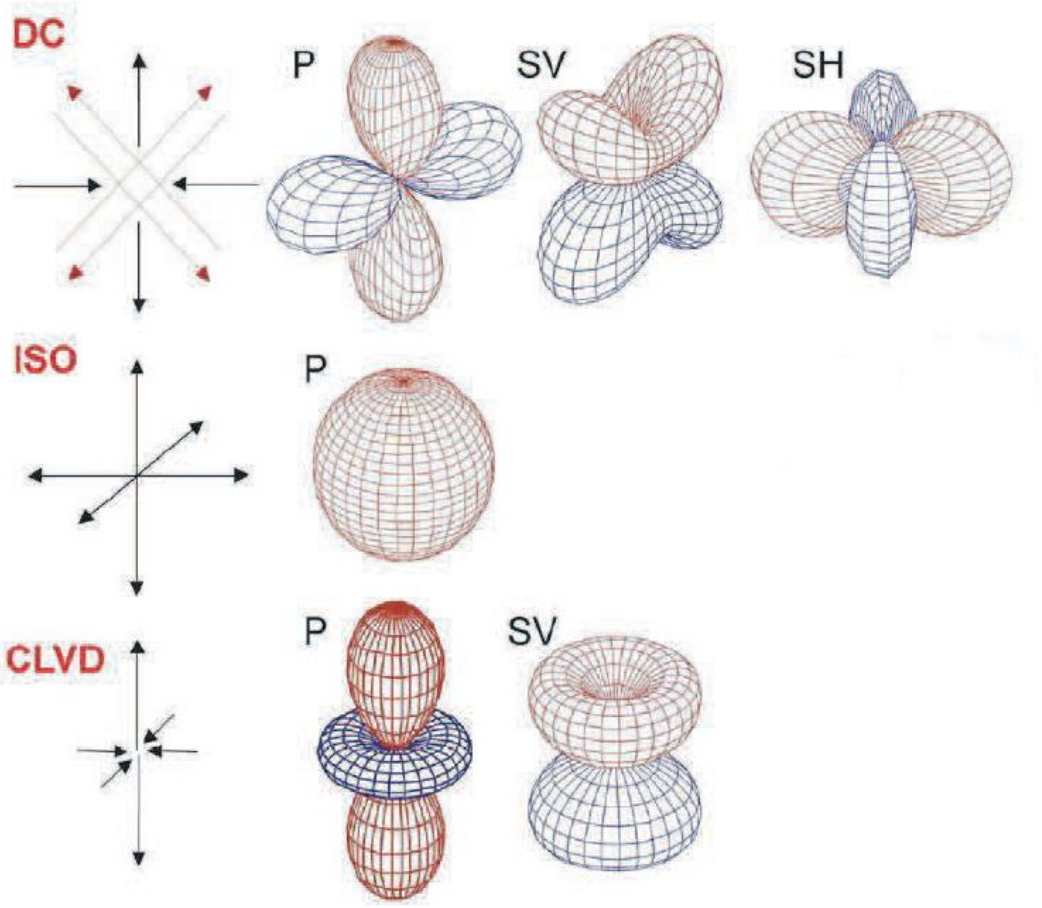

Figure 2.4 Force systems and radiation diagrams of P, SV and SH (compression in red and dilation in blue) for a double-torque source, isotropic and CLVD (Sileny and Milev, 2008).

2.5 Elastodynamic waves

Elastodynamic waves are naturally occurring phenomena caused by the radiation of waves in the continuous medium due to rapid stress relief. In geological settings it occurs when there is a sudden stress redistribution in the rock due to internal changes and alterations in its structure (fracturing, granular crushing, bond

breakage) caused by one or more internal or external agents (mechanical forces, chemical alteration, temperature changes) (Huang et al., 1998).

The Navier equation of motion has solutions in terms of P and S plane body waves and elastodynamic Green functions for the linear elastic solid (Aki and Richards, 2002). Seismic waves and with them associated additional seismic phases are produced and reflected, transmitted and converted within stress-free surfaces and interfaces that are separating solids with different elastic properties. A solid with a free surface, typically oriented horizontally, is referred to as a half space. Shear waves with horizontal polarisation within the horizontal half space or within horizontally layered media are called SH waves. These waves excite on a horizontal plane due to a single stress component ($\sigma_{zy,}$ where z is normal to the horizontal plane and y is the polarization direction). On the contrary, the corresponding S waves with vertical polarisation are called SV waves, and they excite on horizontal planes due to other two stress components (σ_{zx} and σ_{zx}) (Lay and Wallace, 1995).

Any wavefield can be represented using only plane waves as they do account for a complete basis of functions (Kuster and Toksöz, 1974). In practice, they are useful and are mainly used to solve problems within the Cartesian coordinate system and geometry (planar surfaces where boundary conditions must be met) as well as in high-frequency seismology where the wave travel distance is much greater than the wavelength. The other two sets of functions that are used to solve seismological problems are Bessel/Henkel solutions and spherical harmonics (Kuster and Toksöz, 1974). The Bessel/Henkel method is used to solve problems involving cylindrical or spherical geometry while spherical harmonics provide a natural representation of the Earth's free oscillations as well as are used to solve low-frequency problems such as surface waves.

The elastodynamic Green function is used to describe wave propagation in an unbound homogeneous solid medium. The function has P and S wave components.

$$G_{ij}(x, x', t) = G_{ij}^{P} + G_{ij}^{S} \tag{2.42}$$

where

$$G_{ij}^{P} = -\left(\frac{\partial^2}{\partial x_i \partial x_j}\right) h(r, t; v_P) \tag{2.43}$$

and

$$G_{ij}^{S} = -\left(\frac{\delta_{ij}\nabla^2 - \partial^2}{\partial x_i \partial x_j}\right) h(r,t;v_S)$$

(2.44)

with

$$h(r,t;c) = -\frac{1}{4\pi\rho r}\left(t - \frac{r}{c}\right) H\left(t - \frac{r}{c}\right).$$

(2.45)

In equations 2.42 to 2.45, the source has a zero time, r denominates distance between source and receiver, v_P and v_S are P and S wave velocities, respectively, and H is the Heaviside unit step function (Aki and Richards, 2002). The simplest definition of the Heaviside function is as the derivative of the ramp function:

$$H = \frac{\partial}{\partial x}\max\{x, 0\}$$

(2.46)

The elastodynamic Green function for the waves can be expressed in the frequency domain as

$$G_{ij}(x,x',\omega) = \frac{1}{4\pi\rho\omega^2}\left\{\delta_{ij}k_S^2 g(k_S r) - \frac{\partial}{\partial x_i}\frac{\partial}{\partial x_j}[g(k_P r) - g(k_S r)]\right\}$$

(2.47)

where ω is angular frequency, $k_S = \omega/v_S$ while $k_P = \omega/v_P$, $g(kr) = \exp(-ikr)/r$ when dealing with 3D solid and $g(kr) = i\pi H_0(kr)$ in the cases of the 2D solid with H_0 being the Hankel function of zero order.

The displacement field in an unbounded homogeneous isotropic medium generated by a distribution of the moment tensor m_{jk} can be described as

$$u_i\ (x,t) = u_i^P + u_i^S$$

(2.48)

where

$$u_i^{P\ or\ S}(x,t) = O_{ijk}^{P\ or\ S}\int_V \int_{-\infty}^{t} h(r, t-t'; v_{P\ or\ S}) \times m_{jk}(x't')dt'd^3x'$$

(2.49)

with

$$O_{ijk}^{P} = \partial^3/\partial x_i \partial x_j \partial x_k$$

(2.50)

and

$$O_{ijk}^{S} = \frac{1}{2}\left(\frac{\delta_{ij}\partial}{\partial x_k} + \frac{\delta_{ik}\partial}{\partial x_j}\right)\nabla^2 - \partial^3/\partial x_i \partial x_j \partial x_k$$

(2.51)

Combining equation 2.49 to 2.51 gives us far field approximation valid in cases where $r \gg \lambda$ and $r \gg a$ where λ is wavelength and a is source dimension (length of the rupture surface).

$$u_i^{P\ or\ S}(x,t) = \frac{R_{ijk}^{P\ or\ S}}{4\pi\rho r_o v_{P or S}^3} \int_V m_{jk}\left(x', t - r_o^{\cdot} - \frac{\gamma_\iota x'_\iota}{v_{P\ or\ S}}\right) d^3x'$$

(2.52)

where r_o is the distance between source and receiver, $\gamma_i = \partial r/\partial x_i = x_i/r$ are components of the unit vector in the source receiver direction, the integral term composites the source effect, while $R_{ijk}^{P\ or\ S}$ denotes radiation pattern function

$$R_{ijk}^{P} = \gamma_i\gamma_j\gamma_k$$

(2.53)

and

$$R_{ijk}^{S} = \frac{1}{2}(\delta_{ij}\gamma_k + \delta_{ik}\gamma_j) - \gamma_i\gamma_j\gamma_k$$

(2.54)

where R_{ijk}^{P} and R_{ijk}^{S} are radiation pattern functions for P and S waves respectively. The simplest case of fault slip is a unidirectional slip in the x_1 direction on the x_1-x_3 plane (Fig. 2.5), the corresponding far field displacement for this scenario is

$$u_i^{P\ or\ S}(x,t) = \frac{R_{i12}^{P\ or\ S} v_S^2}{2\pi\rho r_o v_{P or S}^3} \int_S \Delta u_1\,[x'_1, x'_3, t + (\gamma_1 x'_1 + \gamma_3 x'_3 + r_o)/v_{P\ or\ S}]d^2x'$$

(2.55)

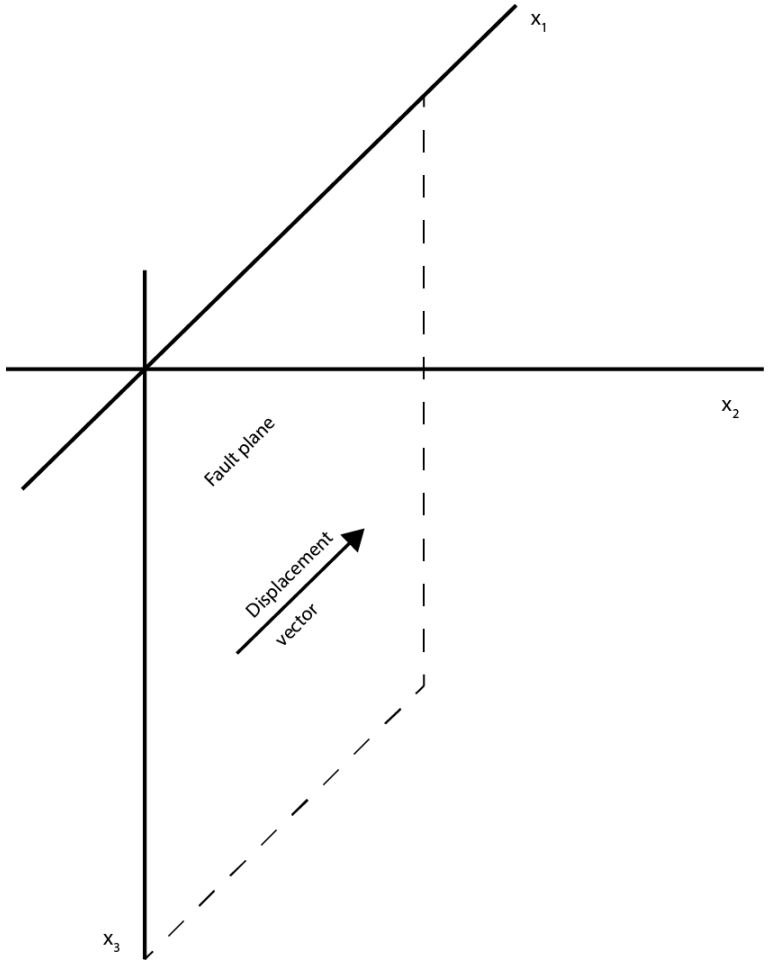

Figure 2.5. Schematic illustration of the unidirectional strike-slip fault, where the fault is located in the x_1-x_3 plane with slip occurring along x_1 axis.

The conditions for the far field $r \gg \lambda$ and $r \gg a$ are equivalent to the high frequency criterion $\omega \gg v_{P\ or\ S}/r$. This means that equation 2.55 does not represent the full extent of the low frequency components from the slip. Contrary to the limiting factors of the far field displacement, low frequency components are associated with more limiting conditions at the source. The point source approximation is valid for $\lambda \gg a$ and $r \gg \lambda$. This allows us to fully subdivide the displacement field into three components depending on the distance (near, intermediate, far) of the receiver as the medium response will differ in the terms of elasto-plasticity.

$$m_{jk} * G_{ij} = u_n^N(t) + u_n^{IP}(t) + u_n^{IS}(t) + u_n^{FP}(t) + u_n^{FS}(t)$$

(2.56)

where

$$u_n^N(t) = \left(\frac{15\gamma_i\gamma_j\gamma_k - 3\gamma_i\delta_{jk} - 3\gamma_j\delta_{ik} - 3\gamma_k\delta_{ij}}{4\pi\rho}\right) \times \frac{1}{r^4}\int_{r/v_P}^{r/v_S} \tau m_{jk}(t-\tau)d\tau$$

(2.57a)

$$u_n^{IP}(t) = \left(\frac{6\gamma_i\gamma_j\gamma_k - \gamma_i\delta_{jk} - \gamma_j\delta_{ik} - \gamma_k\delta_{ij}}{4\pi\rho {v_P}^2}\right) \times \frac{1}{r^2} m_{jk}\left(t - \frac{r}{v_P}\right)$$

(2.57b)

$$u_n^{IS}(t) = -\left(\frac{6\gamma_i\gamma_j\gamma_k - \gamma_i\delta_{jk} - \gamma_j\delta_{ik} - 2\gamma_k\delta_{ij}}{4\pi\rho {v_S}^2}\right) \times \frac{1}{r^2} m_{jk}\left(t - \frac{r}{v_S}\right)$$

(2.57c)

$$u_n^{FP}(t) = -\frac{\gamma_i\gamma_j\gamma_k}{4\pi\rho {v_P}^3}\frac{1}{r} m_{jk}\left(t - \frac{r}{v_P}\right)$$

(2.57d)

$$u_n^{FS}(t) = -\frac{(\gamma_j\gamma_k - \delta_{jk})\gamma_k}{4\pi\rho {v_S}^3}\frac{1}{r} m_{jk}\left(t - \frac{r}{v_S}\right)$$

(2.57e)

where u is displacement at observation point x at the time t, m_{jk} is a general moment tensor at a point source, γ_n, γ_p, γ_q are cosines with the Cartesian coordinate system axes, and G_{ij} is a Green's function. When we consider the relation between internal force and moment tensor given by equation 2.56, we can find that the near field term has no time dependence (eq. 2.57a), but the intermediate and far field term has time dependence (eq. 2.57b to 2.57e). Therefore, the near field term represents the permanent static displacement due to the source, and the far field term represents the dynamic response or transient

seismic waves that are radiated by the source that cause no permanent displacement (Fig 2.6).

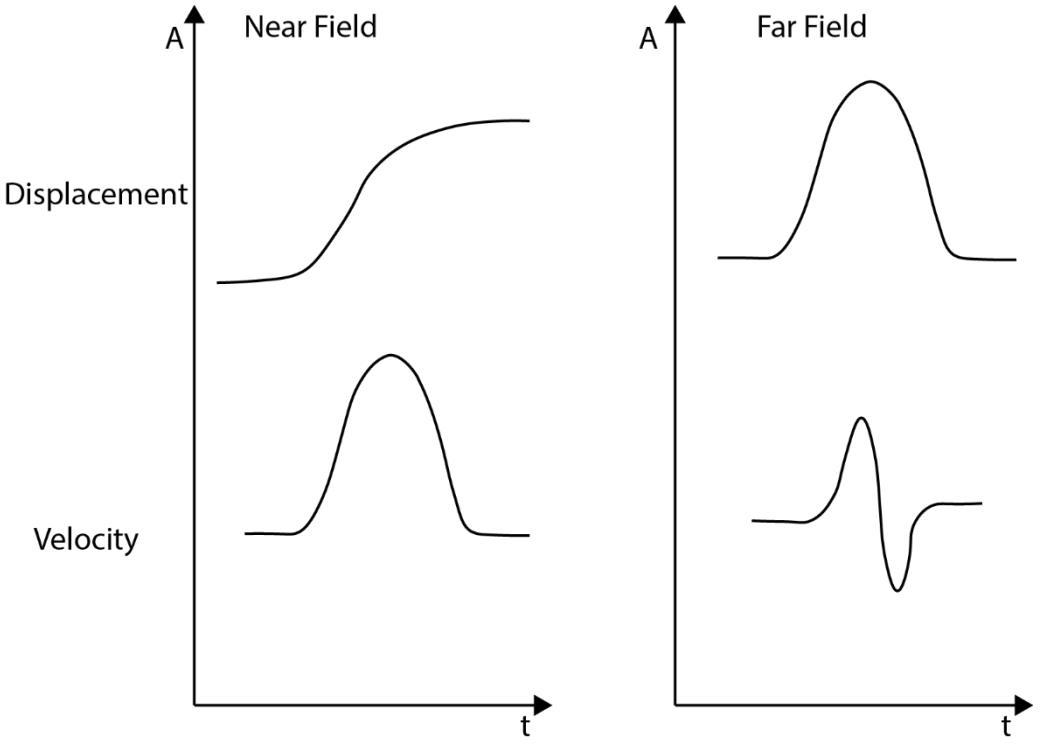

Figure 2.6. Relative particle displacement and velocity caused by seismic wavefield observed from a single point throughout the single rupturing event. Near field term represents permanent plastic displacement while far field show elastic response with no permanent displacement.

It can be seen that the decay rate of the displacement is increasing geometrically towards the source as it is $\frac{1}{r}$ for the far field waves, $\frac{1}{r^2}$ for intermediate field waves and $\frac{1}{r^4}$ for the near field waves. Near field, displacement can be usually observed within the direct proximity of the source while intermediate wave displacement can be seen up to a wavelength of a distance away from the source. If the distance from the source to the observation point is $r \gg \lambda$ (λ denotes wavelength), near field and intermediate field terms in the equation 2.52 are ignored.

2.5.1 Tensile fault slip geometries and moment tensor

To look at the motion along the fault surface during the event, which has a tensile component to it, we need to define the terms using the Cartesian coordinate system (Fig. 2.7). ϕ_s denotes strike of a fault as an angle measured clockwise from north so that the fault plane dips down to the right when looking in the direction of the strike. The dip of the fault is denoted as δ, which is an angle between the

horizontal surface downwards to the fault surface of the footwall. The slip λ_s is the angle of motion of the hanging wall relative to the footwall and it is measured in the counter clockwise direction. As we are using the Cartesian coordinate system the three planes and directions are north(x_1), east (x_2) and down (x_3). This gives us the unit slip vector $\hat{f}$ and unit normal $\hat{n}$ expressed via upper-mentioned fault parameters $(\phi_s, \delta, \lambda_s)$ as

$$\begin{aligned}\hat{f} = &(\cos\lambda_s \cos\phi_s + \cos\delta \sin\ \lambda_s \sin\phi_s)\hat{x}_1 \\ &+(\cos\lambda_s \sin\phi_s - \cos\delta \sin\ \lambda_s \cos\phi_s\ )\hat{x}_2 \\ &-\sin\delta \sin\ \lambda_s\, \hat{x}_3\end{aligned} \tag{2.58}$$

$$\hat{n} = -\sin\delta \sin\phi_s\, \hat{x}_1 + \sin\delta \cos\phi_s\, \hat{x}_2 - \cos\delta\, \hat{x}_3 \tag{2.59}$$

(Aki and Richards, 1980; Aki and Richards, 2002) where $\hat{x}_1$, $\hat{x}_2$ and $\hat{x}_3$ are unit vectors towards the north, east and down and can be seen as

$$\hat{x}_1 = \begin{bmatrix}1\\0\\0\end{bmatrix} \tag{2.60a}$$

$$\hat{x}_2 = \begin{bmatrix}0\\1\\0\end{bmatrix} \tag{2.60b}$$

and

$$\hat{x}_3 = \begin{bmatrix}0\\0\\1\end{bmatrix}. \tag{2.60c}$$

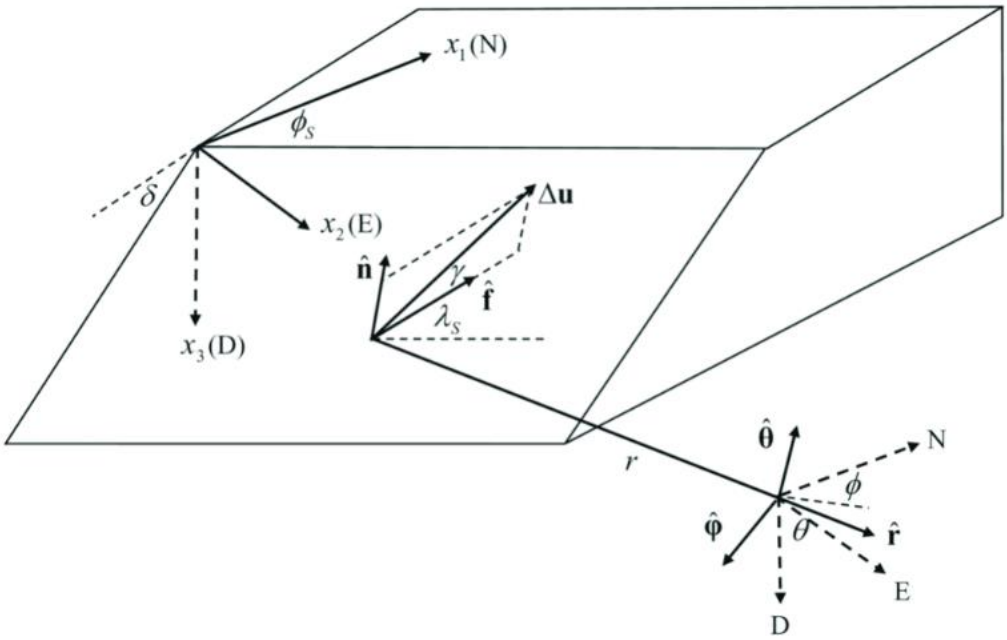

Figure 2.7. Tensile fault segment with relative values denoted in the Cartesian system, where x_1 is North, x_2 is East, x_3 is down. , Δu is the amount of the slip of the hanging wall relative to the footwall which can be subdivided into unit slip vector $\hat{f}$ and unit normal $\hat{n}$. Angles relative to the fault geometries are ϕ_s, δ and λ_s. ϕ_s denotes strike of a fault as an angle measured clockwise from the north so that fault plane dips down to the right when looking in the direction of the strike. The dip of the fault is denoted as δ, which is an angle between measured between the horizontal surface downwards to the fault surface of the footwall. The slip λ_s is the angle of motion of the hanging wall relative to the footwall and it is measured in the counter clockwise direction. $\hat{r}$ is the seismic ray propagation vector while $\hat{\theta}$ and $\hat{\varphi}$ are the other two of the three orthogonal vectors in the spherical coordinates perpendicular relatively to $\hat{r}$. Angles associated with $\hat{r}$ are θ - incident angle measured from the downward vertical axis and ϕ - azimuthal angle of the ray (Aki and Richards, 2002).

The scalar seismic moment is expressed as

$$M_0 = A\Delta u\mu \tag{2.61}$$

where A is the surface area of the fault, Δu is the amount of the slip of the hanging wall relative to the footwall and μ is the rigidity of the rock. Then the displacement vector function $\Delta u(t)$ can be further decomposed into a shear component tangent to the fault and into a tensile component normal to the fault surface

$$\Delta u(t) = \Delta u_{(n)}(t)\hat{n} + \Delta u_{(f)}(t)\hat{f} \tag{2.62}$$

where $\Delta u_{(n)}(t)$ is the tensile function and $\Delta u_{(f)}(t)$ is the shear function of the fault segment.

If the fault movement is purely shear (Mode II), the moment tensor can be expressed as a function of seismic moment and vector components of $\hat{f}$ and $\hat{n}$ as

$$m_{jk} = M_0(f_k n_j + f_j n_k)$$

(2.63)

The moment tensor for the tensile fault segment is also represented by the set of nine force couples with the forces and arms in *j* and *k* directions as a function of $\hat{n}$ and $\Delta u(t)$ in the isotropic medium as

$$m_{jk}(t) = A\{\lambda\delta_{jk}\Delta u_i(t)n_i + \mu[\Delta u_j(t)n_k + \Delta u_k(t)n_j]\}.$$

(2.64)

If we apply the terms expressed in equation 2.59 to the moment tensor equation for the tensile fault segment 2.64 and decompose it into nine components that can be expressed from geometrical properties and observations, we get

$$M_{11}(t) = \mu A[\left(\frac{\lambda}{\mu} + 2\,sin^2\delta\,sin^2\phi_s\right)\Delta u_{(n)}(t) - (sin\,\delta\,cos\,\lambda_s\,sin\,2\phi_s + sin\,2\delta\,sin\,\lambda_s sin^2\phi_s)\Delta u_{(f)}(t)]$$

(2.65a)

$$M_{22}(t) = \mu A[\left(\frac{\lambda}{\mu} + 2\,sin^2\delta\,cos^2\phi_s\right)\Delta u_{(n)}(t) + (sin\,\delta\,cos\,\lambda_s\,sin\,2\phi_s - sin\,2\delta\,sin\,\lambda_s\,cos^2\,\phi_s)\Delta u_{(f)}(t)]$$

(2.65b)

$$M_{33}(t) = \mu A[\left(\frac{\lambda}{\mu} + 2\,cos^2\delta\right)\Delta u_{(n)}(t) + sin\,2\delta\,sin\,\lambda_s\,\Delta u_{(f)}(t)]$$

(2.65c)

$$M_{12}(t) = \mu A[-sin^2\delta\,sin\,2\phi_s\,\Delta u_{(n)}(t) + (sin\,\delta\,cos\,\lambda_s\,cos\,2\phi_s + 0.5sin\,2\delta\,sin\,\lambda_s\,sin\,2\phi_s)\Delta u_{(f)}(t)]$$

(2.65d)

$$M_{13}(t) = \mu A[sin2\delta\,\sin 2\phi_s\,\Delta u_{(n)}(t) - (cos\,\delta\,cos\,\lambda_s\,cos\,\phi_s + cos\,2\delta\,sin\,\lambda_s\,sin\,\phi_s)\Delta u_{(f)}(t)]$$

(2.65e)

$$M_{23}(t) = \mu A[-sin2\delta\,cos\phi_s\,\Delta u_{(n)}(t) - (cos\,\delta\,cos\,\lambda_s\,sin\phi_s - cos\,2\delta\,sin\,\lambda_s\,cos\phi_s)\Delta u_{(f)}(t)]$$

(2.65f)

The symmetrical matrix components, in this case, are identical, such as

$$M_{12}(t) = M_{21}(t)$$

(2.65g)

$$M_{13}(t) = M_{31}(t)$$

(2.65h)

and

$$M_{23}(t) = M_{32}(t)$$

(2.65i)

In the case of hydrofracturing, we are dealing with relatively small fractures with limited heterogeneity, therefore, strike ϕ_s, dip δ, and slip λ_s can be assumed to be constants. The two parameters μ and λ are Lame parameters, which describe the physical properties of the rock and can be expressed by Poisson's ratio *v* as:

$$\frac{\lambda}{\mu} = \frac{2\sigma}{1-2\sigma}$$

(2.66)

2.5.2 P and S wave description in the homogeneous media for tensile fault

When the jump on the tensile fault segment occurs, a part of the energy generated is released as elastic waves (Lockner, 1993). The strength of the generated waves depends on the source parameters such as fault area and displacement amount as well as the radiation direction. The force couples can be decomposed into two components: the longitudinal component, which is a linear dipole with forces along the radiate direction, and the transverse component, which is a shear couple with the forces along the plane normal to the radiate direction. This linear force dipole will contribute to the generation of the P waves carrying the same strength and travelling in two opposite directions with the velocity *a*, whereas the shear force couple will generate S waves which are travelling with the velocity *β*. As was also demonstrated in the sections above, displacements generated by the P and S waves are proportional to the time derivatives of the moment tensor (Aki and Richards, 1980; Pujol and Hermann, 1990) as a function of the linear dipole and the shear couple. They will vary with regards to the radiation direction of the source.

Firstly, to deal with the geometrical solution for this problem, we have to define the three-unit column vectors for the principal axis in the Cartesian coordinate system, respectively, north, east, and down (Fig. 2.7)

$$\hat{r} = \sin\theta\cos\phi\,\hat{x}_1 + \sin\theta\sin\phi\,\hat{x}_2 + \cos\theta\,\hat{x}_3 \tag{2.67}$$

$$\hat{\theta} = \cos\theta\cos\phi\,\hat{x}_1 + \cos\theta\sin\phi\,\hat{x}_2 - \sin\theta\,\hat{x}_3 \tag{2.68}$$

$$\hat{\varphi} = -\sin\phi\hat{x}_1 + \cos\phi\hat{x}_2 \tag{2.69}$$

where θ is the incident angle measured from the downward vertical axis and ϕ is the azimuthal angle of the ray.

Next, if we rewrite the displacement equation for the P waves for the far field in the terms of the source couple radiating in the direction $\hat{r}$ and $\dot{M}$ being time derivative of the moment tensor for the tensile fault, we obtain

$$u^P = \frac{1}{4\pi\rho\alpha^3}\frac{1}{r}\left[\hat{r}^T\dot{M}(t - r/a)\hat{r}\right]\hat{r} \tag{2.70}$$

where super index *T* in $\hat{r}^T$ indicates a matrix transpose. The displacement by the S waves then is obtained by subtracting the longitudinal component $(\hat{r}^T M\hat{r})\hat{r}$ from $M\hat{r}$ at the source. As per expression in homogeneous media, it is given as

$$u^S = \frac{1}{4\pi\rho\beta^3}\frac{1}{r}\left\{\dot{M}(t - r/\beta)\hat{r} - \left[\hat{r}^T\dot{M}(t - r/a)\hat{r}\right]\hat{r}\right\} \tag{2.71}$$

The u^S is orthogonal to the $\hat{r}$ and is composed of the vertical and horizontal components. Decomposing u^S into u^{SV} and u^{SH} is achieved by introducing the other two of the three orthogonal vectors $\hat{\theta}$ and $\hat{\varphi}$ in the spherical coordinates. The SV and SH displacements, obtained by projecting $M\hat{r}$ in $\hat{\theta}$ and $\hat{\varphi}$ in the homogenous media is expressed as

$$u^{SV} = \frac{1}{4\pi\rho\beta^3}\frac{1}{r}\left[\hat{\theta}^T\dot{M}(t - r/\beta)\hat{r}\right]\hat{\theta} \tag{2.72}$$

and

$$u^{SH} = \frac{1}{4\pi\rho\beta^3}\frac{1}{r}\left[\hat{\varphi}^T\dot{M}(t - r/\beta)\hat{r}\right]\hat{\varphi} \tag{2.73}$$

2.5.3 Radiation patterns generated by P and S waves in tensile faults

To investigate the radiation patterns created by the P and S waves on a tensile fault segment, we need to rewrite the displacement equation as the function of the tensile opening angle

$$\Delta u(t) = \Delta u(t)(\sin\gamma\,\hat{n} + \cos\gamma\,\hat{f}) \tag{2.74}$$

where $\Delta u(t)$ is the magnitude of the displacement and γ is the tensile angle of the displacement measured from the slip vector $\hat{f}$ towards the fault normal $\hat{n}$ as shown in Figure 2.7 (Kwiatek and Ben-Zion, 2013). This allows to rewrite the three displacement components *P, SV*, and *SH* for the tensile fault segment as

$$u^{P} = \frac{\mu A \Delta\dot{u}(t - \frac{r}{\alpha})}{4\pi\rho\alpha^{3}} \frac{(\hat{r}^{T} S \hat{r})}{r} \hat{r} \tag{2.75}$$

$$u^{SV} = \frac{\mu A \Delta\dot{u}(t - \frac{r}{\beta})}{4\pi\rho\beta^{3}} \frac{(\hat{\theta}^{T} S \hat{r})}{r} \hat{\theta} \tag{2.76}$$

$$u^{SH} = \frac{\mu A \Delta\dot{u}(t - \frac{r}{\beta})}{4\pi\rho\beta^{3}} \frac{(\hat{\varphi}^{T} S \hat{r})}{r} \hat{\varphi} \tag{2.77}$$

where the S is called the symmetric dislocation tensor. S is expressed in terms of the Cartesian directions of north, east and down as

$$S_{11} = \left[\frac{2\sigma}{1-2\sigma} + 2sin^{2}\delta\, sin^{2}\phi_{s}\right]\sin\gamma - (sin\,\delta\, cos\,\lambda_{s}\, sin2\phi_{s} + sin\,2\delta\, sin\,\lambda_{s}\, sin^{2}\phi_{s})\cos\gamma \tag{2.78a}$$

$$S_{22} = \left[\frac{2\sigma}{1-2\sigma} + 2sin^{2}\delta\, cos^{2}\phi_{s}\right]\sin\gamma + (sin\,\delta\, cos\,\lambda_{s}\, sin2\phi_{s} - sin\,2\delta\, sin\,\lambda_{s}\, cos^{2}\phi_{s})\cos\gamma \tag{2.78b}$$

$$S_{33} = \left[\frac{2\sigma}{1-2\sigma} + 2cos^{2}\delta\right]\sin\gamma + sin2\delta\, sin\lambda_{s}\cos\gamma \tag{2.78c}$$

$$S_{12} = -sin^2\delta\ sin2\phi_s\ sin\gamma + (sin\delta\ sin\lambda_s\ cos2\phi_s + sin2\delta\ sin\lambda_s\ sin2\phi_s/2)\ cos\gamma \quad (2.78d)$$

$$S_{13} = sin2\delta\ sin2\phi_s\ sin\gamma - (cos\delta\ cos\lambda_s\ cos\phi_s + cos2\delta\ sin\lambda_s\ sin\phi_s)\ cos\gamma \quad (2.78e)$$

$$S_{23} = -sin2\delta\ cos\phi_s\ sin\gamma - (cos\delta\ cos\lambda_s\ sin\phi_s - cos2\delta\ sin\lambda_s\ cos\phi_s)\ cos\gamma \quad (2.78f)$$

As in previous cases, symmetrical elements of the source dislocation tensor are identical, such as:

$$S_{12} = S_{21} \quad (2.78g)$$

$$S_{13} = S_{31} \quad (2.78h)$$

and

$$S_{23} = S_{32} \quad (2.78i)$$

This gives us fives degrees of freedom for the source dislocation tensor: strike ϕ_s, dip δ, slip λ_s, tensile angle γ, and Poisson's ratio σ. Finally, the Radiation pattern equation, which depends on the radiate direction $\hat{r}$ (θ, ϕ) for P and S waves, for the tensile faults can be expressed as:

$$R_P = \hat{r}^T S \hat{r} \quad (2.79)$$

$$R_{SV} = \hat{\theta}^T S \hat{r} \quad (2.80)$$

$$R_{SH} = \hat{\varphi}^T S \hat{r} \quad (2.81)$$

and

$$R_S = \left[\left({R_{SV}}^2 + {R_{SH}}^2\right)\right]^{0.5} = \left[\left(\hat{\theta}^T S \hat{r}\right)^2 + \left(\hat{\varphi}^T S \hat{r}\right)^2\right]^{0.5} \quad (2.82)$$

As terms $\hat{\theta}^T$, $\hat{\varphi}^T$, $\hat{r}$ are expressed as matrixes, for the calculation purposes in the programming language C, we need to fully expand these equations as follows, which results in the following formulas (Ou, 2008). The radiation pattern for P waves is:

$$R_P = cos\theta(cos\theta\left(sin\gamma\left(2cos^2\delta - \frac{2\sigma}{2\sigma-1}\right) + sin2\delta\ cos\gamma\ sin\lambda\right)$$
$$-cos\phi\ sin\theta(cos\gamma(cos2\delta\ sin\lambda\ sin\varphi + cos\delta\ cos\lambda\ cos\varphi) - sin2\delta\ sin\gamma\ sin\varphi)$$
$$+sin\phi\ sin\theta(cos\gamma(cos2\delta\ cos\varphi\ sin\lambda - cos\delta\ cos\lambda\ sin\varphi) - sin2\delta\ sin\gamma\ cos\varphi))$$
$$+sin\phi\ sin\theta(cos\theta(cos\gamma(cos2\delta\ cos\varphi\ sin\lambda - cos\delta\ cos\lambda\ sin\varphi) - sin2\delta\ sin\gamma\ cos\varphi))$$
$$+cos\phi\ sin\theta(cos\gamma(cos2\varphi\ cos\lambda\ sin\delta + (sin2\delta\ sin2\varphi\ cos\lambda)/2) - sin2\varphi\ sin^2\delta\ sin\gamma)$$
$$+sin\phi\ sin\theta(cos\gamma(sin2\varphi\ cos\lambda\ sin\delta - sin2\delta\ cos^2\varphi\ sin\lambda)$$
$$-sin\gamma\ (\frac{2\sigma}{2\sigma-1} - 2cos^2\varphi\ sin^2\delta)))$$
$$-cos\phi\ sin\theta(cos\theta(cos\gamma(cos2\delta\ sin\varphi\ sin\lambda + cos\delta\ cos\lambda\ cos\varphi) - sin2\delta\ sin\gamma\ sin\varphi)$$
$$-sin\phi\ sin\theta\big((cos\gamma(cos2\varphi\ cos\lambda\ sin\delta + (sin2\delta\ sin2\varphi\ sin\lambda)/2) - sin2\varphi\ sin^2\delta\ sin\gamma\big)$$
$$+cos\phi\ sin\theta(cos\gamma(sin2\delta\ sin\lambda\ sin^2\varphi + sin2\varphi\ cos\lambda\ sin\delta)$$
$$-sin\gamma\ (\frac{2\sigma}{2\sigma-1} - 2sin^2\delta\ sin^2\varphi)))$$

(2.83)

Accordingly, radiation pattern equations for SH and SV waves are:

$$R_{SH} = cos\theta(cos\phi(cos\gamma(cos2\delta\ cos\varphi\ sin\lambda - cos\delta\ cos\lambda\ sin\varphi) - sin2\delta\ cos\varphi\ sin\gamma)$$
$$+sin\phi(cos\gamma(cos2\delta\ sin\lambda\ sin\varphi + cos\delta\ cos\lambda\ cos\varphi) - sin2\delta\ sin\gamma\ sin\varphi))$$
$$-sin\phi\ sin\theta(sin\phi(cos\gamma(cos2\varphi\ cos\lambda\ sin\delta - sin2\delta\ cos^2\varphi\ sin\lambda)/2)$$
$$-sin2\varphi\ sin^2\delta\ sin\gamma) - cos\phi(cos\gamma(sin2\varphi\ cos\lambda\ sin^2\varphi + sin2\varphi\ cos\lambda\ sin\delta)$$
$$+sin\gamma(\frac{2\sigma}{2\sigma-1} - 2sin^2\delta\ sin^2\varphi))$$
$$+cos\phi(cos\gamma(cos2\varphi\ cos\lambda\ sin\delta + (sin2\delta\ sin2\varphi\ sin\lambda)/2)$$
$$-sin2\varphi\ sin^2\delta sin\gamma))$$

(2.84)

and

$$R_{SV} = sin\phi\ sin\theta(cos\phi\ cos\theta(cos\gamma(cos2\delta\ cos\lambda\ sin\delta + (sin2\ sin2\varphi\ sin\lambda)/2)$$
$$-sin2\varphi\ sin^2\delta\ sin\gamma) - sin\theta(cos\gamma(cos2\delta\ cos\varphi\ sin\lambda - cos\delta\ cos\lambda\ sin\varphi)$$
$$-sin2\delta\ cos\varphi\ sin\gamma) + cos\theta\ sin\phi(cos\gamma(sin2\varphi\ cos\lambda\ sin\delta - sin2\delta\ cos^2\varphi\ sin\lambda)$$
$$-sin\gamma\left(\frac{2\sigma}{2\sigma-1} - 2cos^2\delta - \frac{2\sigma}{2\sigma-1}\right)$$
$$+sin2\delta\ cos\gamma\ sin\lambda) + cos\phi\ cos\theta(cos\gamma(cos2\delta\ sin\lambda\ sin\varphi + cos\delta\ cos\lambda\ cos\varphi)$$
$$-sin2\delta\ sin\gamma\ sin\varphi)$$
$$-cos\theta\ sin\phi(cos\gamma(cos2\delta\ cos\varphi\ cos\lambda - cos\delta\ sin\lambda\ sin\varphi) - sin2\delta\ cos\varphi\ sin\gamma))$$
$$+cos\phi\ sin\theta(sin\theta(cos\gamma(cos2\delta\ cos\varphi\ sin\lambda + \ cos\delta\ sin\lambda\ cos\varphi) - \ sin2\delta\ sin\varphi\ sin\gamma)$$

$$+cos\theta sin\phi(cos\gamma(cos2\delta\ cos\lambda\ sin\delta + (sin2\delta\ sin\lambda\ sin2\varphi/2) - sin2\varphi\ sin^2\delta\ sin\gamma)$$
$$- cos\phi\ cos\theta(cos\gamma(sin2\delta\ sin\lambda\ sin^2\varphi + sin2\varphi\ cos\lambda\ sin\delta)$$
$$+sin\gamma(\frac{2\sigma}{2\sigma - 1} - 2sin^2\delta\ sin^2\varphi)))$$

(2.85)

Lastly R_S can be derived from the upper mentioned equation as a square root of the sum of R_{SV} and R_{SH} squared, such as $R_S = \left[\left({R_{SV}}^2 + {R_{SH}}^2\right)\right]^{0.5}$.

2.5.4 Wave propagation directivity

The seismic records reflect the position of a seismic receiver relative to the seismic source due to the radiation pattern, the fault length and rupture velocity (Lay and Wallace, 1995). Since the rupture velocity is smaller than the propagation velocity of shear waves, body waves generated by the rupture of the early stages of the fault segment will arrive earlier than body waves generated during later rupturing processes. The time difference between subsequent arrival depends on the azimuth between the source and the receiver (Fig. 2.8).

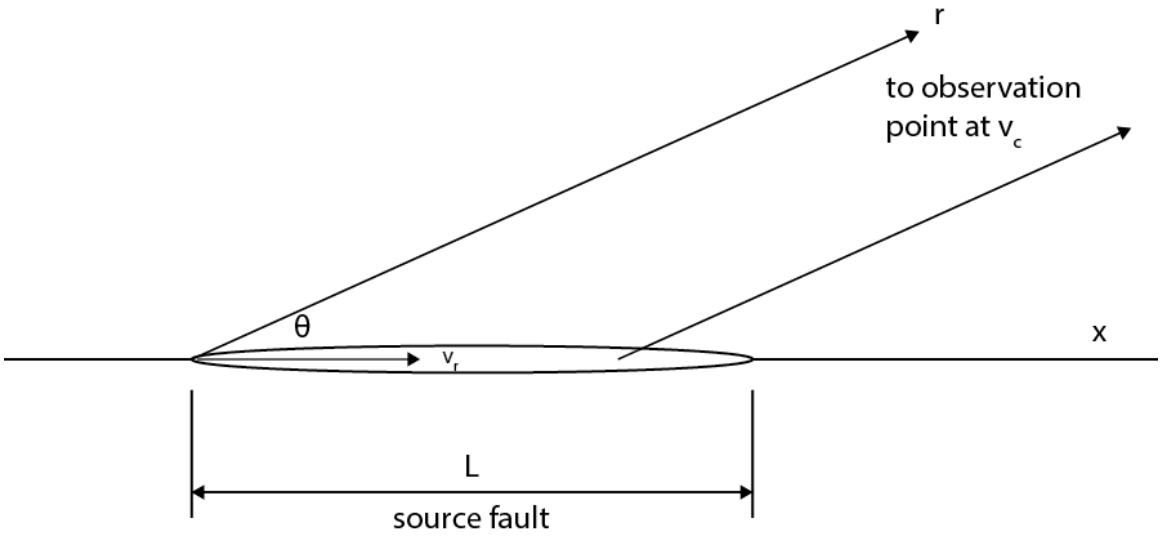

Figure 2.8. Fault section propagating along the x axis with a velocity of v_r. The arrival time as well as longevity of the signal is dependent upon the fault length L and orientation of the fault surface towards the observation point governed by the angle θ.

The travel time of a body wave with a velocity v_c from the origin at the fault and the observation station is

$$t_x = \frac{x}{v_r} + \frac{(r - \cos\theta)}{v_c}$$

(2.86)

The arrival time difference τ_c, where subscript c indicates a time difference for either P or S waves originating at the beginning and the end of the fault segment (apparent rupture duration), can be expressed as

$$\tau_c = \left[\frac{L}{v_r} + \frac{(r - L\ \cos\theta)}{v_c}\right] - \left(\frac{r}{v_c}\right) = \frac{L}{v_r} - \frac{L\cos\theta}{v_c} \tag{2.87}$$

where v_r denotes the rupture propagation velocity, L is the Length of the fault segment and θ is the azimuth between the fault and wave travel vector to the observation station.

Azimuthal variability of signals (apparent source time functions) for rupturing a fault segment introduce variability to the amplitude and the duration of the received signals. However, seismic moment M_0, which is represented by the time interval (can be viewed as "area" of source time function), does not change (Figure 2.9).

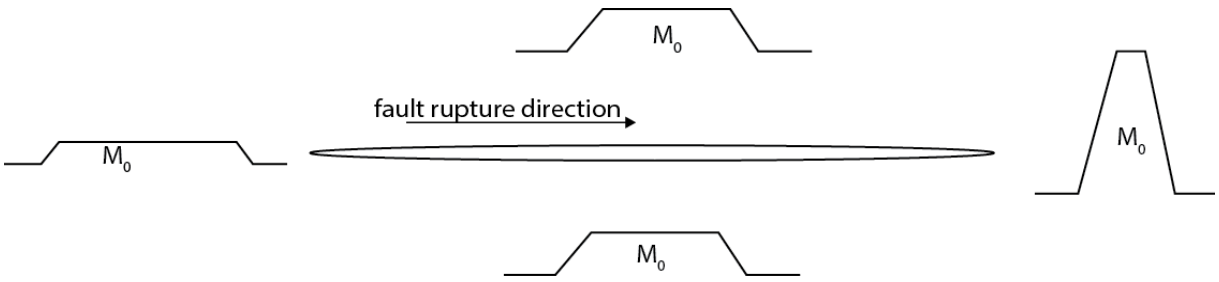

Figure 2.9. Depending on the orientation of the observation point towards the propagating fault, the duration and amplitude of the received signal will vary, however, the area of the time-source ramp function will stay the same and equal to the seismic moment M_0.

2.5.5 Seismic response modelling

As discussed in the above sections, seismogram $ss(t)$ is a convolution of the source $s(t)$, elastic response of the medium $G(t)$ (Green's function), the inelastic response of the medium $a(t)$ and instrumental response $i(t)$ (Kelly et al., 1976; Chapman, 1978; Panza, 1985; Geller and Ohminato 1994; Herrmann, 2002).

$$ss(t) = s(t) * G(t) * a(t) * i(t) \tag{2.88}$$

We have already discussed parametrisation of the source in terms of the moment tensor as well as an elastic response in terms of the Green's function and radiation patterns which together account for displacement observed

$$u(t) = s(t) * G(t)$$

(2.89)

The displacement $u(t)$ is initially expressed in the acceleration units m/s^2. To produce seismograms, we need to convert displacement into the frequency domain. A source function for the wave k (P or S wave) in the frequency domain is expressed as

$$\Delta\dot{S}(\omega) = TF\dot{s}(t - t_p^k)$$

(2.90)

where T is rupture time, F is Fourier transform, $\dot{s}$ is the convolution of the displacement source function over a time period $(ta\ - t_p^k)$ which is wave travel time delayed by fault propagation time.

The source function time profile has two components to it. Firstly, the rupture time is the time required for the fault segment to propagate fully and is assumed from the empirical studies to be 75% of the S-wave propagation speed for the given type of rock (Hartzell and Heaton, 1983; Kame et al., 2003). Secondly, the rise time which is the time required for the particles to reach their final position during the dislocation. Both functions are modelled in the far field by boxcar functions. Hence, the final function is calculated via convolution of the two boxcar functions to give a ramp function. The convolution yields no change in the area of the function, thus seismic moment remains the same (Fig. 2.10).

Fourier transform of a boxcar function of a height $1/T$ and length T is

$$F(\omega) = \int_{-T/2}^{T/2} \frac{1}{T} e^{i\omega T/2} dt = \frac{1}{Ti\omega}\left(e^{i\omega T/2} - e^{-i\omega T/2}\right) = \frac{\sin(\frac{\omega T}{2})}{\omega T/2} = sinc(\frac{\omega T}{2})$$

(2.91)

Since the source time function is the convolution of T_R and T_D boxcar functions, the spectral amplitude of the source signal is the product of the seismic moment of two *sinc* terms:

$$|A(\omega)| = M_0 \left|\frac{\sin(\frac{\omega T_R}{2})}{\omega T_R/2}\right| \left|\frac{\sin(\frac{\omega T_D}{2})}{\omega T_D/2}\right|$$

(2.92)

where T_R is the rupture time while T_D is the rise time.

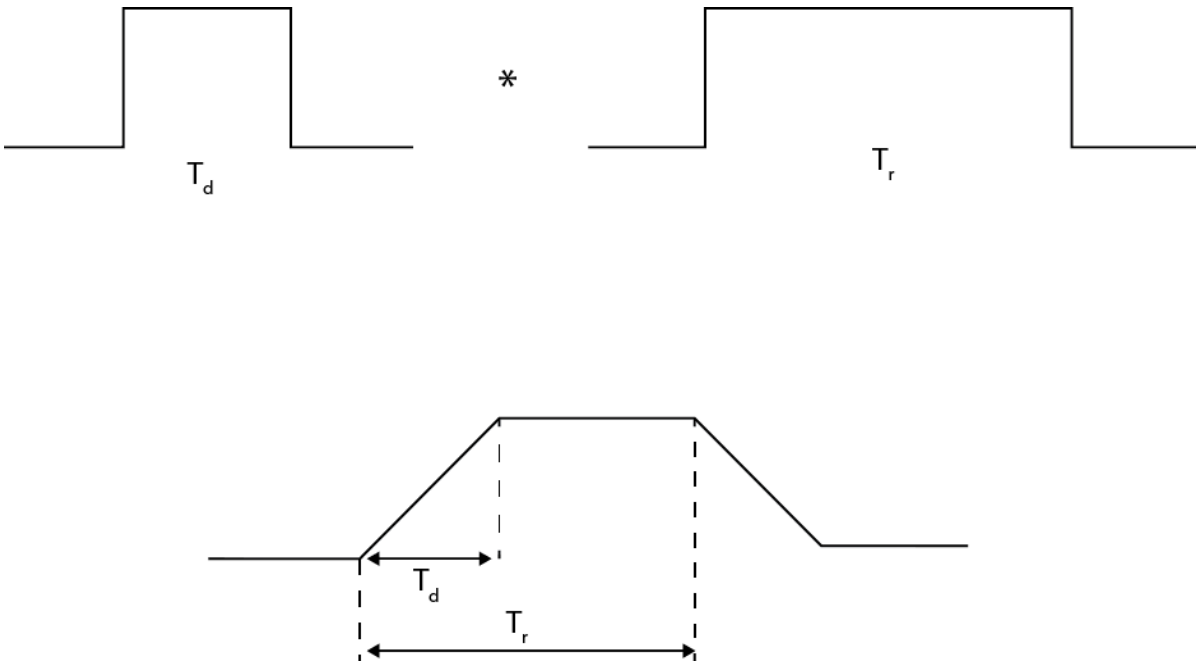

Figure 2.10. Source time function is a convolution of the two boxcar functions: T_D – rise time and T_R – rupture time. The end result is a ramp function, where the duration of the slope is equal to T_D while the length of the rising slope and plateau phase.

Unfortunately, T_R and T_D are usually derived from the observed signal, thus it created a challenge to forward model synthetic seismogram. Therefore, we have to rely on empirical approximations. Fortunately, a lot of work has been carried out on the studies of earthquakes' self-similarity (Aki, 1967). One of the cornerstone parameters that can be scaled from seismic moment M_0 is the corner frequency f_c where $M_0 \propto f_c^{-3}$. It was first observed by Aki (1967) and then confirmed by several empirical studies (Iio, 1986; Abercrombie, 1995; Ogasawara et al., 2002; Hiramatsu et al., 2002). In this study, Aki (1967) assumes that the wave spectrum ratio produced is independent from the seismic moment and is related to the fault geometry which allows the possible scaling laws.

This works in a way that when the signal is recorded by the instrument, the signal decays at a certain rate depending on the frequencies generated by the earthquake. The decay is governed by the total duration of rupturing when signal decays with $1/\omega$ rate and time length of rupturing slowing down and stopping (the downwards slope of the trapezoid time-source function) when signal decays at $1/\omega^2$ rate. The point of the spectrum where decay changes from 0 to at $1/\omega^2$ is known as the corner frequency f_c. And, since $M_0 \propto f_c^{-3}$, the components associated with corner frequency can be scaled from fault properties. M_0 can be further rewritten to better illustrate fault geometry as:

$$M_0 = A\mu u = fL^2\mu u$$

(2.93)

Where *L* and *f* represent length of the fault and ratio of width to length. It has to be noted that in this case rectangular geometry of the fracture is assumed.

From the empirical study of Aki (1967) the following ratio between the fault geometry and rise-time has been derived:

$$T_D = 16Lf^{\frac{1}{2}}/(7\beta\pi^{1.5})$$

(2.94)

It is then possible to create an amplitude spectrum from the emitted signal. Since we are working with the trapezoidal boxcar function, it is useful to approximate *sinc* as 1 for $x<1$ and as $1/x$ for $x>1$. This approach yields:

$$\log|A(\omega)| = \begin{cases} \log M_0 & \omega < 2/T_R \\ \log M_0 - \log(T_R/2) - \log\omega & 2/T_R < \omega < 2/T_D \\ \log M_0 - \log(T_R T_D/4) - 2\log\omega & 2/T_D < \omega \end{cases}$$

(2.95)

The end result is the power spectrum of the received signal in the frequency domain with two corner frequencies.

Equation 2.95 shows that elastic energy produced by the fracturing and faulting decreases over the distance. There are other effects such as scattering and multi-pathing, which are not taken into account in this work, assuming that we are dealing with the isotropic homogeneous medium. However, when looking at the seismograms, even all these effects are not enough to explain for the total loss of the elastic energy. In reality, the earth behaves as an absorbent for the seismic energy. This effect is referred to as an Anelastic attenuation or intrinsic attenuation where elastic energy is partially converted to plastic energy (Anderson and Hart, 1978).

Anelastic attenuation is expressed as a transfer function of a wave (P or S) propagation speed t_p^k in the frequency domain as

$$A_{nc}^k(\omega) = \exp\left(\frac{-\omega t_p^k}{2Q^k}\right)$$

(2.96)

where Q^k is the quality factor for the P or S wave propagation. This dimensionless term is similar to the damping factor of an oscillating system, and so it describes the ability of the medium to attenuate a wave that passes through it. The Dirac convolution of this transfer function gives a centered impulse around the

propagation time $t_p = x/c$ (where x is fault length and c is fault propagation speed). Thus, when represented on the seismogram, the attenuation of the elasticity has the dephasing effect on the signal, which causes the arrival of the low frequency (high amplitude) component before the theoretical arrival time. This is known as the non-causality phenomenon. To work around this problem, it is required to use the causal transfer function (Carpenter and Flinn, 1965, Pennington and Isacks, 1979).

$$A_c^k(\omega) = \exp\left(\frac{-\omega t_p^k}{2Q^k} + i\frac{\omega t_p^k}{\pi Q^k}\left[\ln\left(\frac{\omega}{\omega_N}\right) - 2\right]\right) \tag{2.97}$$

where ω_N is the Nyquist frequency. Thus high frequencies arrive first while the low frequencies have a delay in arrival time depending on the Q^k value.

Q^k usually has a significant role when dealing with large inhomogeneouties over large distances, such as in cases of tectonic earthquakes. In practice, when dealing with microseismic signals, Q^k is usually assumed to be ~1000 as it has a very small effect on the actual seismogram production. Thus, microseismic signals tend to have close to harmonic signal appearance.

The final term composing the seismogram, which needs to be taken into account, is the response of the sensor used to record the waves. In the case of a standard velocimeter, the transfer function is

$$I_{vel}(\omega) = -g\frac{(i\omega)^2}{(i\omega)^2 + 2h\omega_0(i\omega) + \omega_0^2} \tag{2.98}$$

where ω_0 is the natural frequency of the sensor, h is the damping factor and g is the sensitivity in V/m/s.

Finally, synthetic seismograms are obtained by convoluting all the above-mentioned elements. The fact that they are all already given in the frequency domain, makes it a relatively simple process which directly produces synthetic seismograms. To convert seismogram to velocity units (velocigram), it suffices to use not the displacement but its derivative which in frequency domain means that displacement needs to be multiplied by $i\omega$. The synthetic seismogram is then obtained via the inverse Fourier transform

$$ss_{vel}(\vec{x}, t) = TF^{-1}[SS_{vel}(\vec{x}, \omega)] = TF^{-1}[i\omega U(\vec{x}, \omega).A(\omega).I_{vel}(\omega)]. \tag{2.99}$$

3 Methodology

3.1 Elle

In order to numerically simulate the development of fractures assisted by the fluid, we employ a discrete element model initially proposed by Ghani et al. (2013). The code associated with this setup is part of the software package “Latte”, which is a part of the “Elle” package (Bons et al., 2007), which in turn operates in the C/C++ language domain that is an object-oriented code. The software is capable of simulating several dynamic processes of the Earth’s crust. The Latte module is initially based upon the work by McNamara et al. (2000), Flekkøy & Malthe-Sorenssen (2002), Koehn et al. (2005), Vinningland (2007), Niebling et al. (2010), and Goren et al. (2010; 2011) who studied fracture propagation in the discrete elastic solid medium.

Due to large number of variables, some symbols are used for different variables in different chapter subsections. The summary for all the variables will be provided in every Chapter subsection. Table 3.1 provides summary of variables used in Chapter 3.1.

Table 3.1. Table of variables used in Chapter 3.1.

k	Intrinsic stiffness coefficient
E	Young's modulus
v	Poisson ratio
l_m	Thickness of the model
m_s	Mass of the solid
ρ_f and ρ_s	Densities of fluid and solid
v_s	Solid particle velocity
F_i	Interparticle force
∇P	Fluid pressure gradient
V_s	Volume of the solid
ϕ	Porosity
ρ_{eff}	Effective density
g	Gravitational acceleration
σ_t	Critical tensile stress
τ	Critical shear stress
E_c	Critical strain
β	Fluid compressibility
P	Fluid pressure deviation from hydrostatic
K	Permeability
μ	Fluid viscosity
D	Diameter of a single particle in DEM
F_n^i	Sum all interacting forces
f_e	Elastic interparticle forces
f_p	Fluid pressure
f_g	External forces (gravity + large scale tectonic strain)
P_0	Total fluid pressure
σ_{eff}	Effective stress
u, U_{tot}	Particle total displacement
ϕ_a	Displacement azimuth (2D)
U_t, U'_t	Tensile displacement
U_s, U'_s	Shear displacement
a, b, c, d, e, f	Supplementary inter-calculation variables, defined in each subsection individually

3.1.1 Discrete elastic medium (DEM)

This Model is built upon a 2D small scale triangular setup coupled with a square grid fluid pressure continuum. In the model, the triangular network is constructed of disk-shaped particles of constant radius interconnected by springs (discrete element model or DEM). Such model configuration in 2D mimics the isotropic elastic behavior of solid materials and can be used to model deformation problems

in systems described by linear elastic theory (Flekkøy et al., 2002). The intrinsic stiffness coefficient *k* is governed by the macro-scale parameters *E* and *v* (Young's modulus and Poisson ratio) through the consistency measures of strain energy between the 2D elastic lattice of the triangular network and solid continua (Flekkøy et al., 2002)

$$k = \frac{\sqrt{3}}{2} E l_m \tag{3.1}$$

where l_m stands for the thickness of the two-dimensional model. The model runs as a step function, and therefore plain strain deformation is produced for each time step Δt. Deformation of the elastic media is caused by a net force acting on every solid particle. The net force is derived as a sum of fluid and gravitational forces acting on the particle as well as interaction forces acting between the neighbouring particles (interparticle force). Thus, the deformation can be expressed as the following time-dependent force balance equation:

$$m_s \left(1 + \frac{\rho_f \phi}{\rho_s (1-\phi)}\right) \frac{dv_s}{dt} = F_i - \nabla P \frac{V_s}{1-\phi} + \rho_{eff} V_s g \tag{3.2}$$

where m_s denotes the mass of the solid, ρ_f and ρ_s are densities of fluid and solid respectively, v_s is the velocity of the solid particle, F_i is the interparticle force preventing particles from overlapping each other, ∇P is the fluid pressure gradient, V_s is the volume of the solid, ϕ is the porosity, $\rho_{eff} = \rho_s - \rho_f$ is the effective density of the solid and g is the gravitational acceleration (Ghani et al., 2013; Ghani et al., 2015).

The model is of a quasi-static nature, meaning it runs using a time step function. At the end of every time step all springs are checked, and if the predetermined stress threshold for a spring is reached, it breaks releasing elastic energy, the spring is removed from the lattice and a fracture forms. The elastic energy contained in the removed spring is further redistributed among the neighbouring springs via a relaxation algorithm. The solution for such equation results in a heterogeneous force network where the load is then transmitted and redistributed along the solid particles (Vinningland et al., 2007). The breakage occurs once either the critical tensile normal stress σ_t or the critical shear stress τ is reached.

In order to include combinations of tensile and shear failure, it is assumed that

the critical strain value E_c is seen as a sum of tensile (U_t) and shear (U_c) energies (Sachau & Koehn, 2014). There are separate critical values for both tensile (Ec,σ) and shear (Ec,τ) criterions, and their relationship can be expresses as

$$\frac{U_s}{E_c} + \frac{U_t}{E_c} = \left(\frac{\sigma_t}{\sigma_0}\right)^2 + \left(\frac{\tau}{\tau_0}\right)^2 = 1 \tag{3.3}$$

which describes an ellipse in σ_t-τ space (Sun & Jin, 2011). Therefore, the failure can occur as a combination of both shear and tensile factors, or if one of the two components is absent, it will be equivalent to pure tensile or pure shear failure.

3.1.2 2D Pressure diffusion field

The 2D DEM lattice is overlain by a square grid of fluid pressure nodes. The spacing of the fluid continuum grid is twice the size of the solid lattice. The fluid pressure diffusion is derived from mass conservation of the fluid and solid using Darcy's law to express the seepage velocity through the porous medium (Ghani et al., 2013, Ghani et al., 2015)

$$\phi\beta(\partial_t P + u_s \nabla \cdot P) = \nabla \cdot \left[(1+\beta P)\frac{K}{\mu}\nabla P\right] - (1+\beta P)\nabla \cdot u_s \tag{3.4}$$

where φ is the porosity, β is the fluid compressibility, P is the fluid pressure deviation from hydrostatic, and u_s is the solid velocity field. K and μ stand for permeability and fluid viscosity respectively. The left hand side of the equation is the Lagrangian derivative of pore pressure following the solid matrix, which solves for the rate of fluid pressure change as a function of solid particle acceleration. The first term on the right expresses the Darcy fluid pressure diffusion relative to the particles. It is calculated using the Pressure Alternating Direction Implicit algorithm from Teukolsky et al. (1992). The last term is a source term that expresses pressure change as a function of a change in the solid if particles move apart in the local reference of the Darcy flow (Ghani et al., 2013). The Kozeny-Carman relation is used to express K as a function of local porosity φ

$$K(\rho) = \frac{D^2(\phi)^3}{180(1-\phi)^2}$$

(3.5)

where *D* is the particle diameter and 1/180 is an empirical constant for packing of spheres (Ghani et al., 2013; Ghani et al., 2015).

Deformation mechanics are driven by the momentum exchange between the two phases: solid and fluid. The total force applied to the particles is compiled from three main constituents

$$F_n^i = f_e + f_p + f_g$$

(3.6)

where f_e is the interaction force between the particles either due to a connection with the spring or repulsive, fluid pressure force f_p and external force f_g applied due to the gravity and large scale tectonic strain. In this instance, f_e is expressed as a function of the spring elasticity constant *k* and an equilibrium distance between particles a_i and a_j, which equals the sum of the initial radii of the two connected particles

$$f_e = \sum_j k_{ij}\left(|\vec{a}_{ij}| - |\vec{x}_i - \vec{x}_j|\right) \cdot \hat{n}_{ij}$$

(3.7)

where x_i and x_j are the positions of the connected particles, $\hat{n}_{ij}$ is unit vector pointing from the centroid of particle *i* to particle *j* and the sum runs over all the connected neighbours *j*.

The fluid force f_p that acts on the surface normal *dA* of the unit cell is a function of the fluid flow due to the pressure gradient and is described as

$$f_p = \int P_0 dA$$

(3.8)

where $P_0 = P + \rho_f gz$ *is* the local total fluid pressure, *z* depth, ρ_f density of the fluid and *g* gravity constant. It is the sum of a term due to viscous forces arising in the case of fluid flow through the solid, $\int PdA$, and a buoyancy term, $\int \rho f\ gz\ dA$.

Lastly, the gravity force that is acting on every particle is calculated according to

$$f_i^g = \rho_s \pi R_i^2 gC$$

(3.9)

where ρ_s denotes the solid mass density, $R_i^2 = r_i^2 S$, where S is the dimension of the real system (1000m), g is the gravitational constant and *C =2/3* is a scale factor (after Ghani et al., 2015) used to acquire a compatible one dimensional lithostatic stress that can be applied to an isotropic 2D linear elastic solid.

The buoyancy term itself can be written according to Ostrogradsky's theorem as $\int \rho f \; gz \, dA = -\rho_f \pi R_i^2 gC$ (Mory, 2013), so that the total effect of gravity, the direct one plus the buoyancy effect, is $(\rho_s - \rho_f)\pi R_i^2 gC$. This expression incorporates the effects that gravity has on both solid and fluid: this drives the effective stress field $\sigma_{eff} = (\rho_s - \rho_f)gz$ in the system (Niebling et al., 2010).

The solid porosity that is used for the fluid pressure evolution in the fluid lattice is described by the solid mass fraction of solid particles within a fluid cell and changes due to compression, solid movement or fracturing. The solid movement itself between two deformation steps affects the source term in equation 3.4.

3.1.3 Coupling of solid and fluid phases

Finally, the model is set up in a way that the fluid continuum grid overlies the DEM, so that their boundaries coincide. Coupling between the two grids is based on a process where values in either are passed onto the other lattice. Since the fluid grid is set to be twice as large as the DEM matrix, the model uses the "cloud in the cell" method to facilitate the two-way interaction between the porous matrix and the hydrodynamic phase (Ghani et al., 2013, Johnsen et al., 2006, Vinningland et al., 2007). The interaction between the porous solid and hydrodynamic phases is accomplished through the projection operator from the discrete space to the fluid grid space by the help of the smoothing function $s(r_i - r_0)$, which distributes the weight of the particle over the four nearest fluid grid nodes

$$s(r - r_0) = \begin{cases} \left(1 - \frac{w_1}{\Delta x}\right)\left(1 - \frac{w_2}{\Delta z}\right) & if\ w_1 < \Delta x, w_2 < \Delta z \\ 0 & otherwise \end{cases} \tag{3.10}$$

where $r(x,z)$ and $r_o(x_o,z_o)$ are the positions of the particle and the continuum node respectively, $w_1 = |x - x_o|$ and $w_2 = |z - z_o|$ are the relative distances.

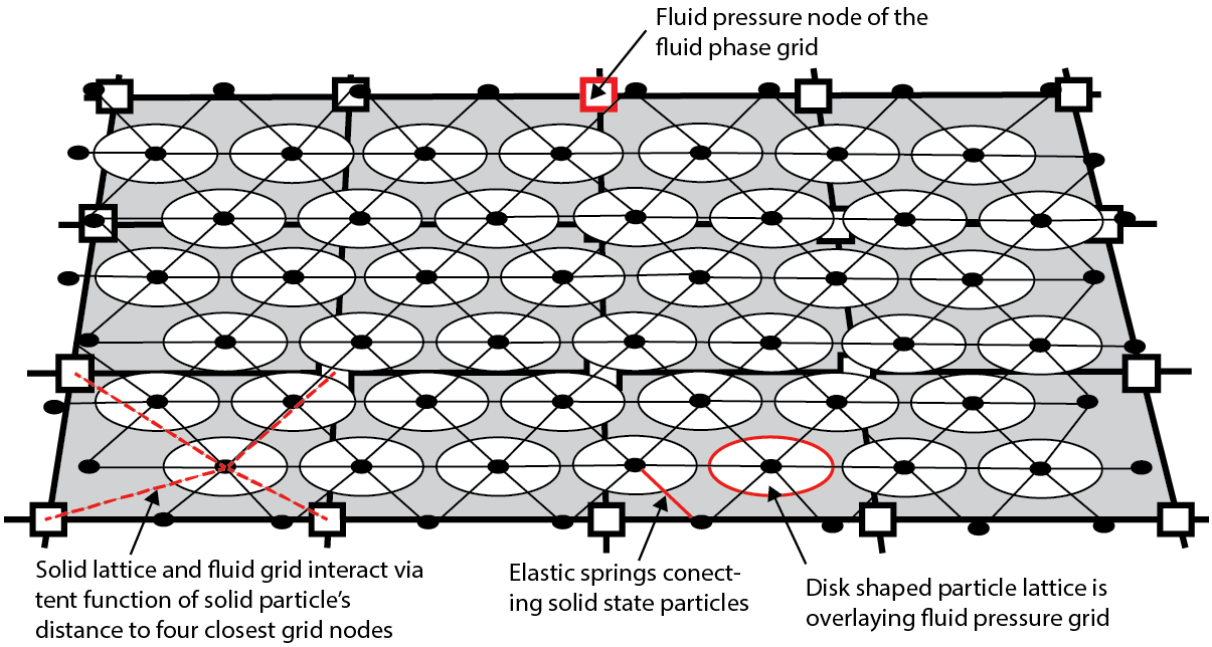

Figure 3.1. Schematic illustration of the DEM (discrete element model) grid overlying the fluid pressure nodes. The DEM grid is triangular whereas the fluid grid is square and larger than the DEM. Both grids are mapped onto each other using tent functions to minimize grid effects. The fluid grid is stationary whereas the DEM grid can move.

This function allows creating a weight map for nodes where nearby particle properties such as weight and velocity are transferred as a sum of ratios that are calculated as a function of the distance between the particle and the node. The particle that is closest to the node will have the heaviest impact on the node properties, while the furthest particle will have the smallest impact. The "cloud in a cell" method works in both ways. This means that fluid pressure forces can be transferred from the pressure nodes to the solid particles using the same weighting principle. Once the fluid pressures are calculated, they are transferred onto the solids and converted to forces that act individually on every particle. The combination of these forces then causes elastic deformation, which can result in fracturing if the deformation exceeds predefined critical breaking values of single elastic bonds. The breaking threshold of a spring is defined as the maximum stress it can withstand without breaking. This is also done as a ratio of critical tensile and shear stress, which is described in Eq. 3.3. The breaking strength of the springs is not uniform and has a normal distribution over the system. In general, however, the overall system strength is larger than the individual spring strength. This is done to closely mimic real-world setups where there are natural inequalities of strength within the rocks. The distribution of the breaking strength plays a major

role in the system as it can to an extent predetermine the dominant mode of fracturing (Koehn et al., 2005).

3.1.4 Model setup

The simulated area represents a cross section in the crust which is 1 km^2 in area. It is represented by the lattice of solid particles, which was 200x200 in its original dimensions, but was changed to a grid of 400x400 particles in later stage simulations. This was done to increase the resolution of the simulations. The depth of the cross-section can be varied, but most experiments were carried out with the overburden rock column of 3000 m (meaning that the modelled area is located between the depth of 3000 and 4000 meters). The boundary conditions confine both the solid and the fluid lattice. The solid lattice is constrained by the walls on the sides and at the bottom of the model that cannot break or deform and are considered as free-slip boundaries with repulsive characteristics. The upper boundary is an open boundary where the overlying sediments exert vertical (gravitational) forces upon the particles within the simulation box. Similarly, the fluid lattice is confined by the periodic boundaries on the side where no fluid can escape. The top and bottom boundaries are given pre-assigned fixed pressure gradient values, using a homogeneous hydrostatic pressure gradient swithin the model box. Therefore, the fluid pressure is a function of the height of the box and height of the overlying sediment column. The fluid has a density of 1000 kg/m^3 and a viscosity of 8.90×10^{-4} Pa s.

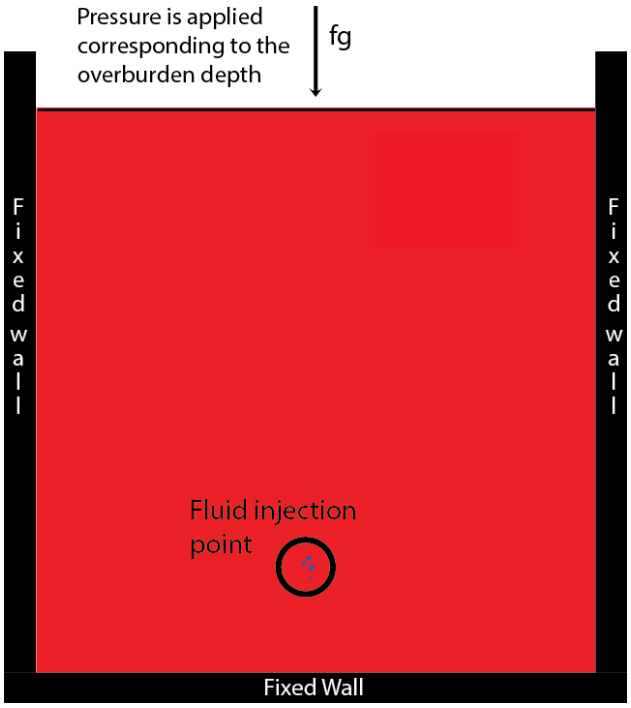

Figure 3.2. The setup of the numerical model is 2D, bound by fixed walls on the right and left hand sides and the bottom while a stress corresponding to the weight of the overburden, arising from gravitational forces, is applied from the top. Fluid is injected in the centre of the lower part of the model.

The model is of quasi-static nature, meaning it runs using a constant time step algorithm. All simulations start in a completely relaxed state. The particles then settle according to the gravitational and fluid forces. Hydrostatic gradient is applied to the model. This means that if the height of the box represents 1 km of rock, the fluid pressure gradient vertically across the unaltered system is going to be 10 KPa/m. The initial time step operation is a fluid pressure increase in one of the nodes of the fluid phase grid. Pressure gradient is then calculated on the scale of the neighbouring nodes. As the new pressure gradients are obtained, the lattice relaxes and the particles start to move according to the new forces acting on them to obtain the new equilibrium state. The system then checks for the breaking strength of the springs. The spring breaking (fracturing) depends not only on its breaking strength but also on the probability. This means that if multiple springs' breaking strength is exceeded, just one with the largest excess stress will be removed at a time. Once it is removed, the relaxation algorithm is run again redistributing stress released from the broken spring among the neighbouring springs. Springs can break and be removed until no other spring has stress exceeding the breaking strength. The relaxation algorithm is run until the model

comes close to a resting state. A pre-setup threshold for the “relaxed state” is required as theoretically the model does not become ever fully relaxed as relaxation criterion has a tendency of $lim \to 0$. Without a pre-determined relaxation threshold value this algorithm would be run indefinitely. The relaxation threshold is chosen such that the model converges reasonably fast towards semi-constant stress states. When the elastic spring medium is relaxed, the local porosity is calculated. Porosity is determined as a function of the particle diameters and their distance between their centres of mass and the pressure node. When spring is removed, it causes particle to get pushed away from the node, thus increasing local porosity. Once changes in the the local porosity are accounted for, the pressure field diffusion calculation is carried out. This terminates one-time step and the model loops into the next one. Time steps in the model are 30 seconds each and the models typically run between 5,000 and 10,000 time steps. This means every simulation has the time frame of 41.6 to 83.3 hours in total. As the aim of the numerical experiment was to test fracturing dynamics under different conditions most of the parameters used in the model were altered throughout the experiments. However, one case was used as a default parameter set and then its parameters were altered one at a time. The following values were used in the default case. The Poisson ratio in the model is 0.3. This value was derived from the continuum form of the stress tensor on an arbitrary lattice site and the standard two-dimensional continuum expression (Flekkoy et al., 2002). The initial setup had a Young’s modulus (E) value assigned to 6 and 12 GPa. Fluid pressure increase rate due to fluid injection is 80000Pa/30s. The average porosity throughout the system is ~1%. The mean tensile strength of the overall system is set to 34 MPa. A normal distribution is then applied to randomise the breaking strength with the two confidence intervals equal to 60% of the mean value (34 MPa) leading to a material breaking strength of around 13 MPa. Throughout the experiments, both, the mean and percentage for the confidence intervals were altered. The values that were used for parameter alteration are outlined in Chapter 4.

3.1.5 Analytical numerical module

The Elle environment is well fitted for the simulation of hydrofracturing processes. However, it lacked the potential to record the data produced in-depth required

for a detailed analysis. As the model is built in the C++ language, additional modules were written in order to record and output data. In this paragraph, I will discuss the analytical methodology used to accomplish this undertaking.

The very basic parameters that we need to record for any dynamical displacement data is the amount of displacement and its vector. To accomplish this task, one requires baseline data. The first step was to create a temporary data library of all particle locations in the XY coordinate system. This data library was then updated and overwritten every successive time step. The positions of the particles of interest at the end of the time step would be recorded and analysed against the baseline positions. The absolute displacement is calculated as $u = \sqrt{\Delta x^2 + \Delta y^2}$ where Δx and Δy are particle position changes along horizontal and vertical axis. Displacement vector azimuth is defined as an angle between the *y* (vertical) axis and the particle movement path (vector) measured clockwise from the *y* axis. The calculation of displacement vector azimuth is more complicated as equations change depending on the quadrangle into which the specific particle vector moves relative to its starting position. There are also special cases when particles move parallel to one of the axes (Fig 3. 3).

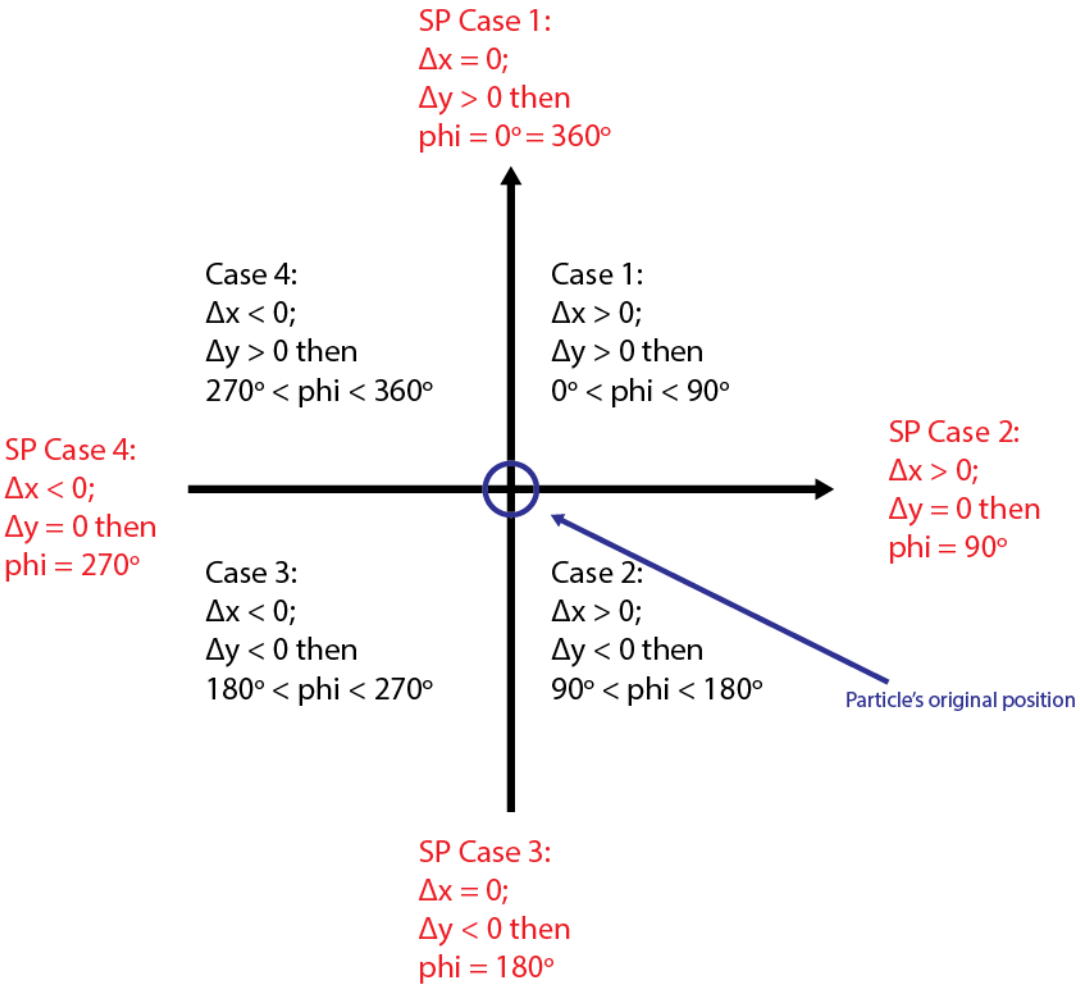

Figure 3.3. Schematic illustration of the case specific quadrangle distribution. Depending on the positive or negative or same changes in the vertical and horizontal coordinates of the particle position before and after the dislocation, specific equation sets have to be used for calculating displacement azimuth.

The cases where particle move along one of the axis are simple as then there is only one possible azimuth value. For all the other scenarios case-specific equations had to be used.

Case 1:

$$\phi_a = atan\sqrt{\frac{\Delta x^2}{\Delta y^2}} \tag{3.11a}$$

Case 2:

$$\phi_a = \pi - atan\sqrt{\frac{\Delta x^2}{\Delta y^2}} \tag{3.11b}$$

Case 3:

$$\phi_a = \pi + atan\sqrt{\frac{\Delta x^2}{\Delta y^2}} \tag{3.11c}$$

Case 4:

$$\phi_a = 2\pi - atan\sqrt{\frac{\Delta x^2}{\Delta y^2}} \tag{3.11d}$$

As described above, the model runs in time steps, meaning that during one-time step there may be no fractures generated or multiple bonds can break at once. The second issue was that no means of recording, which bonds are broken, were provided. Therefore, the next step was to add a routine in the code which would check all the particles for broken bonds and set a “freshly fractured” flag to particles with bonds broken during the current time step. If such bonds were found, that would initiate a statistical data collection routine. Since the model is unable to track the order in which the bonds break, we have to assume that all the spring that break in one-time step break at the same time and form one fracture unit. Broken bonds typically are clustered and form a singular fracture. However, in some cases there are isolated broken bonds formed that are not connected to an existing fracture or other bonds that broke in the given time step. This is typically caused by having too large overpressure in a single time step. To make this approximation have as little effect as possible on the integrity of the model, time steps and fluid pressure increase must be kept to a minimum. At the end of the data collection routine the “freshly fractured” flag would be removed to avoid data duplication in the following time steps.

Fracture dynamics

Once we start dealing with a fracture, we need to define what a "fracture" in our model is. In this case, my approach is to determine fracture as an imaginary line that intersects a broken bond between two particles perpendicular and in the middle (Fig. 3. 4).

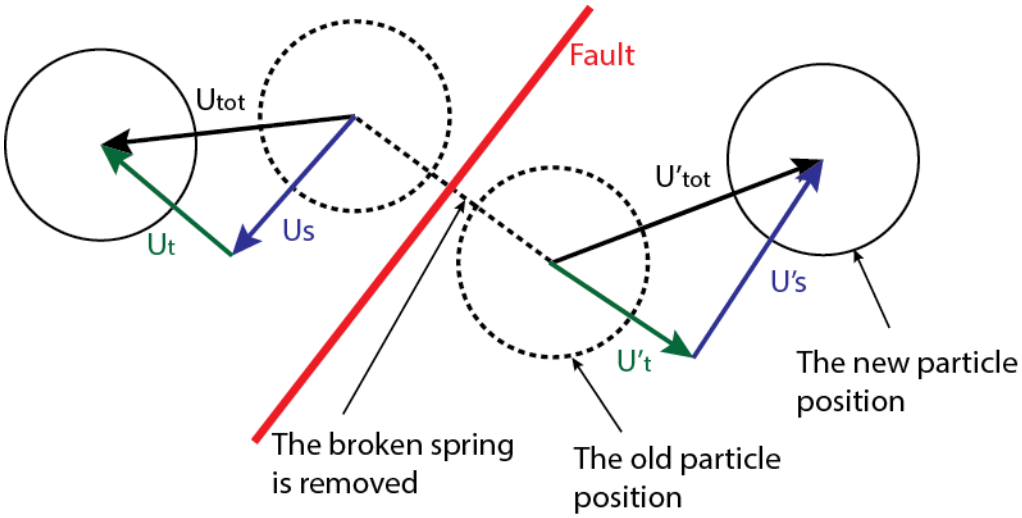

Figure 3.4. Calculation of the Moment Tensor after failure takes place (spring between particles breaks). The figure shows the decomposition of total particle displacement (U_{tot}) into shear (U_s) and tensile components (U_t), which are respectively parallel and perpendicular to the imagined failure surface. The failure surface lies perpendicularly to the broken elastic spring.

One of the parameters we wanted to look at was fracturing mode. As already described, Mode I displacement is perpendicular to the fracture plane while Mode II is parallel. To measure these two vector proportions, we needed to know what the orientation of the reference plane is (e.g., the failure surface). For this, a similar approach to the one used for the azimuth calculation was employed (Fig. 3.5).

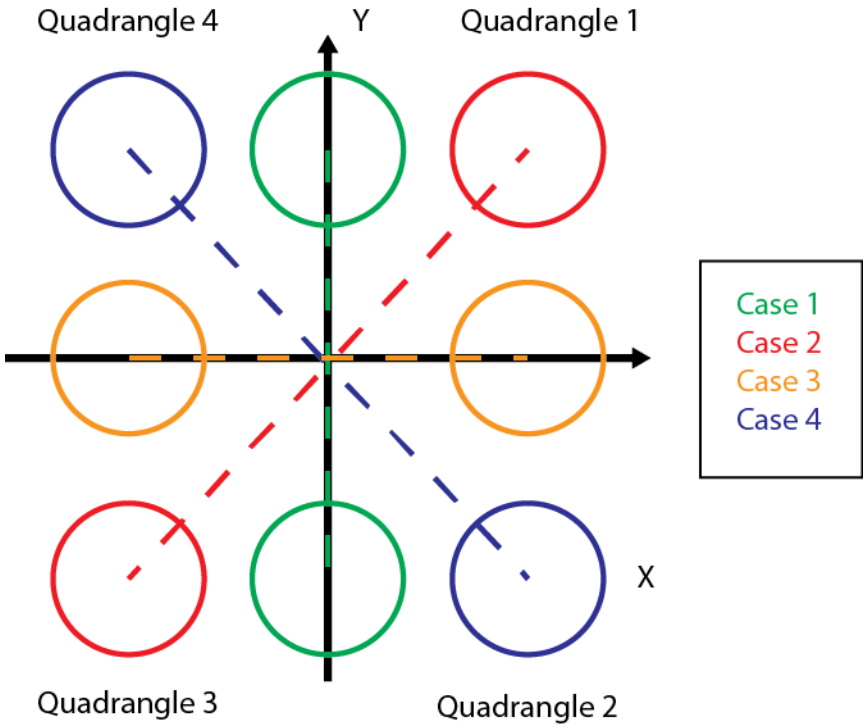

Figure 3.5. Schematic illustration of case specific possible orientations of particles relative to the X and Y axis. Depending on the case, specific set of equations has to be used to calculate Mode I versus Mode II displacement ratio.

Again, there are two cases where particles lie directly on the axis, making the fault plane parallel to either the X axis (Case 3) or Y axis (Case 1). In the other two cases the calculation approach is dependent upon which quadrangle is the particle located in. Calculations are also complicated by the fact that fracture plane orientation has an interval of 90 degrees within which it can be located. The allocation to the respective quadrangle is decided according to the following conditions:

$$Quadrange\ 1\ if\ \begin{cases} x' > x \\ y' > y \end{cases};$$

$$Quadrange\ 2\ if\ \begin{cases} x' > x \\ y' < y \end{cases};$$

$$Quadrange\ 3\ if\ \begin{cases} x' < x \\ y' < y \end{cases};$$

$$Quadrange\ 4\ if\ \begin{cases} x' < x \\ y' > y \end{cases};$$

where x' and y' are the new particle positions while x and y are particle positions prior to fracturing. Once the coordinate quadrangle of the particle is determined, an algorithm specific for each quadrangle is employed to calculate tensile and shear movement components. Within each quadrangle, again two possible cases

are presented depending on whether or not more movement occurred along the x- or y-axis (Fig. 3.6.).

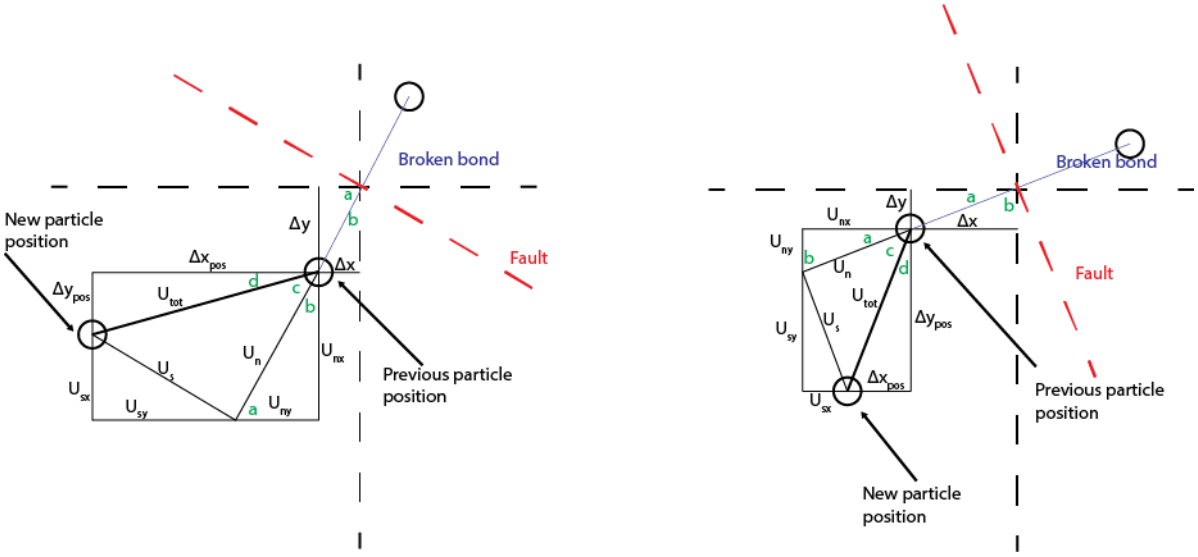

Figure 3.6. Geometric illustration of the tensile (U_t) and shear (U_s) displacement vector components as well as vectors and angles that are required for the calculation process. Depending on the orientation of the broken bond relative to the fault surface, two scenarios are possible. They can be distinguished by comparing and identifying the larger parameter among the Δx and Δy. The equation sets are different for each case. Calculations are the same for both particles connected by the broken spring as the diagram can be mirrored across the fault surface, meaning all the variables remain the same in the absolute values.

In a setup illustrated in Figure 3.6 we need to solve the given problem for the U_t and U_s, which are the tensile and shear movement components respectively. This operation requires several steps. First, we can derive Δx and Δy. We assume that the fault line crosses the broken bond in the middle. We know the coordinates of both connected particles in the *xy* coordinate system, therefore we can calculate the absolute distance value between them by subtracting both particles' *x* and *y* values from each other. Δx and Δy are then half of that value. Further, we define the angle between the broken bond and the *x*-axis as *a*, and the angle between bond and y-axis as *b*. These can be then calculated as

$$a = atan\frac{\Delta y}{\Delta x} = \frac{\pi}{2} - b; \tag{3.12}$$

$$b = atan\frac{\Delta x}{\Delta y} = \frac{\pi}{2} - a. \tag{3.13}$$

At this stage, we introduce two new angles: *c* is an angle between the total displacement vector U_{tot} and its normal to the fault component U_t, while angle *d*

lies between U_{tot} and its vector component along one of the coordinate axes. These vectors are denoted as Δx_{pos} and Δy_{pos}. Which angle is needed for the calculation depends on whether more movement occurred along the *x*- or *y*-axis. If more movement occurred along the *x*-axis, the angle *d* is going to be next to the displacement vector along the *y*-axis and vice versa. We can then solve for angles *c* and *d*:

$$if\ \Delta x > \Delta y\ then \begin{cases} d = atan\dfrac{\Delta y_{pos}}{\Delta x_{pos}} \\ c = \dfrac{\pi}{2} - b - d \end{cases} \tag{3.14a}$$

$$if\ \Delta x < \Delta y\ then \begin{cases} d = atan\dfrac{\Delta x_{pos}}{\Delta y_{pos}} \\ c = \dfrac{\pi}{2} - a - d \end{cases} \tag{3.14b}$$

From this point, we can derive U_t and U_s as U_{tot} is known from the previous calculations:

$$U_t = U_{tot}\cos(c);$$
$$U_s = U_{tot}\sin(c).$$

Lastly, we can acquire *x* and *y* vector component values for U_t and U_s:

$$if\ \Delta x > \Delta y\ then \begin{cases} U_{nx} = U_t\cos(a) \\ U_{ny} = U_t\sin(a) \\ U_{sx} = U_s\sin(a) \\ U_{sy} = U_s\cos(a) \end{cases} \tag{3.15a}$$

$$if\ \Delta x < \Delta y\ then \begin{cases} U_{nx} = U_t\cos(b) \\ U_{ny} = U_t\sin(b) \\ U_{sx} = U_s\sin(b) \\ U_{sy} = U_s\cos(b) \end{cases} \tag{3.15b}$$

As we have both pure tensile and pure shear movements, we introduce the concept of movement mode ratio which is defined as U_s/U_t.

Microseismicity

When looking at seismicity calculations, the classic Aki & Richards (2002) approach uses a point source on the fracture for the elastic wave emission. Due to this reason the fracture orientation and location determination approaches described in the section above had to be redefined. In the previous method, we used every bond's perpendicular plane as a fault surface. For this approach, a single fault plane with central point location and plane orientation had to be defined. To do this, the algorithm that records *x* and *y* positions of all the particles that have been flagged as "freshly fractured", as mentioned in the above section, is implemented. The middle point is then derived as an average of the *x* and *y* values. This brings us to the problem of determining the orientation of the fault plane. To do that, we employ a linear regression algorithm, which treats the broken particles as points in a *XY* scatterplot and puts the best fit line through it. The linear regression equation has the following form:

$$y = ax + b \tag{3.17}$$

Where a is a slope and b is an intercept (x value at which $y = 0$). If we know the midpoint (average *x* and *y* values), and we know the length and dip (slope), we can fit the average fault plane at that location. The length of the plane is acquired simply is a sum of diameters of half of the broken particles (The fracture has two walls; hence only half of the total number of particles is used). The most common method for fitting a regression line is the method of least-squares. This method calculates the best-fitting line for the observed data by minimising the sum of the squares of the vertical deviations from each data point to the line (if a point lies on the fitted line exactly, then its vertical deviation is 0). Because the deviations are first squared, then summed, there are no cancellations between positive and negative values. To calculate the regression, the following series of equations are used:

$$a = \frac{c - d}{e - f} \tag{3.18}$$

$$b = \frac{g - h}{n} \tag{3.19}$$

Where

$$c = n * \sum^{n} x * y \tag{3.20}$$

$$d = \sum^{n} x * \sum^{n} y \tag{3.21}$$

$$e = n * \sum^{n} x^2 \tag{3.22}$$

$$f = \left(\sum^{n} x \right)^2 \tag{3.23}$$

$$g = \sum^{n} y \tag{3.24}$$

$$h = a + \sum^{n} x \tag{3.25}$$

where n is the total number of particles along the fault walls marked as “freshly fractured”.

Once the location and orientation of the fracture plane are known, we need to calculate parameters which depend upon its reference to the observation point. For these simulations, we are using a setup where there is a grid of observation points, which can vary in depth. The grid is located in a way that its middle point is right above the middle point of the simulation box projection on the surface (Fig. 3.7).

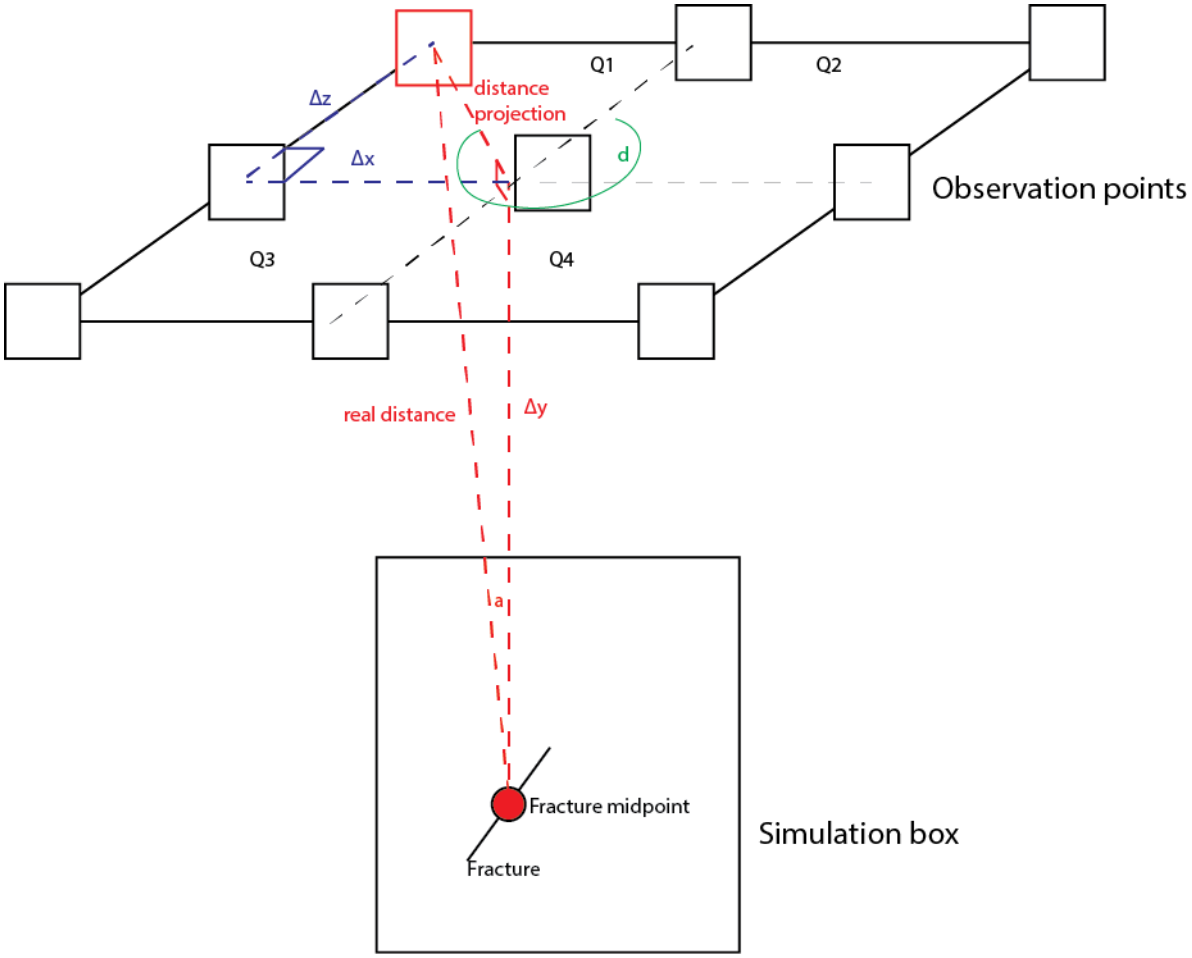

Figure 3.7. Schematic illustration of the observation point grid setup. Simulation box is located along the x axis with y coordinate being the depth. The central observation point is right above the midpoint of the simulation box. Third dimension is introduced via the z coordinate. Observation point grid is 3 by 3 in size but the number of stations in a line as well as distance between them can be varied. From knowing the x coordinate of the fracture midpoint and coordinates of the observation points it is possible to calculate the length of the seismic wave pathway's projection on to the surface. Using that and knowing the depth of the fracture midpoint it is then possible to calculate the length of the seismic wave's pathway itself. Lastly it is then possible to determine the azimuth of the wave as depending on its value and into which case quadrangle case can be referred to, case specific equations will be used for further calculations.

Since *x* and *y* coordinates are used to represent horizontal and vertical orientations in the original 2D model, *z* coordinate is going to be used to represent third dimension. From this setup, we know Δz as it is the distance of the observation point from the grid middle line along the x-axis. We can also calculate Δx and Δy as it is the difference between the *x* coordinate and *y* coordinate of the fracture midpoint and the *x* coordinate and *y* coordinate of the observation point. The distance projection (l_p) can be than simply calculated via triangulation formula $l_p = \sqrt{\Delta z^2 + \Delta x^2}$. From there, using the same approach, we can calculate the real distance (l) from the fracture midpoint to the observation point as $l =$

$\sqrt{\Delta y^2 + {l_p}^2}$. Finally, from these parameters we can determine the angle a as $a = \arctan\frac{l_p}{\Delta y}$. Once the angle a is calculated, it is going to stay the same, and we can project geometries on a 2D plane to simplify the required calculations. Once again, there are several geometrical configurations possible depending on the fault plane orientation and juxtaposition of the source point versus observation point (Fig. 3.8).

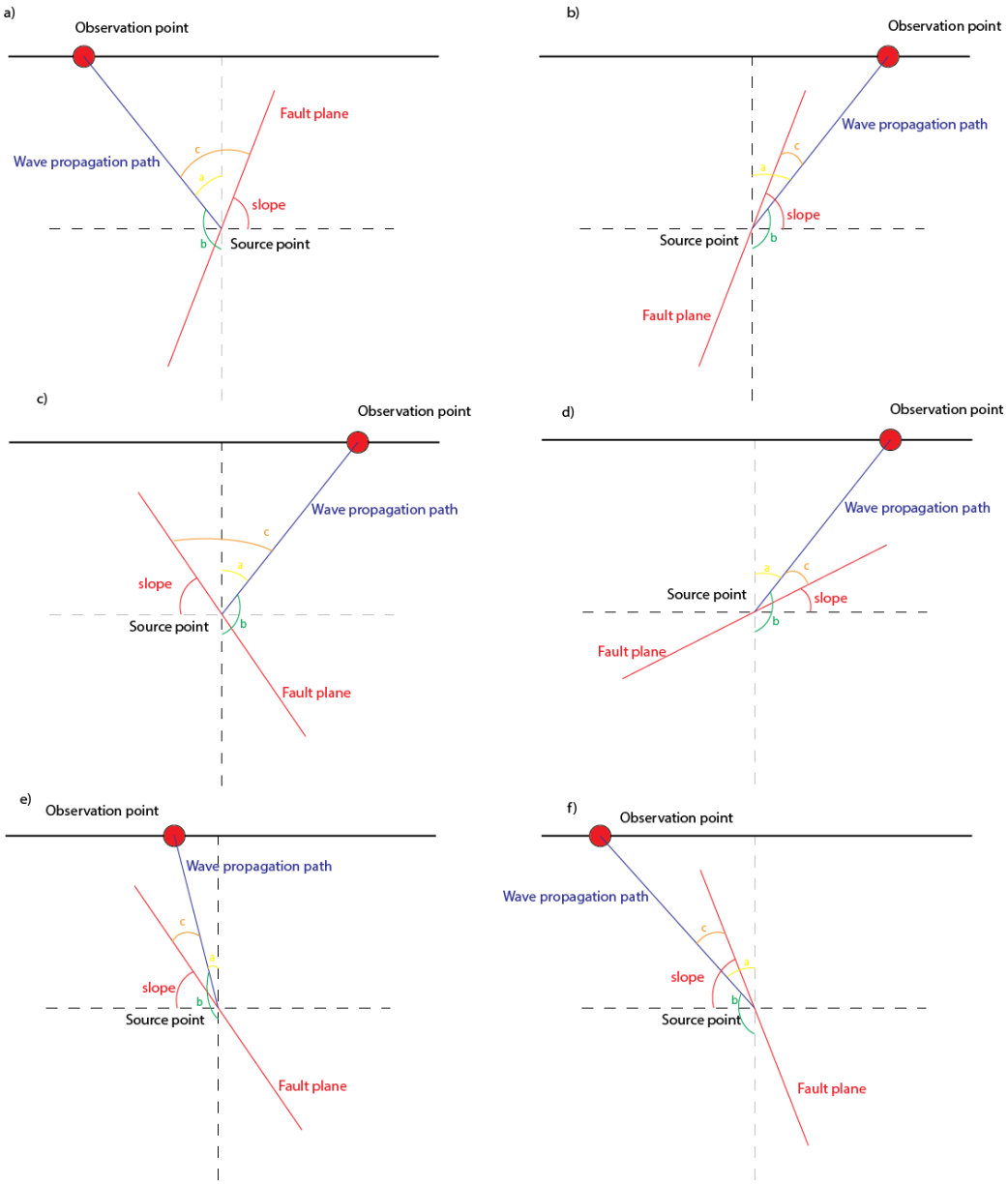

Figure 3.8. Different cases of juxta positioning fault surface and observation point. Differentiation depends upon the observation point and top half of the fault surface being in the same or different quadrangles and wave propagation path being located above or below the fault surface. Depending on the case, specific equations must be used to calculate directivity angle c, which lies between the wave propagation path and the fault surface.

The first angle that we can calculate is "slope" which is equal to the dip of the fault. It can be derived from the slope value a in the regression equation, where the value a essentially is a ratio between the values along the *x*- and *y*-axis. Therefore, if we assume that in the equation $y = ax + b$ $x = 1$ and $b = 0$, $y = a$. We can then plug these values into the slope angle value calculation as

$$slope = \operatorname{atan}\left|\frac{\Delta y}{\Delta x}\right| = \operatorname{atan}\left|\frac{a}{1}\right| = \operatorname{atan}|a| \tag{3.26}$$

The regression equation will also show if the slope value is positive (cases a, b, d in Figure 3.8) or negative (cases c, e, f in Figure 3.8). From this point, we can calculate all the required angles for the seismic wave propagation calculations. In Figure 3.7 the angle d is azimuth, measured clockwise from the z-axis to the wave propagation path surface projection, in Figure 3.8 the angle b is a take-off angle, which is measured from the vertical axis upwards to the wave propagation path and c is the directivity angle, which is measured between the fault plane and the propagation path. a in Figure 3.8 is a supplementary angle measured downwards from the vertical axis to the wave propagation path and required for the calculations. The take-off angle is the easiest to calculate as it is simply $b = \pi - a$. For the directivity angle c the calculations are case dependant. Cases a) and c) in Figure 3.8 are mirrored versions of one another, so the same calculation applies

$$c = \frac{\pi}{2} - slope + a \tag{3.27}$$

Cases d) and e) are also mirrored versions of each other, so for both of them c can be calculated as:

$$c = \frac{\pi}{2} - slope - a \tag{3.28}$$

The same applies to b) and f):

$$c = -\left(\frac{\pi}{2} - slope - a\right) \tag{3.29}$$

The azimuth d determination is again case sensitive depending on the juxtaposition of the source point and observation point. It can be calculated as a cosine function of the propagation path projection and Δx

$$if\ Q1\ \ d = 2\pi - \cos\frac{\Delta x}{dist_p} \tag{3.30a}$$

$$if\ Q2\ \ d = \cos\frac{\Delta x}{dist_p} \tag{3.30b}$$

$$if\ Q3\ \ d = \pi - \cos\frac{\Delta x}{dist_p} \tag{3.30c}$$

$$if\ Q4\ \ d = \pi + \cos\frac{\Delta x}{dist_p} \tag{3.30d}$$

This does not apply to special cases where $\Delta x = 0$ or $\Delta z = 0$. Then

$$if\ \Delta x = 0\ \begin{cases} d = 0 = 2\pi\ \ if\ \Delta z \geq 0 \\ d = \pi\ if\ \Delta z < 0 \end{cases} \tag{3.31a}$$

$$if\ \Delta z = 0\ \begin{cases} d = \frac{\pi}{2}\ if\ \Delta x > 0 \\ d = \frac{3\pi}{4}\ if \Delta x < 0 \end{cases} \tag{3.31b}$$

The last two angles required for the calculations are rake and strike. As we assume, all the fault movement is taking place in 2D space, and there is no out of plane movement we can assign permanent values of 90° ($\frac{\pi}{2}$) to these parameters. Once all these values are calculated, it is now possible to carry them over to the scripts in MatLab responsible for the creation of radiation patterns (Appendix C) and synthetic seismograms (Appendix D).

3.2 MiniTab software and Logistic Distribution

MiniTab is a commercial statistical analysis software developed by Pennsylvania State University. It automates calculations and the creation of graphs, which allows a user to better analyse and interpret data. As experiments have been run multiple times for the same parameters, results had to been accumulated and analysed as complex data. For this purpose, we are employing logistic probability distributions. It is in its essence similar to the normal distribution as it has a bell-shaped curve, however, due to the nature of the results, some of its properties

are more preferential for our experiments. Table 3.2 provides summary for the variables described in Chapter 3.2.

Table 3.2. Table of variables used in Chapter 3.2.

σ	Scale parameter
μ	Location parameter
$f(x)$	Probability density function
$N(x)$	Normal distribution function
$l(x)$	Logistic distribution function

In the probability theory and statistics, the logistic distribution is described as a continuous probability distribution. As for its cumulative distribution function, a logistic function is used, which is taken from the logistic regression theory. It has also been extensively used in modelling life data, electron physics and hydrology processes (Balakrishnan, 1991; Rost, 1991; Singh, 1997;). It is symmetric and unimodal. It has no shape parameter, which means it has only one shape (bell shape), and thus it is in its appearance similar to the normal distribution, however, it tends to have heavier tails. It has two input parameters: μ, the location parameter, and σ, the scale parameter. As this is symmetrical function, μ is determined as the function's mean and mode. The probability density function (PDF) can be described as:

$$f(x) = \frac{e^z}{\sigma(1+e^z)^2} \tag{3.32}$$

Where

$$z = \frac{x-\mu}{\sigma} \tag{3.33}$$

The variance of the logistic distribution is described by equation

$$Var(x) = \frac{1}{3}(\pi\sigma)^2 \tag{3.34}$$

The normal distribution is described as $N(x) = (\mu, \sigma^2)$, where standard deviation is used as σ. The logistic distribution is described only as $l(x) = (\mu, \sigma)$, where the scaling parameter σ is proportional to the variance. The proportion scale is typically set to 1 but can be changed in accordance to the input parameters and desirable shape of the bell curve. This means that the logistic PDF would be

exactly the same as the normal distribution, but only if the standard deviation is $\pi/\sqrt{3}$. Due to the nature of our samples, they can vary massively in scale. This means that by using normal distributions, we would either have to exclude far end members of the data set as outliers or run experiments a number of magnitudes more times to accumulate enough data points, so that these outlying data points would not skew the probability distribution curves. The fact that the logistic distribution equals mean to mode and allows to account for the outliers by setting variance independently of sample values makes it extremely useful to manage and analyse the current data. Interestingly, USA Chess Federation and World Chess Federation switched to logistic distribution from normal distribution when calculating players' skill levels for the same reason (Fenner et al., 2012).

The logistic probability density function has the following properties:

- When the mean μ is increased, PDF shifts to the right, when decreased – shifts to the left (Fig 3.9);
- When the scaling parameter is decreased, PDF gets taller and arms shift closer to the mean. When scaling parameter is increased, PDF becomes shorter and its arms become heavier (Fig 3.9).

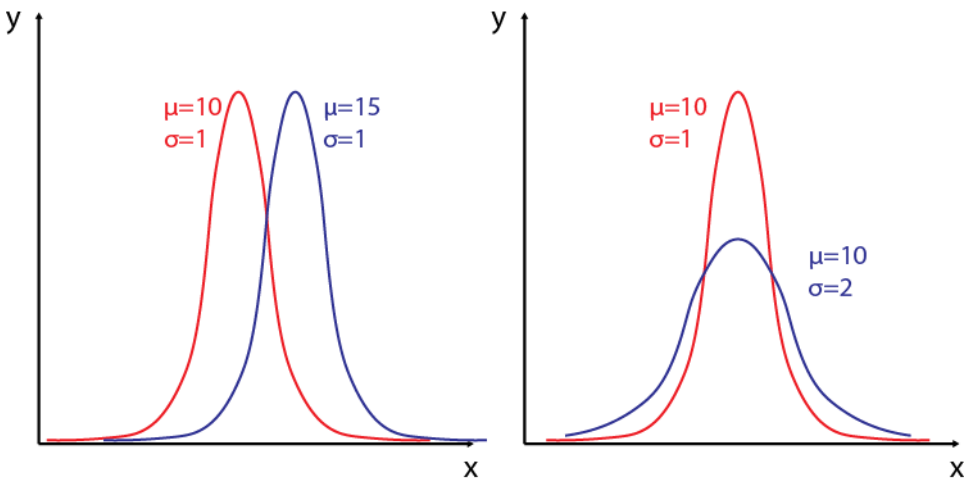

Figure 3.9. Illustration of the changes in the logistic probability distribution function if the changes are applied to the mean μ (left) and scaling parameter σ (right). When mean is altered, the distribution curve will move along the x axis, while if the scaling parameter is increased, the function height will decrease and arms will become heavier.

3.3 Hele-Shaw cell

A Hele-Shaw cell used for these experiments is constructed of two glass plates that are 70 x 32 cm in dimension. The plates are placed on top of each other separated by a distance of 1.5 mm. Equidistant spacing across the cell is provided by aluminum spacers, which are situated close to the edges of the cell. For the experiments that we were carrying out in this study, we made three boundaries completely impermeable and one boundary semi-permeable. The semi-permeable boundary consisted of a steel mesh securely located on the top boundary. The mesh size was 50 μm, and this was sufficiently small to keep the granular material within the cell while allowing for fluid to escape the system. One of the plates has an injection inlet, which is used for applying pressurised air to the system. It is located midway along the shorter fully impermeable boundary at the height of 3 cm above the clamps. The cell is then filled with non-expanded polystyrene sphere shaped grains that are 80 μm in diameter $\pm$ 1 μm called Ugelstadt spheres. The density of the spheres is 1.005 g/cm^3. The mass of the cell fill can vary between 50 and 170 g depending on the proportion of the space which has been filled. This corresponds to 52 $\pm$ 5% of solid fraction, which is within the error margin of the 57% random loose packing of monodispersed grains (Ciamara et al., 2010). However, this figure is a subject to an error of the 1.5 mm space measured between the plates which can reach up to 10%. Lastly, in contrast to the theoretical calculations, electrostatic forces and humidity can also have a real life effect on the experimental beads and decrease the solid fraction.

Before filling the cell, roughly 1-3% of the beads are coloured using Indian ink. This is done to provide markers and texture to the infill allowing for the better resolution of displacement measurements using optical data. The velocity, displacement and strain are then derived using digital image correlation analysis (a process that is described in detail in the following chapter paragraph).

The schematic illustration of the Hele-Shaw setup is shown in Figure 3.10. The sides of the Hele-Shaw cell are clamped using steel clamps after sealing them with double sided rubber sealing tape. To protect the glass from the stress, rubber sealing rings are used in between the clamps, screws and the glass. The two glass plates that are bound together by that point are then placed vertically, and beads

are poured into space between the two plates. The steel mesh is then glued using an epoxy glue gun to provide for the semi-permeable boundary.

As a part of the preparations, the Hele-Shaw cell, after the filling is completed, has the inlet hole plugged and is rotated vertically, so that the semi-permeable boundary is at the bottom. This allows the solid fraction within the cell to decompact and homogenise through gravitational settling of the beads. The cell is then rotated by 180 degrees, so that the semi-permeable boundary is on top. This allows for the repeated homogenisation process to occur. The glass is then thoroughly tapped on upon by a rubber hammer to compact the grains. This is done with a purpose to maximally increase friction between the grains in order to simulate conditions that are as close as possible to those of solid rock. Aside from friction, small amount of cohesion between the grains is present, mainly due to capillary bridges caused by humidity. Next, the cell is laid down horizontally. This has to be done as slowly and as carefully as possible to limit grain decompaction to a minimum. Once the Hele-Shaw cell is in a horizontal position, the plug from the inlet hole is removed, and an air tube leading to the compressor is attached. The cell then is once again slowly and carefully repositioned and fixed vertically with the semi-permeable boundary on top. Particular attention to the lifting is then still required in order to avoid the air channel backfilling with grains.

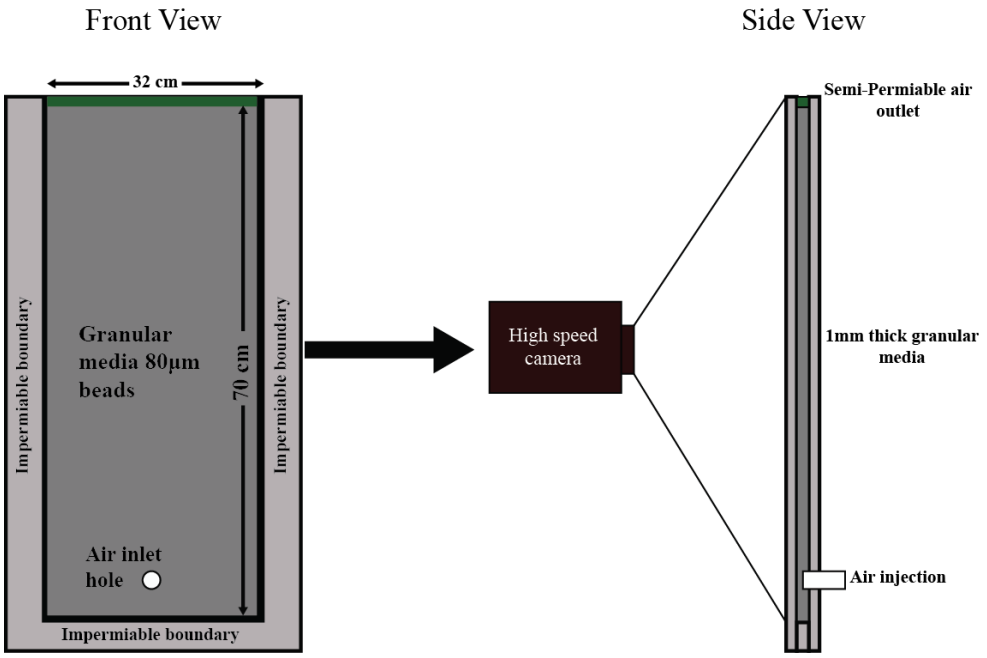

Figure 3.10. Schematic illustration of the Hele-Shaw cell used in the experiments. The 1mm thick space occupied by beads is 32cm wide and 70cm high. It is bound by impermeable boundaries from the sides and the bottom. Steel mesh is glued to the top to provide a semi-permeable boundary, which lets the air out but prevents the beads from escaping. Air inlet hole is located 3cm above the bottom boundary. Hele-Shaw cell is vertically oriented and high speed camera is positioned opposite it for the recording of the experiments.

During the experiments, the cell is positioned in a vertical orientation and stabilised to prevent any displacement caused by the vibration, as it is crucial for the image analysis that the image is not distorted. A black background matt is attached in the back. This is done to identify fracture space during the image analysis. Air injection is done by connecting a pressure tank via tubing to the Hele-Shaw cell. An electronic valve is placed close to the air inlet and the injection is started and ceased via a digital trigger signal being sent to the valve. A selected overpressure is set at the pressure tank outlet and is verified by a Honeywell pressure sensor with an accuracy of ± 4 kPa. Positioned opposite the cell is a Photron SA5 high speed camera, recording the air invasion into the cell at a framerate of 5000 frames per second and a resolution of 1024x1024 pixels (1 pixel ~ 0.7mm in the cell). Such high framerate filming requires extra abundance of lighting. We were using a 400 W Dedolight studio lamp which provides uniform, flicker-free illumination upon the beads in the cell. During the experiments, we recorded acoustic emission caused by the air injection and intergranular friction. The data were recorded by shock accelerometers positioned and fixed on the glass along the central vertical line at different distances from the injection inlet. The sensitivity range of the sensors is 200-900 kHz. The signal was then amplified with a Bruel and Kjaer Nexus Charge Amplifier – Type 2692-A. The amplified/conditioned signal was then transmitted to the computer via a Ni-DAQ mx PCI-6133 acquisition card with multiple channels at 1 MHz sampling rate. The TTL signal was used to trigger valve, camera and acoustic acquisition equipment – all at once – thus allowing to synchronise in time data acquired from all the apparatus pieces.

3.4 MatLAB

MatLAB is one of the most widely used scientific programming platforms. It is mostly renowned for its excessive computational and visualisation capacities and has been long used by scientific, engineering, mathematical and computational communities.

3.4.1 Digital Image correlation (DIC) and NCorr software package

For the Hele-Shaw experiments, a high-speed camera for recording was used. The experiments were recorded at a rate of 5000 frames per second. We have used the basic image subtraction technique written in MatLAB script, however, that provided only the basic insights into the deformation process. For a more advanced approach, we used the Digital Image Correlation (DIC) method.

Digital Image Correlation is a robust non-contact method for measuring deformation occurring in the material. It uses image registration algorithms to track the relative displacement of the points within the material between the reference baseline image (typically, the initial image of the undeformed material) and the following images (typically, images with progressive deformation). Such analysis can be carried out on a very wide scale ranging from tens of meters to nanometers as long as image sequences are properly recorded and are recognisably patterned. The DIC has been used to study behavior of diverse systems such as biological materials (Okahara et al., 2002; Sutradhar et al., 2014), shape memory alloys (Gall et al., 2002), metal alloys (Reynolds & Duvall, 1999; Pan et al., 2009) porous metals (Lefebvre et al., 2008) and others.

NCorr is an open source 2D digital image correlation MatLAB software package that carries out the function of DIC where it can calculate the value of displacement vectors from the particles as well as strains. It does so by scanning the reference image and subdividing it into subsets of predefined size. In each subset, a number of reference points are chosen. Points are given an arbitrary shape, their patterns and greyscale values are recorded, and reference coordinates are stored in the database.

Variables used in this Section are presented in Table 3.3.

Table 3.3. Table of variables used in Chapter 3.4.

x_{curr} and y_{curr}	Current point coordinates
x_{ref} and y_{ref}	Coordinates of the point in the reference image
u	Unilateral movement
v	Vertical movement
p	Transformation vector
C_{cc}	Cross-correlation coefficient
C_{LS}	Least-squares coefficient
f	Grayscale value function for refference image
g	Grayscale value function for current image
f_m and g_m	Mean grayscale values
E_{ij}	Lagrangian strain

The transformation of the initial reference image subset to the state of the following image is constrained to a linear, first order transformation as:

$$x_{curr} = x_{ref} + u_{rc} + \frac{\partial u}{\partial x_{rc}}\left(x_{ref} - x_{ref_c}\right) + \frac{\partial u}{\partial y_{rc}}\left(y_{ref} - y_{ref_c}\right) \tag{3.35}$$

$$y_{curr} = y_{ref} + v_{rc} + \frac{\partial v}{\partial x_{rc}}\left(x_{ref} - x_{ref_c}\right) + \frac{\partial v}{\partial y_{rc}}\left(y_{ref} - y_{ref_c}\right) \tag{3.36}$$

Where x_{curr} and y_{curr} are current point coordinates, x_{ref} and y_{ref} are coordinates of the same point in the reference image. u and v denote unilateral and vertical movement respectively. Subscript *c* points to the central point in the reference subset while subscript *rc* is meant to signify that the transformation is from the reference coordinate system to the current coordinate system. From this, the general transformation vector p is defined as

$$p = \left\{u \;\; v \;\; \frac{\partial u}{\partial x} \;\; \frac{\partial u}{\partial y} \;\; \frac{\partial v}{\partial x} \;\; \frac{\partial v}{\partial y}\right\}^T \tag{3.37}$$

This accounts for all the possible transformation modes possible to the subset to endure as seen in Figure 3.11.

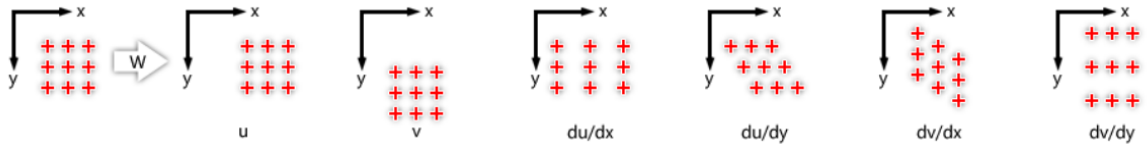

Figure 3.11. Illustration of all the possible deformation modes. From left to right: original reference point positioning, uniform shift along the x axis, uniform shift along the y axis, uniform extension along the x axis, strain along the x axis, strain along the y axis, uniform extension along the y axis.

The next step is to provide a quantitative value between the final reference subset and final current subset. This is done by comparing the grayscale values of both subsets. The two metrics that are used in this and most other DIC is the cross-correlation (C_{cc}) and least square (C_{LS}) criterions.

$$C_{cc} = \frac{\sum \left(f(\tilde{x}_{ref}, \tilde{y}_{ref}) - f_m\right)\left(g(\tilde{x}_{curr}, \tilde{y}_{curr}) - g_m\right)}{\sqrt{\sum\left[f\left((\tilde{x}_{ref}, \tilde{y}_{ref}\right) - f_m\right]^2 \sum\left[g(\tilde{x}_{curr}, \tilde{y}_{curr}) - g_m\right]^2}} \tag{3.38}$$

$$C_{LS} \sum \left[\frac{f(\tilde{x}_{ref}, \tilde{y}_{ref}) - f_m}{\sqrt{\sum\left[f\left((\tilde{x}_{ref}, \tilde{y}_{ref}\right) - f_m\right]^2}} - \frac{g(\tilde{x}_{curr}, \tilde{y}_{curr}) - g_m}{\sqrt{\sum\left[g((\tilde{x}_{curr}, \tilde{y}_{curr}) - g_m\right]^2}}\right]^2 \tag{3.39}$$

Where f and g are grayscale value functions for refference and current images, respectively, and return the grayscale value to the specified (x,y) point. f_m and g_m are the mean greayscale values for the given reference and current subsets and are expressed as:

$$f_m = \frac{\sum f(\tilde{x}_{ref}, \tilde{y}_{ref})}{n(S)} \tag{3.40}$$

$$g_m = \frac{\sum g(\tilde{x}_{curr}, \tilde{y}_{curr})}{n(S)} \tag{3.41}$$

Where $n(S)$ is the number of the elements in the given subset. A good match is indicated when C_{cc} is close to 1 and C_{LS} is close to 0. Both of these criterions are related and are aimed to provide numerical solution for the same problem, however, each respective criterion is easier to calculate in the certain situations, which is why both of them are used.

This allows then to calculate the displacement fields for a single material point located at the center of an initial reference subset. This is done by selecting region of interest (ROI) within the image and determining displacement data in a grid of ROI. As a result, we obtain an array of displacement values. The displacements are then either reduced or incorporated into "continuous displacement" values. This is done by selecting arbitrary points within the ROI, calculating C_{cc} and C_{LS} for points neighboring the reference point. If there is no correlation, the point is "deactivated", otherwise the script goes into another loop and calculates C_{cc} and C_{LS} for all the points neighboring that point. This is done until all the points have been deactivated or all the values in the potential points in the give ROI have been checked.

Once the displacement array map is created it is possible to calculate for the Green-Lagrangian strains (E_{ij}) which are obtained using the displacement gradients:

$$E_{xx} = \frac{1}{2}\left(2\frac{\partial u}{\partial x} + \left(\frac{\partial u}{\partial x}\right)^2 + \left(\frac{\partial v}{\partial x}\right)^2\right) \tag{3.42}$$

$$E_{xy} = \frac{1}{2}\left(\frac{\partial u}{\partial y} + \frac{\partial v}{\partial x} + \frac{\partial u}{\partial x}\frac{\partial u}{\partial y} + \frac{\partial v}{\partial x}\frac{\partial v}{\partial y}\right) \tag{3.43}$$

$$E_{yy} = \frac{1}{2}\left(2\frac{\partial v}{\partial y} + \left(\frac{\partial u}{\partial y}\right)^2 + \left(\frac{\partial v}{\partial y}\right)^2\right) \tag{3.44}$$

4. Modelling hydraulic fracturing

This Chapter demonstrates the complexity of the behaviour of the hydraulically fractured system. The simulations focus on the dynamics of the solid-state deformation, geometries of the created fractures as well as a seismic component of the fracturing. The aim of this Chapter is to look into the dynamics of the solid and fluid phases during the fracture propagation and which mechanical parameters of the solid have the biggest impact upon the developed fracture networks. This Chapter further investigates how geometries of the fracture networks change when altering the natural and anthropogenic parameters as well as monitors the stress change in the system during hydrofracturing. The summary of the parameters used in most of the experiments that are discussed is given in Table 4.1.

Table 4.1. Sets of varied parameters throughout the experiments.

	Depth (m)	Young's moduli (GPa)	Poisson's Ratio	Porosity	Injection rate	Tensile Strength (MPa)	No. of simulations conducted
Default	3000	6	0.3	~1%	80000Pa/30s	44.2	10x10000 time steps (each setting)
Young's modulus	3000	4.5; 6; 7; 8; 9; 10; 12.5; 15; 20; 30 ;40			80000Pa/30s	44.2	
Lower injection rate	3000				**50000Pa/30s**	44.2	
Shallower depth	**1000**				80000Pa/30s	44.2	
Variable tensile strength	3000				80000Pa/30s	**27.2; 34; 44.2; 54.4**	

Note: Main parameters of interest are the depth (column height of the overburden rock), Young's modulus, Poisson's ratio, porosity, fluid pressure injection rate and tensile strength of the rock.

First, the general dynamics of a single experiment is discussed. Then a comparison of the dynamics is presented depending on characteristic changes in the experiments. In total, almost 800 simulations have been run to provide data for this part of the project.

4.1. Analysis of a single fracturing event

For the simulations the coupled hydro-mechanical DEM is used. DEM is composed of the triangular network of solid particles inter-connected with springs, which is overlain by the fluid phase continuum grid. The fluid and solid phases are coupled using tent function. The experiments were carried out in a vertically oriented simulation box where the gravity force is acting upon the particles. The fluid pressure was then locally increased in one of the nodes closer to the bottom margin using the time step function (Fig. 4.1).

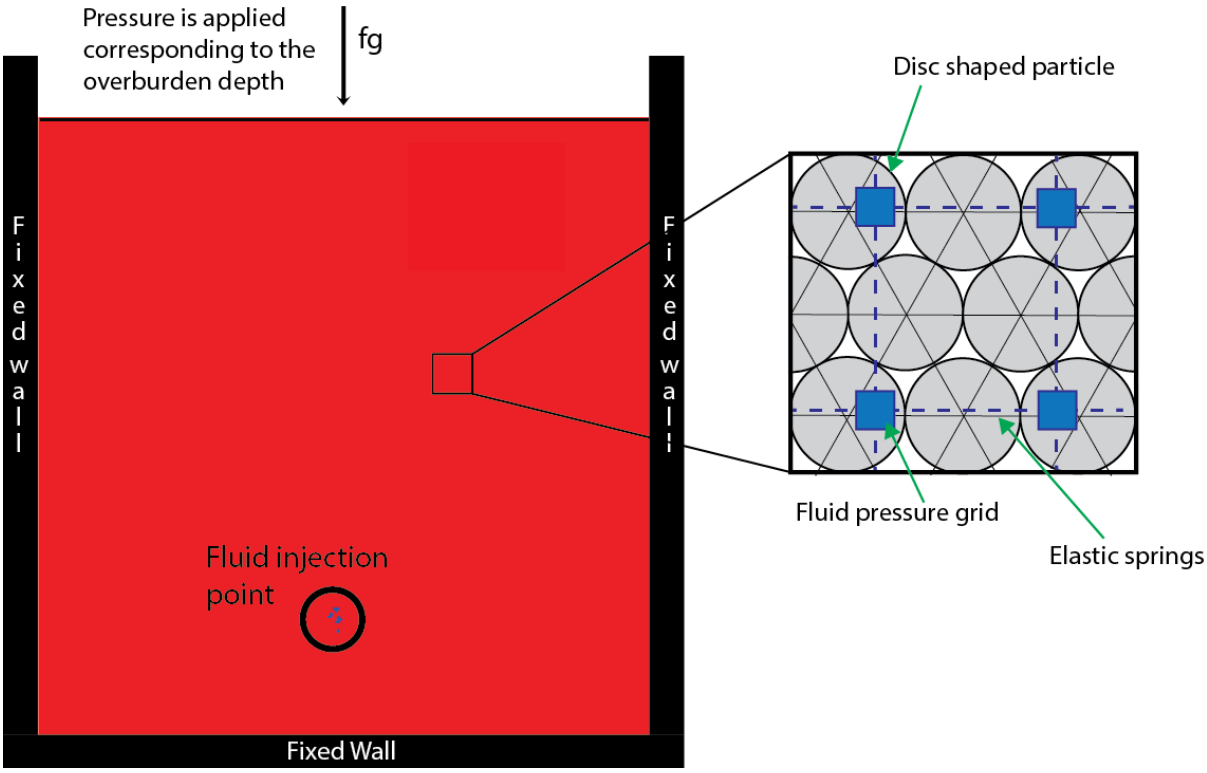

Figure 4.1. Setup of the vertically oriented simulation box. DEM is composed of disc shaped particles that are connected by elastic springs and overlain by the fluid pressure grid. Pressure is applied to correspond to the overburden depth.

4.1.1. Particle displacement

In this Section, snapshots of the same experiment are presented showing different properties at the same time step.

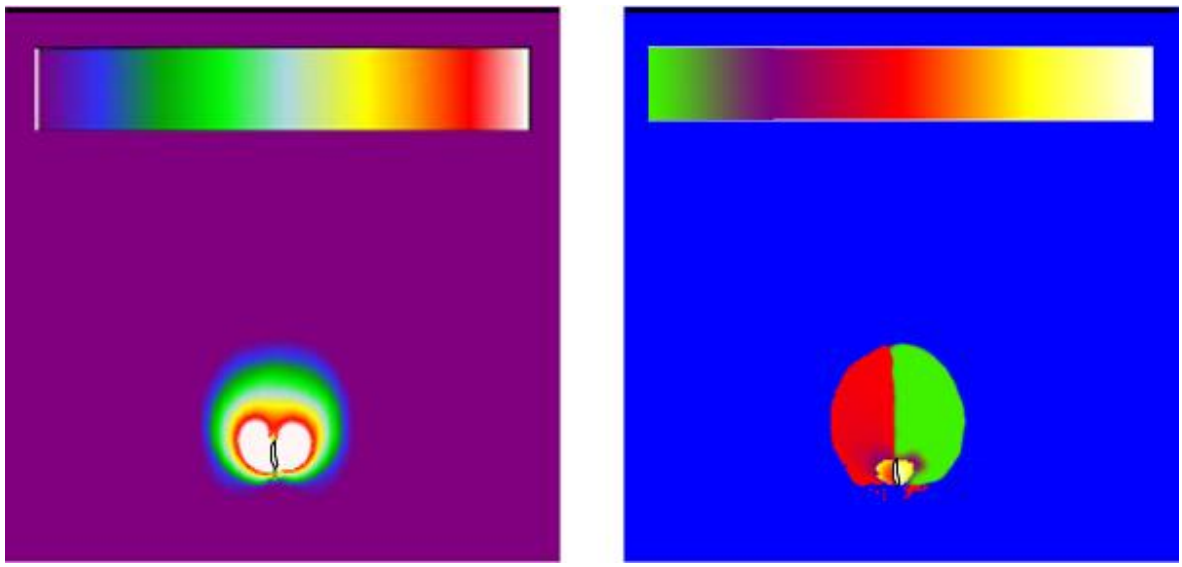

Figure 4.2. Left: relative particle displacement amount where purple colour indicates no displacement and white is the maximum displacement in the given time step. The displacement cloud has an ellipsoid shape and there is a gradual decrease of the displacement amount from the centre, where fracturing is occurring towards the edge of the ellipsoid. Right: azimuth (angle of the displacement vector of the particles) calculated counter-clockwise from the vector pointing to the right (pointing East = 0^0).Green indicates movement to the right, purple indicates upwards (90^o), red – left (180^o), yellow – down (270^o), white also right (360^o). Purple colour gradients indicate movement to the right and upwards, while gradients between white and yellow indicate movements to the right and downwards. Two colours are assigned to "right" direction, as the azimuth was calculated in radians and two values were required for 0 and 2π. Contrasts in colours between the inner smaller circle and the outer larger circle indicate the rebound effect of the compaction field created around the fracture. Approximate fracture outline is indicated by black line in both panels.

Figure 4.2 shows one time step in a simulation with the figure on the left illustrating particle displacement and the figure on the right showing movement angle of the particles. For this experiment, the injection rate was intentionally set 100 times stronger to exaggerate the effect it causes on the elastic media. Figure 4.2 illustrates the relative displacement of particles from the beginning of the time step and at the end of the time step, where purple colour indicates zero displacements and white indicates a relative maximum. The displacement cloud has ellipsoid shape, and there is a gradual decrease of the displacement amount from the centre, where fracturing is occurring towards the edge of the ellipsoid. An interesting feature is that there is a relatively smaller amount of displacement right on top of the fracture compared to the displacement on the sides (top diagonals from the fracture). This would potentially create differences in the stress states. This is illustrated by the horizontal stress change in that time step (Fig. 4.3).

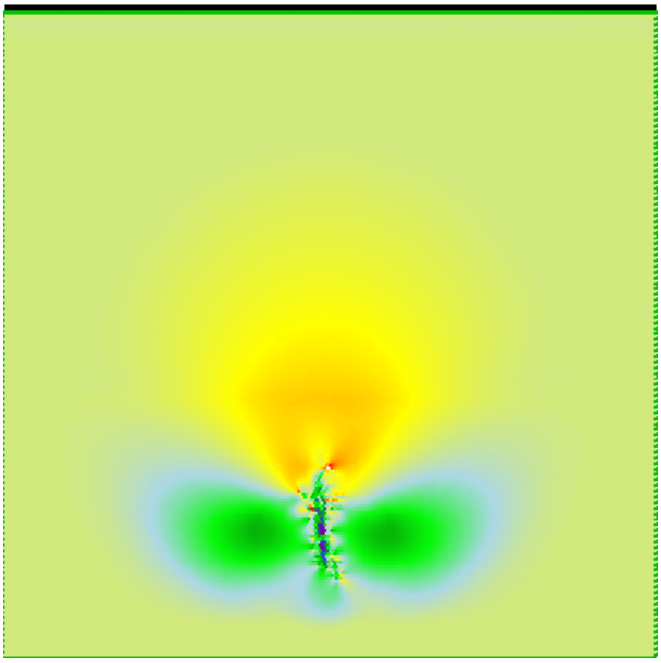

Figure 4.3. Changes in the horizontal (XX) stress throughout one-time step. Engineering convention is used, meaning that cold colours (blues and greens) indicate an increase in stress, while warm colours (yellows and reds) show a decrease. Due to the occurring fracturing, the system is horizontally stressed both to the left and right of the fracture walls while the drop in horizontal stress is observed in the area above the fracture top tip.

In this figure, the engineering convention is used, meaning that warm colours depict the drop-in stress while cold colours show the increase. It can be observed that tensile movement of the fracture walls cause the stress increase to the left and right of the fracture, while a decrease in horizontal stress can be observed in the area above the fracture. Another interesting aspect that we can observe is the directivity of the particle displacement. In Figure 4.2 (right), four colours represent the main directions: blue and white – right, purple – up, red – left and yellow – down. Two colours are assigned to "right" as the full azimuthal circle includes values 0 and 2π, thus two values are required for the end members in the colour scheme. Most of the displacement vectors show particle movement along the horizontal axis. However, alterations between the particles can be seen when they are being pushed either upwards or downwards indicated by a vector component with a rather sharp boundary between them. The boundary lies just to the middle of the area where fracturing is occurring. This observation leads to two conclusions. First, there is the obvious plane of weakness, which can trigger sideways fracturing with the potential of becoming mode II fracture. Second, it means that particles are being pushed aside from the predominant, purely

horizontal vector, which is dominant across the rest of the system. That, in a combination with the relative displacement map and horizontal stress map, shows that diversion happens just before the area of the maximum stress. This indicates the presence of a compaction zone, which particles try to avoid by diverting their movement vector. The significance of these two observations will be discussed further in Chapter 5.

4.1.2 Differentiation of fracture network patterns.

A series of experiments were carried out to examine the behaviour of the system depending on the amount of fluid being injected in one-time step and the breaking strength of the bonds.

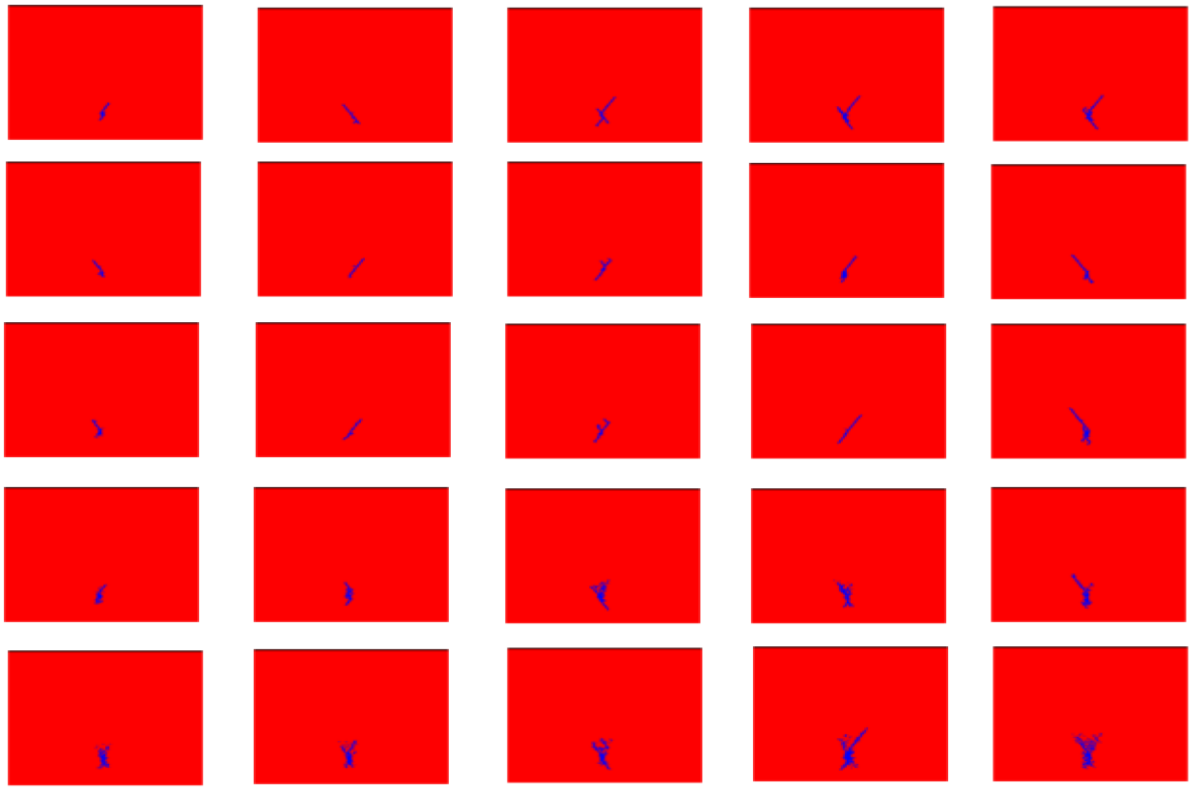

Figure 4.4. Series of 25 experiments illustrating changes in the fracture network geometries when changing the distribution of the breaking strength of the system and amount of the fluid pressure increase per time step at the injection node. From left to right: fluid pressure increase in the injection node per time step is 400 kPa, 500 kPa, 600 kPa, 700 kPa and 800 kPa. From top to bottom: variance interval (maximum and minimum boundaries) of the bond breaking strength are $\pm$ 40%, 50%, 60%, 70% and 80% of the mean 33.4 MPa value.

Figure 4.4 shows the results obtained throughout the 25 experiments. Experiments were carried out with the 3000m high overburden column, 0.3 Poisson ratio and 10 GPa Young's modulus. The fluid pressure change per time step increases from

left to right, and the values used are 400 kPa, 500 kPa, 600 kPa, 700 kPa, 800 kPa. The second parameter that was changed was the distribution of the breaking strength values of the rock. This means that the mean tensile strength value for all the experiments was 33.4 MPa and then the maximum variance of the bond strength could be $\pm$ 40%, 50%, 60%, 70% and 80% (from top to bottom) of that value.

Changes in the values produce a different effect. This is expected as brittle rocks in nature are heterogeneous and fracturing patterns are highly dependent upon the internal microstructures (Tapponier and Brace, 1976; Wong, 1982). Sedimentary rocks are composed of grains varying in sizes and internal tensile strength. Grain contact anisotropy (distribution in length and angles of the contacts between grains) introduce the second parameter influencing the system's tensile strength heterogeneity (Fredrich et al., 1990; Wong et al., 1996). Tensile failure mechanism on a microscale plays important role as microfractures tend to nucleate in the area of small tensile strength, propagate and coalesce into macrofractures (Fredrich et al., 1995; Wong et al., 2006)

Change in the brittleness of the rock causes the formation of more divergent fracture networks. Examples in the top row of Figure 4.4 show either one or two predominant fractures, which tend to form conjugates and have very few offspring fractures. However, with an increase in heterogeneity (amount of bonds that have more both more extreme low and high tensile strength value), the pattern of the fracture network becomes less uniform. More offspring fractures are present, and the conjugate system is not so profound. In some cases, fluid was able to seep through the pores and cause bond breakage outside the main connected fracture network. The increase in the fluid pressure injected per time step had a linear effect on the number of broken bonds breaking, and thus the size of the total fracture network. This can be explained by the fact that in between the injection stages fluid was seeping away through pores, and while the seepage rate is the same, residual fluid pressure in the fracture would be higher when more fluid is injected. That means that the only way to relieve the built-up stress is through further fracturing.

4.1.3 Single fracturing event description

In this Section, the characteristics of a typical fracturing event are discussed. The numerical model follows a similar behaviour and fracturing pattern in all presented cases that show hydrofracturing. In cases where the injection rate is too low or the porosity too high the fluid just seeps away, and no fractures develop. Hydrofracturing typically takes place in four distinct stages: 1) build-up of stress, 2) fracturing, 3) residual fracturing, 4) seeping (Fig. 4.5; 4.6; 4.10).

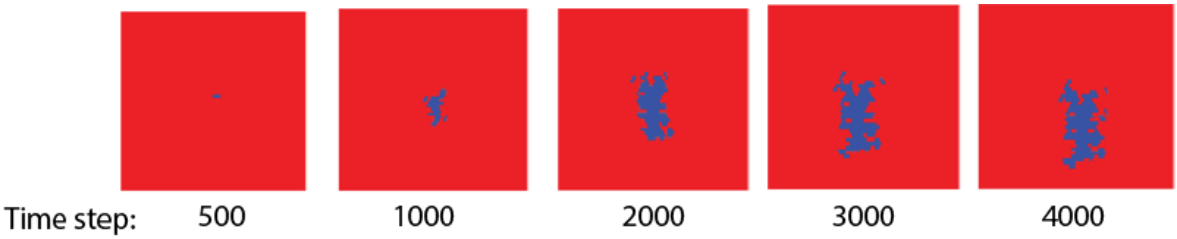

Figure 4.5. Zoom in on the fracture evolution through four different stages. Up to time step 1000 mostly stress build up is occurring with very limited fracturing. Time steps 1000 to 2000 are in the active fracturing where most of the fracture network is developed. Interval between time steps 2000 and 3000 shows residual fracturing where rate of fracture development significantly slows down. Last interval shows the seeping stage where almost no new fractures are created.

In the first stage, the fluid is injected at the centre of the model in several intervals. The fluid pressure diffuses into the pore space slower than the injection rate so that sufficient fluid pressure gradients build up that lead to fracturing. This continues until the most pore spaces surrounding the injection point are filled and the system becomes saturated. Stage two resembles the active hydrofracturing where most of the seismic events can be observed. This stage typically lasts for about 1500-2000 model steps. During the third stage, residual fracturing takes place. In this stage, the overall porosity and permeability of the system have increased enough due to fracturing and fracture opening for the fluid to seep away. At this point, it takes quite long time to build up enough pressure to overcome the tensile breaking strength of the rock so that only minor fracturing events take place. In the fourth and final stage, the system reaches a steady state where porosity and permeability have increased enough for the fluid to seep away and no additional fractures develop.

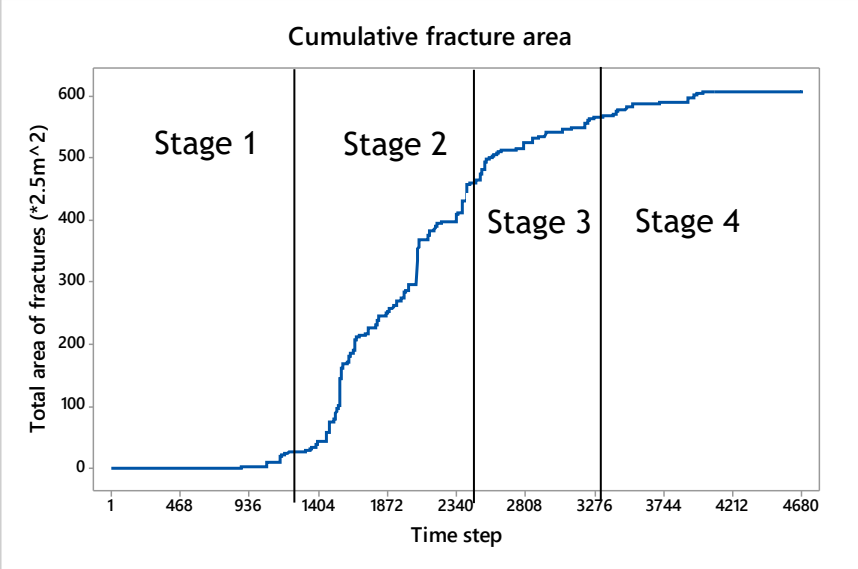

Figure 4.6. The model of a single fracturing event shows four stages of fracture evolution: 1) build-up of stress, 2) fracturing, 3) residual fracturing, 4) seeping. Timing and intensity of the fracturing depend upon the parameters, for the default setting time step intervals for these stages are 1) 0-1300, 2) 1300-2400, 3) 2400-3300, 4) >3300.

Figure 4.7 shows the fluid pressure gradient evolution. The dynamics of fluid pressure gradient changes correspond to the fracturing events where the growth of fractures decreases proportionally to the increase in the cumulative fractured area. The system comes to the status quo once the overall porosity and permeability have increased to the point where all the input fluid seeps away without putting any extra stress on the system. At this stage, it is just enough to prevent the fractures from closing.

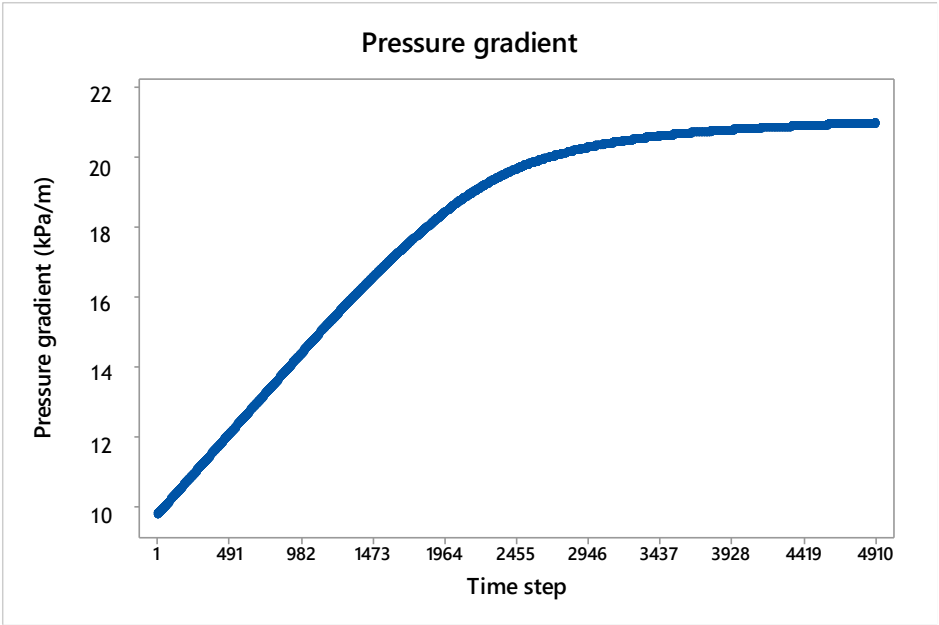

Figure 4.7. The figure shows changes in the fluid pressure gradient. In the default setting the fluid pressure gradient is less susceptible to changes due to a low initial porosity and relatively high fluid injection rate. Timing in the drop in the increasing rates of the fluid pressure gradient corresponds with the timing of the fracturing rate decline.

The effect of depth change

As mentioned earlier, this is a very dynamic system which has a multitude of factors affecting the process. One of the most important factors is the height of the overburden rock column. Figure 4.8 shows the cumulative fractured area for experiments carried out at 1 km, 2 km and 3 km. The major difference that can be seen is the total number of broken bonds, where the shallowest experiment produced the least amount of fracturing while the deepest one has produced the most. The gradient of all the curves during the active phase of fracturing is the same. Also, the active phase of fracturing in all three cases starts at around time step 1200.

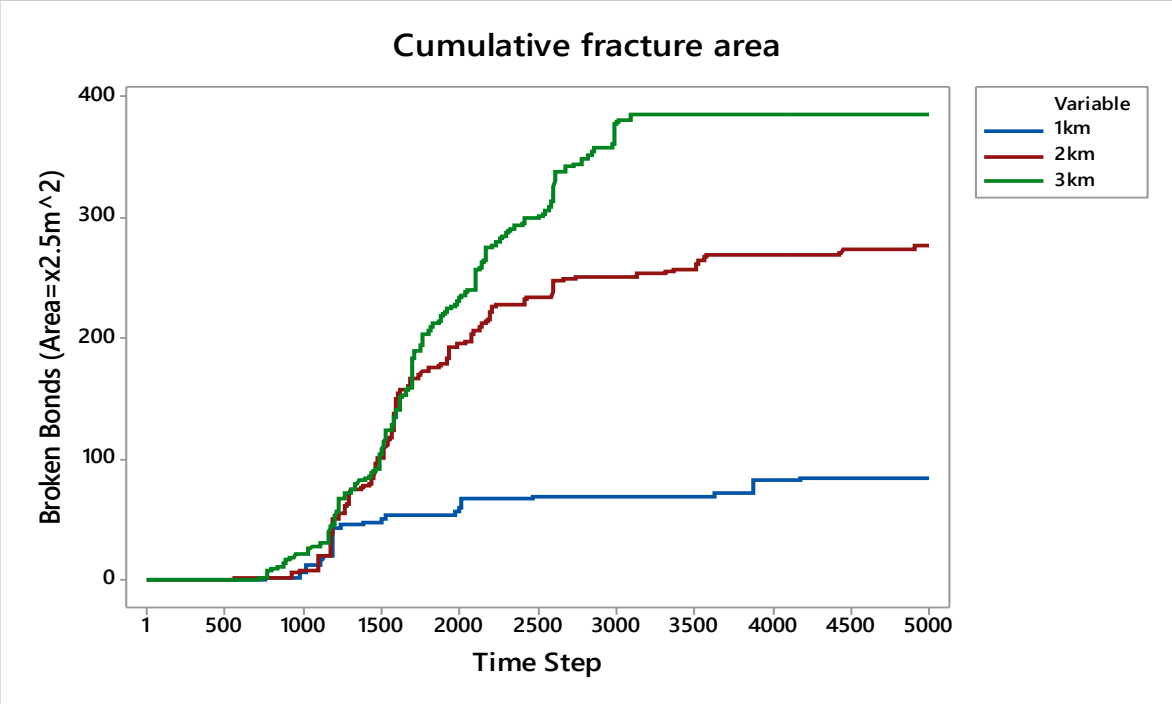

Figure 4.8. The total fractured area increases with the increase of the overburden rock column thickness.

Figure 4.9 shows the fluid pressure gradients for three different depths. The shapes of all three depths are almost the same with a shift in time, where shallower experiments have growth in gradient drop first. Despite the slope of curves being the same for the initial stages of the experiment, flattening out of the line is more gradual for the shallower case. From these two graphs, a tradeoff between the intensity of fracturing and how fast it drops towards the later stages of the experiment can be seen.

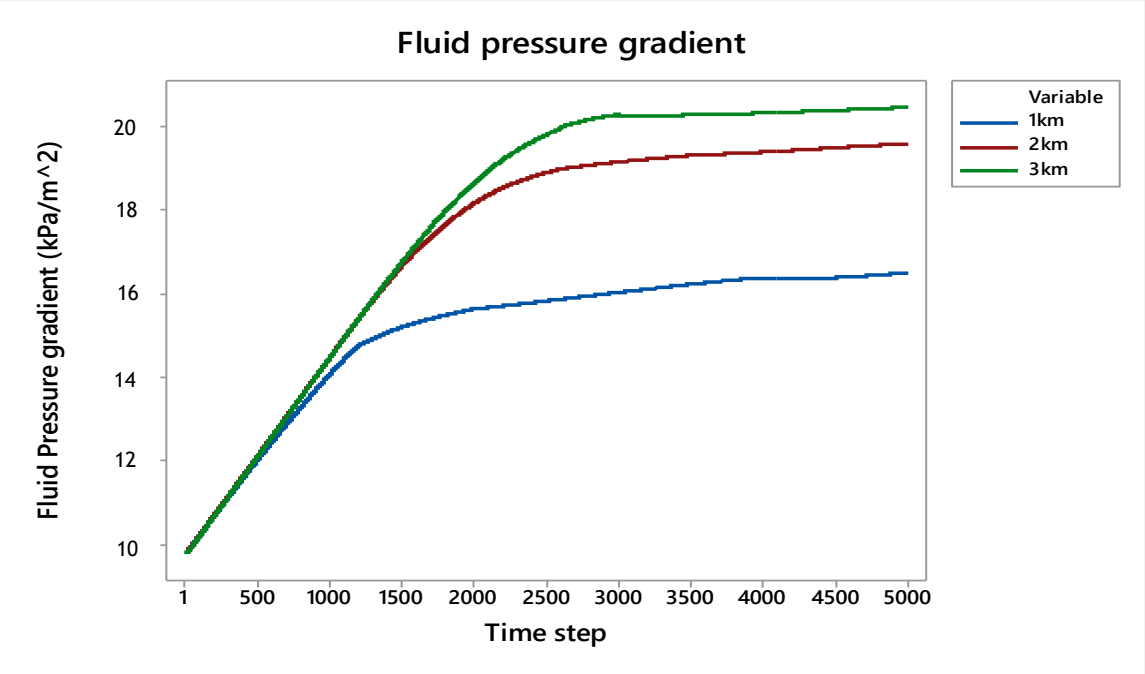

Figure 4.9. Shapes of fluid pressure gradient growth curves are similar for all three depths. Experiments at the deeper depths provide the larger final value of the fluid pressure gradient, however, the curve and plateauing of the trend is more gradient for the experiments at the shallower depths.

The effect of decreased injection pressure

For the following experiments, fluid injection pressure was decreased from 80’000 Pa to 50’000 Pa per interval (time step) of 30 s. Experiments were simulated to be at 3 km depth. Figure 4.10 shows how both cumulative fracturing and fluid pressure gradient compared to the experiments of 80’000 Pa per 30 s at 3 km and 1 km depth.

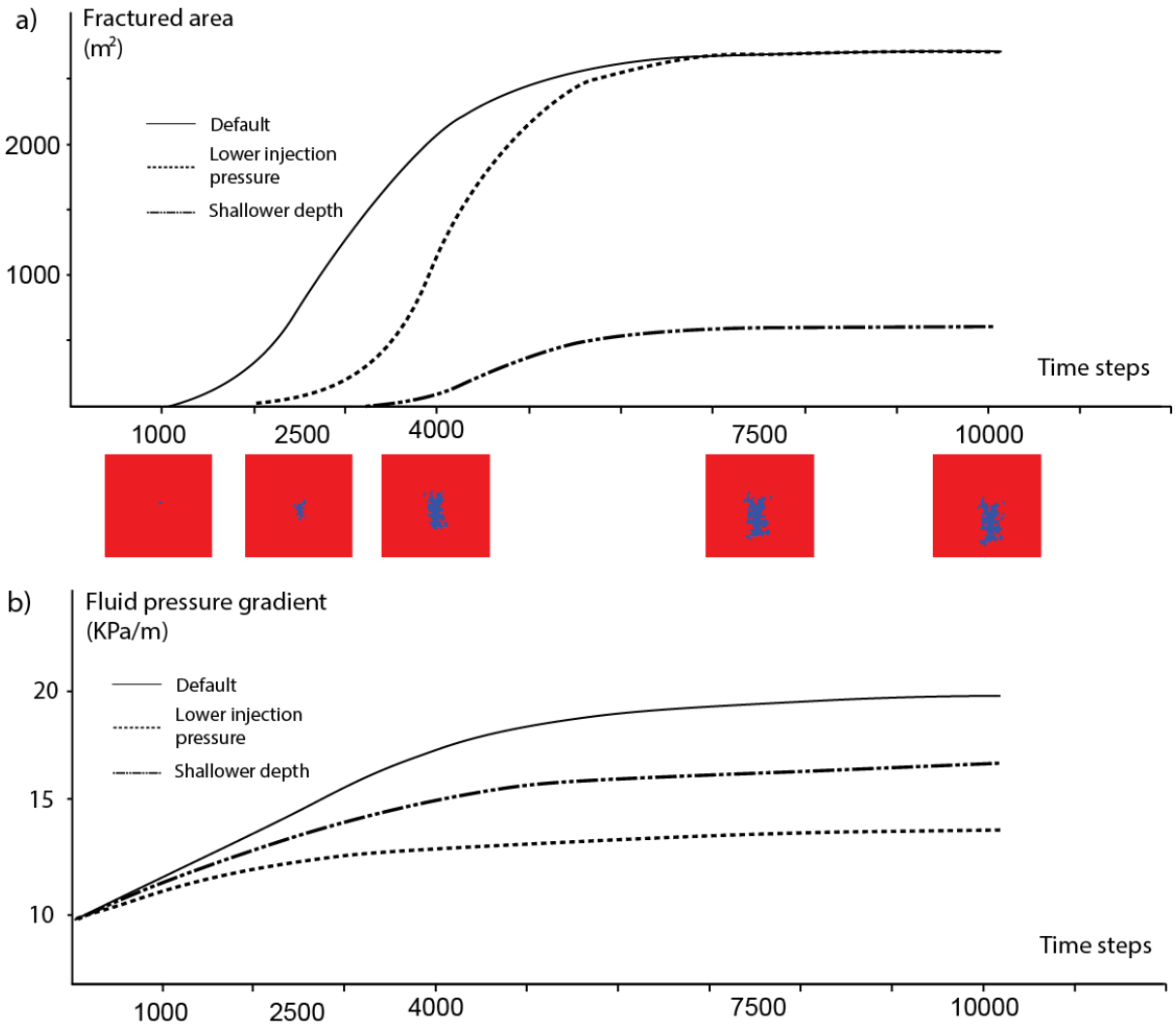

Figure 4.10. Changing the parameters of the model moderates the timing and intensity of the fracturing, however, the overall pattern is preserved in all cases. In the default setting the fluid pressure gradient is less susceptible to changes due to a low initial porosity and relatively high fluid injection rate. Once the injection rate is lowered or seepage is increased via an increase in porosity, it becomes more sensitive to further overall porosity increase through fracturing.

For the fractured area, the trend is exactly the same as for the default setting case with a temporal delay. It can be explained by the fact that more time is required for the pore fluid pressure to grow to the point where tensile failure starts to occur. Once it does, it follows at the same rate as the default case due the system pores being saturated and no fluid injected seeping away. As for the fluid pressure gradient, since the injection rate is smaller, the slope of the gradient growth is smaller from the beginning of the experiment. However, all three cases show the same behaviour that the slope becomes flat once the system has fractured and fluid is actively seeping away. All three experiments converge to a constant fluid pressure gradient, which is expected of a system reaching

equilibrium state. The experiment with the lower injection pressure has a lower fluid pressure gradient as there is less fluid pressure introduced per time step in the injection point. The shallower depth experiment has a smaller degree of compaction due to smaller vertical force, accounting for the height of the overburden column, applied. Smaller compaction results in the increased porosity and thus permeability of the system. This again causes for the lower final pressure gradient in the system compared to the 3 km experiment.

4.2. Effect of changing Young's modulus

Throughout the run of several numerical experiments, we discovered that the greatest effect on changing the behaviour of the fracture propagation was due to modifying the Young's modulus. The following results are a representation of at least ten experiments run for each parameter set and binned using the logistic distribution. This was done to reduce uncertainty, gather more data and to verify experiment integrity. The logistic distribution was chosen as it is better equipped to deal with data sets with large variable spreads. More details on the use of the logistic distribution is provided in Chapter 3. In the first set of experiments, the Young's modulus (E) was varied from 4.5 GPa to 6, 7, 8, 9, 10, 12.5, 15, 20, 30 and 40 GPa. In order to illustrate the model behaviour, we studied 4 parameters, the moment magnitude release during model runs (Figure 4.13), the distribution of fracture wall displacement or aperture (Figure 4.11), the distribution of the amount of broken bonds for single fracture events (Figure 4.12) and the distribution of movement mode ratios in model runs (mode I versus mode II, Figure 4.14). The moment magnitude is derived from the seismic moment M_0 using the approach by (Hanks & Kanamori, 1979) via the equation

$$M_w = \frac{2}{3} log_{10}(M_0) - 10.7 \tag{4.1}$$

The moment magnitude scale is a modern analogue to the outdated Richter scale. It is an analytical approach that relies on the seismic moment rather than recorded seismogram wave amplitude to quantify the energy released, as the wave amplitude approach proved to be inaccurate when dealing with very large or very small earthquakes (Hanks & Kanamori, 1979).

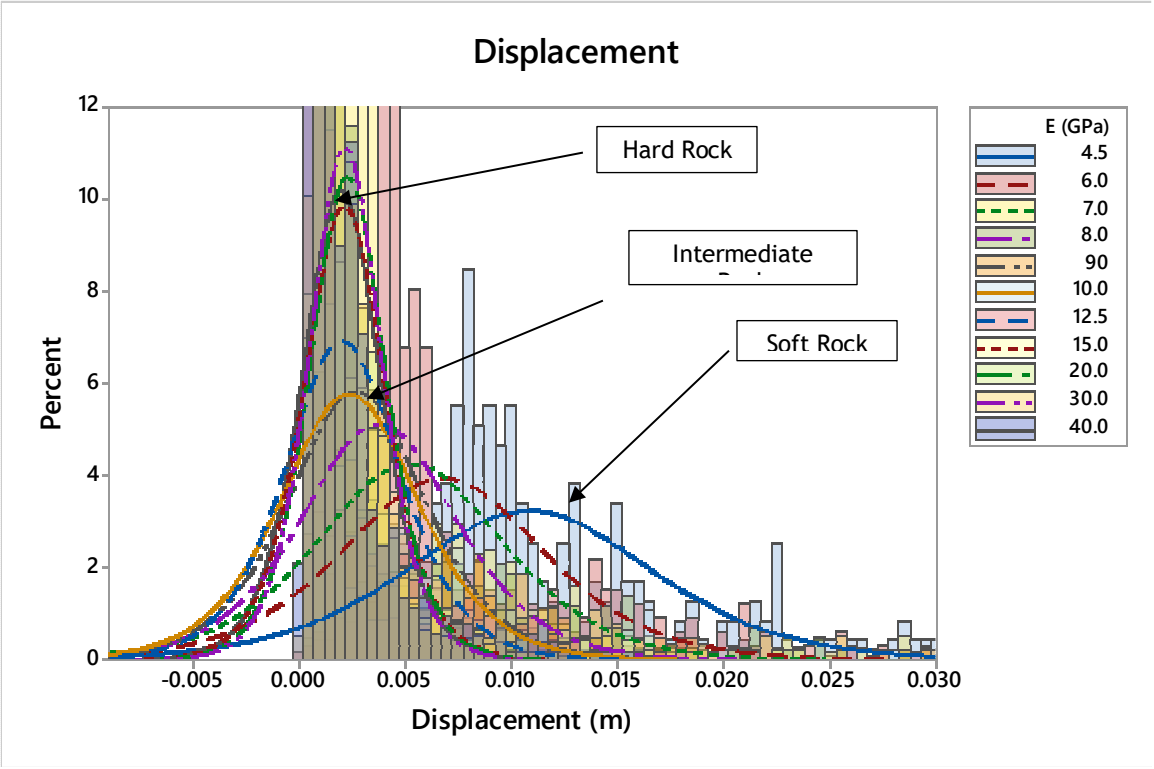

Figure 4.11. Binning of the results according to the amount of relative displacement of the opposing fracture walls. Curves represent the best fit logistic distribution probability density functions. Each column along the x axis represents an interval of 0.0005 m or 0.5 mm. y axis shows the percentage of all the results falling into particular interval along the x axis. Percentage along the y axis is required as experiments with different Young's modulus produced the unequal amount of data points and thus comparing absolute values would prove inefficient. Smaller Young's modulus values tend to have a larger mean and greater variance meaning larger abundance of the results further away from the x axis, with the increase in Young's modulus, the mean shifts closer to 0. For the experiments with Young's modulus values above 10 GPa mean stays almost the same, but variance decreases, meaning a further reduction in the abundance in the larger wall relative displacement values.

The average displacement of the fractures shows clearly that the displacement median/mode is becoming smaller with an increase of the Young's modulus until 12.5 GPa from where it stays constant (Fig. 4.11). Most of the displacement values show that the aperture of the fractures did not exceed 1 cm. Almost no values are above 1 cm for the rocks above 10 GPa and only about a third of the values exceed this amount for the soft rocks rocks (4.5, 6 GPa). The overall distribution becomes smaller with increasing Young's modulus leading to a constant displacement at high values.

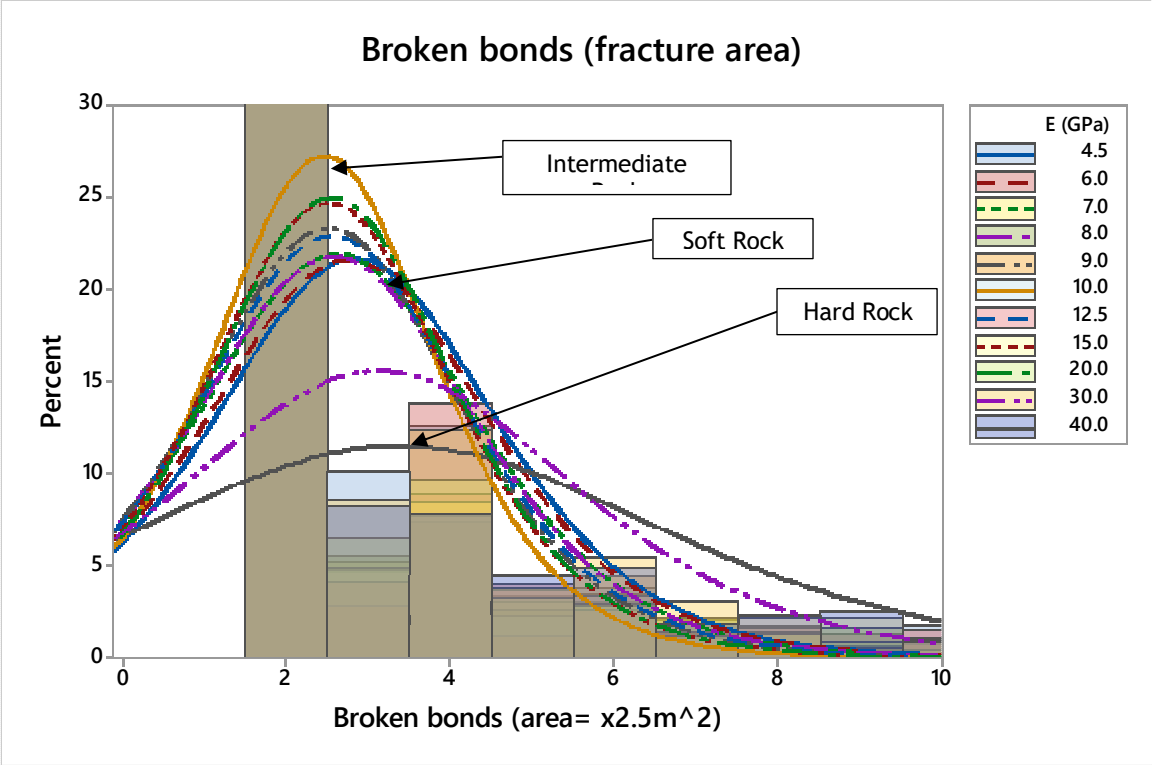

Figure 4.12. Binning of the results according to the number of particles with broken bonds (x axis), which serve as a proxy for the fracture area. Minimum binning value is 2 as one bond holds together two particles. An odd number of particles with broken bonds is possible as one particle might have several bonds broken in the triangular lattice setup. Particle diameter ($2.5m^2$) is used as an area unit. >50% of the results for all Young's modulus experiments are binned within the first category and <2% exceed the fracture area of $25m^2$. Logistic probability distribution curve has a bimodal dynamic. Young's modulus values from 4.5 GPa to 10 GPa distribution curves' means decrease and arms move closer to the mean. Experiments for values above 10 GPa have their means move towards the right along x axis and arms become heavier. This indicates that throughout the series of experiments, the area of the fractures first decreases and later again increases with the turning point for both trends being 10 GPa Young's modulus value.

The fracture area shows a minor initial decrease from 4.5GPa to 10GPa and then an increase in area (Fig. 4.12). The increase in fracture area is most pronounced from 20 to 30 and 40 GPa. Simulations with the highest elastic constants seem to have events where a larger amount of bonds break accounting for longer fractures and thus a larger fracture area. For all Young's modulus values half of the results are binned in the first column, meaning none of them exceeded 2.5 m^2 in area. The right side of the graph has very low numbers of results binned and for all the results, less than 25% of data exceeded 10 m^2 in area.

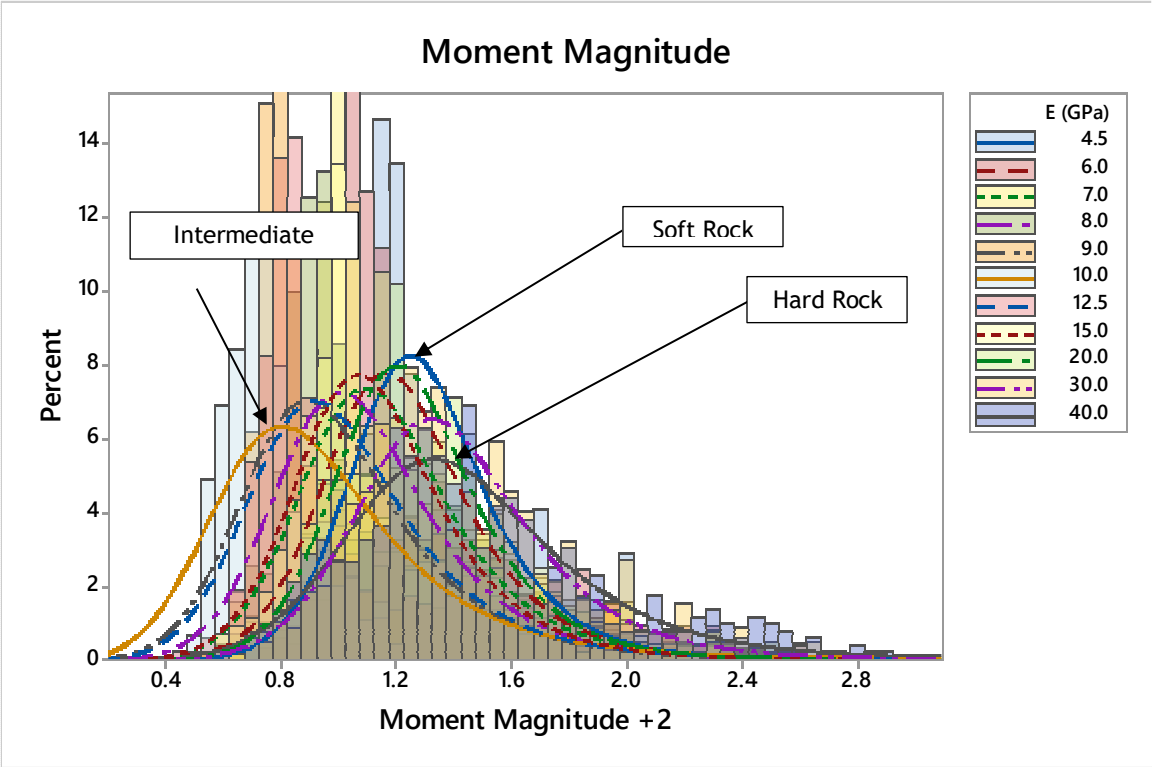

Figure 4.13. Binning of the results according to the moment magnitude produced by the fractures opening. x axis values are artificially increased by 2 as logistic probability density curve calculations require for all the values to be of a positive value. This approach does not interfere with the data objectivity as the value derived from the seismic moment is already artificially diminished by -10.7 (Eq. 4.1) to have values fit closer to the previously used Richter scale. Since the x axis is on a logarithmic scale, log-logistic probability density curves are calculated instead. One binning column equals to an interval of 0.05.

The moment magnitude (Fig. 4.13) changes in a complicated, non-linear manner as a function of changes in the Young's modulus. From 4.5 to 10 GPa the moment magnitude decreases followed by an increase towards higher Young's modulus values. Seismic moment is calculated as a function of fracture's aperture and area, therefore, moment magnitude can be viewed as a convolution of the dynamics discussed in Figure 4.11 and 4.12.

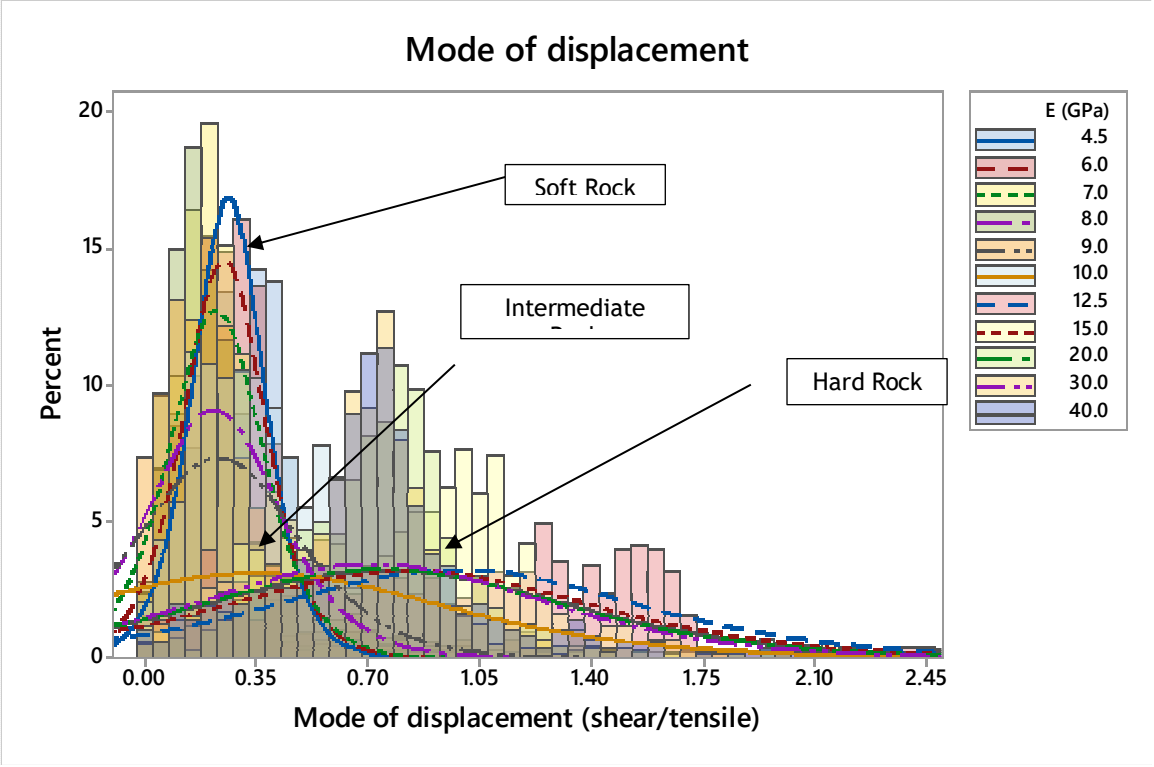

Figure 4.14. Binning of the results according to the displacement mode of the fracture walls relative to the fracture surface. The mode is calculated as shear component versus tensile component. Values above 1 have more shear component while values below 1 are predominantly tensile. Each binning column represents an interval of 0.05. Two trends are visible, experiments with Young's modulus values of up to 10 GPa have smaller means and probability distribution arms are close to the mean. Very few values exceed the value of 1 meaning most events are tensile. Values above 10 GPa have means twice as large and probability density curve arms are very heavy, indicating an abundance of events with the shear component being dominant.

A change of Young's modulus has a strong influence on the fracture mode ratio during the simulations (Fig. 4.14). At low Young's modulus (from 4.5 to 10 GPa) the fracture mode is mainly extensional with a relatively narrow distribution whereas higher Young's moduli (12.5 to 40 GPa) show a much higher amount of shear fractures in addition to mixed extensional/shear failure. The transition between these two regimes is very rapid between the values of 10 and 12.5 GPa followed by unchanging behaviour at greater values. The mean value of the logistic distribution is almost constant, around 1 to 3 (0.3-0.5) ratio of shear versus tensile movement, for the lower Young's moduli, and becomes constant again, around 1 to 1 (1.0) ratio, once the fracture mode changes at higher Young's moduli.

In summary, an increase in Young's modulus has a strong influence on the mode of fracturing changing from extensional mode dominated at Young's moduli below 10 GPa to a mixed mode with a higher amount of shear fractures at higher values. The behaviour of the moment magnitude as a function of Young's modulus is

complex. Fracture wall displacement or aperture of the fractures decreases with an increase of Young's modulus and becomes stationary at high values (>20GPa). The amount of broken bonds or the fracture area is not changing much for small Young's modulus values but increases from values of 20GPa and higher (Fig. 4.15).

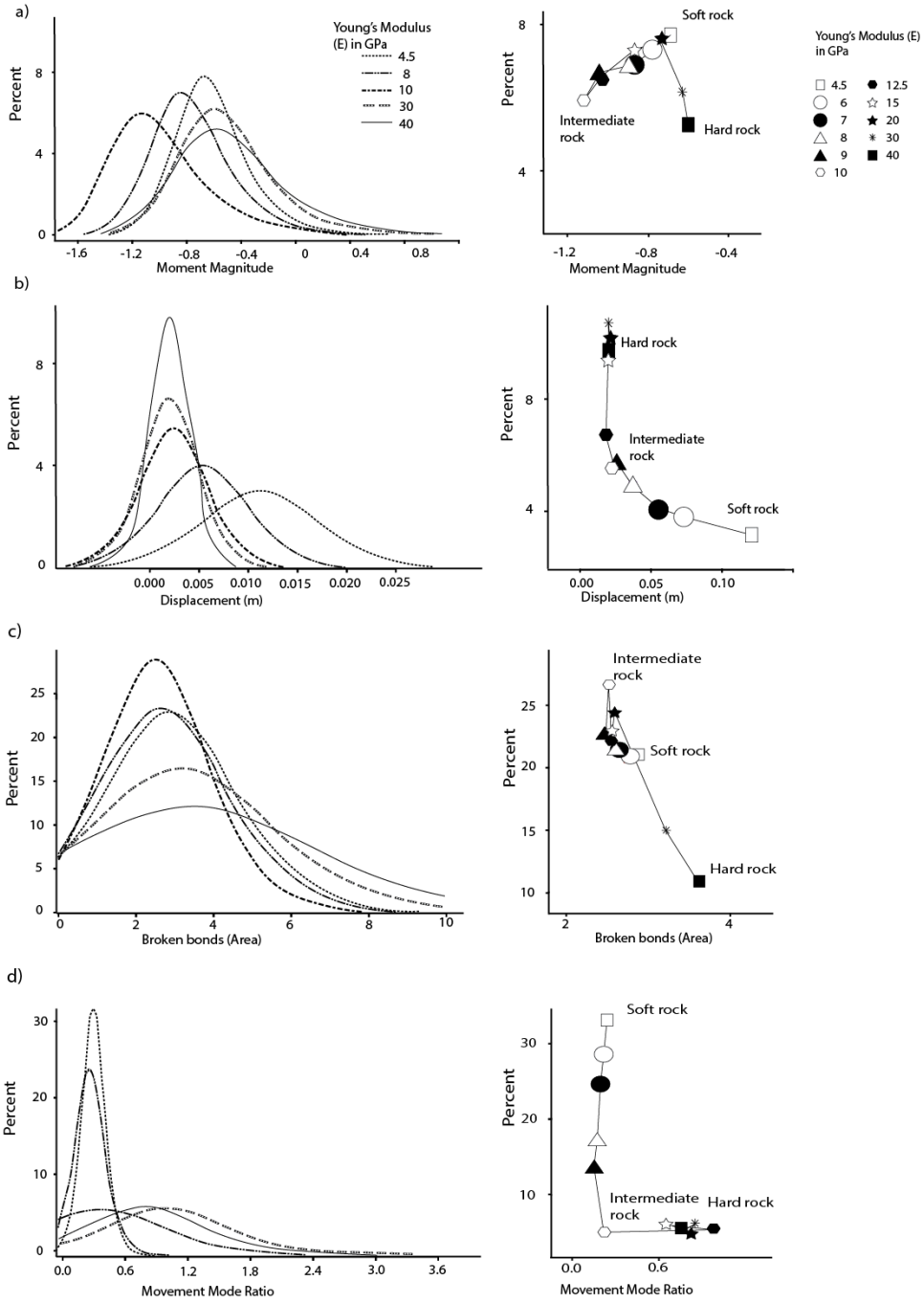

Figure 4.15. Summary figure for the data from Chapter 4.2. Logistic distribution curves on the left hand side and means on the right hand side as a function of changes in Young's modulus. Soft, intermediate and hard rocks are indicated. A) Moment magnitude variation shows a decrease from soft to intermediate rock followed by an increase towards the hardest rocks. B) Displacement or aperture of fracture shows a clear trend from a uniform very thin crack for hard rocks followed by a non-linear increase of the displacement or aperture towards soft rocks. C) the Area of the fracture or amount of broken bonds shows a relatively stable value for soft to intermediate rocks and then an increase in area towards hard rocks. D) The movement mode ratio or the amount of extensional versus shear fracture shows an increase in shear fracturing towards harder rock whereas intermediate and soft rocks show dominant extensional fracturing

4.3. The effect of depth change

To see how the change in load on the system would influence the fracturing process, the depth of the simulation was changed from 3 km to 1 km and the Young's modulus was varied between the simulations in a similar fashion to the default case. Reducing the overburden produced a significant decrease in fracturing in general to an extent where the results yielded as much as ten times fewer fractures than at 3 km. The lower overburden stress led to an increased porosity, which also meant that the fluid pressure gradients were lower and fewer fractures developed (Fig. 4.10). As a result, sample sizes for different Young's modulus experiments was as much as ten times smaller as the equivalent ones for the 3 km depth simulations despite having the same number of runs for each set of parameters. This led to poorer result distributions when looking at probability density functions.

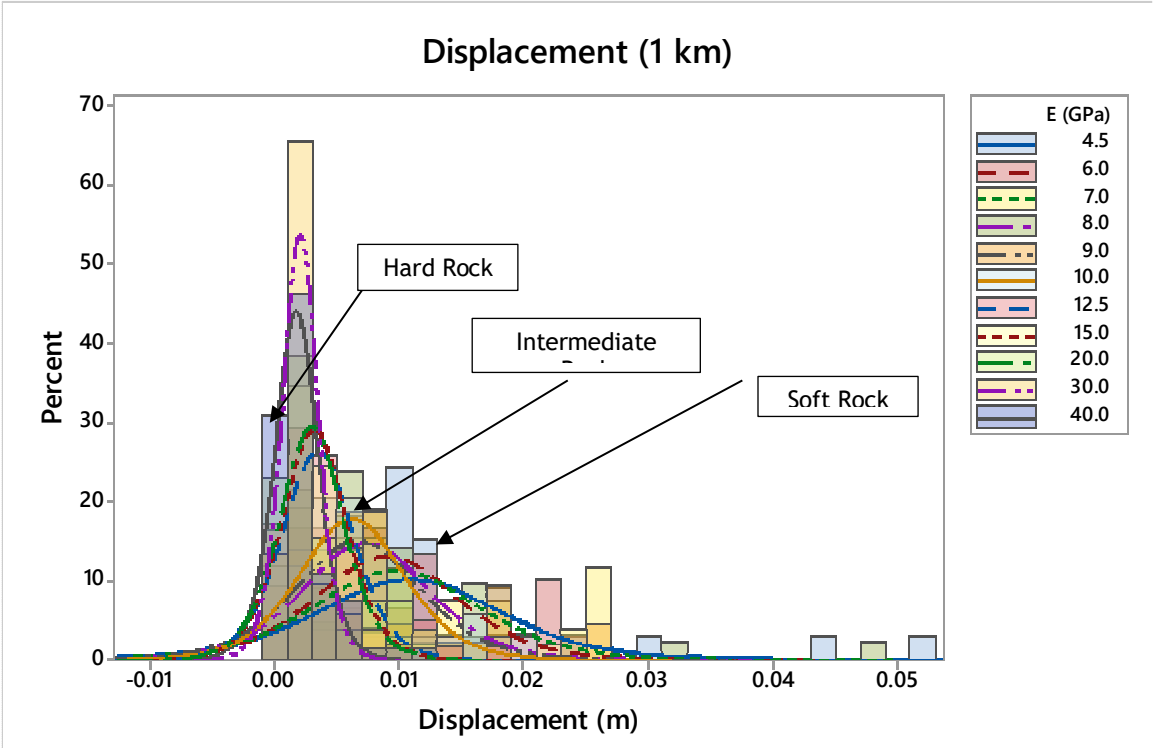

Figure 4.16. Binning of the displacement data for the experiments where rock overburden column height has been reduced to 1 km. Binning value of one column represents an interval of 0.002 m or 2 mm. Displacement trend is very similar to the experiments carried out at 3 km depth, where mean becomes progressively smaller and probability density function arms becoming lighter with the increase in Young's modulus value.

When analysing the fracture displacement or aperture data (Fig. 4.16), a very similar trend to the 3 km cases can be observed where there is a rapid decrease

of wall displacement with an increase in Young's modulus followed by a steady aperture growth with the turning point at around 15 GPa.

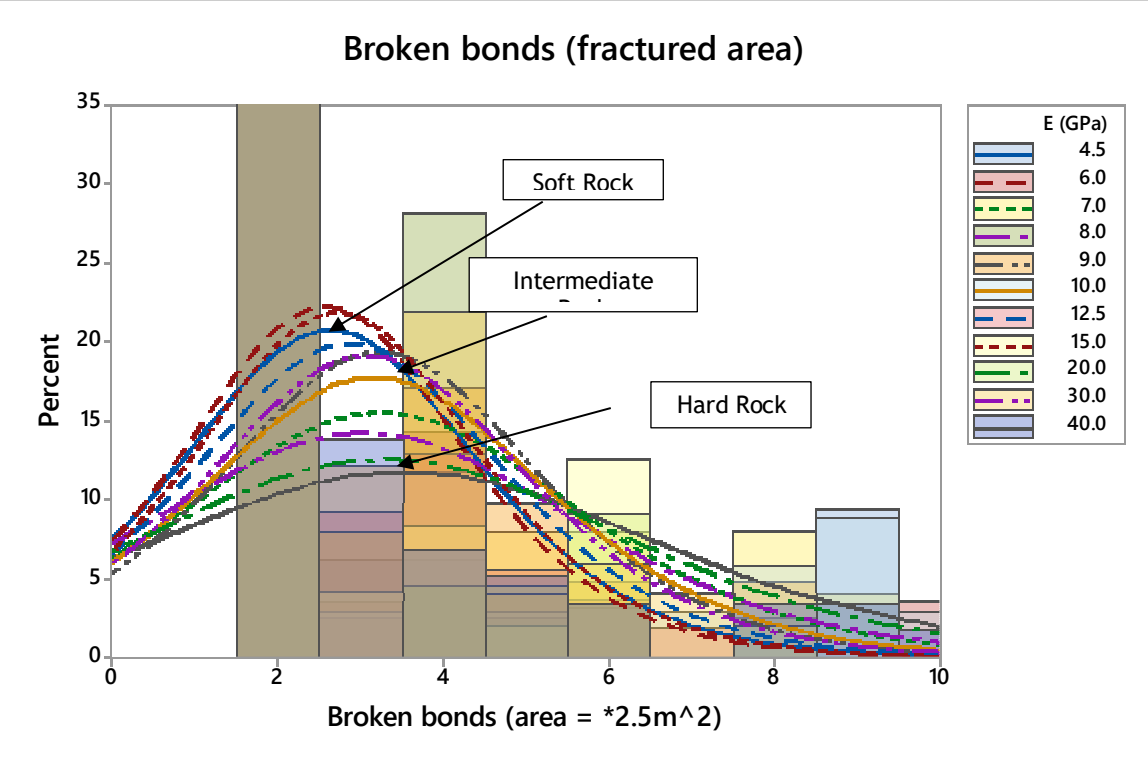

Figure 4.17. Binning of the results according to the area of the fractures created in the single time steps for the experiments where rock overburden column height has been reduced to 1 km. Each binning value represents one particle with a broken bond. The area is obtainable as a square of the single particle diameter (2.5m^2) multiplied by the number of particles with the broken bonds. Similarly, to the results of the 3 km depth experiments, a trend, where area decreases and then increases, is observable, however, more noise is present to the trend due to smaller data point sample size.

Data from the fractured area provides behaviour which is similar to the 3 km scenario, however the data trends are a lot more sporadic and more noise is present (Fig. 4.17). There is clear evidence that the fracture area is increasing with an increase in Young's modulus. As mentioned before, this effect is due to a low number of sample data points, the assumption is that with more data points, distribution means and spreads would become more normalised and aligned to the trend, similarly to the 3 km case.

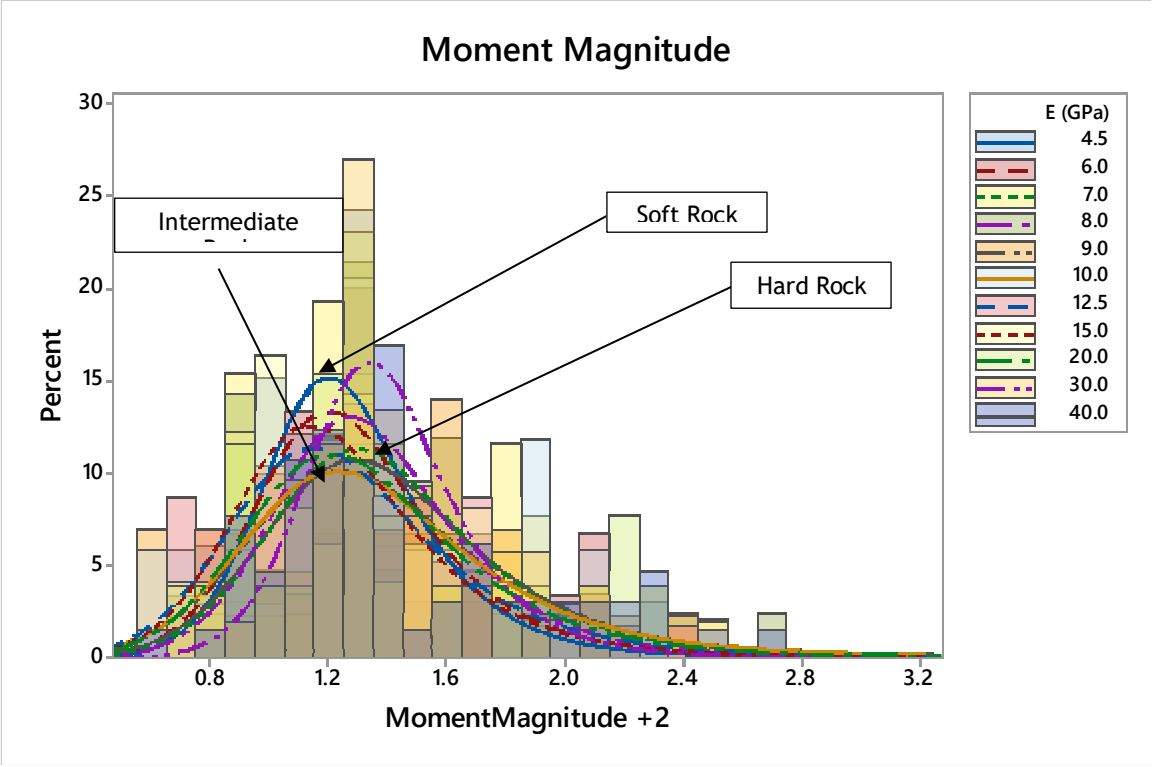

Figure 4.18. Binning of the results according to the moment magnitude created by the fractures opening in single time steps for the experiments where the rock overburden column height has been reduced to 1 km. Binning interval of one column is 0.4. Log-logistic probability density curve is used instead of a logistic curve. X axis is artificially increased by 2 as all data points required to be of a positive value for the density curve calculations. As in previous graphs for 1km depth experiments, the bimodal regime is seen (decrease in mean followed by an increase), however, the trend is not as clear, and more noise is present.

The same can be observed with the moment magnitude (Fig. 4.18) and mode of displacement data (Fig. 4.19): there is a clear division between the result of low Young's modulus and high Young's modulus experiments, however, the results of the intermediate values do not provide a linear progression.

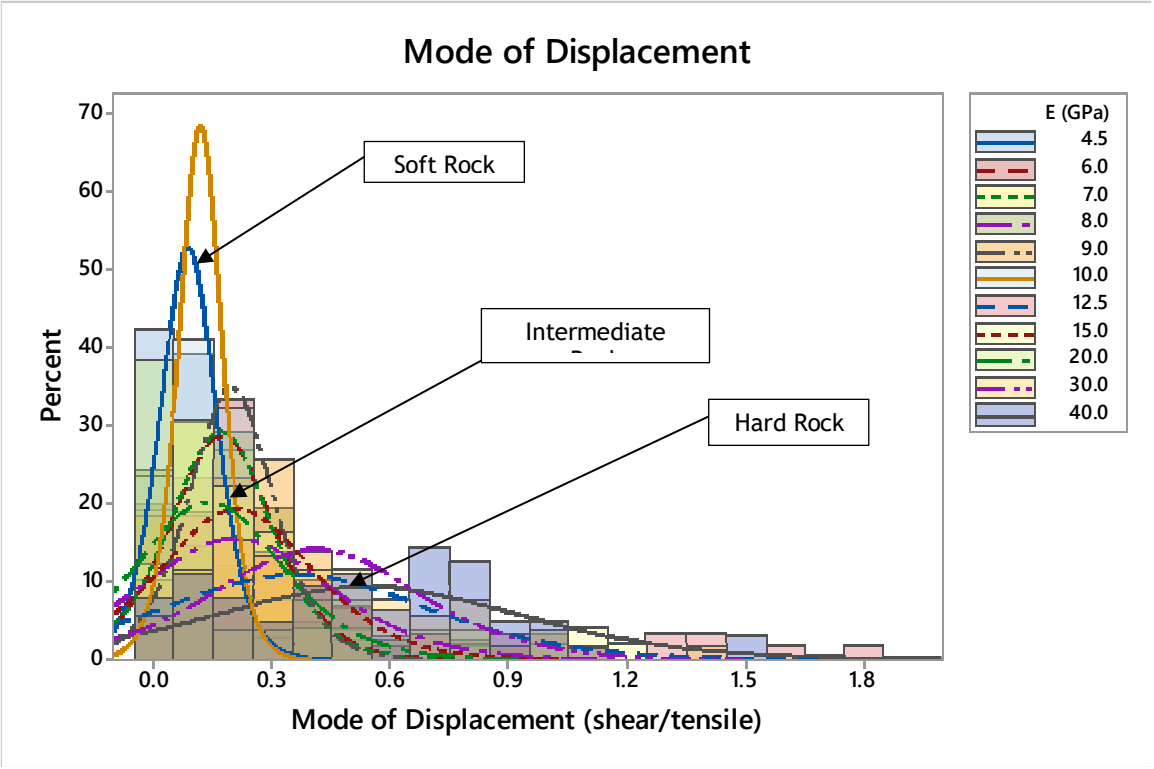

Figure 4.19. Binning of the results according to the displacement mode of fracture walls relative to fault surface for the experiments where rock overburden column height has been reduced to 1 km. Binning interval of one column is 0.1. Data is very noisy but a trend of a general shift towards more shear like behaviour with an increase in Young's modulus is present.

4.4. The effect of tensile strength change

Tensile strength of the rock accounts for the amount of the fluid pressure required to sufficiently decrease effective stress to the stage where the tensile failure occurs. To investigate what effect differentiated breaking strength of the rock has on fracturing dynamic of the system, I have carried out a series of experiments by varying the mean tensile strength of the rock. All the experiments described in the previous Sections of this Chapter (4.1, 4.2, 4.3) were done with the elastic springs between the bonds having the pre-assigned mean tensile strength of 34 MPa. The following experiments had the additional mean tensile strengths of 27.2, 44.2 and 54.2 MPa tested. As mentioned in Section 4.1, there is a distribution of tensile value strength assigned to the springs throughout the system. Following experiments have the distribution with the variance of 60% of the mean value applied to randomize the breaking strength of the system. The summary of the breaking strength distribution is presented in Table 4.2.

Table 4.2. Maximum and minimum values for tensile strength within the system depending on the chosen mean tensile strength value.

Mean tensile strength (MPa)	Minimum tensile strength (MPa)	Maximum tensile strength (MPa)
27.2	10.88	43.52
34	13.6	54.4
44.2	17.68	70.72
54.2	21.68	86.92

First, we want to look at the dynamics of single experiments at varying breaking strength to see how the fractures develop. Figures 4.20 to 4.23 present the number of cumulative bonds broken through a single experiment for different Young's modulus values when the mean tensile strength of the springs is changed.

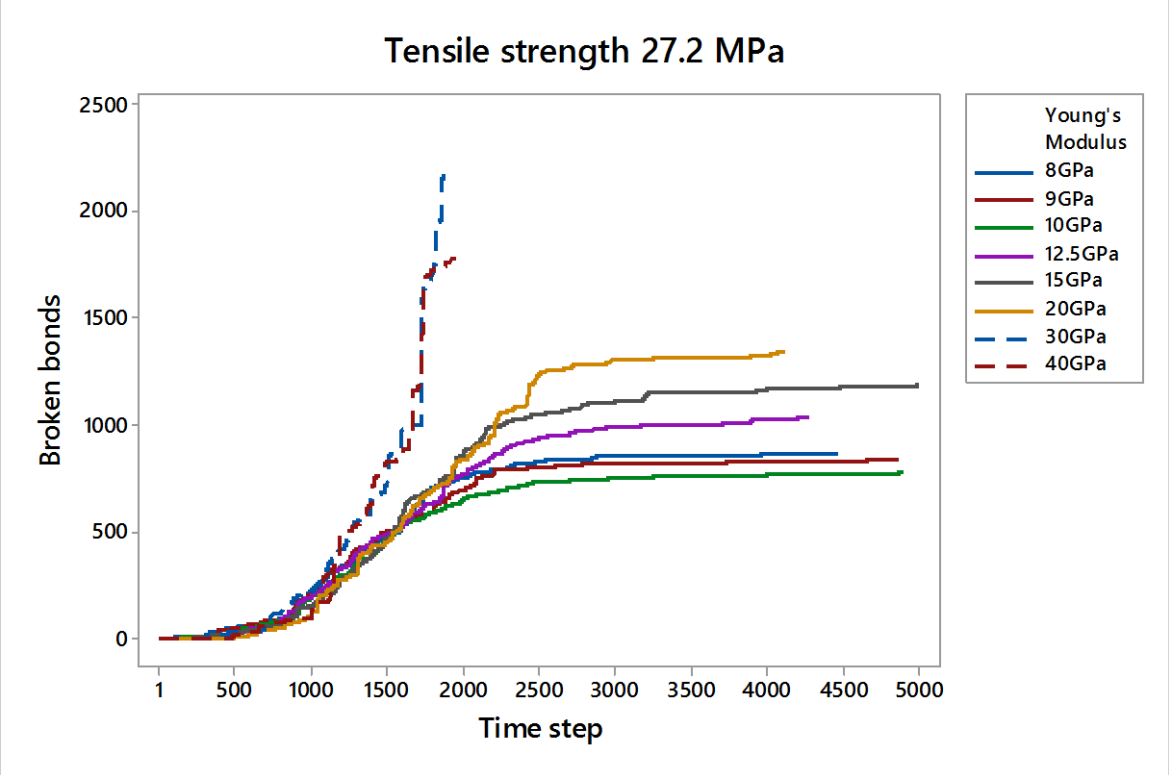

Figure 4.20. Cumulative number of broken bonds for experiments of different Young's modulus and mean tensile strength of the rocks being 27.2 MPa. Increase in Young's modulus produces larger cumulative fracture area at the end of the experiment. 30 and 40 GPa Young's modulus experiments failed as the system became too brittle and collapsed under the gravitational force applied.

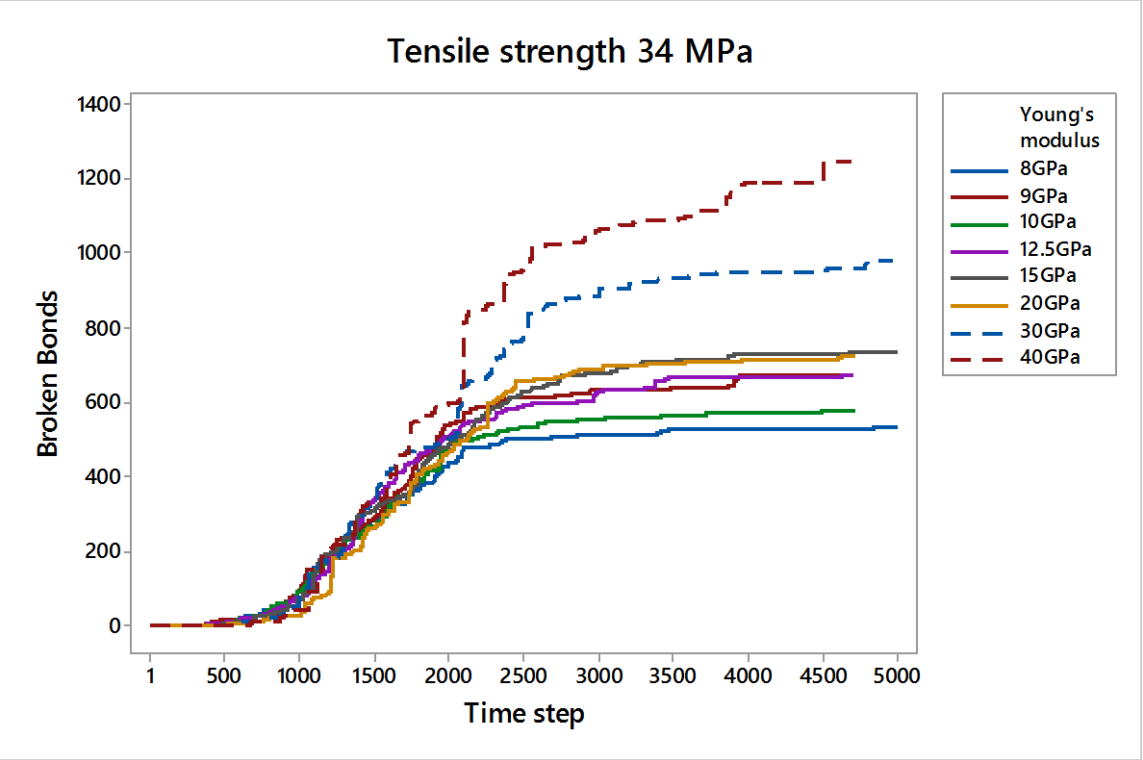

Figure 4.21. Cumulative number of broken bonds for experiments of different Young's modulus and mean tensile strength of the rocks being 34 MPa. The same trend of increase in cumulative fracture area with an increase in Young's modulus is observed, however, the fracture area is smaller with an increase in the mean tensile strength of the rock. Fracturing initiates at the later stages compared to 27.2 MPa mean tensile strength experiments.

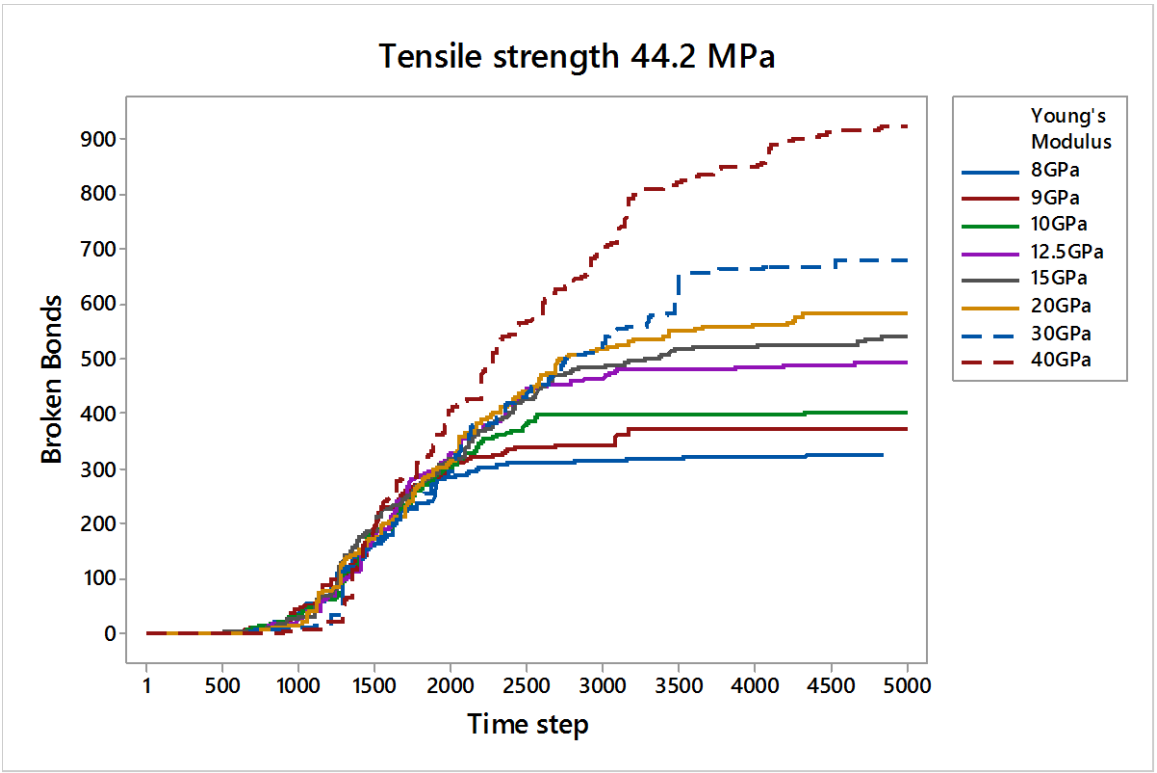

Figure 4.22. Cumulative number of broken bonds for experiments of different Young's modulus and mean tensile strength of the rocks being 44.2 MPa.

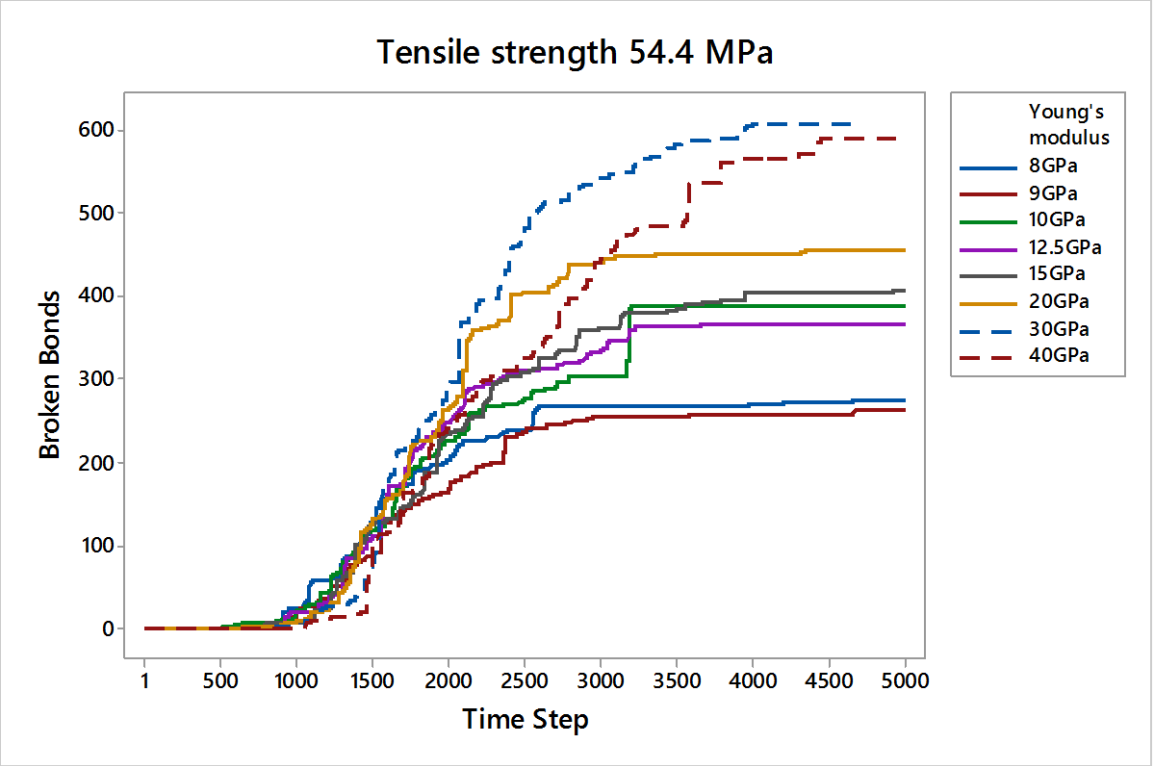

Figure 4.23. Cumulative number of broken bonds for experiments of different Young's modulus and mean tensile strength of the rocks being 54.4 MPa. Increase in the mean tensile strength of the rock produces further decrease in the fracture area and later initiation of active fracturing.

All the graphs provide the same profile as the initial experiments where there is an initial build-up stage, active fracturing, a decrease in fracturing rate and plateauing. Experiments with lower Young's modulus tend to start producing fractures earlier and plateau sooner. Experiments with high Young's modulus produce fractures at later time steps but have a steeper slope and stabilise later. This effect is more pronounced with an increase in the breaking strength. The exception are the 30 and 40 GPa experiments for rocks with 27.2 MPa mean tensile strength. In this case, the number of fractured bonds was so high that the remaining bonds could not provide support for the gravitational forces and the model would "collapse" in a fashion where bonds would start breaking in an uncontrolled manner. The model can also behave unstably at the large breaking strength values. In Figure 4.23 the experiment with 10 GPa Young's modulus was in a plateau stage when the erratic large-scale failure occurred. In all the experiments show an increase in fracturing depending on the Young's modulus of the rock. No exact conclusion can be drawn from these experiments as they depict single model run results. For this reason, I have gathered an average number of total broken bonds for ten experiments with the same parameter set and plotted

them against a non-dimensional parameter of Young's modulus scaled to mean tensile strength (Fig. 4.24).

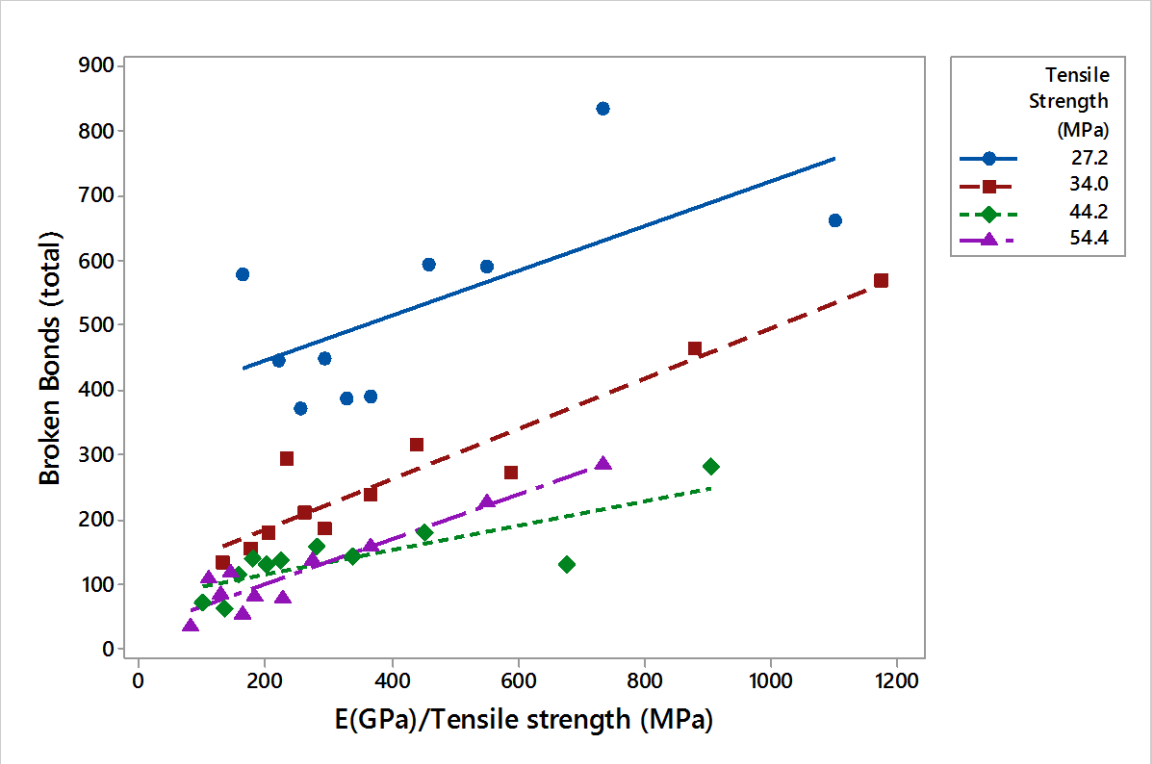

Figure 4.24. The figure shows the number of bonds broken during an experiment for a series of Young's moduli normalized by the mean tensile breaking strength of the rock. Increasing Young's modulus and decreasing the breaking strength both lead to more fractures. All the regression curves for Young's moduli show roughly the same slope.

In Figure 4.24 each point represents a number of total broken bonds averaged over 10 experiments. The slope of all four mean tensile strength values is the same with the exception of 44.2 MPa value, which is slightly less steep. There is a non-linear decrease of total broken bonds depending on the increase of the breaking strength of the springs where the last two values are almost the same. The inverse trend is observed for the variability of the results where smallest breaking strength rocks show the largest variability, while 44.2 MPa and 54.4 MPa results show an almost linear trend.

The next step is to look at the fluid pressure gradient dynamics depending on the mean tensile strength and Young's modulus changes in the rock (Fig 4.25 to 4.28).

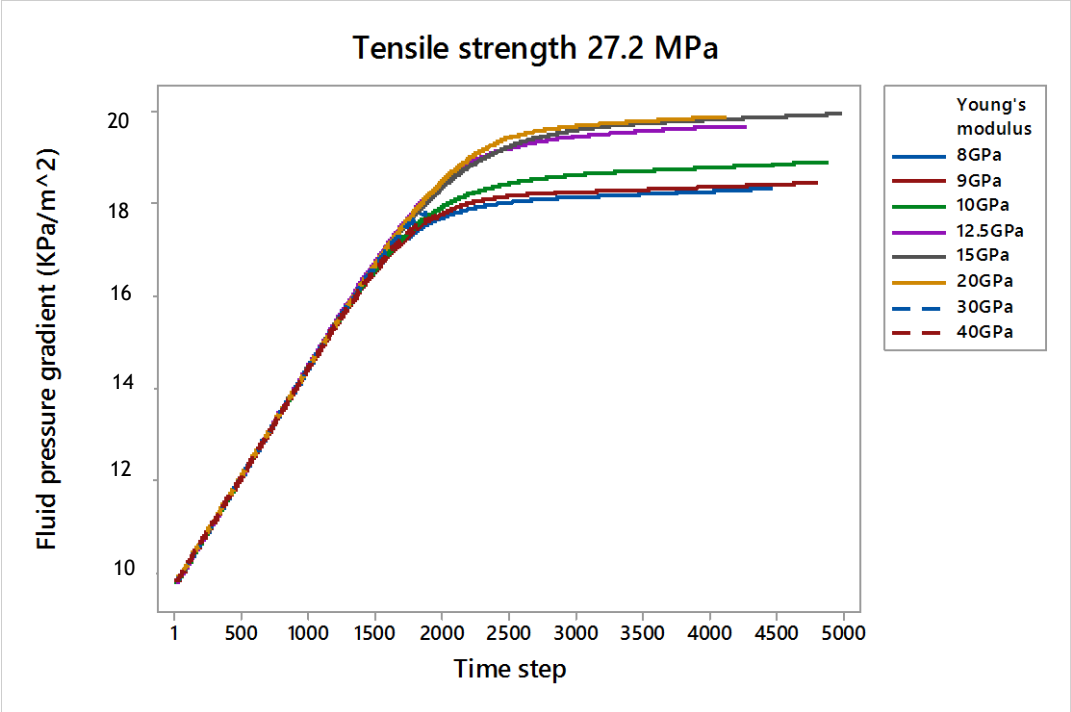

Figure 4.25. Fluid pressure gradient for different Young's modulus experiments for rocks with a mean tensile strength of 27.2 MPa. Smaller values (8-10 GPa) and medium values (12.5-20 GPa) are clustered together while larger values (30-40 GPa) are absent due to simulation failing. Curve plateauing coincides in time with the initiation of active fracturing stage.

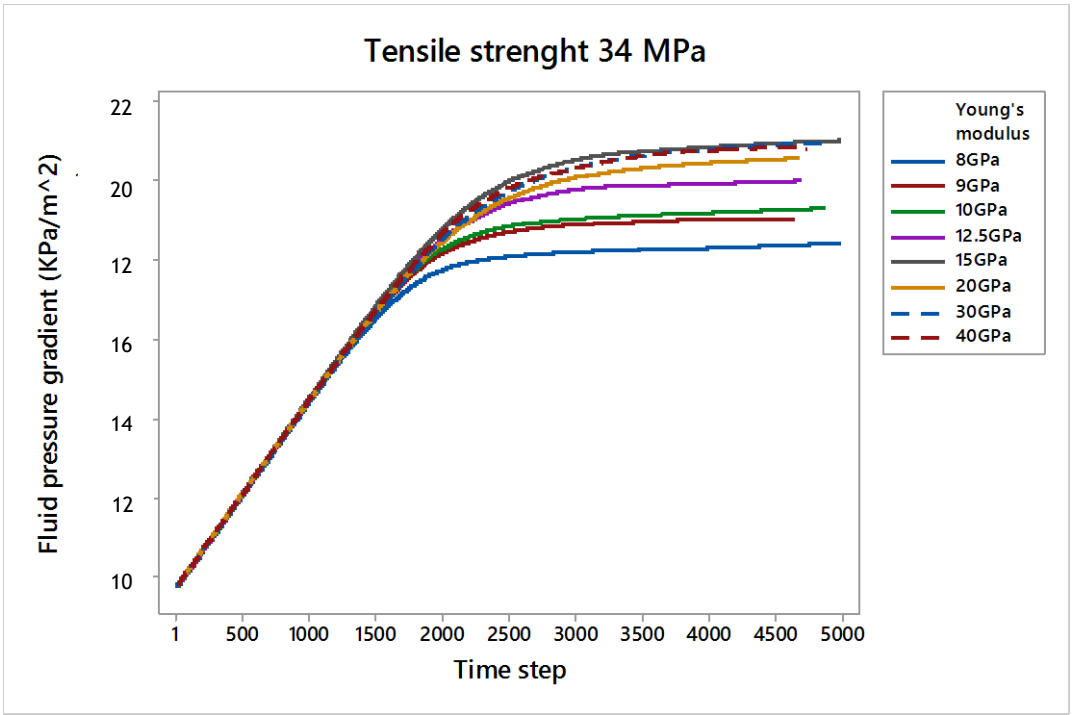

Figure 4.26. Fluid pressure gradient for different Young's modulus experiments for rocks with a mean tensile strength of 34 MPa. The end value of the fluid pressure gradient is higher compared to 27.2 MPa mean tensile strength experiments. The smaller Young's modulus values become less clustered while medium and high Young's modulus values still produce relatively similar results.

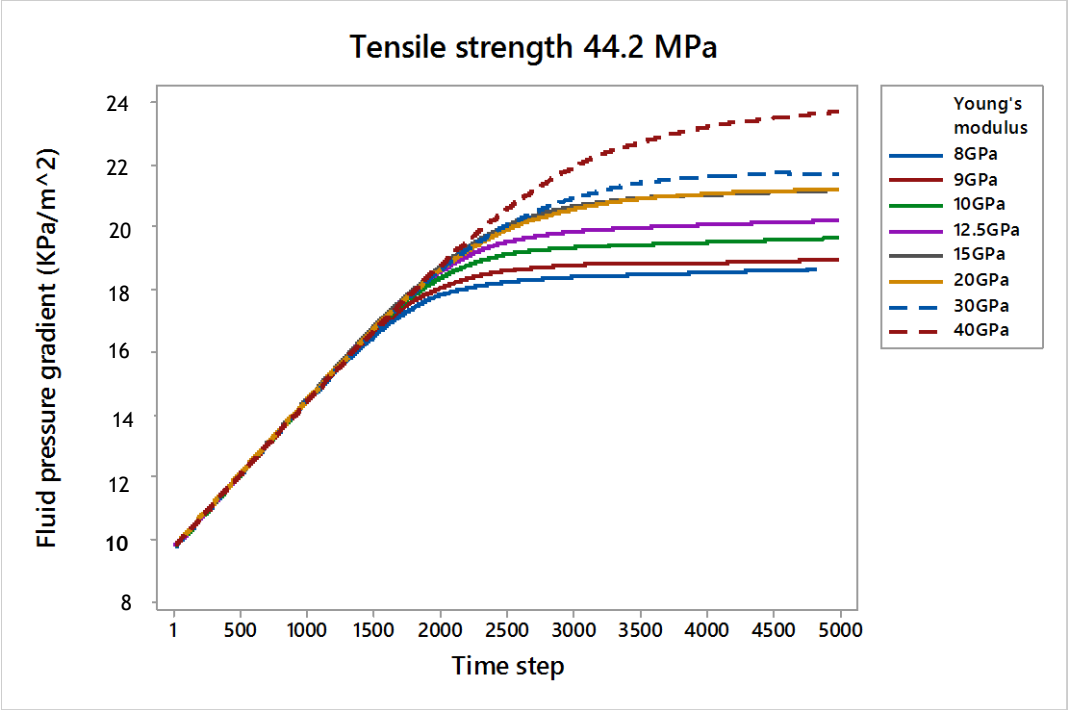

Figure 4.27. Fluid pressure gradient for different Young's modulus experiments for rocks with a mean tensile strength of 44.2 MPa. Further, increase in the end fluid pressure gradient value compared to lower mean tensile strength value experiments. Values for separate Young's modulus experiments are better set apart from each other due to differentiated fracturing initiation time.

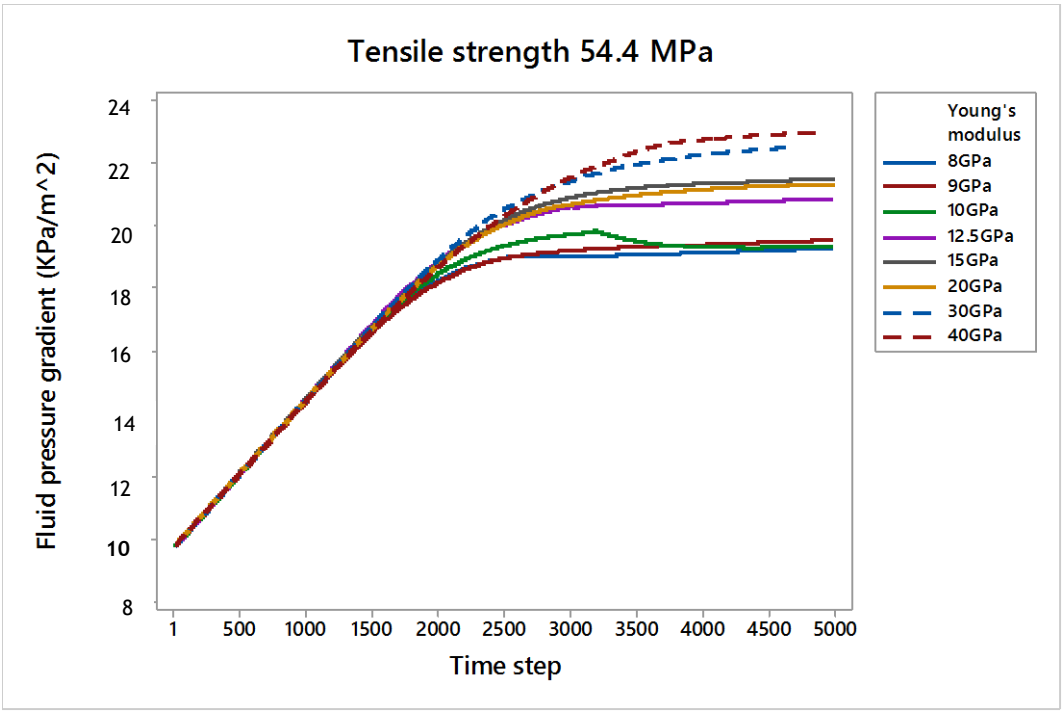

Figure 4.28. Fluid pressure gradient for different Young's modulus experiments for rocks with a mean tensile strength of 54.4 MPa. Drop in 10 GPa Young's modulus fluid pressure gradient in a plateau stage is due to an erratic large-scale failure occurring at the same time step.

Figures 4.25 to 4.28 show a clear relationship where the final fluid pressure gradient is increasing with an increase in Young's modulus. All values start at the same gradient while the smaller Young's modulus values start to change slope first. The slope change is more abrupt than for the larger Young's modulus values. This can be explained by the fact that the lower Young's modulus simulations developed fractures earlier and fluid seeps away easier. For the smaller mean tensile strength value pressure gradients, the smaller and intermediate Young's modulus values tend to group together and cannot be well distinguished. With the increase in breaking strength of the rock the distinction between the values becomes clearer. To better understand the relationship between all the variables, the end value of the fluid pressure gradient is plotted against the dimensionless value of Young's modulus / mean tensile strength of the rock (Fig. 4.29).

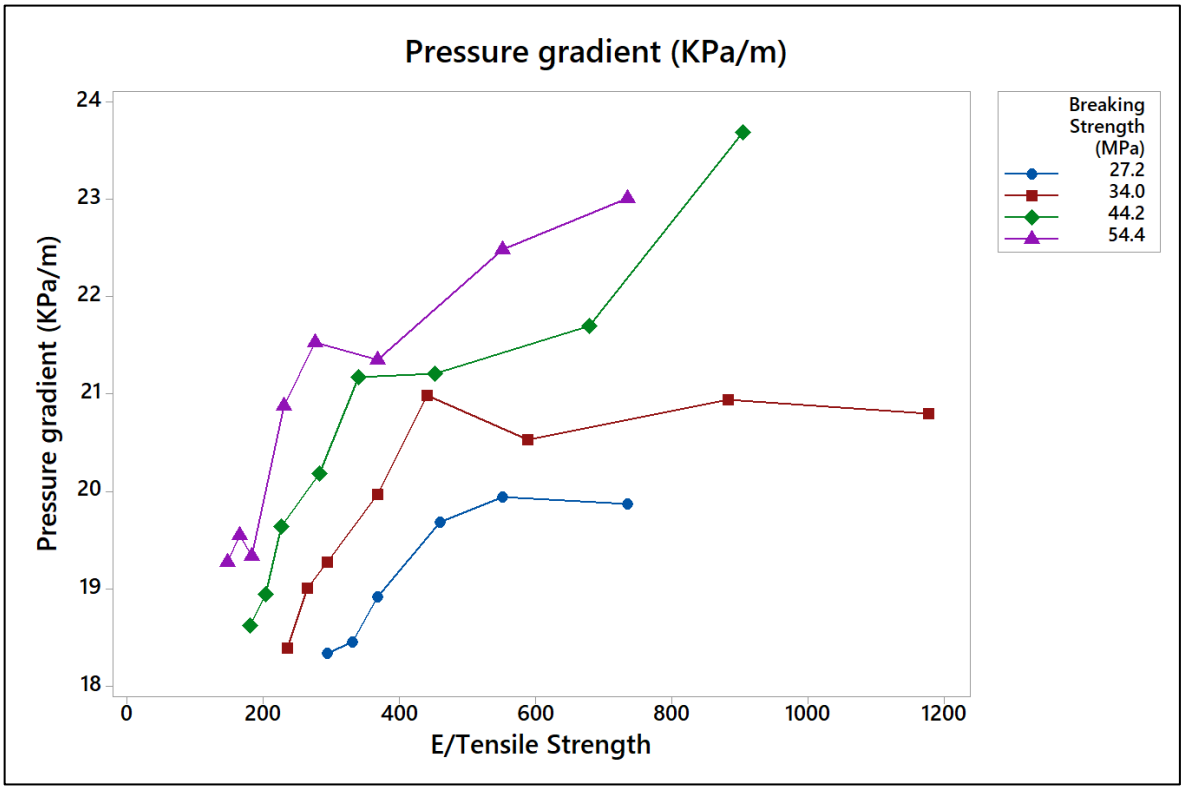

Figure 4.29. The figure shows a fluid pressure gradient for a series of Young's modulus normalized by the tensile breaking strength of the rock. Increase in the mean tensile strength of the rock leads to an overall increase in the fluid pressure gradient.

Figure 4.29 clearly illustrates that the fluid pressure gradient increases with the mean tensile strength. The increase in non-linear in regards of the change in Young's modulus as values past 15 GPa show smaller change in the final fluid pressure gradient relative to the increase in Young's modulus.

Figures 4.30 to 4.33 present parameters that were observed before (displacement, area, moment magnitude and mode of displacement). Due to a larger number of

variables being changed the lesser amount of experiments could be run for each set. Only up to two simulations for each set of variables were carried out. This resulted in a smaller number of data points and greater uncertainty. Despite noise in the data the general trends can still be distinguished.

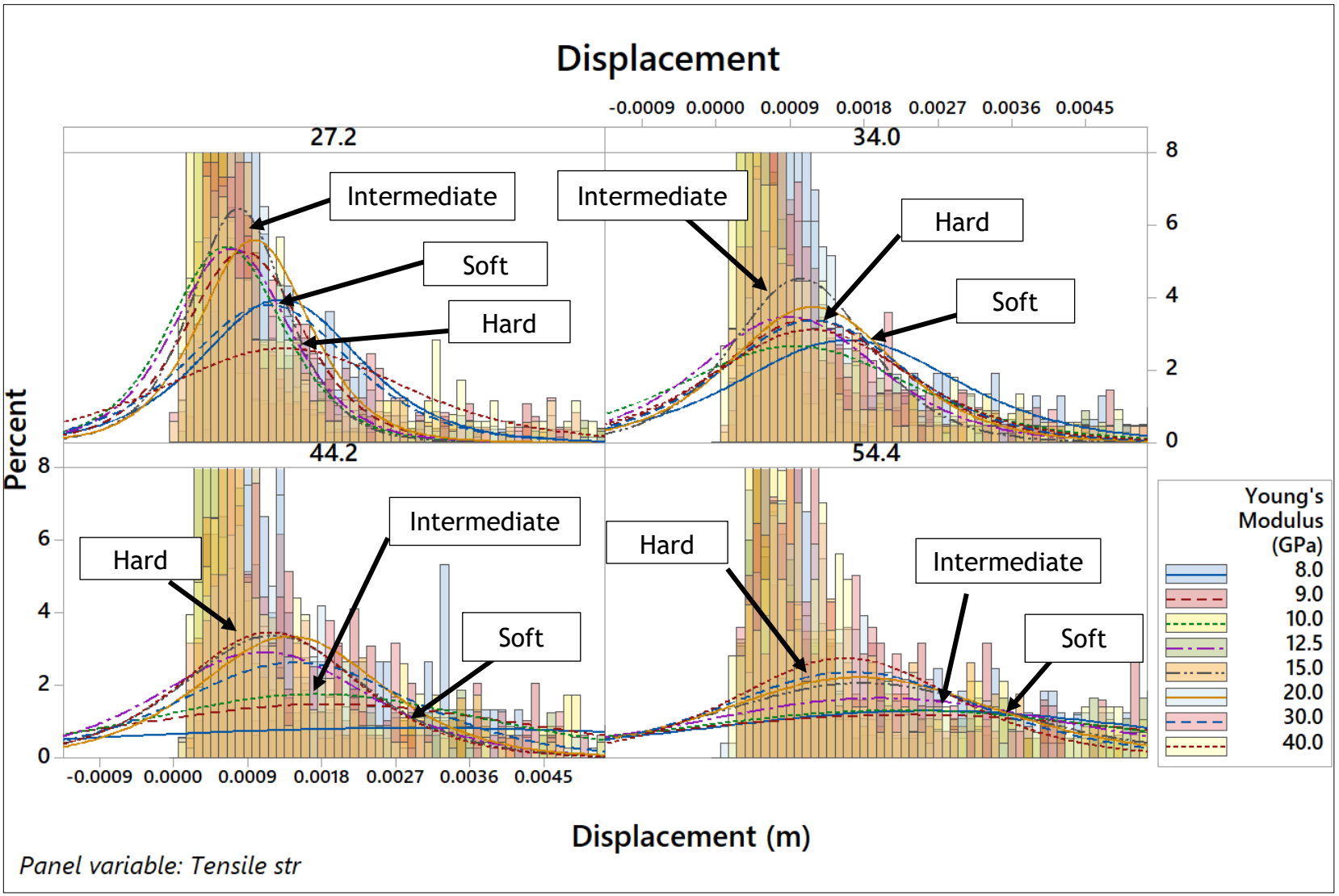

Figure 4.30. Binning of the displacement data points for series of Young's modulus for different mean tensile strength experiments. Binning value of a single column is 0.1mm. Y axis represents the percentage of all the results for the given Young's modulus experiment data points following into each column. Such an approach is used to normalize against a different number of total data points for each Young's modulus value.

Figure 4.30 shows the distributions of the displacement or fracture aperture data. The mean tensile strength used in the Section 4.2.2 was 44.2 MPa. The same trend can be seen in these repeated experiments. Distribution peaks for 8 and 9 GPa Young's modulus values are low, meaning the spread of the results is wide and values that are further on the x-axis are more abundant. That means that in general a lower Young's modulus of the rock prompts wider fracture opening. The distribution peaks stay low until 10 GPa, above which they become a higher meaning a significant drop in the larger aperture data points. This behaviour is more pronounced with an increase in the breaking strength. For 54.4 MPa mean tensile strength experiments, all peaks are relatively low and the difference between them becomes smaller. Experiments of values 8, 9 and 10 GPa show almost identical data point distribution and the increase in the subsequent distribution peaks is very gradual. For the experiments of 34 and 27.2 MPa, the mean tensile strength displacement changes show non-linear behaviour. Compared to the other two mean tensile strength value experiments, these peaks are significantly higher, meaning that there is a lack of large aperture data points. For both experiments at the low and high end, the Young's modulus values are located further to the right on the x-axis while the medium values are located closer to the 0 value and have higher peaks, meaning smaller aperture data points. In both cases, a turning point for the trends is 10 GPa Young's modulus. Comparing all four mean tensile strength experiments at 40 GPa Young's modulus the results present almost no change in the data point while the 8 GPa value has significant growth in the average aperture of the fracture with the increase of the breaking strength of the rock. This illustrates that the Young's modulus has a significant effect on the behaviour of the fracture-opening irrespective of the breaking strength of the rock.

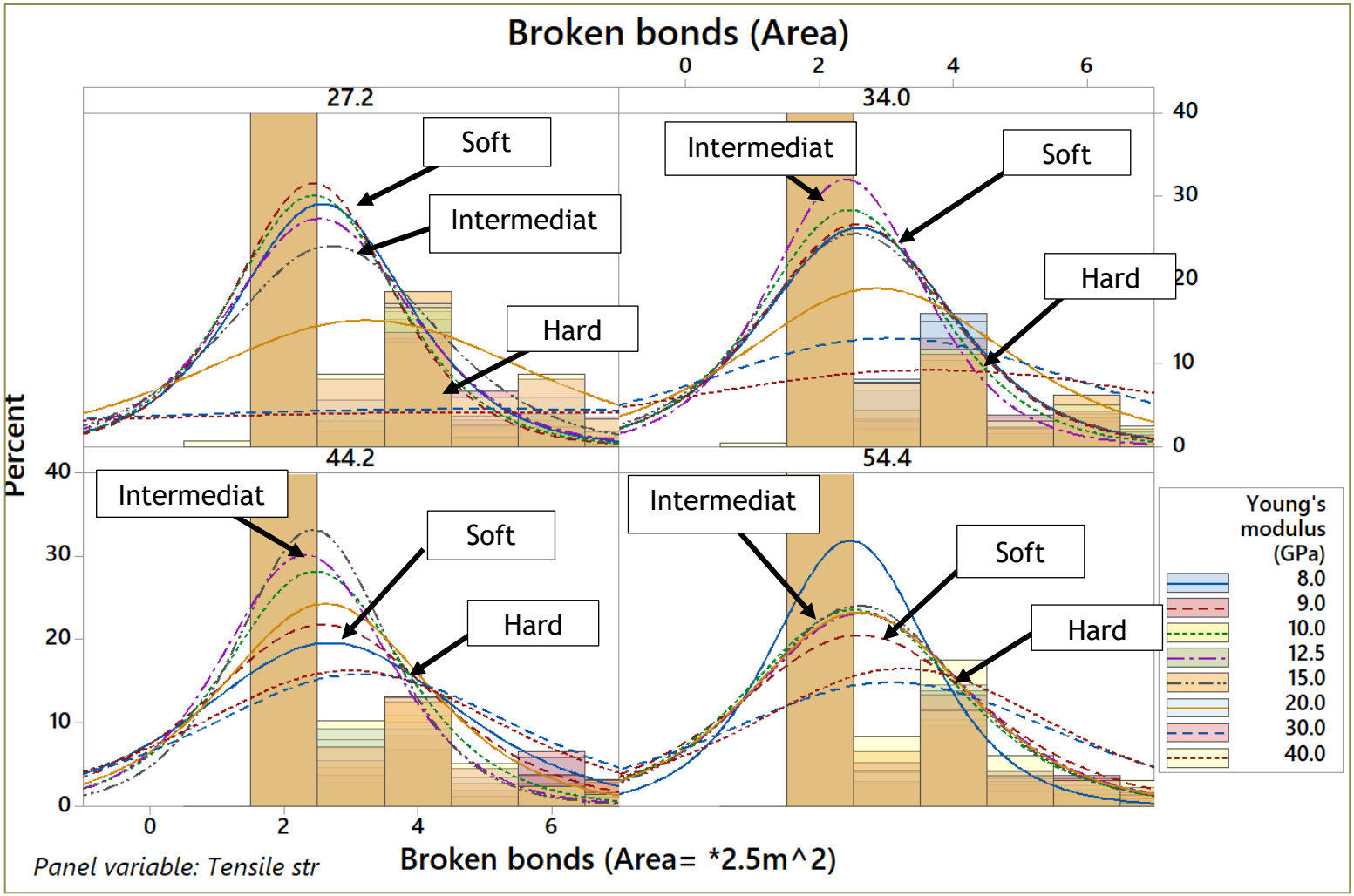

Figure 4.31. Binning of the data points of the broken bonds for series of Young's modulus for different mean tensile strength experiments. Broken bonds serve as a proxy for the area of the fracture, where a number of broken bonds has to be multiplied by the diameter of the single particle squared ($2.5m^2$). More than half of the results do not exceed the area of $5m^2$. All of the differentiates mean tensile strength experiments show bimodal behaviour where mean first shifts closer to 0 and then shifts away from 0 when progressively increasing Young's modulus. The turning point Young's modulus value increases with the growing mean tensile strength of the rock. The probability distribution curve peaks become higher and arms lighter with the increase in the mean tensile strength, meaning a decrease in the abundance of the large fracture area data points.

Figure 4.31 provides the fracture area distribution data. More than 50% of the data points represent a single bond between two particles breaking, which creates 5m^2 large fractures. Very few of the results exceed the area of 25m^2. When increasing the Young's modulus of the rock, the data sets in all the four mean tensile strength experiments present bimodal behaviour. When increasing the Young's modulus value from 8 GPa onwards, the distribution peaks become higher and move leftwards, indicating the overall decrease in the fracture area created. Then at the intermediate values towards the 40 GPa value, the peaks become lower and move towards the right-hand side indicating growth in the fracture area. The switching point is dependent on the mean tensile strength. For the 27.2 MPa mean tensile strength experiments the switch in the trend occurs at 9 GPa Young's modulus value, for the 34 MPa mean tensile strength it is 12.5 GPa and for 44.2 MPa it is at 15 GPa. The exception is the 55.4 MPa experiments where there is an abnormal 8 GPa distribution curve and switching point is not easy to distinguish. This is due to the effect that with an increase in the breaking strength of the rock, the distribution curves tend to become more uniform. With the increase in breaking strength, the high Young's modulus values have a significant drop in the high area values which results in the curve peaks becoming higher and moving towards the left. The low Young's modulus values are increasing in the distribution spread, which is illustrated in a small drop of the peaks and a shift towards the right. The most stable value, showing the least amount of change, is 10 GPa. This decrease/increase bi-modal behaviour explains the change in the turning point among the data of different tensile value distribution curves. The data provided shows that changes in the breaking strength of the rocks have a significant impact on the behaviour of the system.

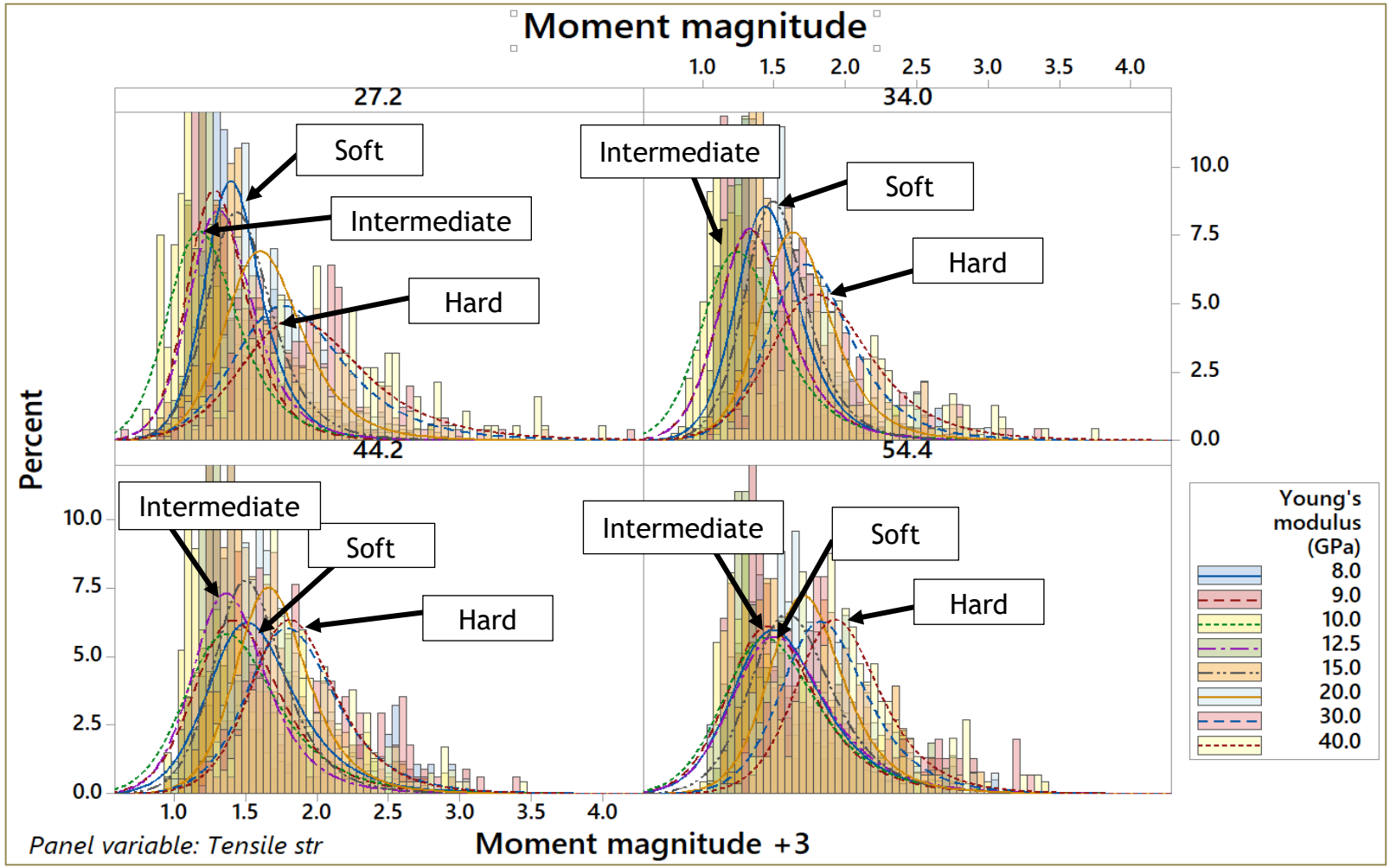

Figure 4.32. Binning of the moment magnitude data points for series of Young's modulus for different mean tensile strength experiments. Binning interval of a single column is 0.05. Values along x axis represent moment magnitude values, which artificially have been increased by 3. This is done as log-logistic probability density curves cannot be calculated for negative values. All four mean tensile strength experiment series show bimodal behaviour, where moment magnitude mean first shifts to the left along the x axis and then shifts to the right with Young's modulus value being progressively increased. For all the experiments turning Young's modulus value is 10 GPa.

Figure 4.32 shows the distribution of the moment magnitude of the seismicity generated by the fracturing events. The moment magnitude calculation is a function of the fracture area and aperture. Most of the values are in the negative range and only about 1% of all the results exceed the magnitude of 0.5. The magnitude values are slightly lower for the high breaking strength rocks. All four mean tensile strength value experiments show that the different Young's modulus data distribution curves become more uniform towards the high breaking strength rocks. The distribution curves further provide non-linear bimodal behaviour where values first decline until they reach values of 10 GPa Young's modulus followed by an increase towards high Young's modulus values. When observing the dynamic of the curve it can be seen that it changes depending on the mean tensile strength, with the 10 GPa curve being once again most stable. The 8 and 9 GPa curves become smaller in height and move towards the left hand side. This behaviour of the graphs shows that the number of large events does not change by much, but that there is an increase in the number of lower magnitude events and thus an increase in the spread of the results and decrease of the mean. The 8, 9 and 10 GPa value graphs provide almost the identical distribution curves for the rock with 54.4 MPa mean tensile strength. Tough rocks (30 and 40 GPa Young's modulus) maintain the same mean with an increase in the breaking strength, but the spread decreases, indicating a decrease in abundance at both the small and large end of the result spectrum.

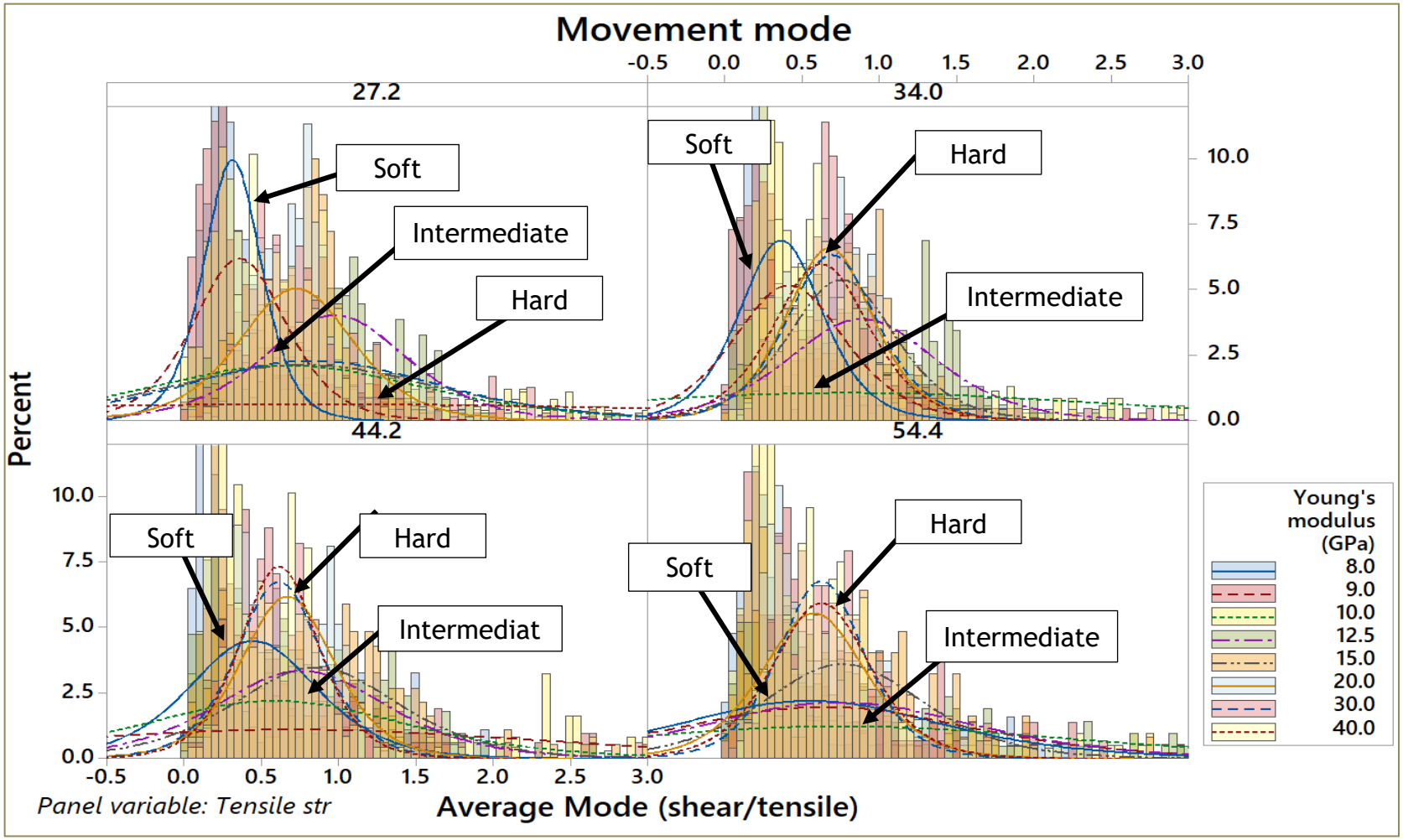

Figure 4.33. Binning of the movement mode data points for the series of Young's modulus for different mean tensile strength experiments. Binning interval of a single column is 0.05. Movement mode is calculated as shear component versus tensile component for every particle and then averaged over the number of particles broken during that time step. There is an overall shift towards displacement having more shear component with an increase in the rock's breaking strength. Value of 10 GPa has the least change in the probability distribution curve location and shape throughout the all four mean tensile strength experiments.

Figure 4.33 shows the distribution of the displacement mode ratio. This data set is the hardest to analyse. The initial experiments required a large number of data points for a clear trend to be identified. For this reason, the current results do not show a clear relationship between the different Young's modulus values. There is an overall shift towards a greater proportion of shear movement components with an increase in mean tensile strength as well as a Young's modulus of 10 GPa having the least amount of change in the distribution curve throughout all four mean tensile strength experiments.

To better illustrate the effects that breaking strength change has on the fracture opening dynamics, it is helpful to plot the parameters of interest against the non-dimensional value of Young's modulus / mean tensile strength (Fig. 4.34 to 4.37).

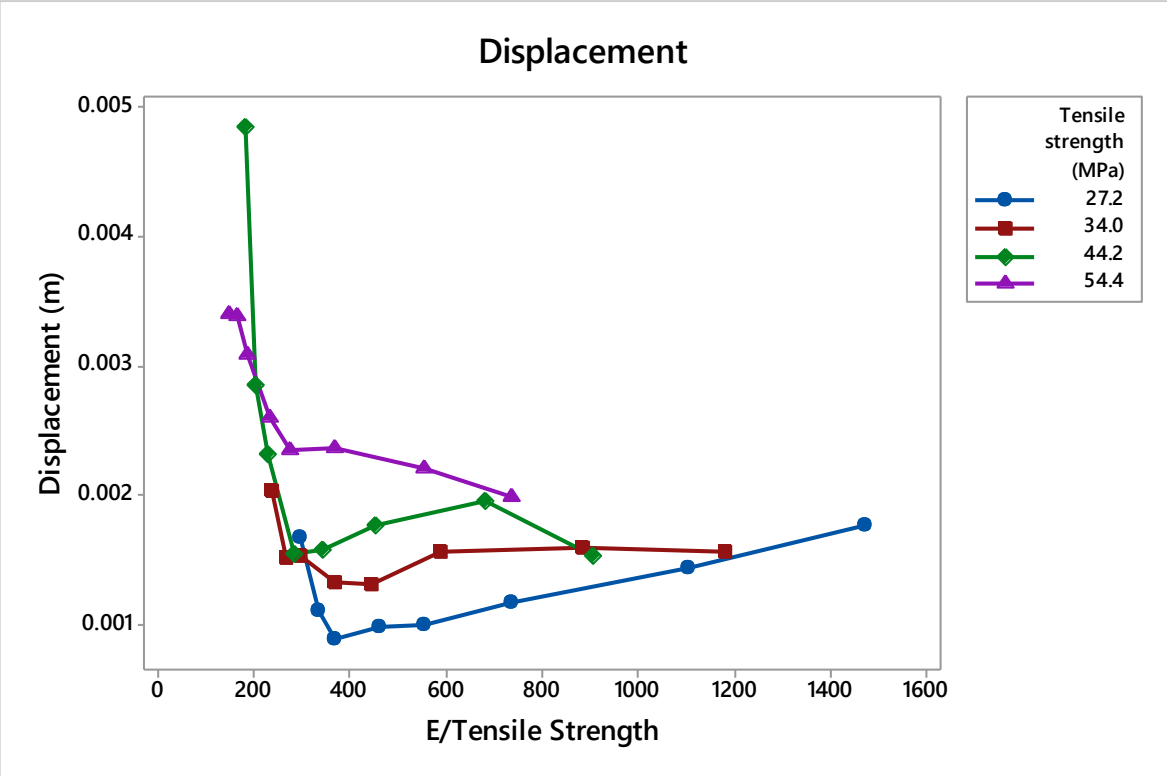

Figure 4.34. The figure shows the displacement data for a series of Young's moduli normalized by the tensile breaking strength of the rock. All data series show a bimodal non-linear relationship with the overall increase in the amount of displacement and shift in Young's modulus value being a turning point for the trend.

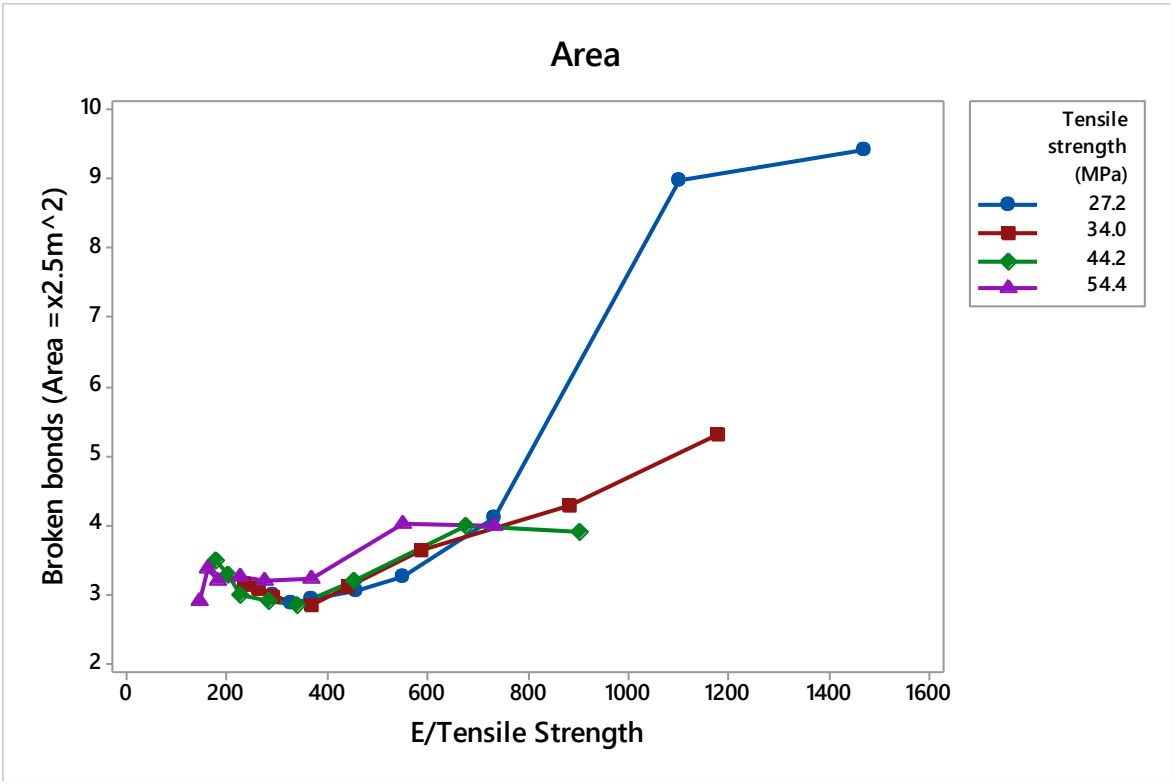

Figure 4.35. Area data for a series of Young's moduli normalized by the tensile breaking strength of the rock. Data shows almost identical non-linear behaviour. Two end-member points for the 27.2 MPa can be disregarded as a large number of broken bonds was produced by collapse of the solid particle lattice under its own weight.

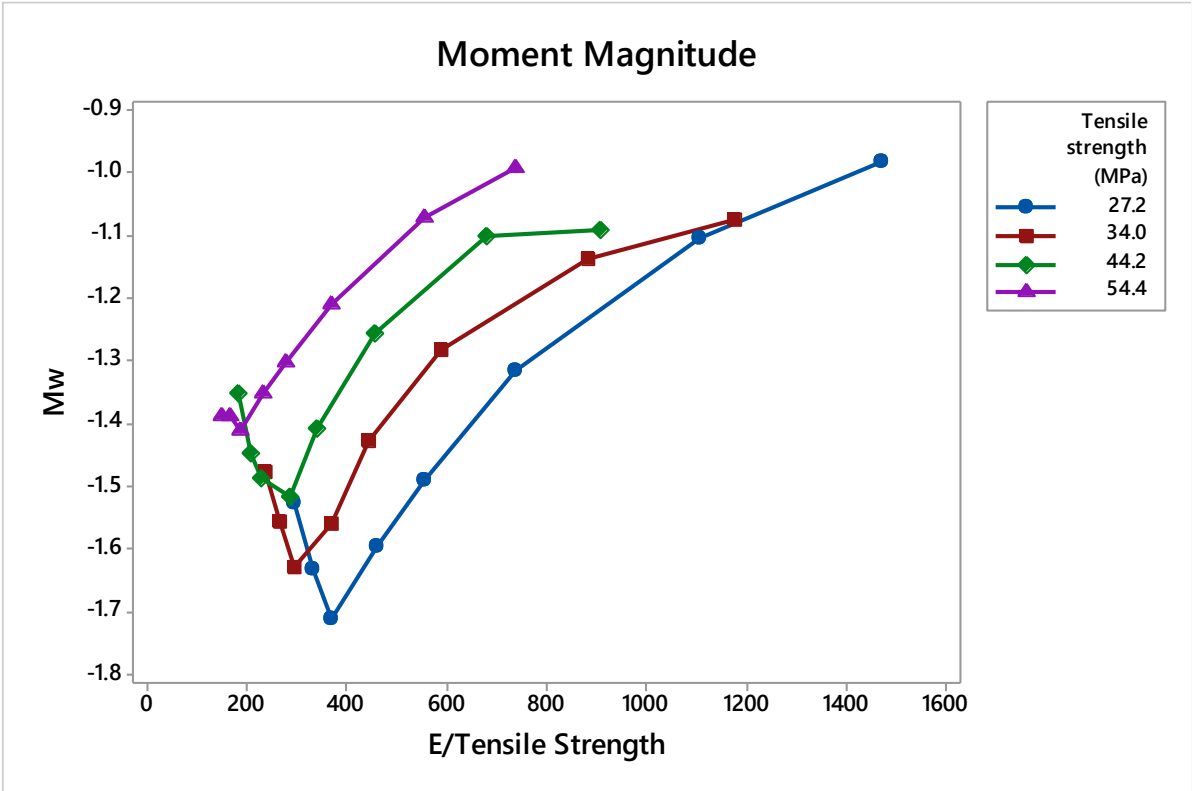

Figure 4.36. Moment magnitude data for a series of Young's moduli normalized by the tensile breaking strength of the rock. All four mean tensile strength experiment series show non-linear behaviour with the switch at 10 GPa. With the increase of the breaking strength of the rock, the spread of the data values becomes smaller.

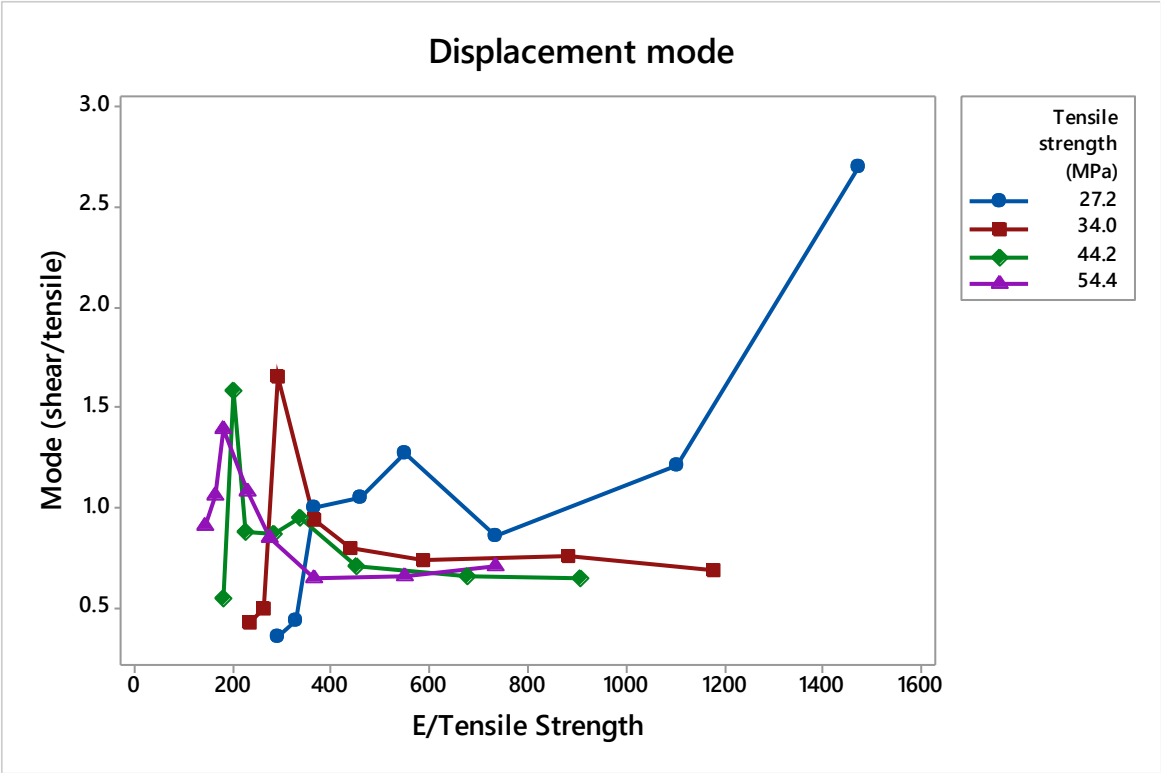

Figure 4.37. Displacement mode data for a series of Young's moduli normalized by the tensile breaking strength of the rock. All data series show non-linear behaviour. Two end-member points for the 27.2 MPa mean tensile strength can be disregarded as the model failed during given simulations.

Figures 4.34 to 4.37 illustrate the means of fracture aperture or displacement, fracture area, moment magnitude and fracture wall movement mode versus the non-dimensional parameter of Young's modulus / mean tensile strength of the bonds. The aperture of the fracture walls shows clearly a bimodal regime where it is high for smaller Young's modulus values and decreases inversely with an increase in Young's modulus until it starts increasing again after a certain value (Fig. 4.34). The turning point value increases with the an increase in breaking strength as it is 10 GPa (Young's modulus) for the experiments of 27.2 MPa bond mean tensile strength and progresses to 20 GPa for the experiments of 54.4 MPa mean tensile strength. The area data shows behavior similar to the displacement data (Fig. 4.35). There is an initial decrease and a following increase in the mean with the more gentle transition from one regime to another. The turning point in the trends for all experiments is either 10 GPa or 12.5 GPa. Very clear changes from the decrease to increase can be seen in Figure 4.36 which shows the mean moment magnitude, which is the function of the fracture aperture, area and rigidity of the rock. All data but the 44.2 MPa mean tensile strength line has a turning point at 10 GPa. It also shows that a fracturing rock with 10 GPa Young's

modulus will have the lowest seismicity impact irrespective of the breaking strength of that rock.

4.5. Discussion

The simulations indicate that a change in Young's modulus has a pronounced effect on the fracture behaviour. At a lower Young's modulus, the fracture mode is dominated by extension, the amounts of broken bonds are low, and the fracture wall movement or aperture is large. At higher Young's moduli the fracture mode becomes mixed with a larger amount of shear fractures, the fracture aperture becomes constant while the number of broken bonds and thus the fracture area increase. The fracture behaviour changes quite abruptly at around 10 GPa. Below 10 GPa the rock is quite soft and forms elliptically shaped fractures which almost "inflate" and do not really propagate. Above 10 GPa the rock is tougher; thus it is much more prone to tensile movement and stress is relieved through the propagation of fractures and thus more shear like movement.

To explain this behaviour we look at the stress increase at the tip of a mode I fracture (Fig. 4.38), which is calculated using equation 4.2.

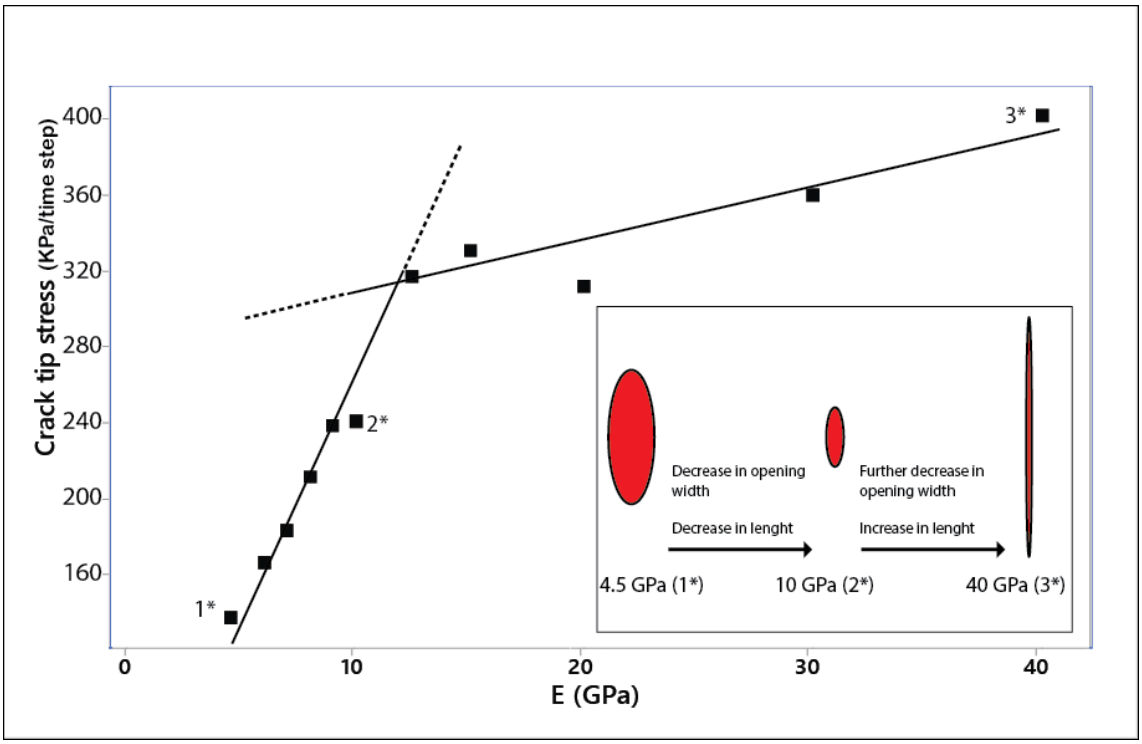

Figure 4.38. The figure shows the calculated crack tip stress from the crack aperture and length as a function of Young's modulus (E). The plot shows two regimes, below 10 to 11 MPa Young's modulus the crack tip stress increases rapidly, whereas at Young's moduli higher than 11 MPa the crack tip stress increase is only minor. These two regimes represent two failure regimes, below the critical of Young's modulus the fractures, are soft and open whereas at higher values the aperture is constant the crack propagates by an increase in length.

These values are obtained using fracture geometrical parameters averaged over multiple runs of the same Young's modulus values. The rest of parameters are as of a "default" scenario as described in Table 4.1.

The Stress at the crack tip σ (used for the *y* axis in the Figure 4.38), is a function of σ_0, the external stress (as a function of the fluid pressure gradient), length *L* of the crack and the radius of curvature *r* at the crack tip according to (Irwin, 1957)

$$\sigma = 2\sigma_0 \sqrt{\frac{L}{2r}} \tag{4.2}$$

Two different geometrical factors affect stress at the crack tip, the aperture and the fracture length. Soft rocks have larger elasticity and tend to be more easily compressed leading to wide open fractures with the change in fracture aperture is strongly sensitive to changes in elasticity. In this regime, the fracture length is fairly stable and in fact, slowly decreases with increasing Young's modulus. At larger Young's moduli the change in fracture aperture halts, whereas the change in fracture length becomes important. Although we do know the critical tensile strength as it is a prescribed value within the model, it is not easily possible to calculate the critical fracture strength based on rock mechanical properties alone without observing precise geometries of individual fractures e.g J-integral (Rice, 1968), which is not possible in the current model setup.

In the cases where the rock is harder the fracture aperture is small, and the stress is relieved through fracturing at the crack tip because the critical fracture toughness is exceeded before a critical tensile stress was reached. These fractures tend to be narrow but have greater length and occur in rocks which have Young's modulus greater than 10GPa. This change can also be observed from the microseismic observations where there is a dynamic shift within the average magnitude of the fracturing event as well as a shift in the dominating mode (mode I or mode II) of fracturing.

Further to better understand the dynamics at the fracture tip the XX and YY net stress change was constructed between the initial and final time steps in profile lines oriented vertically and horizontally through the simulated fractured area (Fig. 4.39, 4.40)

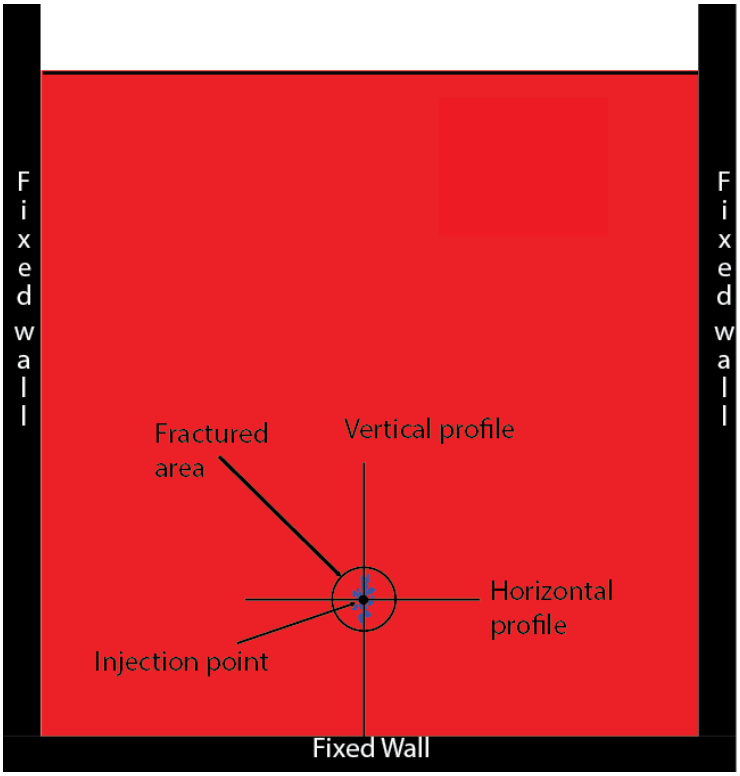

Figure 4.39. The figure shows the schematic placement of the profiles used to calculate the difference in XX (lateral) and YY (vertical) stress between the first and last time steps in the experiments. The profiles cover fracture networks rather than single fractures and thus show fluctuations in stress.

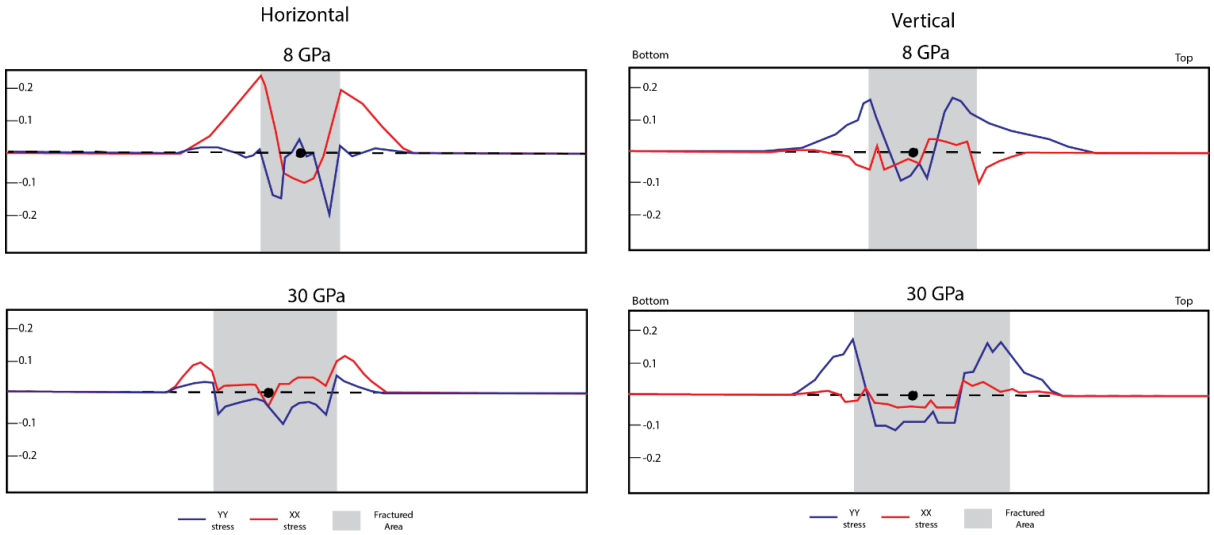

Figure 4.40. Profiles of change in XX (lateral) and YY (vertical) stress throughout the experiment along the horizontal (left) and vertical (right) lines of the profile. The horizontal profile shows an increase in XX stress on each side of the fractured area representing a compaction wave, which is much more pronounced in the soft rock. The vertical profile shows a significant difference of XX stress for soft versus hard rocks with hard rocks showing the only compression whereas soft rocks have a tensile region at the top of the fracture. Both vertical profiles are anisotropic reflecting gravity.

The data line is uneven as rather than going through a single fracture, it crosses a fracture network, and this causes fluctuations. After performing this procedure

multiple times for several cases, we can observe certain patterns emerge, which are schematically depicted in Figure 4.41.

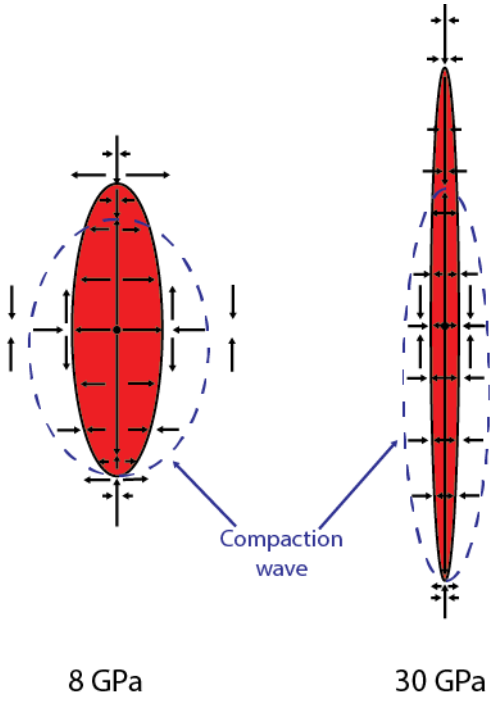

Figure 4.41. The figure shows a schematic illustration of stress in soft and hard rocks. Arrows pointing towards the centre of fracture indicate compressive stress while arrows pointing outwards – extensional.

Both cases (soft and hard rock fractures) have isotropic (explosive) behaviour at the injection point and tend to have stress changes on the left and right-hand side. The XX (lateral) stress in both cases shows an increase on both sides of the crack representing a compaction wave. This compaction wave is much more pronounced in the soft rock. The YY (vertical) stress behaviour is different for soft and hard rocks. In the case of a soft rock, it tends to be slightly extensional at the boundary of the fracture and then changes to compressive further away. When looking at the hard rock, the stress is mainly positive with a small negative area at the very centre and the switch from negative to positive is more abrupt. At the crack tip, soft and hard rocks behave quite differently, especially at the top of the fractured area. Both soft and hard rock scenarios show a bimodal behaviour where both XX and YY stresses change from extensional to compressive closer to the end of the fractured area. However, in the case of soft rocks, the XX stress becomes sharply extensional just outside the fractured area, while in the case of the hard rock scenario, no sudden change in stress is observed. This backs up the theory that fracture development in the case of soft rocks is mostly governed through lateral extension and increase of the fracture aperture as the stress regimes readily allow for lateral expansion at the crack tip. The relatively higher XX stress values at the

sides of the fracture suggest extensive expansion in that direction. In the case of the hard rock, the length is the key value behind the crack growth. In the case of the soft rock, the fracture tip is already an extension before the crack propagates and the fluid pushes outwards to pull the solid apart for further fracturing. This behaviour is very similar to fracturing in granular media where grains are being pushed apart (Niebling et al, 2012) and would represent pure mode I extensional failure. In contrast, the hard rock fracture tip is actually under compression. The stress concentration in the hard rock case is very high at the crack tip so that almost any tensile stress at the tip extends the breaking strength and leads to fracture propagation. The effect of these different mechanisms results in different slopes for hard rocks in Figure 4.38.

Figure 4.38 illustrates that in soft rocks the cracks are shorter and have a rounder shape. In this case, the fluid is potentially filling the whole crack and pushing at the walls (creating gradients depending on seepage) for further fracturing. In the case of hard rocks, the upper fracture tip is quite far from the centre. In this case, the fluid may not reach the tip for fracturing to occur. This leads to a dry crack tip if the solid is not water saturated or in the case of saturated rocks to a low fluid pressure crack tip. Many authors recognize this to be a multiscale problem (Bunger et al., 2007; Adachi et al., 2007; Detournay, 2016) as many factors are involved which are hard to test under laboratory circumstances. However, experiments in dry, impermiable material by Lecampion et al. (2016) show there is indeed a temporal lag in fluid filling the whole fracture when fracturing occurs. Unluckily, due to model's limitation, it is impossible to see or test a scenario where fluid would travel directly through fracture, thus allowing the possibility to observe a dry crack tip. This would require a different model setup rather than DEM coupled with fluid grid continiuum, which is used in our case.

It is unclear if the fracture tip remains dry in the same experimental circumstances when material is porous rather than impermiable, as used in experiments by by Lecampion et al. (2016) (scenario which would closer resemble real world conditions), which would allow fluid to fill the pores in the solid prior to fracturing.

4.6. Conclusions

This contribution shows numerically how hydrofracturing during fluid injection develops in 4 distinct stages: 1) build-up of stress, 2) fracturing, 3) residual

fracturing, 4) seeping. The Young's modulus of rocks and their breaking strength change the fracturing behaviour resulting in two predominant fracturing mechanisms. In the cases when the fractured rock is soft, fracturing occurs due to a critical tensile strength or cohesion being exceeded, change in the stress at the crack tip as a function of Young's modulus is then governed by the change in the fracture aperture and the fracture tip is constantly under extension. When the rock is hard, the fracture aperture is small and constant, and the fracture length becomes the key driver of the stress change. The fracture tip is under compression and fracturing is driven strongly by stress intensification at the tip, causing fractures to propagate in more shear like a failure.

It is shown that the relationship between Young's modulus and the two failure mechanisms works independently of the breaking strength of the rock as changes in Young's modulus for rocks with different breaking strengths produce the same relative increase in the amount of fracturing. The number of fractures that develop is a non-linear function of the breaking strength.

Changes in secondary parameters such as the amount of overburden or fluid injection rate have an impact on the number of fractures that develop but have little to no effect on the described failure mechanisms. The transition between the failure due to a critical tensile strength for soft rocks versus a strong dependence on stress intensification for hard rock lies at Young's modulus of about 10 GPa in the simulations. Since Young's moduli for natural shales vary from 8 to 50 GPa one has to be careful to use the right failure criterion depending on the shale type.

Change in the breaking strength of the rock produces an effect where data points can vary in their distribution fashion, but it has no effect on the nature of the effect of having two separate failure mechanisms. The change in the breaking strength has the following effect on the observed parameters:

- **Pressure gradient**: increase in the breaking strength of the rock results in larger values of the fluid pressure gradient at the end of the experiment. This is explained by the larger amount of fluid being required to fracture the rock as the tensile failure criterion is higher.
- **Cumulative number of broken bonds**: the lower breaking strength of the rock allows for a larger number of cumulative broken bonds to develop during the hydrofracturing process. This is the effect of the brittle rock allowing for easier fracturing.

- **Fracture area, displacement and moment magnitude**: Increasing the breaking strength of the rock provides a trade-off relationship between the abundance of the events and their magnitude. Lower breaking strength rocks produce large numbers of fractures in a single fracturing event that have small aperture and area and thus small moment magnitude. Rocks with increased breaking strength are harder to fracture and are able to accumulate a larger amount of stress before failing. Once they fail, fractures produced in a single event have larger aperture and area and thus have higher seismicity generated.

5. Hele-Shaw cell experiments

The purpose of this Chapter is to replicate the simulation processes described in Chapter 4 under laboratory conditions to the best possible standard. Numerous laboratory methods for studying rock physical properties and hydrofracturing processes, described in Chapter 2, have been looked into and considered before opting for a Hele-Shaw cell approach. The main reasons for choosing this approach are:

- The Hele-Shaw cell geometry and setup mimic the simulation "box" parameters used in experiments described in Chapter 4 very well.
    - Limiting the possible deformation to the thin space in between the glass plates is very close to copying the 2D environment of the "Latte" simulation platform.
    - The compacted granular nature of the solid phase of the Hele-Shaw cell resembles the triangular setup of the DEM lattice used in the simulations.
- The experiments are easily repeatable and require no additional cost for acquiring rock samples and measuring their physical properties. The ability to reproduce single experiments multiple times enables for greater data availability.
- The Hele-Shaw cell experiments are time efficient, meaning that little time was required to carry out this part of the study and the method was well established in the laboratory at the University of Strasbourg.

A total number of 56 experiments was carried out with the variable characteristics described in Table 5.1. A full log of all the experiments can be found in Appendix B.

The significant difference between the experiments described in Chapter 5 and simulations discussed in Chapter 4 is the forces that are acting on the solid and opposing its displacement. In the simulations it is the tensile, cohesive strength of the solid that has to be overcome for the material to fracture. Experiments are, however, carried out using granular material. This means there is almost no cohesion between the grains. The displacement of the material is opposed by the frictional forces between the beads themselves and between beads and the glass plates. This difference has to be considered when analysing the results.

Table 5.1. Summary of the parameters used in the Hele-Shaw cell experiments.

Overburden (m)	Overpressure (Bar)	Injection duration (sec)	Room t° (C°)	Relative humidity (%)	Type
0.2	0.05-0.2	0.1-0.5	24.9°-25.4°	50-58	A, B, C
0.25	0.05-0.2	0.1-0.3	24.9°-25.4°	50-58	B
0.5	0.1-0.2	0.2-1.0	26.6°-28.4°	56.6-61-7	A, B
0.6	0.1-0.6	0.5-1.5	27.2°-29.1°	55.4-59	B, C

Note: Overburden, overpressure and injection duration parameters were varied. Room temperature and relative humidity of the air could not be controlled in the conditions, where the experiments were carried out, however, they potentially could influence the cohesion of the granular media in the Hele-Shaw cell. Types of experiments are indicated, and are dependent upon the calibration between the overburden, overpressure and injection duration.

By the design, the change in the amount of granular media within the cell (overburden) should provide laboratory analogues to the simulation experiments with altered depth. On the other hand, altering overpressure and duration of the injection interval would mimic systems with fairly intense fluid injection.

Experiments are carried out in a vertically oriented Hele-Shaw cell. The cell itself is represented by two glass plates that are fixed by three impermeable boundaries from both sides and the bottom and a semi permeable boundary from the top. Glass plates are positioned 1.5 mm apart from each other. The space in between the plates is filled with polysterene ugelstad beads that are 80 microns in diameter. The top boundary is made of metallic mesh, which in size is smaller than the diameter of the beads. That allows for the injected fluid to escape while retaining the beads within the cell. Injection point is located centered, 3cm above the bottom boundary. The experiments are then recorded using high speed camera (Fig. 5.1).

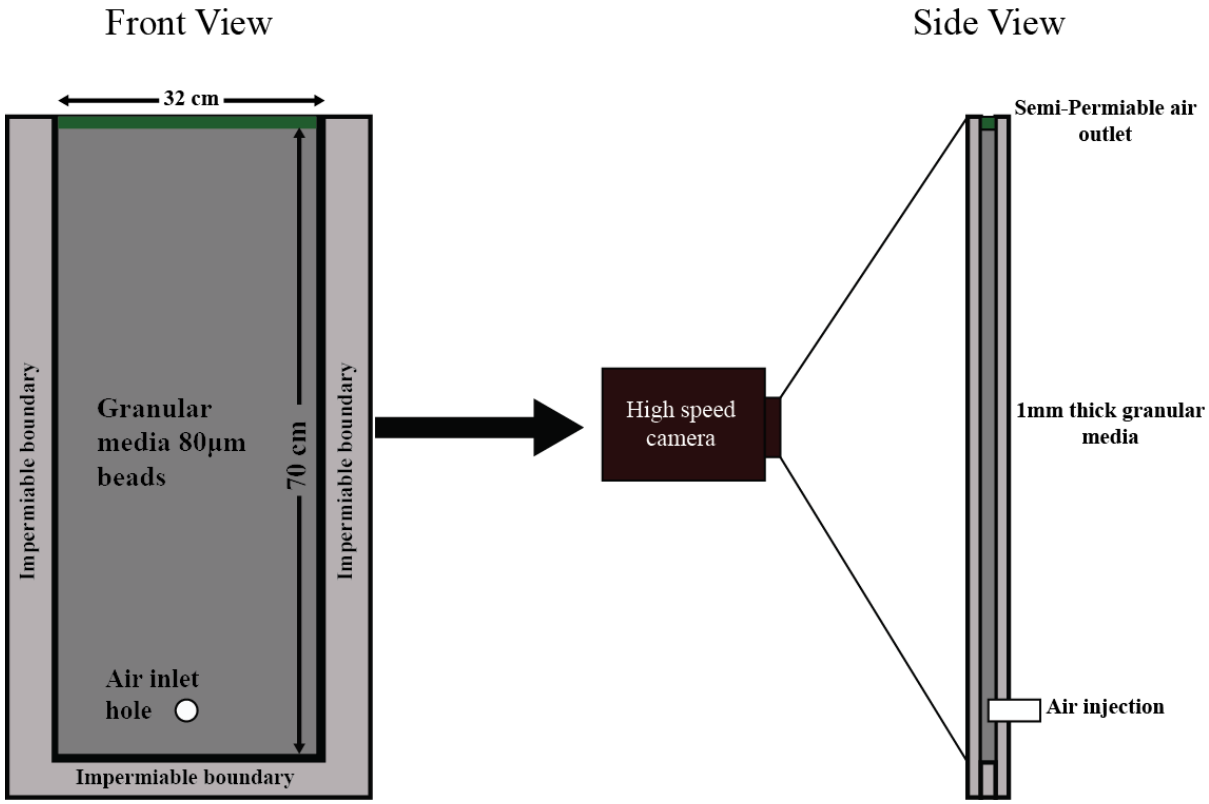

Figure 5.1. Schematic illustration of the Hele-Shaw cell used in the experiments. It is composed of two glass plates positioned 1.5 mm apart from each other. Plates are bound by three impermeable boundaries from the bottom and from both sides. The space in between the boundaries is filled with poysterene beads, which are 80 microns in diameter. Top boundary is made of semi-permeable metallic mesh, with gridding smaller then diameter of the beads. This allows for retaining of the beads within the cell while the injected fluid can escape. During the experiments the cell is positioned vertically and experiments are recorded using high speed camera.

5.1. Single experiment description

This Section focuses on the underlying processes taking place over a single hydro or air-fracture experiment. Depending on the calibration between the overburden height, the applied air overpressure and the duration of the air impulse, the system can act in multiple ways (Table 5.1). Three scenarios depending on the amount of system disturbance caused will be presented. To look at the initial dynamics, a simple image subtraction technique has been applied using MATLAB. As described in Chapter 3, about 3% of the silica beads in the Hele-Shaw cell are dyed black. When movement occurs, dark beads can move into space previously occupied by white beads and vice versa. The image subtraction technique rasterizes a series of images creating a matrix with values corresponding to every pixel's hue position along the greyscale. Values of the matrix are then subtracted from each other for every one of the following images in the sequence and

accumulated in a separate result matrix. The outcome is a matrix that in its dimensions is the same as the analysed images but shows the numerical cumulative value for the change in light intensity in the image series. This can be interpreted as a heat map representing displacement intensity in the system. Two types of the analysis using this method have been carried out:

- Cumulative – shows the difference between the reference image and the initial image at the sequence, representing the system state prior to the experiment. This approach shows the total system disturbance occurring throughout the experiment.
- Differential – represents the difference between the two images in the course of the experiment running with the predefined interval between them. This approach shows the dynamic change in the system disregarding disturbance occurring prior to the first reference image.

5.1.1. Experiment type A

This type of experiment represents the scenario when fluid pressure within the rock is too small to open a fracture. Summary of the parameters under which this type of the outcome occurred is presented in Table 5.2. It can be seen that such outcome is typical of experiments with low overpressure.

Table 5.2. Summary of the parameters under which Type A experiments occurred.

Overburden (m)	Overpressure (Bar)	Injection duration (sec)
0.2; 0.5	<0.1	0.2-2

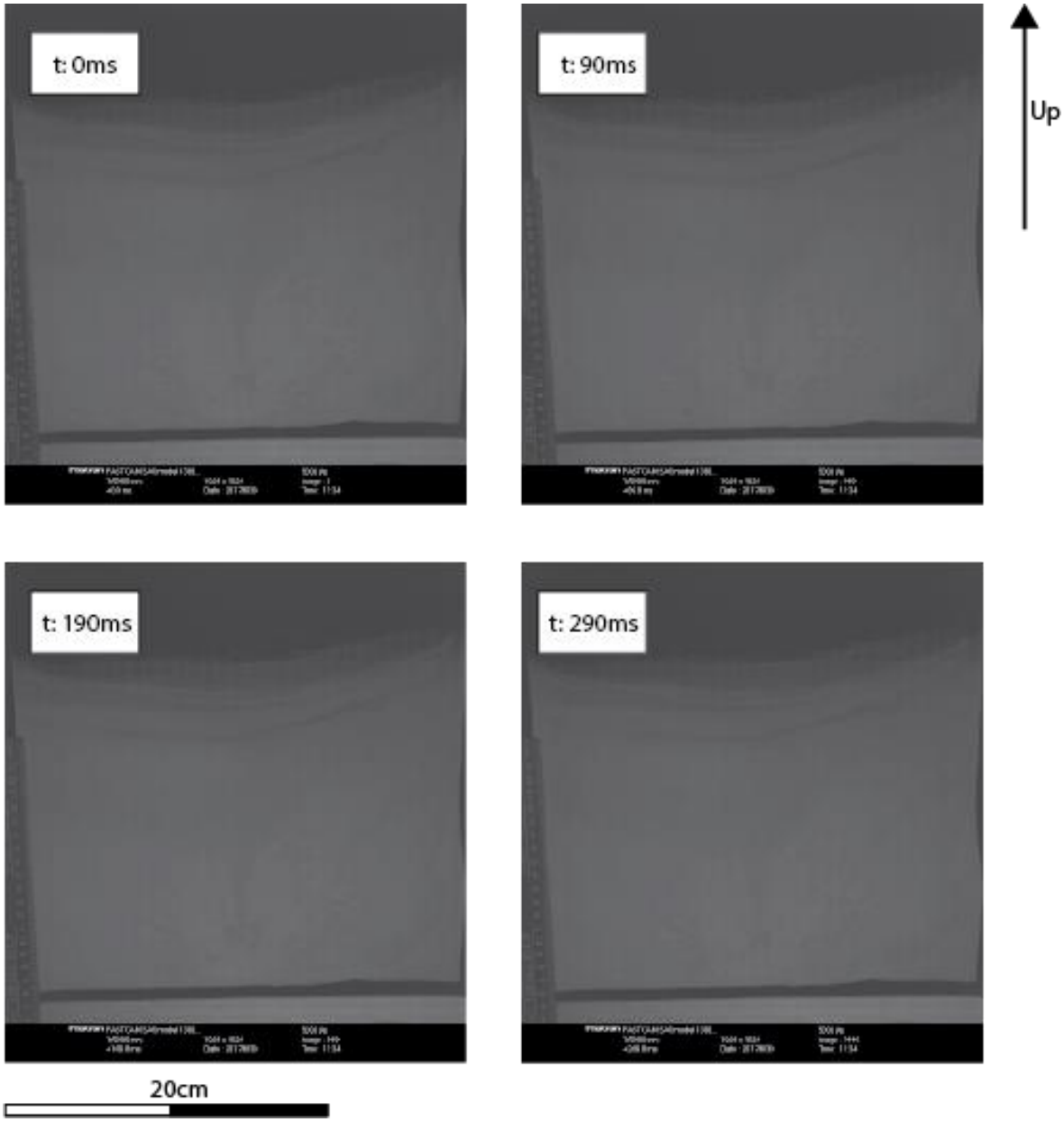

Figure 5.2. The camera recorded frames of the experiment, where fluid injection pressure and duration were low enough not to produce visible fractures. The length of the experiment is 0.3s. The time interval between the two following images is 0.01s.

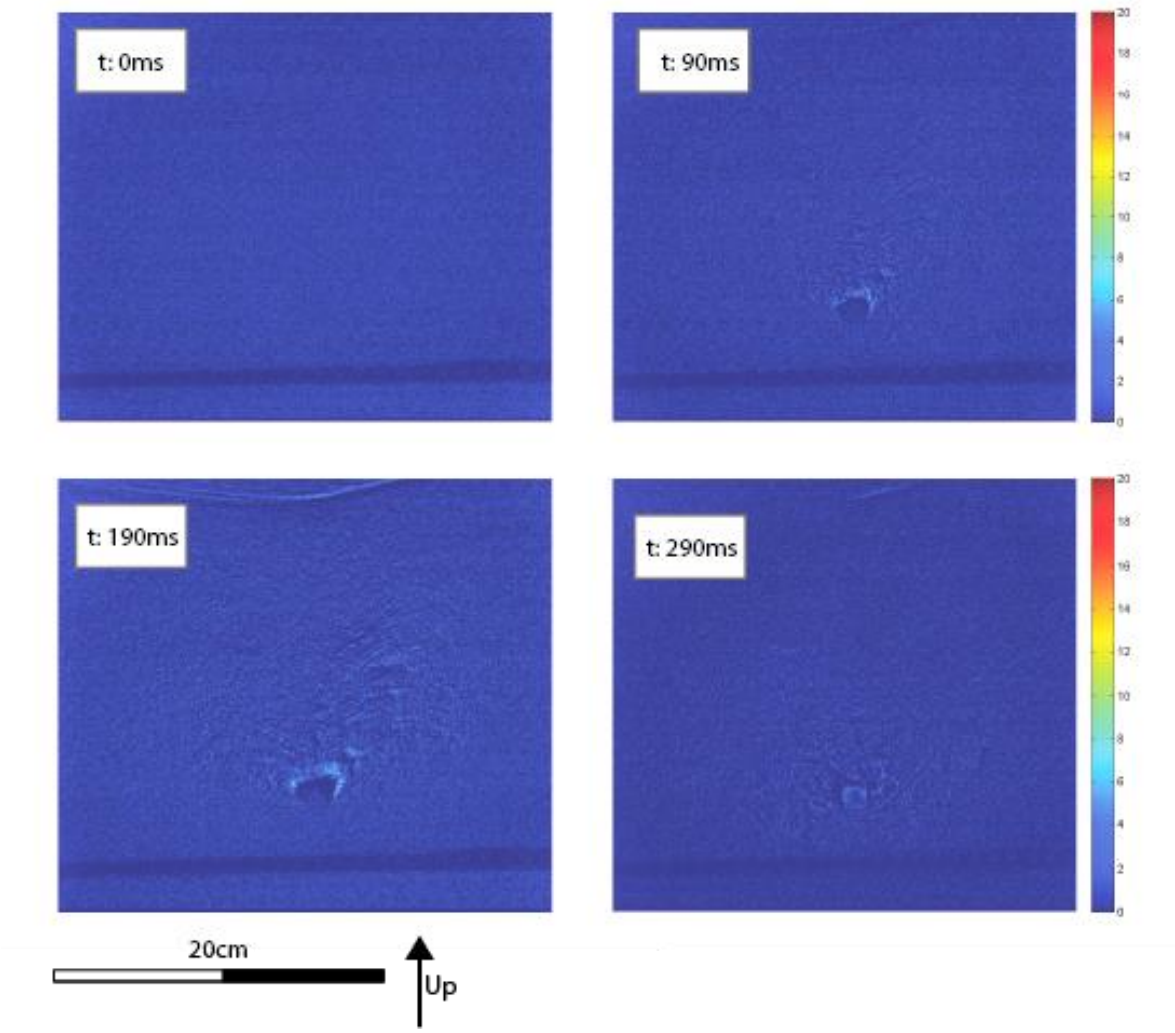

Figure 5.3. Series of the images representing the cumulative difference in the displacement in the reference to the state of the media prior to the experiment beginning. The length of the experiment is 0.3s. The time interval between the two following images is 0.1s. Scale represents relative change according to the grayscale gradient, maximum is a change from white to black and vice versa. As it is impossible to cancel all the vibrations in the given laboratory setup, some noise is visible throughout all the image. As air is injected, particles surrounding the inlet hole start to decompact creating a compaction wave. Following the initial compaction wave, smaller movement waves can be seen forming in a radial fashion relative to the fluid injection point. Last image represent the experiment stage where air injection has been ceased and grains recompact. Amount of the final compaction is smaller than the initial state of the granular media.

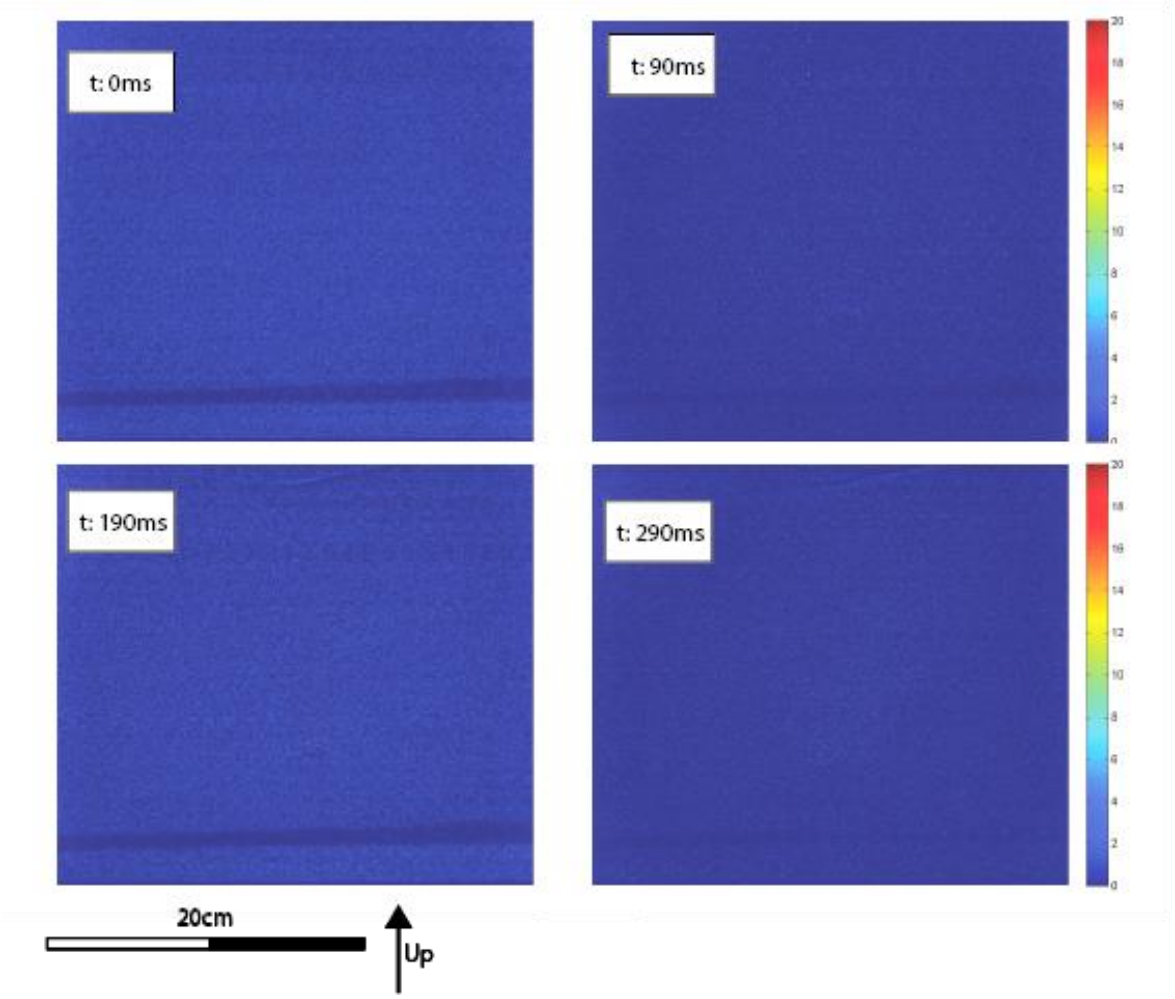

Figure 5.4. Series of images representing heat map of movement between every two following images. The length of the experiment is 0.3s. The time interval between the two following images is 0.01s. The absence of any visual traces indicates that decompaction is very gradual and produces very little disturbance in a short timescale.

Figure 5.2 shows the actual recorded images from the experiment with 0.2 m high infill column of granular media where 0.05 bar overpressure has been applied for 0.2 seconds. No displacement can be seen from a simple visual inspection of the footage as the fluid pressure was too small to open fractures. Figure 5.3 depicts the amount of relative displacement per pixel of the image for the same system. The fluid injected can be seen to cause particle decompaction. Decompaction is created by air pushing particles away from the injection site and away from each other once it seeps into space between them. This creates area where the particle density is lower than average density throughout the cell. This creates a radial compaction wave surrounding the air inlet hole and the decompacted zone. The decompaction of the central area causes smaller displacement and compaction ripples throughout the whole system. Ripple effect is caused by small scale

particle movement throughout the whole system as particles are being pushed away from the injection hole. When the local porosity of the system is increased, the system maintains status quo, meaning all the injected air seeps away through local pores and the system does not decompact any further, even if more fluid is being injected. Once the air injection is ceased, the system recompacts under the gravitational force. At the final stage, particles can be seen to be less compacted compared to the initial state of the system. The main aim of the differential image subtraction is to see the intensity of the displacement in the system. Images in Figure 5.4 show very little to no signal. This indicates that the decompaction of the particles causes very uniform and gradual displacement with only small differences throughout the system. Last image shows that recompaction under gravity is by far more rapid than the decompaction and faster than can be recorded by the differential image subtraction. This indicates that introducing fluid/gas to the solid system and then removing it causes irreversible changes to the solid media.

5.1.2. Experiment type B

With the gradual increase over a series of experiments in the overpressure and fluid/gas injection duration time, the fluid/gas is able to open up a fracture. The fluid/gas overpressure is barely exceeding the resistance of the frictional forces within the system and only a single, vertically orientated fracture develops (Fig. 5.5 to 5.7). The summary of the parameters used that caused Type B outcome in the experiment is presented in Table 5.3.

Table 5.3. Summary of the parameters under which Type B experiments occurred.

Overburden (m)	Overpressure (Bar)	Injection duration (sec)
0.2; 0.25; 0.5; 0.6	0.05 – 0.4	0.1 – 2

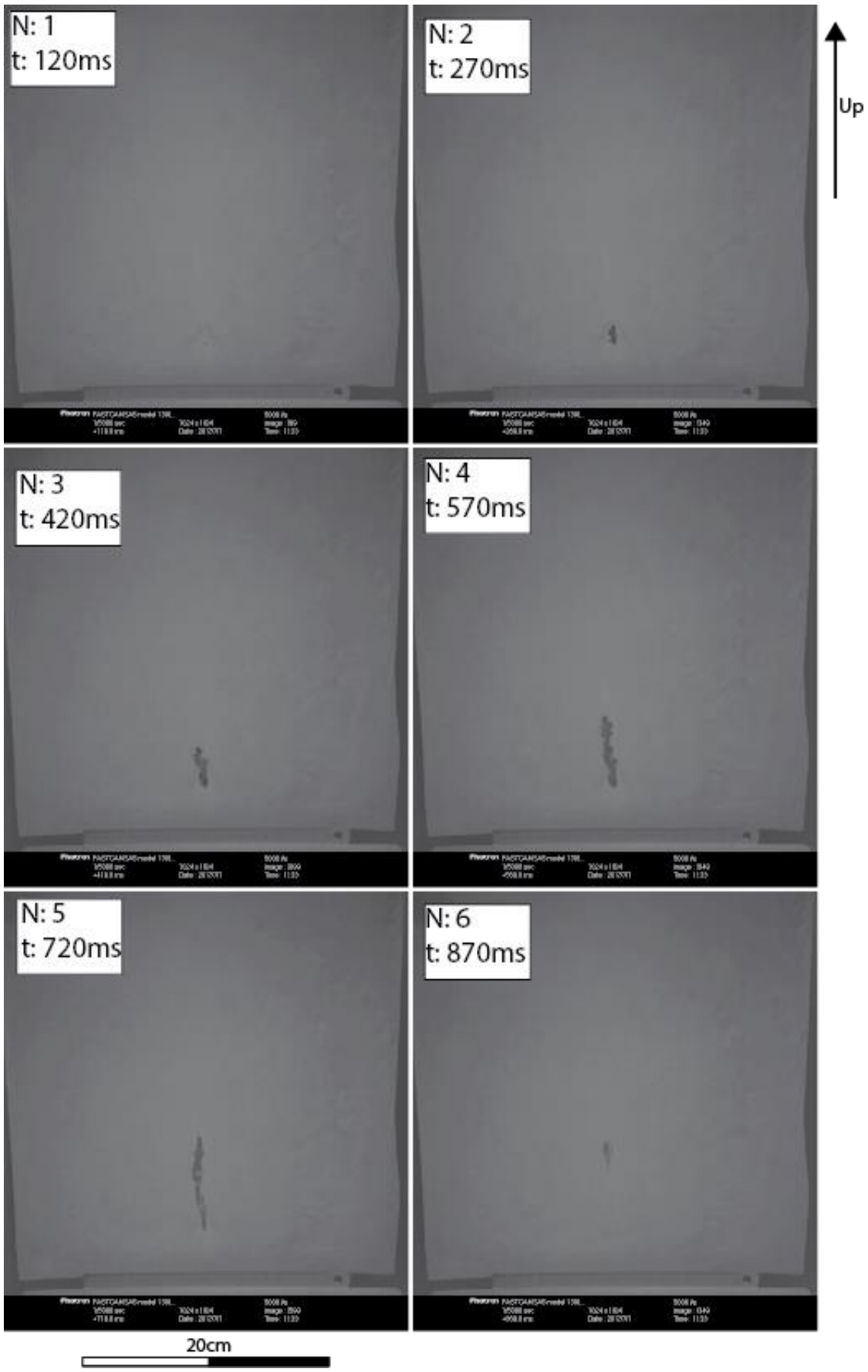

Figure 5.5. The camera recorded frames for the experiment, where fluid overpressure was high enough to produce a single, vertically oriented fracture. Length of the experiment is 0.9s with the fluid injection phase lasting 0.7s (last image in the sequence represenst the closing down of the system). The time interval between any two frames is 0.15s.

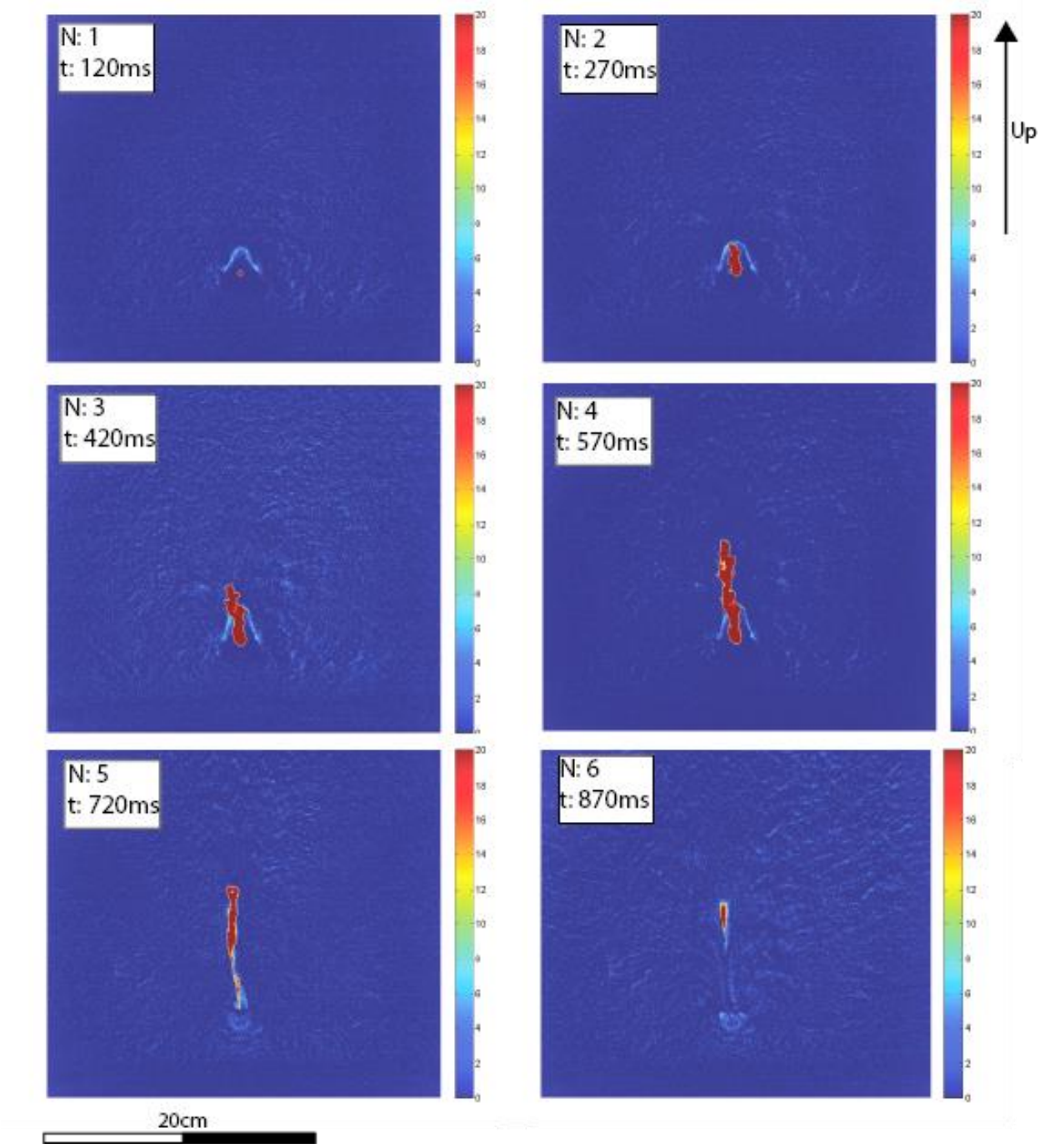

Figure 5.6. Series of the images representing the cumulative difference in the displacement in the reference to the state of the media prior to the experiment beginning. The length of the experiment is 0.9s. The time interval between any two following images is 0.15s. Fracture opening is marked in red, while relative particle displacement is indicated using the chart, which is linked to a change of value on a grayscale bar. Events recorded can be subdivided into several episodes. First image shows system decompaction, forming a radial feature where fluid seeps to. Following images show fracture initially opening in an isotropic fashion: it forms a circular feature and opens in all directions uniformly. Opening process is continued in a vertical direction with a slight variation of crack tip propagation direction. Fracture thickness is mostly uniform throughout the system. Last frame shows the fracture closing down once the fluid injection is ceased. Fracture propagation is halted before the air injection is ceased. This occurs due to fracture surface being sufficiently large to allow for all the injected air to seep away.

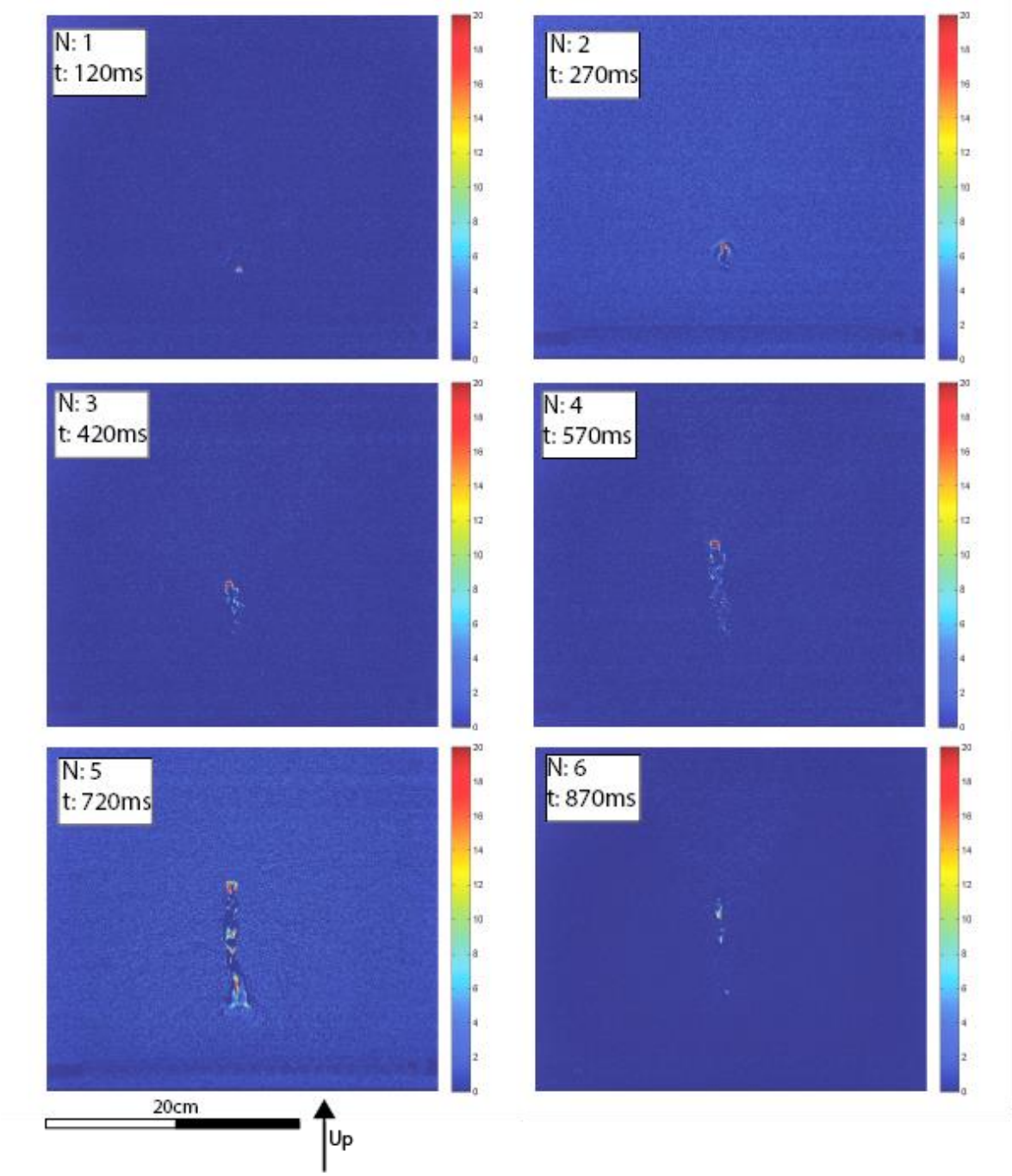

Figure 5.7. Series of images representing heat map of movement between every two following images. The length of the experiment is 0.9s. The time interval between any two following images is 0.15s. This figure allows observing the dynamics of different fracture opening stages. The first image shows decompaction occurring, forming a radial feature, where most of the particles are being pushed slightly upwards. This is followed by fracture's vertical propagation. Bright colours within the opened fracture are due to the granular material being picked out of the fracture walls by the flowing air turbulence. Last image represent the closure of the fracture, once the fluid injection is ceased.

In this type of the experiment, the fracture opening, and particle movement are clearly seen (Fig. 5.5) in contrast to the Experiment Type A (Fig. 5.2). This experiment type's initial phase is identical to the previous: the injected fluid/gas firstly increases the local pore pressure and decompacts the system in the radial

area around the injection point. As the fluid/gas injection rate in this scenario is higher than the seepage rate, the local pressure gradient keeps increasing, which causes for the tensile failure of the material. The initial fracture opening is isotropic (equal displacement in all directions) (Fig. 5.6, Image 1). This is followed by the fracture progressively opening in a predominantly vertical orientation with some lateral component variability. An interesting feature can be seen in the Image 2 in Figure 5.6. When the fracture propagation reaches the stage where it bypasses the compaction wave created by the initial particle decompaction, it exploits the decompacted area by branching into it. This feature will be further explored in more detail in the following DIC analysis and discussion sections. Figure 5.6 shows that fracture propagation happens through increasing the area in front of the fracture tip and to a lesser extent the area around it. Furthermore, as the fracture propagates, it forms linear features that are oriented at an angle towards main channel of the fracture (Fig. 5.6). This indicates that there is a differential particle movement along both sides of these features. The downside of the image subtraction technique is that one cannot distinguish the vector (direction) of displacement, just the value of displacement in this area (relative amount of change of pixel colour value). Fracture propagation is halted before the air injection is ceased. This occurs due to fracture surface being sufficiently large to allow for all the injected air to seep away through pore space.

5.1.3. Experiment type C

The third type of experiments is represented by a setup where the fluid injection is done in a rapid manner. This causes fractures to branch out and form conjugates. If an overpressure is not set to a limit, the system can fluidize, i.e. grains loose cohesion because they loose contact with each other and retain no friction. The summary of the parameters used that caused Type C outcome in the experiment is presented in Table 5.4.

Table 5.4. Summary of the parameters under which Type C experiments occurred.

Overburden (m)	Overpressure (Bar)	Injection duration (sec)
0.2; 0.6	0.1 – 0.6	0.2 – 1

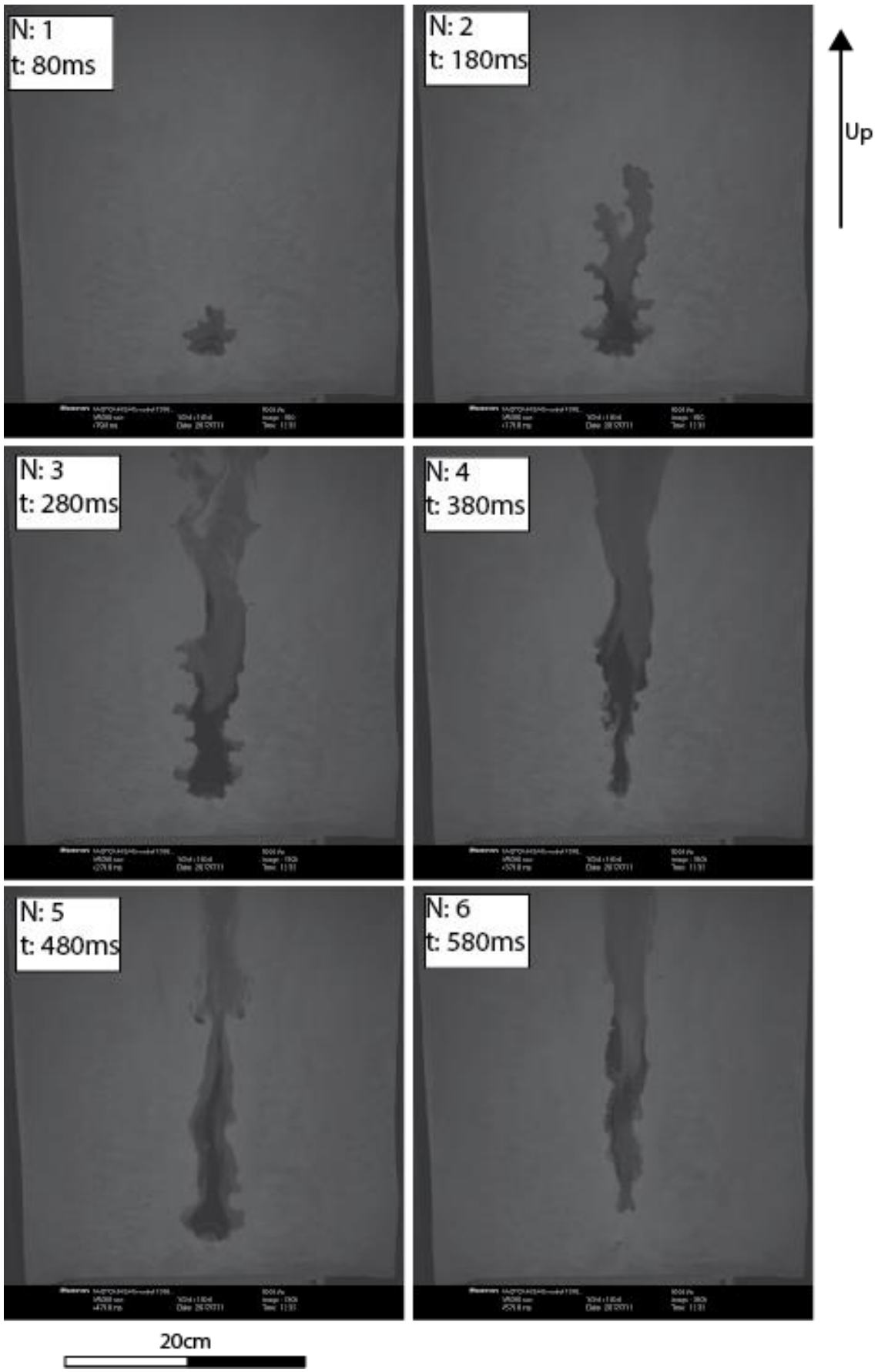

Figure 5.8. Camera recording frames for the experiment, where fluid overpressure was increased to the stage where it causes granular media to fluidize. Length of the experiment is 0.6s with the fluid injection phase lasting 0.5s (last four images in the sequence represent the closing down of the system). The time interval between any two frames is 0.1s.

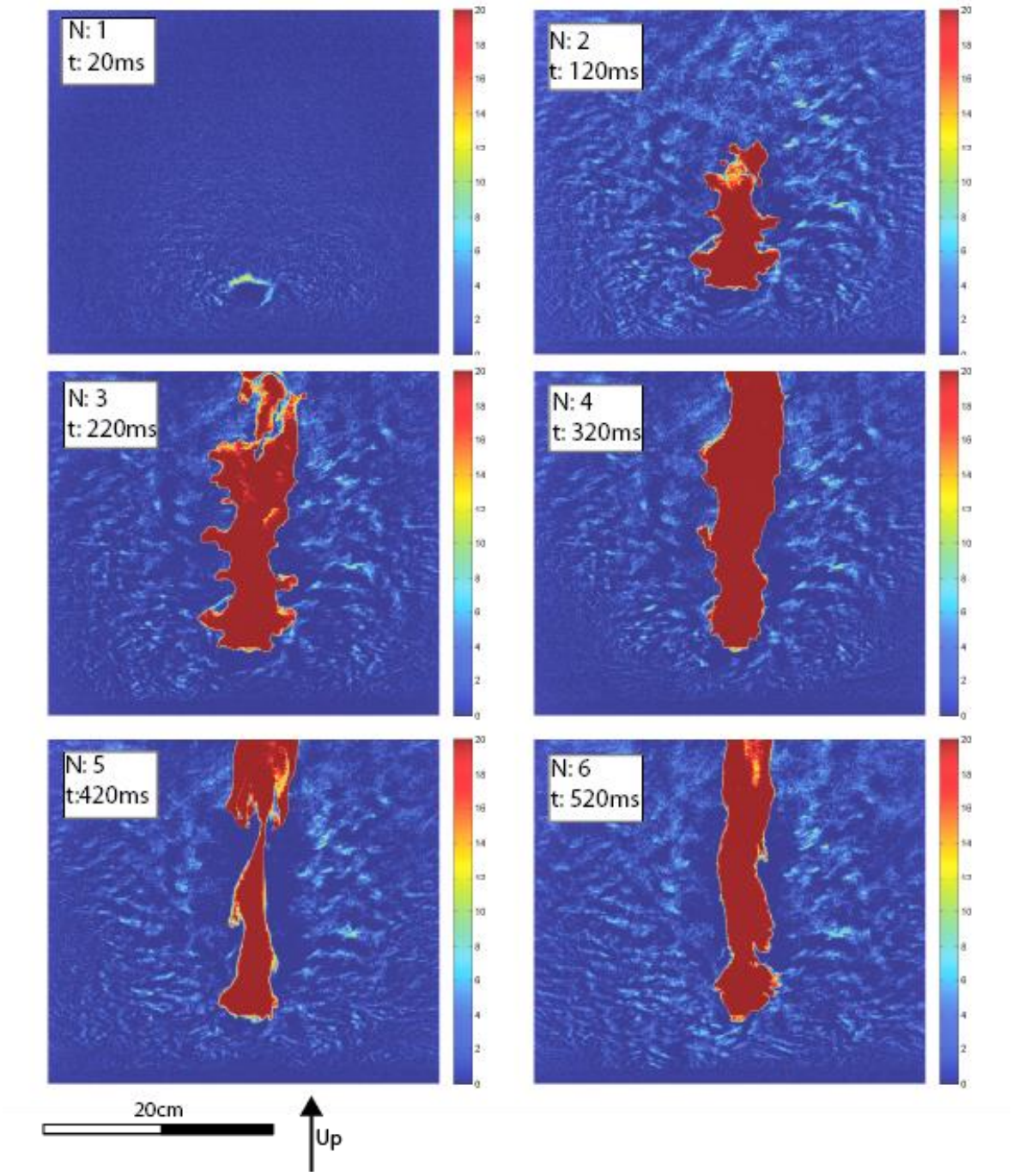

Figure 5.9. Series of the images representing the cumulative difference in the displacement in the reference to the state of the media prior to the experiment beginning. The length of the experiment is 0.6s. The time interval between the two following images is 0.1s. Initial stages of the experiment are the same as previous types: initial air dissipation through pore spaces and local decompaction followed by isotropic fracture opening. There is a relationship in fracture width versus the injected fluid overpressure, as the fracture width is larger than the previous experiment type. Due to high fluid injection rate air increases pore pressure to an extent where frictional forces between the grains are lost and granular media start to behave as a fluid. The second image shows fluid forming a separate pocket to the top right of the fracture front. The fluid content is so high in between the grains that they detach from the main mass and get carried together with the air flow in the fracture (same image, bright yellow sector).

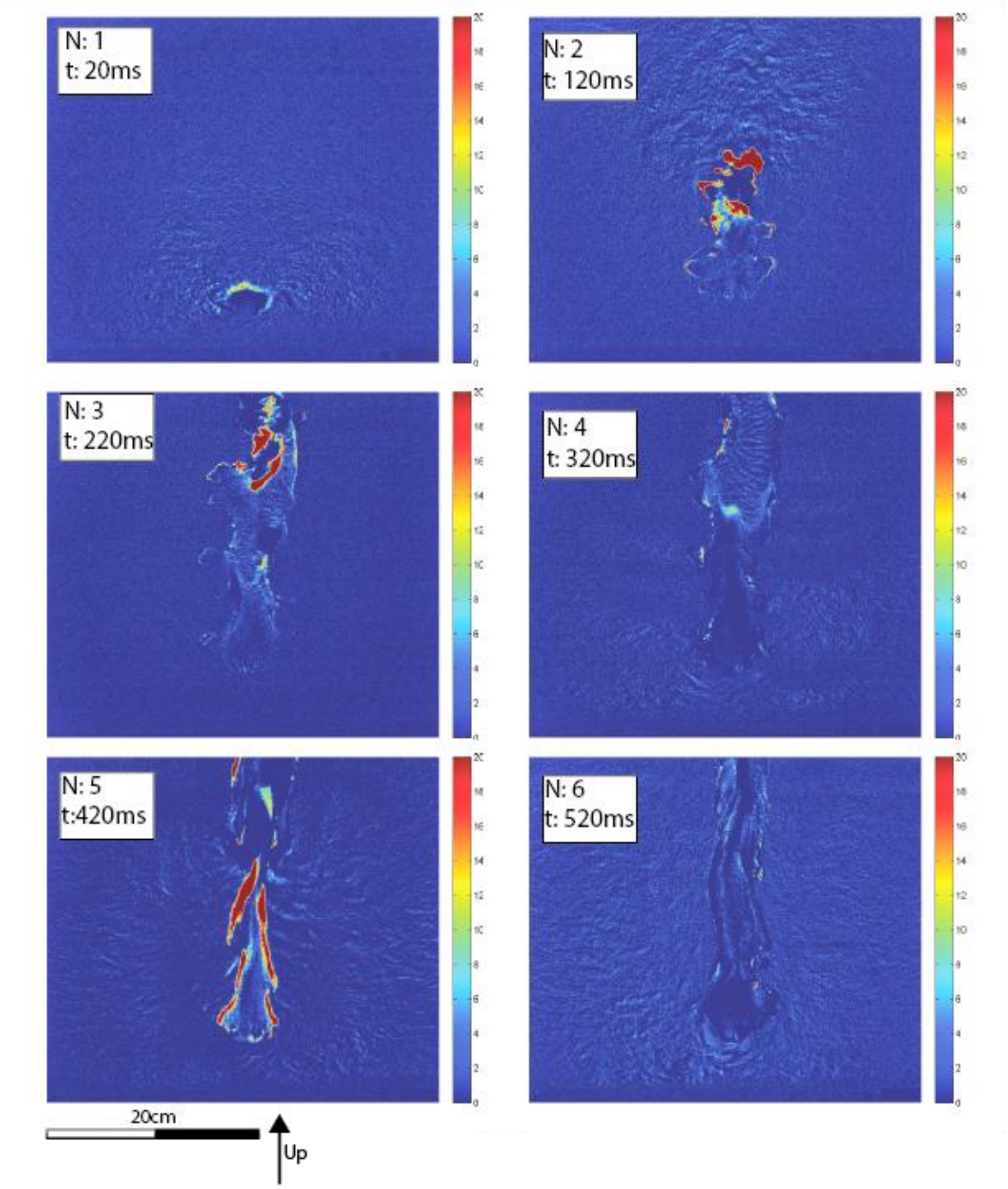

Figure 5.10. Series of images representing heat map of movement between every two following images. The length of the experiment is 0.6s. The time interval between the two following images is 0.1s. Initial image show the same fracture opening dynamics as the previous two experiment types. In the later stages of the experiment mass movements along the fracture walls and fracture, a channel can be seen. Dynamics lead to show that the injected fluid is behaving in a turbulent way, which is not the case in hydrofracturing, where the fluid flow is considered to be laminar.

This type of experiment shows a fracture that is much wider and that has many fracture offspring side-branches (Fig. 5.8). There is a relationship between the amount overpressure of he injected fluid/gas and the width of the main fracture

channel. The initial stages of the experiment coincide with the dynamics described in the previous two types of experiments: an initial granular decompaction happens as pore the pressure increases due to fluid injection, followed by an isotropic radial fracture opening (Fig. 5.9). Once the fracture is open, it propagates vertically, and is creating horizontal offspring branches. The branches are predominantly created by exploiting planes of weakness created by particle movement duirng earlier stages of the experiment. In the setup with high pressure, the amount of fluid/gas increases the pore pressure around single grains to the extent where grains lose contact and friction with their surrounding neighbour particles. This causes the system to fluidize as fluid saturated particle clusters behave as a fluid rather than a solid. The process of the fluidization can be seen in Figure 5.9 (Image 2); fluid/air seeps through the particles and exploits previously decompacted planes (because of differential particle movement) where it creates a bubble. In the same image area (top right) the fracture front is being decompacted on a granular level, and in the next frame, it is carried by injected fluid along the main fracture channel in a turbulent manner. This behaviour is referred to as viscous fingering. Turbulent fluid flow can be seen in Figure 5.10 and they present a problem as they further enhance viscous fingering. Neither viscous fingering nor turbulent flow are present in the actual hydrofracturing processes as rock walls are solid and do not become fluidized and fracture openings are typically small enough for all the fluid flow to be laminar.
When using the Hele-Shaw cell for looking at hydrofracturing dynamics one must be aware of the possible drawbacks and the system experiment design (amount of overburden and injected fluid overpressure) must be calibrated to resemble real rock conditions as close as possible.

5.2. DIC analysis

The image subtraction method described in Section 5.1 is relatively easy to carry out and provides a good glossary of the ongoing dynamics. However, one of its biggest drawbacks is the inability to distinguish the direction of displacement, but only its magnitude. For this reason, we need to employ an approach that recognizes and follow the whole pattern, rather than individual image pixels. In order to achieve this, the MATLAB code based NCorr software package is operated

as discussed in Chapter 3. The main purpose of this software package is to analyse the displacement vectors and calculate Lagrangian strains.
The analysis is computationally intensive and requires a large amount of memory. The algorithm, despite taking rotational factors into account, cannot always cope with the complex nature of the displacement patterns within the material. This causes some drawbacks, which have to be taken into account when analysing the data. Experiments, which could be used for the DIC analysis had to be hand-picked as only a limited amount of continuous frames could be analysed due to RAM limitations.

5.2.1. Initial injection stage analysis

The aim of this part of the analysis is to look at displacements and strains in the system during the particle decompaction stage shortly after fluid injection is initialised. For this part, the same data that is used to demonstrate Type A experiments is taken. This is done so that the original, unaltered frames could be seen in Figure 5.2. The data are presented in four parts (Fig 5.11, from top to bottom): vertical displacement component, lateral displacement component and (Fig. 5.12 from top to bottom) vertical (YY) strain, lateral (XX) strain. The results that were gained are very intuitive. The vertical displacement is predominantly upwards orientated and, as fluid seeps through the pores, decompaction is occurring on an expanding area. A similar trend is seen for the lateral movement: More movement is occurring towards the right hand side than the left hand side meaning there is an unequal distribution of displacement. The total vector of lateral displacement is slightly upward oriented. Both lateral and vertical displacements do not exceed the value of 5 pixels which equals 1.5 mm. If we consider the diameter of a single particle to be 80 microns, the particles may displace up to 20 times their own diameter. This shows that even if the system does not open visible fractures, the decompaction and local porosity increase is substantial. This is also illustrated by the fact that the system is stable once it is decompacted and all the fluid injected is able to seep away. This is further shown by the strain analysis where the extensional regime around the injection point is dominant, despite the compaction wave that was created around the injection point. When looking at the XX strain, the area and magnitude of the extension are

greater than the sum of the two compaction fronts on either side of the injection hole. A similar observation can be made about the YY strain plot. The vertical strain indicates the area of high compaction in front of the fracture tip. As the expansive area is becoming larger, it bypasses the compacted grains towards the right upper side. This phenomenon helps to explain why in the later experiment stages there is an increase in the displacement towards the right-hand side. The images in the last rows show the state of the system once the fluid/air injection is ceased. Once the fluid/air pressure is removed, areas, which have been compacted create a rebound effect. This can be particularly well seen in the lateral displacement plot, where particles move in opposite directions. In the vertical plot, the final displacement is still orientated upwards. Despite that, once the system comes to rest, it has more positive strain components, meaning that it has a higher porosity compared to the start of the experiment. The results gained from the DIC analyses produce a behaviour that is similar to the one observed when running the numerical model.

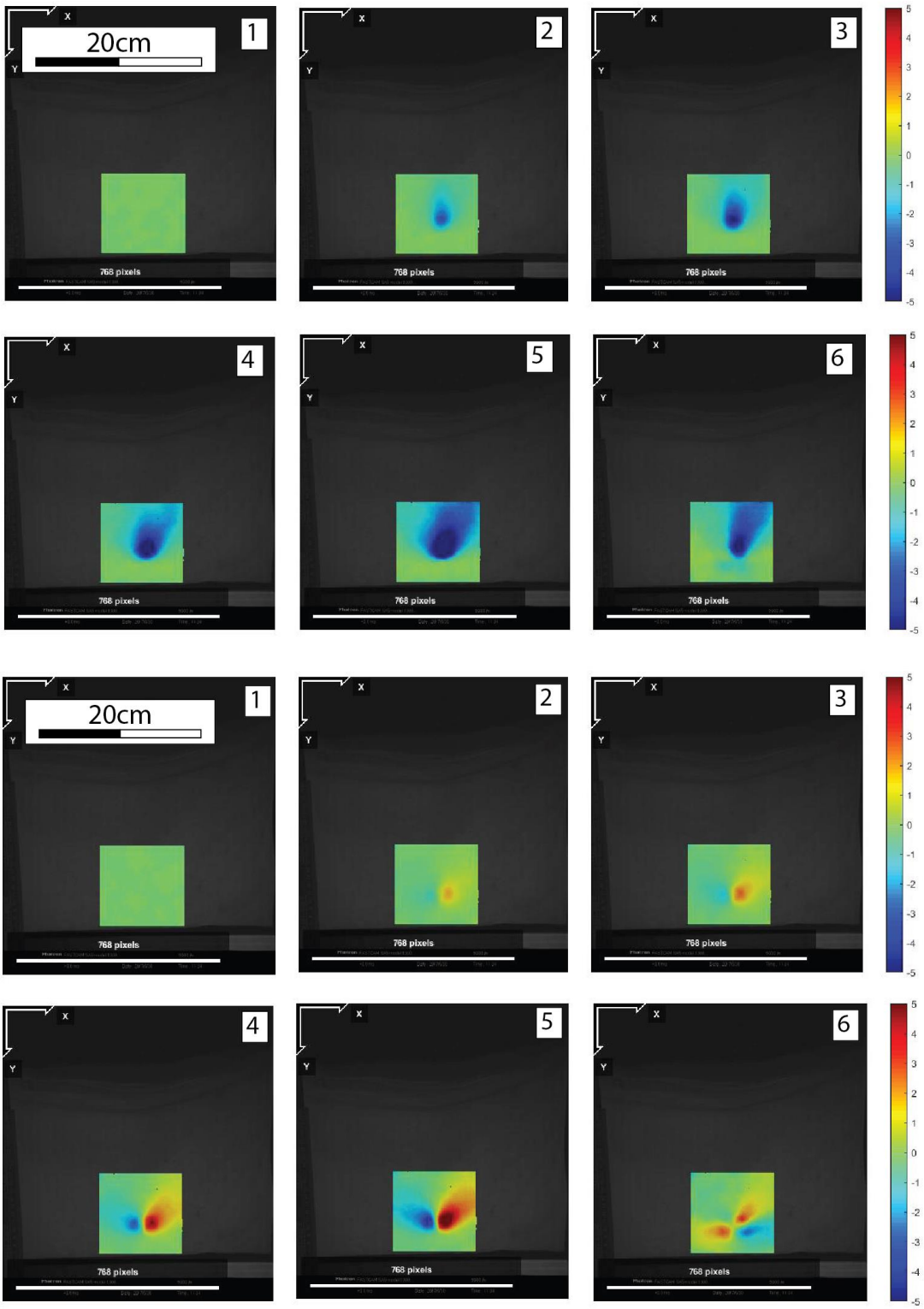

Figure 5.11. Series of digitally correlated images representing (from top to bottom): vertical displacement, horizontal displacement. Displacement units are in pixels, where one pixel represents 0.3mm and a 768-pixel scale bar provided is equal to 25cm. For the vertical displacement component, upwards movement is represented by cold (blue) colours, while downward movement is shown by warm (yellow and red colours). For lateral displacement, cold colours correspond to leftwards movements while warm colours show rightwards movement. The duration of the experiment is 0.4s, with every two frames having a time interval of 0.08s between them. The last frame shows the result once the fluid injection has been ceased.

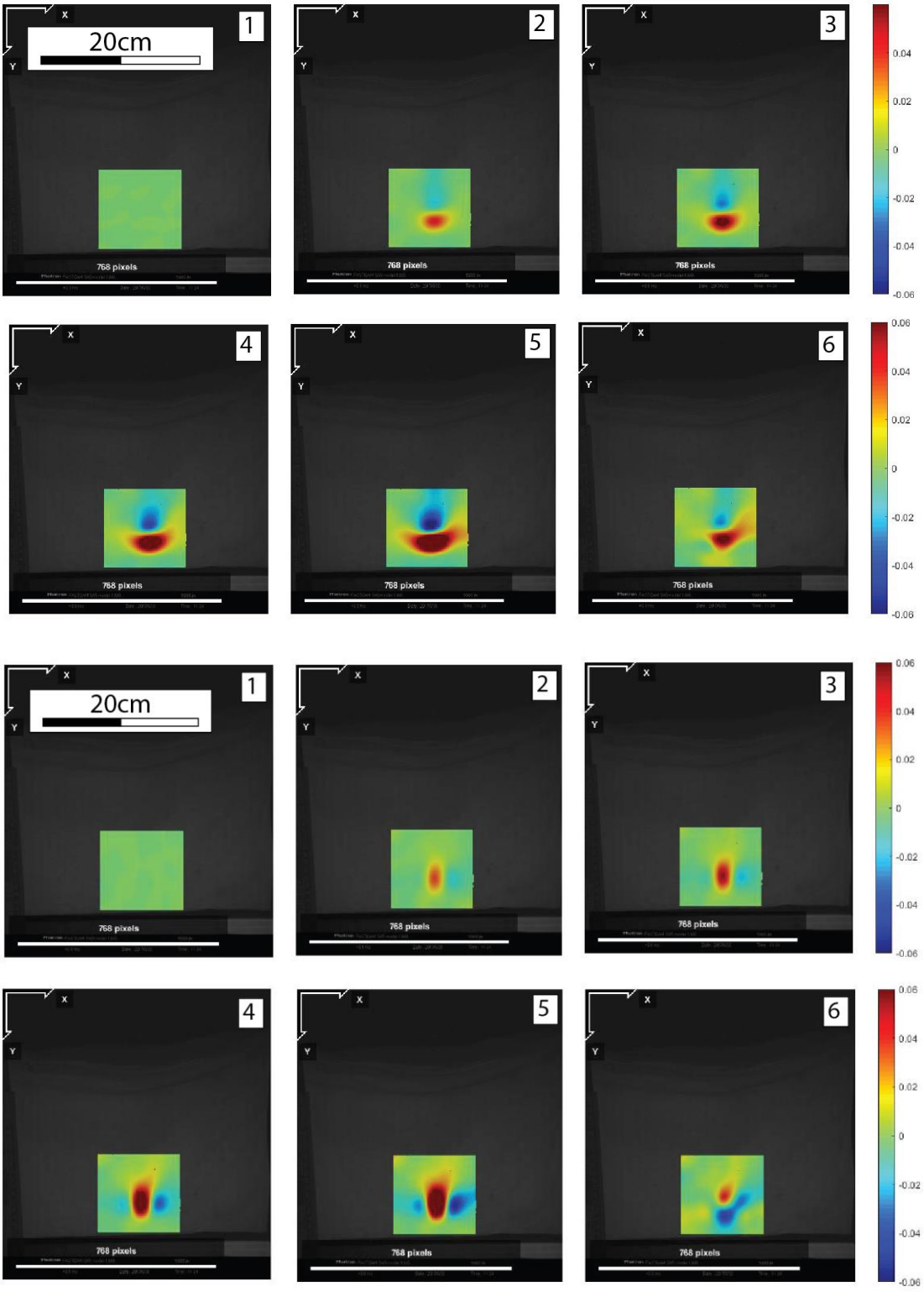

Figure 5.12. Series of digitally correlated images representing (from top to bottom): horizontal (XX) strain, vertical (YY) strain. The strain is represented as a ratio between the initial solid media state and state at the given time step in the experiment, where the positive values indicate extension while negative values show compaction. The duration of the experiment is 0.4s, with every two frames having a time interval of 0.08s between them. The last frame shows the result once the fluid injection has been ceased.

5.2.2. Fracture opening stage analysis

This paragraph describes the internal dynamics of the system during the initial opening and fracture propagation, which occurs after the decompaction stage. For this purpose, DIC data from type B experiments is provided with accompanying original footage frames (Fig. 5.13).

Figures 5.14 and 5.15 show the displacement data (vertical and horizontal, respectively). The initial isotropic fracture opening provides particle displacements that are predominantly upwards on the vertical axis and uniform in both lateral directions. Once the initial fracture opening is complete, conjugates start to form. This can be seen in the images 4 to 6 (Fig. 5.15), where new displacement front "clouds" start to form (Image 6, Fig. 5.15). Both conjugates' displacement fields are operating independently of each other. Displacement trends towards the right hand side show interesting dynamics. During the first three frames, a clear rightwards directed displacement front forms to the right hand side of the fracture. As the conjugates form, the right fracture arm continues to propagate upwards. The arm then forms a new rightwards directed displacement front, which is independent of the previous displacement stage. This shows that fracture propagation is occurring in segments or pulses rather than being a continuous process. The strain analysis shows predictable behaviour during the initial opening (Images 1 to 3): for the horizontal axis (XX) (Fig. 5.16) there is decompaction in the middle with compaction waves created on either side of the injection hole; for the vertical component (YY) (Fig. 5.17) there is decompaction around the inlet hole with a smaller compaction zone above. The vertical positive strain zone, which indicates decompaction, is laterally more extensive than the negative (compaction) zone. As the experiment progresses, decompaction zone "curls" around the compacted zone. This is an onset of the conjugate fracture formation. As conjugates form, the fractures propagate around the compacted zone. Image 6 of the XX strain analysis (Fig. 5.16) shows that the extension field reverts from being inclined towards the right back to a vertical position once the fracture has progressed beyond the compaction zone. Afterwards a new separate compaction wave forms on both sides of the facture. Next step in the analysis is to see how far the conjugates propagate during the initial fracturing. This can be achieved by looking at the cumulative image subtraction of the experiment for the extended duration of the same experiment (Fig. 5.18). Figure 5.18 shows that

fracture conjugates propagate rapidly within the decompacted area of the solid that are created in the early stages of the experiment (Images 1 to 8). Once the boundary of the decompacted area is reached, the propagation is halted and fractures increase in width rather than propagate further (Images 9 to 11). Finally, one of the dominant branches “breaches” into the compacted media. The propagation within the compacted media is discussed in the following subsection.

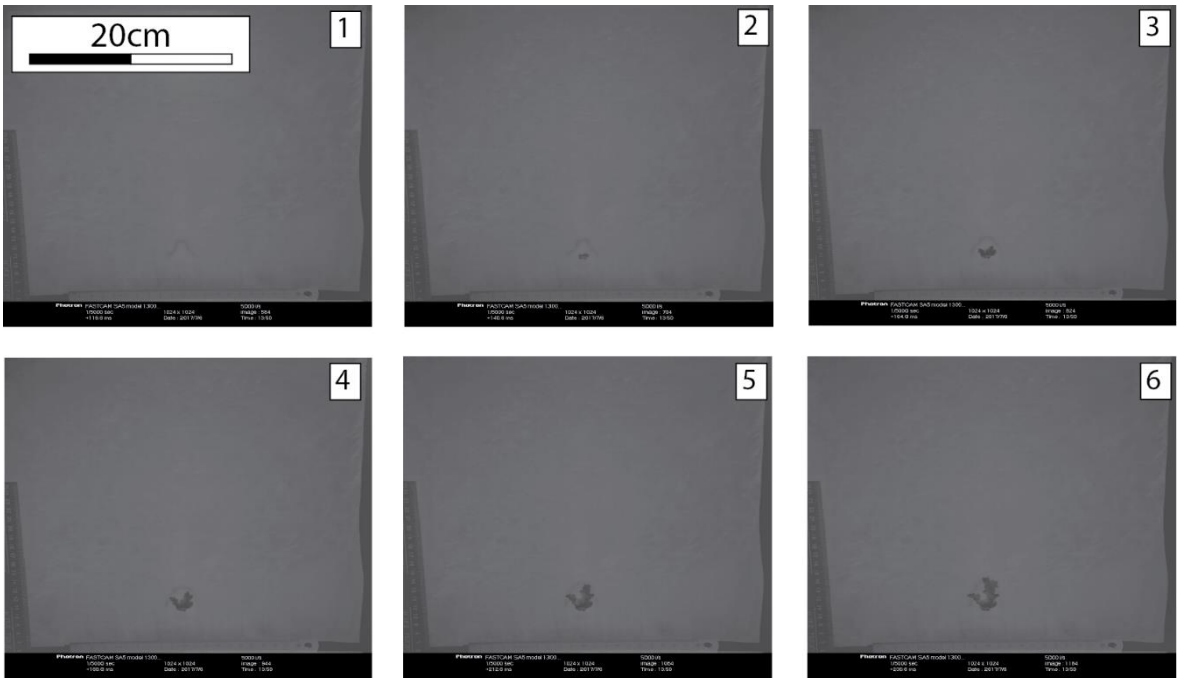

Figure 5.13. The original experiment footage frames that were analysed in this paragraph. Displacement units are in pixels, where one pixel represents 0.3mm and a 768-pixel scale bar provided is equal to 25cm. The length of the shown experiment is 0.12s with an interval of 0.02s in between every two frames

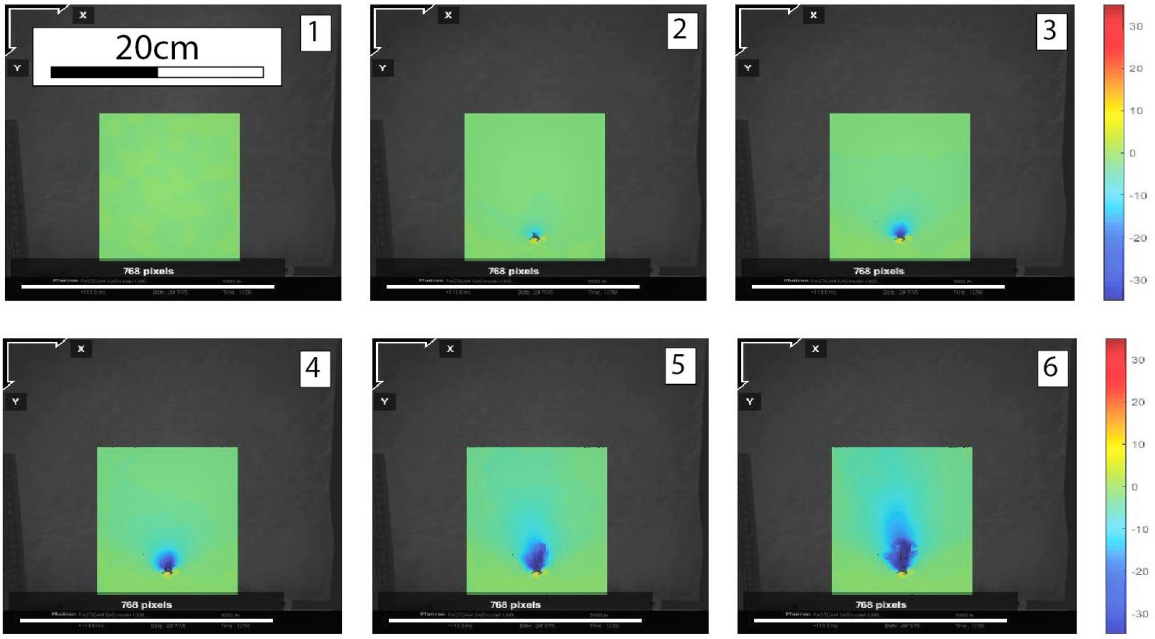

Figure 5.14. Series of digitally correlated images representing vertical displacement. Displacement units are in pixels, where one pixel represents 0.3mm. The length of the shown experiment is 0.12s with an interval of 0.02s in between every two frames.

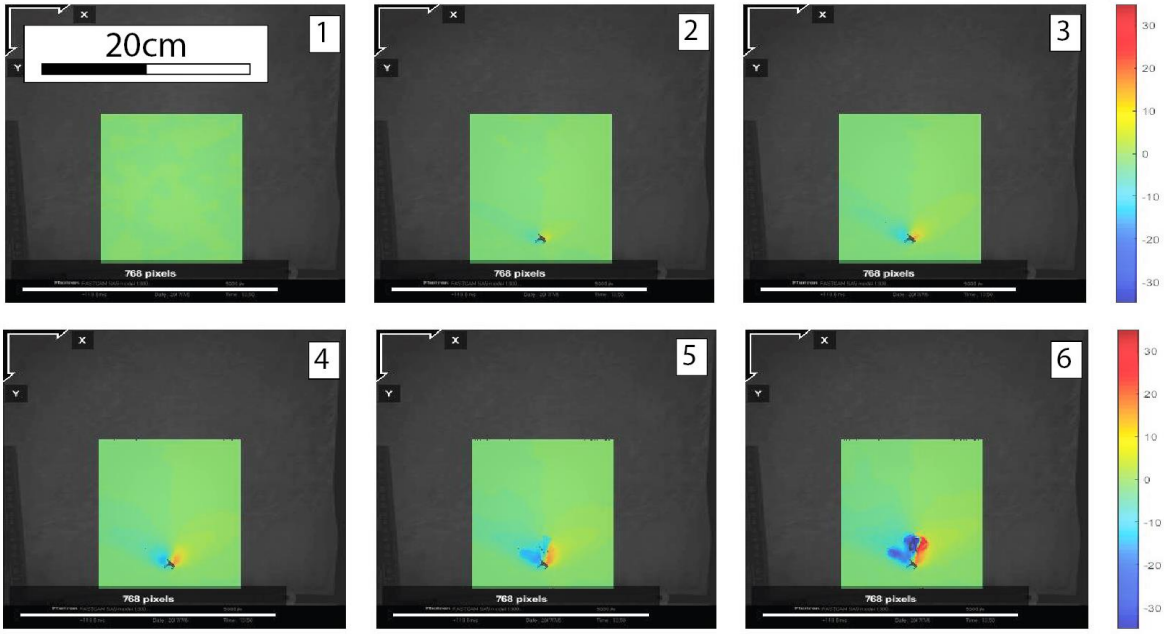

Figure 5.15. Series of digitally correlated images representing horizontal displacement. Displacement units are in pixels, where one pixel represents 0.3mm. The length of the shown experiment is 0.12s with an interval of 0.02s in between every two frames.

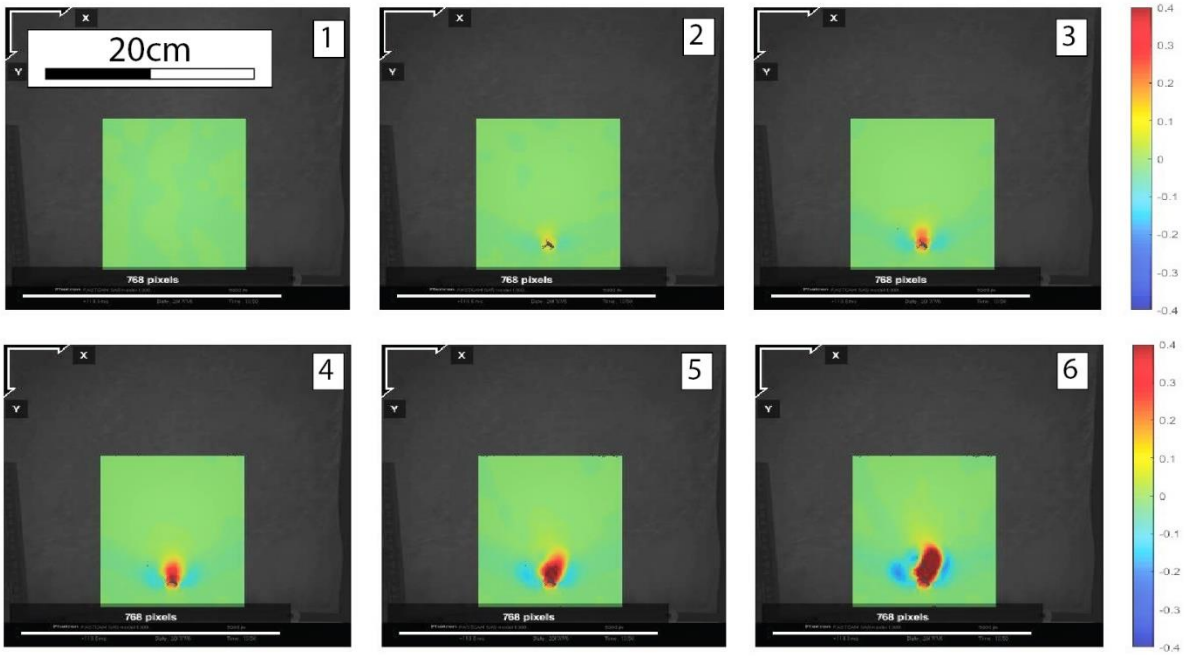

Figure 5.16. Series of digitally correlated images representing horizontal strain. The length of the shown experiment is 0.12s with an interval of 0.02s in between every two frames.

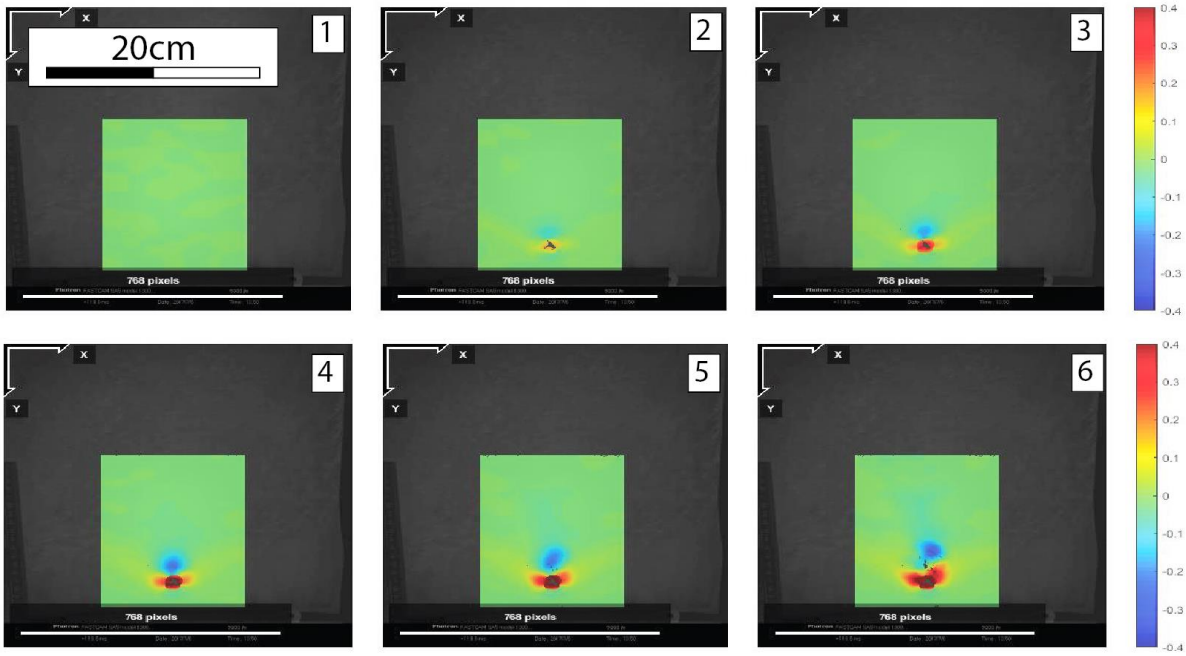

Figure 5.17. Series of digitally correlated images representing horizontal strain. The length of the shown experiment is 0.12s with an interval of 0.02s in between every two frames.

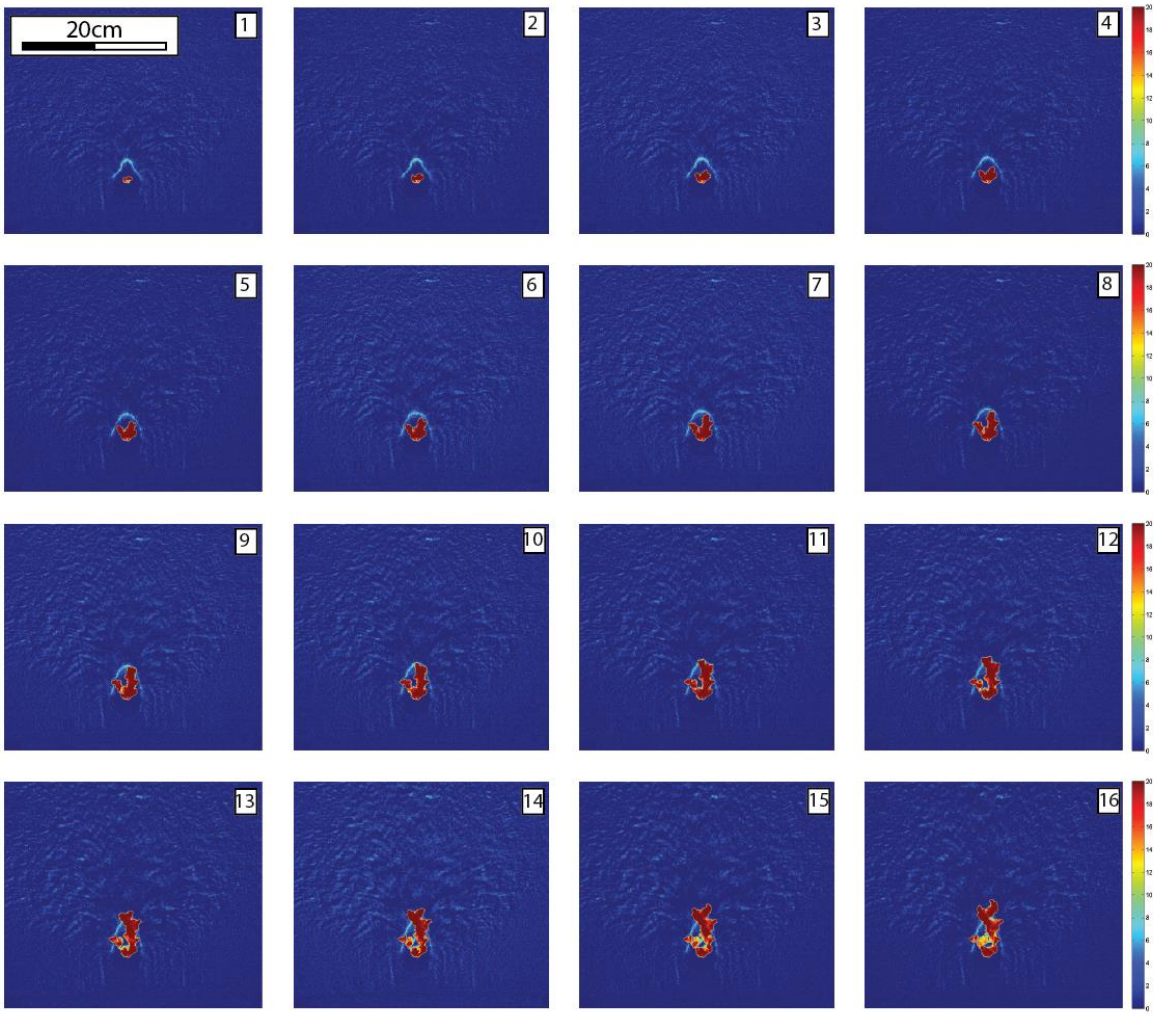

Figure 5.18. Image subtraction sequence for the experiment used in Section 5.2.1.. Sequence duration is 0.24s with the interval between any two frames of 0.02s. The total duration is twice the length of the sequence represented in Fig. 5.13-5.17. As fracture initiates, there is still an ongoing decompaction front advancement. Conjugates advance rapidly through decompacted solid. Once they reach the boundary of the decompacted media, the existing fractures open within the decompacted area, fracture boundaries are following the boundary of the decompacted area.

5.2.3. Fracture propagation in advanced stages

In advanced stages of the experiment, the fracture has localized into one predominant channel and branching is occurring on a very small scale. Figures 5.19 to 5.23 show the dynamics of a single fracture propagation over a relatively short time period. Type B experiment footage was used for this figure.

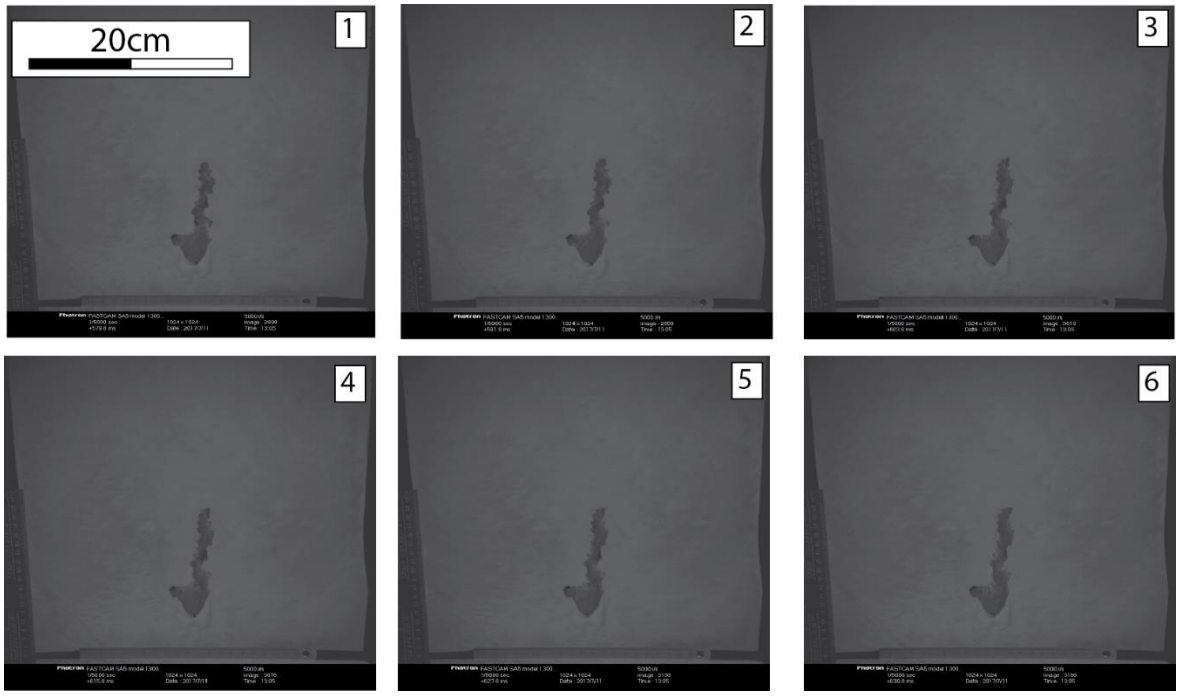

Figure 5.19. The original experiment footage frames that were analysed. Length of the experiment segment represented equals to 0.06s with the 0.01s interval between every two frames.

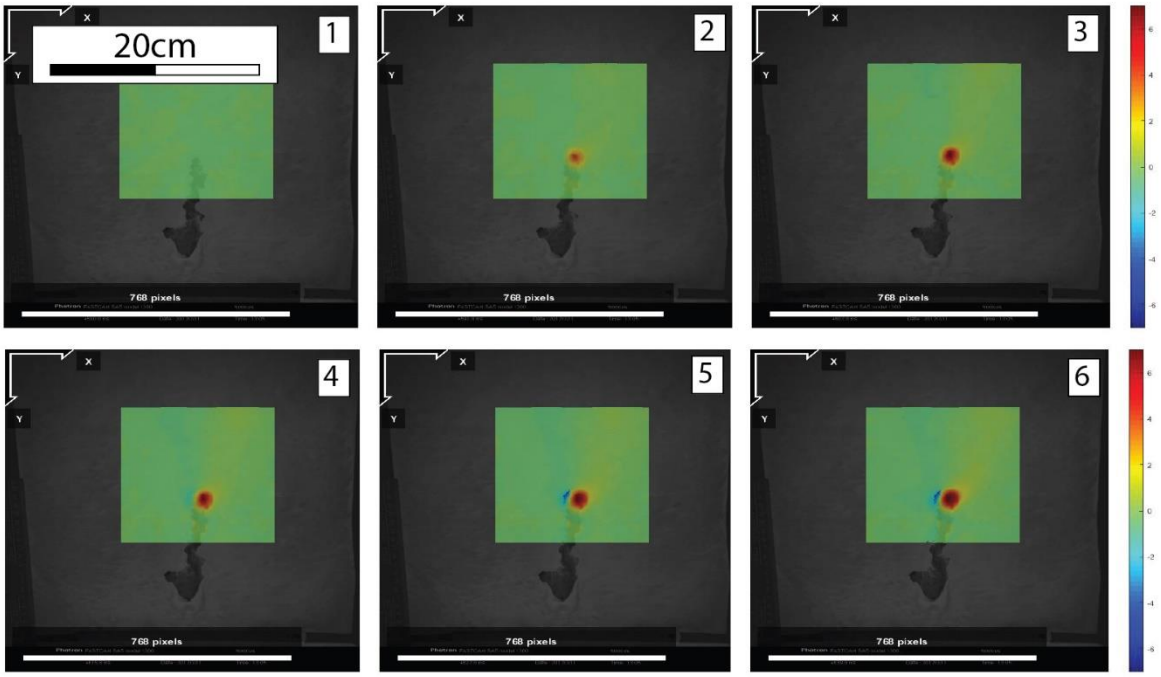

Figure 5.20. . Series of digitally correlated images representing horizontal displacement. Displacement units are pixels, where one pixel represents 0.3mm and a 768-pixel scale bar provided is equal to 25cm. Length of the experiment segment represented equals to 0.06s with the 0.01s interval between every two frames.

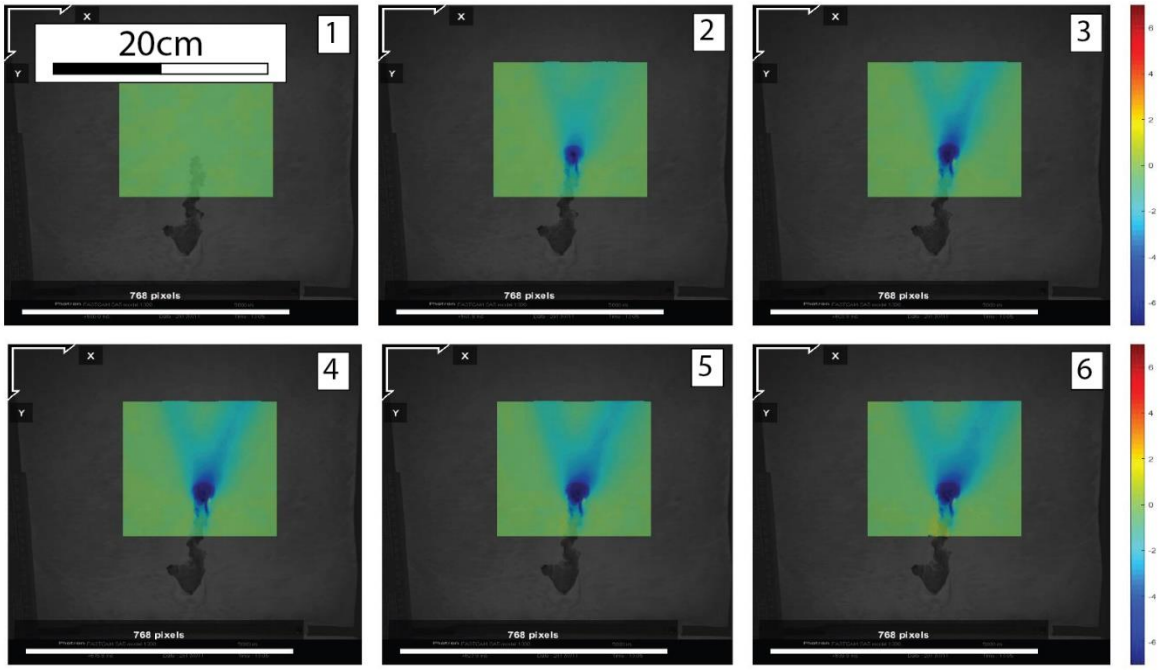

Figure 5.21. Series of digitally correlated images representing vertical displacement. Displacement units are pixels, where one pixel represents 0.3mm and a 768-pixel scale bar provided is equal to 25cm. Length of the experiment segment represented equals to 0.06s with the 0.01s interval between every two frames.

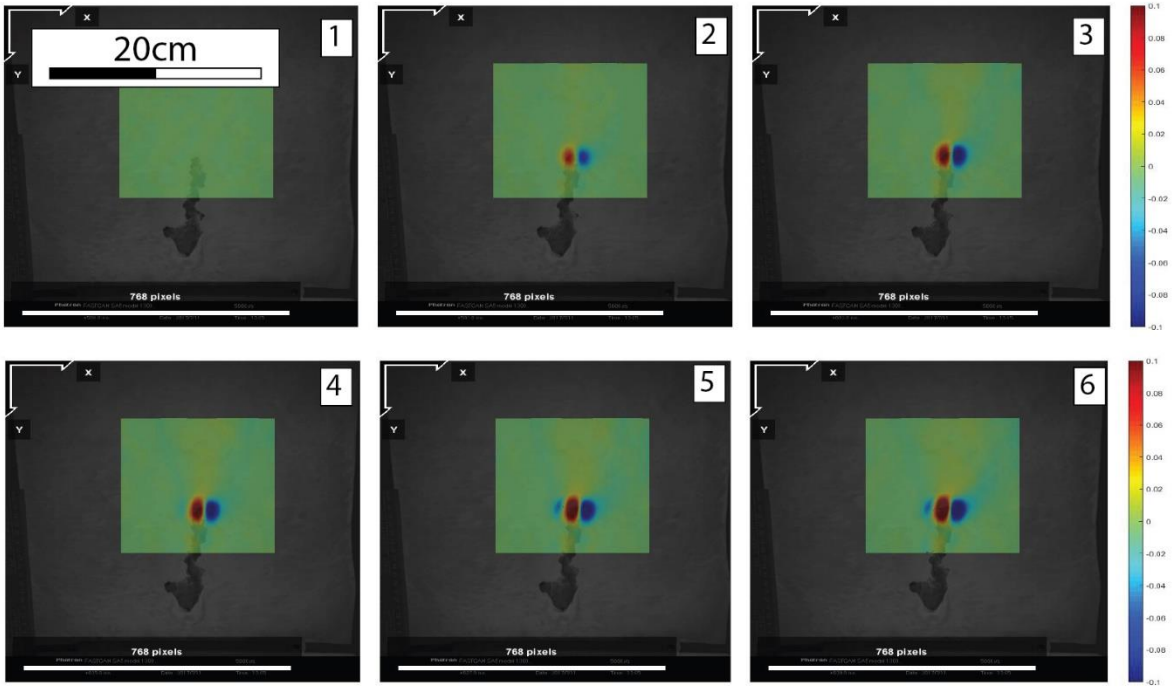

Figure 5.22. Series of digitally correlated images representing horizontal strain. Length of the experiment segment represented equals to 0.06s with the 0.01s interval between every two frames.

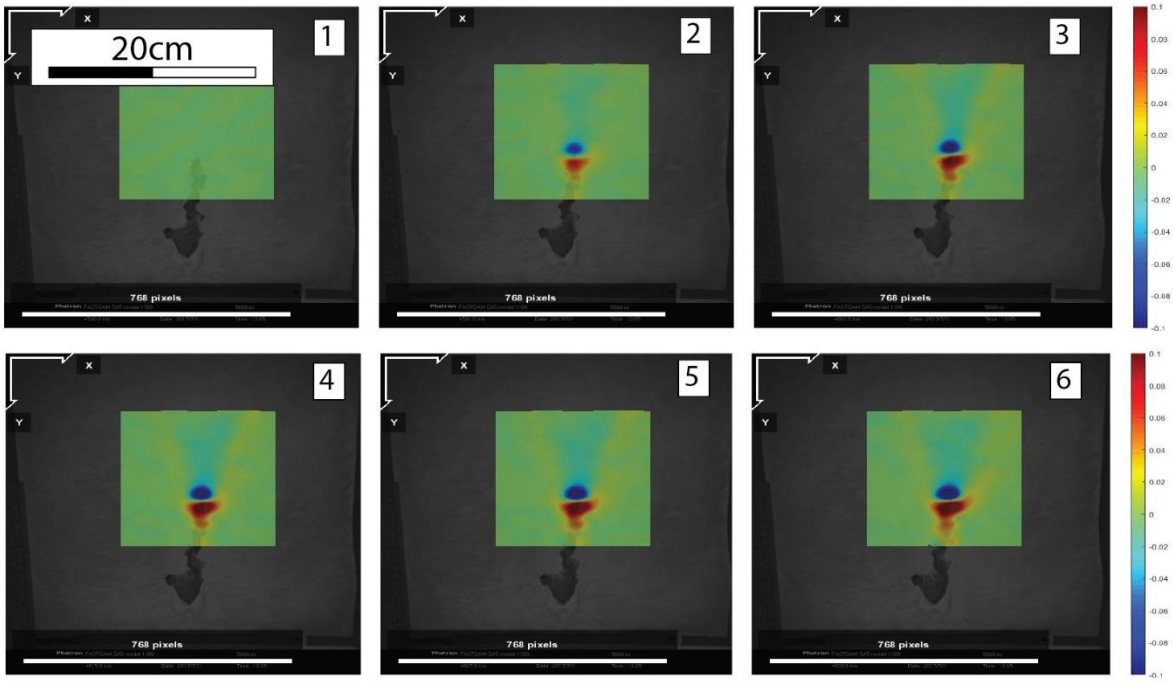

Figure 5.23. Series of digitally correlated images representing horizontal strain. Length of the experiment segment represented equals to 0.06s with the 0.01s interval between every two frames.

At this stage of the experiment, large-scale branching has ceased due to fluid/air injection being sufficient only to hold open the existing branches and propagate only via the channel that has the most favourable stress conditions for fracture opening. The vertical displacement component (Fig. 5.21) is purely directed upwards. As the propagation is localized it can be seen that despite the area in front of the fracture tip vertical displacement is observable in two channels that are orientated at 60º to each other. The lateral displacement component (Fig. 5.20) for the first three frames is orientated purely towards the right hand side and only in the second half of the footage (Images 4 to 6) the leftward oriented component is observable. This shows that the fracture does not open in both lateral directions uniformly but rather at different stages. This is further confirmed by the lateral strain analysis of the media (Fig. 5.22). In the images 1 to 3 the positive strain field (extension) is forming around the fracture tip and has only one compaction zone (negative strain) forming to the right hand side of it. The experiment footage (Fig. 5.19) shows that at this stage the fracture opens and propagates towards the right-hand side. Later, in the images 4 to 6, a compaction wave can be seen that also develops to the left hand side of the fracture tip. The experiment footage indicates that at this stage rather than to propagate, the fracture tip inflates as its aperture increases. The last DIC image series shows the vertical strain (Fig. 5.23). A similar behaviour to the behaviours described in

previous experiments is observable, where a smaller compaction zone is forming on top of the fracture tip while the area around the fracture tip shows expansive behaviour. The positive strain zone is larger in its area than the negative strain zone. When combining vertical strain analysis images with observations from the fracture propagation itself, it can be seen that the fracture, once it reaches the compaction zone, despite of σ^1 being vertical, halts its upwards propagation and the fracture tip in further frames becomes inclined to the right hand side (Images 4 to 6), propagating into an area around the compaction zone. This is further shown by positive vertical zone "curling" around the compaction zone to the right hand side. The mechanics of this behaviour are further looked into in the discussion section.

5.3. Effect of decreased overburden column

As a separate case, it is worth looking at experiment types with low height overburden column and fluid injections at a low overpressure over a prolonged period of time (Fig. 5.24-5.28). During this type of experiment, the overpressure is high enough to open the fracture, however, its propagation is very minimal. This combination of the experimental input variables produces thin horizontally, rather than vertically, orientated fractures. The effect of horizontal fractures and more specifically formation of "beef" veins has been studied and formation mechanisms have been proposed by Cobbold & Rodirgues (2007). They propose a mechanism, where "beef" horizontal veins tend to form in shallow basins under compressional tectonic regimes, which allows for the principal stresses σ_1 and σ_3 to switch places. This means that the least principal stress becomes vertical and the difference in pore fluid pressure accounts for a lifting force. It is then equal to the force created by the gravitational pull of the overburden column plus the tensile strength of the material.

Horizontal fracture opening can be further investigated by looking at Figures 5.24-5.28. The movement component is predominantly upwards on the vertical axis (Fig. 5.26) and rightwards orientated on the horizontal axis (Fig. 5.25). The unidirectional movement on the horizontal axis explains the dual nature of the XX strain with only one compaction wave being created (Fig. 5.27). The upward movement of the solid media creates the compaction zone above the injection point, which can be seen on the YY strain map (Fig. 5.28). In this scenario, because

the least principal stress is vertical, instead of propagating into or around the compaction zone, the fracture opens in a horizontal manner in between the expansion and compaction areas. In contrast to other experiments, this setup produces almost equal in area compaction and expansion zones on the YY strain map. This further contributes to the creation of horizontal fractures as a compaction zone prevents vertical propagation.

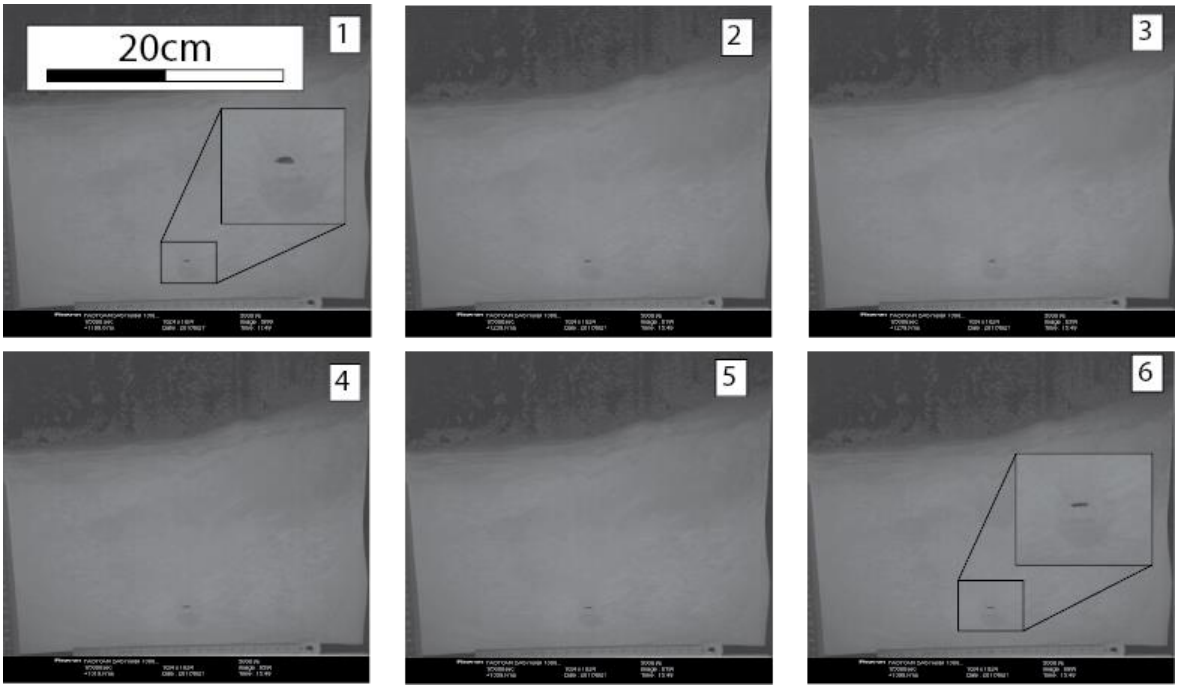

Figure 5.24. Series of original experiment footage frames showing the formation of the horizontal fracture. Length of the experiment is 0.2s with an interval of 0.03s between every two frames.

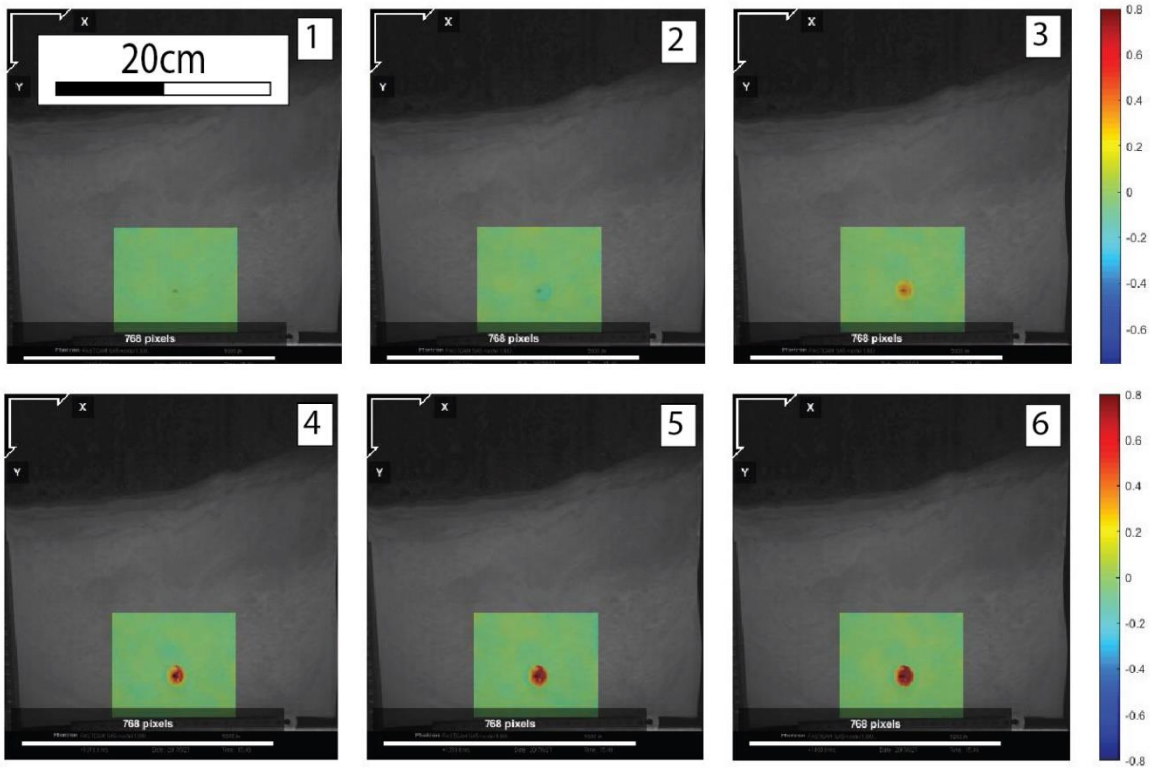

Figure 5.25. Series of digitally correlated images showing the horizontal displacement during the formation of the horizontal fracture. Length of the experiment is 0.2s with an interval of 0.03s between every two frames.

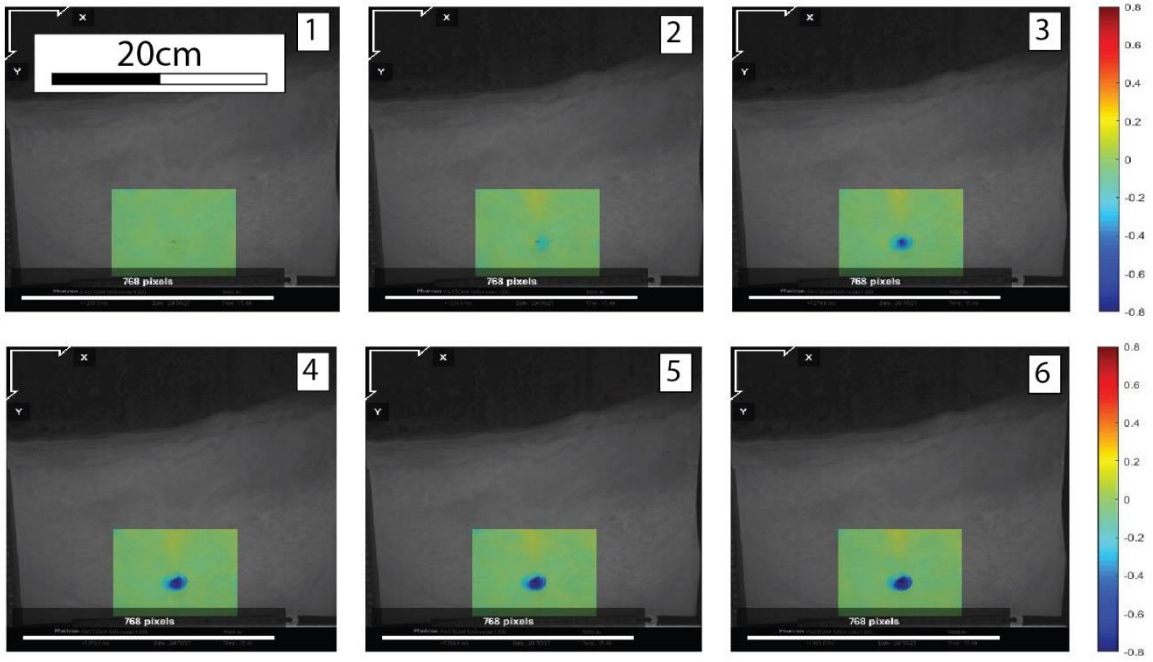

Figure 5.26. Series of digitally correlated images showing the vertical displacement during the formation of the horizontal fracture. Length of the experiment is 0.2s with an interval of 0.03s between every two frames.

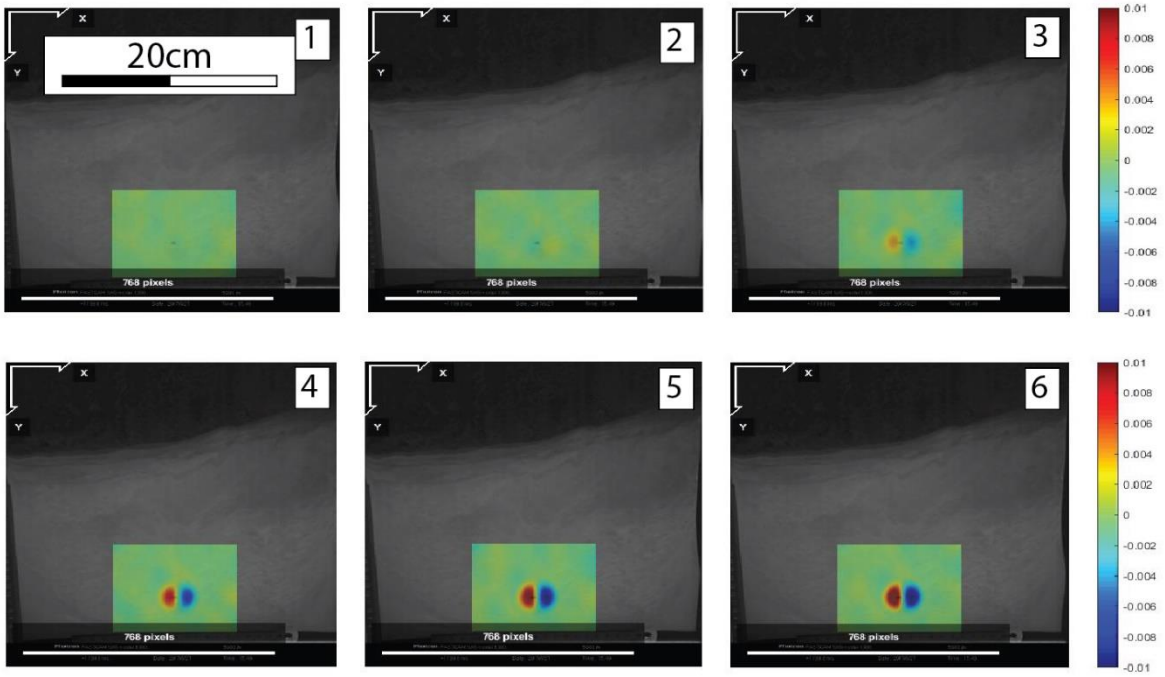

Figure 5.27. Series of digitally correlated images showing the horizontal strain during the formation of the horizontal fracture. Length of the experiment is 0.2s with an interval of 0.03s between every two frames.

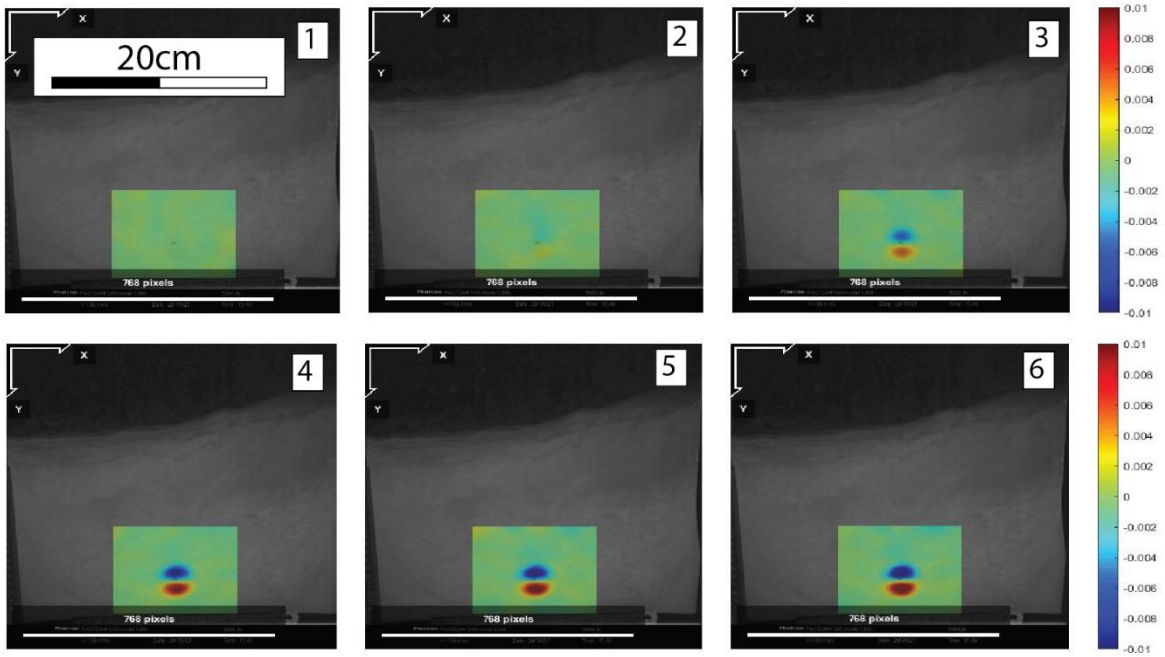

Figure 5.28. Series of digitally correlated images showing the vertical strain during the formation of the horizontal fracture. Length of the experiment is 0.2s with an interval of 0.03s between every two frames.

5.4. Acoustic emissions

In order to look into acoustic emissions produced by the fluid injections, three accelerometers were attached to the Hele-Shaw cell on a vertical axis along the injection hole. The amplitude of the recorded signals during the experiments was

recorded and stored using MATLAB. A Type B experiment, where a singular fracture would develop, produced the seismogram that is shown in Figure 5.29.

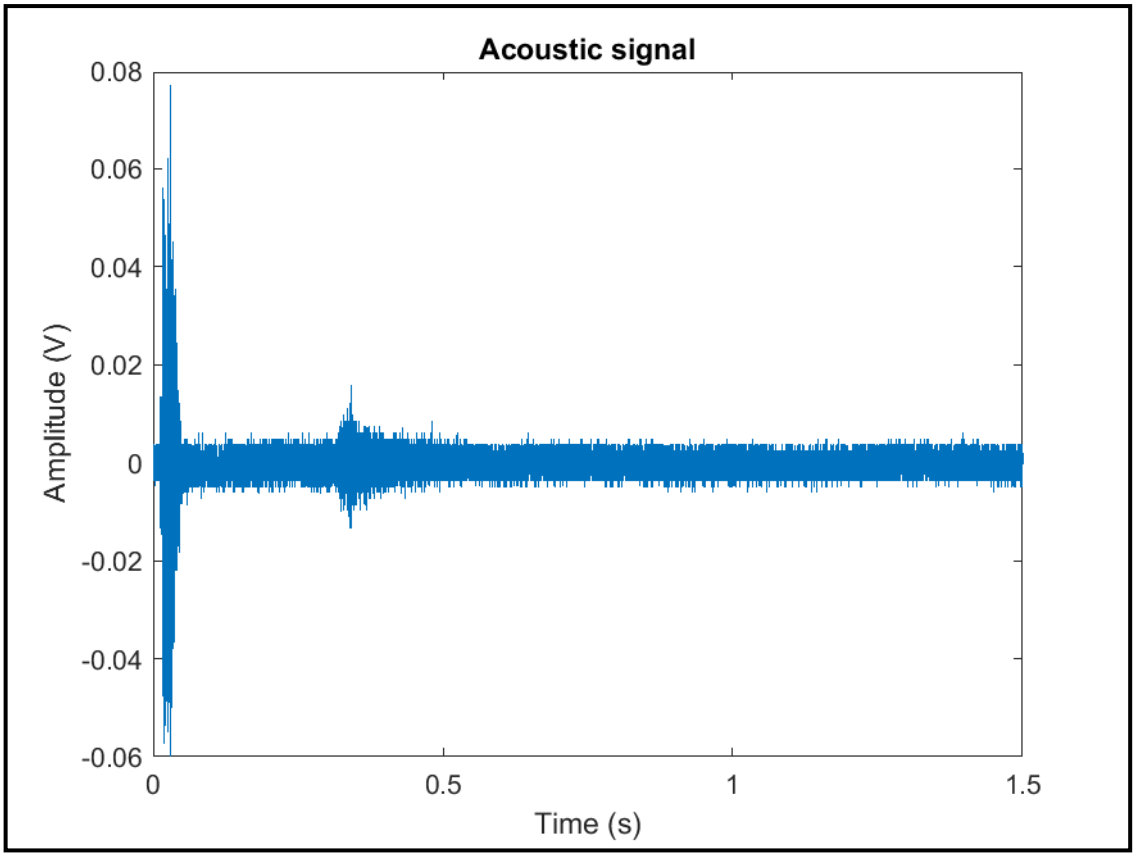

Figure 5.29. Acoustic signal emitted by the Type B experiment. Fluid injection phase length is 0.3s. The initial high amplitude signal is an artefact due to air pressure "hitting" the system as it covers the distance in the tubing between the valve and Hele-Shaw cell. The second peak and higher amplitude signals are recorded as the fluid injection is ceased and granular media system "collapses". The signal during the actual fracture propagation is indistinguishable from the background noise observable past the experiment conclusion.

The high amplitude signals produced at the initial stages of the experiment are an artefact of the overpressured fluid/gas colliding with the solid as it travels from the valve to the inlet hole in the cell. The second pulse of high amplitude signals is produced by the granular media colliding into empty fracture space as the pressurised fluid is removed from the system. The signal during the actual fracture propagation process does not differ from the background noise recorded past the experiment completion. As a control measure, an experiment was carried out with fluid injection tubing filled up to the valve with granular material.

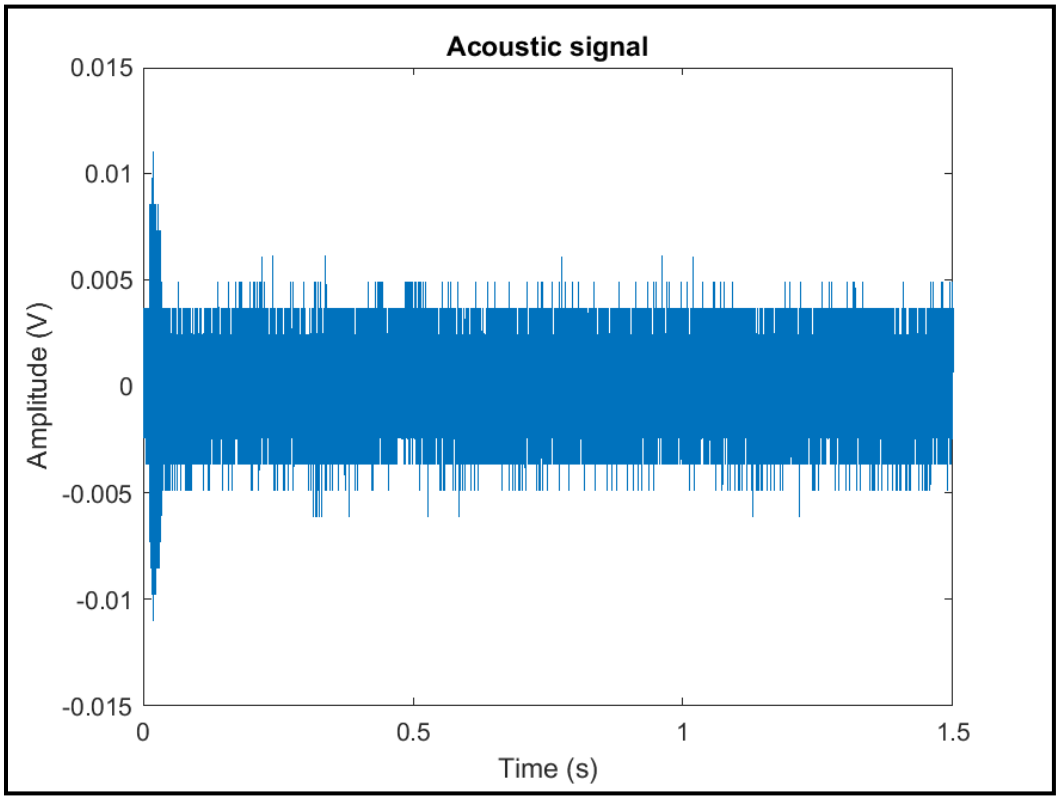

Figure 5.30. A control experiment with the same parameters as shown in Figure 5.15. The fluid inlet tubing was filled with the granular media up to the valve thus preventing overpressured fluid "hitting" the granular media. There is still a small spike in signal amplitude due to valve opening motion. It is not fracturing associated as fracturing did not occur at that time interval.

Figure 5.30 shows that there is still a small spike in signal amplitudes at the initial stages. Knowing from the experiment footage that no fracturing initiated at this time interval, it can be ruled out that this spike in signal is related to fracturing. Only Type C experiments were able to produce a distinguishable signal (Fig. 5.31).

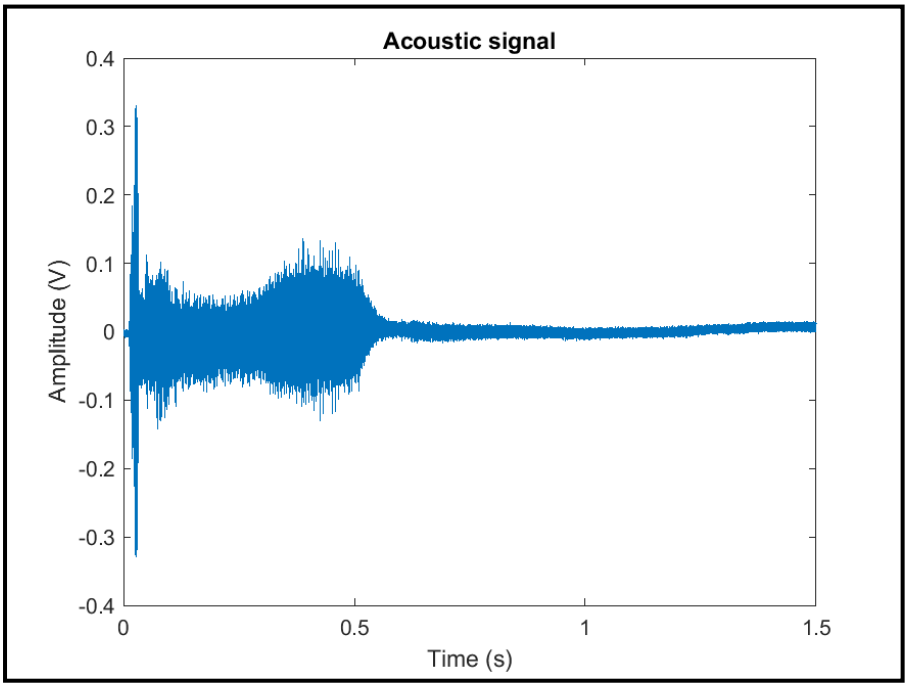

Figure 5.31. Acoustic signal recording from Type C experiment. Fluid injection phase duration is 0.5s.

Despite the fact that the initial fluid and the solid collision caused shock, there is a clearly distinguishable fracturing that caused a signal.

It is then possible to carry out a Fourier transformation of the signal to look at the power spectrum (Fig. 5.32, 5.33). In all the following cases, Fourier transformation was applied for the time period corresponding to the length of the active air injection phase.

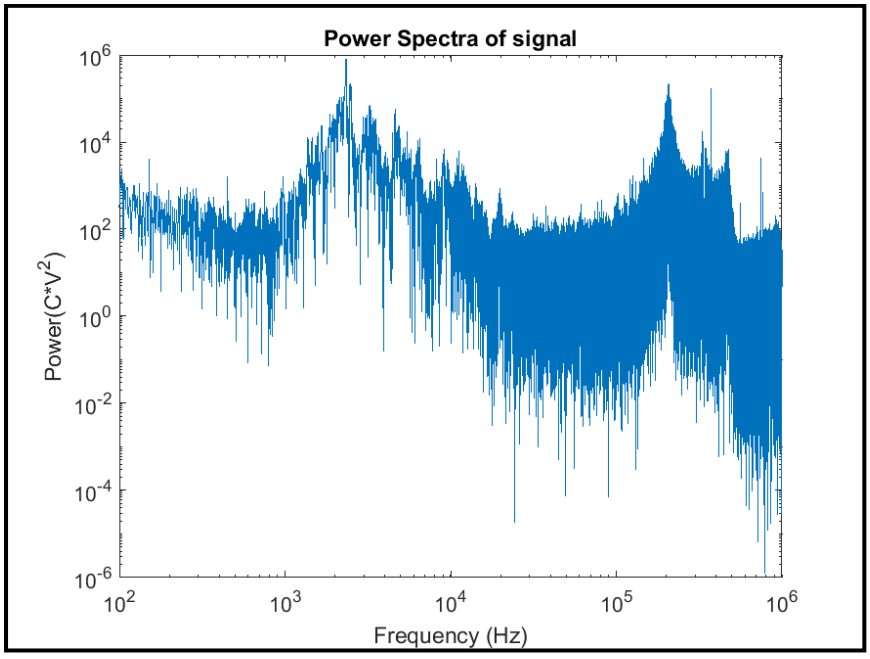

Figure 5.32. The power spectrum of the signal recorded during the Type C experiment.

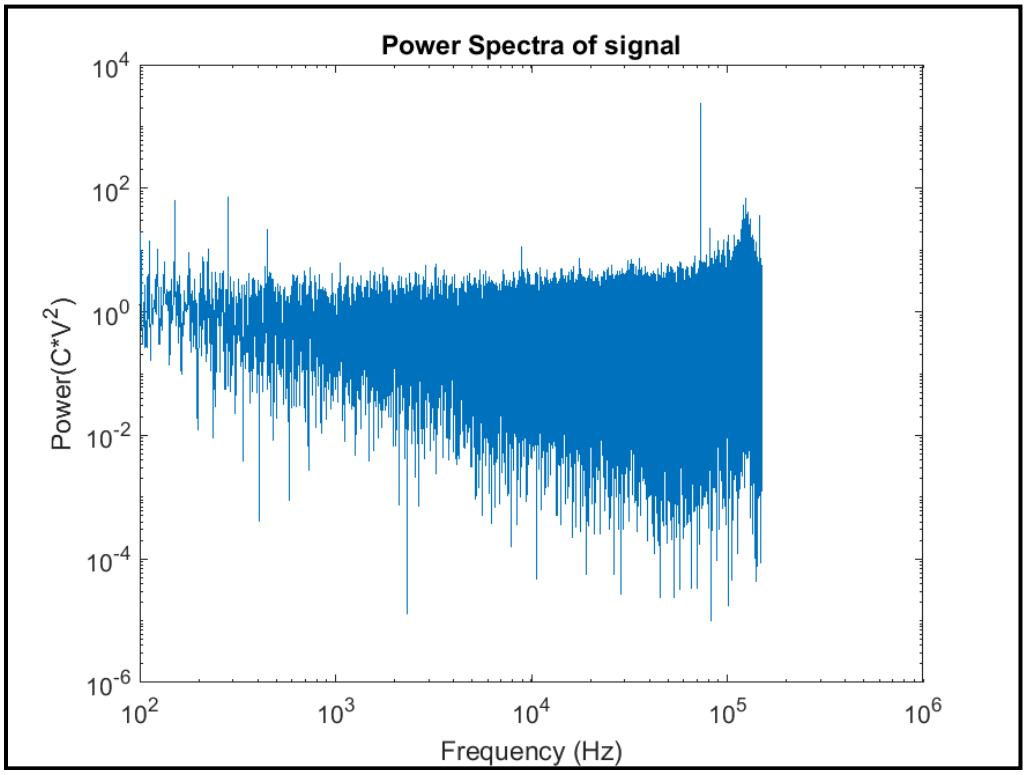

Figure 5.33. The power spectrum of the signal recorded during the Type B experiment.

Type C experiments clearly produces signals of frequencies, which can theoretically be used to calculate the corner frequency (Fig. 5.32), while the only signals distinguishable that were created during type B experiments are the ones caused by fluid and solid collision at the experiment initiation.

Due to this, the acoustic emissions recorded as part of Hele-Shaw experiments cannot be properly used as Type C experiments very poorly represent hydrofracturing processes due to granular media fluidization during them. Potentially this experiment could be repeated if a more a sensitive equipment was used.

5.5. Discussion

5.5.1. Scaling of the fracture geometries

To quantify the experimental findings, a number of the parameters from the created fractures were recorded and systemized. The observation criterions include main channel length (height) and width, decompaction time and number of branches.

The first question is whether there is any correlation between the amount of injection fluid (parametrized by the amount of overpressure and duration of the injection) and geometries of the fracture.

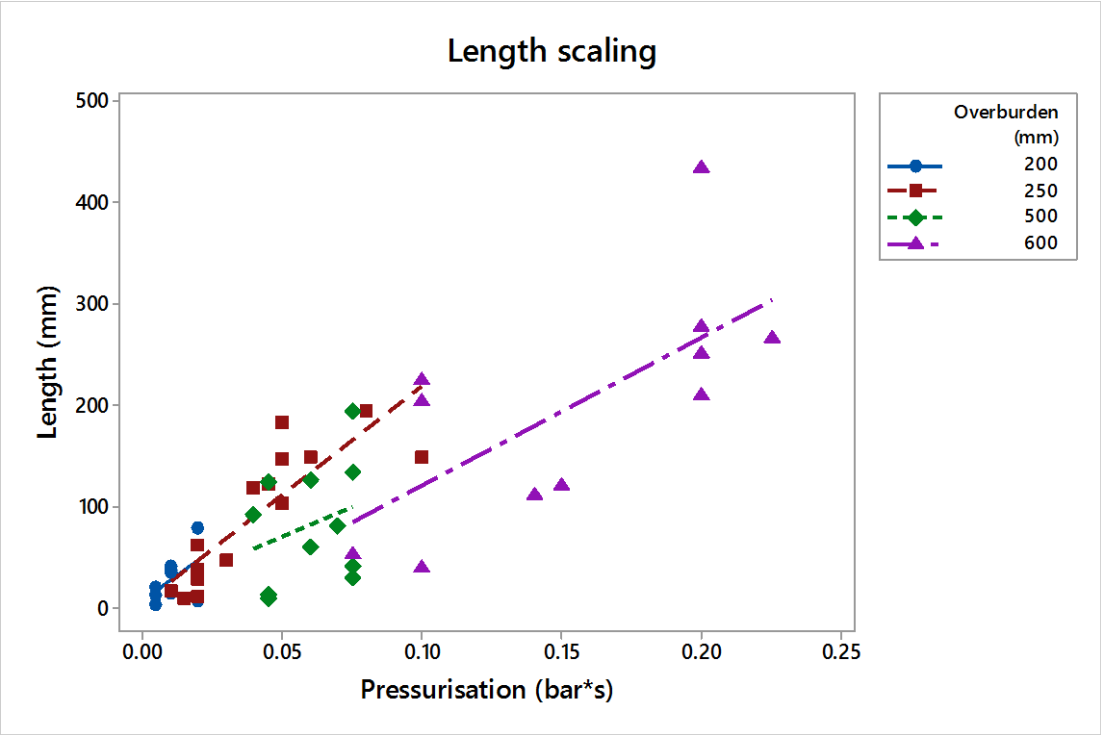

Figure 5.34. Scatterplot of the main fracture channel length versus pressurisation expressed as the amount of overpressure multiplied by the injection time. The line represents a linear regression.

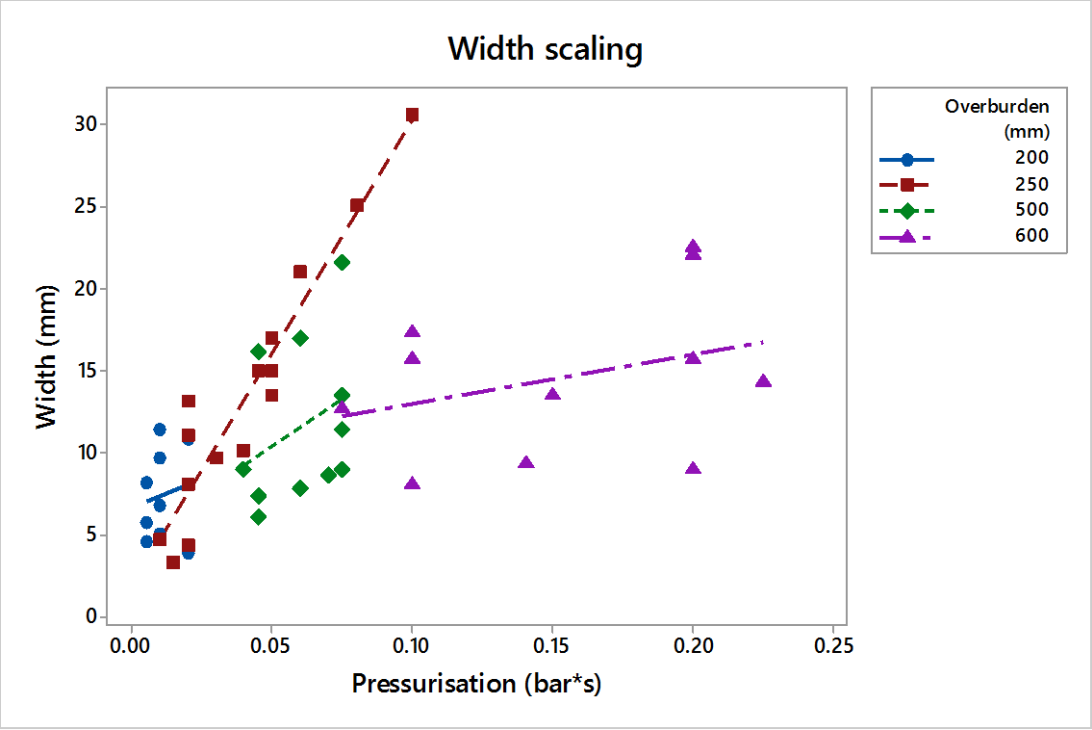

Figure 5.35 Scatterplot of the main fracture channel width versus pressurisation expressed as the amount of overpressure multiplied by the injection time. The line represents a linear regression.

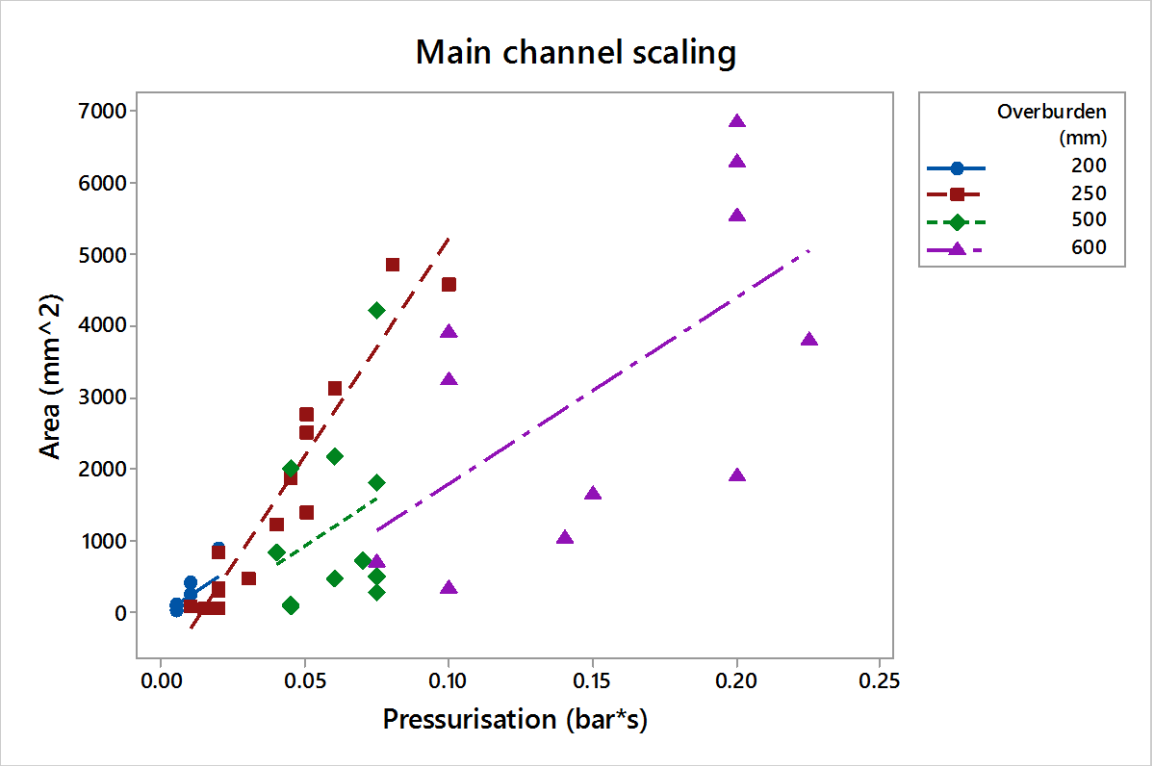

Figure 5.36. Scatterplot of the main fracture channel area versus pressurisation expressed as the amount of overpressure multiplied by the injection time. The line represents a linear regression.

Figures 5.34 to 5.36 show the basic scaling of the fracture length, width and area versus the amount of fluid injected expressed as overpressure amount times the duration of the injection. Although the correlation is good for experiments with 250 mm overburden for all three criteria, where R^2 values reach 0.84, it is poor with increasing overburden as R^2 drops to 0.69 for 600 mm, 0.31 for 500 mm and 0.27 for 200 mm overburdens. This is explained by the fact that with an increase in overburden it takes longer for the particles around the injection hole to decompact. However, lower overburden values shift the system into a state where the principal stresses change their orientation and different fracturing mechanisms are effective producing horizontal hydrofractures. Figure 5.37 shows how the area scales versus the pressurization using only the time past the fracturing initiation.

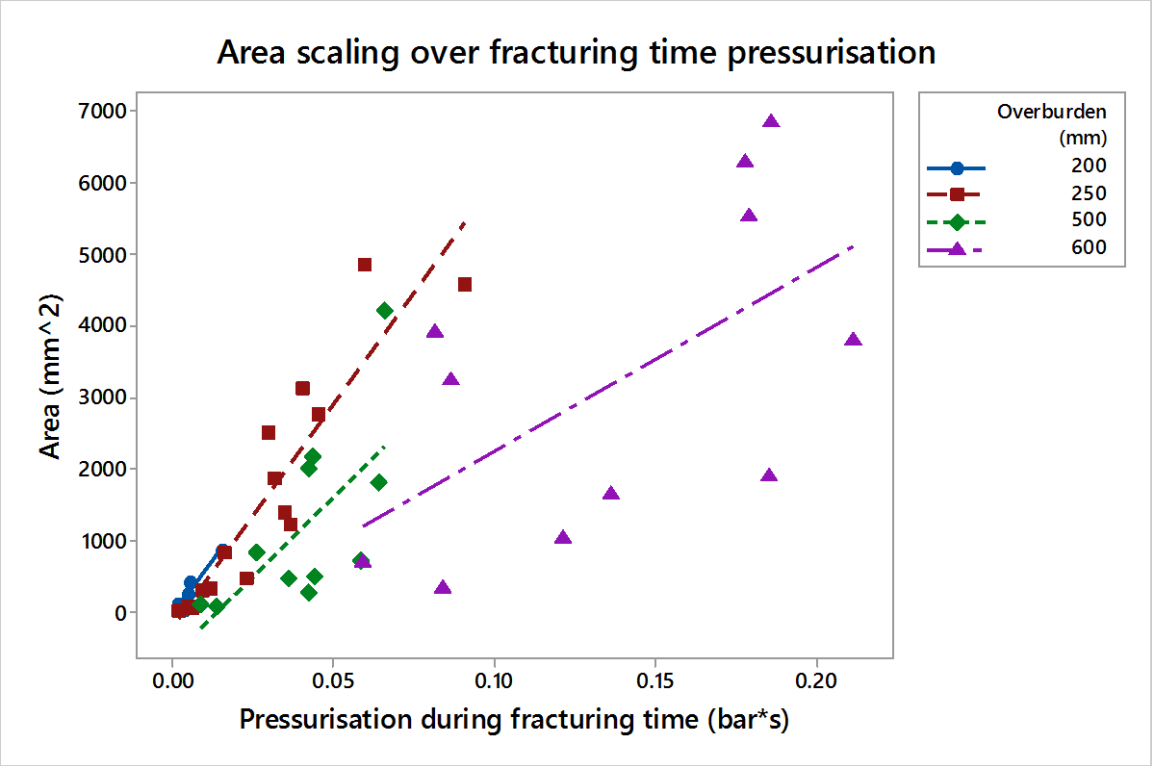

Figure 5.37. Scatterplot of the main fracture channel area versus pressurisation expressed as the amount of overpressure multiplied by the injection time past the fracturing initiation. The line represents a linear regression.

Such an approach greatly improves the regression fit as R^2 values increase to 0.9 for 200 mm overburden and are 0.84, 0.5 and 0.65 for 250, 500 and 600 mm overburden experiments respectively. While R^2 values drop slightly for 250 and 600, they increase significantly for the other two overburden experiments and such an approach yields a net improvement in precision.

This is explained by the fact that with increasing overburden, the variability of the branching increases, therefore the total area of the fractured area changes more dynamically. To account for this fact I tried scaling area versus the overburden alone (Fig. 5.38) and compare it to the same relation but with a number of branches being taken into account (Fig. 5.39).

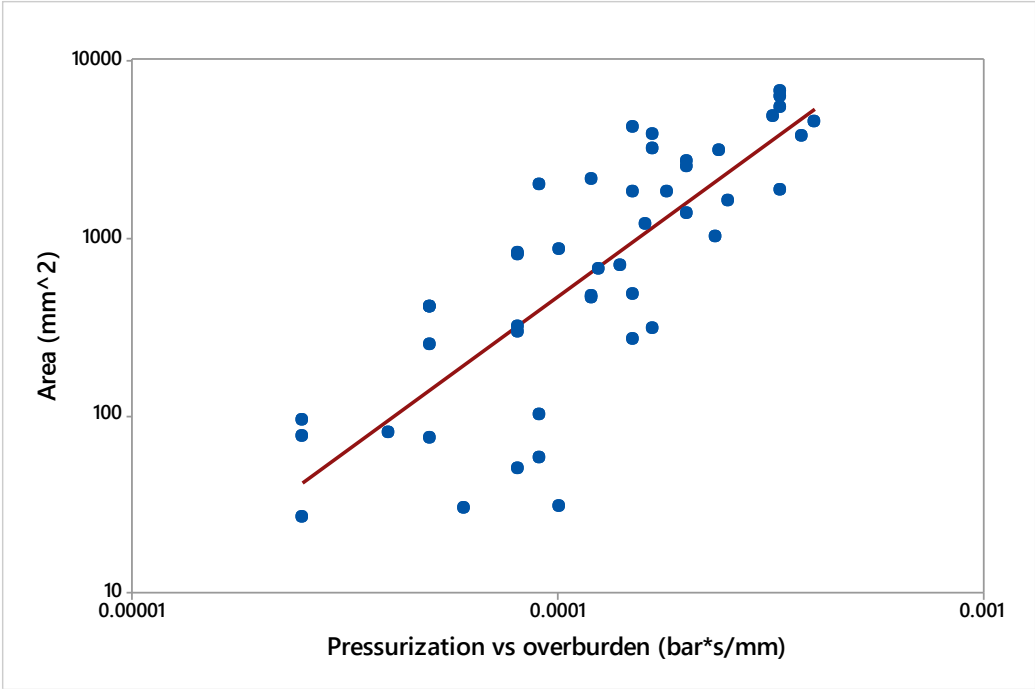

Figure 5.38. Scatterplot of main channel area scaled versus pressurization expressed as the amount of overpressure multiplied by the injection time past the fracturing initiation. That is then normalized versus overburden column height. The line represents power law regression.

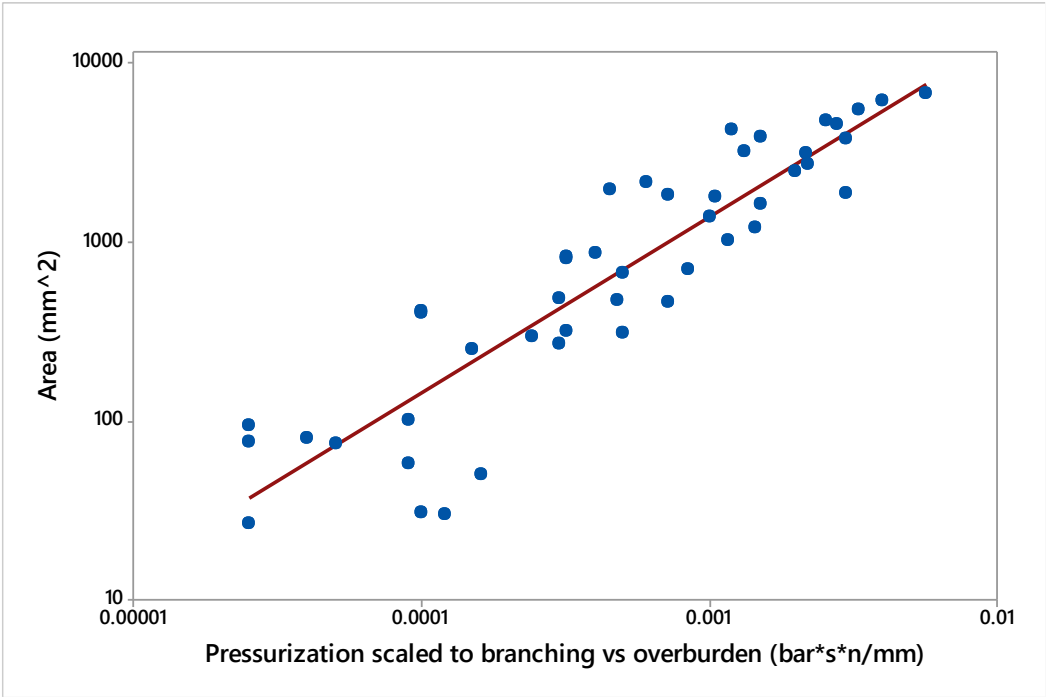

Figure 5.39. Scatterplot of main channel area scaled versus pressurization expressed as the amount of overpressure multiplied by the injection time past the fracturing initiation. That is then normalized versus overburden column height and number of the branch conjugates. The line represents power law regression.

The best fit line, in this case, is a power law regression which is expressed as

$$y = ax^b \tag{5.1}$$

This application of branching scaling criterion greatly improved the regression line fit as R^2 value increased from 0.68 for adding only overburden scaling parameter to 0.85 when branching parameter was further included. When using a time interval of the active fracturing the R^2 value further improves up to 0.89 providing an even better fit. These observations give us several equations that can be used to account for the area of the main fracture channel created, depending on the number of variables known (Table 5.5).

Table 5.5. List of best-fit equations for main fracture area channel calculations depending on which input parameters are known. Data fit increases with the number of parameters known. Variables are A – main fracture channel area (mm^2); P – overpressure (bar), t – total duration of injection phase (s); t_f - time of active fracturing (s); h - height of the overburden column (mm), n_b - number of branch conjugates.

Overpressure, time, overburden	Fracturing time	Number of branches	Scaling relation	R^2
X			$A = 7.37E+09\left(\frac{P*t}{h}\right)^{1.798}$	0.68
X	X		$A = 2.54E+08\left(\frac{P*t_f}{h}\right)^{1.347}$	0.84
X		X	$A = 1.46E+06\left(\frac{P*t*n_b}{h}\right)^{0.9998}$	0.85
X	X	X	$A = 5.54E+05\left(\frac{P*t_f*n_b}{h}\right)^{0.822}$	0.89

In a typical hydrofracturing operation, one would not know the number of branches or fracturing initiation time unless microseismic monitoring is in place. Applying only one extra parameter to the equation greatly improves data fit. For this reason, it is worth to estimate the number of branching conjugates (Fig. 5.40) as a function of time periods, which precede the active fracturing greatly, they vary and are not consistent, especially for the higher values along the x axis (Fig. 5.41).

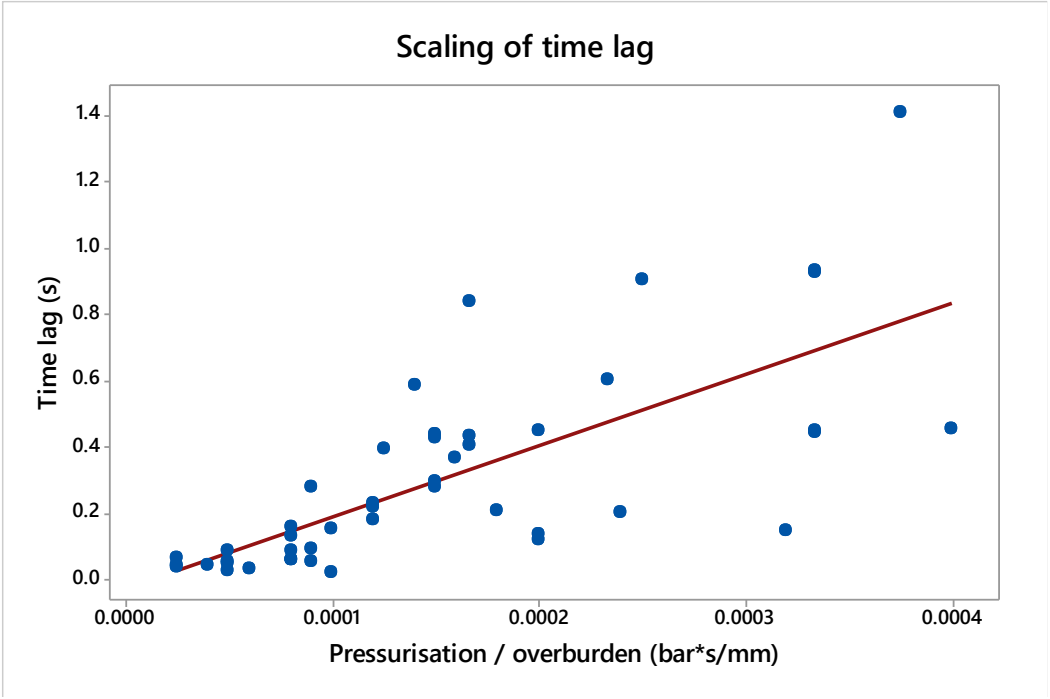

Figure 5.40. Scaling of the time lag between the fluid injection initiation and the start of the active fracturing versus pressurisation normalized by overburden column height. The line represents linear regression with an R^2 value of 0.55. The variability increases rapidly with the increase of the value along the x axis.

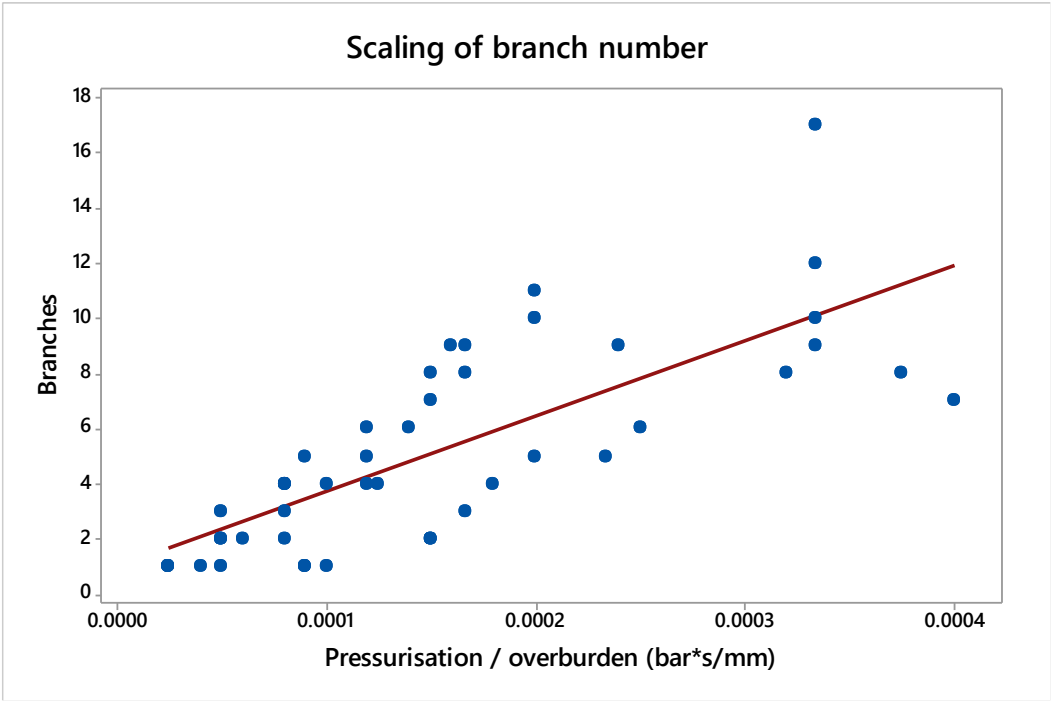

Figure 5.41. Scaling of branch number versus pressurisation normalized by overburden column height. The line represents linear regression with an R^2 value of 0.68.

It can be seen that it is possible to estimate additional parameters that can be used to predict the area of the main fracture channel. However, there is increasing variability with an increase of overpressure and time over which it is applied.

From this analysis, it can be concluded that it is possible to an extent to predict the geometries of the main fracture channel based on the overpressure and time over which it is applied. The increase in overpressure tends to cause for growth in the channel width while duration of the injection causes for longer fractures. Both fracture width and length are inversely proportional to the overburden column height. Scaling using only overpressure, injection duration and overburden height shows significant uncertainty in the projected fracture channel area. This uncertainty can be greatly decreased by introducing into scaling equation either time it takes for active fracturing to initiate or number of branching fractures created.

The equation presented works only for the granular media in the Hele-Shaw cell. For the solid rock variations in the elastic parameters such as tensile strength, Poisson's ratio and Young's modulus would also have to be taken into account. This presents opportunity for the future work in this direction.

5.5.2. Fracture propagation

A detailed analysis of the fracture propagation was carried out using the image subtraction technique and the digital image correlation. This shows several interesting patterns in the fracture propagation mechanics. Both methods have shown that fracture tip propagation causes disturbances along the whole solid system. Figure 5.42 shows a close up and annotated image of cumulative image subtraction during the fracture tip propagation.

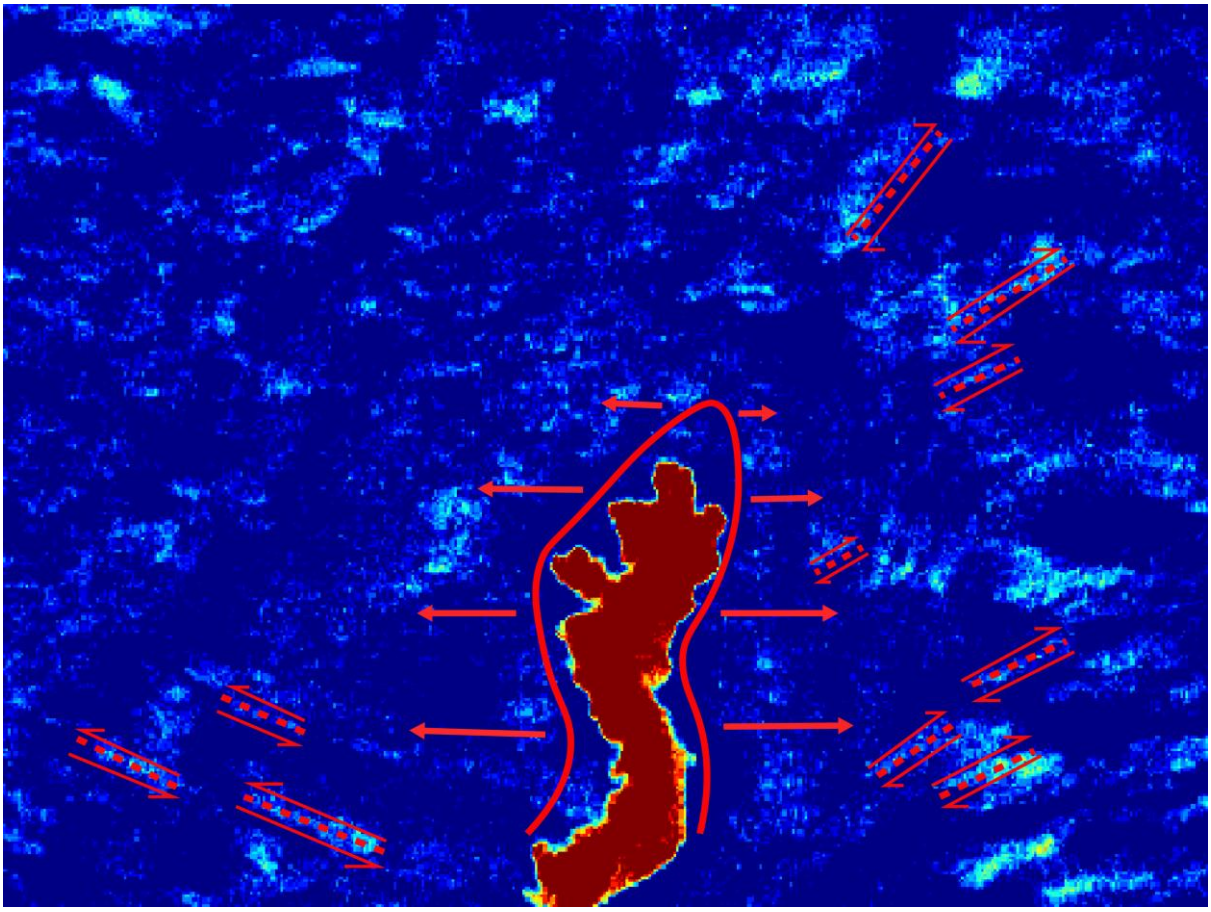

Figure 5.42. Zoomed in the frame of cumulative difference image subtraction. Image shows the propagation of the fracture front. Fracture opens in a tensile mode, however, it causes shear movement bands to occur on the sides in the solid. The frame is 10cm in width.

It can be seen that the main fracture is opening in a predominantly tensile fashion. However, as it does, linear structures form away from the main fracture which are aligned at an angle towards the main fracture channel. These features indicate that there is unequal movement occurring on either side of the feature shearing the material.

The Image subtraction technique shows that there is movement on these planes, however the level of detail is small and therefore DIC is required (Fig. 5.43).

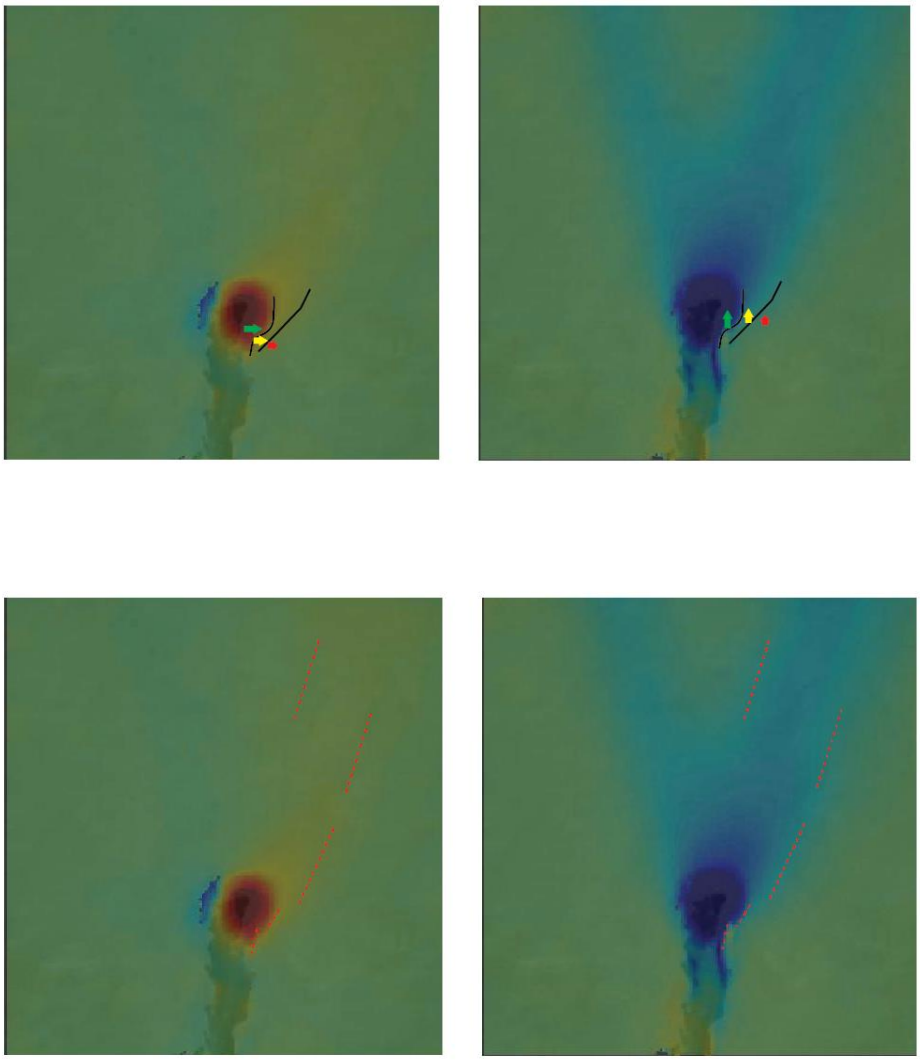

Figure 5.43. Digitally correlated images of horizontal displacement (left) and vertical displacement (right). Each frame is 10 cm in width. For horizontal displacement images, warm colours indicate rightwards movement, while cold colours – leftwards. For vertical displacement, warm colours indicate downward movement, while cold colours show upwards movement. In the upper row images, black lines show clear distinction boundaries between the differential movements within the solid surrounding fracture tip. Both vertical and horizontal displacement areas overlap. Bottom row images show that the displacement front can be seen far above the fracture tip.

DIC analysis images show displacement fronts coinciding with both horizontally and vertically directed displacement vectors. They further show a sharp separation for magnitudes of displacement. This indicates that there is shear movement along these surfaces. It must be taken into account that this is granular media. If dealing with a solid rock, this would amount in stress build up due to the strain, which could eventually lead to a mode II failure. It can be further seen that the displacement front is extending upwards far beyond the fracture tip.

Differential movement, once it triggers even minor shear movements, creates a plane of weakness as it has lost cohesion locally. This is an important notion to look into as fracture propagation is not a straight unidirectional process. Figure 5.42 shows a fracture as a linear feature which propagates in the predominantly vertical area, with minor horizontal deviations. Figure 5.43 shows horizontal displacement being predominantly orientated towards the right (red) and only slightly towards the left (blue). From that we can conclude that the fracture tip propagation is a multi-stage process:

- As the fracture propagates, it builds up a compaction zone in front of it. It also causes minor mode II events around it, which creates planes of weakness;
- Once the material is too compacted to fail, the fracture increases in aperture rather than propagating. This causes for the compaction waves to build on either side of the fracture walls. The fracture aperture increase does not occur in both lateral directions simultaneously but does so in stages/pulses. This leads to a fracture tip being surrounded by compacted solid;
- Fluid pressure increase within the main channel builds stress, which is easiest released by exploiting one of the previously created planes of weakness;
- The process repeats itself, the next exploited plane of weakness is typically orientated almost parallel to σ^1.

5.5.3. Comparing Hele-Shaw results to modelling data

One of the objectives for these experiments was to see if the Hele-Shaw environment can replicate the data acquired through modelling using the Latte code. It would be problematic to compare the created fracture dimension ratios as the modelled data accounts also for elastic parameters (Young's modulus, tensile strength, Poisson's ratio), which are very hard to replicate using a Hele-Shaw cell. However, it is possible to look at the stress maps of the Hele-Shaw cell, which can be seen from the accumulated strain and compared the horizontal and vertical stress profiles of the Latte model (Fig. 5.44).

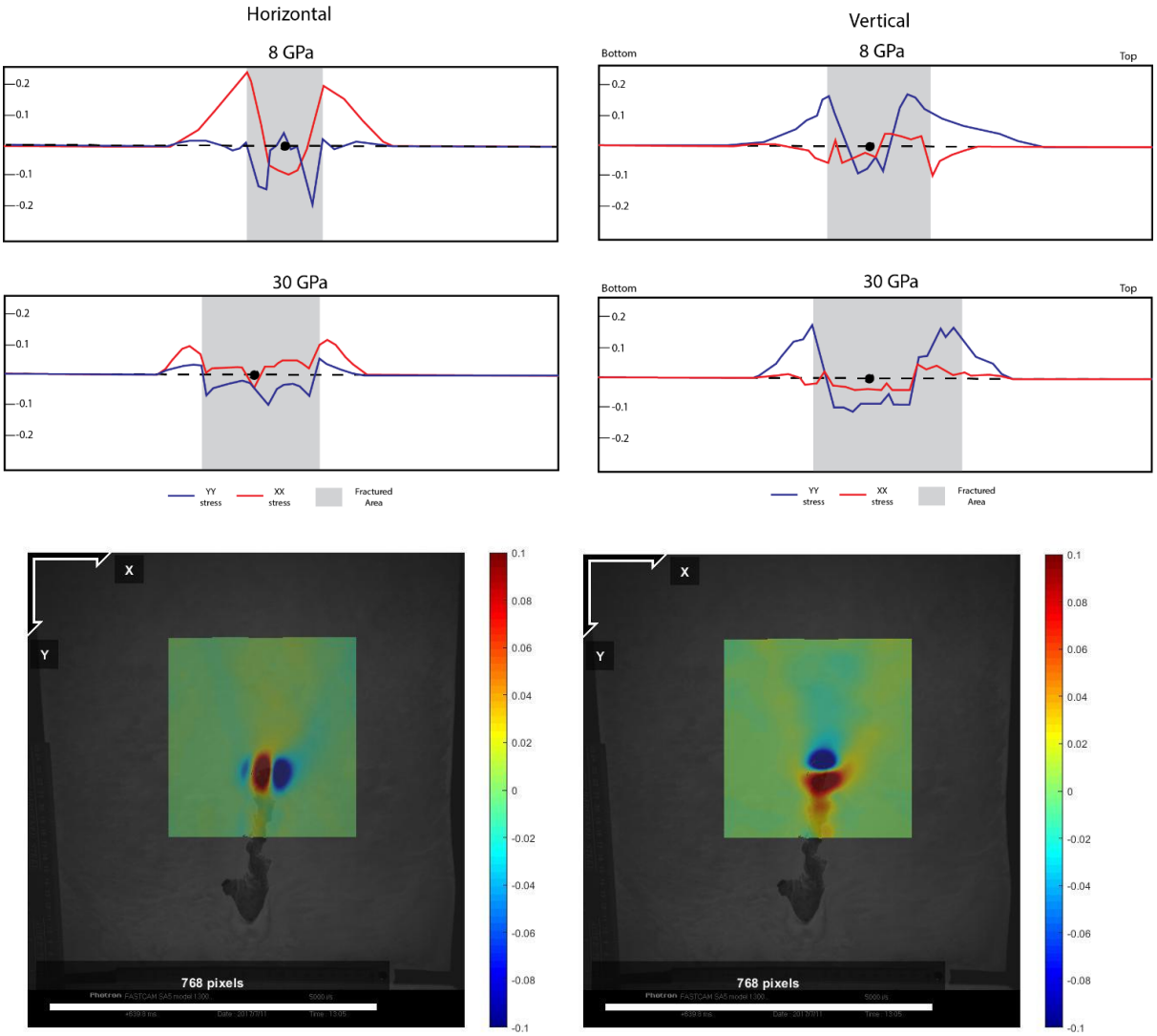

Figure 5.44. Comparison between modelled stress data and strain fields obtained from DIC of Hele-Shaw cell experiments. Top: Profiles of change in XX (lateral) and YY (vertical) stress throughout the experiment along the horizontal (left) and vertical (right) lines of the profile for soft and hard rocks. Bottom: images from DIC analysis of the Hele-Shaw experiments showing horizontal (left) and vertical (right) amounts of strain.

When looking at the horizontal cross-section of the stress regimes, the modelled and experimental data correspond well for the soft rock numerical experiments (8 GPa Young's modulus). There is a clear rapid change from negative to positive horizontal (XX) stress once the profile crosses from the fractured area into the unfractured solid. This is a clear indication of the compaction wave being created. The strain data for the Hele-Shaw experiment shows extension where the fracture channel is located and compaction on either side, which corresponds to the modelled data. The vertical stress (YY) is negative across the fractured area but does not become strongly positive outside of it. The experimental data shows a large extensive regime area where the fracture is with no compaction on either

side. For the vertical stress profile, there is a clear indication of the extensional regime for XX stress and compactional for the YY stress. This explains why the experimental and modelled fractures in the soft rock have the tendency to inflate. That behaviour of the solid media can be also clearly seen in the strain regimes for the experimental data. The stress regimes for the hard rocks correspond with the experimental data to a lesser extent. The horizontal profile's XX stress also shows a compactional wave present on either side of the fractured area, however, it is less pronounced and the fractured area itself is dominated by compaction rather than extension. Further, there is a clear positive value trend for YY stress within and outside the fractured area, whereas no compactional vertical strain is observable in the experimental data. Vertical data, although corresponding in having the YY compaction zone in front of the fracture tip, does not coincide for the XX stress. The modelled data shows that there is compactional XX stress while the experimental data shows an extensional regime.

It can be concluded that experiments with granular media within a vertically oriented Hele-Shaw cell do demonstrate features that would be expected within the hydrofractured rocks with low Young's modulus. As already discussed in Chapter 4, rocks with high Young's modulus have different fracturing dynamics. Due to that reason, the Hele-Shaw cell, which has granular media with limited cohesion, is not completely suitable to carry out experiments aimed at studying hydrofracturing in hard rocks but can be used to understand soft rock hydrofracturing.

5.6. Conclusions

In this chapter it was shown that experiments in a vertically orientated Hele-Shaw cell can vary in their general behaviour depending on the input parameters and can be subdivided into three types:

- Type A: only decompaction around the injection hole occurs with no active fracturing developing;
- Type B: active fracturing develops after a decompaction stage and is expressed through a fracture with a single main channel and minor branching conjugates;

- Type C: due to a high fluid injection rate, the granular media particles become detached, lose frictional cohesion and the granular media becomes fluidised (loses properties of the solid media).

Only Type B and, to an extent, Type A experiments can be used to study processes related to hydrofracturing and thus calibration of the experimental parameters is essential.

The image subtraction and digital image correlation techniques reveal the complexity in the behaviour of a propagating fracture. It has been shown that despite predominant channel opening in the main mode I fashion, fracture propagation results in a system-wide solid media disturbance. The unequal opening of the fracture tip causes differential movement of the solid media in the surrounding area resulting in minor mode II events and creation of weakness planes. The fracture opening process itself has multiple stages:

1) Initial decompaction around the fluid injection source as fluid seeps into nearby pores and raises pore fluid pressure;
2) Rapid isotropic fracture opening, the extent of which is typically limited by the area of the decompaction zone from the previous stage;
3) Main fracture channel propagation by 1) fracture tip opening until it is halted by a compacted region, 2) fracture tip inflation via lateral movement, which is typically unsymmetrical in proportions regarding to the amount of displacement in both directions, 3) fracture tip's further propagation by exploiting previously created planes of weakness.

As a case of special interest experiments with low overburden column were carried out. They corresponded with the observation carried out by Rodrigues & Cobbold (2007), which confirmed that Hele-Shaw experiments enable the creation of horizontal fractures in appropriate conditions.

This research showed that it is possible to scale the geometries of the fractures developed to the input parameters such as overburden column height, amount of overpressure and duration of the fluid injection. The precision of prediction increases with the number of known variables, such as the amount of time it takes for the system to initiate active fracturing and the number of the branches created. This scaling relationship is relevant for the granular media and elastoplastic parameters would have a significant effect on the observed properties of the fractures. There is a potential for future research to see how the

incorporation of such parameters as Young's modulus, Poison's ratio and tensile strength of the material would fit into the scaling relationship.

The effort to investigate the acoustic emissions generated by the fracturing in the granular media was made. Only strong, type C, experiments produced a signal that could be reasonably analysed. However, type C experiments poorly represent the hydrofracturing processes and are not of particular interests within the spectrum of this study. It is possible to repeat the attempts to look into acoustic emissions with more sensitive equipment.

Results obtained from the strain analysis in the DIC was compared to the stress analysis from the Latte model simulations described in Chapter 4. The behaviour of the solid media correlates well for the cases where simulations were run for the rock with a low Young's modulus. Simulations with the rocks of high Young's modulus, despite having some similarities, show significantly different fracture propagation behaviour.

It can be concluded that vertically oriented Hele-Shaw cell experiments can be used to study hydrofracturing processes if they are properly conducted and calibrated despite having some drawbacks and limits to which these processes can be portrayed.

6. Modelled microseismicity

The purpose of this chapter is to look into the microseismic signals generated by modelled hydrofracturing. The gathered analytical data from the simulations will be presented and the functionality of the developed forward seismicity modelling tool that was added to the Elle package will be illustrated. The research questions in this chapter are:

- Is there a correlation between the moment magnitude, mode of fracture opening and distance from the injection point?
- What effect does a change in the Young's modulus and the breaking strength of the rock has on the source mechanism, radiation pattern and the received signal generated by the hydraulic fracturing?

6.1. Characterisation of the generated seismicity

The first point is to present a single experiment in terms of the seismicity generated. Figure 6.1 shows the moment magnitude of the seismic events generated via fracturing. The data is stacked from five experiments.

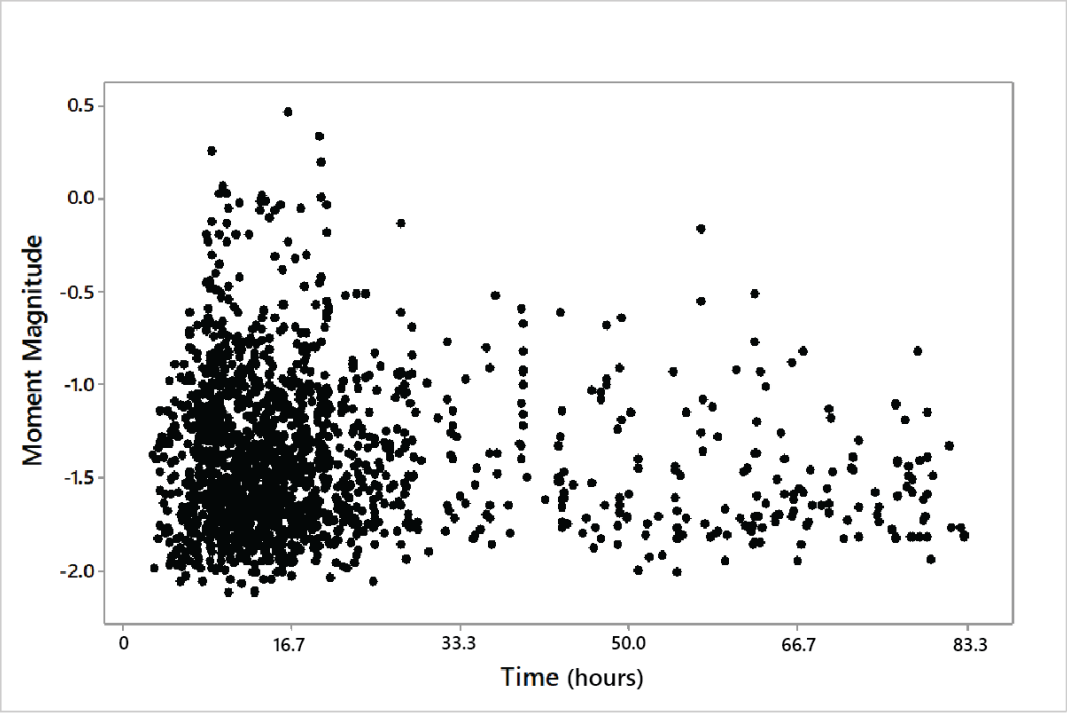

Figure 6.1. Moment magnitude of the events depending on the time when they occurred through the experiment. The length of the experiment is 5000 time-steps, where one time-step is 30s. The x scale has been converted to show time in the hour format. Data is stacked from five consecutive model runs. The greatest moment magnitude values can be observed during the phase of the most active fracturing (time-step 500-2000, 8-30 hours) and tend to decrease towards the later phases of the model evolution.

Most of the larger events occur in the initial stages of the experiment when most of the fracturing events are recorded. As the active fracturing decreases in the later stages of the model, the frequency of occurrence for higher value events drops. All the events are below 0.5 of magnitude. The lower boundary is around -2.0 due to the limitation of the minimum area of the fracture, which is the diameter of the single solid particle (2.5m). During natural hydrofracturing operations, events as small as -4.0 can be recorded if the sensitivity of the recording equipment permits it (Eaton and Forouhideh, 2010).

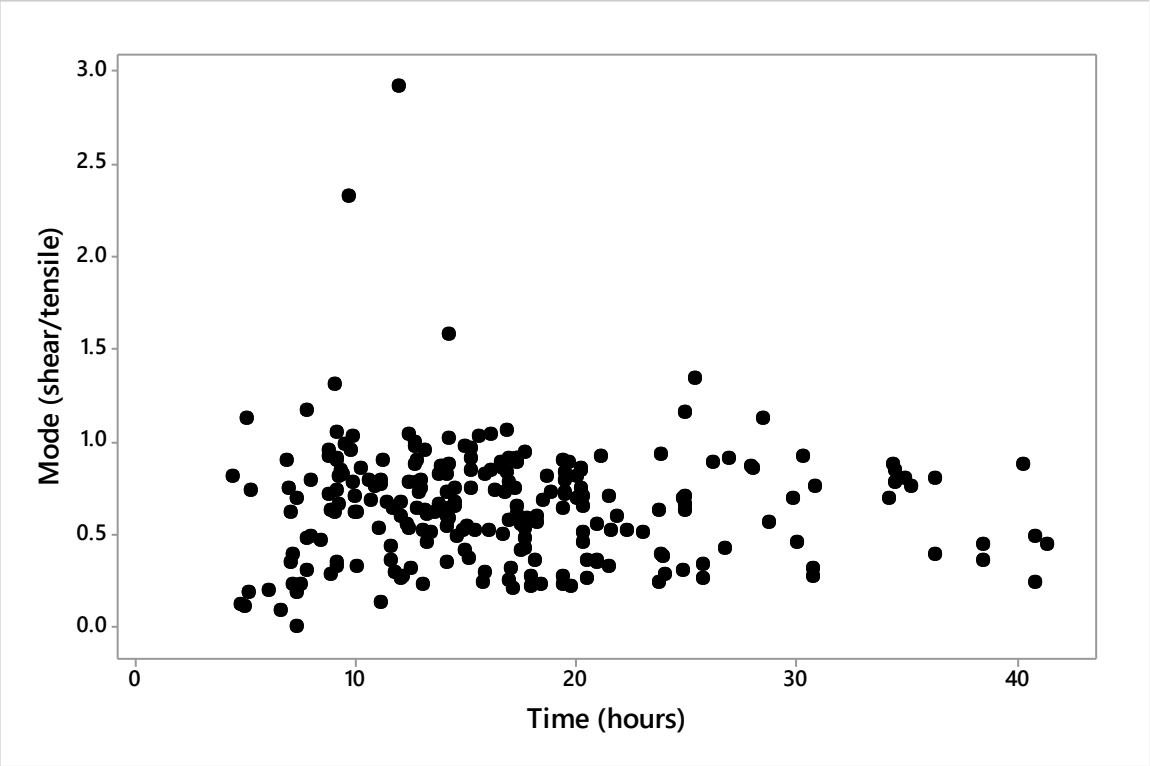

Figure 6.2. Mode of fracturing versus time of the fracturing event occurring. There is no apparent correlation between the mode of fracturing and stage of the experiment when the fracturing event is occurring. Most of the events are below value 1.0 meaning that tensile (Mode I) component is dominating.

Figure 6.2 shows that there is no obvious correlation between the amount of shear component present with regards to the stage of the experiment when the fracturing is occurring. The majority of the recorded events are below the ratio value of 1.0, meaning that the tensile component is more dominant than the shear component.

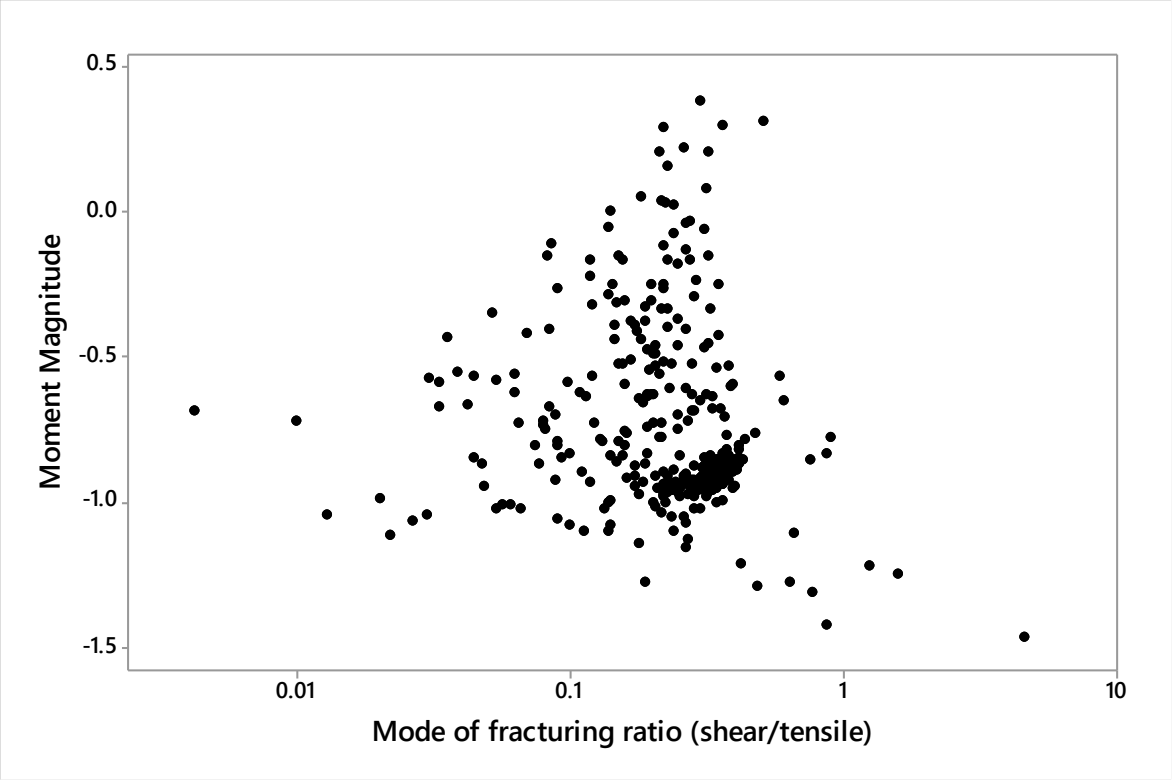

Figure 6.3. Moment magnitude of the recorded seismic events versus mode of their fracturing. All results produce an observable trend of an initial moment magnitude increase as fracturing becomes more shear-like followed by a decrease of magnitude and increase of the shear component.

Figure 6.3 shows the relationship between the mode of the fracturing and the moment magnitude. Most of the fracturing events in the simulations were mode I dominated (mode of fracturing ratio < 1) with the mode II fracture proportion increasing with the magnitude of the event. However, this trend is not linear and it can be seen that there are some mixed mode I – mode II events that have a very low magnitude.

Lastly, Figures 6.4 to 6.6 illustrate the effect that the distance from the injection point has on the moment magnitude and mode of the displacement. The data has been stacked from five consecutive model runs.

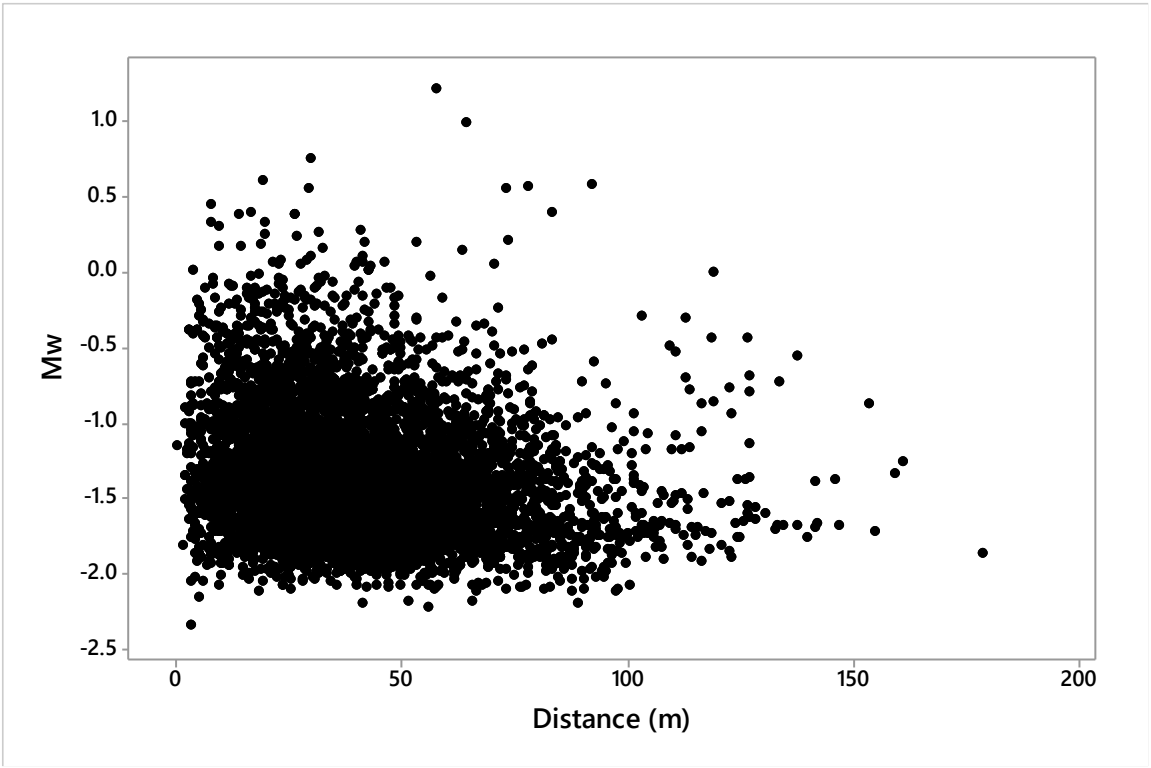

Figure 6.4. Distribution of moment magnitude (Mw) of the events relative to the distance from the injection point (m).

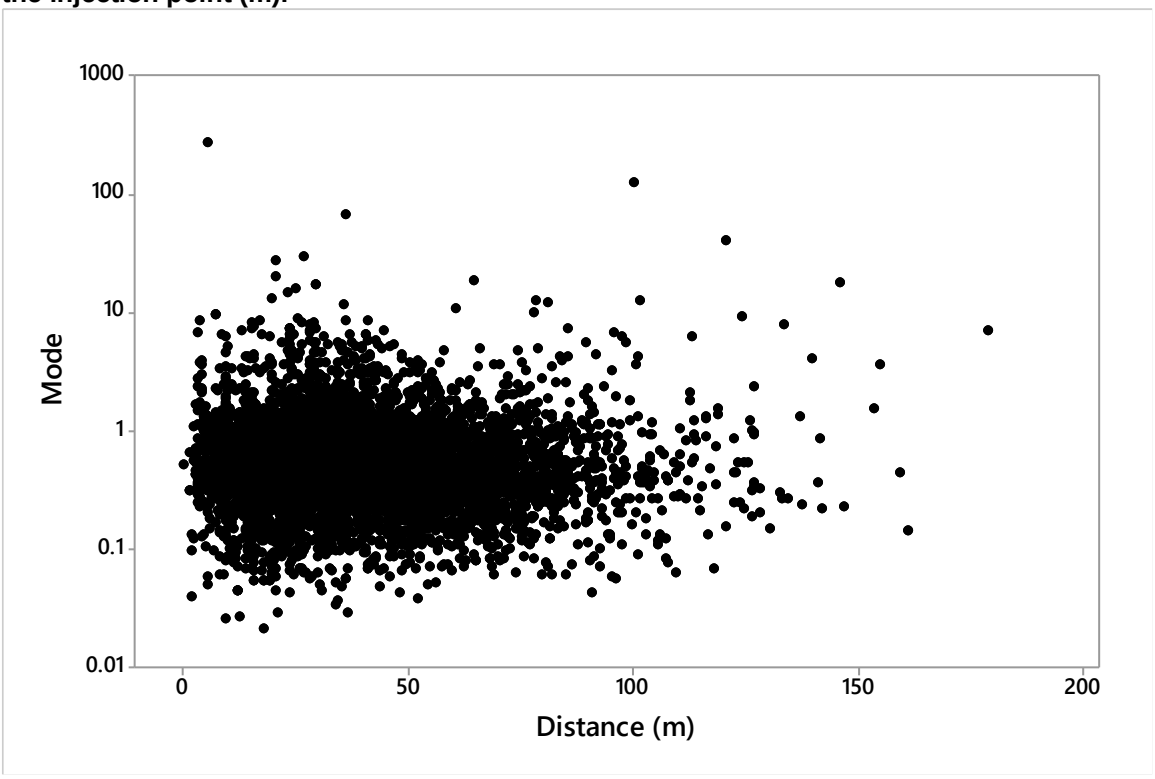

Figure 6.5. Distribution of fracturing mode (shear/tensile) of the events relative to the distance from the injection point (m).

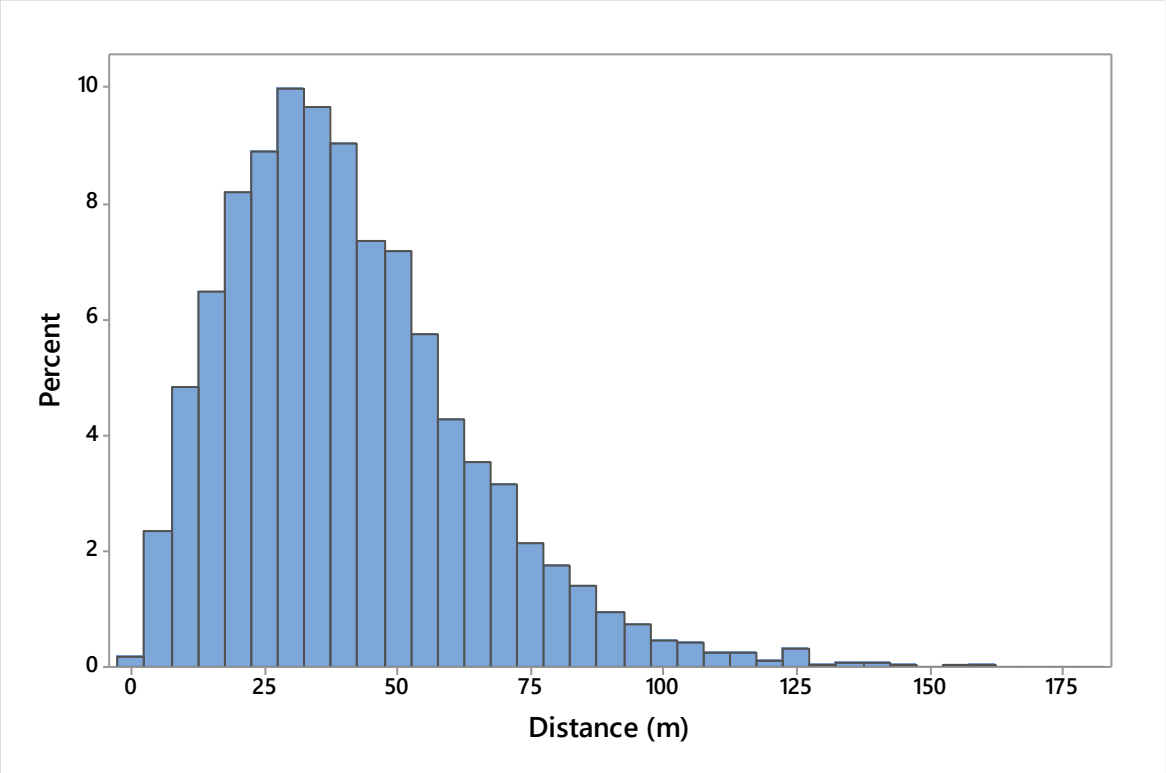

Figure 6.6. Histogram of the fracturing events sorted by their distance from the injection point (m). Y-axis represents the percentage of all the events being binned in each interval, which is 5m. The distribution shows a skewed bell-shaped curve, where most events occur 30m from the injection point with the frequency of fracturing events decreasing towards the boundaries of the model.

The density of the events in both Figure 6.4 and Figure 6.5 follow the distribution of the frequency of the events corresponding to their distance as shown in Figure 6.6. That shows that the distance of the occurrence of the fracturing events from the injection point has no significant effect on the moment magnitude or mode of fracturing.

6.2. Aseismic activity

Aseismic activity is characterised by a fault displacement which does not cause an earthquake (Guglielmi et al., 2015). Its main feature is that movement along the fault is in its nature closer to a slow creep rather than fracture tip propagation. Fluid injection into existing fracture network also causes minor solid fracture wall movements that do not have rupturing nature typical for the seismic events. Several studies show that anthropogenic fluid induced fracturing can cause aseismic activity (Scotti and Cornett, 1994; Guglielmi et al., 2015).

The Elle model is limited in the possibility to observe aseismic events due to logging only the position of the particles at the end of each time step. Therefore the dynamics of the particle movement during the relaxation phase of the lattice are not observed or recorded. However, there is significant potential for aseismic activity. To illustrate this it was possible to log the average amount of movement of particles located along the fracture wall during the time steps when no active fracturing took place. The amount of movement is an order of magnitude lower than that during time steps when bond breakage occurs, however it follows the same pattern where there is a greater increase in values in the initial stages of fracturing and subsequent decline in the later stages (Figure 6.7). It is more challenging to compare the potential seismic signal magnitude as the model is very limited in dealing with the temporal component. The formula for the seismic moment is $M_o = uA\mu$, where u is displacement, A is the area of the fracture and μ is the rigidity of rock. The aseismic movement along the fault would be occurring in clusters along the system as the fluid travels from the injection point towards the edges of the fracture network. The quasi-static nature of the model allows us to look at snapshots only before every fluid pressure injection step and therefore it is impossible to tell which segment of the fault moved at which time. The area of the active fracture segment is one of the key components in calculating the seismic moment. This is calculation of a theoretical seismic moment as even in nature it would be extremely hard to define an area of the aseismic slip. Not knowing the area makes the task of calculating the moment magnitude challenging for aseismic movement. If we can calculate the average displacement for all the particles, this approach cannot be used to calculate the average area of a "cluster" for the fracture area being active at any single time. Assuming that the aseismic activity period is going to be longer with the increase of the fracture network size, one approach how to tackle this challenge is to scale the seismic moment against the time (Tr) it would take the whole fracture area to rupture where $Tr = L/Vr = L/(0.75 \times Vs)$ where L is fracture length and Vr and Vs are rupture velocity and s-wave velocity.

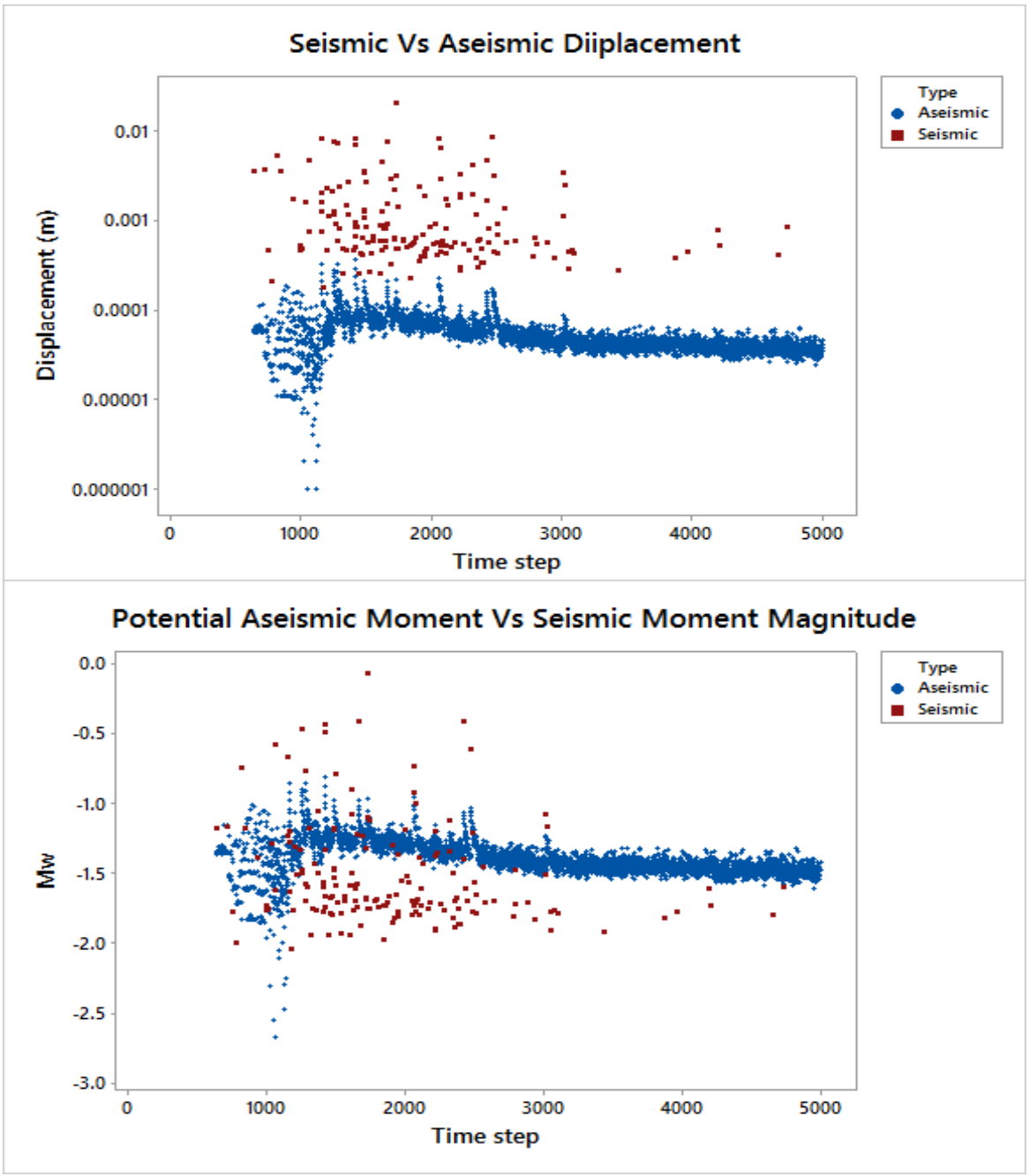

Figure 6.7. Top: Average displacement of particles during the time steps when active fracturing (seismic) takes place versus average displacement of all the particles across the fracture walls during time steps when no active fracturing is occurring (aseismic). Botton: Moment magnitude caused by the seismic fracturing versus potential moment magnitude caused by the fracture wall movements during time steps when no active fracturing occurs (aseismic). In this case, moment magnitude is a potential cumulative, which would occur if all the particles would move at once, which is not the case. As moment magnitude function is directly proportional to the fracture area, it would keep progressively increasing with the increase in fracture area throughout the experiment, therefore this effect is avoided by scaling it to fracture propagation time.

This still shows us only a total potential seismic moment as it would imply that the movement occurs along the whole fractured area simultaneously, which is not the case, as the movement occurs in different segments of the fractured area at

different times. The inability to observe which segment moves at a given time is a limiting factor for this model. However, the approximation makes it possible to see that the smaller peaks in the aseismic data array correspond to the fracturing events. This would be indicative of the fact that large amounts of energy are being released aseismically alongside the energy created during active fracturing and may not be directly observed.

6.3. Radiation Patterns

Another feature that can be used to analyse the fractures is the radiation patterns of the generated seismicity. Radiation pattern plots can be used as an alternative to so-called “beach ball” diagrams, as they represent strength and polarity (compressional, extensional) of the emitted seismic signals depending on the geometry of the fault. As discussed in Chapter 3, the variables required for radiation pattern calculation are Poisson’s ratio, dip, strike, rake, tensile angle, take-off angle and azimuth. The Poisson’s ratio is a pre-assigned value in the Elle model equal to 0.3. For the purposes of the representation of the general nature of the events, I will use all the potential take-off angles and azimuth values (360^{o}). This will show the whole spectrum rather than the value at a single point. The task can be further simplified by the fact that the Elle model is operating in a 2D environment, which eliminates the possibility of the out-of-plane movement. This allows assuming constant strike and rake values. At this point, there are only two variables remaining: dip and tensile angle. For this part, the data which has been stacked from up to three experiments with differentiated sets of varying Young’s modulus and breaking strength values are presented. These values have been selected as variables to be in consensus with the experimental setup used in Chapter 4.

The first step is to look at the effect that differentiating the Young’s modulus and tensile strength of the rock has on the dip and tensile angle of the fracture wall slip.

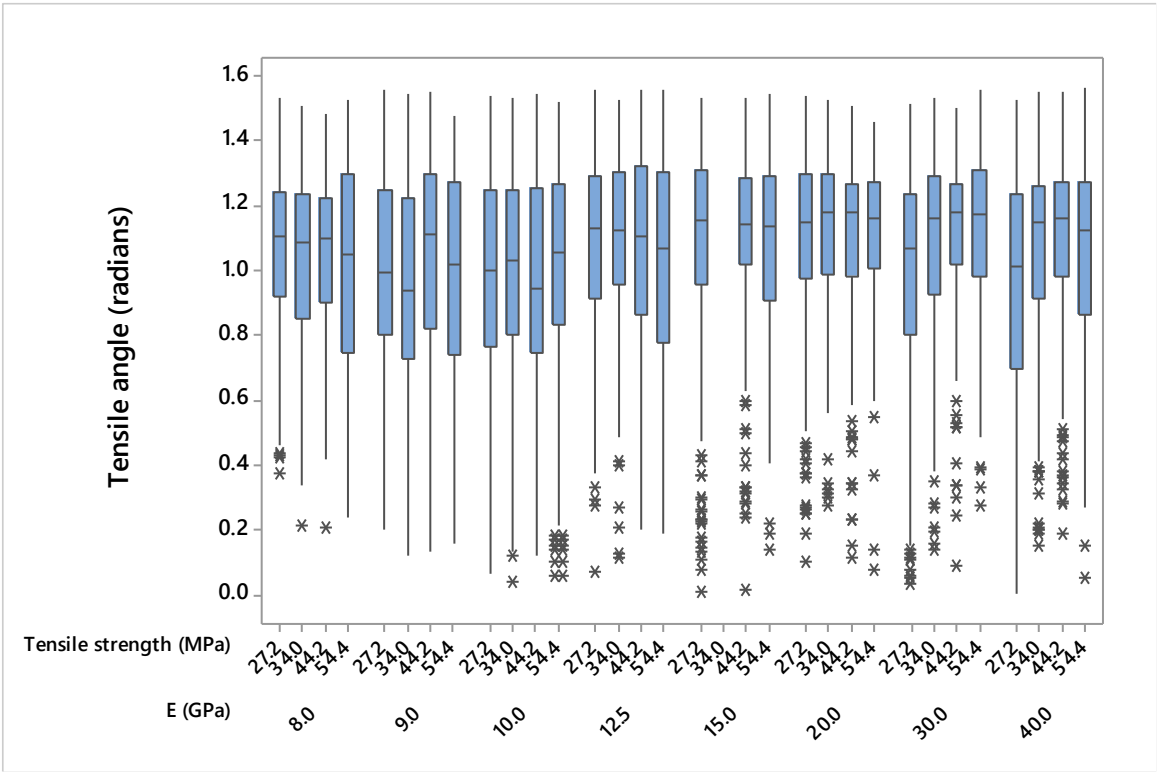

Figure 6.8. Boxplot of tensile angle values depending on the variations in Young's modulus (E) and tensile strength of the rock. Despite all the means and two quartiles of the data being relatively close to the same value, data covers most of the spectrum of values (0º-90º). Stars represent the data points, which are considered outliers (fir outside 95% confidence interval).

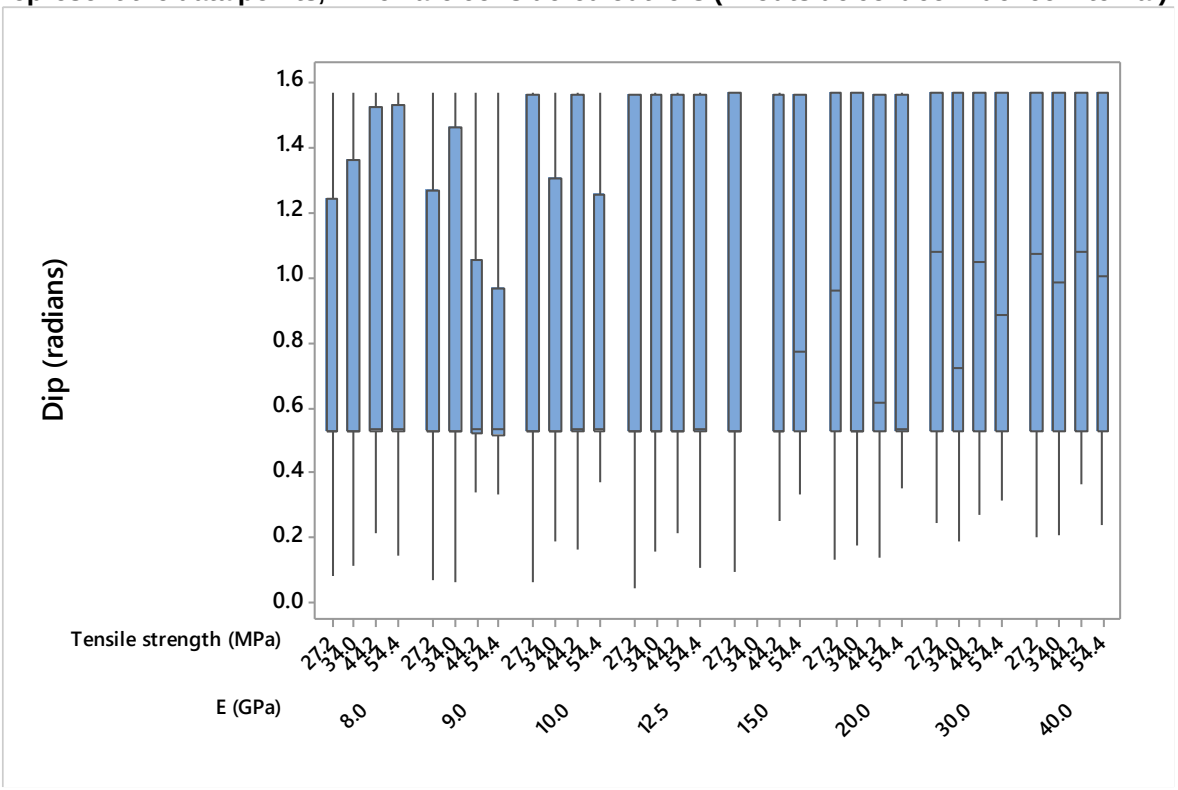

Figure 6.9. Boxplot of fracture dip data values depending on the variations in Young's modulus (E) and tensile strength of the rock. There can be seen a shift of the means towards higher values with increasing Young's modulus. Data covers most of the spectrum (0º-90º), however, there is lack of values of shallower dip. This might be an artefact of the triangular lattice setup.

The result distributions shown by the boxplots in Figures 6.8 and 6.9 show that the result spread covers most of the possible 90-degree spectrum for both dip and tensile angle values. There is little variability in the shift of the mean and quartiles for the tensile angle data irrelevant to the change in Young's modulus or breaking strength. The dip data appears to show a shift in means and quartiles towards steeper dips with the increase in both Young's modulus and tensile strength of the rock. Figure 6.9 shows very little data with shallower dip values. There is a possibility that such effect is an artefact created by the triangular grid structure of the DEM, where most springs are either at 60 or 0-degree dip. Nevertheless, since dip data is generated as a function of multiple broken springs, a shift in the means still provides valuable information on the effects of changing Young's modulus and tensile strength. Also, the dips would be expected to be steep due to the gravity's effect in the system. Further, change in Young's modulus produces significant change in dip data, therefore artefact effect created by the lattice cannot be dominating.

To completely understand if the effect of changing the elastic parameters of the rock is significant, a statistical analysis must be carried out. For this purpose, the one way ANOVA analysis is used, which tells if the difference in the means of a data sets is significant enough with regards to the confidence interval for the mean. A standard 95% confidence interval is being used, meaning that the significance level $a=0.05$. The ANOVA analysis confirms that a change in one of the variables creates a statistically significant difference in the means if the calculated P-value is below a.

Figures 6.10 and 6.11 show the calculated sequence of 95% confidence intervals for the dip and tensile angle means respectively in regards to varying Young's modulus.

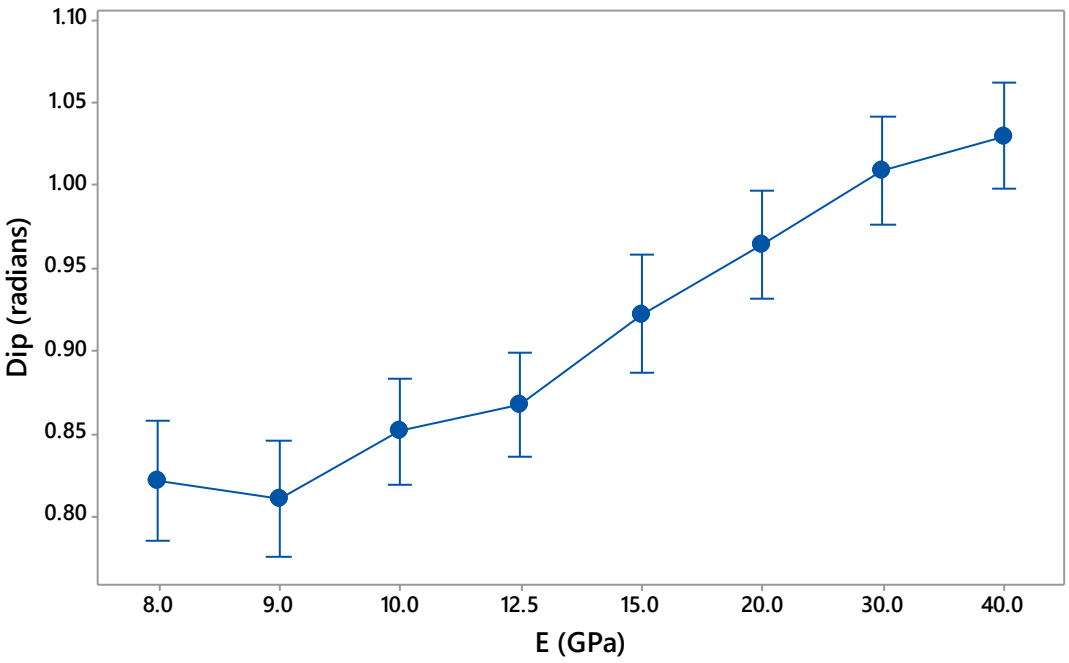

The pooled standard deviation was used to calculate the intervals.

Figure 6.10. 95% confidence intervals for the data means of dip values in regards to changing rock's Young's modulus (E). There is a clear trend in the dip becoming steeper with the increase in Young's modulus.

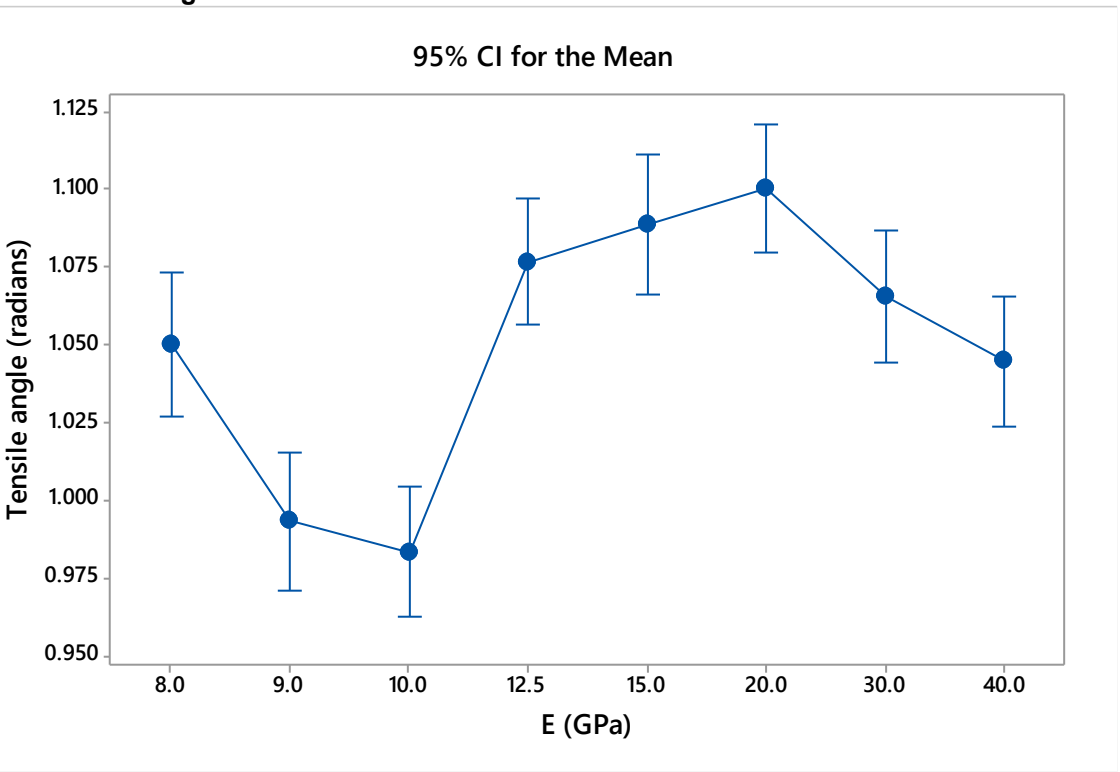

Figure 6.11. 95% confidence intervals for the data means of tensile angle values in regards to changing rock's Young's modulus (E). Increase in Young's modulus produces non-linear behaviour in the tensile angle response. Changing E from 8 to 10 GPa produces a decrease in tensile angle, meaning shift to larger shear component present. This is followed by a rapid increase in the tensile angle for the intermediate E values (10-15 GPa) with the subsequent repeated decrease for larger E values (30-40 GPa).

Figures 6.10 and 6.11 show that there is a significant effect on changes in the data means as a result of differentiating the Young's modulus. There is a linear trend for the dip to become steeper with an increase in Young's modulus. The tensile angle variations with respect to a change in the Young's modulus are more complex. The initial increase in Young's modulus from 8 to 10 GPa causes the tensile angle to decrease, which indicates the greater presence of shear component in the fracture opening. This is followed by a shift to higher tensile angles for values of 12.5 GPa and a further increase to a value of 20 GPa. This increase is then followed by a repeated drop in tensile angle mean value for the 30 and 40 GPa Young's modulus simulations. The behaviour coincides with the data provided in Chapter 4, as it shows 2 or 3 different regimes of fracture opening behaviour depending on the Young's modulus of the rock.

The one way ANOVA analysis carried out showed that the P-values for both dip and tensile angle datasets is 0, indicating that there is a statistically significant difference in the mean response to the change in Young's modulus.

Figures 6.12 and 6.13 show the responses in the dip and tensile angle means with regards to changes in the mean tensile strength of the rock.

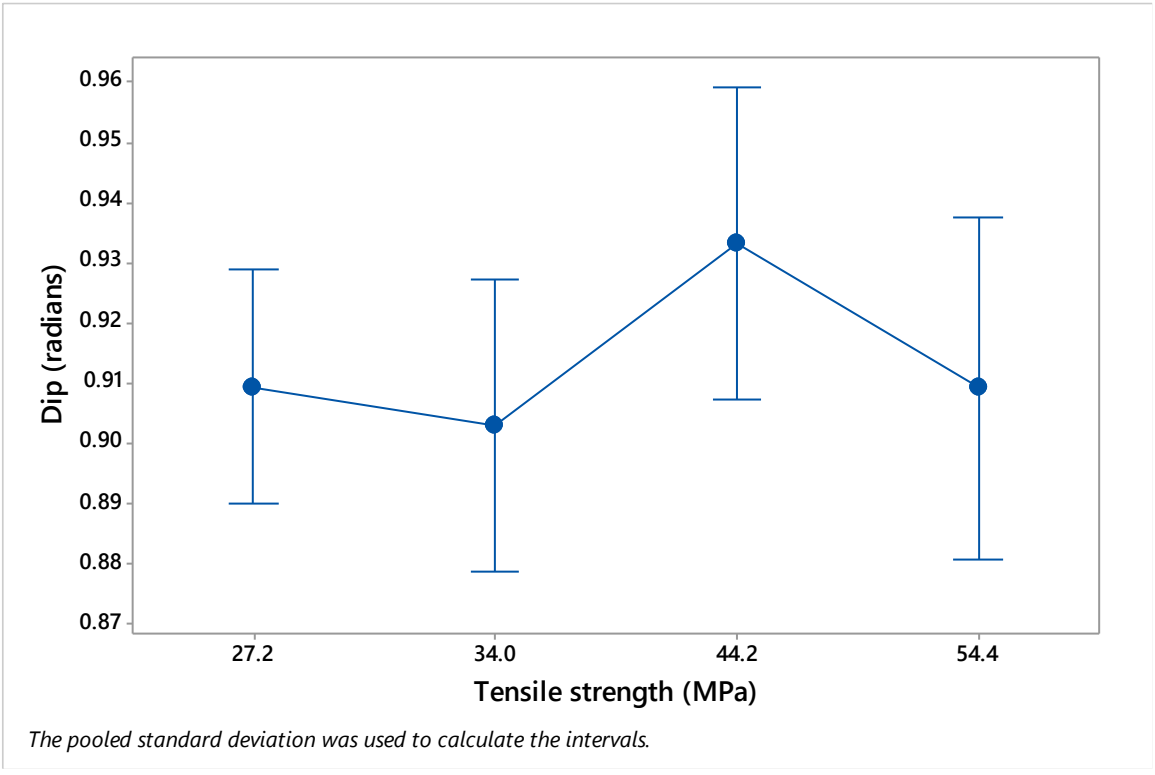

Figure 6.12. 95% confidence intervals for the data means of dip values in regards to changing rock's tensile strength. All tensile strength values but 44.2 MPa produce similar results.

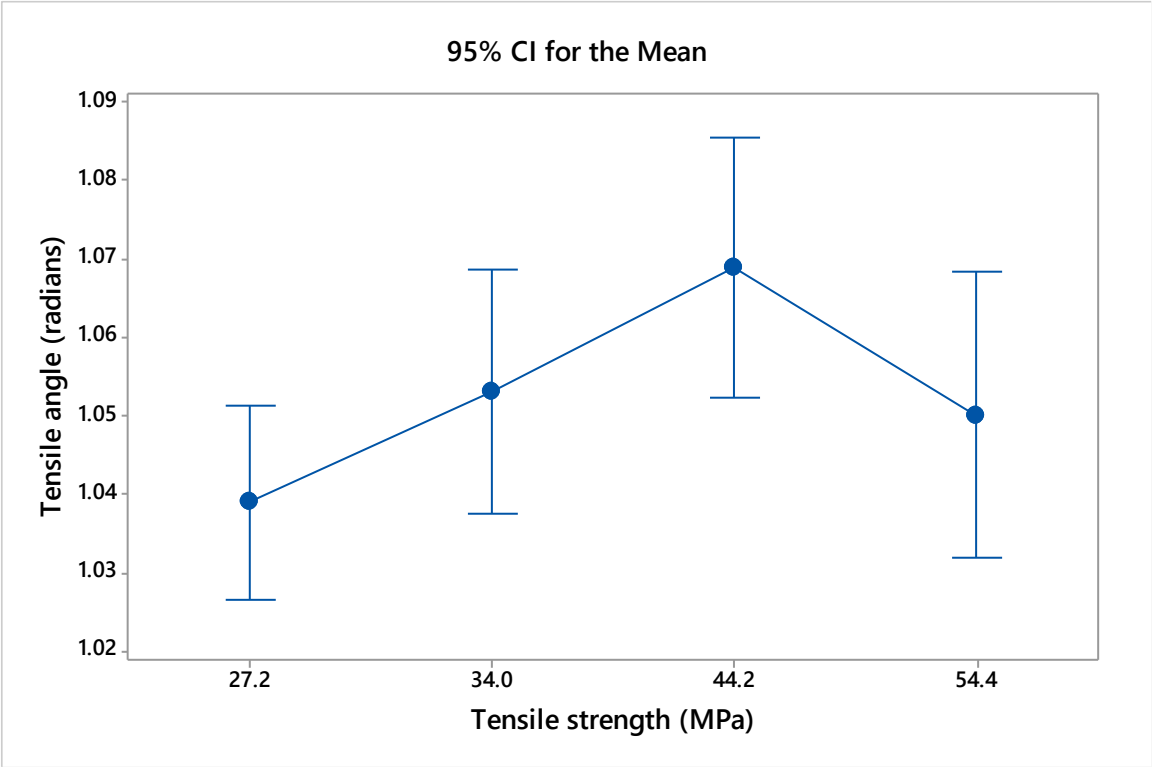

Figure 6.13. 95% confidence intervals for the data means of tensile angle values in regards to changing rock's tensile strength. Data shows the bimodal behaviour of increasing tensile angle (higher Mode I component) with higher tensile strength values, followed by a drop in the 54.4 MPa data.

The means for the dip of all but the 44.2 MPa tensile strength value show similar results. The ANOVA analysis produces a P-value of 0.366 and with the P-value being greater than $\alpha = 0.05$ there is not enough evidence to reject the hypothesis that all means are statistically significantly different.

The tensile angle mean values show the tendency to increase linearly with an increase in the breaking strength of the rock and then the values decrease at a mean tensile strength of 55.4 MPa. This can be interpreted as an increase and a following decrease in the amount of shear component in the fracture wall opening vector. The ANOVA analysis of the mean data gives the P-value of 0.044, which is lower than α, meaning that there is sufficient statistical evidence to say that a change in the tensile strength of the rock leads to a significant difference in the response variable (tensile angle).

As the ANOVA analysis produced three out of four positive results, it can be concluded that changes in Young's modulus and breaking strength of the rock significantly influence the nature of the seismic radiation pattern produced.

The next step in the analysis is to look at the actual radiation pattern values created for the given mean values. For the purpose of better understanding, the data provided in Figure 6.14 shows the reference radiation patterns for the vertically orientated fracture where the tensile angle of the fracture opening is varied. Figure 6.15 presents the calculated radiation patterns for P and S waves using the mean dip and tensile angle values derived from experiments with varied Young's modulus and tensile strength of the rock.

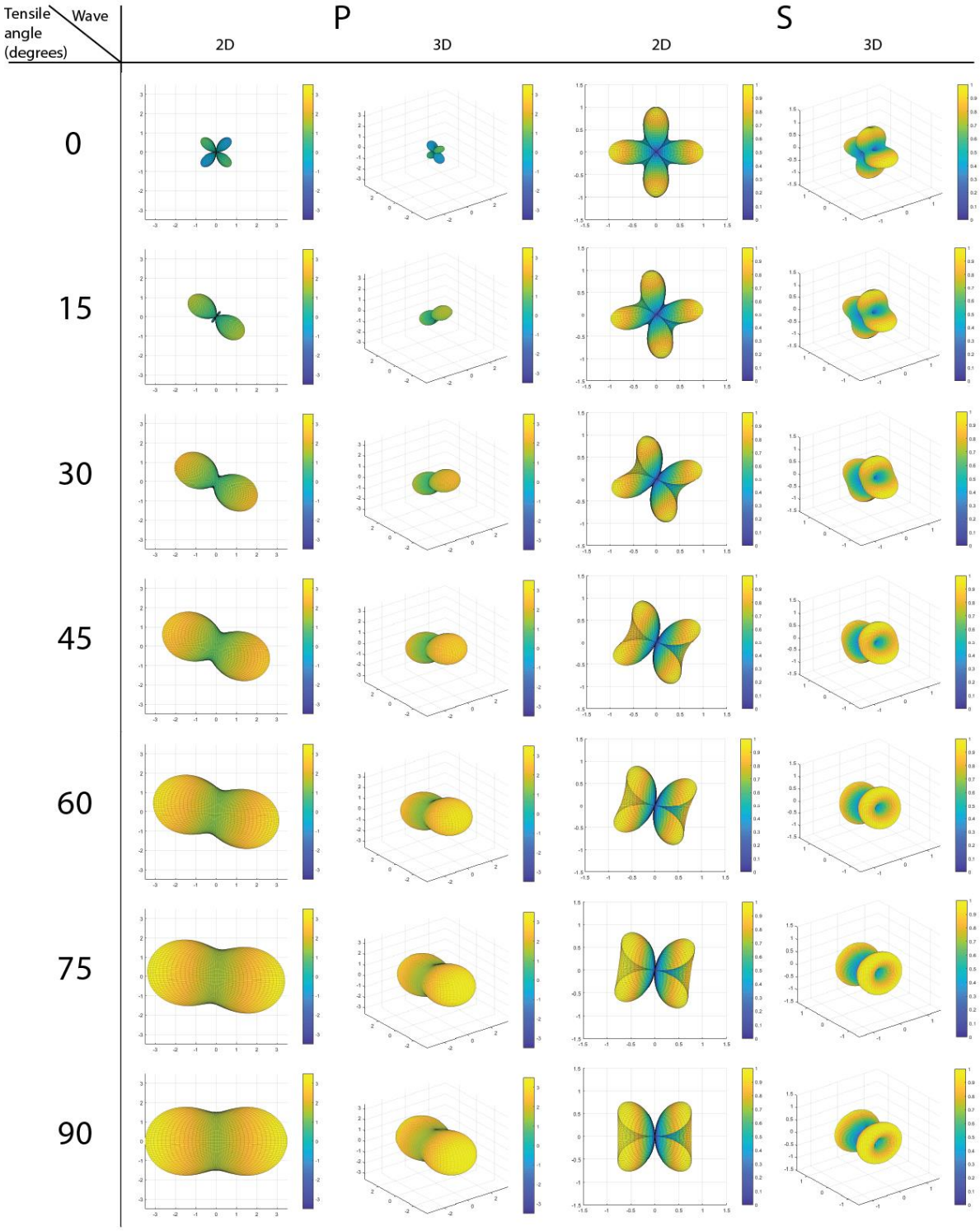

Figure 6.14. Radiation patterns for a vertical fracture for P and S waves in 2D and 3D for varying tensile angle values. 0 degrees correspond to pure Mode II event while 90 degrees – to Pure Mode I event. P wave radiation pattern values vary from -1 to 3.5, while S wave radiation pattern values range from 0 to 1. For P wave tensile angle determines both the absolute value and magnitude of the radiation pattern. For S waves, the range of values stays the same for all the tensile angles, however, the orientation and shape of the pattern value cloud is altered.

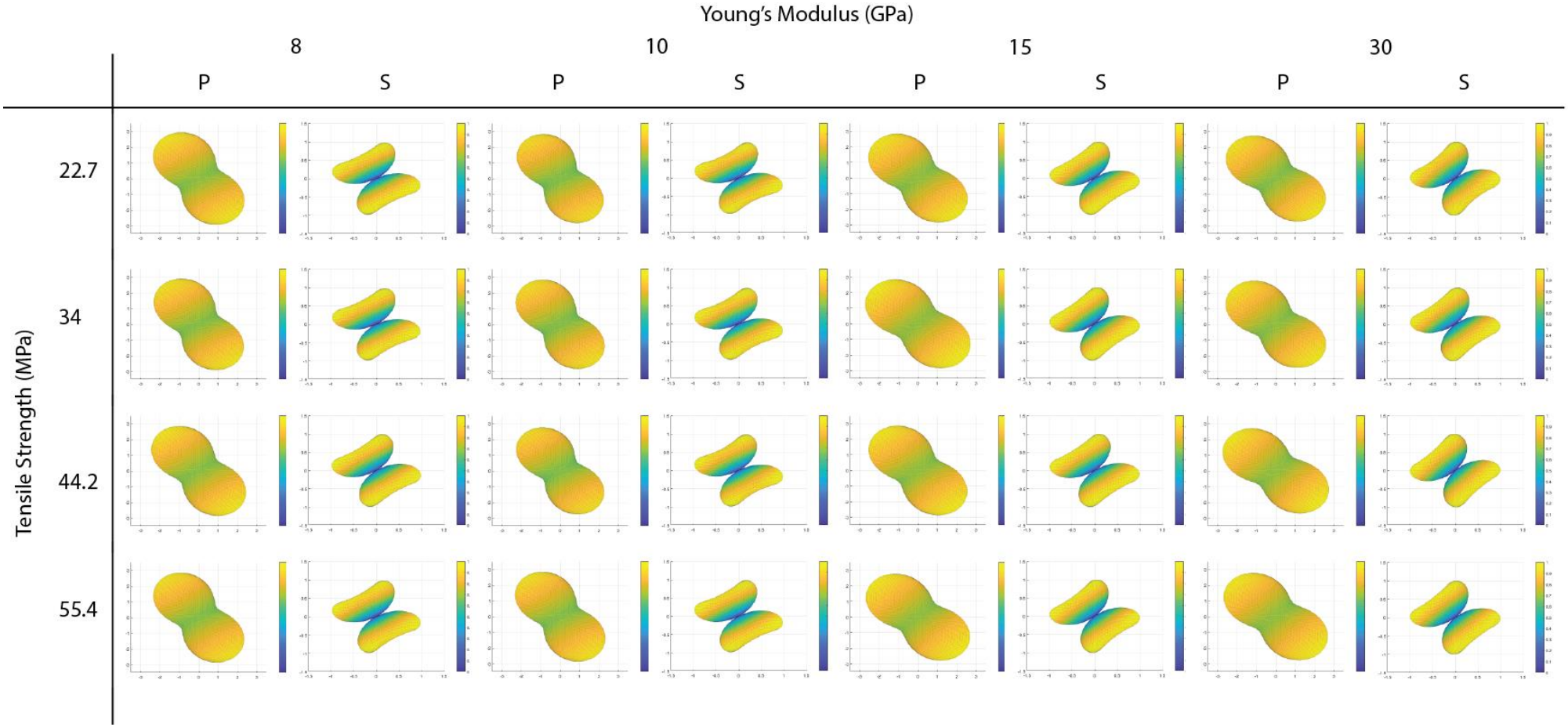

Figure 6.15. P and S wave radiation patterns for the varying Young's modulus and tensile strength values. Derived mean dip and tensile angle values have been used for the pattern calculations. Dip variability accounts for the variations in the inclination of the radiated pattern, while variation in the tensile angle mostly influences the magnitude of the P wave pattern. Magnitude change is expressed through slight changes in the P wave pattern size.

Figure 6.15 illustrates that there is very minimal variability in the radiation patterns across different Young's modulus and tensile strength values despite dips and tensile value means being statistically different.

The first motion of the arrival P wave can be either negative or positive depending on whether it is compressional or extensional. In Figure 6.14 it can be seen that the compressional component becomes absent if the value of the tensile angle is above 15º. Figure 6.15 shows that none of the P wave radiation patterns derived from the mean dip and tensile angle values show compressional behaviour. Therefore it is important to investigate under which circumstances it is still possible to receive compressional first motion of the arrival P wave. For the next part of the analysis, the data was tagged in a binary fashion according to the tensile angle values. The cut-off value was chosen to be 15º as events with larger tensile angle did not produce a compressional front (Kwiatec and Ben-Zion, 2013). Figure 6.16 shows the proportion of all the events that are producing only an expansive front depending on the Young's modulus, while Figure 6.17 – when changing the breaking strength of the rock.

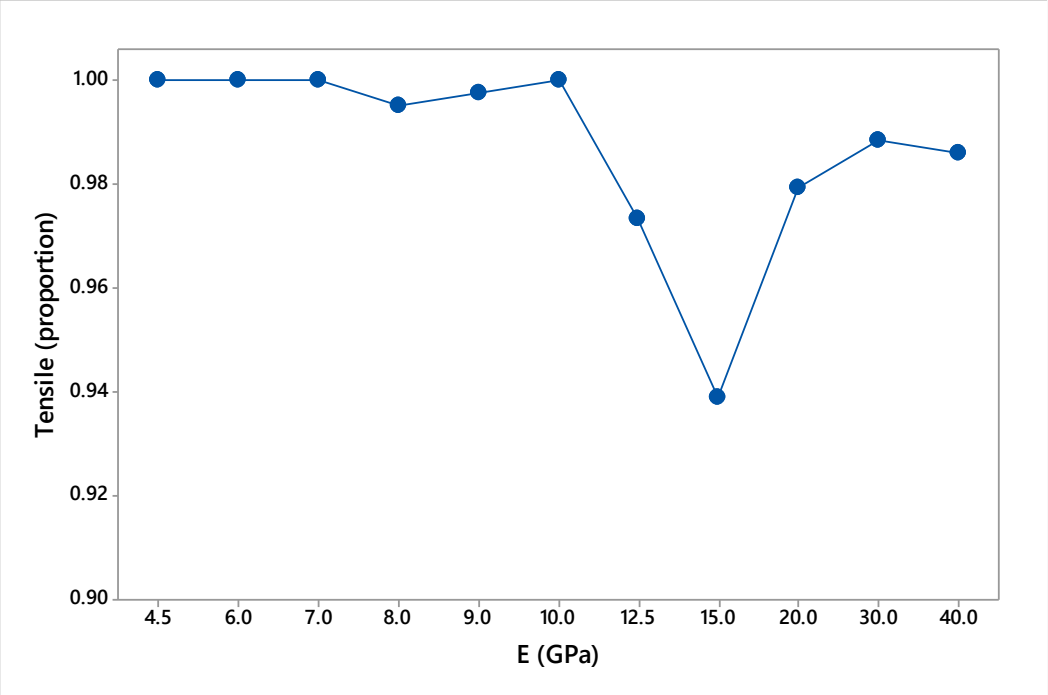

Figure 6.16. The proportion of the events producing only tensile or expansive component of the P wave depending on Young's modulus of the rock. The figure shows a non-linear regime where soft rock (>10 GPa Young's modulus) produce almost exclusively expansive component. Above 10 GPa value, there is a rapid increase in the events with the compressive component present (up to 6%), with a repeated decrease for hard rocks (30-40 GPa) with less than 2% of the events showing compression.

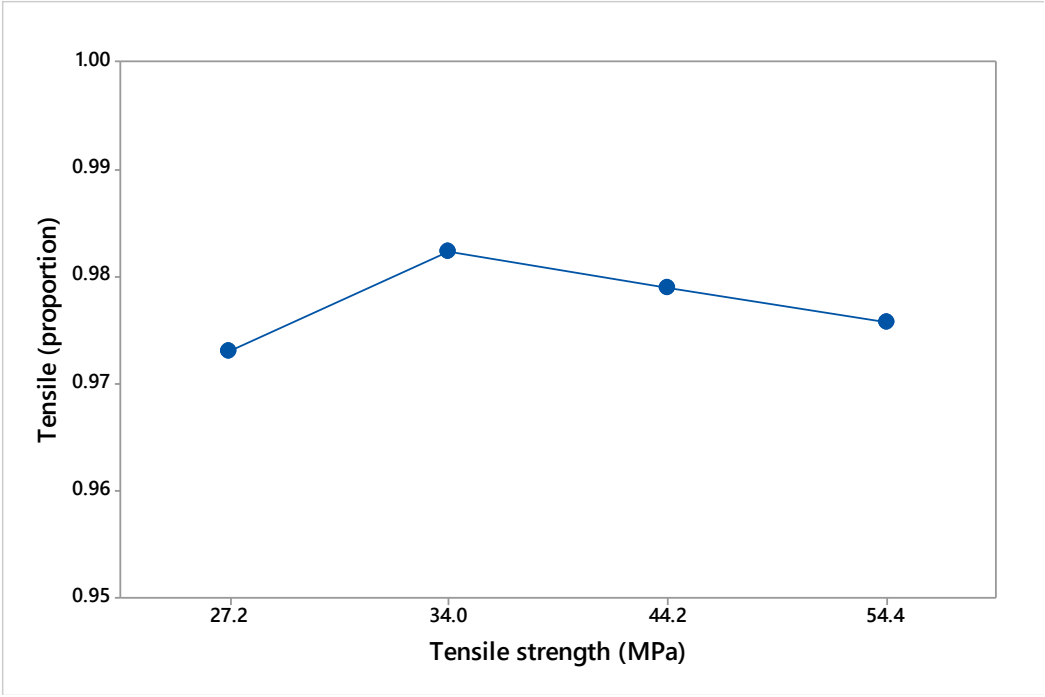

Figure 6.17. The proportion of the events producing only tensile or expansive component of the P wave depending on the tensile strength of the rock. Change in the tensile strength provides little change in the amount of the events showing compressional component with the total variability being less than 2% of the total number of events.

It can be seen that Young's modulus has a stronger effect upon the possibility of having a compressional component in the radiation pattern of the P wave. An increase in Young's modulus produces a non-linear response to the proportion of the events producing compression. Soft rocks with Young's modulus values of up to 10 GPa produce almost exclusively extensional components. This is followed by an increase of up to 6% of the events having a compressional component for the experiments with a Young's modulus of 15 GPa. Finally, the compressional value proportion drops again to 2% for the hard rock experiments with Young's modulus values of 30-40 GPa.

Experiments with a variation in breaking strength of the rock produce very little change in the proportion of the events having compressional components. The total amount of variability is less than 2%.

From the results presented in this Chapter, it can be concluded that the change in Young's modulus is the key driver behind the dynamic of changes in the radiation patterns. Despite of the fact that the dip and tensile angle means show a statistically significant evidence to be considered different for the series of Young's modulus values, they produce little alteration across the calculated radiation patterns for both P and S waves. A small variability in the orientation of the emitted radiation pattern shows that the optimal receiver position would not

greatly vary for rocks with differentiated Young's modulus and breaking strength. However, it has to be taken into consideration that this is in the homogenous rocks with no layering, which would otherwise cause ray scattering and reflectivity issues that would call for more detailed placement consideration.

6.4. Received signal

In addition to the radiation pattern which is an important aspect of calculating the intensity of the received signal, it is also important to look at the energy received itself. The two main components in the energy are the total displacement generated and time parameters, such as rupture time and rise time. Rise time can be defined as time required for rupture velocity to reach its optimum value (≈70% of S wave velocity) from the point of initiation while rupture time is time required for fracture to propagate along its length. These are then used to construct a velocigram at the observation point, which accounts for the displacement per second. Figure 6.18 demonstrates the rupture time of the fractures for differentiated Young's modulus and breaking strengths of the rock. The logistic distribution probability density function is then applied to better illustrate the results generated. The relationship is exactly the same as for the fracture area distribution data in Chapter 4 as the rupture time is directly proportional to the area of the fracture.

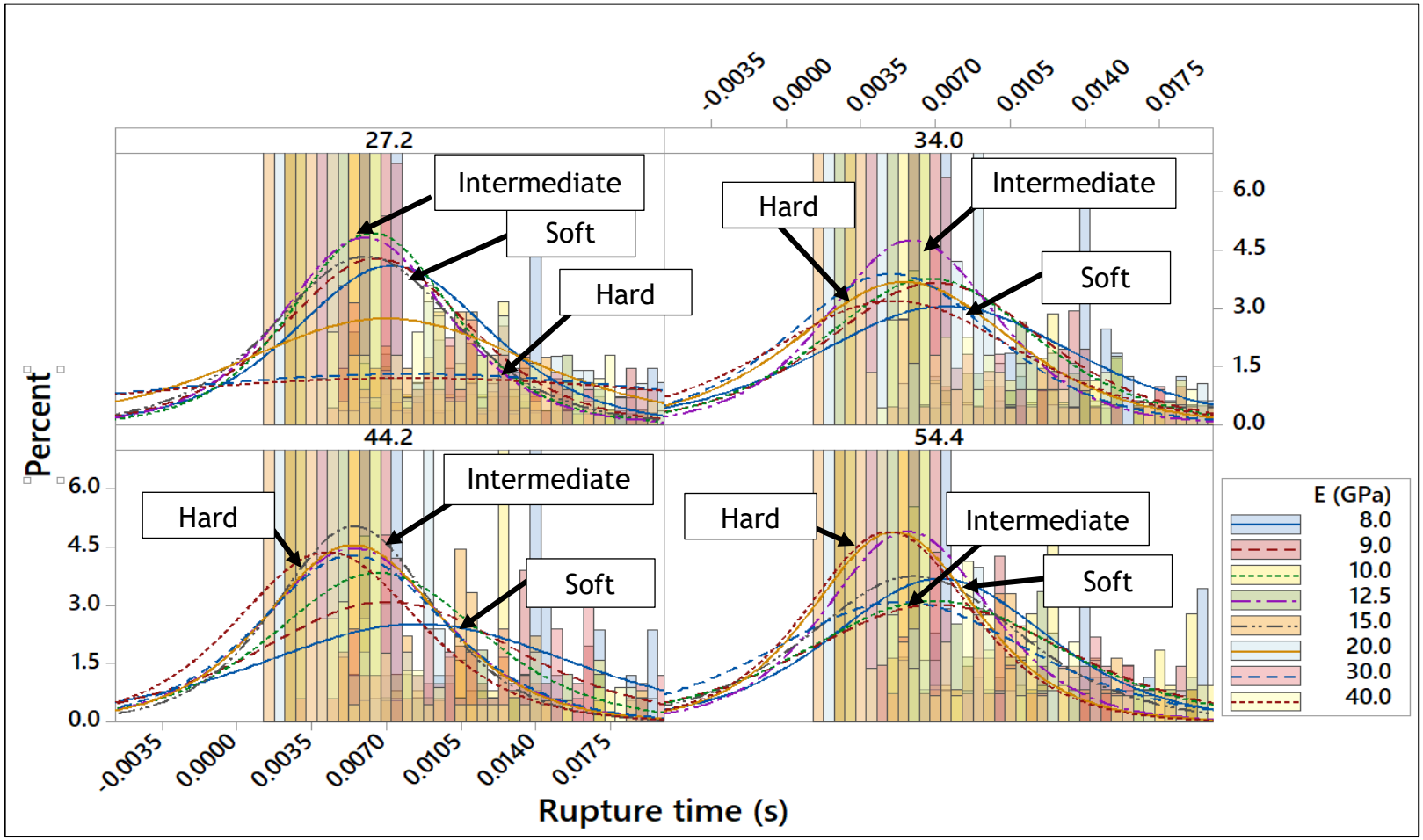

Figure 6.18. Binning of the data points of the fracture rupture time for series of Young's modulus (E) for different tensile strength experiments. Binning interval for a single column is 0.0005s. Curves represent logistic distribution probability density functions. The results show the same non-linear behaviour as for the area experiments in Chapter 4. All of the tensile strength experiments show bimodal behaviour where mean first shifts closer to 0 and then shifts away from 0 when progressively increasing Young's modulus. The turning point Young's modulus value increases with the growing tensile strength of the rock. The probability distribution curve peaks become higher and arms lighter with the increase in the tensile strength, meaning a decrease in the abundance of the large fracture area data points.

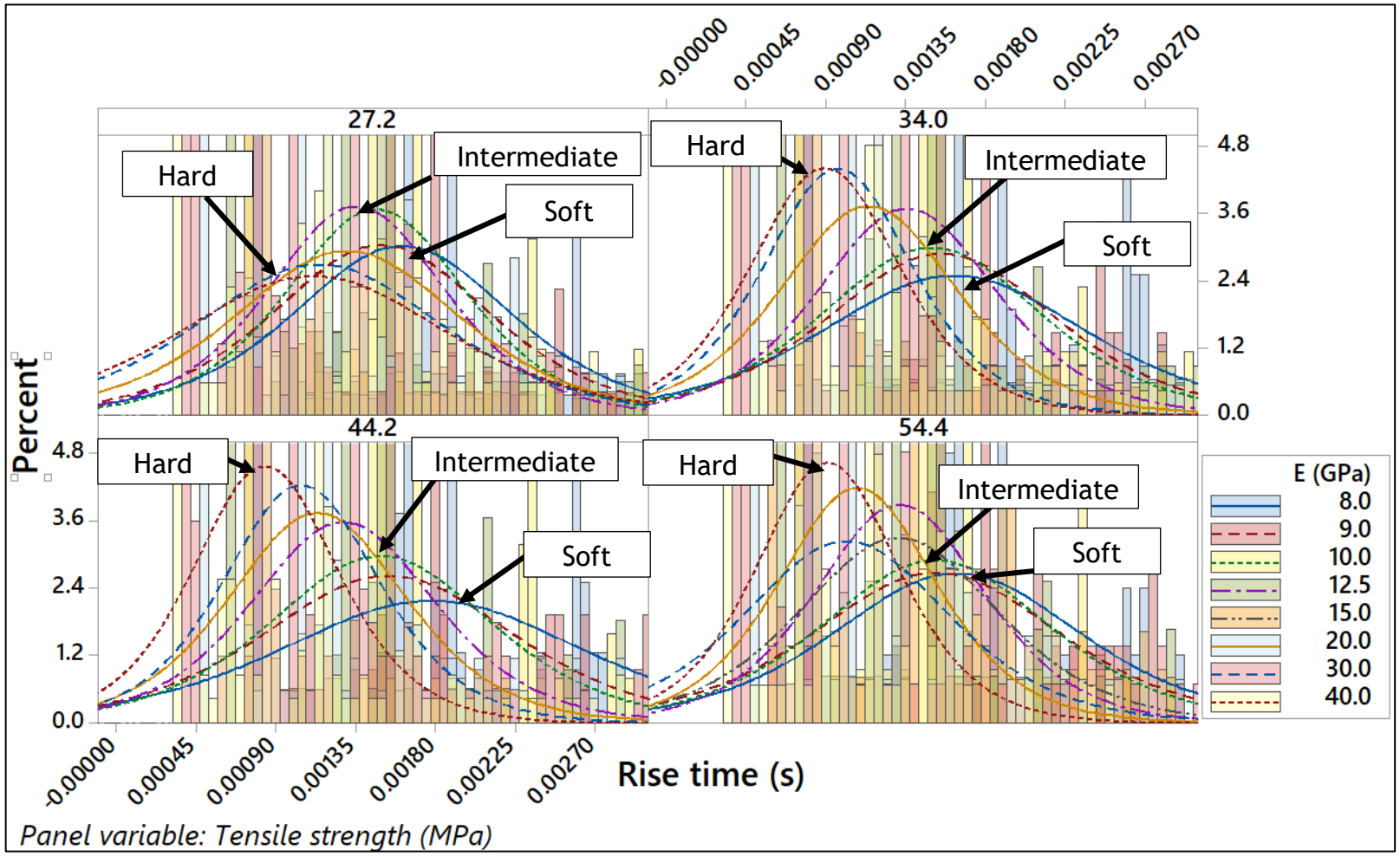

Figure 6.19. Binning of the data points of the fracture rise time for series of Young's modulus (E) for different tensile strength experiments. Binning interval for a single column is 5×10^{-6}s. Curves represent logistic distribution probability density functions. Rise time parameter shows non-linear behaviour for the smallest tensile strength value, which becomes progressively more linear as the tensile strength of the rock is increased.

A calculation for the rise time parameter, which accounts for the lengths of the slope in the ramp-shaped source time function, is more complex (Fig. 6.19).
The rise time (as expected) is an order of magnitude lower than the rupture time. The data probability distribution curves are showing non-linear behaviour for the smallest breaking strength experiments as the data peaks initially become higher and then again drop with progressive increase in Young's modulus. This means that for the intermediate Young's modulus values (10-12.5 GPa), there is a drop in the abundance of the larger rise time values. There is, however, a steady tendency for the rise time to decrease with the increase of Young's modulus. As the breaking strength of the rock is increased, the probability density function curve evolution becomes more linear as, with the increase in Young's modulus, the peaks of the curves become higher and move towards 0 while the arms of the function become lighter. For the highest breaking strength experiment data, there is a tendency for the soft rocks (8-10 GPa) to produce almost identical distribution curves. Similar behaviour was observed in the fracture geometry analysis data sets presented in Section 4.2.4.
The second parameter responsible for the parametrization of the ramp function is the amount of total displacement at the observation point. For this purpose, we are looking at an observation point that is located on the surface diagonally relative to the simulation box midpoint projection on the surface. Figure 6.20 presents the displacement data for the P wave while Figure 6.21 – for the S wave.

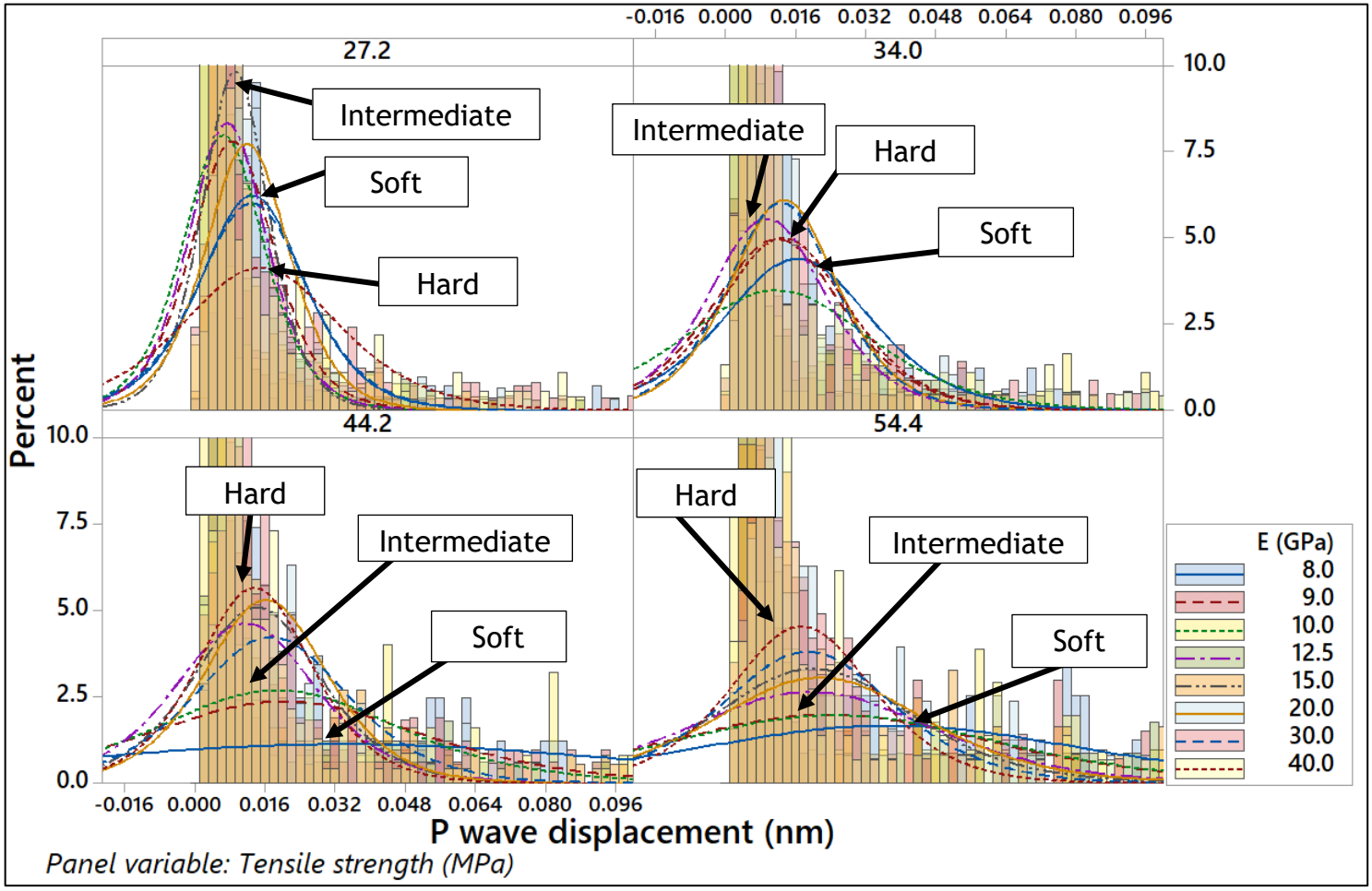

Figure 6.20. Binning of the data points of the observed displacement due to P waves for series of Young's modulus (E) for different tensile strength experiments. Binning interval for a single column is 0.002 µm. Experiments with the lowest tensile strength show bimodal behaviour where, while increasing Young's modulus, peaks of the probability density functions first move closer to 0 and get higher until 15 GPa value, after which the trend reverses. Increasing the tensile strength of the rock causes peaks for all Young's modulus values to become lower and move rightwards along the x axis. The amount of transformation is dependent upon Young's modulus where low E values are affected by it the most.

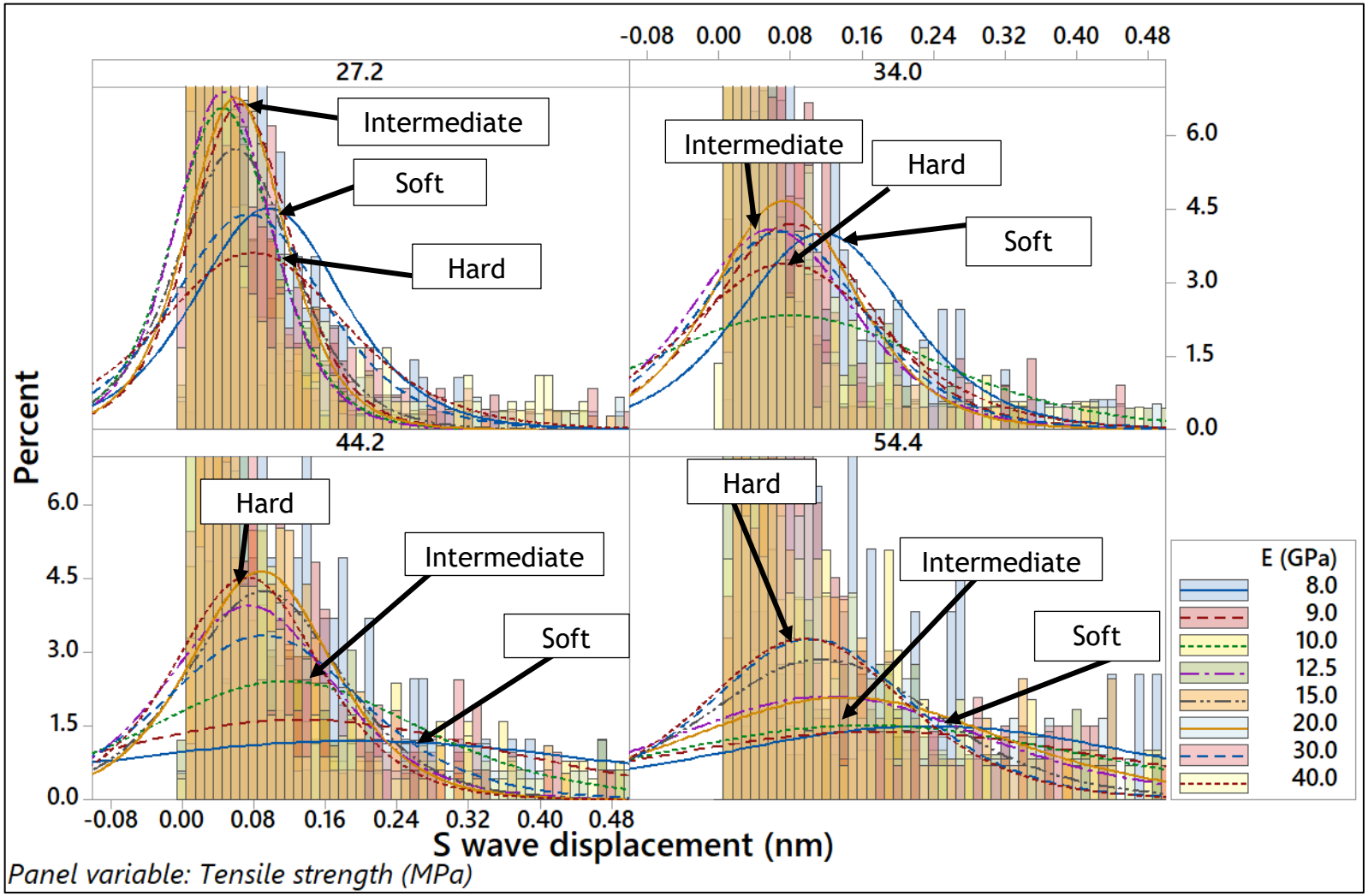

Figure 6.21. Binning of the data points of the observed displacement due to S waves for series of Young's modulus (E) for different tensile strength experiments. Binning interval for a single column is 0.01 µm. Data shows a very similar dynamic trend to P wave data in Figure 6.20. S wave displacement is an order of magnitude higher.

The total displacement at the observation point is highly dependent upon the Young's modulus and breaking strength of the rock. For the low breaking strength experiments, there is a clear nonlinear trend as a function of increasing Young's modulus. The probability density curves become higher and move towards zero in the initial stages, meaning that there is a decrease in the abundance of the events with larger times of seismic response. This can be seen up to a Young's modulus of 15 GPa, past which the trend reverses to the point where the 40 GPa Young's modulus curve location and shape are similar to the 8 GPa Young's modulus curve. Increasing the breaking strength of the rock causes peaks of all Young's modulus value experiments to become lower and for them to move further towards the right hand side along the x axis meaning that there is a great increase in the longer duration response events. This occurs at different rates where the probability distribution curve transformation of the low Young's modulus values is most noticeable, while the distribution of the high Young's modulus experiment results is affected the least. Progressive increase in the breaking strength of the rock causes the dynamics to evolve to the stage where there is no "reverse" trend point with higher Young's moduli. At 55.4 MPa mean tensile strength experiments, a clear trend can be seen where an increase in Young's modulus causes distribution peaks to move closer to zero and become higher in an almost linear fashion.

Obtaining both the duration and amount of total displacement at the observation point allows to calculate for the final component – the velocity of the displacement (Figure. 6.22, 6.23). That would represent the height of the ramp velocigram function.

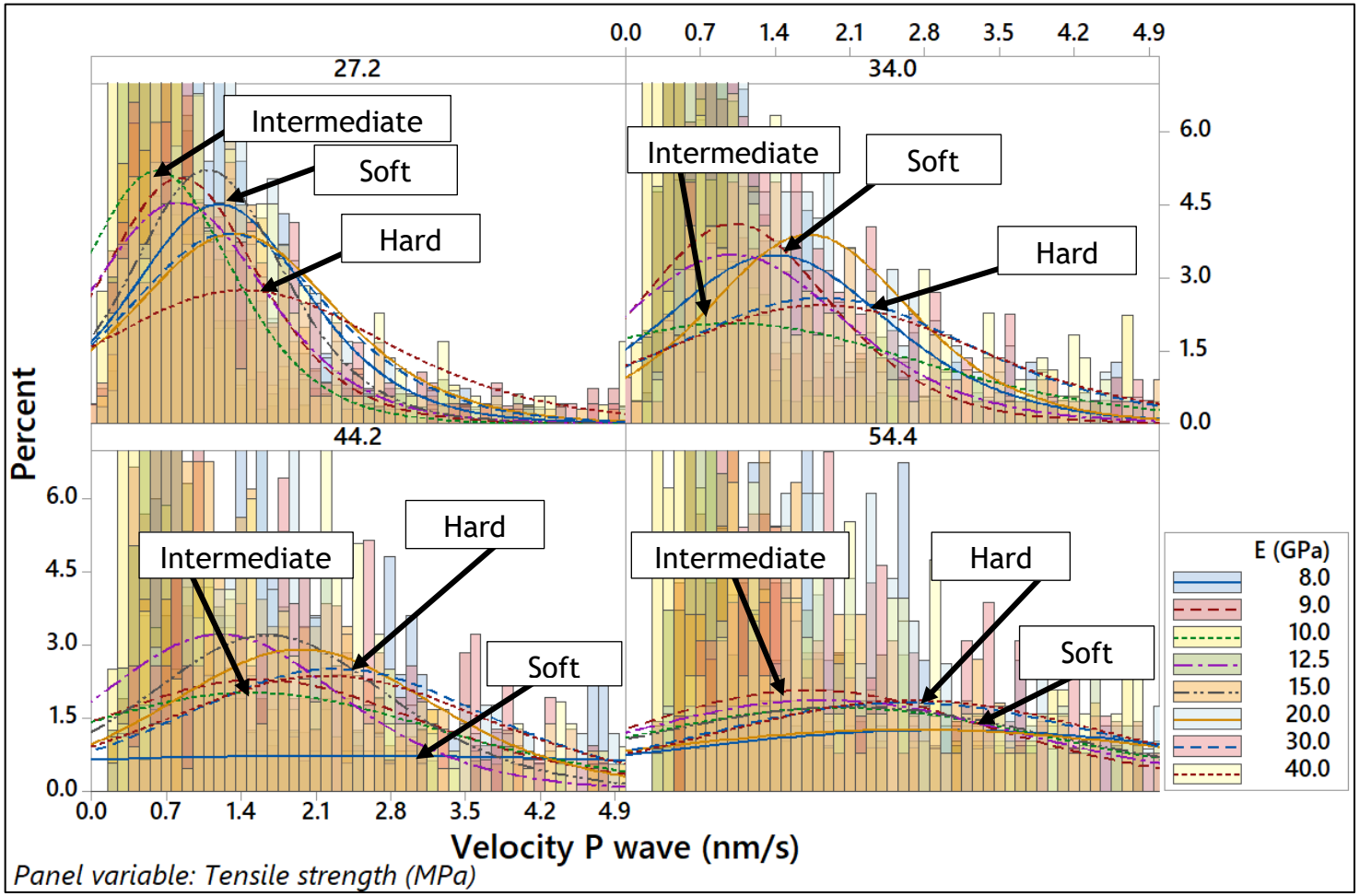

Figure 6.22. Binning of the data points of the observed displacement velocity due to P waves for series of Young's modulus (E) for different tensile strength experiments. Binning interval for a single column is 0.1 µm/s. A similar dynamic can be seen as in Figure 6.20 where there is a bimodal trend for increasing Young's modulus values in experiments with smaller tensile strength and increase in tensile strength causes value peaks to become lower and move rightwards along the x axis. Low Young's modulus value results are affected by this the most while high E values are affected the least. It further causes all results to become more uniform, as can be seen in 54.4 MPa tensile strength experiment panel.

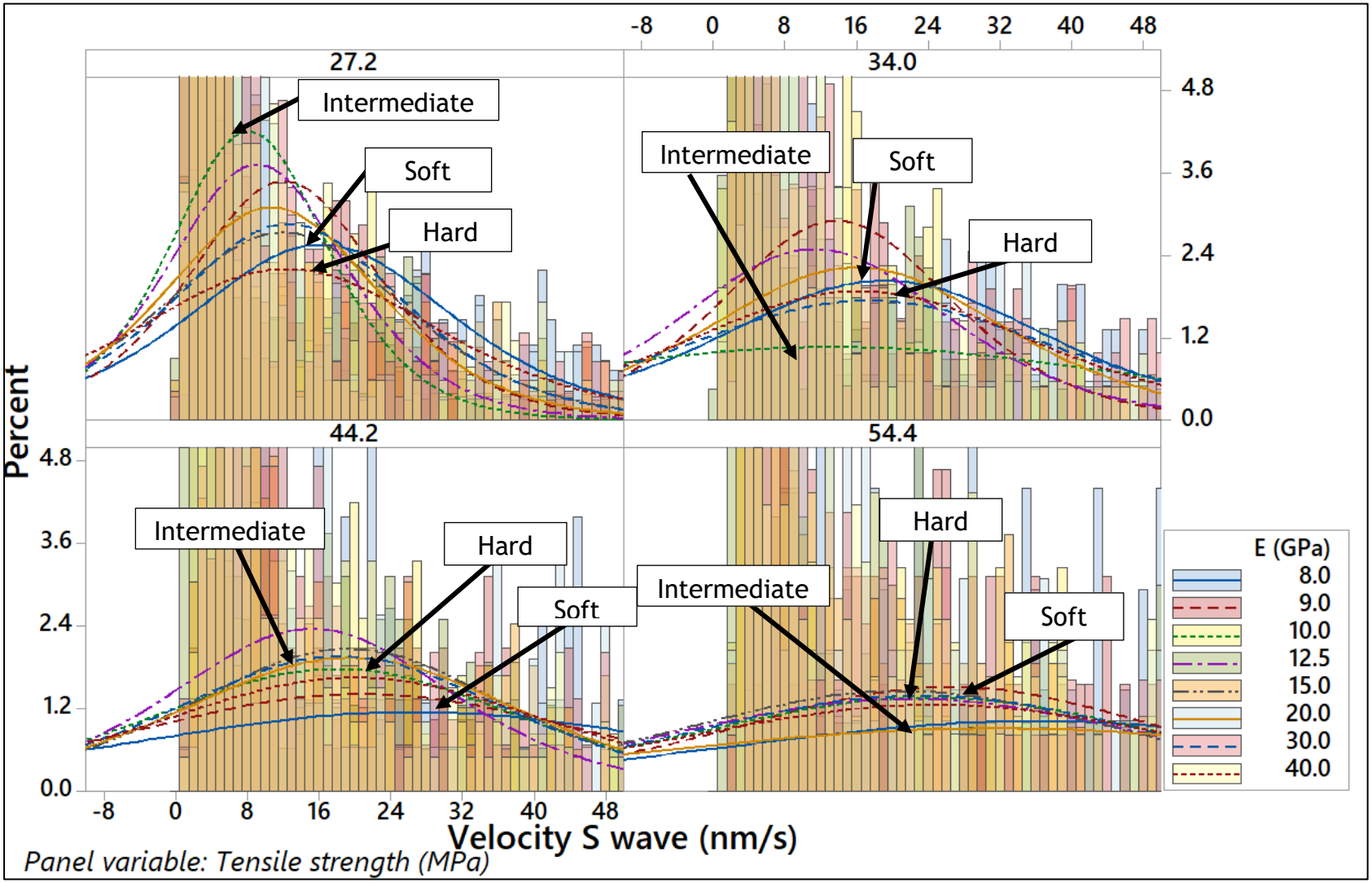

Figure 6.23. Binning of the data points of the observed displacement velocity due to S waves for series of Young's modulus (E) for different tensile strength experiments. Binning interval for a single column is 1 μm/s. The dynamic trend observable is analogue to the P wave trend described in Figure 6.22. The S wave velocity results are of a magnitude higher than those of P wave.

For the velocity of the displacement, the dynamics are similar to the one observed in the total displacement data. For the low breaking strength values an increase in Young's modulus values causes the probability density curves first to move closer to zero and to become higher. This can be seen to happen up to a Young's modulus of 10 GPa after which the trend reverses and the distribution peaks become lower and move further to the right hand side along the x axis. An increase in the breaking strength of the rock causes the peaks of all experiment distributions to become lower and to move towards the right hand side, which means that an increase in the tensile strength of the rock causes a higher velocity of the seismic pulses. Once the mean tensile strength of 55.4 MPa is reached, there appears to be very minimal variability between the different Young's modulus value distributions.

Lastly, as a part of the seismicity factor analysis, a MatLab module was created that is able to generate synthetic seismograms using variables derived from the Elle suite (Appendix D). Figure 6.24 presents synthetic seismograms for the fracturing event from the single experiment of 30 GPa Young's modulus and 44.2 MPa mean tensile strength, where the average values for moment magnitude and fracture geometry for the whole experiment have been used. The signal shows differentiated arrival times, amplitude and shape of the received signal depending on the location of the observation point and the angle between the fault surface and the travel route of the seismic ray towards the observation station.

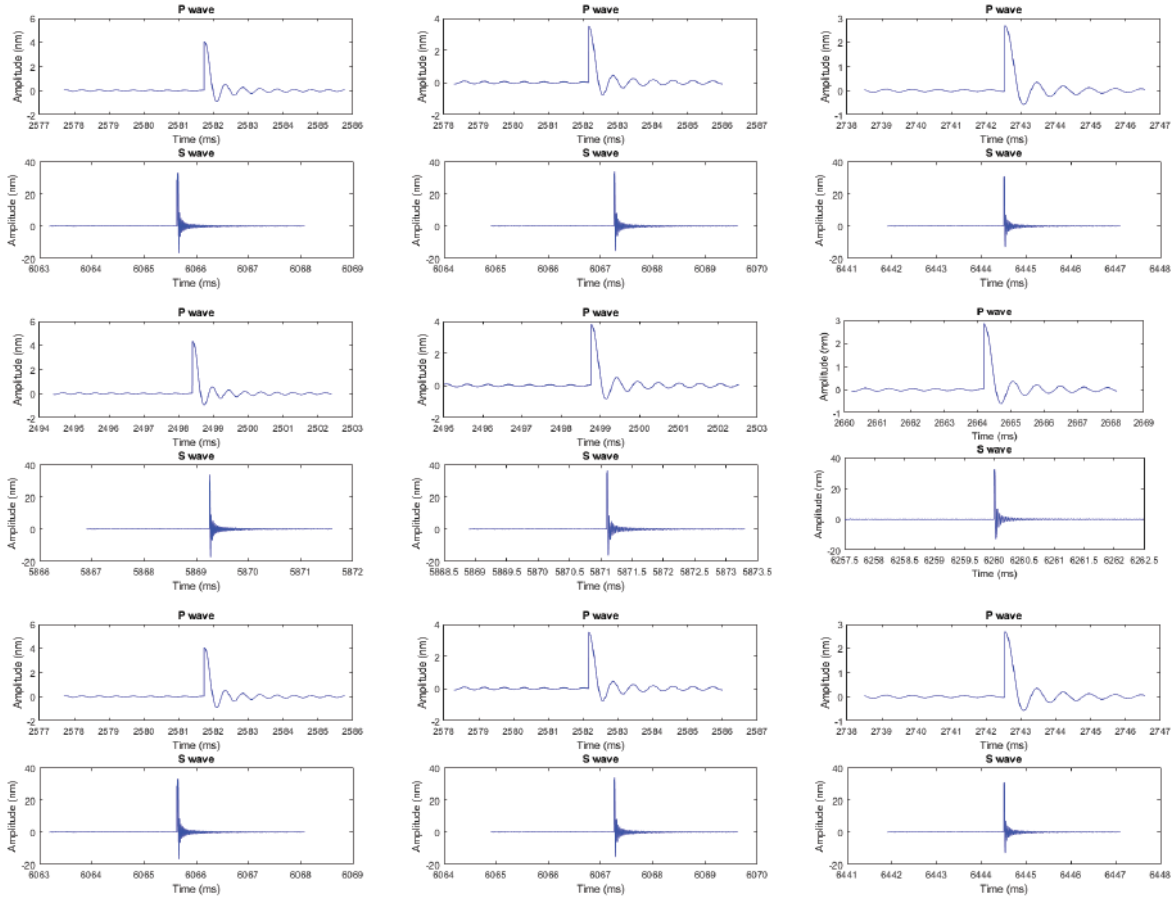

Figure 6.24. Synthetic seismograms for P and S waves produced for an average moment magnitude and geometry parameters derived from an experiment of a rock with 30 GPa Young's modulus and 44.2 MPa tensile strength. For this setup, observation grid is located on a surface, while the experiment is carried out at 3000m depth. The central observation point is located above the simulation box midpoint while the distance between every two observation points along the horizontal or vertical axis is 1000m. Signals show differentiated amplitude, arrival time and shape of the signal depending on the location of the observation point and its juxtapositioning relative to the fault surface.

6.5. Discussion

As shown in this chapter, the seismicity characterization depends on the multitude of variables at the source. Therefore it would be useful to use one single entity to bring together all the variables representing the source mechanism. As discussed in Chapter 2.4.2, the classic way of representing the source mechanism is via the moment source tensor. The nine-element matrix then can be further decomposed into three components: a double couple (DC), a compensated linear vector dipole (CLVD) and an isotropic (ISO).

To derive this moment tensor, components have been calculated for every fracturing event within all the experiments. Figures 6.25 to 6.27 show the boxplots representing the variability of the three moment tensor components depending on Young's modulus value and breaking strength.

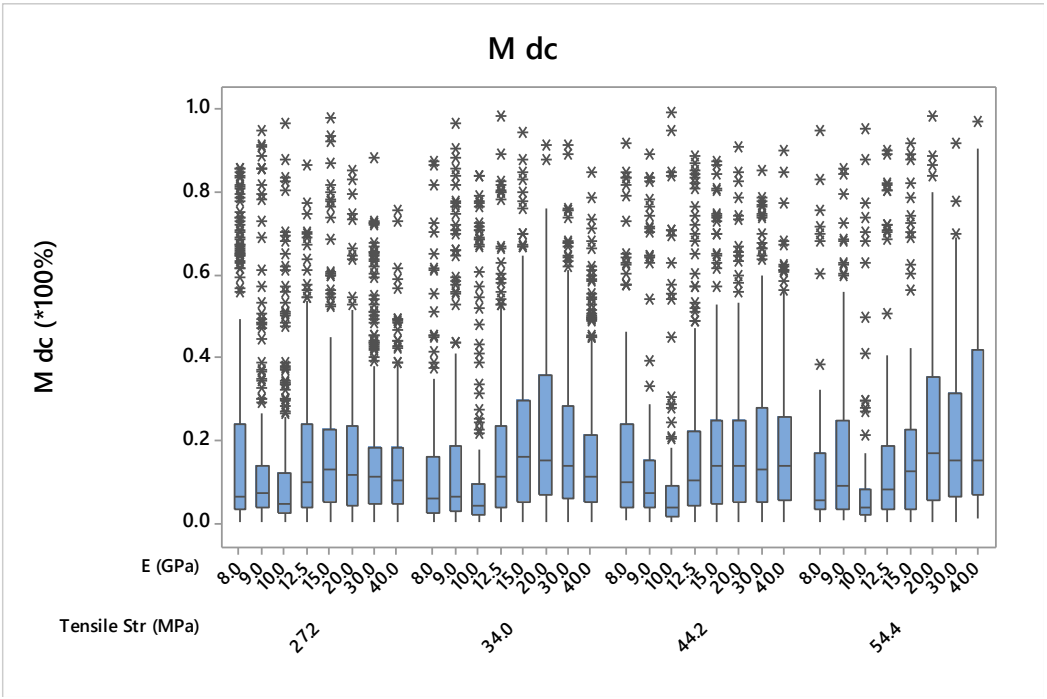

Figure 6.25. Boxplot representing the amount in the percentage of DC component for the varying Young's modulus and tensile strength values.

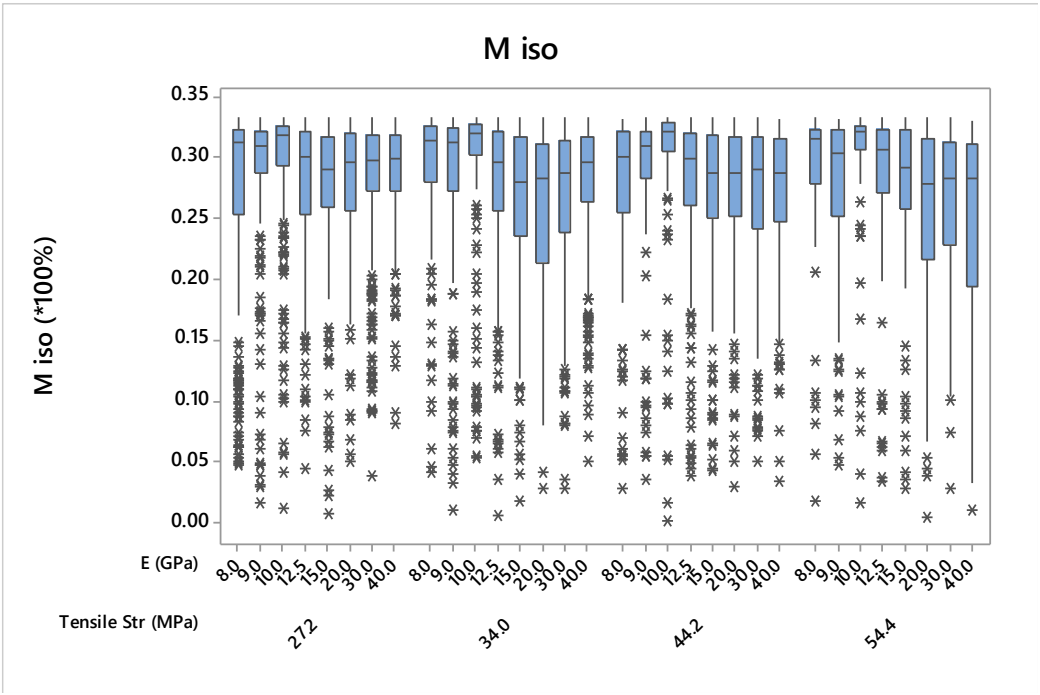

Figure 6.26. Boxplot representing the amount in the percentage of ISO component for the varying Young's modulus and tensile strength values.

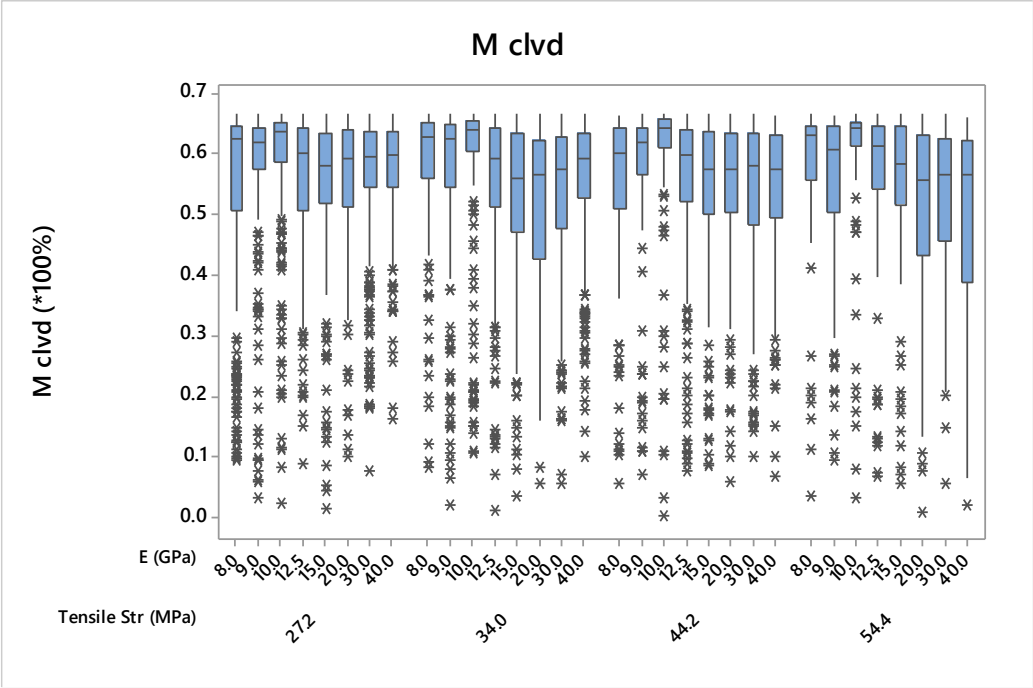

Figure 6.27. Boxplot representing the amount in the percentage of CLVD component for the varying Young's modulus and tensile strength values.

Figure 6.25 shows relatively low amounts for the DC component, which is representative of the amount of the slip along the fault surface. This is in consensus with the data shown in Chapter 4.2.4 and Figure 6.5 which show relatively small mode II components. In Section 6.3 it was observed that fracturing events with a tensile angle larger than 15º do not produce compressive radiation patterns that are typical of the strike-slip and DC fault displacements. The ratio of mode I versus mode II movement components should be above 3.73 as calculated from $ctan(15^o)$. Figure 6.5 shows the majority of the events to be below that value. The remainder of the moment tensor is then split between ISO and CLVD components. A pattern where there is a predominating CLVD component with a proportion of ISO is to be expected of the tensile fracture opening. Most of the movement is perpendicularly away from the fracture plane, which accounts for the large amount of CLVD. However, pure CLVD would assume that all the solid that displaced perpendicularly away from the fault plane would be compensated by the solid moving parallel towards the midpoint of the fracture plane. Since this is not the case, the volume change is compensated by the ISO component.

The next step is to look at how the changes in Young's modulus and breaking strength of the rock influence the proportional breakdown of the moment tensor components.

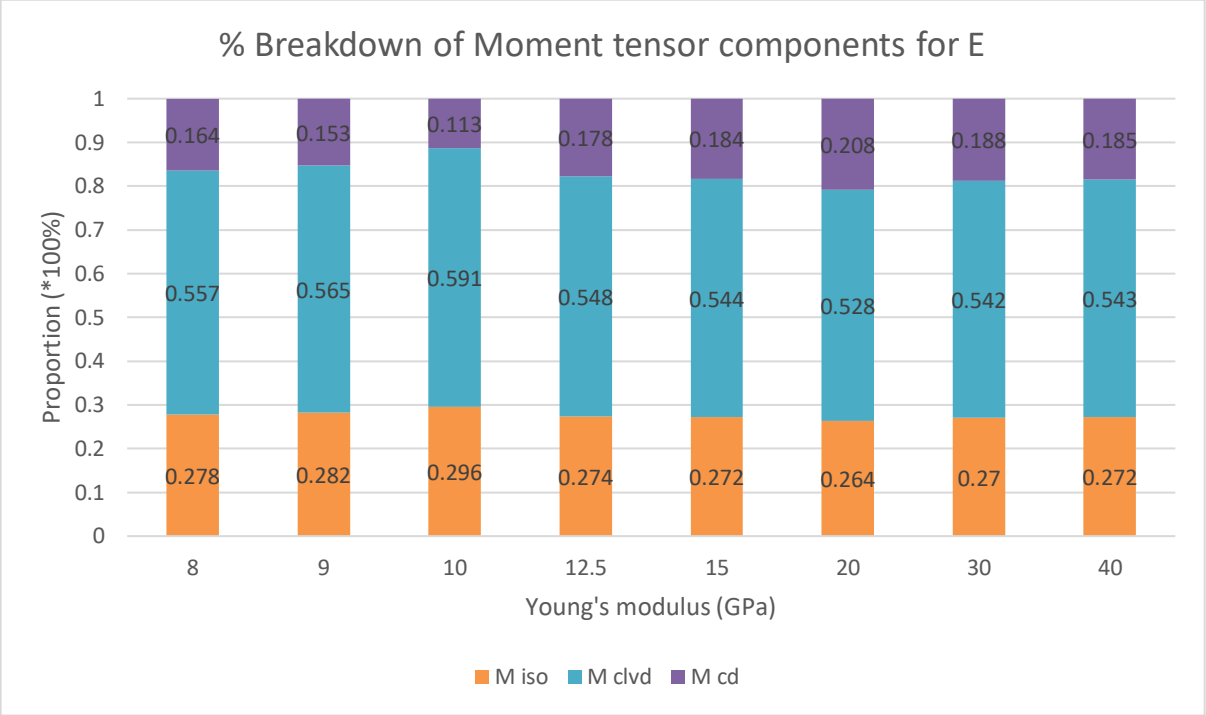

Figure 6.28. Proportional breakdown of the moment tensor components depending on Young's modulus.

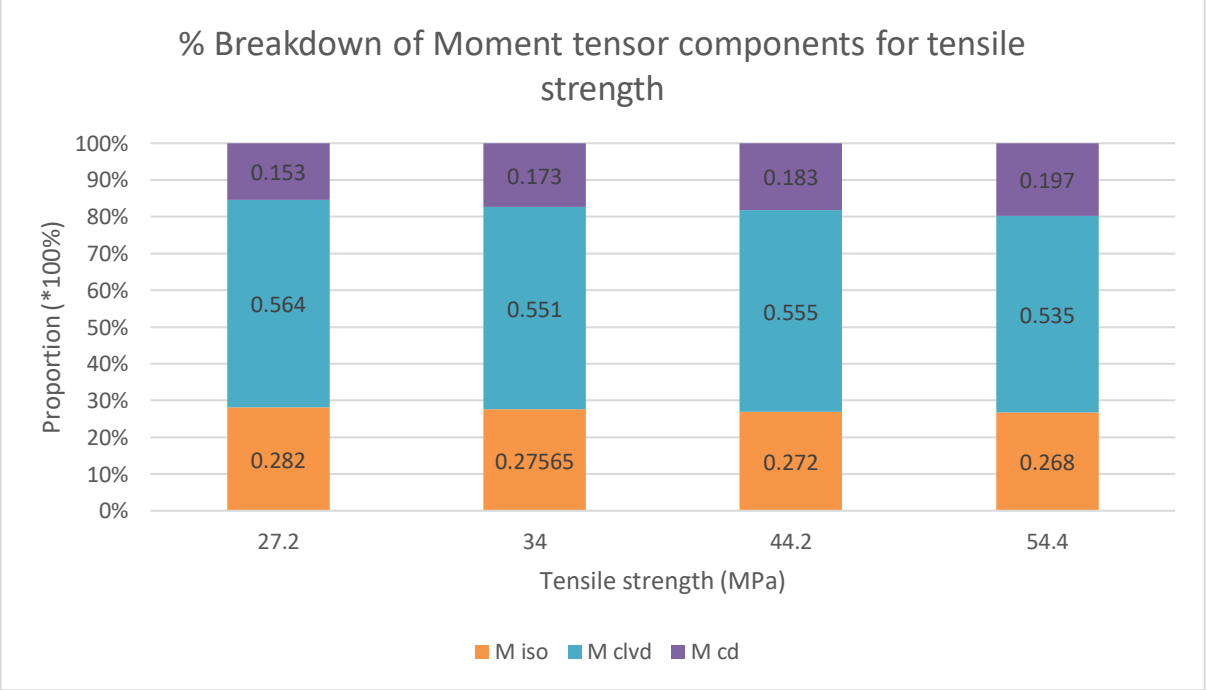

Figure 6.29. Proportional breakdown of the moment tensor components depending on the tensile strength of the rock.

Figures 6.28 and 6.29 show that there seems to be a variation in the DC component depending on the Young's modulus and breaking strength of the rock. To see if

the difference is statistically significant, the data mean variances were calculated and an ANOVA analysis was carried out.

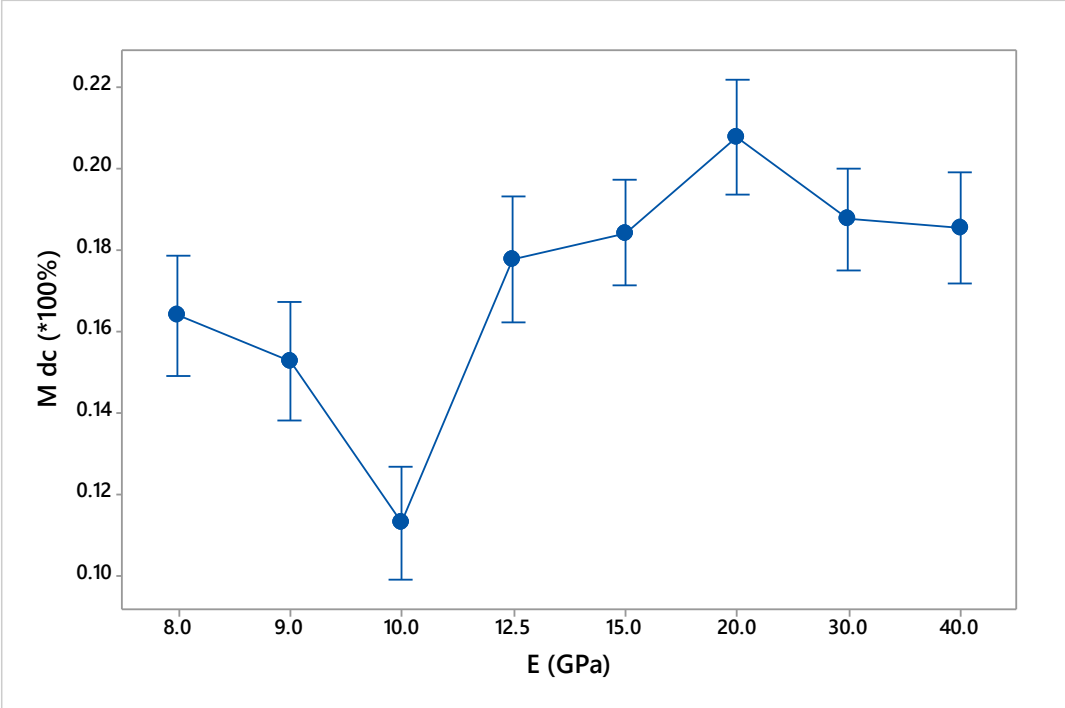

Figure 6.30. Mean variances for differentiated Young's modulus values. Data shows non-linear behaviour where there is drop in DC component for soft rocks when increasing Young's modulus value from 8 to 10 GPa with following values (12.5 to 40 GPa) showing relatively uniform behaviour and higher DC component than the soft rock.

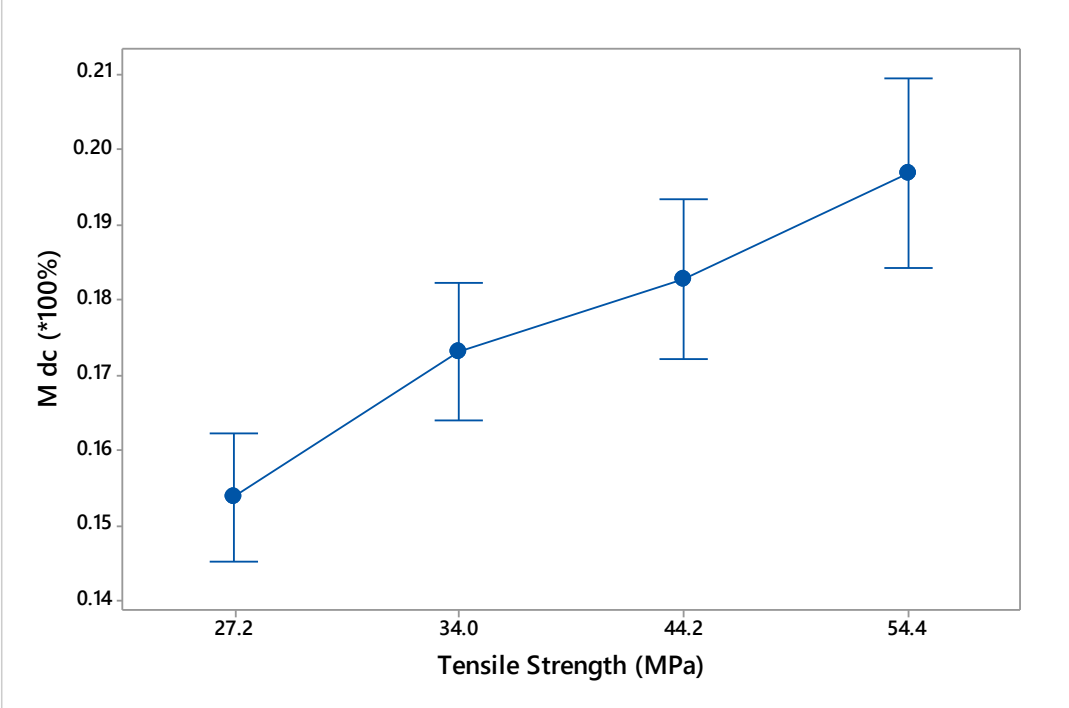

Figure 6.31 Mean variances for differentiated tensile strength values. Data shows an almost linear increase in the presence of the DC component with the increase in the tensile strength of the rock.

Figures 6.30 and 6.31 show the calculated variances for the means for Young's modulus and breaking strength of the rock. From the visual analysis, it can be seen that the increase in Young's modulus first creates a decrease in the DC component (8 to 10 GPa) and then the behaviour changes rapidly and a further rise in Young's modulus provides a relatively high DC component with very minor changes (12.5 to 40 GPa).

ANOVA analysis provided P-values of 0.0 for both variables indicating that they have a statistically significant impact on the proportion of DC element in the generated moment tensor.

6.6. Conclusions

Several important conclusions have been made throughout the observations from the experiments described in this chapter.

Looking at the relationships between the stages of the experiment, the distance from the injection point and the mode of the displacement it has been concluded that:

- The greatest moment magnitude values can be observed during the phase of the most active fracturing (time-step 500-2000, 8-30 hours) and tend to decrease towards the later phases of the model evolution;
- There is no apparent correlation between the mode of fracturing and stage of the experiment when the fracturing event is occurring;
- Fracturing event's occurrence distance from the injection point has no significant effect on the moment magnitude or mode of fracturing.

Special attention has been paid to the aseismic aspect of the fracturing experiment as fracture wall displacement and movement relative to the opposing sides of the fracture plane can happen even when there is no active fracture propagation. There is a limitation to this model due to its quasi-static nature that prevents recording which segments were moving at the same time throughout a single time step. This prevents direct moment magnitude calculation as the area parameter is unknown. However, without that, the displacement data shows a behaviour, which in its trend is similar to the fracturing moment magnitude data. There is an increase in the average displacement in the time steps 500-2000 with the subsequent drop. It can be concluded that aseismic activity fault movement

is an important part of the hydrofracturing process along the seismic component and provides a significant portion of the seismic disturbance in the surrounding area.

The characteristics of the received seismic signal are highly dependent upon the geometries of the fault and displacement vectors. In this Chapter, it has been shown that changes in Young's modulus of the rock cause statistically significant alterations in the dip angle of the fractures created as well as the tensile angle of the opening fractures. Similarly to conclusions in Chapter 4, we can see that there are two different trends and responsible mechanisms present.

The radiation pattern analysis shows that there is little variability for the values and characteristics for the radiation patterns calculated using the average fault geometry parameters. However, it is established that little to no compressional P wave element can be seen for the faults, which have tensile angles exceeding 15° (Kwiatec and Ben-Zion, 2013). The simulations show that once again there are two regimes present with almost no events having tensile angles below 15° for soft rocks with Young's modulus up to 10 GPa, and a rapid increase in them for rocks with larger Young's modulus values.

The same division in two different fracture development mechanisms has an effect on the characteristics of the observed signal such as duration on the rupture time and rise time of the source time function, total displacement and displacement velocities of the received P and S wave signals. A Young's modulus of 10 GPa is showing to be the turning point for the switch in dynamics. An increase in the breaking strength of the rock causes for the drop-in variability of the signal parameters for the soft (8-10 GPa) rocks. This is further represented by the synthetic seismogram module, which was developed to specifically work with the ELLE package. The received signal amplitude and initiation time for the same fracturing event varies depending on the observation point's location relative to the fracture orientation.

The best way to describe the seismic signal source is through the moment tensor term. It was possible to decompose it into three main constituents. Special interest was paid to the double couple (DC) element of it, which represents the amount of mode II component to the relative fracture wall displacement. It can be concluded that the a variation of the Young's modulus repeatedly shows non-linear behaviour, where there is a drop in the DC component for values up to 10

GPa, which is followed by a rapid increase for the following, higher Young's modulus values. A breaking strength increase shows a predictable increase in the shear component of the seismic tensor as the rock is harder to fracture to produce mode I fractures.

It can be concluded that the observation and results shown in this section prove that a Young's modulus change provides statistically significant variability to the geometry of the fault and from that to the characteristics of the received seismic signal. It also provides more evidence showing that there are two mechanisms of fracture propagation depending on Young's modulus. As previously discussed in Chapter 4, the switching point between the two regimes is 10 GPa, which produces a visible change in the observed seismic signals, which are discussed in this Chapter.

7. Conclusions

In this thesis fracture dynamics associated with hydrofracturing and the analysis of the generated microseismic signals were studied. The work was undertaken through numerical modelling, physical experiments in a vertically orientated Hele-Shaw cell and image analysis techniques. Nearly 800 numerical simulations have been carried out and more than 50 Hele-Shaw experiments were done to acquire all the data. In this chapter, the answers to the research questions raised in Chapter 1.4 are presented and a general conclusion that can be drawn from this work is summarized.

- What are the dynamics of the solid and fluid phases in the system during hydrofracturing?

Hydrofracturing is a highly, temporally and spatially, dynamic process that depends upon the mechanical properties of the solid material. All hydrofracturing experiments show the same overall dynamic where, after an initial fluid pressure injection at the point source the system eventually reaches saturation and equilibrium state. This is observed in Chapter 4.1.1 where all the experiments have an active fracturing stage, but eventually, despite fluid still being introduced to the system, active fracturing stops and fluid pressure gradient changes in the system cease. Simulations show that hydrofracturing during fluid injection develops in 4 distinct stages.

- Which mechanical rock properties, natural conditions and anthropologically controlled factors have the largest effect on the characteristics of the developed fracture networks?

Simulations were carried out with numerous properties varied throughout them: breaking strength of the rock, the height of the overburden rock column, injected fluid pressure, Young's modulus. It has been shown that the largest variability in the hydrofracturing dynamics is introduced by the alteration of the Young's modulus and, to a lesser extent, the breaking strength of the rock.

- How do the fracture network geometries change in response to alteration of the before-mentioned variables?

An increase in Young's modulus leads to a non-monotonic change in the fracture area and aperture. In cases when the fractured rock is soft, fracturing occurs due to a critical tensile strength or cohesion being exceeded. Changes in the stress at the crack tip as a function of the Young's modulus is then governed by the change in the fracture aperture and the fracture tip is constantly under extension. When the rock is hard, the fracture aperture is small and constant, and the fracture length becomes the key driver of the stress change. The fracture tip is under compression and fracturing is driven strongly by stress intensification at the tip, causing fractures to propagate in a more shear like failure.

- How does the stress state evolve in the system during hydrofracturing?

Both, the numerical and Hele-Shaw experiments show that a compaction wave is created on both sides of the propagating hydrofracture expressed through an increase in horizontal stress. This effect is more pronounced in the soft rock. In the area in front of the propagating hydrofracture, hard rocks show the compaction regime, while soft rocks have an area of negative horizontal stress, which is a favourable condition for the creation of tensile fracture. Further, Hele-Shaw cell experiment analysis shows negative horizontal strain in the area in front of the fracture tip, which corresponds to the numerical simulation solution. This further supports the finding that there are different fracture propagation mechanisms for rocks depending on the Young's modulus value.
Hele-Shaw experiments show that displacements around the main fracture tip cause non-uniform shearing disturbances throughout the system, which contribute to a multitude of minor mode II events and create a network of weakness planes surrounding the main fracture channel.

- What are the dynamics of a single propagating fracture?

As already discussed, numerical models show that all hydrofractures have multiple stages. Hele-Shaw cell experiments then allowed to look at the dynamics in more detail. Several stages of fracture propagation have been observed in detail:

1) Initial pore pressure increase in the area surrounding the fluid injection source and a local drop in the effective stress;
2) Initial opening of the fracture has a relatively high isotropic component, however, the fracture aligns with the orientation of the largest principal stress relatively fast. The first fracturing events occur rapidly throughout the zone where the fluid seeped to and decreased effective stress prior to the fracture opening;
3) Once the fracture has developed into a linear orientation, fracture tip propagation of the main channel happens in several stages: 1) fracture tip opening until it is halted by a compacted region, 2) fracture tip inflation via lateral movement, which is typically unsymmetrical in proportions regarding the amount of displacement in both lateral directions, 3) fracture tip's further propagation by exploiting previously created planes of weakness.

- Can we quantify possible fracture network geometries from the input parameters?

Analysis of the Hele-Shaw experiment data shows that the area of the main fracture channel can be estimated from knowing the height of the overburden column, the amount of overpressure and duration of the fluid injection period with a certain degree of uncertainty (R-squared value of 0.68). The amount of uncertainty can be decreased by knowing either the time it takes for active fracturing to initiate or the number of branching structures to the main channel that are created. The R-squared value can then be increased up to 0.84.

- Can we observe any patterns in the generated seismicity depending on the characteristics of the hydrofracturing operation?

The received seismic signal is highly dependent upon the geometry of the fault. It has been shown that having two fracture propagation mechanisms due to varying Young's modulus results in a non-linear response in the seismic signal. Changes in Young's modulus produce a bimodal distribution of the moment magnitude. Increase in Young's modulus up to 10 GPa causes for the average moment magnitude to drop. When the Young's modulus is increased to more than 10 GPa,

there is a subsequent growth in the average moment magnitude of the fracturing events. Changes in Young's modulus further have an effect on the radiation pattern value and properties of the received signal, such as rupture and rise time, the total amount of displacement and displacement velocity.

This thesis has presented a significant enhancement in the earlier developed hybrid numerical model Elle. The model uses coupling between solid and fluid phases to simulate hydrofracturing processes (Chapter 3.1). The analytical module for the model has been developed to specifically deal with the statistical parameter recording and analysis (Chapter 3.1.5, Appendix A). It has been tested against a variation in a number of crucial internal (mechanical properties of the rock, overburden rock column height variation) and external (variation in the injected fluid overpressure) factors (Chapter 4.1). The most significant changes in fracture geometries (total area, average aperture) and associated seismic parameters (mode of displacement and moment magnitude) have been associated with the alteration of the Young's modulus within the rock. It has been shown that increasing Young's modulus from 4.5 to 40 GPa results in a non-linear behaviour of the changes in the parameters described. This is due to different mechanisms of fracturing being present. For the soft rocks the fracture mechanism is driven by tensile failure of the rock and thus a fracture grows through an increase in aperture. For the hard rocks, the fracture tip is under stress and the fracture grows by stress intensification at the tip, which produces more shear-like, mode II typical behaviour.

Another aspect of the developed analytical module was the ability to analyse the seismicity parameters. The non-linear change in the fracture's aperture and area evolution due to Young's modulus increase provides a specific distribution of the moment magnitude values. This work has shown that if the Young's modulus and breaking strength of the rock are known, it is possible to calculate a probability density function for the moment magnitude responses. The rocks with Young's modulus of 10 GPa produce the smallest moment magnitude response while both decrease and increase of this Young's modulus value cause greater responses in seismic signal magnitude. This is an important discovery that can have a multitude of applications across the industrial sectors such as unconventional hydrocarbon

extraction and the geothermal energy sector, where induced seismicity is of a great public concern. Knowing the probability of causing a seismic event of larger magnitude than 0.5 is of a special interest in the UK as all the operations must be ceased if such event is recorded.

As an additional analytical module, a MatLab based package to illustrate radiation patterns (Appendix C) and generate synthetic seismograms (Appendix D) has been created to further enhance the possibilities of the given modelling package. It has been shown that alterations in Young's modulus have a statistically significant effect on the generated response in parameters used to calculate both radiation patterns and synthetic seismograms.

Lastly, in an effort to investigate into the possibility to reproduce the given numerical simulation experiments in the laboratory conditions, a number of vertically oriented Hele-Shaw cell experiments were conducted. These experiments produced a response which is similar to the one that was obtained for the soft rock numerical simulations. The fracture was propagating through an increase in aperture rather than fracture tip propagation. The stress regime created in the area surrounding the fracture was almost identical to the one in the numerical simulations for the soft rocks. The experiments also provided a very detailed insight into the dynamics of a single fracture tip rupture event and showed that it propagates through separate segments depending on the local strain distributions within the surrounding media. Further, besides the main mode I channel opening, there a swarm of minor mode II events was recorded in the surrounding media. This could account for the fact that a lot of microseismicity, which is picked up during hydrofracturing in industrial operations has almost pure mode II nature (Kamei et al., 2015).

7.1 Further works

Understanding the characteristics of the hydrofracturing process has a number of possible applications in the industry and academia. As previously mentioned, the ability to predict the seismicity generated from knowing the parameters of input has a great potential in the unconventional hydrocarbon industry as well as in the geothermal sectors. Due to the great amount of time required to develop the

numerical code and run the simulations, only the scenario with a centralized fluid injection point source has been tested. There are, however, a number of other scenarios that have a potential of developing:

1) Geothermal well stimulation would require a connected network of fractures in the basement rock to be created for the system to work. Therefore, one of the further model developments would be to test the possibility of connectivity by using a multitude of injection points to create a single fracture network. This could then be further developed by introducing a layer of reduced cohesion to test the scenario of fluid seeping into nearby fault structures.
2) An emerging industry of carbon capture and storage (CCS) is putting lots of effort into understanding the behaviour of CO_2 once it is injected into depleted hydrocarbon reservoirs. The experiments described here are using fluid properties that are characteristic of water. Seeing how the fluid with the properties that are close to "supercritical" would influence the solid phase has a great potential for research using this modelling setup.
3) This work has presented an ability to acquire a range of the seismic parameters from the fracturing events. However, the scenarios tested are all of the anthropogenic origins. As discussed in Chapter 1.3.1, most of the naturally induced mode I seismicity is associated with volcano-tectonic processes (Majer et al., 2007). There is potential, despite being quite ambitious, to attempt to model fracturing and generated seismicity in such areas using the Elle package.
4) A reference on the "beef-vein" generation research by Cobbold and Rodrigues (2007) has been done in Chapters 2.1.3 and 5.3. Beef veins can form due to overpressure in shallow, horizontally stressed basins. There is a possibility to fine-tune the model to conditions described in the research and see if it is possible to model both fracturing and generated seismicity dynamics for "beef-vein" forming processes.
5) There is potential to further develop Hele-Shaw cell experiments. One possibility is to use cell infill material that has higher internal friction to better mimic solid materials. Another scenario is having layered media in the cell

(e.g. layers of different diameter silica beads) to see how a fracture propagates when facing changes in layers.

Appendices

A Developed Elle code for calculating fracture mechanical and seismological dynamics.

Code is written in C++ language.

```
// set the baseline coordinates for all the particles
void Lattice::Initialize_Movement_Energy_Difference()
{
        int i;

        for (i = 0; i < numParticles; i++)    // look which particles are
in the
    // box
    {
                runParticle->xpos_prev = runParticle->xpos;
                runParticle->ypos_prev = runParticle->ypos;
                runParticle->eEl_prev = runParticle->eEl;

      runParticle = runParticle->nextP;
    }
}

// Calculate the displacement amount and azimuth of the displacement vector


void Lattice::Calculate_Movement_Energy_Difference()
{
        int i;

        for (i = 0; i < numParticles; i++)    // look which particles are
in the
    // box
    {
runParticle->posx_diff_time = runParticle->xpos_prev - runParticle->xpos;
runParticle->posy_diff_time = runParticle->ypos_prev - runParticle->ypos;
runParticle->total_move  =  sqrt((runParticle->posx_diff_time*runParticle-
>posx_diff_time)+(runParticle->posy_diff_time*runParticle-
>posy_diff_time));
runParticle->eEl_diff_time = runParticle->eEl_prev - runParticle->eEl;

if  ((runParticle->xpos_prev  ==  runParticle->xpos)  &&  (runParticle-
>ypos_prev > runParticle->ypos))// For cases when particle movement is
either horizontal or vertical
{       runParticle->move_angle = 3 * PI / 2; // 270 deg
                        }
else if ((runParticle->xpos_prev == runParticle->xpos) && (runParticle-
>ypos_prev < runParticle->ypos))
{
runParticle->move_angle = PI / 2; // 90 degrees
}
else if ((runParticle->xpos_prev > runParticle->xpos) && (runParticle-
>ypos_prev == runParticle->ypos))
{
runParticle->move_angle = 2 * PI; // 0 degrees
}
```

```
else if ((runParticle->xpos_prev < runParticle->xpos) && (runParticle-
>ypos_prev == runParticle->ypos))
{
runParticle->move_angle = PI; // 180 degrees
                        }
else if ((runParticle->xpos_prev > runParticle->xpos) && (runParticle-
>ypos_prev < runParticle->ypos))
// For all the other cases
{
runParticle->move_angle         =         atan         ((sqrt(runParticle-
>posx_diff_time*runParticle->posx_diff_time))     /     (sqrt(runParticle-
>posy_diff_time*runParticle->posy_diff_time)));       //90-180
runParticle->move_angle = PI - runParticle->move_angle;
}
else if ((runParticle->xpos_prev < runParticle->xpos) && (runParticle-
>ypos_prev < runParticle->ypos))
{
runParticle->move_angle         =         atan         ((sqrt(runParticle-
>posx_diff_time*runParticle->posx_diff_time))     /     (sqrt(runParticle-
>posy_diff_time*runParticle->posy_diff_time)));       //0-90
runParticle->move_angle = 0 + runParticle->move_angle;
}
else if ((runParticle->xpos_prev > runParticle->xpos) && (runParticle-
>ypos_prev > runParticle->ypos))
{
runParticle->move_angle         =         atan         ((sqrt(runParticle-
>posx_diff_time*runParticle->posx_diff_time))     /     (sqrt(runParticle-
>posy_diff_time*runParticle->posy_diff_time)));       //180-270
runParticle->move_angle = PI + runParticle->move_angle;
}
else if ((runParticle->xpos_prev < runParticle->xpos) && (runParticle-
>ypos_prev > runParticle->ypos))
{
runParticle->move_angle         =         atan         ((sqrt(runParticle-
>posx_diff_time*runParticle->posx_diff_time))     /     (sqrt(runParticle-
>posy_diff_time*runParticle->posy_diff_time)));       //270-360
runParticle->move_angle = 2 * PI - runParticle->move_angle;
}
else runParticle->move_angle = 0.0;



runParticle->xpos_prev = runParticle->xpos;
runParticle->ypos_prev = runParticle->ypos;
runParticle->eEl_prev = runParticle->eEl;

runParticle = runParticle->nextP;
}
}

// Calculate the shear and tensile displacement components relative to the
fault surface


void Lattice::Calculate_Seismic_Moment()
{
int i,j, ii, jj, k;

double mov, movx, movy, alpha, beta, phi, theta;

for (i = 0; i<8; i++)
        {
if (!fault[0]->fault_orientation[i][0])
```

```
        {
        ii = i-1;
        break;
        }
        }
for (i = 0; i<8; i++)
        {
if (!fault[1]->fault_orientation[i][0])
        {
        jj = i-1;
        break;
        }
        }

// Calculate for one wall of the fracture

if              ((fault[0]->frac_pos[0]+fault[0]->frac_pos[1])>(fault[1]-
>frac_pos[0]+fault[1]->frac_pos[1]))
{
movx = (fault[0]->xpos-fault[1]->xpos) - (fault[0]->frac_pos[0]-fault[1]-
>frac_pos[0]);
movy = (fault[0]->ypos-fault[1]->ypos) - (fault[0]->frac_pos[1]-fault[1]-
>frac_pos[1]);

mov = sqrt((movx*movx)+(movy*movy));

//fault[0]->fault_orientation[ii][0] this is the fault orientation, x is 0
and 1 is y
//for the equation then x is y etc.

alpha   =   atan   ((sqrt((fault[0]->fault_orientation[ii][0])   *(fault[0]-
>fault_orientation[ii][0])))              /              ((sqrt((fault[0]-
>fault_orientation[ii][1])*(fault[0]->fault_orientation[ii][1])))));
beta = (PI / 2) - alpha;

if (alpha<beta)
{

phi = atan ((sqrt(movy *movy)) / (sqrt(movx *movx)));
theta = (PI / 2) - beta - phi;

if (theta < 0)
{
phi = atan ((sqrt(movx *movx)) / (sqrt(movy *movy)));
theta = (PI / 2) - alpha - phi;
}
else
{
phi=phi;
theta=theta;
}
}
else if
(alpha>beta)
{
phi = atan ((sqrt(movx *movx)) / (sqrt(movy *movy)));
theta = (PI / 2) - beta - phi;
if (theta < 0)
{
phi = atan ((sqrt(movy *movy)) / (sqrt(movx *movx)));
theta = (PI / 2) - alpha - phi;
}
else
```

```
{
phi=phi;
theta=theta;
}
}
else
{
phi = PI / 4;
theta = 0;
}
fault[1]->movement_normal[jj]  =  fault[0]->movement_normal[ii]  =  cos
(theta) * mov;
fault[1]->movement_shear[jj]  = fault[0]->movement_shear[ii] = sin (theta)
* mov;
fault[1]->movement_vector_n[jj][0] = fault[0]->movement_vector_n[ii][0] =
cos (alpha) * fault[0]->movement_normal[ii];
fault[1]->movement_vector_n[jj][1] = fault[0]->movement_vector_n[ii][1] =
sin (alpha) * fault[0]->movement_normal[ii];
fault[1]->movement_vector_s[jj][0] = fault[0]->movement_vector_s[ii][0] =
sin (alpha) * fault[0]->movement_shear[ii];
fault[1]->movement_vector_s[jj][1] = fault[0]->movement_vector_s[ii][1] =
cos (alpha) * fault[0]->movement_shear[ii];
fault[1]->seismic_mode[jj]  =  fault[0]->seismic_mode[ii]  =  fault[0]-
>movement_shear[ii] / fault[0]->movement_normal[ii];

// Setup the "just broken" flags

fault[1]->just_broken = fault[0]->just_broken = fault[0]->just_broken + 1;
fault[1]->fractured = fault[0]->fractured = fault[0]->fractured + 1;
// %%%%%%%
}

// Calculate for second wall of the fracture

else
{
movx = (fault[1]->xpos-fault[0]->xpos) - (fault[1]->frac_pos[0]-fault[0]-
>frac_pos[0]);
movy = (fault[1]->ypos-fault[0]->ypos) - (fault[1]->frac_pos[1]-fault[0]-
>frac_pos[1]);

mov = sqrt((movx*movx) + (movy*movy));
alpha  =  atan  ((sqrt((fault[1]->fault_orientation[jj][0])  *(fault[1]-
>fault_orientation[jj][0])))            /            ((sqrt((fault[1]-
>fault_orientation[jj][1])*(fault[1]->fault_orientation[jj][1])))));
beta = (PI / 2) - alpha;
if (alpha<beta)
{
phi = atan ((sqrt(movy *movy)) / (sqrt(movx *movx)));
theta = (PI / 2) - beta - phi;
if (theta < 0)
{
phi = atan ((sqrt(movx *movx)) / (sqrt(movy *movy)));
theta = (PI / 2) - alpha - phi;
}
else
{
phi=phi;
=theta;
}
}
else if
(alpha>beta)
```

```
{
phi = atan ((sqrt(movx *movx)) / (sqrt(movy *movy)));
theta = (PI / 2) - beta - phi;
if (theta < 0)
{
phi = atan ((sqrt(movy *movy)) / (sqrt(movx *movx)));
theta = (PI / 2) - alpha - phi;
}
else
{
phi=phi;
theta=theta;
}
}
else
{
phi = PI / 4;
theta = 0;
}
fault[0]->movement_normal[ii]   =   fault[1]->movement_normal[jj]   =   cos
(theta) * mov;
fault[0]->movement_shear[ii] = fault[1]->movement_shear[jj] = sin (theta)
* mov;
fault[0]->movement_vector_n[ii][0] = fault[1]->movement_vector_n[jj][0] =
cos (alpha) * fault[1]->movement_normal[jj];
fault[0]->movement_vector_n[ii][1] = fault[1]->movement_vector_n[jj][1] =
sin (alpha) * fault[1]->movement_normal[jj];
fault[0]->movement_vector_s[ii][0] = fault[1]->movement_vector_s[jj][0] =
sin (alpha) * fault[1]->movement_shear[jj];
fault[0]->movement_vector_s[ii][1] = fault[1]->movement_vector_s[jj][1] =
cos (alpha) * fault[1]->movement_shear[jj];
fault[0]->seismic_mode[ii]   =   fault[1]->seismic_mode[jj]   =   fault[1]-
>movement_shear[jj] / fault[1]->movement_normal[jj];

// Setup the "just broken" flag
fault[0]->just_broken = fault[1]->just_broken = fault[1]->just_broken + 1;
fault[1]->fractured = fault[0]->fractured = fault[0]->fractured + 1;
// %%
}
}


// Function set to calculate all seismicity associated parameters

void Lattice::Calculate_Moment_tensor(double pos_y, double depth)
{
        FILE *stat;
        FILE *stat2;
        FILE *stat3;
        FILE *stat4;
int n, mode_count, error, part_count, i, j, k, l, o, m, part_count_2;
double drop_1, drop_2, slope_1, slope_2, frequency, freq_value, interval_1,
interval_2,   inj_distance,   barrier_1_s,   barrier_2_s,   barrier_1_p,
barrier_2_p, time_ratio, fc, rise_t_p, rise_t_s, pos_x, pos_z, V_us, V_up,
omega_0_s, omega_0_p, omega_s, omega_p, length, length_f, real_length,
surface_dist, delta, Up, Us, thet, r1, r2, r3, vect_thet_1, vect_thet_2,
vect_thet_3, vect_phi_1, vect_phi_2, rad_pat_p, rad_pat_s, rad_pat_s_1,
rad_pat_s_2, s, M_max, M_max_p, M_max_s, distance, fdistance, x_distance2,
y_distance2, mode_total, mode_final, mode_fcount, seismic_moment, slip,
average_slip,   elastic,   moment_magn,   f_error,   real_area,   theta,
average_density, average_density_f, part_count_f, ave_x, ave_y, x_min,
y_min,  x_max,  y_max,  dif_x,  dif_y,  total_x,  alpha,  beta,  lame1,
total_young, total_poisson, ave_poisson, ave_young, my, total_y, area, a,
```

```
b, c, d, g, f, slope, xy, x2, y_angle, x_angle, count_f, area_f, u_tot,
u_totx, u_toty, u_t, u_tx, u_ty, u_tot_final, u_totx_final, u_toty_final,
u_t_final, u_tx_final, u_ty_final, m11, m12, m13, m21, m22, m23, m31, m32,
m33, Vs, Vp, Vr, ceta, dist_x, dist_y, dist, t_ini_swave, t_ini_pwave,
t_diff_swave, t_diff_pwave, t_end_swave, t_end_pwave, lambda_s, phi,
phi_s, s11, s22, s33, s12, s13, s23, nx, ny, nz, vx, vy, vz, Mt[3][3],
V[3][3], v[3], Ev1, Ev2, Ev3, trace, M_iso, M_clvd, M_dc, epsilone;

// Open/create statistical output files

 stat = fopen ("moment_tensor.txt", "a");
 stat2 = fopen ("radiation_pattern.txt", "a");
 stat3 = fopen ("displacement.txt", "a");
 stat4 = fopen ("fft.txt", "a");

// Assigning default values to all the variables

// !!!!  Variables are present in two columns to save space in word
document. To use in C each variable has to be presented in its own row !!!!

mode_count = 0;         // number of broken bonds
mode_total = 0;         // total of shear vs normal movement
mode_fcount = 0;        // printable value of broken bonds (not int)
slip = 0;               // total movement of all particles that had bonds
broken
elastic = 0;    // total of elastic energy released
error = 0;                                u_tot = 0;
f_error = 0;                              u_totx = 0;
length = 0;                               u_toty = 0;
length_f = 0;                             u_tx = 0;
real_length = 0;                          u_ty = 0;
distance = 0;                             u_t_final = 0;
x_distance2 = 0;                          u_tot_final = 0;
y_distance2 = 0;                          u_totx_final = 0;
average_density = 0;                      u_toty_final = 0;
part_count = 0;                           u_tx_final = 0;
part_count_2 = 0;                         u_ty_final = 0;
part_count_f = 0;                         m11 = 0;
ave_x = 0;                                m12 = 0;
ave_y = 0;                                m13 = 0;
x_min = 0;                                m21 = 0;
y_min = 0;                                m22 = 0;
x_max = 0;                                m23 = 0;
y_max = 0;                                m31 = 0;
dif_x = 0;                                m32 = 0;
dif_y = 0;                                m33 = 0;
total_x = 0;                              total_young = 0;
total_y = 0;                              total_poisson = 0;
area = 0;                                 my = 0;
a = 0;                                    lame1 = 0;
b = 0;                                    ave_poisson = 0;
c = 0;                                    ave_young = 0;
d = 0;                                    alpha = 0;
g = 0;                                    beta = 0;
f = 0;                                    Vs = 0;
xy = 0;                                   Vp = 0;
slope = 0;                                Vr = 0;
x2 = 0;                                   ceta = 0;
y_angle = 0;                              dist_x = 0;
x_angle = 0;                              dist_y = 0;
count_f = 0;                              dist = 0;
area_f = 0;                               t_ini_swave = 0;
u_t = 0;                                  t_ini_pwave = 0;
```

```
t_diff_swave = 0;
t_diff_pwave = 0;
t_end_swave = 0;
t_end_pwave = 0;
theta = 0;
real_area = 0;
average_density_f = 0;
M_max = 0;
M_max_p = 0;
M_max_s = 0;
lambda_s = 0;
phi = 0;
phi_s = 0;
s11 = 0;
s22 = 0;
s33 = 0;
s12 = 0;
s13 = 0;
s23 = 0;
s = 0;
thet = 0;
r1 = 0;
r2 = 0;
r3 = 0;
vect_thet_1 = 0;
vect_thet_2 = 0;
vect_thet_3 = 0;
vect_phi_1 = 0;
vect_phi_2 = 0;
rad_pat_p = 0;
rad_pat_s = 0;
rad_pat_s_1 = 0;
rad_pat_s_2 = 0;
Up = 0;
Us = 0;
delta =0;
surface_dist =0;
omega_0_s = 0;
omega_0_p = 0;
omega_s = 0;
omega_p = 0;
V_us = 0;
V_up = 0;
fc = 0;
rise_t_p =0;
rise_t_s =0;
time_ratio =0;
barrier_1_s=0;
barrier_2_s=0;
barrier_1_p=0;
barrier_2_p=0;
inj_distance =0;
frequency =0;
freq_value=0;
interval_1=0;
interval_2=0;
drop_1=0;
drop_2=0;
slope_1=0;
slope_2=0;
```

```
runParticle = &refParticle;    // start

for (n = 0; n < numParticles; n++)    // look which particles are in the
    // box
{
if   (runParticle->mode_n   !=   -1   and   runParticle->just_broken   >0)
//just_broken is the counter to see if the particle was broken, made
positive Calculate_Seismic_Moment function, lines 15970 and 16047
{
//Calculate      seismic      moment      and      displacement      mode
```

```
mode_count++;
mode_total = mode_total + runParticle->mode_n;
slip = slip + (runParticle->total_move * (runParticle->real_radius * 2 *
particlex));
elastic = elastic + runParticle->eEl_diff_time;
total_young = total_young + (runParticle->young * 1000000 * 1000);
total_poisson = total_poisson + runParticle->poisson_ratio;
area   =   area   +   ((((runParticle->real_radius)*2)   *   ((runParticle-
>real_radius)*2)));
length = length + ((runParticle->radius)*2);
x_distance2 = (runParticle->xpos - 0.5) * (runParticle->xpos - 0.5);
y_distance2 = (runParticle->ypos - 0.2) * (runParticle->ypos - 0.2);
distance = distance + sqrt(x_distance2 + y_distance2);
// insert coresponding x and y divided by 100 positions of the injection
point
runParticle->just_frac = runParticle->just_frac + 1;
// return counter to 0 (default) value
```

```
}

else if (runParticle->mode_n = -1 and runParticle->just_broken >0) // to
see the number of particles which were broken but were ignored by the relax
function
{
error++;
runParticle->just_broken   =   runParticle->just_broken   -   runParticle-
>just_broken;
}
runParticle = runParticle->nextP;
}

 f_error = 0 + error;
 mode_fcount = mode_count + 0;
 mode_final = mode_total / mode_count; // average shear vs normal movement
 average_slip = slip / mode_count;
 ave_poisson = total_poisson / mode_count;
 ave_young = total_young / mode_count;
 area = area + 0;
 my = ave_young / (2.0 * ave_poisson + 2.0);
 seismic_moment = my * average_slip * area;
 moment_magn  =  (log10((seismic_moment  *  10000000))  /  1.5)  -  10.73;
//converts seismic moment from joules to dynes
 fdistance = distance / mode_count;
 length_f = length + 0;

  for (i = 0; i < numParticles; i++)  // look which particles are in the
    // box
{
if (runParticle->just_broken >0)
                                {
        part_count++;

        total_x = total_x + runParticle->xpos;
        total_y = total_y + runParticle->ypos;
        xy = xy + runParticle->xpos * runParticle->ypos;
        x2 = x2 + runParticle->xpos * runParticle->xpos;

        real_area   =   real_area   +   ((((runParticle->real_radius)*2)   *
((runParticle->real_radius)*2)));
        real_length = real_length + ((runParticle->real_radius*2));


}
runParticle = runParticle->nextP;
}
count_f = part_count + 0;
area_f = area + 0;
a = part_count * xy;                    // Calculates the slope
b = total_x * total_y;
c = part_count * x2;
d = total_x * total_x;
slope = (a-b) / (c-d);
ave_x = total_x / part_count;  //Calculates the midpoint
ave_y = total_y / part_count;
inj_distance = sqrt(((ave_x-0.5)*(ave_x-0.5))+((ave_y-0.2)*(ave_y-0.2))) *
2.5; // numbers are injection cpprdinates x,y
y_angle =(atan(1/(sqrt(slope*slope)))); //Calculates the dip
```

```
dif_y = (cos (y_angle)) * (length_f/2); //calculates the x and y differeces
dif_x = (sin (y_angle)) * (length_f/2);

if (slope > 0 and slope < 1000)     //calculates the endpoints of trendline
depending
{
                //on the placement of the trendline.
                x_max = ave_x + dif_x;
                y_max = ave_y + dif_y;
                x_min = ave_x - dif_x;
                y_min = ave_y - dif_y;
}

else if (slope < 0 and slope > (-1000))
                                {
                x_max = ave_x + dif_x;
                y_max = ave_y - dif_y;
                x_min = ave_x - dif_x;
                y_min = ave_y + dif_y;
}

else if (slope == 0)
                                {
                x_max = ave_x + dif_x;
                y_max = ave_y + 0;
                x_min = ave_x - dif_x;
                y_min = ave_y - 0;
}

else if (slope >1000 or slope < (-1000))
                                        {
                x_max = ave_x + 0;
                y_max = ave_y + dif_y;
                x_min = ave_x - 0;
                y_min = ave_y - dif_y;
}

                for (j = 0; j < numParticles; j++)
                {
                        if (runParticle->just_broken >0)
                                {
                                part_count_2++;
// calculating the Ut (n vector) and Utot (v vector) in accordance with
the trendline

        if (runParticle->posy_diff_time == 0)

        {
        g = 0;
        }
        else
        {
g       =       atan       ((sqrt(runParticle->posx_diff_time*runParticle-
>posx_diff_time))/(sqrt(runParticle->posy_diff_time*runParticle-
>posy_diff_time)));
}
f = PI - g - y_angle;
u_tot = u_tot + (((sin (f)) * runParticle->total_move * (runParticle-
>real_radius * 2 * particlex))/sin (f));
```

```
u_t = u_t + ((sin (f)) * runParticle->total_move * (runParticle->real_radius * 2 * particlex));
u_tx = u_tx + ((cos(y_angle)) * ((sin (f)) * runParticle->total_move* (runParticle->real_radius * 2 * particlex)));
u_ty = (sin(y_angle)) * ((sin (f)) * runParticle->total_move* (runParticle->real_radius * 2 * particlex));
u_totx = sqrt((runParticle->posx_diff_time*runParticle->posx_diff_time))* (runParticle->real_radius * 2 * particlex);
u_toty = sqrt((runParticle->posy_diff_time*runParticle->posy_diff_time))* (runParticle->real_radius * 2 * particlex);
average_density = average_density + runParticle->real_density;

//Remove "just fractured" flags
runParticle->just_frac = runParticle->just_frac - runParticle->just_frac;
runParticle->just_broken = runParticle->just_broken - runParticle->just_broken;
//
}
runParticle = runParticle->nextP;
}
part_count_f = part_count_2 + 0;
average_density_f = average_density / part_count_f;
lame1 = ave_young * ave_poisson / (1.0-(2.0*ave_poisson)*(1.0+ave_poisson));
u_t_final = u_t / part_count_2;
u_tot_final = u_tot / part_count_2;
u_totx_final = u_totx / part_count_2;
u_toty_final = u_toty / part_count_2;
u_tx_final = u_tx / part_count_2;
u_ty_final = u_ty / part_count_2;
beta = asin(sqrt((u_t_final*u_t_final)/(u_tot_final*u_tot_final)));
alpha = (PI/2) - beta;
        if (part_count_2%2 == 0)
        {
        real_length = real_length / 2;
        }
        else
        {
        real_length = (real_length + (1000/400)) / 2; //change number in (1000/x) where x is particle count in a row in the box and number is the real scale distance of the box
        }


// Calculating Source-Time function

// first calculate wave propagation velocity

Vs = sqrt(my / average_density_f);
Vp = sqrt( (lame1 + (2 * my)) / average_density_f);

// asume that propagation velocity is 75% of Vs

Vr = Vs * 0.75;

// calculate corner frequency

fc = pow (10, (((13-(log10(seismic_moment)))/3)+1.1));

/*!Following function calculates seismic response for
 * square grid of 5x5 points located around the central plane where
 * x 0 -> 1 as in grid settings and z intersects model plane at 0
 * and goes -0.5 -> 0.5
```

```
 */
for (pos_x = 0; pos_x < 2.01; pos_x = pos_x + 0.5)

{
for (pos_z = -1; pos_z < 1.01; pos_z = pos_z + 0.5)
{

// calculate distance to observation station

dist_x = (sqrt ((ave_x - pos_x)*(ave_x - pos_x))) * (runParticle-
>real_radius * 2 * particlex);        //distance from frac midpoint to
observ point along x axis if traced on surface
dist_y = (pos_y - ave_y) * (runParticle->real_radius * 2 *
particlex);           //vertical depth from frac point to observation
point

if (pos_z == 0)
{
surface_dist = dist_x;
}
else
{
surface_dist = sqrt((pos_z* (runParticle->real_radius * 2 * particlex)*
pos_z* (runParticle->real_radius * 2 * particlex))+(dist_x*dist_x));
       //trace of the distance on the surface
}
dist       =       sqrt(((dist_y       +       depth)*(dist_y       +
depth))+(surface_dist*surface_dist));
//absolute distance from frac midpoint to observ point

// calculate rake

lambda_s = PI/2;       //assuming all movement is in 2D and fault is
oriented along N-S line (x coordinates go 0->1 as S->N)

// calculate strike

phi_s = PI/2;          //same as above


// calculate azimuth


if (pos_z == 0 and pos_x < ave_x)
{
phi = PI;
}
else if (pos_z == 0 and pos_x > ave_x)
{
phi = 0;
}
else if (pos_z == 0 and pos_x == ave_x)
{
phi = 0;
}
else if (pos_x < ave_x and pos_z > 0)
{
phi = PI + acos(dist_x/surface_dist);
}
else if (pos_x < ave_x and pos_z < 0)
{
phi = PI - acos(dist_x/surface_dist);
}
```

```
else if (pos_x > ave_x and pos_z > 0)
{
phi = 2*PI - acos(dist_x/surface_dist);
}
else if (pos_x > ave_x and pos_z < 0)
{
phi = acos(dist_x/surface_dist);
}
else if (pos_x == ave_x and pos_z > 0)
{
phi = 3*PI/4;
}
else if (pos_x == ave_x and pos_z > 0)
{
phi = PI/2;
}
else
{
phi = 0;
}

// next calculate relative positioning of fault orientation and observation
station coordinates

ceta = acos((dist_y+depth)/dist);

if (ave_x > pos_x and slope > 0)
{
thet = sqrt((PI/2 - y_angle + ceta)*(PI/2 - y_angle + ceta));
}
else if (ave_x > pos_x and slope < 0 )
{
thet   =   sqrt((PI/2   -   (sqrt(y_angle*y_angle))   -   ceta)*(PI/2   -
(sqrt(y_angle*y_angle)) - ceta));
}
else if (ave_x < pos_x and slope > 0)
{
thet   =   sqrt((PI/2   -   (sqrt(y_angle*y_angle))   -   ceta)*(PI/2   -
(sqrt(y_angle+y_angle)) - ceta));
}
else if (ave_x < pos_x and slope < 0)
{
thet   =   sqrt((PI/2   -   (sqrt(y_angle*y_angle))   +   ceta)*(PI/2   -
(sqrt(y_angle*y_angle)) + ceta));
else if (slope == 0)
{
thet = PI/2 -ceta;
}
else
{
thet = ceta +0;
}

// take-off angle

theta = PI - (acos((dist_y+depth)/dist));

// calculate initial travel time

t_ini_swave = ((real_length/2) / Vr) + ((dist - ((real_length/2) * cos
(thet))) / Vs);
t_ini_pwave = ((real_length/2) / Vr) + ((dist - ((real_length/2) * cos
(thet))) / Vp);
```

```
// calculate arrival time difference

t_diff_swave = (real_length / Vr) - ((real_length * cos (thet)) / Vs);
t_diff_pwave = (real_length / Vr) - ((real_length * cos (thet)) / Vp);

//calculate rise time

 rise_t_s = (((16 * real_length * (sqrt((1000/400)/real_length))) / (7 *
Vs * (sqrt(PI*PI*PI)))) * t_diff_swave);

// calculate arrival end-time

t_end_swave = t_ini_swave + t_diff_swave + rise_t_s;
t_end_pwave = t_ini_pwave + t_diff_pwave + rise_t_s;


// calculate the height of boxcar function (Amplitude in dynes)

M_max_p = seismic_moment / (t_diff_pwave);
M_max_s = seismic_moment / (t_diff_swave);

// calculate Source Tensor

s11                          =                          ((((2*ave_poisson)/(1-
(2*ave_poisson)))+(2*((sin(y_angle))*(sin(y_angle)))*((sin(phi_s))*(sin(p
hi_s)))))*(sin(beta)))-
((((sin(y_angle))*(cos(lambda_s))*(sin(2*phi)))+((sin(2*y_angle))*(sin(la
mbda_s))*((cos(phi_s*2))*(cos(phi_s*2)))))*cos(beta));
s22                          =                          ((((2*ave_poisson)/(1-
(2*ave_poisson)))+(2*((sin(y_angle))*(sin(y_angle)))*((cos(phi_s))*(cos(p
hi_s)))))*(sin(beta)))+((((sin(y_angle))*(cos(lambda_s))*(sin(2*phi)))-
((sin(2*y_angle))*(sin(lambda_s))*((cos(phi_s*2))*(cos(phi_s*2)))))*cos(b
eta));
s33                          =                          ((((2*ave_poisson)/(1-
(2*ave_poisson)))+(2*((cos(y_angle))*(cos(y_angle)))))*(sin(beta)))+((sin
(2*y_angle))*(sin(lambda_s))*cos(beta));
s12                                  =                                  ((-
((sin(y_angle))*(sin(y_angle))))*(sin(2*phi_s))*(sin(beta)))+((((sin(y_an
gle))*(cos(lambda_s))*(cos(2*phi_s)))+(((sin(2*y_angle))*(sin(lambda_s))*
(sin(2*phi_s)))/2))*(cos(beta)));
s13            =            (((sin(2*y_angle)))*(sin(phi_s))*(sin(beta)))-
((((cos(y_angle))*(cos(lambda_s))*(cos(phi_s)))+(((cos(2*y_angle))*(sin(l
ambda_s))*(sin(phi_s)))))*(cos(beta)));
s23          =          ((-((sin(2*y_angle)))*(cos(phi_s))*(sin(beta))))-
((((cos(y_angle))*(cos(lambda_s))*(sin(phi_s)))-
(((cos(2*y_angle))*(sin(lambda_s))*(cos(phi_s)))))*(cos(beta)));

// Calculate Moment Tensor

               nx = -((sin(y_angle)) * (sin(phi_s)));
               ny = (sin(y_angle)) * (cos(phi_s));
               nz = -(cos(y_angle));
               vx = ((((cos(lambda_s)) * (cos(phi_s)))+((cos(y_angle)) *
(sin(lambda_s))   *   (sin(phi_s))))   *   (cos(beta)))-((sin(y_angle))   *
(sin(phi_s)) * (sin(beta)));
               vy = ((((cos(lambda_s)) * (sin(phi_s)))-((cos(y_angle)) *
(sin(lambda_s))   *   (cos(phi_s))))   *   (cos(beta)))+((sin(y_angle))   *
(cos(phi_s)) * (sin(beta)));
               vz    =    (-((sin(lambda_s))*(sin(y_angle))*(cos(beta))))-
((cos(y_angle))*(sin(beta)));
               Mt[0][0] = 2*nx*vx;
               Mt[0][1] = ((nx*vy)+(ny*vx));
```

```
                Mt[0][2] = ((nx*vz)+(nz*vx));
                Mt[1][0] = ((nx*vy)+(ny*vx));
                Mt[1][1] = 2*ny*vy;
                Mt[1][2] = ((ny*vz)+(nz*vy));
                Mt[2][0] = ((nx*vz)+(nz*vx));
                Mt[2][1] = ((ny*vz)+(nz*vy));
                Mt[2][2] = 2*nz*vz;

  trace = (Mt[1][1] + Mt[0][0] + Mt[2][2]);


  eigen_decomposition(Mt, V, v);

  Ev1=v[2];
  Ev2=v[1];
  Ev3=v[0];
  M_iso = (trace /3)/(sqrt(Ev1*Ev1));
// deviatoric moment tensor

                Mt[0][0] = (2*nx*vx) - (trace/3);
                Mt[1][1] = (2*ny*vy) - (trace/3);
                Mt[2][2] = (2*nz*vz) - (trace/3);
// Diagonolize moment tensor
    eigen_decomposition(Mt, V, v);

  Ev1=v[2];
  Ev2=v[1];
  Ev3=v[0];

  epsilone = -(Ev3/Ev1);


// Proportionalise moment tensor

   M_clvd = 2*(sqrt(epsilone*epsilone))*(1-M_iso);
   M_dc = 1-M_iso-M_clvd;

   if (M_dc<0)
   {
           M_clvd = M_clvd+(2*M_dc);
           M_dc = 1-M_iso-M_clvd;
           }
// Calculate Radiation Patterns

rad_pat_p                                                                =
cos(theta)*(cos(theta)*(sin(beta)*(2*cos(y_angle)*cos(y_angle)           -
(2*ave_poisson)/(2*ave_poisson              -             1))            +
sin(2*y_angle)*cos(beta)*sin(lambda_s))                                  -
cos(phi)*sin(theta)*(cos(beta)*(cos(2*y_angle)*sin(lambda_s)*sin(phi_s)  +
cos(y_angle)*cos(lambda_s)*cos(phi_s))                                   -
sin(2*y_angle)*sin(beta)*sin(phi_s))                                     +
sin(phi)*sin(theta)*(cos(beta)*(cos(2*y_angle)*cos(phi_s)*sin(lambda_s)  -
cos(y_angle)*cos(lambda_s)*sin(phi_s))                                   -
sin(2*y_angle)*cos(phi_s)*sin(beta)))                                    +
sin(phi)*sin(theta)*(cos(theta)*(cos(beta)*(cos(2*y_angle)*cos(phi_s)*sin
(lambda_s)        -        cos(y_angle)*cos(lambda_s)*sin(phi_s))        -
sin(2*y_angle)*cos(phi_s)*sin(beta))                                     +
cos(phi)*sin(theta)*(cos(beta)*(cos(2*phi_s)*cos(lambda_s)*sin(y_angle)  +
(sin(2*y_angle)*sin(2*phi_s)*sin(lambda_s))/2)                           -
sin(2*phi_s)*sin(y_angle)*sin(y_angle)*sin(beta))                        +
sin(phi)*sin(theta)*(cos(beta)*(sin(2*phi_s)*cos(lambda_s)*sin(y_angle)  -
sin(2*y_angle)*cos(phi_s)*cos(phi_s)*sin(lambda_s))                      -
sin(beta)*((2*ave_poisson)/(2*ave_poisson          -          1)         -
```

```
2*cos(phi_s)*cos(phi_s)*sin(y_angle)*sin(y_angle))))                    -
cos(phi)*sin(theta)*(cos(theta)*(cos(beta)*(cos(2*y_angle)*sin(lambda_s)*
sin(phi_s)        +        cos(y_angle)*cos(lambda_s)*cos(phi_s))        -
sin(2*y_angle)*sin(beta)*sin(phi_s))                                    -
sin(phi)*sin(theta)*(cos(beta)*(cos(2*phi_s)*cos(lambda_s)*sin(y_angle) +
(sin(2*y_angle)*sin(2*phi_s)*sin(lambda_s))/2)                          -
sin(2*phi_s)*sin(y_angle)*sin(y_angle)*sin(beta))                       +
cos(phi)*sin(theta)*(cos(beta)*(sin(2*y_angle)*sin(lambda_s)*sin(phi_s)*s
in(phi_s)        +        sin(2*phi_s)*cos(lambda_s)*sin(y_angle))       +
sin(beta)*((2*ave_poisson)/(2*ave_poisson          -          1)         -
2*sin(y_angle)*sin(y_angle)*sin(phi_s)*sin(phi_s))));

rad_pat_s_1                                                             =
cos(theta)*(cos(phi)*(cos(beta)*(cos(2*y_angle)*cos(phi_s)*sin(lambda_s)
-                 cos(y_angle)*cos(lambda_s)*sin(phi_s))                -
sin(2*y_angle)*cos(phi_s)*sin(beta))                                    +
sin(phi)*(cos(beta)*(cos(2*y_angle)*sin(lambda_s)*sin(phi_s)            +
cos(y_angle)*cos(lambda_s)*cos(phi_s))                                  -
sin(2*y_angle)*sin(beta)*sin(phi_s)))                                   -
sin(phi)*sin(theta)*(sin(phi)*(cos(beta)*(cos(2*phi_s)*cos(lambda_s)*sin(
y_angle)      +      (sin(2*y_angle)*sin(2*phi_s)*sin(lambda_s))/2)     -
sin(2*phi_s)*sin(y_angle)*sin(y_angle)*sin(beta))                       -
cos(phi)*(cos(beta)*(sin(2*phi_s)*cos(lambda_s)*sin(y_angle)            -
sin(2*y_angle)*cos(phi_s)*cos(phi_s)*sin(lambda_s))                     -
sin(beta)*((2*ave_poisson)/(2*ave_poisson          -          1)         -
2*cos(phi_s)*cos(phi_s)*sin(y_angle)*sin(y_angle))))                    +
cos(phi)*sin(theta)*(sin(phi)*(cos(beta)*(sin(2*y_angle)*sin(lambda_s)*si
n(phi_s)*sin(phi_s)    +    sin(2*phi_s)*cos(lambda_s)*sin(y_angle))    +
sin(beta)*((2*ave_poisson)/(2*ave_poisson          -          1)         -
2*sin(y_angle)*sin(y_angle)*sin(phi_s)*sin(phi_s)))                     +
cos(phi)*(cos(beta)*(cos(2*phi_s)*cos(lambda_s)*sin(y_angle)            +
(sin(2*y_angle)*sin(2*phi_s)*sin(lambda_s))/2)                          -
sin(2*phi_s)*sin(y_angle)*sin(y_angle)*sin(beta)));

rad_pat_s_2                                                             =
sin(phi)*sin(theta)*(cos(phi)*cos(theta)*(cos(beta)*(cos(2*phi_s)*cos(lam
bda_s)*sin(y_angle)   +   (sin(2*y_angle)*sin(2*phi_s)*sin(lambda_s))/2)  -
sin(2*phi_s)*sin(y_angle)*sin(y_angle)*sin(beta))                       -
sin(theta)*(cos(beta)*(cos(2*y_angle)*cos(phi_s)*sin(lambda_s)          -
cos(y_angle)*cos(lambda_s)*sin(phi_s))                                  -
sin(2*y_angle)*cos(phi_s)*sin(beta))                                    +
cos(theta)*sin(phi)*(cos(beta)*(sin(2*phi_s)*cos(lambda_s)*sin(y_angle) -
sin(2*y_angle)*cos(phi_s)*cos(phi_s)*sin(lambda_s))                     -
sin(beta)*((2*ave_poisson)/(2*ave_poisson          -          1)         -
2*cos(phi_s)*cos(phi_s)*sin(y_angle)*sin(y_angle))))                    -
cos(theta)*(sin(theta)*(sin(beta)*(2*cos(y_angle)*cos(y_angle)          -
(2*ave_poisson)/(2*ave_poisson              -             1))           +
sin(2*y_angle)*cos(beta)*sin(lambda_s))                                 +
cos(phi)*cos(theta)*(cos(beta)*(cos(2*y_angle)*sin(lambda_s)*sin(phi_s) +
cos(y_angle)*cos(lambda_s)*cos(phi_s))                                  -
sin(2*y_angle)*sin(beta)*sin(phi_s))                                    -
cos(theta)*sin(phi)*(cos(beta)*(cos(2*y_angle)*cos(phi_s)*sin(lambda_s) -
cos(y_angle)*cos(lambda_s)*sin(phi_s))                                  -
sin(2*y_angle)*cos(phi_s)*sin(beta)))                                   +
cos(phi)*sin(theta)*(sin(theta)*(cos(beta)*(cos(2*y_angle)*sin(lambda_s)*
sin(phi_s)        +        cos(y_angle)*cos(lambda_s)*cos(phi_s))        -
sin(2*y_angle)*sin(beta)*sin(phi_s))                                    +
cos(theta)*sin(phi)*(cos(beta)*(cos(2*phi_s)*cos(lambda_s)*sin(y_angle) +
(sin(2*y_angle)*sin(2*phi_s)*sin(lambda_s))/2)                          -
sin(2*phi_s)*sin(y_angle)*sin(y_angle)*sin(beta))                       -
cos(phi)*cos(theta)*(cos(beta)*(sin(2*y_angle)*sin(lambda_s)*sin(phi_s)*s
in(phi_s)        +        sin(2*phi_s)*cos(lambda_s)*sin(y_angle))       +
```

```
sin(beta)*((2*ave_poisson)/(2*ave_poisson - 1) -
2*sin(y_angle)*sin(y_angle)*sin(phi_s)*sin(phi_s))));

rad_pat_s = sqrt((rad_pat_s_1*rad_pat_s_1)+(rad_pat_s_2*rad_pat_s_2));

// Calculate far field displacement

Up = (rad_pat_p / (4*PI*Vp*Vp*Vp*dist*average_density_f))*M_max_p*1000000;
//converting to nm from m scale
Us = (rad_pat_s / (4*PI*Vs*Vs*Vs*dist*average_density_f))*M_max_s*1000000;

// Calculate displacement velocities

V_us = Us / (t_diff_swave + rise_t_s);
V_up = Up / (t_diff_pwave + rise_t_p);

// Calculate source spectrum knickpoints

barrier_1_s = 2 / t_diff_swave;
barrier_2_s = 2 / rise_t_s;


// Create source spectrum

freq_value = 0;
frequency = 0;
interval_1 = barrier_1_s / 5;
interval_2 = ((barrier_2_s - barrier_1_s) / 5);

for (l = 0; l < 5; l++)
{
freq_value = freq_value + interval_1;
frequency = log10(seismic_moment);

if (l == 0)
{
fprintf (stat4, "%f", freq_value);
fprintf (stat4, " %f", frequency);
}
else
{
fprintf (stat4, " %f", freq_value);
fprintf (stat4, " %f", frequency);
}
}
for (o = 0; o < 5; o++)
{
if      ( o==1 )                //calculating slope
{
drop_1 = frequency;
}
freq_value = freq_value + interval_2;
frequency   =   (log10(seismic_moment))-   (log10(t_diff_swave   /   2))   -
(log10(freq_value));
drop_1 = drop_1 - frequency;
slope_1 = drop_1 / interval_2;
fprintf (stat4, " %f", freq_value);
fprintf (stat4, " %f", frequency);
}
for (m = 0; m < 5; m++)
{
if      ( m==1 )                //calculating slope
{
```

```
drop_2 = frequency;
}
freq_value = freq_value + interval_2;
frequency = (log10(seismic_moment)) - (log10((t_diff_swave * rise_t_s) /
4)) - (2*(log10(freq_value)));
drop_2 = drop_2 - frequency;
slope_2 = drop_2 / interval_2;

// Create output files

fprintf (stat4, " %f", freq_value);
fprintf (stat4, " %f", frequency);


                                }


        fprintf (stat4, " %f", barrier_1_s);
        fprintf (stat4, " %f", barrier_2_s);
        fprintf (stat4, " %f", fc);
        fprintf (stat4, " %f", slope_1);
        fprintf (stat4, " %f\n", slope_2);



          fprintf (stat2, "%f", phi_s);
          fprintf (stat2, " %f", y_angle);
          fprintf (stat2, " %f", lambda_s);
          fprintf (stat2, " %f", beta);



          fprintf (stat3, "%f", pos_x);
          fprintf (stat3, " %f", pos_z);
          fprintf (stat3, " %f", moment_magn);
          fprintf (stat3, " %f", inj_distance);
          fprintf (stat3, " %f", Vp);
          fprintf (stat3, " %f", Vs);
          fprintf (stat3, " %f", u_tot_final);
          fprintf (stat3, " %f", u_t_final);
          fprintf (stat3, " %f", part_count_f);
          fprintf (stat3, " %f", real_length);
          fprintf (stat3, " %f", Up);
          fprintf (stat3, " %f", Us);
          fprintf (stat3, " %f", t_ini_pwave);
          fprintf (stat3, " %f", t_end_pwave);
          fprintf (stat3, " %f", t_ini_swave);
          fprintf (stat3, " %f", t_end_swave);
          fprintf (stat3, " %f", t_diff_pwave);
          fprintf (stat3, " %f", t_diff_swave);
          fprintf (stat3, " %f", rise_t_s);
          fprintf (stat3, " %f", barrier_1_s);
          fprintf (stat3, " %f", barrier_2_s);
          fprintf (stat3, " %f", fc);
          fprintf (stat3, " %f", theta);
          fprintf (stat3, " %f", thet);
          fprintf (stat3, " %f", phi);
          fprintf (stat3, " %f", phi_s);
          fprintf (stat3, " %f", y_angle);
          fprintf (stat3, " %f", lambda_s);
          fprintf (stat3, " %f", beta);
          fprintf (stat3, " %f", rad_pat_p);
          fprintf (stat3, " %f", rad_pat_s);
```

```
          fprintf (stat3, " %f", epsilone);
          fprintf (stat3, " %f", M_iso);
          fprintf (stat3, " %f", M_clvd);
          fprintf (stat3, " %f", M_dc);
          fprintf (stat3, " %f\n", ave_poisson);
}
}
        fprintf (stat, "%f", mode_total);
         fprintf (stat, " %f", mode_final);
         fprintf (stat, " %f", seismic_moment);
         fprintf (stat, " %f", average_slip);
         fprintf (stat, " %f", moment_magn);
         fprintf (stat, " %f", elastic);
         fprintf (stat, " %f", f_error);
         fprintf (stat, " %f", fdistance);
         fprintf (stat, " %f", mode_fcount);
        fprintf (stat, " %f", part_count_f);
         fprintf (stat, " %f", y_angle);
         fprintf (stat, " %f", ave_x);
         fprintf (stat, " %f", ave_y);
         fprintf (stat, " %f", u_t);
         fprintf (stat, " %f", u_tot);
         fprintf (stat, " %f", u_t_final);
         fprintf (stat, " %f", u_tot_final);
         fprintf (stat, " %f\n", t_end_pwave);
        fprintf (stat2, " %f\n", ave_poisson);

fclose (stat);
fclose (stat2);
fclose (stat3);
fclose (stat4);
}

// Function to create horizontal pressure and stress profiles across
injection point


void
Lattice::DumpPressureProfile (int particle_row)
{
  FILE *stat;          // file pointer
  FILE *stat2;
  FILE *stat3;
  FILE *stat4;
  FILE *stat5;
  FILE *stat6;

  int i,j;     // counters
  runParticle = &refParticle;  // start of list

        for (i=0;i<(particle_row*particlex);i++)
        {
                runParticle = runParticle->nextP;
        }
        stat = fopen ("PressureProfile.txt", "a");    //  open  statistic
output
        stat2 = fopen ("PorosityProfile.txt", "a");   //  open  statistic
output
        stat3 = fopen ("FractureProfile.txt", "a");
        stat4 = fopen ("Profile_Fluid_Pr_Gradient.txt", "a");
        stat5 = fopen ("Profile_Stress_xx.txt", "a");
        stat6 = fopen ("Profile_Stress_yy.txt", "a");
```

```
        for (j=0;j<particlex-1;j++)
        {

                if (j>(particlex*0.33) and j<(particlex*0.66))
                {
                fprintf (stat, ";%f", runParticle->temperature);
                fprintf (stat2, ";%f", runParticle->average_porosity);
                fprintf (stat3, ";%f", runParticle->fractured);
                fprintf         (stat4,         ";%f",         runParticle-
>fluid_pressure_gradient);
                fprintf (stat5, ";%f", runParticle->sxx);
                fprintf (stat6, ";%f", runParticle->syy);

                runParticle = runParticle->nextP;
        }
                else
                {
                        runParticle = runParticle->nextP;
                        }


        }
        fprintf (stat, ";%f\n", runParticle->temperature);
        fprintf (stat2, ";%f\n", runParticle->average_porosity);
        fprintf (stat3, ";%f\n", runParticle->fractured);
        fprintf (stat4, ";%f\n", runParticle->fluid_pressure_gradient);
        fprintf (stat5, ";%f\n", runParticle->sxx);
        fprintf (stat6, ";%f\n", runParticle->syy);

  fclose (stat);                // close file
  fclose (stat2);
  fclose (stat3);
  fclose (stat4);
  fclose (stat5);
  fclose (stat6);

}

// Function to create horizontal pressure and stress profiles above the
injection point


void
Lattice::DumpPressureProfileUp (int particle_row)
{
  FILE *stat;           // file pointer
  FILE *stat2;
  FILE *stat3;
  FILE *stat4;
  FILE *stat5;
  FILE *stat6;

  int i,j;      // counters


  runParticle = &refParticle;  // start of list

        for (i=0;i<(particle_row*particlex);i++)
        {
                runParticle = runParticle->nextP;
        }
```

```
        stat = fopen ("PressureProfileUP.txt", "a");  //  open  statistic
output
        stat2 = fopen ("PorosityProfileUP.txt", "a"); //  open  statistic
output
        stat3 = fopen ("FractureProfileUP.txt", "a");
        stat4 = fopen ("Profile_Fluid_Pr_GradientUP.txt", "a");
        stat5 = fopen ("Profile_Stress_xxUP.txt", "a");
        stat6 = fopen ("Profile_Stress_yyUP.txt", "a");

        for (j=0;j<particlex-1;j++)
        {

                if (j>(particlex*0.33) and j<(particlex*0.66))
                {
                fprintf (stat, ";%f", runParticle->temperature);
                fprintf (stat2, ";%f", runParticle->average_porosity);
                fprintf (stat3, ";%f", runParticle->fractured);
                fprintf         (stat4,         ";%f",         runParticle-
>fluid_pressure_gradient);
                fprintf (stat5, ";%f", runParticle->sxx);
                fprintf (stat6, ";%f", runParticle->syy);

                runParticle = runParticle->nextP;
        }
                else
                {
                        runParticle = runParticle->nextP;
                        }


        }
        fprintf (stat, ";%f\n", runParticle->temperature);
        fprintf (stat2, ";%f\n", runParticle->average_porosity);
        fprintf (stat3, ";%f\n", runParticle->fractured);
        fprintf (stat4, ";%f\n", runParticle->fluid_pressure_gradient);
        fprintf (stat5, ";%f\n", runParticle->sxx);
        fprintf (stat6, ";%f\n", runParticle->syy);

  fclose (stat);              // close file
  fclose (stat2);
  fclose (stat3);
  fclose (stat4);
  fclose (stat5);
  fclose (stat6);

}

// Function to create vertical pressure and stress profiles across
injection point


void
Lattice::DumpVertPressureProfile      (int      particle_collumn,      int
start_particle_row, int end_particle_row)
{
  FILE *stat;          // file pointer
  FILE *stat2;
  FILE *stat3;
  FILE *stat4;
  FILE *stat5;
  FILE *stat6;

  int i,j,k;   // counters
```

```
  runParticle = &refParticle;  // start of list

        for (i=0;i<(particle_collumn + (400 * start_particle_row));i++)
        {
                runParticle = runParticle->nextP;
        }

        stat = fopen ("PressureVertProfile.txt", "a");        //       open
statistic output
        stat2 = fopen ("PorosityVertProfile.txt", "a");       //       open
statistic output
        stat3 = fopen ("FractureVertProfile.txt", "a");
        stat4 = fopen ("Profile_VertFluid_Pr_Gradient.txt", "a");
        stat5 = fopen ("Profile_VertStress_xx.txt", "a");
        stat6 = fopen ("Profile_VertStress_yy.txt", "a");

        for (j=0;j<(end_particle_row - start_particle_row);j++)
        {
                fprintf (stat, ";%f", runParticle->temperature);
                fprintf (stat2, ";%f", runParticle->average_porosity);
                fprintf (stat3, ";%f", runParticle->fractured);
                fprintf         (stat4,         ";%f",         runParticle-
>fluid_pressure_gradient);
                fprintf (stat5, ";%f", runParticle->sxx);
                fprintf (stat6, ";%f", runParticle->syy);


                        for (k=0; k<400; k++)
                        {
                                runParticle = runParticle->nextP;
                                }


        }
        fprintf (stat, ";%f\n", runParticle->temperature);
        fprintf (stat2, ";%f\n", runParticle->average_porosity);
        fprintf (stat3, ";%f\n", runParticle->fractured);
        fprintf (stat4, ";%f\n", runParticle->fluid_pressure_gradient);
        fprintf (stat5, ";%f\n", runParticle->sxx);
        fprintf (stat6, ";%f\n", runParticle->syy);

  fclose (stat);                // close file
  fclose (stat2);
  fclose (stat3);
  fclose (stat4);
  fclose (stat5);
  fclose (stat6);


}
```

B Data logs for all the conducted Hele-Shaw cell experiements.

Nr.	Overburden (mm)	Overpressure (bar)	Duration (s)	Width (mm)	Length (mm)	Branches	Init time (s)	t^o	Rel Hum(%)
0507_01	250	0.1	0.2	3.9	7.8	1	0.178	24.9	58
3006_06	250	0.05	0.2	6.8	37	3	0.112	25.4	50
0507_02	250	0.1	0.2	10.8	80.4	4	0.049	24.9	58
0507_03	250	0.1	0.1	5	15	1	0.072	24.9	58
0507_04	250	0.1	0.1	11.4	35.7	2	0.049	24.9	58
0507_05	250	0.1	0.1	9.7	42.1	2	0.045	24.9	58
0507_06	250	0.05	0.1	5.7	13.3	1	0.055	24.9	58
0507_07	250	0.05	0.1	8.1	3.3	1	0.035	24.9	58
0507_08	250	0.05	0.1	4.5	21	1	0.065	24.9	58
0607_01	500	0.2	0.2	9	93	4	0.071	26.6	61.7
0607_02	500	0.1	0.3	NA	NA	NA	NA	26.6	61.7
0607_03	500	0.2	0.3	7.8	60.9	4	0.121	26.6	61.7
0607_04	500	0.15	0.3	16.1	123.9	5	0.02	26.6	61.7
0607_05	500	0.15	0.3	6	9.7	1	0.21	26.6	61.7
0607_06	500	0.15	0.5	9	30.3	2	0.22	26.6	61.7
0607_07	500	0.15	0.5	11.4	42.3	2	0.207	26.6	61.7
0707_01	500	0.15	0.3	7.3	14	1	0.246	28.4	56.6
0707_02	500	0.2	0.3	17	126.9	5	0.083	28.4	56.6
0707_03	500	0.15	0.5	13.5	134.5	7	0.075	28.4	56.6
0707_04	500	0.05	0.5	NA	NA	NA	NA	28.4	56.6
0707_05	500	0.15	0.5	21.6	195.5	8	0.062	28.4	56.6
0707_06	500	0.1	0.7	8.6	82	6	0.116	28.4	56.6
0707_07	500	0.05	1	NA	NA	NA	NA	28.4	56.6
0707_08	500	0.2	1	16.2	225	9	0.148	28.4	56.6
1007_01	600	0.2	0.5	15.7	205.1	8	0.069	29.1	59
1007_02	600	0.15	0.5	12.7	53.3	4	0.107	29.1	59
1007_03	600	0.1	1	8	39	3	0.163	29.1	59
1007_04	600	0.2	0.7	9.3	111.3	5	0.096	29.1	59
1007_05	600	0.2	1	9	210.3	9	0.075	29.1	59
1007_07	600	0.4	0.5	22	251	10	0.053	29.1	59
1007_08	600	0.6	0.5	30.7	600	17	0.047	29.1	59

1107_01	600	0.2	0.5	17.3	225.6	9	0.093	27.2	55.4
1107_02	600	0.2	1	15.7	435.4	17	0.071	27.2	55.4
1107_03	600	0.4	0.5	22.5	278.9	12	0.055	27.2	55.4
1107_04	600	0.6	0.5	30	442.1	14	0.045	27.2	55.4
1107_05	600	0.15	1	13.5	121	6	0.095	27.2	55.4
1107_06	600	0.15	1.5	14.3	265.9	8	0.092	27.2	55.4
2706_01	200	0.05	2	NA	NA	NA	NA	28.8	60.3
2706_02	200	0.1	1	NA	NA	NA	NA	28.8	60.3
2706_03	200	0.2	0.5	30.6	149.3	7	0.047	28.8	60.3
2706_04	200	0.1	0.4	10.1	119.5	9	0.036	28.8	60.3
2706_05	200	0.1	0.5	15	182.9	11	0.049	28.8	60.3
2706_06	200	0.1	0.2	13.1	62.1	4	0.041	28.8	60.3
2706_07	200	0.1	0.1	4.7	17	1	0.055	28.8	60.3
2706_08	200	0.15	0.3	15	123.8	4	0.09	28.8	60.3
2706_09	200	0.2	0.1	11	29	4	0.042	28.8	60.3
2706_10	200	0.4	0.2	25	194.1	8	0.052	28.8	60.3
2706_11	200	0.05	2	8.3	4	1	0.05	28.8	60.3
3006_01	200	0.25	0.2	17	148.1	10	0.081	25.4	50
3006_02	200	0.1	0.2	NA	NA	NA	NA	25.4	50
3006_03	200	0.2	0.3	21	149	9	0.099	25.4	50
3006_04	200	0.1	0.3	9.7	47.9	6	0.073	25.4	50
3006_05	200	0.1	0.2	4.3	11.8	2	0.14	25.4	50
3006_07	200	0.05	0.3	3.3	9	2	0.268	25.4	50
3006_08	200	0.25	0.2	13.5	103.6	5	0.062	25.4	50
3006_09	200	0.1	0.2	8	37.4	3	0.112	25.4	50

C MatLAB routine for producing radiation pattern visualisations (after Kwiatek & Ben-Zion, 2013)

```
AZIMUTH = (0:4:360)*pi/180;
TAKEOFF = (0:2:180)*pi/180;
[AZIMUTH,TAKEOFF] = meshgrid(AZIMUTH,TAKEOFF);


% These are the values that come out of Elle
strike = 1.570796;
dip = 0.9892;
rake = 1.570796;
gamma = 1.0448;
sigma = 0.3;
%%%%

[GP, GS, GSH, GSV] = rpgen(strike,dip,rake,gamma,sigma, TAKEOFF*180/pi,
AZIMUTH*180/pi);

%Change first parameter for visualisation of desired pattern (GP, GS, GSH,
%GSV)

scale = abs(GP);
YP = scale.*cos(AZIMUTH) .* sin(TAKEOFF);
XP = scale.*sin(AZIMUTH) .* sin(TAKEOFF);
ZP = scale.*-cos(TAKEOFF);

%Change forth parameter for visualisation of desired pattern (GP, GS, GSH,
%GSV)

surf(XP,YP,ZP,GP,'EdgeColor','none','AmbientStrength',0.7,'EdgeColor','k'
,'EdgeAlpha',0.1);
axis ([-3.5 3.5 -3.5 3.5 -3.5 3.5]);
colorbar;
caxis ([-3.5 3.5]);
view ([90 0]);

%%%%%%%%%%
function [Gp, Gs, Gsh, Gsv] = rpgen(strike, dip, rake, gamma, sigma, TKO,
AZM)
   TKO = TKO * pi / 180;
   AZM = AZM * pi / 180;

if nargout == 1
  Gp      =      cos(TKO).*(cos(TKO).*(sin(gamma).*(2.*cos(dip).^2      -
(2.*sigma)./(2.*sigma   -   1))   +   sin(2.*dip).*cos(gamma).*sin(rake))   -
cos(AZM).*sin(TKO).*(cos(gamma).*(cos(2.*dip).*sin(rake).*sin(strike)    +
cos(dip).*cos(rake).*cos(strike)) - sin(2.*dip).*sin(gamma).*sin(strike))
+ sin(AZM).*sin(TKO).*(cos(gamma).*(cos(2.*dip).*cos(strike).*sin(rake)  -
cos(dip).*cos(rake).*sin(strike))                                        -
sin(2.*dip).*cos(strike).*sin(gamma)))                                   +
sin(AZM).*sin(TKO).*(cos(TKO).*(cos(gamma).*(cos(2.*dip).*cos(strike).*si
n(rake)          -          cos(dip).*cos(rake).*sin(strike))            -
sin(2.*dip).*cos(strike).*sin(gamma))                                    +
cos(AZM).*sin(TKO).*(cos(gamma).*(cos(2.*strike).*cos(rake).*sin(dip)    +
(sin(2.*dip).*sin(2.*strike).*sin(rake))./2)                             -
sin(2.*strike).*sin(dip).^2.*sin(gamma))                                 +
sin(AZM).*sin(TKO).*(cos(gamma).*(sin(2.*strike).*cos(rake).*sin(dip)    -
```

```
sin(2.*dip).*cos(strike).^2.*sin(rake))                                  -
sin(gamma).*((2.*sigma)./(2.*sigma          -          1)               -
2.*cos(strike).^2.*sin(dip).^2)))                                       -
cos(AZM).*sin(TKO).*(cos(TKO).*(cos(gamma).*(cos(2.*dip).*sin(rake).*sin(
strike)          +          cos(dip).*cos(rake).*cos(strike))           -
sin(2.*dip).*sin(gamma).*sin(strike))                                   -
sin(AZM).*sin(TKO).*(cos(gamma).*(cos(2.*strike).*cos(rake).*sin(dip)   +
(sin(2.*dip).*sin(2.*strike).*sin(rake))./2)                            -
sin(2.*strike).*sin(dip).^2.*sin(gamma))                                +
cos(AZM).*sin(TKO).*(cos(gamma).*(sin(2.*dip).*sin(rake).*sin(strike).^2
+                 sin(2.*strike).*cos(rake).*sin(dip))                  +
sin(gamma).*((2.*sigma)./(2.*sigma          -          1)               -
2.*sin(dip).^2.*sin(strike).^2)));
X = [Gp];
 disp (X);

elseif nargout == 2
  Gp      =      cos(TKO).*(cos(TKO).*(sin(gamma).*(2.*cos(dip).^2      -
(2.*sigma)./(2.*sigma   -   1))   +   sin(2.*dip).*cos(gamma).*sin(rake))   -
cos(AZM).*sin(TKO).*(cos(gamma).*(cos(2.*dip).*sin(rake).*sin(strike)   +
cos(dip).*cos(rake).*cos(strike)) - sin(2.*dip).*sin(gamma).*sin(strike))
+ sin(AZM).*sin(TKO).*(cos(gamma).*(cos(2.*dip).*cos(strike).*sin(rake) -
cos(dip).*cos(rake).*sin(strike))                                       -
sin(2.*dip).*cos(strike).*sin(gamma)))                                  +
sin(AZM).*sin(TKO).*(cos(TKO).*(cos(gamma).*(cos(2.*dip).*cos(strike).*si
n(rake)          -          cos(dip).*cos(rake).*sin(strike))           -
sin(2.*dip).*cos(strike).*sin(gamma))                                   +
cos(AZM).*sin(TKO).*(cos(gamma).*(cos(2.*strike).*cos(rake).*sin(dip)   +
(sin(2.*dip).*sin(2.*strike).*sin(rake))./2)                            -
sin(2.*strike).*sin(dip).^2.*sin(gamma))                                +
sin(AZM).*sin(TKO).*(cos(gamma).*(sin(2.*strike).*cos(rake).*sin(dip)   -
sin(2.*dip).*cos(strike).^2.*sin(rake))                                 -
sin(gamma).*((2.*sigma).*(2.*sigma          -          1)               -
2.*cos(strike).^2.*sin(dip).^2)))                                       -
cos(AZM).*sin(TKO).*(cos(TKO).*(cos(gamma).*(cos(2.*dip).*sin(rake).*sin(
strike)          +          cos(dip).*cos(rake).*cos(strike))           -
sin(2.*dip).*sin(gamma).*sin(strike))                                   -
sin(AZM).*sin(TKO).*(cos(gamma).*(cos(2.*strike).*cos(rake).*sin(dip)   +
(sin(2.*dip).*sin(2.*strike).*sin(rake))./2)                            -
sin(2.*strike).*sin(dip).^2.*sin(gamma))                                +
cos(AZM).*sin(TKO).*(cos(gamma).*(sin(2.*dip).*sin(rake).*sin(strike).^2
+                 sin(2.*strike).*cos(rake).*sin(dip))                  +
sin(gamma).*((2.*sigma).*(2.*sigma          -          1)               -
2.*sin(dip).^2.*sin(strike).^2)));
  Gs                                                                    =
((sin(AZM).*sin(TKO).*(cos(AZM).*cos(TKO).*(cos(gamma).*(cos(2.*strike).*
cos(rake).*sin(dip)   +   (sin(2.*dip).*sin(2.*strike).*sin(rake))./2)   -
sin(2.*strike).*sin(dip).^2.*sin(gamma))                                -
sin(TKO).*(cos(gamma).*(cos(2.*dip).*cos(strike).*sin(rake)             -
cos(dip).*cos(rake).*sin(strike)) - sin(2.*dip).*cos(strike).*sin(gamma))
+ cos(TKO).*sin(AZM).*(cos(gamma).*(sin(2.*strike).*cos(rake).*sin(dip) -
sin(2.*dip).*cos(strike).^2.*sin(rake))                                 -
sin(gamma).*((2.*sigma).*(2.*sigma          -          1)               -
2.*cos(strike).^2.*sin(dip).^2)))                                       -
cos(TKO).*(sin(TKO).*(sin(gamma).*(2.*cos(dip).^2 - (2.*sigma)./(2.*sigma
-        1))        +        sin(2.*dip).*cos(gamma).*sin(rake))         +
cos(AZM).*cos(TKO).*(cos(gamma).*(cos(2.*dip).*sin(rake).*sin(strike)   +
cos(dip).*cos(rake).*cos(strike)) - sin(2.*dip).*sin(gamma).*sin(strike))
- cos(TKO).*sin(AZM).*(cos(gamma).*(cos(2.*dip).*cos(strike).*sin(rake) -
cos(dip).*cos(rake).*sin(strike))                                       -
sin(2.*dip).*cos(strike).*sin(gamma)))                                  +
cos(AZM).*sin(TKO).*(sin(TKO).*(cos(gamma).*(cos(2.*dip).*sin(rake).*sin(
strike)          +          cos(dip).*cos(rake).*cos(strike))           -
```

```
sin(2.*dip).*sin(gamma).*sin(strike))                                    +
cos(TKO).*sin(AZM).*(cos(gamma).*(cos(2.*strike).*cos(rake).*sin(dip)    +
(sin(2.*dip).*sin(2.*strike).*sin(rake))./2)                             -
sin(2.*strike).*sin(dip).^2.*sin(gamma))                                 -
cos(AZM).*cos(TKO).*(cos(gamma).*(sin(2.*dip).*sin(rake).*sin(strike).^2
+                  sin(2.*strike).*cos(rake).*sin(dip))                  +
sin(gamma).*((2.*sigma)./(2.*sigma           -           1)              -
2.*sin(dip).^2.*sin(strike).^2))))).^2                                   +
(cos(TKO).*(cos(AZM).*(cos(gamma).*(cos(2.*dip).*cos(strike).*sin(rake)  -
cos(dip).*cos(rake).*sin(strike)) - sin(2.*dip).*cos(strike).*sin(gamma))
+      sin(AZM).*(cos(gamma).*(cos(2.*dip).*sin(rake).*sin(strike)       +
cos(dip).*cos(rake).*cos(strike))                                        -
sin(2.*dip).*sin(gamma).*sin(strike)))                                   -
sin(AZM).*sin(TKO).*(sin(AZM).*(cos(gamma).*(cos(2.*strike).*cos(rake).*s
in(dip)       +       (sin(2.*dip).*sin(2.*strike).*sin(rake))./2)       -
sin(2.*strike).*sin(dip).^2.*sin(gamma))                                 -
cos(AZM).*(cos(gamma).*(sin(2.*strike).*cos(rake).*sin(dip)              -
sin(2.*dip).*cos(strike).^2.*sin(rake))                                  -
sin(gamma).*((2.*sigma)./(2.*sigma           -           1)              -
2.*cos(strike).^2.*sin(dip).^2)))                                        +
cos(AZM).*sin(TKO).*(sin(AZM).*(cos(gamma).*(sin(2.*dip).*sin(rake).*sin(
strike).^2         +         sin(2.*strike).*cos(rake).*sin(dip))        +
sin(gamma).*((2.*sigma)./(2.*sigma - 1) - 2.*sin(dip).^2.*sin(strike).^2))
+      cos(AZM).*(cos(gamma).*(cos(2.*strike).*cos(rake).*sin(dip)       +
(sin(2.*dip).*sin(2.*strike).*sin(rake))./2)                             -
sin(2.*strike).*sin(dip).^2.*sin(gamma))))).^2).^(1./2);


elseif nargout == 3
  Gp      =      cos(TKO).*(cos(TKO).*(sin(gamma).*(2.*cos(dip).^2       -
(2.*sigma)./(2.*sigma   -   1))   +   sin(2.*dip).*cos(gamma).*sin(rake))   -
cos(AZM).*sin(TKO).*(cos(gamma).*(cos(2.*dip).*sin(rake).*sin(strike)    +
cos(dip).*cos(rake).*cos(strike)) - sin(2.*dip).*sin(gamma).*sin(strike))
+ sin(AZM).*sin(TKO).*(cos(gamma).*(cos(2.*dip).*cos(strike).*sin(rake)  -
cos(dip).*cos(rake).*sin(strike))                                        -
sin(2.*dip).*cos(strike).*sin(gamma)))                                   +
sin(AZM).*sin(TKO).*(cos(TKO).*(cos(gamma).*(cos(2.*dip).*cos(strike).*si
n(rake)           -           cos(dip).*cos(rake).*sin(strike))          -
sin(2.*dip).*cos(strike).*sin(gamma))                                    +
cos(AZM).*sin(TKO).*(cos(gamma).*(cos(2.*strike).*cos(rake).*sin(dip)    +
(sin(2.*dip).*sin(2.*strike).*sin(rake))./2)                             -
sin(2.*strike).*sin(dip).^2.*sin(gamma))                                 +
sin(AZM).*sin(TKO).*(cos(gamma).*(sin(2.*strike).*cos(rake).*sin(dip)    -
sin(2.*dip).*cos(strike).^2.*sin(rake))                                  -
sin(gamma).*((2.*sigma)./(2.*sigma           -           1)              -
2.*cos(strike).^2.*sin(dip).^2)))                                        -
cos(AZM).*sin(TKO).*(cos(TKO).*(cos(gamma).*(cos(2.*dip).*sin(rake).*sin(
strike)           +           cos(dip).*cos(rake).*cos(strike))          -
sin(2.*dip).*sin(gamma).*sin(strike))                                    -
sin(AZM).*sin(TKO).*(cos(gamma).*(cos(2.*strike).*cos(rake).*sin(dip)    +
(sin(2.*dip).*sin(2.*strike).*sin(rake))./2)                             -
sin(2.*strike).*sin(dip).^2.*sin(gamma))                                 +
cos(AZM).*sin(TKO).*(cos(gamma).*(sin(2.*dip).*sin(rake).*sin(strike).^2
+                  sin(2.*strike).*cos(rake).*sin(dip))                  +
sin(gamma).*((2.*sigma)./(2.*sigma           -           1)              -
2.*sin(dip).^2.*sin(strike).^2)));
  Gs                                                                     =
((sin(AZM).*sin(TKO).*(cos(AZM).*cos(TKO).*(cos(gamma).*(cos(2.*strike).*
cos(rake).*sin(dip)   +   (sin(2.*dip).*sin(2.*strike).*sin(rake))./2)   -
sin(2.*strike).*sin(dip).^2.*sin(gamma))                                 -
sin(TKO).*(cos(gamma).*(cos(2.*dip).*cos(strike).*sin(rake)              -
cos(dip).*cos(rake).*sin(strike)) - sin(2.*dip).*cos(strike).*sin(gamma))
+ cos(TKO).*sin(AZM).*(cos(gamma).*(sin(2.*strike).*cos(rake).*sin(dip)  -
```

```
sin(2.*dip).*cos(strike).^2.*sin(rake))                                  -
sin(gamma).*((2.*sigma)./(2.*sigma          -          1)               -
2.*cos(strike).^2.*sin(dip).^2)))                                       -
cos(TKO).*(sin(TKO).*(sin(gamma).*(2.*cos(dip).^2 - (2.*sigma)./(2.*sigma
-       1))       +       sin(2.*dip).*cos(gamma).*sin(rake))           +
cos(AZM).*cos(TKO).*(cos(gamma).*(cos(2.*dip).*sin(rake).*sin(strike)   +
cos(dip).*cos(rake).*cos(strike)) - sin(2.*dip).*sin(gamma).*sin(strike))
- cos(TKO).*sin(AZM).*(cos(gamma).*(cos(2.*dip).*cos(strike).*sin(rake) -
cos(dip).*cos(rake).*sin(strike))                                       -
sin(2.*dip).*cos(strike).*sin(gamma)))                                  +
cos(AZM).*sin(TKO).*(sin(TKO).*(cos(gamma).*(cos(2.*dip).*sin(rake).*sin(
strike)          +          cos(dip).*cos(rake).*cos(strike))           -
sin(2.*dip).*sin(gamma).*sin(strike))                                   +
cos(TKO).*sin(AZM).*(cos(gamma).*(cos(2.*strike).*cos(rake).*sin(dip)   +
(sin(2.*dip).*sin(2.*strike).*sin(rake))./2)                            -
sin(2.*strike).*sin(dip).^2.*sin(gamma))                                -
cos(AZM).*cos(TKO).*(cos(gamma).*(sin(2.*dip).*sin(rake).*sin(strike).^2
+                 sin(2.*strike).*cos(rake).*sin(dip))                  +
sin(gamma).*((2.*sigma)./(2.*sigma          -          1)               -
2.*sin(dip).^2.*sin(strike).^2)))).^2                                   +
(cos(TKO).*(cos(AZM).*(cos(gamma).*(cos(2.*dip).*cos(strike).*sin(rake) -
cos(dip).*cos(rake).*sin(strike)) - sin(2.*dip).*cos(strike).*sin(gamma))
+      sin(AZM).*(cos(gamma).*(cos(2.*dip).*sin(rake).*sin(strike)       +
cos(dip).*cos(rake).*cos(strike))                                       -
sin(2.*dip).*sin(gamma).*sin(strike)))                                  -
sin(AZM).*sin(TKO).*(sin(AZM).*(cos(gamma).*(cos(2.*strike).*cos(rake).*s
in(dip)       +       (sin(2.*dip).*sin(2.*strike).*sin(rake))./2)      -
sin(2.*strike).*sin(dip).^2.*sin(gamma))                                -
cos(AZM).*(cos(gamma).*(sin(2.*strike).*cos(rake).*sin(dip)             -
sin(2.*dip).*cos(strike).^2.*sin(rake))                                 -
sin(gamma).*((2.*sigma)./(2.*sigma          -          1)               -
2.*cos(strike).^2.*sin(dip).^2)))                                       +
cos(AZM).*sin(TKO).*(sin(AZM).*(cos(gamma).*(sin(2.*dip).*sin(rake).*sin(
strike).^2        +        sin(2.*strike).*cos(rake).*sin(dip))         +
sin(gamma).*((2.*sigma)./(2.*sigma - 1) - 2.*sin(dip).^2.*sin(strike).^2))
+      cos(AZM).*(cos(gamma).*(cos(2.*strike).*cos(rake).*sin(dip)       +
(sin(2.*dip).*sin(2.*strike).*sin(rake))./2)                            -
sin(2.*strike).*sin(dip).^2.*sin(gamma)))).^2).^(1./2);
  Gsh                                                                   =
cos(TKO).*(cos(AZM).*(cos(gamma).*(cos(2.*dip).*cos(strike).*sin(rake)  -
cos(dip).*cos(rake).*sin(strike)) - sin(2.*dip).*cos(strike).*sin(gamma))
+      sin(AZM).*(cos(gamma).*(cos(2.*dip).*sin(rake).*sin(strike)       +
cos(dip).*cos(rake).*cos(strike))                                       -
sin(2.*dip).*sin(gamma).*sin(strike)))                                  -
sin(AZM).*sin(TKO).*(sin(AZM).*(cos(gamma).*(cos(2.*strike).*cos(rake).*s
in(dip)       +       (sin(2.*dip).*sin(2.*strike).*sin(rake))./2)      -
sin(2.*strike).*sin(dip).^2.*sin(gamma))                                -
cos(AZM).*(cos(gamma).*(sin(2.*strike).*cos(rake).*sin(dip)             -
sin(2.*dip).*cos(strike).^2.*sin(rake))                                 -
sin(gamma).*((2.*sigma)./(2.*sigma          -          1)               -
2.*cos(strike).^2.*sin(dip).^2)))                                       +
cos(AZM).*sin(TKO).*(sin(AZM).*(cos(gamma).*(sin(2.*dip).*sin(rake).*sin(
strike).^2        +        sin(2.*strike).*cos(rake).*sin(dip))         +
sin(gamma).*((2.*sigma)./(2.*sigma - 1) - 2.*sin(dip).^2.*sin(strike).^2))
+      cos(AZM).*(cos(gamma).*(cos(2.*strike).*cos(rake).*sin(dip)       +
(sin(2.*dip).*sin(2.*strike).*sin(rake))./2)                            -
sin(2.*strike).*sin(dip).^2.*sin(gamma)));


elseif nargout == 4
  Gp       =       cos(TKO).*(cos(TKO).*(sin(gamma).*(2.*cos(dip).^2       -
(2.*sigma)./(2.*sigma   -   1))   +   sin(2.*dip).*cos(gamma).*sin(rake))   -
cos(AZM).*sin(TKO).*(cos(gamma).*(cos(2.*dip).*sin(rake).*sin(strike)   +
```

```
cos(dip).*cos(rake).*cos(strike)) - sin(2.*dip).*sin(gamma).*sin(strike))
+ sin(AZM).*sin(TKO).*(cos(gamma).*(cos(2.*dip).*cos(strike).*sin(rake) -
cos(dip).*cos(rake).*sin(strike))                                       -
sin(2.*dip).*cos(strike).*sin(gamma)))                                  +
sin(AZM).*sin(TKO).*(cos(TKO).*(cos(gamma).*(cos(2.*dip).*cos(strike).*si
n(rake)          -          cos(dip).*cos(rake).*sin(strike))           -
sin(2.*dip).*cos(strike).*sin(gamma))                                   +
cos(AZM).*sin(TKO).*(cos(gamma).*(cos(2.*strike).*cos(rake).*sin(dip)   +
(sin(2.*dip).*sin(2.*strike).*sin(rake))./2)                            -
sin(2.*strike).*sin(dip).^2.*sin(gamma))                                +
sin(AZM).*sin(TKO).*(cos(gamma).*(sin(2.*strike).*cos(rake).*sin(dip)   -
sin(2.*dip).*cos(strike).^2.*sin(rake))                                 -
sin(gamma).*((2.*sigma)./(2.*sigma          -          1)               -
2.*cos(strike).^2.*sin(dip).^2)))                                       -
cos(AZM).*sin(TKO).*(cos(TKO).*(cos(gamma).*(cos(2.*dip).*sin(rake).*sin(
strike)          +          cos(dip).*cos(rake).*cos(strike))           -
sin(2.*dip).*sin(gamma).*sin(strike))                                   -
sin(AZM).*sin(TKO).*(cos(gamma).*(cos(2.*strike).*cos(rake).*sin(dip)   +
(sin(2.*dip).*sin(2.*strike).*sin(rake))./2)                            -
sin(2.*strike).*sin(dip).^2.*sin(gamma))                                +
cos(AZM).*sin(TKO).*(cos(gamma).*(sin(2.*dip).*sin(rake).*sin(strike).^2
+                 sin(2.*strike).*cos(rake).*sin(dip))                  +
sin(gamma).*((2.*sigma)./(2.*sigma          -          1)               -
2.*sin(dip).^2.*sin(strike).^2)));
  Gs                                                                    =
((sin(AZM).*sin(TKO).*(cos(AZM).*cos(TKO).*(cos(gamma).*(cos(2.*strike).*
cos(rake).*sin(dip)   +   (sin(2.*dip).*sin(2.*strike).*sin(rake))./2)  -
sin(2.*strike).*sin(dip).^2.*sin(gamma))                                -
sin(TKO).*(cos(gamma).*(cos(2.*dip).*cos(strike).*sin(rake)             -
cos(dip).*cos(rake).*sin(strike)) - sin(2.*dip).*cos(strike).*sin(gamma))
+ cos(TKO).*sin(AZM).*(cos(gamma).*(sin(2.*strike).*cos(rake).*sin(dip) -
sin(2.*dip).*cos(strike).^2.*sin(rake))                                 -
sin(gamma).*((2.*sigma).*(2.*sigma          -          1)               -
2.*cos(strike).^2.*sin(dip).^2)))                                       -
cos(TKO).*(sin(TKO).*(sin(gamma).*(2.*cos(dip).^2 - (2.*sigma)./(2.*sigma
-        1))        +        sin(2.*dip).*cos(gamma).*sin(rake))         +
cos(AZM).*cos(TKO).*(cos(gamma).*(cos(2.*dip).*sin(rake).*sin(strike)   +
cos(dip).*cos(rake).*cos(strike)) - sin(2.*dip).*sin(gamma).*sin(strike))
- cos(TKO).*sin(AZM).*(cos(gamma).*(cos(2.*dip).*cos(strike).*sin(rake) -
cos(dip).*cos(rake).*sin(strike))                                       -
sin(2.*dip).*cos(strike).*sin(gamma)))                                  +
cos(AZM).*sin(TKO).*(sin(TKO).*(cos(gamma).*(cos(2.*dip).*sin(rake).*sin(
strike)          +          cos(dip).*cos(rake).*cos(strike))           -
sin(2.*dip).*sin(gamma).*sin(strike))                                   +
cos(TKO).*sin(AZM).*(cos(gamma).*(cos(2.*strike).*cos(rake).*sin(dip)   +
(sin(2.*dip).*sin(2.*strike).*sin(rake))./2)                            -
sin(2.*strike).*sin(dip).^2.*sin(gamma))                                -
cos(AZM).*cos(TKO).*(cos(gamma).*(sin(2.*dip).*sin(rake).*sin(strike).^2
+                 sin(2.*strike).*cos(rake).*sin(dip))                  +
sin(gamma).*((2.*sigma).*(2.*sigma          -          1)               -
2.*sin(dip).^2.*sin(strike).^2)))).^2                                   +
(cos(TKO).*(cos(AZM).*(cos(gamma).*(cos(2.*dip).*cos(strike).*sin(rake) -
cos(dip).*cos(rake).*sin(strike)) - sin(2.*dip).*cos(strike).*sin(gamma))
+      sin(AZM).*(cos(gamma).*(cos(2.*dip).*sin(rake).*sin(strike)       +
cos(dip).*cos(rake).*cos(strike))                                       -
sin(2.*dip).*sin(gamma).*sin(strike)))                                  -
sin(AZM).*sin(TKO).*(sin(AZM).*(cos(gamma).*(cos(2.*strike).*cos(rake).*s
in(dip)       +       (sin(2.*dip).*sin(2.*strike).*sin(rake))./2)      -
sin(2.*strike).*sin(dip).^2.*sin(gamma))                                -
cos(AZM).*(cos(gamma).*(sin(2.*strike).*cos(rake).*sin(dip)             -
sin(2.*dip).*cos(strike).^2.*sin(rake))                                 -
sin(gamma).*((2.*sigma).*(2.*sigma          -          1)               -
2.*cos(strike).^2.*sin(dip).^2)))                                       +
```

```
cos(AZM).*sin(TKO).*(sin(AZM).*(cos(gamma).*(sin(2.*dip).*sin(rake).*sin(
strike).^2        +        sin(2.*strike).*cos(rake).*sin(dip))        +
sin(gamma).*((2.*sigma)./(2.*sigma - 1) - 2.*sin(dip).^2.*sin(strike).^2))
+      cos(AZM).*(cos(gamma).*(cos(2.*strike).*cos(rake).*sin(dip)      +
(sin(2.*dip).*sin(2.*strike).*sin(rake))./2)                            -
sin(2.*strike).*sin(dip).^2.*sin(gamma)))).^2).^(1./2);
  Gsh                                                                   =
cos(TKO).*(cos(AZM).*(cos(gamma).*(cos(2.*dip).*cos(strike).*sin(rake)   -
cos(dip).*cos(rake).*sin(strike)) - sin(2.*dip).*cos(strike).*sin(gamma))
+      sin(AZM).*(cos(gamma).*(cos(2.*dip).*sin(rake).*sin(strike)      +
cos(dip).*cos(rake).*cos(strike))                                       -
sin(2.*dip).*sin(gamma).*sin(strike)))                                  -
sin(AZM).*sin(TKO).*(sin(AZM).*(cos(gamma).*(cos(2.*strike).*cos(rake).*s
in(dip)       +       (sin(2.*dip).*sin(2.*strike).*sin(rake))./2)      -
sin(2.*strike).*sin(dip).^2.*sin(gamma))                                -
cos(AZM).*(cos(gamma).*(sin(2.*strike).*cos(rake).*sin(dip)             -
sin(2.*dip).*cos(strike).^2.*sin(rake))                                 -
sin(gamma).*((2.*sigma)./(2.*sigma            -           1)            -
2.*cos(strike).^2.*sin(dip).^2)))                                       +
cos(AZM).*sin(TKO).*(sin(AZM).*(cos(gamma).*(sin(2.*dip).*sin(rake).*sin(
strike).^2        +        sin(2.*strike).*cos(rake).*sin(dip))        +
sin(gamma).*((2.*sigma)./(2.*sigma - 1) - 2.*sin(dip).^2.*sin(strike).^2))
+      cos(AZM).*(cos(gamma).*(cos(2.*strike).*cos(rake).*sin(dip)      +
(sin(2.*dip).*sin(2.*strike).*sin(rake))./2)                            -
sin(2.*strike).*sin(dip).^2.*sin(gamma)));
  Gsv                                                                   =
sin(AZM).*sin(TKO).*(cos(AZM).*cos(TKO).*(cos(gamma).*(cos(2.*strike).*co
s(rake).*sin(dip)    +    (sin(2.*dip).*sin(2.*strike).*sin(rake))./2)    -
sin(2.*strike).*sin(dip).^2.*sin(gamma))                                -
sin(TKO).*(cos(gamma).*(cos(2.*dip).*cos(strike).*sin(rake)             -
cos(dip).*cos(rake).*sin(strike)) - sin(2.*dip).*cos(strike).*sin(gamma))
+ cos(TKO).*sin(AZM).*(cos(gamma).*(sin(2.*strike).*cos(rake).*sin(dip) -
sin(2.*dip).*cos(strike).^2.*sin(rake))                                 -
sin(gamma).*((2.*sigma)./(2.*sigma            -           1)            -
2.*cos(strike).^2.*sin(dip).^2)))                                       -
cos(TKO).*(sin(TKO).*(sin(gamma).*(2.*cos(dip).^2 - (2.*sigma)./(2.*sigma
-        1))        +        sin(2.*dip).*cos(gamma).*sin(rake))        +
cos(AZM).*cos(TKO).*(cos(gamma).*(cos(2.*dip).*sin(rake).*sin(strike)    +
cos(dip).*cos(rake).*cos(strike)) - sin(2.*dip).*sin(gamma).*sin(strike))
- cos(TKO).*sin(AZM).*(cos(gamma).*(cos(2.*dip).*cos(strike).*sin(rake) -
cos(dip).*cos(rake).*sin(strike))                                       -
sin(2.*dip).*cos(strike).*sin(gamma)))                                  +
cos(AZM).*sin(TKO).*(sin(TKO).*(cos(gamma).*(cos(2.*dip).*sin(rake).*sin(
strike)          +          cos(dip).*cos(rake).*cos(strike))           -
sin(2.*dip).*sin(gamma).*sin(strike))                                   +
cos(TKO).*sin(AZM).*(cos(gamma).*(cos(2.*strike).*cos(rake).*sin(dip)    +
(sin(2.*dip).*sin(2.*strike).*sin(rake))./2)                            -
sin(2.*strike).*sin(dip).^2.*sin(gamma))                                -
cos(AZM).*cos(TKO).*(cos(gamma).*(sin(2.*dip).*sin(rake).*sin(strike).^2
+                 sin(2.*strike).*cos(rake).*sin(dip))                  +
sin(gamma).*((2.*sigma)./(2.*sigma            -           1)            -
2.*sin(dip).^2.*sin(strike).^2)));



end
```

D MatLAB routine for plotting synthetic seismograms using the Elle output parameters for the hydrofracturing experiments.

```
clear all
dts=.001; % Sampling interval for signal
dti=.01; % Sampling interval for empty space

%%%%%%%%%%%%%% Input variables %%%%%%%%%%%%%%%%%%%%%%%%%%
Tini_p=2660.2;   % Start time of P wave (ms)
Tini_s=6257.5; % Start time of S wave (ms)
Trp=7.961; % Rupture time for P wave (ms)
Trs=4.981; % Rupture time for S wave (ms)
Tdp=0.013; % Rise time for P wave
Tds=0.013; % Rise time for S wave (ms)
Sp=2.831; % Displacement velocity for P wave, negative if radiation
pattern is compressional (nm/ms)
Ss=54.91; % Displacement velocity for S wave(nm/ms)

%%%%%%%%%%%%%%%%%%%%%%%%%%%%%%%%%%%%%%%%%%%%%%%%%%%%%%%%%%%%

EndP=Tini_p+Trp+Tdp+Tdp;
EndS=Tini_s+Trs+Tds+Tds+0.1;
breakt=Tini_s-EndP;

% Create ramp function for P wave

t0=[(Tini_p-0.01):dti:Tini_p];
t1=[Tini_p:dts:(Tini_p+Tdp)];
t2=[(Tini_p+Tdp):dts:(Tini_p+Trp)];
t3=[(Tini_p+Trp):dts:(Tini_p+Trp+Tdp)];
t4=[(Tini_p+Trp+Tdp):dti:(EndP)];
SP0=size(t0);
sp0=0;
sp0_1=repmat(sp0,SP0);
SP4=size(t4);
sp4=0;
sp4_1=repmat(sp4,SP4);
sp1=((t1-Tini_p)*Sp)/Tdp;
sp2=Sp;
SP2=size(t2);

sp2_1=repmat(sp2,SP2);

sp3=Sp-(Sp*((t3-(Tini_p+Trp))/Tdp));


% Create ramp function for S wave

t6=[Tini_s:dts:(Tini_s+Tds)];
t7=[(Tini_s+Tds):dts:(Tini_s+Trs)];
t8=[(Tini_s+Trs):dts:(Tini_s+Trs+Tds)];
t9=[(Tini_s+Trs+Tds):dti:(EndS)];

SP9=size(t9);
sp9=0;
sp9_1=repmat(sp9,SP9);
sp6=((t6-Tini_s)*Ss)/Tds;
```

```
sp7=Ss;
SP7=size(t7);

sp7_1=repmat(sp7,SP7);

sp8=Ss-(Ss*((t8-(Tini_s+Trs))/Tds));

% Create cumulative displacement profile for P and S waves
s_start=[sp0_1];
sp=[sp1 sp2_1 sp3];
ss=[sp6 sp7_1 sp8];
s_end=[sp9_1];

Up=zeros(size(sp));
   Up(1)=dts*sp(1);
   Up(2)=dts*sp(2);

   for i=3:1:(length(sp))

       Up(i)=Up(i-1)+sp(i)*dts;

   end

Us=zeros(size(ss));
   Us(1)=dts*ss(1);
   Us(2)=dts*ss(2);

   for j=3:1:(length(ss))

       Us(j)=Us(j-1)+ss(j)*dts;

   end

% Create combined time profiles for P and S waves
t_start=[t0];
tp=[t1 t2 t3];
ts=[t6 t7 t8];
t_end=[t9];



%Fourier transform

y=fftshift(Sp*(sinc(Up)));
z=fftshift(Ss*(sinc(Us)));


%Apply attenuation effect
% ... for P wave

A = y*Trp/(pi*1000);
B = (-y*Trp)/2000;
C = (log(y/((dts/2))))-2;
D = exp(B+(1i*A.*C));
E = (D.*(y));

% ... for S wave
A1 = z*Trs/(pi*1000);
B1 = (-z*Trs)/2000;
```

```
C1 = (log(z/((dts/2))))-2;
D1 = exp(B1+(1i*A1.*C1));
E1 = (D1.*(z));

%Plot the graph

figure
ax1 = subplot (2,1,1);
plot(tp, E, 'b');
title('P wave');
xlabel('Time (ms)')
ylabel('Amplitude (nm)');

ax2 = subplot (2,1,2);
plot(ts, E1, 'b');
title('S wave');
xlabel('Time (ms)');
ylabel('Amplitude (nm)');
```

List of References

Aamodt, L. and Kuriyagawa, M., 1981, Measurement of instantaneous shut-in pressure in crystalline rock (No. LA-UR-82-782; CONF-811240-1). Los Alamos National Lab., NM (USA).

Abercrombie, R.E., 1995, Earthquake source scaling relationships from− 1 to 5 ML using seismograms recorded at 2.5-km depth. *Journal of Geophysical Research: Solid Earth* 100(B12): 24015–24036.

Abramson, L.W., Lee, T.S., Sharma. S, 2002, *Slope stability and stabilization methods*. John Wiley & Sons.

Agarwal, R.G., Carter, R.D., Pollock, C.B., 1979, Evaluation and performance prediction of low-permeability gas wells stimulated by massive hydraulic fracturing. *Journal of Petroleum Technology* 31(03): 362–372.

Aki, K., Richards, P.G., 2002), *Quantitative Seismology*. University Science Books.

Aki, K., 1967, Scaling law of seismic spectrum. *Journal of Geophysical Research* 72(4): 1217–1231.

Aki, K., 1984, Asperities, barriers, characteristic earthquakes and strong motion prediction. *Journal of Geophysical Research: Solid Earth* 89(B7): 5867–5872.

Aki, K., Richards, P.G., 1980, Quantative seismology: Theory and methods. *New York* 801.

Anderson, D.L., Hart, R.S., 1978, Q of the Earth. *Journal of Geophysical Research: Solid Earth* 83(B12): 5869–5882.

Anderson, T.L., Anderson, T.L., 2005, *Fracture mechanics: fundamentals and applications*. CRC Press.

Andrews, M.J., O'rourke, P.J., 1996, The multiphase particle-in-cell (MP-PIC) method for dense particulate flows. *International Journal of Multiphase Flow* 22(2): 379–402.

Aoyagi, K., Kazama, T., 1980, Transformational changes of clay minerals, zeolites and silica minerals during diagenesis. *Sedimentology* 27(2): 179–188.

Ashurst, W.T., Hoover, W.G., 1976, Microscopic fracture studies in the two-dimensional triangular lattice. *Physical Review B* 14(4): 1465.

Avallone, E., Baumeister, T., 2017, *Mark's standard handbook for mechanical engineers*. McGraw-Hill.

Baig, A., Urbancic, T., 2010, Microseismic moment tensors: A path to understanding frac growth. *The Leading Edge* 29(3): 320–324.

Balakrishnan, N., 1991, *Handbook of the logistic distribution*. CRC Press.

Banks, D., Odling, N.E., Skarphagen, H., 1996, Permeability and stress in crystalline rocks. *Terra Nova* 8(3): 223–235.

Baria, R., Baumgärtner, J., Rummel, F., 1999, HDR/HWR reservoirs: concepts, understanding and creation. *Geothermics* 28(4): 533–552.

Barker, C., 1972, Aquathermal pressuring--role of temperature in development of abnormal-pressure zones. *AAPG Bulletin* 56(10): 2068–2071.

Beer, F.P., Johnston Jr, E.R., DeWolf, J.T., 2001, *Mechanics of materials. Third*. New York: McGraw-Hill.

Bell, F.G., 2004, *Engineering geology and construction*. CRC Press.

Bell, F.G., 2013, *Engineering in rock masses*. Elsevier.

Ben-Zion, Y., 2003, Key formulas in earthquake seismology. *International handbook of earthquake and engineering seismology* 81: 1857–1875.

Ben-Zion, Y,. 2003, *Seismic Motion, Lithospheric Structures, Earthquake and Volcanic Sources: The Keiiti Aki Volume*. Springer.

Biot, M.A., Masse, L., Medlin, W.L., 1986, A two-dimensional theory of fracture propagation. *SPE Production Engineering* 1(01): 17–30.

Bird, R.B., 2002, Transport phenomena. *Applied Mechanics Reviews* 55(1): R1-R4.

Bishop, W., Henkel, D.J., 1957, *The measurement of soil properties in the triaxial test*. Edward Arnold (Publishers) Ltd; London.

Bishop, A.W. and Donald, I.B., 1961, July. The experimental study of partly saturated soil in the triaxial apparatus. *In Proceedings of the 5th international conference on soil mechanics and foundation engineering*, Paris, Vol. 1, pp. 13-21.

Bobok, E., 1993, *Fluid mechanics for petroleum engineers*. Elsevier.

Bohnhoff, M., Baisch, S., Harjes, H., 2004, Fault mechanisms of induced seismicity at the superdeep German Continental Deep Drilling Program (KTB) borehole and their relation to fault structure and stress field. *Journal of Geophysical Research: Solid Earth* 109(B2).

Bonamy, D., Bouchaud, E., 2011, Failure of heterogeneous materials: A dynamic phase transition? *Physics Reports* 498(1): 1–44.

Bons, P., Koehn, D., Jessell, M.W., 2007, *Microdynamics simulation*. Springer Science & Business Media.

Borowski, S., 2012, Idea for “fracking” came from Civil War battlefield. *AAAS MemberCentral*.

Boucher, G., Ryall, A., Jones, A.E., 1969, Earthquakes associated with underground nuclear explosions. *Journal of Geophysical Research* 74(15): 3808–3820.

Bower, A.F., 2009, *Applied mechanics of solids*. CRC Press.

Bowker, K.A., 2007, Barnett shale gas production, Fort Worth Basin: Issues and discussion. *AAPG Bulletin* 91(4): 523–533.

Brown, E.T., 2007, *Block Caving Geomechanics: International Caving Study 1997-2004*. Julius Kruttschnitt Mineral Research Centre, The University of Queensland.

Bunger, A.P., Detournay, E., 2008, Experimental validation of the tip asymptotics for a fluid-driven crack. *Journal of the Mechanics and Physics of Solids* 56(11): 3101–3115.

Bunger, A.P., Detournay, E., Garagash, D.I., 2005, Toughness-dominated hydraulic fracture with leak-off. *International Journal of Fracture* 134(2): 175–190.

Carman, P.C., 1939, Permeability of saturated sands, soils and clays. *The Journal of Agricultural Science* 29(2): 262–273.

Carpenter, E.W., Flinn, E.A., 1965, Attenuation of teleseismic body waves. *Nature* 207(4998): 745.

Castagna, J.P., Batzle, M.L., Eastwood, R.L., 1985, Relationships between compressional-wave and shear-wave velocities in clastic silicate rocks. *Geophysics* 50(4): 571–581.

Chapman, C.H., 1978, A new method for computing synthetic seismograms. *Geophysical Journal of the Royal Astronomical Society* 54(3): 481–518.

Chareyre, B., Cortis, A., Catalano, E., 2012, Pore-scale modeling of viscous flow and induced forces in dense sphere packings. *Transport in porous media* 94(2): 595–615.

Chen, S., Doolen, G.D., 1998, Lattice Boltzmann method for fluid flows. *Annual review of fluid mechanics* 30(1): 329–364.

Cheng, X., Xu, L., Patterson, A., 2008, Towards the zero-surface-tension limit in granular fingering instability. *Nature Physics* 4(3): 234.
Chiu, C., Wang, T., Weng M., 2013, Modeling the anisotropic behavior of jointed rock mass using a modified smooth-joint model. *International Journal of Rock Mechanics and Mining Sciences* 62: 14–22.
Chouet, B., 2003, Volcano seismology. In: Ben-Zion Y (ed.) *Seismic Motion, Lithospheric Structures, Earthquake and Volcanic Sources: The Keiiti Aki Volume:* Springer, pp. 739–788.
Chouet, B.A., 1996, Long-period volcano seismicity: its source and use in eruption forecasting. *Nature* 380(6572): 309.
Ciamarra, M.P., Coniglio, A., Candia, A., 2010, Disordered jammed packings of frictionless spheres. *Soft Matter* 6(13): 2975–2981.
Ciarlet, P.G., Lions, J., 1990, Handbook of numerical analysis. Vol. 1. *Amsterdam and New York, North-Holland, 1990, 658.*
Clément, C., Toussaint, R., Stojanova, M., 2018, Sinking during earthquakes: Critical acceleration criteria control drained soil liquefaction. *Physical review E* 97(2): 22905.
Cobbold, P.R., Rodrigues, N., 2007, Seepage forces, important factors in the formation of horizontal hydraulic fractures and bedding-parallel fibrous veins (‘beef’and ‘cone-in-cone’). *Geofluids* 7(3): 313–322.
Cornet, F.H., Helm, J., Poitrenaud, H., 1997, Seismic and aseismic slips induced by large-scale fluid injections. *Pure and Applied Geophysics* 150(3-4): 563–583.
Cornet, F.H., Helm, J., Poitrenaud, H., 1997, Seismic and aseismic slips induced by large-scale fluid injections. *Pure and Applied Geophysics* 150(3-4): 563–583.
Cornet, F.H., Jianmin, Y., 1995, Analysis of induced seismicity for stress field determination and pore pressure mapping. *Pure and Applied Geophysics* 145(3): 677–700.
Cox, S., 2005, Coupling between deformation, fluid pressures, and fluid flow in ore-producing hydrothermal systems at depth in the crust.
Cuenot, N., Charléty, J., Dorbath, L., 2006, Faulting mechanisms and stress regime at the European HDR site of Soultz-sous-Forêts, France. *Geothermics* 35(5): 561–575.
Cundall, P.A., 2001, A discontinuous future for numerical modelling in geomechanics? *Proceedings of the institution of civil engineers-geotechnical engineering* 149(1): 41–47.
Cundall, P.A., Hart, R.D., 1992, Numerical modelling of discontinua. *Engineering computations* 9(2): 101–113.
Cundall, P.A., Strack, O.D.L., 1979, A discrete numerical model for granular assemblies. *geotechnique* 29(1): 47–65.
Damjanac, B., Detournay, C., 2013, *Three-dimensional numerical model of hydraulic fracturing in fractured rock masses*. International Society for Rock Mechanics.
Dean, R.G., Dalrymple, R.A., 1991, *Water wave mechanics for engineers and scientists*. World Scientific Publishing Company.
Deichmann, N., Giardini, D., 2009, Earthquakes induced by the stimulation of an enhanced geothermal system below Basel (Switzerland). *Seismological Research Letters* 80(5): 784–798.
Deshpande, V.S., Fleck, N.A., 2001 Multi-axial yield behaviour of polymer foams. *Acta Materialia* 49(10): 1859–1866.

Detournay, E., Cheng, A.H., 1991, Plane strain analysis of a stationary hydraulic fracture in a poroelastic medium. *International Journal of Solids and Structures* 27(13): 1645–1662.

Detournay, E.,Cheng, A.H, 1993, Fundamentals of poroelasticity1. *Chapter 5 in Comprehensive Rock Engineering: Principles, Practice and Projects, II*: 113–171.

Detournay, E., Cheng, A.H., 1995, Fundamentals of poroelasticity. In: *Analysis and design methods:* Elsevier, pp. 113–171.

DiPippo, R., 2012, *Geothermal power plants: principles, applications, case studies and environmental impact*. Butterworth-Heinemann.

Dorren, L.K.A., 2003, A review of rockfall mechanics and modelling approaches. *Progress in Physical Geography* 27(1): 69–87.

Dyer, B.C., Schanz, U., Spillmann, T., 2010, Application of microseismic multiplet analysis to the Basel geothermal reservoir stimulation events. *Geophysical Prospecting* 58(5): 791–807.

Eaton, D.W., Forouhideh, F., 2012, Solid angles and the impact of receiver-array geometry on microseismic moment-tensor inversion. *Geophysics*.

Eberhardt, E., Stimpson, B., Stead, D., 1999, Effects of grain size on the initiation and propagation thresholds of stress-induced brittle fractures. *Rock Mechanics and Rock Engineering* 32(2): 81–99.

Eisner, L., Hulsey, B.J., Duncan, P., 2010, Comparison of surface and borehole locations of induced seismicity. *Geophysical Prospecting* 58(5): 809–820.

Ellsworth, W.L., 2013, Injection-induced earthquakes. *Science* 341(6142): 1225942.

Engelder, T., Lacazette, A., 1990, Natural hydraulic fracturing. *Rock joints: Rotterdam, AA Balkema*: 35–44.

Enoki, M., Kishi, T., 1988, Theory and analysis of deformation moment tensor due to microcracking. *International Journal of Fracture* 38(4): 295–310.

Farrell, W.E., 1972, Deformation of the Earth by surface loads. *Reviews of Geophysics* 10(3): 761–797.

Fay, J.A., 1994, *Introduction to fluid mechanics*. MIT press.

Fehler, M.C., 1989, *Stress control of seismicity patterns observed during hydraulic fracturing experiments at the Fenton Hill hot dry rock geothermal energy site, New Mexico*. Elsevier.

Fenner, T., Levene, M., Loizou, G., 2012, A discrete evolutionary model for chess players' ratings. *IEEE Transactions on Computational Intelligence and AI in Games* 4(2): 84–93.

Fischer, T., Horálek, J., Michálek, J., 2010, The 2008 West Bohemia earthquake swarm in the light of the WEBNET network. *Journal of seismology* 14(4): 665–682.

Flekkøy, E.G., Malthe-Sørenssen, A., Jamtveit, B., 2002, Modeling hydrofracture. *Journal of Geophysical Research: Solid Earth* 107(B8): ECV 1-1-ECV 1-11.

Frank, U., Barkley, N., 1995, Remediation of low permeability subsurface formations by fracturing enhancement of soil vapor extraction. *Journal of hazardous materials* 40(2): 191–201.

Fraser, B.J., 1994, *Context: Classroom and school climate*. Curtin University of Technology.

Fredrich, J.T., Menendez, B., Wong, T., 1995, Imaging the pore structure of geomaterials. *Science* 268(5208): 276–279.

Fredrich, J.T., Evans, B., Wong, T., 1990, Effect of grain size on brittle and semibrittle strength: Implications for micromechanical modelling of failure in compression. *Journal of Geophysical Research: Solid Earth* 95(B7): 10907–10920.

Fyfe, D., Montgomery, D., 1978, Statistical formulation of one-dimensional electron fluid turbulence. *The Physics of Fluids* 21(3): 316–326.

Fyfe, W.S., 2012, *Fluids In The Earth's Crust: Their Significance In Metamorphic, Tectonic And Chemical Transport Process*. Elsevier.

Gall, K., Dunn, M.L., Liu, Y., 2002, Shape memory polymer nanocomposites. *Acta Materialia* 50(20): 5115–5126.

Gallegos, T.J., Varela, B.A., Haines, S.S. and Engle, M.A., 2015. Hydraulic fracturing water use variability in the United States and potential environmental implications. *Water Resources Research*, *51*(7), pp.5839-5845.

Garagash, D.I., 2006, Plane-strain propagation of a fluid-driven fracture during injection and shut-in: Asymptotics of large toughness. *Engineering fracture mechanics* 73(4): 456–481.

Garagash, D. and Detournay, E., 1996. Influence of pressurization rate on borehole breakdown pressure in impermeable rocks. *In Proc. North American Rock Mechanics Symposium* (pp. 1075-1080).

Gasperini, P. and Vannucci, G., 2003, FPSPACK: a package of FORTRAN subroutines to manage earthquake focal mechanism data. *Computers & Geosciences* 29(7): 893–901.

Geller, R.J. and Ohminato, T. 1994, Computation of synthetic seismograms and their partial derivatives for heterogeneous media with arbitrary natural boundary conditions using the Direct Solution Method. *Geophysical Journal International* 116(2): 421–446.

Gercek. H., 2007, Poisson's ratio values for rocks. *International Journal of Rock Mechanics and Mining Sciences* 44(1): 1–13.

Ghani, I., Koehn, D. and Toussaint, R., 2015, Dynamics of hydrofracturing and permeability evolution in layered reservoirs. *Frontiers in Physics* 3: 67.

Ghani, I., Koehn, D., Toussaint, R., 2013, Dynamic Development of Hydrofracture. *Pure and Applied Geophysics* 170(11): 1685–1703.

Goertz-Allmann, B.P., Goertz, A. and Wiemer, S., 2011, Stress drop variations of induced earthquakes at the Basel geothermal site. *Geophysical Research Letters* 38(9).

Goren, L., Aharonov, E., Sparks, D., 2010, Pore pressure evolution in deforming granular material: A general formulation and the infinitely stiff approximation. *Journal of Geophysical Research: Solid Earth* 115(B9).

Goren, L., Aharonov, E., Sparks, D., 2011, The mechanical coupling of fluid-filled granular material under shear. *Pure and Applied Geophysics* 168(12): 2289–2323.

Greaves, G.N., Greer, A.L., Lakes, R.S., 2011, Poisson's ratio and modern materials. *Nature materials* 10(11): 823.

Green, D.H. and Wang, H.F., 1986, Fluid pressure response to undrained compression in saturated sedimentary rock. *Geophysics* 51(4): 948–956.

Green, C.A., Styles, P. and Baptie, B.J., 2012. Preese Hall shale gas fracturing review and recommendations for induced seismic mitigation. *London, UK: Department of Energy and Climate Change*.

Griffith, A.A., 1921, The phenomena of rupture and flow in solids. *Philosophical transactions of the royal society of london. Series A, containing papers of a mathematical or physical character* 221: 163–198.

Grigoli, F., Cesca, S., Rinaldi, A.P., Manconi, A., López-Comino, J.A., Clinton, J.F., Westaway, R., Cauzzi, C., Dahm, T. and Wiemer, S., 2018. The November 2017 Mw 5.5 Pohang earthquake: A possible case of induced seismicity in South Korea. *Science*, *360*(6392), pp.1003-1006.

Groenenboom, J. and van Dam, D.B., 2000, Monitoring hydraulic fracture growth: Laboratory experiments. *Geophysics* 65(2): 603–611.

Guglielmi, Y., Cappa, F., Avouac, J., 2015, Seismicity triggered by fluid injection–induced aseismic slip. *Science* 348(6240): 1224–1226.

Gutenberg, B. and Richter, C.F., 1941, Seismicity of the Earth.

Haas, J.L., 1971, The effect of salinity on the maximum thermal gradient of a hydrothermal system at hydrostatic pressure. *Economic Geology* 66(6): 940–946.

Haimson, B.C., 1978, *The hydrofracturing stress measuring method and recent field results*. Elsevier.

Haimson, B. and Chang, C., 2000, A new true triaxial cell for testing mechanical properties of rock, and its use to determine rock strength and deformability of Westerly granite. *International Journal of Rock Mechanics and Mining Sciences* 37(1-2): 285–296.

Haimson, B.C. and Zhongliang, Z., 1991, *Effect of borehole size and pressurization rate on hydraulic fracturing breakdown pressure*. American Rock Mechanics Association.

Hanson, M.E, Shaffer, R.J. and Anderson, G.D., 1981, Effects of various parameters on hydraulic fracturing geometry. *Society of Petroleum Engineers Journal* 21(04): 435–443.

Hazzard. J.F, and Young, R.P., 2002, Moment tensors and micromechanical models. *Tectonophysics* 356(1): 181–197.

Healy, J.H., Rubey, W.W., Griggs, D.T., 1968, The denver earthquakes. *Science* 161(3848): 1301–1310.

Heaton, T.H., 1982, Tidal triggering of earthquakes. *Bulletin of the Seismological Society of America* 72(6A): 2181–2200.

Heinberg, R., 2013, *A brief history of fracking*.

Hele-Shaw, H.S., 1897, Experiments on the nature of surface resistance in pipes and on ships. *Trans. Inst. Naval Archtects* 39: 145–156.

Hele-Shaw, H.S., 1898, Experiments on the nature of surface resistance of water and streamline motion under certain experimental conditions. *Trans. Inst. Naval Archtects* 40: 21–46.

Hele-Shaw, H.S., 1899, Stream-line motion of a viscous film. *Rep. 68th Meetin& British Assoc. for the Advancement Sci*: 136–142.

Herrmann, R.B., 2002, Computer programs in seismology: An overview of synthetic seismogram computation. *Saint-Louis University, USA, version* 3: 2002.

Hicks, T., Pine, R., Willis-Richards, J., 1996, *A hydro-thermo-mechanical numerical model for HDR geothermal reservoir evaluation*. Elsevier.

Hillis, R.R., 2003, Pore pressure/stress coupling and its implications for rock failure. *Geological Society, London, Special Publications* 216(1): 359–368.

Hiramatsu, Y., Yamanaka, H., Tadokoro, K., 2002, Scaling law between corner frequency and seismic moment of microearthquakes: Is the breakdown of the cube law a nature of earthquakes? *Geophysical Research Letters* 29(8).

Hoek, E. and Franklin, J.A., 1967, *A simple triaxial cell for field or laboratory testing of rock*. Imperial College of Science and Technology, University of London.

Holtz, R.D. and Kovacs, W.D., 1981, *An introduction to geotechnical engineering (No. Monograph)*.
House, L.S. and Flores, R., 2002 Seismological studies of a fluid injection in sedimentary rocks, East Texas. *Pure and Applied Geophysics* 159(1): 371–401.
Housee, S., 2004, Unveiling South Asian female identities post september 11: Asian female students' sense of identity and experiences of higher education. *Institutional racism in higher education*: 59–70.
Howison, S.D., 1986, Bubble growth in porous media and Hele–Shaw cells. *Proceedings of the Royal Society of Edinburgh Section A: Mathematics* 102(1-2): 141–148.
Huang, M., Jiang, L., Liaw, P.K., 1998, Using acoustic emission in fatigue and fracture materials research. *JOM* 50(11): 1–14.
Huang, W., 1998, Application of Mindlin plate theory to analysis of acoustic emission waveforms in finite plates. In: Schafbuch PJ, Thompson RB, Rizzo FJ and Rudolphi TJ., eds, *Review of Progress in Quantitative Nondestructive Evaluation:* Springer, pp. 493–500.
Hubbert, M.K. and Rubey, W.W., 1959, Role of fluid pressure in mechanics of overthrust faulting I. Mechanics of fluid-filled porous solids and its application to overthrust faulting. *Geological Society of America Bulletin* 70(2): 115–166.
Hubbert, M.K. and Willis, D.G., 1972, Mechanics of hydraulic fracturing.
Hutchinson, J.W., 2000, Plasticity at the micron scale. *International Journal of Solids and Structures* 37(1-2): 225–238.
Iio, Y., 1986, Scaling relation between earthquake size and duration of faulting for shallow earthquakes in seismic moment between 1010 and 1025 dyne• cm. *Journal of Physics of the Earth* 34(2): 127–169.
Inglis, C.E., 1913, Stress in a plate due to the presence of sharp corners and cracks. *Trans. Roy. Inst. Naval Architects* 60: 219–241.
Irwin, G.R., 1957, Analysis of Stresses and Strains Near the End of a Crack Traversing a Plate. *J. Appl. Mech.*
Jerry, B., 2005, *Discrete event system simulation*. Pearson Education India.
Jin, L, Sun, B. and Gu, B., 2011, Finite element simulation of three-dimensional angle-interlock woven fabric undergoing ballistic impact. *Journal of the textile institute* 102(11): 982–993.
Jing, L., 2003, A review of techniques, advances and outstanding issues in numerical modelling for rock mechanics and rock engineering. *International Journal of Rock Mechanics and Mining Sciences* 40(3): 283–353.
Jing, L. and Hudson, J.A., 2002, Numerical methods in rock mechanics. *International Journal of Rock Mechanics and Mining Sciences* 39(4): 409–427.
Johns, W.D. and Shimoyama, A., 1972, Clay minerals and petroleum-forming reactions during burial and diagenesis. *AAPG Bulletin* 56(11): 2160–2167.
Johnsen, Ø., Toussaint, R., Måløy, K.J, 2008, Coupled air/granular flow in a linear Hele-Shaw cell. *Physical review E* 77(1): 11301.
Johnsen, Ø, Toussaint, R., Måløy, K.J, 2006, Pattern formation during air injection into granular materials confined in a circular Hele-Shaw cell. *Physical review E* 74(1): 11301.
Johnston, D.H. and Toksöz, M.N., 1980, Thermal cracking and amplitude dependent attenuation. *Journal of Geophysical Research: Solid Earth* 85(B2): 937–942.
Jost, M.L, Büßelberg, T., Jost, Ö., 1998, Source parameters of injection-induced microearthquakes at 9 km depth at the KTB deep drilling site, Germany. *Bulletin of the Seismological Society of America* 88(3): 815–832.

Jost, M. and Herrmann, R.B., 1989, A student's guide to and review of moment tensors. *Seismological Research Letters* 60(2): 37–57.
Julian, B.R., Miller, A.D. and Foulger, G.R., 1997, Non-double-couple earthquake mechanisms at the Hengill-Grensdalur volcanic complex, southwest Iceland. *Geophysical Research Letters* 24(7): 743–746.
Julian, B.R., Miller, A.D. and Foulger, G.R., 1998, Non-double-couple earthquakes 1. Theory. *Reviews of Geophysics* 36(4): 525–549.
Kamei, R., Nakata, N. and Lumley, D., 2015, Introduction to microseismic source mechanisms. *The Leading Edge* 34(8): 876–880.
Kanamori, H., 1994, Mechanics of earthquakes. *Annual Review of Earth and Planetary Sciences* 22(1): 207–237.
Kanamori, H. and Anderson, D.L., 1975, Theoretical basis of some empirical relations in seismology. *Bulletin of the Seismological Society of America* 65(5): 1073–1095.
Keller, G.V. and Frischknecht, F.C., 1966, Electrical methods in geophysical prospecting.
Kelly, K.R., Ward, R.W., Treitel, S., 1976, Synthetic seismograms: a finite-difference approach. *Geophysics* 41(1): 2–27.
Keranen, K.M., Weingarten, M., Abers, G.A., 2014, Sharp increase in central Oklahoma seismicity since 2008 induced by massive wastewater injection. *Science* 345(6195): 448–451.
Knopoff, L., 1964, A matrix method for elastic wave problems. *Bulletin of the Seismological Society of America* 54(1): 431–438.
Knopoff, L., Charmet, J.C., Roux, S., 1990, Disorder and Fracture. *NATO ASI Series B: Physics* 235.
Kochnev, V., Polyakov, V., Goz, I., 2007, *Imaging hydraulic fracture zones from surface passive microseismic data*.
Koehn, D., Arnold, J. and Passchier, C.W., 2005, Fracture and vein patterns as indicators of deformation history: a numerical study. *Geological Society, London, Special Publications* 243(1): 11–24.
Kostrov, V.V., 1974, Seismic moment and energy of earthquakes, and seismic flow of rock. *Izv. Acad. Sci. USSR Phys. Solid Earth* 1: 23–44.
Kraft, T., Herrmann, M., Tormann, T., Karvounis, D., Deichamnn, N. and Wiemer, S., 2018, April. Basel Induced Seismicity-A Never Ending Story?. *In EGU General Assembly Conference Abstracts* (Vol. 20, p. 7077).
Kuster, G.T. and Toksöz, M.N., 1974, Velocity and attenuation of seismic waves in two-phase media: Part I. Theoretical formulations. *Geophysics* 39(5): 587–606.
Kwiatek, G. and Ben-Zion, Y., 2013, Assessment of P and S wave energy radiated from very small shear-tensile seismic events in a deep South African mine. *Journal of Geophysical Research: Solid Earth* 118(7): 3630–3641.
Lake, L.W. and Clegg, J.D., 2007, Petroleum engineering handbook: production operations engineering, vol IV. *Society of Petroleum Engineers, Richardson*.
Lakshminarayana, B., 1995, *Fluid dynamics and heat transfer of turbomachinery*. John Wiley & Sons.
Lay, T. and Wallace, T.C., 1995, *Modern global seismology*. Elsevier.
Le Calvez, J., Malpani, R., Xu, J., 2016, Hydraulic fracturing insights from microseismic monitoring. *Oilfield Review* 28(2).
Lecampion, B., Desroches, J., Jeffrey, R.G., 2017, Experiments versus theory for the initiation and propagation of radial hydraulic fractures in low-

permeability materials. *Journal of Geophysical Research: Solid Earth* 122(2): 1239–1263.
Lefebvre, L., Banhart, J. and Dunand, D.C., 2008, Porous metals and metallic foams: current status and recent developments. *Advanced Engineering Materials* 10(9): 775–787.
Leguillon, D., 2002, Strength or toughness? A criterion for crack onset at a notch. *European Journal of Mechanics-A/Solids* 21(1): 61–72.
Lei, Q., Latham, J., Xiang, J., 2014, Effects of geomechanical changes on the validity of a discrete fracture network representation of a realistic two-dimensional fractured rock. *International Journal of Rock Mechanics and Mining Sciences* 70: 507–523.
Lemaire, E., Levitz, P., Daccord, G., 1991, From viscous fingering to viscoelastic fracturing in colloidal fluids. *Physical review letters* 67(15): 2009.
Li, Q,. Xing, H., Liu, J., 2015, A review on hydraulic fracturing of unconventional reservoir. *Petroleum* 1(1): 8–15.
Lisjak, A. and Grasselli, G., 2014, A review of discrete modeling techniques for fracturing processes in discontinuous rock masses. *Journal of Rock Mechanics and Geotechnical Engineering* 6(4): 301–314.
Liszka, T. and Orkisz, J., 1980, The finite difference method at arbitrary irregular grids and its application in applied mechanics. *Computers and structures* 11(1-2): 83–95.
Lockner, D.A., 1993, *The role of acoustic emission in the study of rock fracture*. Elsevier.
Lockner, D.A., Moore DE and Reches ZE., eds)., 1992, *Microcrack interaction leading to shear fracture*. American Rock Mechanics Association.
Love, A.E.H., 2013, *A treatise on the mathematical theory of elasticity*. Cambridge University Press.
Mader, D., 1989, *Hydraulic Proppant Fracturing and Gravel Packing*. Elsevier Science.
Majer, E.L., Baria R, Stark M, et al.., 2007, Induced seismicity associated with enhanced geothermal systems. *Geothermics* 36(3): 185–222.
Malthe-Sørenssen, A., Walmann, T., Feder, J., 1998, Simulation of extensional clay fractures. *Physical review E* 58(5): 5548.
Malvern, L.E., 1969, *Introduction to the Mechanics of a Continuous Medium*.
Mango, A.J., Schmeeckle, M.W. and Furbish, D.J., 2004, Tidally induced groundwater circulation in an unconfined coastal aquifer modeled with a Hele-Shaw cell. *Geology* 32(3): 233–236.
Mann, D.M. and Mackenzie, A.S., 1990, Prediction of pore fluid pressures in sedimentary basins. *Marine and Petroleum Geology* 7(1): 55–65.
Martin, P.Y., 2003, “Said and done” versus “saying and doing” gendering practices, practicing gender at work. *Gender & society* 17(3): 342–366.
Mas Ivars, D., Potyondy, D.O., Pierce, M., 2008, The smooth-joint contact model. *Proceedings of WCCM8-ECCOMAS* 2008: 8th.
Matthews, S.J., James, B.J., and Hyland, M.M., 2007, Microstructural influence on erosion behaviour of thermal spray coatings. *Materials characterization* 58(1): 59–64.
McBirney, A.R. and Murase, T., 1984, Rheological properties of magmas. *Annual Review of Earth and Planetary Sciences* 12(1): 337–357.
McGarr, A., 1994, Some comparisons between mining-induced and laboratory earthquakes. *Pure and Applied Geophysics* 142(3-4): 467–489.

McGarr, A., Simpson, D., Seeber, L., 2002, Case histories of induced and triggered seismicity. *International Geophysics Series* 81(A): 647–664.
McLean, J.W. and Saffman, P.G., 1981, The effect of surface tension on the shape of fingers in a Hele Shaw cell. *Journal of Fluid Mechanics* 102: 455–469.
McNamara, S., Flekkøy, E.G. and Måløy, K.J., 2000, Grains and gas flow: Molecular dynamics with hydrodynamic interactions. *Physical review E* 61(4): 4054.
Miller, A.D., Stewart, R.C., White, R.A., 1998, Seismicity associated with dome growth and collapse at the Soufriere Hills Volcano, Montserrat. *Geophysical Research Letters* 25(18): 3401–3404.
Miller, B.G., 2004, *Coal energy systems*. Academic Press.
Mitsuhiro, M., Mora, P., Donnellan, A., 2002, *Earthquake processes: Physical modelling, numerical simulation and data analysis part I*. Springer.
Mohammed, I. and Liechti, K.M., 2000, Cohesive zone modeling of crack nucleation at bimaterial corners. *Journal of the Mechanics and Physics of Solids* 48(4): 735–764.
Morgenstern, N. and Price, V.E., 1965, The analysis of the stability of general slip surfaces. *geotechnique* 15(1): 79–93.
Morton, M.Q., 2013, Unlocking the Earth: A Short History of Hydraulic Fracturing.
Mory, M., 2013, *Fluid Mechanics for Chemical Engineering*. John Wiley & Sons.
Mourgues, R. and Cobbold. P.R., 2003, Some tectonic consequences of fluid overpressures and seepage forces as demonstrated by sandbox modelling. *Tectonophysics* 376(1-2): 75–97.
Munjiza, A., Owen, D.R. and Bicanic, N., 1995, A combined finite-discrete element method in transient dynamics of fracturing solids. *Engineering computations* 12(2): 145–174.
Munjiza, A., 1992, Discrete elements in transient dynamics of fractured media, Swansea University.
Murphy, S., O'Brien, G.S., McCloskey J, 2013, Modelling fluid induced seismicity on a nearby active fault. *Geophysical Journal International* 194(3): 1613–1624.
National RC Committee on Fracture Characterization and Fluid Flow, 1996, Rock Fractures and Fluid Flow: Contemporary Understanding and Applications. *National Academy, Washington, DC* 551.
Niebling, M.J., 2013, *Dynamic aerofracture or hydrofracture of dense granular packing: pressure and viscosity control of the fracture patterns*.
Niebling, M.J., Flekkøy, E.G., Måløy, K.J., 2010, Mixing of a granular layer falling through a fluid. *Physical review E* 82(1): 11301.
Niebling, M.J., Flekkøy, E.G., Måløy, K.J., 2010, Sedimentation instabilities: impact of the fluid compressibility and viscosity. *Physical review E* 82(5): 51302.
Niebling, M.J., Toussaint, R., Flekkøy, E.G., 2012, Dynamic aerofracture of dense granular packings. *Physical review E* 86(6): 61315.
Nimmo, J.R., 2004, Porosity and pore size distribution. *Encyclopedia of Soils in the Environment* 3: 295–303.
Nolen-Hoeksema, R.C. and Ruff, L.J., 2001, Moment tensor inversion of microseisms from the B-Sand propped hydrofracture, M-Site, Colorado. *Tectonophysics* 336(1): 163–181.
Nordgren, R.P., 1972, Propagation of a vertical hydraulic fracture. *Society of Petroleum Engineers Journal* 12(04): 306–314.

Nowick, A. and Berry, D., 1972, Anelastic relaxation in crystalline solids, acad. *Press, New York*.

Obeysekara, A., Lei, Q., Salinas, P., 2016, *A fluid-solid coupled approach for numerical modeling of near-wellbore hydraulic fracturing and flow dynamics with adaptive mesh refinement*. American Rock Mechanics Association.

O'connell, R.J. and Budiansky, B., 1978, Measures of dissipation in viscoelastic media. *Geophysical Research Letters* 5(1): 5–8.

Ogasawara, H., Sato, S., Nishii, S., 2002, Semi-controlled seismogenic experiments in South African deep gold mines. *JOURNAL-SOUTH AFRICAN INSTITUTE OF MINING AND METALLURGY* 102(4): 243–250.

Ohta, A., Suzuki, N. and Mawari, T., 1992, Effect of Young's modulus on basic crack propagation properties near the fatigue threshold. *International journal of fatigue* 14(4): 224–226.

Okahara, M., Kiyosue, H., Yamashita, M., 2002, Diagnostic accuracy of magnetic resonance angiography for cerebral aneurysms in correlation with 3D-digital subtraction angiographic images: a study of 133 aneurysms. *Stroke* 33(7): 1803–1808.

Oliver, J., 1986, Fluids expelled tectonically from orogenic belts: Their role in hydrocarbon migration and other geologic phenomena. *Geology* 14(2): 99–102.

Oliver, N.H., 1996, Review and classification of structural controls on fluid flow during regional metamorphism. *Journal of Metamorphic Geology* 14(4): 477–492.

Oliver, N.H. and Bons, P.D., 2001, Mechanisms of fluid flow and fluid–rock interaction in fossil metamorphic hydrothermal systems inferred from vein–wallrock patterns, geometry and microstructure. *Geofluids* 1(2): 137–162.

Olson, J. and Pollard, D.D., 1989, Inferring paleostresses from natural fracture patterns: A new method. *Geology* 17(4): 345–348.

Olson, J.E., Laubach, S.E. and Lander, R.H., 2009, Natural fracture characterization in tight gas sandstones: Integrating mechanics and diagenesis. *AAPG Bulletin* 93(11): 1535–1549.

Osborne, M.J. and Swarbrick, R.E., 1997, Mechanisms for generating overpressure in sedimentary basins: A reevaluation. *AAPG Bulletin* 81(6): 1023–1041.

Ou, G., 2008, Seismological Studies for Tensile Faults. *Terrestrial, Atmospheric & Oceanic Sciences* 19(5).

Pan, B., Qian, K., Xie, H., 2009, Two-dimensional digital image correlation for in-plane displacement and strain measurement: a review. *Measurement science and technology* 20(6): 62001.

Panza, G.F., 1985, Synthetic seismograms. *J. Geophys.*, _: 125–145.

Parez, S., Aharonov, E. and Toussaint, R., 2016, Unsteady granular flows down an inclined plane. *Physical review E* 93(4): 42902.

Park, K., Paulino, G.H., Celes, W., 2012, Adaptive mesh refinement and coarsening for cohesive zone modeling of dynamic fracture. *International Journal for Numerical Methods in Engineering* 92(1): 1–35.

Parvizi, A., Garrett, K.W. and Bailey, J.E., 1978, Constrained cracking in glass fibre-reinforced epoxy cross-ply laminates. *Journal of Materials Science* 13(1): 195–201.

Paterson, L., 1981, Radial fingering in a Hele Shaw cell. *Journal of Fluid Mechanics* 113: 513–529.

Paterson, M.S. and Wong, T., 2005, *Experimental rock deformation-the brittle field*. Springer Science & Business Media.

Pearson, C., 1981, The relationship between microseismicity and high pore pressures during hydraulic stimulation experiments in low permeability granitic rocks. *Journal of Geophysical Research: Solid Earth* 86(B9): 7855–7864.

Penningtin, W.D. and Isacks, B.L., 1979, Analysis of short-period waveforms of P phases from deep-focus earthquakes beneath the Fiji Islands. *Geophysical Journal of the Royal Astronomical Society* 56(1): 19–40.

Perugini, D. and Poli, G., 2005, Viscous fingering during replenishment of felsic magma chambers by continuous inputs of mafic magmas: field evidence and fluid-mechanics experiments. *Geology* 33(1): 5–8.

Peters, W.H. and Ranson, W.F., 1982, Digital imaging techniques in experimental stress analysis. *Optical engineering* 21(3): 213427.

Pierce, M., Cundall, P., Potyondy, D., 2007, *A synthetic rock mass model for jointed rock*.

Place, D., Lombard, F., Mora, P., 2002, Simulation of the micro-physics of rocks using LSMearth. In: Mitsuhiro M, Mora P, Donnellan A and Yin X., eds, *Earthquake processes: Physical modelling, numerical simulation and data analysis part I:* Springer, pp. 1911–1932.

Prasad, M., Kopycinska, M., Rabe, U., 2002, Measurement of Young's modulus of clay minerals using atomic force acoustic microscopy. *Geophysical Research Letters* 29(8).

Prpich, G., Coulon, F. and Anthony, E.J., 2016. Review of the scientific evidence to support environmental risk assessment of shale gas development in the UK. *Science of The Total Environment*, *563*, pp.731-740.

Pujol, J. and Herrmann, R.B., 1990, A student's guide to point sources in homogeneous media. *Seismological Research Letters* 61(3-4): 209–224.

Rao, M. and Ramana, Y.V., 1992, A study of progressive failure of rock under cyclic loading by ultrasonic and AE monitoring techniques. *Rock Mechanics and Rock Engineering* 25(4): 237–251.

Reynolds, A.P. and Duvall, F., 1999, Digital image correlation for determination of weld and base metal constitutive behavior. *WELDING JOURNAL-NEW YORK-* 78: 355-s.

Rost, J., 1991, A logistic mixture distribution model for polychotomous item responses. *British Journal of Mathematical and Statistical Psychology* 44(1): 75–92.

Rubinstein, J.L. and Mahani, A.B., 2015. Myths and facts on wastewater injection, hydraulic fracturing, enhanced oil recovery, and induced seismicity. *Seismological Research Letters*, *86*(4), pp.1060-1067.

Rutledge, J.T. and Phillips, W.S., 2003, Hydraulic stimulation of natural fractures as revealed by induced microearthquakes, Carthage Cotton Valley gas field, east Texas. *Geophysics* 68(2): 441–452.

Rutqvist, J., Rinaldi, A.P., Cappa, F., 2013, Modeling of fault reactivation and induced seismicity during hydraulic fracturing of shale-gas reservoirs. *Journal of Petroleum Science and Engineering* 107: 31–44.

Sachau, T. and Koehn, D., 2014, A new mixed-mode fracture criterion for large-scale lattice models. *Geoscientific Model Development* 7(1): 243–247.

Sachau, T., Bons, P.D. and Gomez-Rivas, E., 2015, Transport efficiency and dynamics of hydraulic fracture networks. *Frontiers in Physics* 3: 63.

Sachau, T., Koehn, D. and Passchier, C., 2013, Mountain-building under extension. *American Journal of Science* 313(4): 326–344.

Sachpazis, C.I., 1990, Correlating Schmidt hardness with compressive strength and Young's modulus of carbonate rocks. *Bulletin of the International Association of Engineering Geology-Bulletin de l'Association Internationale de Géologie de l'Ingénieur* 42(1): 75–83.

Saffman, P.G. and Taylor, G.I., 1958, The penetration of a fluid into a porous medium or Hele-Shaw cell containing a more viscous liquid. *Proc. R. Soc. Lond. A* 245(1242): 312–329.

Satoh, T., Shivakumar, K., Nishizawa, O., 1996, Precursory localization and development of microfractures along the ultimate fracture plane in amphibolite under triaxial creep. *Geophysical Research Letters* 23(8): 865–868.

Sayers, C.M., 2013, The effect of anisotropy on the Young's moduli and Poisson's ratios of shales. *Geophysical Prospecting* 61(2): 416–426.

Schafbuch, P.J, Thompson, R.B, Rizzo, F.J., 1998, *Review of Progress in Quantitative Nondestructive Evaluation*. Springer.

Schmidt, V. and McDonald, D.A., 1979, The role of secondary porosity in the course of sandstone diagenesis.

Schmitt, D.R. and Zoback, M.D., 1992, Diminished pore pressure in low-porosity crystalline rock under tensional failure: Apparent strengthening by dilatancy. *Journal of Geophysical Research: Solid Earth* 97(B1): 273–288.

Scholtès, L. and Donzé, F., 2013, A DEM model for soft and hard rocks: role of grain interlocking on strength. *Journal of the Mechanics and Physics of Solids* 61(2): 352–369.

Scholz, C.H., 2002, *The mechanics of earthquakes and faulting*. Cambridge University Press.

Scotti, O. and Cornet, F., 1994, *In situ evidence for fluid-induced aseismic slip events along fault zones*. Oxford; New York: Pergamon Press, 1974-c1996.

Secor, D.T., 1965, Role of fluid pressure in jointing. *American Journal of Science* 263(8): 633–646.

Segall, P., 1989, Earthquakes triggered by fluid extraction. *Geology* 17(10): 942–946.

Sethian, J.A. and Smereka, P., 2003, Level set methods for fluid interfaces. *Annual review of fluid mechanics* 35(1): 341–372.

Shah, K.R. and Labuz, J.F., 1995, Damage mechanisms in stressed rock from acoustic emission. *Journal of Geophysical Research: Solid Earth* 100(B8): 15527–15539.

Shapiro, S.A., Dinske, C. and Kummerow, J., 2007, Probability of a given-magnitude earthquake induced by a fluid injection. *Geophysical Research Letters* 34(22).

Shearer, P.M., 2009, *Introduction to seismology*. Cambridge University Press.

Sherburn, S., Scott, B.J., Nishi, Y., 1998, Seismicity at White Island volcano, New Zealand: a revised classification and inferences about source mechanism. *Journal of Volcanology and Geothermal Research* 83(3): 287–312.

Shlien, S., 1972, Earthquake-tide correlation. *Geophysical Journal of the Royal Astronomical Society* 28(1): 27–34.

Sibson, R.H., 1977, Fault rocks and fault mechanisms. *Journal of the Geological Society* 133(3): 191–213.

Šílený, J. and Milev, A., 2008, Source mechanism of mining induced seismic events—Resolution of double couple and non double couple models. *Tectonophysics* 456(1-2): 3–15.

Singh, V.P., 1997, The use of entropy in hydrology and water resources. *Hydrological processes* 11(6): 587–626.
Stein, S. and Wysession, M., 2003, An introduction to seismology, earthquakes, and earth structure.
Stork, A.L., Verdon, J.P. and Kendall, J., 2014, The robustness of seismic moment and magnitudes estimated using spectral analysis. *Geophysical Prospecting* 62(4): 862–878.
Sun, Y. and Beckermann, C., 2010, Phase-field modeling of bubble growth and flow in a Hele–Shaw cell. *International Journal of Heat and Mass Transfer* 53(15-16): 2969–2978.
Sutradhar, A., Park, J., Carrau, D., 2014, Experimental validation of 3D printed patient-specific implants using digital image correlation and finite element analysis. *Computers in biology and medicine* 52: 8–17.
Talebi, S. and Boone, T.J., 1998, Source parameters of injection-induced microseismicity. *Pure and Applied Geophysics* 153(1): 113–130.
Tanaka, T., Kawaguchi, T. and Tsuji, Y., 1993, Discrete particle simulation of flow patterns in two-dimensional gas fluidized beds. *International Journal of Modern Physics B* 7(09n10): 1889–1898.
Tandaiya, P., Ramamurty, U., Ravichandran, G., 2008, Effect of Poisson's ratio on crack tip fields and fracture behavior of metallic glasses. *Acta Materialia* 56(20): 6077–6086.
Tang, C.A., Tham, L.G., Lee, P.K., 2002, Coupled analysis of flow, stress and damage (FSD) in rock failure. *International Journal of Rock Mechanics and Mining Sciences* 39(4): 477–489.
Tapponnier, P. and Brace, W.F., 1976, Development of stress-induced microcracks in Westerly granite. *Int. J. Rock Mech. Min. Sci. Geomech. Abstr* 13(4): 103–112.
Terzaghi, K von., 1925, Principles of soil mechanics. *Eng News-Record* 95.
Teska, K., 2011, Patent watch: the deep roots of fracking. *Mechanical Engineering* 133(12): 22.
Teufel, L.W., Rhett, D.W. and Farrell, H.E., 1991, *Effect of reservoir depletion and pore pressure drawdown on in situ stress and deformation in the Ekofisk field, North Sea*. American Rock Mechanics Association.
Teukolsky, S.A., Flannery, B.P., Press, W.H., 1992, Numerical recipes in C. *SMR* 693(1).
Tobin, H.J. and Saffer, D.M., 2009, Elevated fluid pressure and extreme mechanical weakness of a plate boundary thrust, Nankai Trough subduction zone. *Geology* 37(8): 679–682.
Todd, D.K., 1959, *Ground water hydrology*. John Wiley and Sons, Inc, New York.
Tsai, P.A., Riesing, K. and Stone, H.A., 2013, Density-driven convection enhanced by an inclined boundary: Implications for geological CO 2 storage. *Physical review E* 87(1): 11003.
Tsuruoka, H., Ohtake, M. and Sato, H., 1995, Statistical test of the tidal triggering of earthquakes: contribution of the ocean tide loading effect. *Geophysical Journal International* 122(1): 183–194.
Tullis, T.E. and Tullis, J., 1986, Experimental rock deformation techniques. *Mineral and Rock Deformation: Laboratory Studies, Geophys. Monogr. Ser* 36: 297–324.
Ul Islam, T. and Gandhi, P.S., 2017, Spontaneous fabrication of three-dimensional multiscale fractal structures using hele-shaw cell. *Journal of Manufacturing Science and Engineering* 139(3): 31007.

Valko, P. and Economides, M.J. *Hydraulic Fracture Mechanics,(1995)*. Chichester, John Wiley & Sons.
Van Damme, H. and Lemaire, E., 1990, From flow to fracture and fragmentation in colloidal media. In: *Disorder and fracture:* Springer, pp. 83–104.
Van der Pluijm, B.A. and Marshak, S., 2004, *Earth structure*. New York.
Vance, J.M., 2017, Russell Gold, The Boom: How Fracking Ignited the American Energy Revolution and Changed the World. *Environment and History* 23(2): 328–329.
Vavryčuk, V., 2001, Inversion for parameters of tensile earthquakes. *Journal of Geophysical Research: Solid Earth* 106(B8): 16339–16355.
Vavryčuk, V., 2005, Focal mechanisms in anisotropic media. *Geophysical Journal International* 161(2): 334–346.
Vavryčuk, V., 2007, On the retrieval of moment tensors from borehole data. *Geophysical Prospecting* 55(3): 381–391.
Vavryčuk, V., 2011, Tensile earthquakes: Theory, modeling, and inversion. *Journal of Geophysical Research: Solid Earth* 116(B12).
Versteeg, H.K. and Malalasekera, W., 2007, *An introduction to computational fluid dynamics: the finite volume method*. Pearson Education.
Vicsek, T. and Kertész, J., 1988, Laplacian Pattern Formation. *Europhysics News* 19(2): 24–27.
Vinningland, J.L., Johnsen, Ø., Flekkøy, E.G., 2007, Experiments and simulations of a gravitational granular flow instability. *Physical review E* 76(5): 51306.
Vinningland, J.L., Johnsen, Ø., Flekkøy, EG., 2007, Granular rayleigh-taylor instability: Experiments and simulations. *Physical review letters* 99(4): 48001.
Virieux, J., 1986, P-SV wave propagation in heterogeneous media: Velocity-stress finite-difference method. *Geophysics* 51(4): 889–901.
Walmann, T., Malthe-Sørenssen, A., Feder, J., 1996, Scaling relations for the lengths and widths of fractures. *Physical review letters* 77(27): 5393.
Wang, H., Marongiu-Porcu M and Economides MJ., 2016, Poroelastic and poroplastic modeling of hydraulic fracturing in brittle and ductile formations. *SPE Production & Operations* 31(01): 47–59.
Wang, Y. and Mora, P., 2008, Macroscopic elastic properties of regular lattices. *Journal of the Mechanics and Physics of Solids* 56(12): 3459–3474.
Wang, Y., Yin, X., Ke, F., 2000, Numerical simulation of rock failure and earthquake process on mesoscopic scale. *Pure and Applied Geophysics* 157(11-12): 1905–1928.
Warner, B. and Shapiro, J., 2013, Fractured, fragmented federalism: A study in fracking regulatory policy. *Publius: The Journal of Federalism* 43(3): 474–496.
Warpinski, N.R., Steinfort, T.D., Branagan, P.T., 1999, *Apparatus and method for monitoring underground fracturing*. Google Patents.
Warpinski, N., 2009, *Integrating microseismic monitoring with well completions, reservoir behavior, and rock mechanics*. Society of Petroleum Engineers.
Warpinski, N., Wolhart, S. and Wright, C., 2001, *Analysis and prediction of microseismicity induced by hydraulic fracturing*. Society of Petroleum Engineers.
Wells, D.L. and Coppersmith, K.J., 1994, New empirical relationships among magnitude, rupture length, rupture width, rupture area, and surface displacement. *Bulletin of the Seismological Society of America* 84(4): 974–1002.
White, D.E., 1957, Magmatic, connate, and metamorphic waters. *Geological Society of America Bulletin* 68(12): 1659–1682.

White, S.H., Bretan, P.G. and Rutter, E.H., 1986, Fault-zone reactivation: kinematics and mechanisms. *Phil. Trans. R. Soc. Lond. A* 317(1539): 81–97.
Winkler, K.W. and Murphy, W.F., 1995, Acoustic velocity and attenuation in porous rocks. *Rock physics and phase relations. A Handbook of physical constants*: 20–34.
Witherspoon, P.A., Cook, N.G. and Gale, J.E., 1981, Geologic storage of radioactive waste: Field studies in Sweden. *Science* 211(4485): 894–900.
Wong, R., 1996, *Microcracking and grain size effect in Yuen Long marbles*. Oxford; New York: Pergamon Press, 1974-c1996.
Wong, T., Wong, R.H.C., Chau, K.T., 2006, Microcrack statistics, Weibull distribution and micromechanical modeling of compressive failure in rock. *Mechanics of Materials* 38(7): 664–681.
Wong, T., 1982, Shear fracture energy of Westerly granite from post-failure behavior. *Journal of Geophysical Research: Solid Earth* 87(B2): 990–1000.
Wulff, A. and Burkhardt, H., 1997, Mechanisms affecting ultrasonic wave propagation in fluid-containing sandstones under high hydrostatic pressure. *Journal of Geophysical Research: Solid Earth* 102(B2): 3043–3050.
Wulff, A., Hashida, T., Watanabe, K., 1999, Attenuation behaviour of tuffaceous sandstone and granite during microfracturing. *Geophysical Journal International* 139(2): 395–409.
Xia, J., Miller, R.D. and Park, C.B., 1999, Estimation of near-surface shear-wave velocity by inversion of Rayleigh waves. *Geophysics* 64(3): 691–700.
Yong, R.N., 2000, *Geoenvironmental engineering: Contaminated soils, pollutant fate, and mitigation*. CRC Press.
Yoshihisa, I., 1986, Scaling relation between earthquake size and duration of faulting for shallow earthquakes in seismic moment between 1010 and 1025 dyne• cm. *Journal of Physics of the Earth* 34(2): 127–169.
Zang, A., Christian Wagner, F., Stanchits, S., 1998, Source analysis of acoustic emissions in Aue granite cores under symmetric and asymmetric compressive loads. *Geophysical Journal International* 135(3): 1113–1130.
Zeev, S.B., Goren, L., Parez, S., 2017, The Combined Effect of Buoyancy and Excess Pore Pressure in Facilitating Soil Liquefaction. In: *Poromechanics VI:* pp. 107–116.
Zienkiewicz, O.C. and Shiomi, T., 1984, Dynamic behaviour of saturated porous media; the generalized Biot formulation and its numerical solution. *International journal for numerical and analytical methods in geomechanics* 8(1): 71–96.
Zoback, M.D. and Harjes, H., 1997, Injection-induced earthquakes and crustal stress at 9 km depth at the KTB deep drilling site, Germany. *Journal of Geophysical Research: Solid Earth* 102(B8): 18477–18491.
Zoback, M.D., Rummel, F., Jung, R., 1977, *Laboratory hydraulic fracturing experiments in intact and pre-fractured rock*. Elsevier.
Zoback, M.D. and Pollard, D.D., 1978, *Hydraulic fracture propagation and the interpretation of pressure-time records for in-situ stress determinations*. American Rock Mechanics Association.